



AUTOMATED ANALYSIS OF OPTICAL COHERENCE TOMOGRAPHY ANGIOGRAPHY IMAGES FOR AGE-RELATED MACULAR DEGENERATION

A THESIS SUBMITTED TO THE UNIVERSITY OF MANCHESTER
FOR THE DEGREE OF DOCTOR OF PHILOSOPHY
IN THE FACULTY OF SCIENCE AND ENGINEERING

2022

By

Abdullah Alfahaid 

School of Engineering
Department of Computer Science

Contents

Abstract	33
Declaration	35
Copyright	36
Dedication	37
Acknowledgements	38
Abbreviation	39
1 Introduction	42
1.1 Chapter Introduction	42
1.2 Motivations	42
1.2.1 Age-related Macular Degeneration (AMD)	42
1.2.2 Optical Coherence Tomography Angiography (OCTA)	43
1.2.3 Analysis of OCTA Image Texture	44
1.3 Aim and Objectives	46
1.4 Hypotheses	47
1.5 Contributions	47
1.6 Publications	49
1.7 Thesis Outline	50
1.8 Chapter Conclusion	51
2 Image Texture Analysis in Computer Vision	52
2.1 Chapter Introduction	52
2.2 Computer Vision Tasks in Medical Image Analysis	52
2.2.1 Image Classification	53

2.2.2	Image Segmentation	54
2.3	Texture Role	57
2.4	Texture Representation	58
2.4.1	Hand-engineered Category	60
2.4.1.1	Geometrical or Structural	60
2.4.1.2	Statistical	62
2.4.1.3	Model Based	66
2.4.1.4	Signal Processing	69
2.4.1.5	Local Texture Descriptors	71
2.4.2	Learned Category	85
2.5	Classification Approaches	88
2.5.1	Machine Learning Algorithms	89
2.5.1.1	Support Vector Machine (SVM)	89
2.5.1.2	K-Nearest Neighbour (KNN)	92
2.5.2	Similarity Measure Metrics	94
2.5.2.1	Chi-square χ^2 Distance Similarity Metric	95
2.5.2.2	Intersection Distance Similarity Metric	95
2.6	Feature Selection and Reduction	96
2.6.1	Dimensionality Reduction Techniques	98
2.6.2	Feature Selection Techniques	104
2.7	Fundamental Part in Image Texture Analysis Tasks	106
2.8	Evaluation Measures and Resampling Strategies	110
2.8.1	Evaluation Measures	110
2.8.2	Resampling Strategies	115
2.9	Chapter Conclusion	118
3	Application Domain, Data Sets and Related Works	119
3.1	Chapter Introduction	119
3.2	The Human Eye	119
3.2.1	Anatomy and Physiology of The Retina	120
3.2.2	Common Eye Conditions	123
3.2.2.1	Age-related Macular Degeneration (AMD)	123
3.2.2.2	Diabetic Retinopathy (DR)	125
3.2.2.3	Glaucoma	125
3.3	Retinal Vasculature Imaging Modalities	126
3.3.1	Fundus	126

3.3.2	Optical Coherence Tomography (OCT)	129
3.3.3	Optical Coherence Tomography Angiography (OCTA)	131
3.4	Description of OCTA Image Data Sets	131
3.4.1	Manchester Royal Eye Hospital	132
3.4.2	Moorfields Eye Hospital	134
3.5	Related Works	135
3.5.1	Conventional Approaches	136
3.5.1.1	Qualitative Analysis	136
3.5.1.2	Quantitative Analysis	139
3.5.2	Automated Approaches	143
3.5.2.1	Image Segmentation	145
3.5.2.2	Image Classification	151
3.6	Chapter Conclusion	163
4	Classification Algorithm Based on Whole-Local Texture Features	165
4.1	Chapter Introduction	165
4.2	Motivation	165
4.3	Proposed Algorithm	175
4.3.1	Local Texture Feature Extraction	175
4.3.2	Classification	188
4.4	Experimental Evaluation and Results	191
4.4.1	Manchester Royal Eye Hospital	195
4.4.1.1	Superficial Inner Retina Layer	195
4.4.1.2	Deep Inner Retina Layer	196
4.4.1.3	Outer Retina Layer	197
4.4.1.4	Choriocapillaris Layer	199
4.4.1.5	Layer Combination	200
4.4.2	Moorfields Eye Hospital	207
4.4.2.1	Superficial Inner Retina Layer	207
4.4.2.2	Deep Inner Retina Layer	209
4.4.2.3	Outer Retina Layer	211
4.4.2.4	Choriocapillaris Layer	213
4.4.2.5	Layer Combination	215
4.4.3	Cross-Corpora Experiments	229
4.5	Discussion and Performance Comparison	230
4.6	Chapter Conclusion	236

5	Classification Algorithm Based on Reduced-Local Texture Features	237
5.1	Chapter Introduction	237
5.2	Motivation	238
5.3	Proposed Algorithm	240
5.3.1	Local Texture Feature Extraction	241
5.3.2	Data Pre-processing	242
5.3.3	Feature Dimensionality Reduction	244
5.3.4	Classification	246
5.4	Experimental Evaluation and Results	246
5.4.1	Manchester Royal Eye Hospital	249
5.4.1.1	Superficial Inner Retina Layer	249
5.4.1.2	Deep Inner Retina Layer	250
5.4.1.3	Outer Retina Layer	251
5.4.1.4	Choriocapillaris Layer	253
5.4.1.5	Layer Combination	254
5.4.2	Moorfields Eye Hospital	261
5.4.2.1	Superficial Inner Retina Layer	261
5.4.2.2	Deep Inner Retina Layer	263
5.4.2.3	Outer Retina Layer	265
5.4.2.4	Choriocapillaris Layer	267
5.4.2.5	Layer Combination	269
5.4.3	Cross-Corpora Experiments	283
5.5	Discussion and Performance Comparison	284
5.6	Chapter Conclusion	298
6	Localisation Algorithm Based on Local Texture Features	306
6.1	Chapter Introduction	306
6.2	Motivation	306
6.3	Proposed Algorithm	308
6.3.1	Partitioning OCTA Images into Overlapping Patches	308
6.3.2	Local Texture Feature Extraction	310
6.3.3	Similarity Measure	311
6.3.4	Localisation	313
6.4	Experimental Evaluation and Results	314
6.4.1	Manchester and Moorfields Hospitals	315
6.5	Discussion and Performance Comparison	317

6.6	Chapter Conclusion	322
7	Conclusion and Future Work	324
7.1	Chapter Introduction	324
7.2	Main Findings	324
7.3	Conclusion	325
7.4	Future Directions	329
	Bibliography	331
A	Supplementary details for Chapter 2	360
A.1	Learned Category	360
A.2	Support Vector Machine (SVM)	369
A.3	K-Nearest Neighbour (KNN)	378
B	Supplementary details for Chapter 3	383
B.1	Optical Coherence Tomography Angiography (OCTA)	383

Word Count: 79998

List of Tables

2.1	Confusion matrix.	111
3.1	Summary of the total number of images in the OCTA image data set provided by Manchester Royal Eye Hospital.	133
3.2	Summary of the total number of images in the OCTA image data set provided by Moorfields Eye Hospital.	134
3.3	A summary of the multiclass image classification results of the various CNN models.	154
4.1	A summary of classification results (mean AUC scores \pm standard deviations) that measure the performance of the automated classification algorithm that is based on whole-local texture features for solving the healthy vs wet AMD classification task, on the OCTA images of the superficial inner retina layer.	196
4.2	A summary of classification results (mean AUC scores \pm standard deviations) that measure the performance of the automated classification algorithm that is based on whole-local texture features for solving the healthy vs wet AMD classification task, on the OCTA images of the deep inner retina layer.	197
4.3	A summary of classification results (mean AUC scores \pm standard deviations) that measure the performance of the automated classification algorithm that is based on whole-local texture features for solving the healthy vs wet AMD classification task, on the OCTA images of the outer retina layer.	198

4.4	A summary of classification results (mean AUC scores \pm standard deviations) that measure the performance of the automated classification algorithm that is based on whole-local texture features for solving the healthy vs wet AMD classification task, on the OCTA images of choriocapillaris layer.	199
4.5	A summary of classification results (mean AUC scores \pm standard deviations) that measure the performance of the automated classification algorithm that is based on whole-local texture features for solving the healthy vs wet AMD classification task, based on concatenating two feature vectors extracted from the OCTA images of the superficial and the deep retina layers.	201
4.6	A summary of classification results (mean AUC scores \pm standard deviations) that measure the performance of the automated classification algorithm that is based on whole-local texture features for solving the healthy vs wet AMD classification task, based on concatenating two feature vectors extracted from the OCTA images of the superficial and the outer retina layers.	201
4.7	A summary of classification results (mean AUC scores \pm standard deviations) that measure the performance of the automated classification algorithm that is based on whole-local texture features for solving the healthy vs wet AMD classification task, based on concatenating two feature vectors extracted from the OCTA images of the superficial and the choriocapillaris retina layers.	202
4.8	A summary of classification results (mean AUC scores \pm standard deviations) that measure the performance of the automated classification algorithm that is based on whole-local texture features for solving the healthy vs wet AMD classification task, based on concatenating two feature vectors extracted from the OCTA images of the deep and the outer retina layers.	202
4.9	A summary of classification results (mean AUC scores \pm standard deviations) that measure the performance of the automated classification algorithm that is based on whole-local texture features for solving the healthy vs wet AMD classification task, based on concatenating two feature vectors extracted from the OCTA images of the deep retina and the choriocapillaris layers.	203

4.10	A summary of classification results (mean AUC scores \pm standard deviations) that measure the performance of the automated classification algorithm that is based on whole-local texture features for solving the healthy vs wet AMD classification task, based on concatenating two feature vectors extracted from the OCTA images of the outer retina and the choriocapillaris layers.	203
4.11	A summary of classification results (mean AUC scores \pm standard deviations) that measure the performance of the automated classification algorithm that is based on whole-local texture features for solving the healthy vs wet AMD classification task, based on concatenating three feature vectors extracted from the OCTA images of the superficial inner, the deep inner and the outer retina layers.	204
4.12	A summary of classification results (mean AUC scores \pm standard deviations) that measure the performance of the automated classification algorithm that is based on whole-local texture features for solving the healthy vs wet AMD classification task, based on concatenating three feature vectors extracted from the OCTA images of the superficial, the deep inner retina and the choriocapillaris layers.	205
4.13	A summary of classification results (mean AUC scores \pm standard deviations) that measure the performance of the automated classification algorithm that is based on whole-local texture features for solving the healthy vs wet AMD classification task, based on concatenating three feature vectors extracted from the OCTA images of the superficial inner, the outer retina and the choriocapillaris layers.	205
4.14	A summary of classification results (mean AUC scores \pm standard deviations) that measure the performance of the automated classification algorithm that is based on whole-local texture features for solving the healthy vs wet AMD classification task, based on concatenating three feature vectors extracted from the OCTA images of the deep inner, the outer retina and the choriocapillaris layers.	206

4.15	A summary of classification results (mean AUC scores \pm standard deviations) that measure the performance of the automated classification algorithm that is based on whole-local texture features for solving the healthy vs wet AMD classification task, based on concatenating all feature vectors extracted from the OCTA images of all ocular vascular layers..	206
4.16	A summary of classification results (mean AUC scores \pm standard deviations) that measure the performance of the automated classification algorithm that is based on whole-local texture features for solving the dry AMD vs wet AMD classification task, on the OCTA images of the superficial inner retina layer.	208
4.17	A summary of classification results (mean AUC scores \pm standard deviations) that measure the performance of the automated classification algorithm that is based on whole-local texture features for solving the CNV vs non-CNV classification task, on the OCTA images of the superficial inner retina layer.	209
4.18	A summary of classification results (mean AUC scores \pm standard deviations) that measure the performance of the automated classification algorithm that is based on whole-local texture features for solving the dry AMD vs wet AMD classification task, on the OCTA images of the deep inner retina layer.	210
4.19	A summary of classification results (mean AUC scores \pm standard deviations) that measure the performance of the automated classification algorithm that is based on whole-local texture features for solving the CNV vs non-CNV classification task, on the OCTA images of the deep inner retina layer.	211
4.20	A summary of classification results (mean AUC scores \pm standard deviations) that measure the performance of the automated classification algorithm that is based on whole-local texture features for solving the dry AMD vs wet AMD classification task, on the OCTA images of the outer retina layer.	212

4.21	A summary of classification results (mean AUC scores \pm standard deviations) that measure the performance of the automated classification algorithm that is based on whole-local texture features for solving the CNV vs non-CNV classification task, on the OCTA images of the outer retina layer.	213
4.22	A summary of classification results (mean AUC scores \pm standard deviations) that measure the performance of the automated classification algorithm that is based on whole-local texture features for solving the dry AMD vs wet AMD classification task, on the OCTA images of the choriocapillaris layer.	214
4.23	A summary of classification results (mean AUC scores \pm standard deviations) that measure the performance of the automated classification algorithm that is based on whole-local texture features for solving the CNV vs non-CNV classification task, on the OCTA images of the choriocapillaris layer.	215
4.24	A summary of classification results (mean AUC scores \pm standard deviations) that measure the performance of the automated classification algorithm that is based on whole-local texture features for solving the dry AMD vs wet AMD classification task, based on concatenating two feature vectors extracted from the OCTA images of the superficial and the deep retina layers.	216
4.25	A summary of classification results (mean AUC scores \pm standard deviations) that measure the performance of the automated classification algorithm that is based on whole-local texture features for solving the dry AMD vs wet AMD classification task, based on concatenating two feature vectors extracted from the OCTA images of the superficial and the outer retina layers.	217
4.26	A summary of classification results (mean AUC scores \pm standard deviations) that measure the performance of the automated classification algorithm that is based on whole-local texture features for solving the dry AMD vs wet AMD classification task, based on concatenating two feature vectors extracted from the OCTA images of the superficial retina and the choriocapillaris layers.	217

4.27	A summary of classification results (mean AUC scores \pm standard deviations) that measure the performance of the automated classification algorithm that is based on whole-local texture features for solving the dry AMD vs wet AMD classification task, based on concatenating two feature vectors extracted from the OCTA images of the deep and the outer retina layers.	218
4.28	A summary of classification results (mean AUC scores \pm standard deviations) that measure the performance of the automated classification algorithm that is based on whole-local texture features for solving the dry AMD vs wet AMD classification task, based on concatenating two feature vectors extracted from the OCTA images of the deep retina and the choriocapillaris layers.	218
4.29	A summary of classification results (mean AUC scores \pm standard deviations) that measure the performance of the automated classification algorithm that is based on whole-local texture features for solving the dry AMD vs wet AMD classification task, based on concatenating the two feature vectors extracted from the OCTA images of the outer retina and the choriocapillaris layers.	219
4.30	A summary of classification results (mean AUC scores \pm standard deviations) that measure the performance of the automated classification algorithm that is based on whole-local texture features for solving the dry AMD vs wet AMD classification task, based on concatenating three feature vectors extracted from the OCTA images of the superficial inner, the deep inner and the outer retina layers.	219
4.31	A summary of classification results (mean AUC scores \pm standard deviations) that measure the performance of the automated classification algorithm that is based on whole-local texture features for solving the dry AMD vs wet AMD classification task, based on concatenating three feature vectors extracted from the OCTA images of the superficial, the deep inner retina and the choriocapillaris layers.	220

4.32	A summary of classification results (mean AUC scores \pm standard deviations) that measure the performance of the automated classification algorithm that is based on whole-local texture features for solving the dry AMD vs wet AMD classification task, based on concatenating three feature vectors extracted from the OCTA images of the superficial inner, the outer retina and the choriocapillaris layers.	220
4.33	A summary of classification results (mean AUC scores \pm standard deviations) that measure the performance of the automated classification algorithm that is based on whole-local texture features for solving the dry AMD vs wet AMD classification task, based on concatenating three feature vectors extracted from the OCTA images of the deep inner, the outer retina and the choriocapillaris layers.	221
4.34	A summary of classification results (mean AUC scores \pm standard deviations) that measure the performance of the automated classification algorithm that is based on whole-local texture features for solving the dry AMD vs wet AMD classification task, based on concatenating all feature vectors extracted from the OCTA images of all ocular vascular layers.	221
4.35	A summary of classification results (mean AUC scores \pm standard deviations) that measure the performance of the automated classification algorithm that is based on whole-local texture features for solving the CNV vs non-CNV classification task, based on concatenating two feature vectors extracted from the OCTA images of the superficial and the deep retina layers.	223
4.36	A summary of classification results (mean AUC scores \pm standard deviations) that measure the performance of the automated classification algorithm that is based on whole-local texture features for solving the CNV vs non-CNV classification task, based on concatenating two feature vectors extracted from the OCTA images of the superficial and the outer retina layers.	223

4.37	A summary of classification results (mean AUC scores \pm standard deviations) that measure the performance of the automated classification algorithm that is based on whole-local texture features for solving the CNV vs non-CNV classification task, based on concatenating two feature vectors extracted from the OCTA images of the superficial retina and the choriocapillaris layers.	224
4.38	A summary of classification results (mean AUC scores \pm standard deviations) that measure the performance of the automated classification algorithm that is based on whole-local texture features for solving the CNV vs non-CNV classification task, based on concatenating two feature vectors extracted from the OCTA images of the deep and the outer retina layers.	224
4.39	A summary of classification results (mean AUC scores \pm standard deviations) that measure the performance of the automated classification algorithm that is based on whole-local texture features for solving the CNV vs non-CNV classification task, based on concatenating two feature vectors extracted from the OCTA images of the deep retina and the choriocapillaris layers.	225
4.40	A summary of classification results (mean AUC scores \pm standard deviations) that measure the performance of the automated classification algorithm that is based on whole-local texture features for solving the CNV vs non-CNV classification task, based on concatenating the two feature vectors extracted from the OCTA images of the outer retina and the choriocapillaris layers.	225
4.41	A summary of classification results (mean AUC scores \pm standard deviations) that measure the performance of the automated classification algorithm that is based on whole-local texture features for solving the CNV vs non-CNV classification task, based on concatenating three feature vectors extracted from the OCTA images of the superficial inner, the deep inner and the outer retina layers.	226

4.42	A summary of classification results (mean AUC scores \pm standard deviations) that measure the performance of the automated classification algorithm that is based on whole-local texture features for solving the CNV vs non-CNV classification task, based on concatenating three feature vectors extracted from the OCTA images of the superficial, the deep inner retina and the choriocapillaris layers.	226
4.43	A summary of classification results (mean AUC scores \pm standard deviations) that measure the performance of the automated classification algorithm that is based on whole-local texture features for solving the CNV vs non-CNV classification task, based on concatenating three feature vectors extracted from the OCTA images of the superficial inner, the outer retina and the choriocapillaris layers.	227
4.44	A summary of classification results (mean AUC scores \pm standard deviations) that measure the performance of the automated classification algorithm that is based on whole-local texture features for solving the CNV vs non-CNV classification task, based on concatenating three feature vectors extracted from the OCTA images of the deep inner, the outer retina and the choriocapillaris layers.	227
4.45	A summary of classification results (mean AUC scores \pm standard deviations) that measure the performance of the automated classification algorithm that is based on whole-local texture features for solving the CNV vs non-CNV classification task, based on concatenating all feature vectors extracted from the OCTA images of all ocular vascular layers.	228
4.46	The evaluation results (sensitivity scores) of the classifiers trained on the OCTA image data set for the Manchester healthy versus Manchester wet AMD classification task to distinguish the wet AMD cases of Moorfields OCTA image data set.	230
4.47	The evaluation results (sensitivity scores) of the classifiers trained on the OCTA image data set for the Moorfields dry AMD versus Moorfields wet AMD classification task to distinguish the wet AMD cases of Manchester OCTA image data set.	231

4.48	The evaluation results (sensitivity scores) of the classifiers trained on the OCTA image data set for the Manchester healthy versus Moorfields wet AMD classification task to distinguish the wet AMD cases of Manchester OCTA image data set.	232
4.49	The evaluation results (sensitivity scores) of the classifiers trained on the OCTA image data set for the Moorfields dry AMD versus Manchester wet AMD classification task to distinguish the wet AMD cases of Moorfields OCTA image data set.	233
4.50	A summary of best classification results (mean AUC scores \pm standard deviations) as achieved by the automated OCTA image classification algorithm proposed for solving the healthy vs wet AMD classification task based on whole-local texture features.	233
4.51	A summary of best classification results (mean AUC scores \pm standard deviations) as achieved by the automated OCTA image classification algorithm proposed for solving the dry AMD vs wet AMD classification task based on whole-local texture features.	234
4.52	A summary of best classification results (mean AUC scores \pm standard deviations) as achieved by the automated OCTA image classification algorithm proposed for solving the CNV vs non-CNV classification task based on whole-local texture features.	235
5.1	A summary of classification results (mean AUC scores \pm standard deviations) that measure the performance of the automated classification algorithm that is based on reduced-local texture features for solving the healthy vs wet AMD classification task, on the OCTA images of superficial inner retina layer.	250
5.2	A summary of classification results (mean AUC scores \pm standard deviations) that measure the performance of the automated classification algorithm that is based on reduced-local texture features for solving the healthy vs wet AMD classification task, on the OCTA images of deep inner retina layer.	251
5.3	A summary of classification results (mean AUC scores \pm standard deviations) that measure the performance of the automated classification algorithm that is based on reduced-local texture features for solving the healthy vs wet AMD classification task, on the OCTA images of outer retina layer.	252

5.4	A summary of classification results (mean AUC scores \pm standard deviations) that measure the performance of the automated classification algorithm that is based on reduced-local texture features for solving the healthy vs wet AMD classification task, on the OCTA images of choriocapillaris layer.	253
5.5	A summary of classification results (mean AUC scores \pm standard deviations) that measure the performance of the automated classification algorithm that is based on reduced-local texture features for solving the healthy vs wet AMD classification task, based on concatenating two feature vectors extracted from the OCTA images of the superficial and the deep retina layers.	255
5.6	A summary of classification results (mean AUC scores \pm standard deviations) that measure the performance of the automated classification algorithm that is based on reduced-local texture features for solving the healthy vs wet AMD classification task, based on concatenating two feature vectors extracted from the OCTA images of the superficial and the outer retina layers.	256
5.7	A summary of classification results (mean AUC scores \pm standard deviations) that measure the performance of the automated classification algorithm that is based on reduced-local texture features for solving the healthy vs wet AMD classification task, based on concatenating two feature vectors extracted from the OCTA images of the superficial and the choriocapillaris retina layers.	256
5.8	A summary of classification results (mean AUC scores \pm standard deviations) that measure the performance of the automated classification algorithm that is based on reduced-local texture features for solving the healthy vs wet AMD classification task, based on concatenating two feature vectors extracted from the OCTA images of the deep and the outer retina layers.	257
5.9	A summary of classification results (mean AUC scores \pm standard deviations) that measure the performance of the automated classification algorithm that is based on reduced-local texture features for solving the healthy vs wet AMD classification task, based on concatenating two feature vectors extracted from the OCTA images of the deep retina and the choriocapillaris layers.	257

5.10	A summary of classification results (mean AUC scores \pm standard deviations) that measure the performance of the automated classification algorithm that is based on reduced-local texture features for solving the healthy vs wet AMD classification task, based on concatenating two feature vectors extracted from the OCTA images of the outer retina and the choriocapillaris layers.	258
5.11	A summary of classification results (mean AUC scores \pm standard deviations) that measure the performance of the automated classification algorithm that is based on reduced-local texture features for solving the healthy vs wet AMD classification task, based on concatenating three feature vectors extracted from the OCTA images of the superficial inner, the deep inner and the outer retina layers.	258
5.12	A summary of classification results (mean AUC scores \pm standard deviations) that measure the performance of the automated classification algorithm that is based on reduced-local texture features for solving the healthy vs wet AMD classification task, based on concatenating three feature vectors extracted from the OCTA images of the superficial, the deep inner retina and the choriocapillaris layers.	259
5.13	A summary of classification results (mean AUC scores \pm standard deviations) that measure the performance of the automated classification algorithm that is based on reduced-local texture features for solving the healthy vs wet AMD classification task, based on concatenating three feature vectors extracted from the OCTA images of the superficial inner, the outer retina and the choriocapillaris layers.	259
5.14	A summary of classification results (mean AUC scores \pm standard deviations) that measure the performance of the automated classification algorithm that is based on reduced-local texture features for solving the healthy vs wet AMD classification task, based on concatenating three feature vectors extracted from the OCTA images of the deep inner, the outer retina and the choriocapillaris layers.	260

5.15	A summary of classification results (mean AUC scores \pm standard deviations) that measure the performance of the automated classification algorithm that is based on reduced-local texture features for solving the healthy vs wet AMD classification task, based on concatenating all feature vectors extracted from the OCTA images of all ocular vascular layers.	260
5.16	A summary of classification results (mean AUC scores \pm standard deviations) that measure the performance of the automated classification algorithm that is based on reduced-local texture features for solving the dry AMD vs wet AMD classification task, on the OCTA images of superficial inner retina layer.	262
5.17	A summary of classification results (mean AUC scores \pm standard deviations) that measure the performance of the automated classification algorithm that is based on reduced-local texture features for solving the CNV vs non-CNV classification task, on the OCTA images of superficial inner retina layer.	263
5.18	A summary of classification results (mean AUC scores \pm standard deviations) that measure the performance of the automated classification algorithm that is based on reduced-local texture features for solving the dry AMD vs wet AMD classification task, on the OCTA images of deep inner retina layer.	264
5.19	A summary of classification results (mean AUC scores \pm standard deviations) that measure the performance of the automated classification algorithm that is based on reduced-local texture features for solving the CNV vs non-CNV classification task, on the OCTA images of the deep inner retina layer.	265
5.20	A summary of classification results (mean AUC scores \pm standard deviations) that measure the performance of the automated classification algorithm that is based on reduced-local texture features for solving the dry AMD vs wet AMD classification task, on the OCTA images of outer retina layer.	266

5.21	A summary of classification results (mean AUC scores \pm standard deviations) that measure the performance of the automated classification algorithm that is based on reduced-local texture features for solving the CNV vs non-CNV classification task, on the OCTA images of outer retina layer.	267
5.22	A summary of classification results (mean AUC scores \pm standard deviations) that measure the performance of the automated classification algorithm that is based on reduced-local texture features for solving the dry AMD vs wet AMD classification task, on the OCTA images of choriocapillaris layer.	268
5.23	A summary of classification results (mean AUC scores \pm standard deviations) that measure the performance of the automated classification algorithm that is based on reduced-local texture features for solving the CNV vs non-CNV classification task, on the OCTA images of choriocapillaris layer.	269
5.24	A summary of classification results (mean AUC scores \pm standard deviations) that measure the performance of the automated classification algorithm that is based on reduced-local texture features for solving the dry AMD vs wet AMD classification task, based on concatenating two feature vectors extracted from the OCTA images of the superficial and the deep retina layers.	270
5.25	A summary of classification results (mean AUC scores \pm standard deviations) that measure the performance of the automated classification algorithm that is based on reduced-local texture features for solving the dry AMD vs wet AMD classification task, based on concatenating two feature vectors extracted from the OCTA images of the superficial and the outer retina layers.	271
5.26	A summary of classification results (mean AUC scores \pm standard deviations) that measure the performance of the automated classification algorithm that is based on reduced-local texture features for solving the dry AMD vs wet AMD classification task, based on concatenating two feature vectors extracted from the OCTA images of the superficial retina and the choriocapillaris layers.	271

5.27	A summary of classification results (mean AUC scores \pm standard deviations) that measure the performance of the automated classification algorithm that is based on reduced-local texture features for solving the dry AMD vs wet AMD classification task, based on concatenating two feature vectors extracted from the OCTA images of the deep and the outer retina layers.	272
5.28	A summary of classification results (mean AUC scores \pm standard deviations) that measure the performance of the automated classification algorithm that is based on reduced-local texture features for solving the dry AMD vs wet AMD classification task, based on concatenating two feature vectors extracted from the OCTA images of the deep retina and the choriocapillaris layers.	272
5.29	A summary of classification results (mean AUC scores \pm standard deviations) that measure the performance of the automated classification algorithm that is based on reduced-local texture features for solving the dry AMD vs wet AMD classification task, based on concatenating two feature vectors extracted from the OCTA images of the outer retina and the choriocapillaris layers.	273
5.30	A summary of classification results (mean AUC scores \pm standard deviations) that measure the performance of the automated classification algorithm that is based on reduced-local texture features for solving the dry AMD vs wet AMD classification task, based on concatenating three feature vectors extracted from the OCTA images of the superficial inner, the deep inner and the outer retina layers.	273
5.31	A summary of classification results (mean AUC scores \pm standard deviations) that measure the performance of the automated classification algorithm that is based on reduced-local texture features for solving the dry AMD vs wet AMD classification task, based on concatenating three feature vectors extracted from the OCTA images of the superficial, the deep inner retina and the choriocapillaris layers.	274

5.32	A summary of classification results (mean AUC scores \pm standard deviations) that measure the performance of the automated classification algorithm that is based on reduced-local texture features for solving the dry AMD vs wet AMD classification task, based on concatenating three feature vectors extracted from the OCTA images of the superficial inner, the outer retina and the choriocapillaris layers.	274
5.33	A summary of classification results (mean AUC scores \pm standard deviations) that measure the performance of the automated classification algorithm that is based on reduced-local texture features for solving the dry AMD vs wet AMD classification task, based on concatenating three feature vectors extracted from the OCTA images of the deep inner, the outer retina and the choriocapillaris layers.	275
5.34	A summary of classification results (mean AUC scores \pm standard deviations) that measure the performance of the automated classification algorithm that is based on reduced-local texture features for solving the dry AMD vs wet AMD classification task, based on concatenating all feature vectors extracted from the OCTA images of all ocular vascular layers.	275
5.35	A summary of classification results (mean AUC scores \pm standard deviations) that measure the performance of the automated classification algorithm that is based on reduced-local texture features for solving the CNV vs non-CNV classification task, based on concatenating two feature vectors extracted from the OCTA images of the superficial and the deep retina layers.	277
5.36	A summary of classification results (mean AUC scores \pm standard deviations) that measure the performance of the automated classification algorithm that is based on reduced-local texture features for solving the CNV vs non-CNV classification task, based on concatenating two feature vectors extracted from the OCTA images of the superficial and the outer retina layers.	277

5.37	A summary of classification results (mean AUC scores \pm standard deviations) that measure the performance of the automated classification algorithm that is based on reduced-local texture features for solving the CNV vs non-CNV classification task, based on concatenating two feature vectors extracted from the OCTA images of the superficial retina and the choriocapillaris layers.	278
5.38	A summary of classification results (mean AUC scores \pm standard deviations) that measure the performance of the automated classification algorithm that is based on reduced-local texture features for solving the CNV vs non-CNV classification task, based on concatenating two feature vectors extracted from the OCTA images of the deep and the outer retina layers.	278
5.39	A summary of classification results (mean AUC scores \pm standard deviations) that measure the performance of the automated classification algorithm that is based on reduced-local texture features for solving the CNV vs non-CNV classification task, based on concatenating two feature vectors extracted from the OCTA images of the deep retina and the choriocapillaris layers.	279
5.40	A summary of classification results (mean AUC scores \pm standard deviations) that measure the performance of the automated classification algorithm that is based on reduced-local texture features for solving the CNV vs non-CNV classification task, based on concatenating two feature vectors extracted from the OCTA images of the outer retina and the choriocapillaris layers.	279
5.41	A summary of classification results (mean AUC scores \pm standard deviations) that measure the performance of the automated classification algorithm that is based on reduced-local texture features for solving the CNV vs non-CNV classification task, based on concatenating three feature vectors extracted from the OCTA images of the superficial inner, the deep inner and the outer retina layers.	280

5.42	A summary of classification results (mean AUC scores \pm standard deviations) that measure the performance of the automated classification algorithm that is based on reduced-local texture features for solving the CNV vs non-CNV classification task, based on concatenating three feature vectors extracted from the OCTA images of the superficial, the deep inner retina and the choriocapillaris layers.	281
5.43	A summary of classification results (mean AUC scores \pm standard deviations) that measure the performance of the automated classification algorithm that is based on reduced-local texture features for solving the CNV vs non-CNV classification task, based on concatenating three feature vectors extracted from the OCTA images of the superficial inner, the outer retina and the choriocapillaris layers.	281
5.44	A summary of classification results (mean AUC scores \pm standard deviations) that measure the performance of the automated classification algorithm that is based on reduced-local texture features for solving the CNV vs non-CNV classification task, based on concatenating three feature vectors extracted from the OCTA images of the deep inner, the outer retina and the choriocapillaris layers.	282
5.45	A summary of classification results (mean AUC scores \pm standard deviations) that measure the performance of the automated classification algorithm that is based on reduced-local texture features for solving the CNV vs non-CNV classification task, based on concatenating all feature vectors extracted from the OCTA images of all ocular vascular layers.	282
5.46	The evaluation results (sensitivity scores) of the classifiers trained on the OCTA image data set for the Manchester healthy versus Manchester wet AMD classification task to distinguish the wet AMD cases of Moorfields OCTA image data set.	284
5.47	The evaluation results (sensitivity scores) of the classifiers trained on the OCTA image data set for the Moorfields dry AMD versus Moorfields wet AMD classification task to distinguish the wet AMD cases of Manchester OCTA image data set.	285

5.48	The evaluation results (sensitivity scores) of the classifiers trained on the OCTA image data set for the Manchester healthy versus Moorfields wet AMD classification task to distinguish the wet AMD cases of Manchester OCTA image data set.	286
5.49	The evaluation results (sensitivity scores) of the classifiers trained on the OCTA image data set for the Moorfields dry AMD versus Manchester wet AMD classification task to distinguish the wet AMD cases of Moorfields OCTA image data set.	287
5.50	A summary of best classification results (mean AUC scores \pm standard deviations) as achieved by the automated OCTA image classification algorithm proposed for solving the healthy vs wet AMD classification task based on reduced-local texture features.	288
5.51	A summary of best classification results (mean AUC scores \pm standard deviations) as achieved by the automated OCTA image classification algorithm proposed for solving the dry AMD vs wet AMD classification task based on reduced-local texture features.	289
5.52	A summary of best classification results (mean AUC scores \pm standard deviations) as achieved by the automated OCTA image classification algorithm proposed for solving the CNV vs non-CNV classification task based on reduced-local texture features.	290
5.53	Performance comparison based on mean AUC scores \pm standard deviations of the two automated OCTA image classification algorithms proposed for solving the healthy vs wet AMD classification task based on whole-local texture features and reduced-local texture features. . .	291
5.54	Performance comparison based on mean AUC scores \pm standard deviations of the two automated OCTA image classification algorithms proposed for solving the dry AMD vs wet AMD classification task based on whole-local texture features and reduced-local texture features.	292
5.55	Performance comparison based on mean AUC scores \pm standard deviations of the two automated OCTA image classification algorithms proposed for solving the CNV vs non-CNV classification task based on whole-local texture features and reduced-local texture features. . .	293

5.56	An in-depth evaluation of the two automated OCTA image classification algorithms proposed that are based on whole-local texture features and reduced-local texture features on the optimal binary classification task, i.e.: healthy vs wet AMD.	299
6.1	A summary of evaluation results (mean <i>IoU</i> scores \pm standard deviations) that demonstrate the performance of the localisation algorithm on the diseased OCTA images of the outer retina and the choriocapillaris layers.	316
B.1	A comprehensive summary of the differences between the key characteristics of the OCTA, OCT, FA and IGA imaging techniques.	395

List of Figures

1.1	The textural appearance of the blood vessels network in the superficial inner retina, deep inner retina, outer retina, and choriocapillaris layers in OCTA images.	45
2.1	An application example of a whole image classification task for glaucoma detection.	54
2.2	An example of a classification task for distinguishing between texture regions within a breast cancer tissue slide as pathological or normal. .	54
2.3	A classification task for assessing the quality of OCTA image texture appearance.	55
2.4	An example of a region-based segmentation task for the detection of diabetic retinopathy lesions, namely hard exudates, and for monitoring its progression in fundus images.	56
2.5	An example of a boundary-based segmentation task for the detection of various retinal layer boundaries in OCT images for AMD.	56
2.6	An illustrative example of a common procedure normally utilised in many texture representation techniques.	59
2.7	An illustrative example of two simulated tumour images that demonstrate two different textural appearances, namely rough and smooth tumours that share a comparable pixel intensity value distribution. . .	63
2.8	Illustration example of the application of GLCM approach on a greyscale image from.	64
2.9	Basic examples of fractal shapes.	68
2.10	A typical conventional system setup of the texture feature extraction process using signal processing methods.	69
2.11	An illustrative example of extracting local texture features based on the original LBP texture descriptor using a greyscale texture image. . .	74

2.12	An application of the original LBP methodology on real texture data. (a) Shows an input texture image of retinal blood vessels of a human eye.	75
2.13	Visualisation of three different local circularly symmetrical neighbour sets with different (p, r) parameters.	76
2.14	Visualisation of different local texture structures or patterns detected by the $LBP_{p,r}^{2u}$ texture descriptor with 8 neighbourhood of pixels.	79
2.15	Visualisation of all potential rotation invariant uniform circular patterns or structures that comprises unique spatial transitions detected by the rotation invariant uniform $LBP_{p,r}^{2riu}$ texture descriptor with 8 neighbourhood of pixels.	80
2.16	Visualisation of five different sampling points locations strategies that define a set of binary tests using the BRIEF descriptor.	82
2.17	A typical structure of a simple artificial neuron model.	85
2.18	An explanatory instance of a deep learning algorithm applied on a textured image that contains a person.	87
2.19	The separating hyperplane (middle line between two dashed lines \mathbf{H}_1 & \mathbf{H}_2) of an SVM classifier that separates two different classes in a linear separable case.	89
2.20	An illustrative plot that demonstrates the similarity values of randomly generated data samples described by five and by twenty different features.	98
2.21	An application example of the <i>PCA</i> technique to address two highly correlated features used in a predictive modelling task for classifying the segmentation quality of cells in a living organism.	101
2.22	The ROC curves of three different classifiers, namely A, B and random classifiers.	114
2.23	A visualisation of three folds cross-validation strategy.	116
3.1	A cross section view illustrating the anatomy of the human eye.	121
3.2	A cross section view illustrating the anatomy of the retina.	122
3.3	Demonstration of two different visual fields seen by two people, one with healthy vision and the other one with AMD disease.	124
3.4	Visualising images of abnormal retinal blood vessels appearance of a human eye as captured using two different fundus imaging techniques, namely FA and IGA.	127

3.5	Visualising the textural appearance of cross-sectional tomographic images of two different human eyes with different conditions captured using the OCT imaging technique.	130
3.6	Visualising the various retinal and choroidal vascular layers of two randomly selected eyes with different ocular conditions, specifically healthy and wet AMD eyes from the Manchester Royal Eye Hospital OCTA image data set.	133
3.7	Demonstrating the various retinal and choroidal vascular layers of two randomly selected eyes with different ocular conditions, specifically dry AMD and wet AMD eyes, from the Moorfields Eye Hospital OCTA image data set.	135
3.8	Samples of OCTA images that show the textural appearance of two different qualitative features or patterns of CNV regions.	137
3.9	Samples of OCTA images that show the textural appearance of three different qualitative features or patterns of CNV regions.	138
3.10	Illustrating the proportion of computer vision and AI systems that are applied into diagnostic medical imaging data in comparison to other diagnostic medical related data on the PubMed search engine.	144
4.1	Outline of the automated OCTA image texture analysis algorithm that is proposed for AMD disease detection by the means of image classification.	176
4.2	Visualising various OCTA images with their corresponding $LBP_{p,r}$ patterns for a normal eye.	179
4.3	Visualising various OCTA images with their corresponding $LBP_{p,r}$ patterns for an eye with dry AMD.	180
4.4	Visualising various OCTA images with their corresponding $LBP_{p,r}$ patterns for an eye with wet AMD.	181
4.5	Visualising various OCTA images with their corresponding $LBP_{p,r}^{2riu}$ patterns for a normal eye.	184
4.6	Visualising various OCTA images with their corresponding $LBP_{p,r}^{2riu}$ patterns for an eye with dry AMD.	185
4.7	Visualising various OCTA images with their corresponding $LBP_{p,r}^{2riu}$ patterns for an eye with wet AMD.	186
4.8	Visualising various OCTA images with their corresponding $BRIEF_{S,n}$ patterns for a normal eye.	188

4.9	Visualising various OCTA images with their corresponding $BRIEF_{S,n}$ patterns for an eye with dry AMD.	189
4.10	Visualising various OCTA images with their corresponding $BRIEF_{S,n}$ patterns for an eye with wet AMD.	190
5.1	An outline of the automated OCTA image texture analysis algorithm that is proposed for AMD disease detection by the means of image classification based on reduced-local texture features.	241
5.2	Plots of bar charts that demonstrate the percentage of variance explained by the individual PCs in the healthy vs wet AMD classification task for only the occasions in which the classification algorithm that is based on reduced-local texture features achieved better performance. .	295
5.3	Visualising the percentage of variance explained by the individual PCs in the dry AMD vs wet AMD classification task for only the occasions in which the classification algorithm that is based on reduced-local texture features accomplished improved performance.	296
5.4	Visualising the percentage of variance explained by the individual PCs in the CNV vs non-CNV classification task for only the situations in which the classification algorithm that is based on reduced-local texture features demonstrated enhanced classification performance. . . .	297
6.1	An outline of the automated localisation algorithm for localising areas of CNV lesions related to AMD disease in the texture of OCTA images based on local texture features.	309
6.2	Two healthy models of OCTA images that show the typical textural appearance of the outer retina and the choriocapillaris layers.	315
6.3	Two samples of diseased OCTA images of the outer retinal layer in which the CNV areas are more or less correctly localised by the localisation algorithm when varying the similarity measures.	317
6.4	Two samples of diseased OCTA images of the choriocapillaris layer in which the locations of CNV areas are approximately correctly estimated by the localisation algorithm when changing the similarity measures.	318

6.5	Samples of two different diseased OCTA images of the outer retinal layer in which the locations of CNV areas are properly and improperly estimated by the localisation algorithm when changing the similarity measures.	319
6.6	Examples of two diseased OCTA images of the choriocapillaris layer in which the positions of CNV regions are correctly and incorrectly estimated by the localisation algorithm when varying the similarity measures.	320
6.7	Examples of diseased OCTA images of the outer retina and the choriocapillaris layers that do not display perceptible regions associated with CNV lesions.	321
6.8	Examples of two challenging localisation situations where the CNV areas appear in irregular patterns and more or less dominate the whole OCTA image.	321
6.9	Two samples of challenging situations due to movements of the patient's eye or head.	322
A.1	An example of convolution operation applied to a two dimensional input data.	361
A.2	Typical components of the convolutional layer in CNN algorithms. . .	362
A.3	A typical structure of CNN algorithm for an end-to-end learning task.	364
A.4	Three potential benefits when exploiting transfer learning techniques.	368
A.5	Illustrative examples and visualisations of the SVM classifier in practical situations as well as comprehensive explanations of its four fundamental notions.	370
A.6	An illustrative example of the KNN classifier in a binary classification situation.	379
B.1	A basic schematic that illustrates the manner in which the OCTA imaging technique functions in a working example to image the human eye.	385
B.2	Illustration of how the motion contrast technology is employed in the OCTA imaging technique by the means of variance.	386
B.3	Automated retinal and choroidal layers segmentation including visualisations with different fields of view by the OCTA imaging technique for a healthy human eye.	388

B.4	Visualising images of abnormal choroidal and retinal blood vessels captured using various retinal vasculature imaging techniques specifically OCTA, OCT, FA and IGA, for an eye with CNV, a late stage of AMD disease.	391
-----	--	-----

Abstract

AUTOMATED ANALYSIS OF OPTICAL COHERENCE TOMOGRAPHY ANGIOGRAPHY IMAGES FOR AGE-RELATED MACULAR DEGENERATION

Abdullah Alfahaid 

A thesis submitted to the University of Manchester
for the degree of Doctor of Philosophy, 2022

Age-related Macular Degeneration (AMD) is a damaging and threatening retinal condition and the leading cause of visual impairment in the elderly population. Optical Coherence Tomography Angiography (OCTA) is a relatively new imaging technique that enables the visualisation and characterisation of the retina of the human eye. The OCTA imaging technique produces clear images of the retinal and choroidal vascular layers including the superficial inner retina, the deep inner retina, the outer retina and the choriocapillaris layers. The current clinical standard for detecting and evaluating the efficacy of the treatments for AMD disease involves visually examining the textural appearance of OCTA images of these layers. However, this is not a trivial task given the significant amount of data being acquired in each OCTA scan, the pattern variations between individuals, and the fact that areas of abnormalities may appear similar. As a consequence, it may exceed the clinicians' ability to visually diagnose AMD patients accurately. Therefore, this research aims at automating reliable ways of accurately quantifying and finding evidence of AMD presence in the context of OCTA images, as such evidence is not easily perceptible by ophthalmologists. Enabling automated analysis of OCTA images texture could also have a significant impact on ophthalmologists' workload. In this research, three different algorithms have been developed to help in quantifying, localising and classifying AMD disease in OCTA images in an automated manner.

The first algorithm is constructed for conducting image classification based on whole local texture features as developed by testing different texture descriptors including the Local Binary Patterns (LBP) and the Binary Robust Independent Elementary

Features (BRIEF) for measuring the texture of OCTA images and examining various classifiers including the Support Vector Machine (SVM) and the K-Nearest Neighbour (KNN) for performing the classification. The second algorithm is analogous to the first algorithm; however, it is based on reduced-local texture features as transformed by the Principal Component Analysis (PCA) technique to decorrelate the texture features. The third algorithm is created for localising areas of ocular vascular abnormalities related to AMD disease in the texture of OCTA images. This is accomplished by employing the LBP texture descriptor and testing different distance similarity metrics including the chi-square and the histogram intersection for performing the localisation.

The various diagnostic algorithms developed were rigorously evaluated based on diverse OCTA image data sets provided by two different hospitals, namely the Manchester Royal Eye Hospital and the Moorfields Eye Hospital. Several eye conditions involved in the various OCTA image data sets comprised healthy, dry AMD and wet AMD. Broadly, the first algorithm demonstrated to perform best on classifying the healthy cases from the wet AMD disease cases accomplishing a mean area under the receiver operating characteristic curve (AUC) score and a standard deviation = 1.00 ± 0.00 . The second algorithm, on the other hand, showed better performance on distinguishing eyes with dry AMD disease from eyes with wet AMD disease achieving a mean AUC score and a standard deviation = 0.85 ± 0.02 , and on distinguishing eyes with choroidal neovascularisation (CNV) lesions related to AMD disease from eyes with non-CNV (dry AMD) lesions attaining a mean AUC score and a standard deviation = 0.85 ± 0.05 . The third algorithm, however, was shown to provide reasonable estimates for the approximate locations of CNV regions in the diseased OCTA images of the outer retina and the choriocapillaris layers. Overall, the results obtained from the various algorithms developed are very effective and encouraging compared to other well-established methods. These algorithms have the potential to be integrated into the OCTA imaging technique, hence providing an instant diagnosis of AMD disease in a daily clinical practice.

Declaration

No portion of the work referred to in this thesis has been submitted in support of an application for another degree or qualification of this or any other university or other institute of learning.

Copyright

- i. The author of this thesis (including any appendices and/or schedules to this thesis) owns certain copyright or related rights in it (the “Copyright”) and s/he has given The University of Manchester certain rights to use such Copyright, including for administrative purposes.
- ii. Copies of this thesis, either in full or in extracts and whether in hard or electronic copy, may be made **only** in accordance with the Copyright, Designs and Patents Act 1988 (as amended) and regulations issued under it or, where appropriate, in accordance with licensing agreements which the University has from time to time. This page must form part of any such copies made.
- iii. The ownership of certain Copyright, patents, designs, trade marks and other intellectual property (the “Intellectual Property”) and any reproductions of copyright works in the thesis, for example graphs and tables (“Reproductions”), which may be described in this thesis, may not be owned by the author and may be owned by third parties. Such Intellectual Property and Reproductions cannot and must not be made available for use without the prior written permission of the owner(s) of the relevant Intellectual Property and/or Reproductions.
- iv. Further information on the conditions under which disclosure, publication and commercialisation of this thesis, the Copyright and any Intellectual Property and/or Reproductions described in it may take place is available in the University IP Policy (see <http://documents.manchester.ac.uk/display.aspx?DocID=24420>), in any relevant Thesis restriction declarations deposited in the University Library, The University Library’s regulations (see <https://www.library.manchester.ac.uk/about/regulations/>) and in The University’s policy on presentation of Theses.

Dedication

To my parents, children, wife, brothers and sisters.

Acknowledgements

First and foremost, I would like to express my gratitude to Allah Almighty for the completion of my PhD journey and thesis writing.

To my supervisor Dr Tim Morris, my heartfelt acknowledgement for his excellent guidance, encouragement and support to help me finish my PhD study. The same goes to my co-supervisor, Prof Timothy Cootes. Special thanks are due to you both.

Furthermore, I would like to thank my parents, children, wife, brothers, and sisters, who all stand by me and helped me during the period of my study.

Heartfelt appreciation and thanks are also due to Dr Konstantinos Balaskas, for facilitating the access to OCTA image data sets used in this research. The same also goes to Dr Panagiotis Sergouniotis, Dr Pearse A. Keane, Dr Hagar Khalid, and Dr Nikolas Pontikos. Many thanks to all of you for providing feedbacks on this research as well as the valuable help in labelling the OCTA image data sets used.

I also would like to thank all my relatives, friends and office mates.

Abbreviation

AI	Artificial Intelligence
AMD	Age-related Macular Degeneration
ANN	Artificial Neural Networks
AUC	Area Under ROC Curve
BRIEF	Binary Robust Independent Elementary Features
BRIEF_{S,n}	Enhanced Version of BRIEF
BRIEF_{S,n}^{PCA}	Applying <i>PCA</i> on <i>BRIEF_{S,n}</i>
BVD	Blood Vessel Density
CNS	Central Nervous System
CNN	Convolutional Neural Networks
CNV	Choroidal Neovascularisation
CFP	Colour Fundus Photography
CT	Computed Tomography
DR	Diabetic Retinopathy
DN	Dense-Net configuration
FP	False Positive
FN	False Negative
FPR	False Positive Rate
FA	Fluorescein Angiography
FD	Fractal Dimension
GLCM	Grey Level Co-occurrence Matrices

GLD	Grey Level Differences
IOU	Intersection Over Union
IGA	Indocyanine Green Angiography
KNN	K-Nearest Neighbour
LBP	Local Binary Pattern
LC	Local Contrast
LBP_{p,r}	Enhanced Version of LBP
LBP_{p,r}^{ri}	Rotation Invariant Version of LBP
LBP_{p,r}^{2u}	Uniform Version of LBP
LBP_{p,r}^{2riu}	Rotation Invariant Uniform Version of LBP
LBP_{p,r}^{PCA}	Applying <i>PCA</i> on $LBP_{p,r}$
LBP_{p,r}^{2riuPCA}	Applying <i>PCA</i> on $LBP_{p,r}^{2riu}$
LN	Loose-Net configuration
LOOCV	Leave-One-Out Cross-Validation
MRF	Markov Random Field
MFS	MultiFractal Spectrum
MLP	Multilayer Perceptron
MRI	Magnetic Resonance Imaging
OCTA	Optical Coherence Tomography Angiography
OCT	Optical Coherence Tomography
OH	Old Healthy
PCA	Principal Component Analysis
PCs	Principal Components
PPV	Positive Predictive Value
ROC curve	Receiver Operating Characteristic curve
RPE	Retinal Pigment Epithelial
SVM	Support Vector Machine

TP	True Positive
TN	True Negative
TNR	True Negative Rate
YH	Young Healthy

Chapter 1

Introduction

1.1 Chapter Introduction

This chapter introduces the research presented in this thesis. It begins by presenting the main motivations for conducting this research. Provision of the overall aim and objectives as well as the main hypotheses of this research then follows. The main research contributions are summarised next. Finally, the publications produced from the work undertaken are individually listed followed by a brief description of the thesis structure.

1.2 Motivations

The main motivations for conducting the research presented in this thesis are determined by three fundamental components. These are Age-related Macular Degeneration (AMD) disease, a highly threatening eye disorder; Optical Coherence Tomography Angiography (OCTA), which is a novel ocular vascular imaging technique; and the potential outstanding benefits of automating the analysis of OCTA image texture. The rationales for considering these three subjects are justified in the following three subsections 1.2.1, 1.2.2 and 1.2.3.

1.2.1 Age-related Macular Degeneration (AMD)

Age-related Macular Degeneration (AMD) is a very complex, heterogeneous retinal disease that is a primary cause of vision damage in the elderly population [1,2]. AMD primarily affects the macula, the central region of the retina. It is clinically divided into

two different types, namely wet AMD and dry AMD [3]. Wet AMD disease is characterised by the presence of a common, vision-threatening complication called choroidal neovascularisation (CNV) that involves the growth of abnormal blood vessels and may incorporate several typical lesions including the presence of fluid or retinal haemorrhage and retinal pigment epithelial detachments, among others [3]. Dry AMD disease is also known as geographic atrophy, which includes outer retinal thinning and is typically characterised by damage of retinal pigment epithelial cells, underlying choroidal capillaries and overlying photoreceptors [3].

Dry AMD is the common subtype and is linked to gradual vision loss, while wet AMD is associated with a more severe presentation and rapid vision impairment [3]. Remarkably, wet AMD can be successfully treated with intravitreal injections. As a result, early discovery and treatment are critical, and quick diagnosis has been associated with better results [4]. Early detection of areas related to CNV lesions and distinction between subjects with wet AMD and dry AMD are consequently prioritised in terms of effort and healthcare resources.

1.2.2 Optical Coherence Tomography Angiography (OCTA)

To assist in the early detection of AMD disease, numerous retinal vasculature imaging modalities have been developed. Optical Coherence Tomography Angiography (OCTA) is a new and promising imaging technology that combines both dye-free angiography as well as non-invasive volumetric three-dimensional imaging capabilities. This imaging technique has several benefits over the commonly used Optical Coherence Tomography (OCT) imaging technique in that it allows for an in-depth visualisation of blood circulation in both retinal and choroidal vascular layers. In contrast to other recognised fundus imaging modalities such as Fluorescein Angiography (FA) and Indocyanine Green Angiography (IGA), the OCTA imaging technique is quick and non-invasive [5–7]. Notably, the OCTA imaging technique allows for the characterisation of moving and static elements in both retinal and choroidal blood vessels, as well as the visualisation of vascular abnormalities, e.g.: areas of CNV lesions, and other vascular details that can assist in the differentiation between the appearance of healthy vascular from dry and wet AMD.

The OCTA imaging technique generates images of four different retinal and choroidal vascular layers namely the superficial inner retina, the deep inner retina, the outer retina and the choriocapillaris layers. The OCTA images of the superficial

inner retina layer are determined as a projection of the vasculature located in two retinal layers, namely the nerve fibre layer and the ganglion cell layer [7]. The OCTA images of the deep inner retina layer, on the other hand, are defined as a projection of a combination of the vascular plexuses situated at the edge of the inner plexiform layer and the inner nuclear layer and the edge of the inner nuclear layer and the outer plexiform [7].

The current clinical standard for detecting CNV lesions and assessing the effectiveness of the treatments given for patients with wet AMD comprises visually examining and evaluating the textural appearance of OCTA images of the outer retina and the choriocapillaris layers [8,9]. Nevertheless, this is not a trivial task given the enormous quantity of image data in each OCTA scan, the textural pattern differences among individuals, and the appearance of regions of CNV and non-CNV lesions as well as the healthy vascular in the various OCTA images, which may seem identical when comparing various subjects [10].

As a result of the challenges inherent in the interpretation process, it is not uncommon for clinicians to frequently seek a second opinion. The textural appearance of the retinal and choroidal vascular layers in the OCTA images for eyes with different conditions are given in Figure 1.1. OCTA images of different ocular vascular layers from various eyes with no vascular pathologies, dry AMD and wet AMD are demonstrated. The complexity in the texture of blood vessel patterns between the OCTA images of different ocular vascular layers can be appreciated.

1.2.3 Analysis of OCTA Image Texture

The texture of images is very rich with extremely important details that describe complex visual patterns which can be distinguished by colour, brightness, size, or shape [11]. Texture information, in the context of medical imaging, relates to the macro and micro structural properties of images representing biomedical tissues [12]. Clinicians are typically trained to perform tasks like interpreting, establishing standardised qualitative features and creating links between visual texture appearance patterns and particular pathologies in medical images. Among the early attempts to identify ocular vascular pathologies related to AMD disease in the context of OCTA image data are, therefore, the qualitative analysis approaches [8,9,13–18].

The qualitative approaches typically attempt to visually establish standardised patterns, i.e.: qualitative features, for the areas of CNV lesions. Examples of qualitative

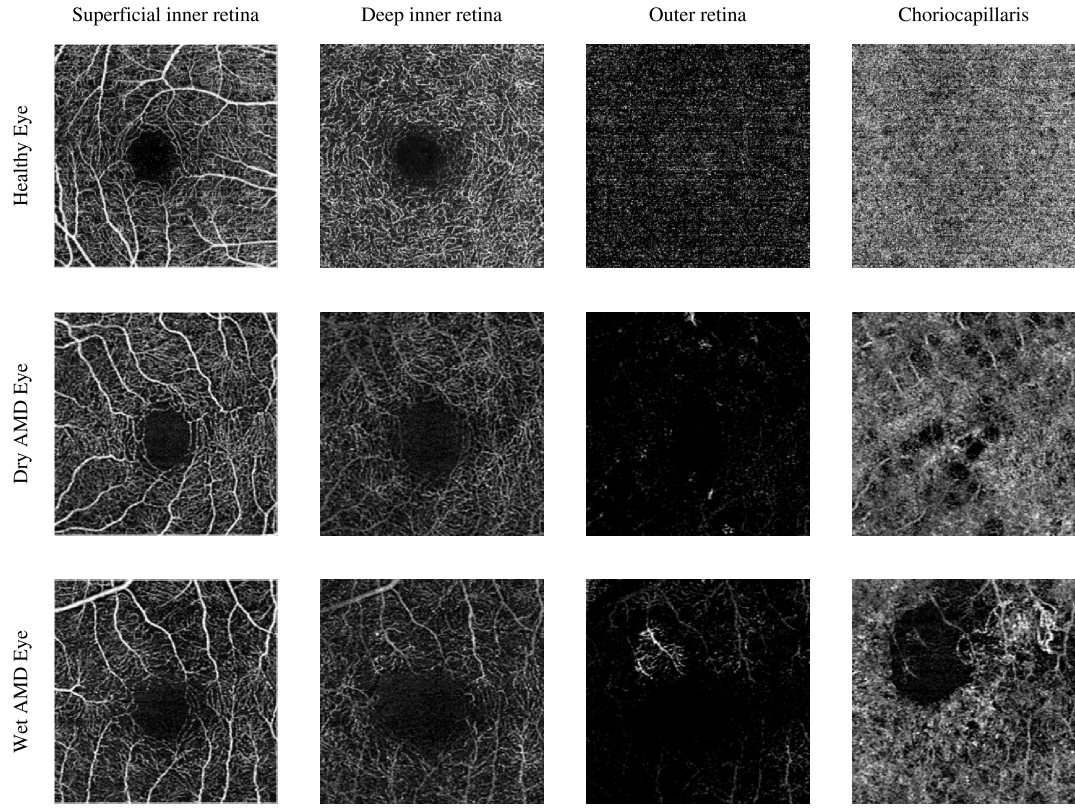


Figure 1.1: The textural appearance of the blood vessels network in the superficial inner retina, deep inner retina, outer retina, and choriocapillaris layers in OCTA images. Each row illustrates a different eye condition from the various ocular vascular layers. The first row shows a healthy eye, the second row shows a dry AMD eye, and the final row shows a wet AMD eye. It can be observed how the similarities appear in the patterns of the abnormalities in all layers for the dry and wet AMD eyes. However, in some layers, the patterns appear very similar among various eye conditions, e.g.: dry AMD, wet AMD and also healthy. The similarities between healthy and pathological vascular patterns appear in the OCTA images of the superficial inner retina and the deep inner retina layers.

features used to describe the structures or textural arrangements of CNV regions include the “medusa”, the “sea fan” and the “indistinct” features that are suggested by Kuehlewein et al. [8]. The term medusa pattern is usually used to describe the textural appearance of the OCTA image that displays a large thick central abnormal blood vessel trunk with abnormal blood vessels that branch out in various directions. The term sea fan pattern is used if more than 90% of the abnormal blood vessels are branched in a single direction from a large thick central blood vessel trunk. The term indistinct pattern, however, is normally used to describe the absence of distinct abnormal blood vessels.

However, these qualitative features are often insufficient to describe texture characteristics since these are generally considered to be as low-level descriptive terms as the general terms usually used to describe textures, namely uniformness, randomness, smoothness and coarseness, while the human visual perception of textures is significantly richer [12]. Significant differences may also occur in this difficult and complex mapping of various patterns and could result in errors during interpretation of the texture of images with possibly undesirable consequences [12, 19–21]. This is largely attributed to the diversity and complexity of human biology and anatomy, including image acquisition techniques, as well as being compounded by observer training [12]. The aforementioned is also amplified by the significant hurdle that still remains with the OCTA imaging technique, which is the lack of specific diagnostic criteria for OCTA image data in the presence of various retinal diseases including AMD disease [22]. Additionally, there is evidence to demonstrate that it is also problematic for the human eye to recognise textural information which is related to higher-order statistics or to the spectral properties of images [23].

Consequently, automating the analysis of OCTA images is extremely necessary as it could assist ophthalmologists to extract features which are meaningful but may be difficult to distinguish visually. Other advantages can also include reducing the burden on ophthalmologists and ensuring greater efficiency, consistency, and reliability in the diagnosis process in daily clinical practice. Likewise, it can also be perfectly beneficial for certain exceptional circumstances, e.g.: epidemic or pandemic situations, as with the current situation with coronavirus disease (COVID-19) when numerous hospitals have restricted the number of hospital visitors. As such, it can not only cut sharply the waiting of patients in the clinic before being seen by one of the medical staff but can also rapidly accelerate the invitation of other patients who are still on the waiting list. Another potentially outstanding advantage includes eliminating or removing the subjectivity of personal interpretation, since it is typically accomplished without requiring the involvement of manual assistance to delineate or measure certain areas of interest, e.g.: the areas of CNV lesions.

1.3 Aim and Objectives

Given the potential outstanding advantages earlier mentioned by automating the analysis of OCTA image texture, the overall aim of this research is to automate ways of quantifying and finding evidence of AMD disease in the context of OCTA image data.

To achieve this overall aim, the main research objectives are:

- To explore ways to automate the analysis of OCTA image texture.
- To investigate texture representation techniques for measuring the texture of OCTA images.
- To identify the main characteristics of the OCTA image data and how these have been exploited by previous studies to facilitate the diagnosis of AMD disease.
- To construct fully automated diagnosis algorithms that can accurately analyse the various OCTA images with different eye conditions related to AMD disease as well as healthy.
- To create a fully automated diagnosis algorithm that can estimate the locations of abnormal ocular blood vessel areas, e.g.: regions of CNV lesions, in the texture of OCTA images.

1.4 Hypotheses

The main research hypotheses of the work presented in this thesis are:

- It is feasible to perform automated diagnosis for eye conditions, e.g.: AMD disease, using the OCTA image data in the raw form purely as extracted by the OCTA imaging technique.
- There is a difference between the blood vessel patterns in the superficial inner retina and the deep inner retina layers of the diseased and healthy OCTA images.

1.5 Contributions

The works undertaken in this research project have resulted in achieving several contributions to knowledge. From a computer science perspective, the works presented in this thesis have contributed to the domain of Artificial Intelligence (AI) and, in particular, the field of computer vision which concerns the design of specialised techniques that typically mimic human vision and perception. As such, a number of domain-specific and novel purely data-driven techniques were developed to facilitate the diagnosis of AMD disease in the context of OCTA image data in fully automated ways. These are summarised by the following points:

- The development of two domain-specific texture descriptors for measuring the presentation of AMD disease in the texture of OCTA image data. The first descriptor is based on employing a supervised pattern recognition technique

via adapting the greyscale and rotation invariant uniform Local Binary Patterns (LBP^{2riu}) texture descriptor of Ojala et al. [24]. The latter descriptor is based on the combination of the LBP^{2riu} texture descriptor and an unsupervised pattern recognition technique via exploiting the Principal Component Analysis (PCA) technique, together forming a single texture descriptor denoted as the $LBP^{2riuPCA}$ texture descriptor. Both descriptors generally demonstrated strong capabilities to capturing very discriminative texture measurements from the texture of OCTA images that are useful for AMD disease detection.

- The construction of two novel fully automated classification algorithms for AMD disease detection in the OCTA images of various ocular vascular layers. The first algorithm is based on whole local texture features purely as extracted by the LBP^{2riu} texture descriptor. The second algorithm is based on reduced-local texture features as transformed by the $LBP^{2riuPCA}$ texture descriptor. These two different algorithms proved able to discriminate accurately between healthy and AMD disease as well as to distinguish between the different stages of AMD disease, e.g.: dry AMD and wet AMD.
- The design of a fully automated localisation algorithm for identifying areas of ocular vascular abnormalities related to AMD disease, e.g.: regions of CNV lesions, in the texture of OCTA images. This algorithm demonstrated great capabilities of localising important areas of CNV lesions wherever they appear to be situated around a particular area in the texture of OCTA images. The main advantage of this algorithm is that it does not rely on manually annotated OCTA image data in which areas of abnormalities are precisely delineated.

The above-mentioned techniques developed have also enabled the design of four different novel diagnostic applications for the diagnosis of vascular pathologies related to AMD disease based on the OCTA images of different ocular vascular layers in their raw form. These diagnostic applications are listed as follows:

1. Classifying healthy OCTA images from OCTA images with wet AMD disease.
2. Classifying OCTA images with dry AMD disease from OCTA images with wet AMD disease.
3. Classifying OCTA images with CNV lesions from OCTA images with non-CNV lesions.
4. Localising important regions related to CNV lesions in the texture of OCTA images.

These four novel diagnostic applications are evaluated based on diverse OCTA

image data sets provided by two different hospitals, namely the Manchester Royal Eye Hospital and the Moorfields Eye Hospital.

The works demonstrated in this thesis have also added further significant contributions to knowledge from the field of ophthalmology perspective. As such, the various techniques developed enabled the identification of novel ocular vasculature texture variations between the various eye conditions related to AMD disease, including healthy, in the texture of OCTA images of two retinal vascular layers. These retinal vascular layers are:

1. The OCTA images of superficial inner retina layer.
2. The OCTA images of deep inner retina layer.

The significant findings here are that these retinal vascular layers are not usually individually used or examined by ophthalmologists, nor in previous attempts to automate the analysis of OCTA images for AMD detection. This is because the differences are not perceived by the human eye. However, the techniques developed in this thesis have successfully identified and quantified these differences by applying supervised and unsupervised statistical pattern recognition techniques, e.g.: the LBP^{2riu} and the $LBP^{2riuPCA}$ texture descriptors, on the texture of OCTA images.

1.6 Publications

Besides the earlier mentioned research contributions, the works undertaken have also resulted in producing a number of peer-reviewed scientific papers [25–27]. These are listed as follows:

- A paper entitled “An Automated Age-Related Macular Degeneration Classification Based on Local Texture Features in Optical Coherence Tomography Angiography” was published at the Medical Image Understanding and Analysis (MIUA 2018) Conference [25].
- An abstract entitled “Machine Learning for the automated interpretation of Optical Coherence Tomography Angiography for Age-related Macular Degeneration” was published at the Association for Research in Vision and Ophthalmology (ARVO 2019) Annual Meeting [26].
- A paper entitled “A Hybrid Machine Learning Approach Using LBP Descriptor and PCA for Age-Related Macular Degeneration Classification in OCTA Images” was published at the MIUA 2019 Conference [27].

1.7 Thesis Outline

The thesis is structured in seven chapters including this Chapter 1 that introduces the works presented in this thesis. The remaining six chapters are, therefore, illustrated as follows:

Chapter 2 Image Texture Analysis in Computer Vision: This chapter provides descriptions of the various typical computer vision tasks in medical image analysis applications. It also delivers a comprehensive technical background for the different techniques typically used to automate the analysis of image texture. The evaluation measures and strategies that could be utilised to quantify the performance of methods developed to perform a particular computer vision task are also given. This chapter works as a roadmap to assist in selecting the most appropriate ways to create and evaluate the diagnosis techniques for AMD disease in the OCTA images.

Chapter 3 Application Domain, Data Sets and Related Works: This chapter covers the related background of the application domain of the work undertaken in this thesis. The various typical ocular vascular imaging modalities are then reviewed. The pros and cons with every single imaging technique are highlighted as well as an illustration of the novelty of the OCTA imaging technique. Comprehensive descriptions of the OCTA image data sets utilised in this thesis are included. Finally, the most recent and notable previous attempts related to the research presented in this thesis are then summarised including their advantages and disadvantages.

Chapter 4 Classification Algorithm Based on Whole-Local Texture Features: This chapter describes a fully automated OCTA image classification algorithm for the diagnosis of AMD disease based on whole-local texture features.

Chapter 5 Classification Algorithm Based on Reduced-Local Texture Features: This chapter provides a fully automated OCTA image classification algorithm for the diagnosis of AMD disease based on reduced-local texture features.

Chapter 6 Localisation Algorithm Based on Local Texture Features: This chapter presents a fully automated localisation algorithm for localising areas of CNV lesions related to AMD disease in the texture of OCTA images based on local texture features.

Chapter 7 Conclusion and Future Work: This chapter concludes the whole work presented in this thesis by firstly summarising the main findings, followed by drawing the conclusion. Afterwards, possible future works for further investigations to address the potential limitations are suggested.

1.8 Chapter Conclusion

The research provided in this thesis is introduced in this chapter. It starts by outlining the major reasons for performing this study. The main aim and objectives, as well as the key hypotheses of this study, are then presented. After that, the significant research contributions are summarised. Finally, the various papers resulting from the work conducted are given, followed by a summary of the thesis structure.

Chapter 2

Image Texture Analysis in Computer Vision

2.1 Chapter Introduction

This chapter provides a comprehensive technical background for the various computer vision domains and techniques used to automate the analysis of image texture. The chapter will start by providing descriptions of the various computer vision tasks in medical applications. However, the focus is purely on image classification and segmentation problems, as these fall within the domain of the research presented in this thesis. This is followed by a presentation of the various techniques used to extract texture features, to classify images, to measure the similarity between images and to decorrelate or select the textural features. Finally, the evaluation measures and strategies that could be utilised to quantify the performance of methods developed to perform a particular computer vision task such as classification are summarised.

2.2 Computer Vision Tasks in Medical Image Analysis

The field of computer vision has emerged as a discipline in itself, yet it can be considered as a multidisciplinary field [28]. Consequently, it can generally be referred to as a subfield of machine learning and Artificial Intelligence (AI) that may include the utilisation of general machine learning algorithms and may make use of specialised methods [29]. As a multidisciplinary field, it can appear formidable since various techniques and details can be borrowed from a wide variety of different fields including mathematics, physics, neurosciences, perceptual psychology and computer science,

among others and reused or applied across various domains [28].

Nevertheless, within the field of computer vision, the means to develop and solve a wide variety of applications and problems such as mobile robot navigation, military intelligence, industrial inspection, facial expression recognition and more importantly medical image understanding, and analysis have been sought [30]. The main goal of computer vision is to extract meaningful information or descriptions from digital data such as images and videos [31]. This is to automate tasks like matching, recognition and prediction and to provide machines with an ability to see and assist in the diagnosis of various diseases in medicine. This gives the machine the same capacity to perform these tasks as the visual system of humans. This also includes making the computer capable of recognising variations under a range of different conditions such as altered lighting, orientations and so on [29].

Computer vision is a very broad field of study and includes numerous specialised tasks and techniques to solve a wide variety of problems. However, as the focus of this research is to automate the analysis of the retinal image texture, the scope of discussion will be narrowed to typical computer vision tasks in medical image analysis applications. Generally, these include image classification and image segmentation tasks. In the following two subsections, 2.2.1 and 2.2.2, comprehensive explanations are provided along with examples for each particular task.

2.2.1 Image Classification

In computer vision, the task of an image or a texture classification is to assign an entire image or a particular texture region within an image as belonging to a class of a predefined set of categories in the training samples [32]. The classification can be conducted as a binary classification problem, such as classifying a whole image as diseased or healthy. Figure 2.1 shows an example of a classification task for detecting glaucoma, a common eye condition, and the classification is performed on the entire image and the result is either a diseased or a healthy image.

Another example of classification application is that of localising a texture region within an image as being inside or outside a given class [32]. Figure 2.2 illustrates this as the task here is to differentiate between pathological and normal texture regions and localise them in breast cancer images.

The task of image classification could also be extended to assist clinicians for not only identifying pathologies in images but also for assessing the quality of medical images. Figure 2.3 demonstrates a classification application to assess the quality of

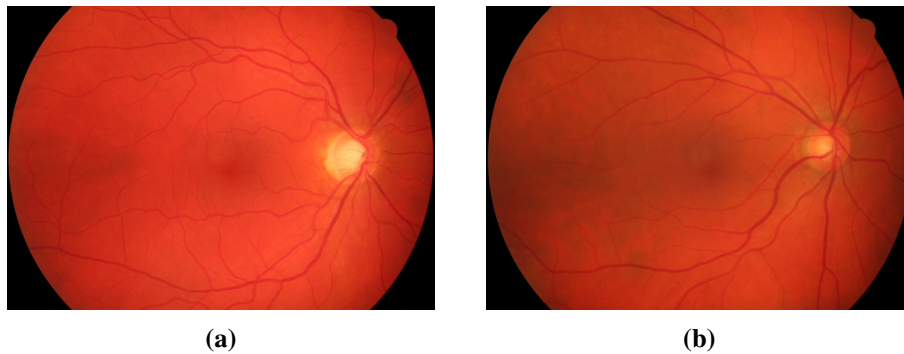


Figure 2.1: An application example of a whole image classification task for glaucoma detection [33]. (a) Represents a healthy human eye and (b) represents a human eye with glaucoma. The final output of the classification is either a healthy or a diseased image.

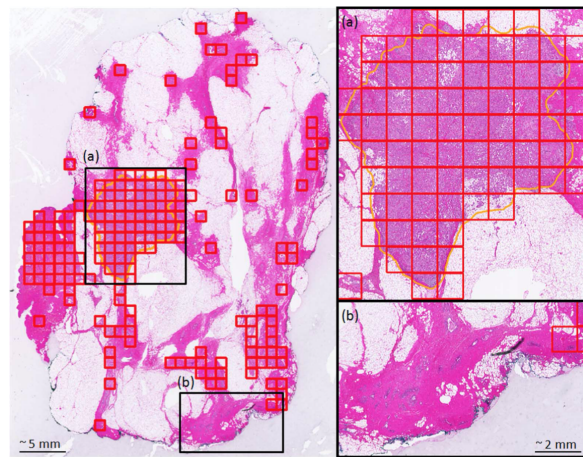


Figure 2.2: An example of a classification task for distinguishing between texture regions within a breast cancer tissue slide as pathological or normal [34]. (a) shows detected regions (the red bounding boxes) which match (the yellow contour) that manually drawn by a trained pathologist as an important region. (b) shows the correctly discarded region indicating that is a normal region. The final output of this is an image with bounding boxes on the potential important areas.

OCTA images that represent the retinal blood vessel texture.

2.2.2 Image Segmentation

The main goal of an image segmentation task is to partition a digital image into multiple disjoint regions. This is to simplify and convert the original image representation into a new representation that is more interpretable and understandable. It might also potentially help for further analysis to be applied or to allow for more information to be derived using the segmented regions. Each region in the partitioned image perhaps

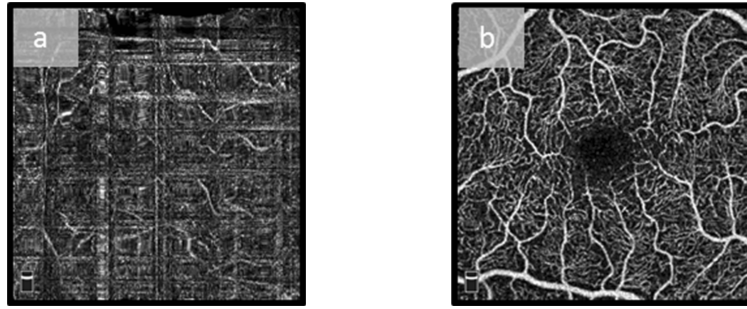


Figure 2.3: A classification task for assessing the quality of OCTA image texture appearance [35]. The two OCTA images show the texture of the superficial vascular layer in the retina. (a) Represents an example of poor-quality image due to noise caused by the patient's motion and (b) represents an image with good quality. The final output of this system is a good or poor image quality based on gold standard data.

shares homogeneous appearance or characteristics such as texture, colour, etc. Image segmentation is one of the most challenging computer vision tasks in image analysis applications. This is because prior knowledge or details about the regions of interest that are to be segmented may not be apparent, such as how many regions, objects and types of textures exist in the image [36]. While it may not be necessary to know these details, being aware of them is the way to tell if the various segmented areas share similarity or if each area is distinct from the other.

Broadly, image segmentation methods can be grouped into two categories based upon the task to be achieved. These are region-based and boundary-based techniques [36]. In the region-based methods, the overall objective is to detect the areas that have a uniform textural appearance or colour. The process then involves merging the detected areas with each other based on their similarity. These methods have the advantage that the boundaries of the areas are normally closed. Hence, areas identified with different texture or colour are well defined and separated. However, these methods have some disadvantages. This is because it may be necessary to define a set of values of parameters before segmenting the image such as a similarity threshold value, the number of distinct regions and so on [36, 37]. Figure 2.4 shows an example of a region-based method.

For the boundary-based methods, the main aim is to identify the boundaries of

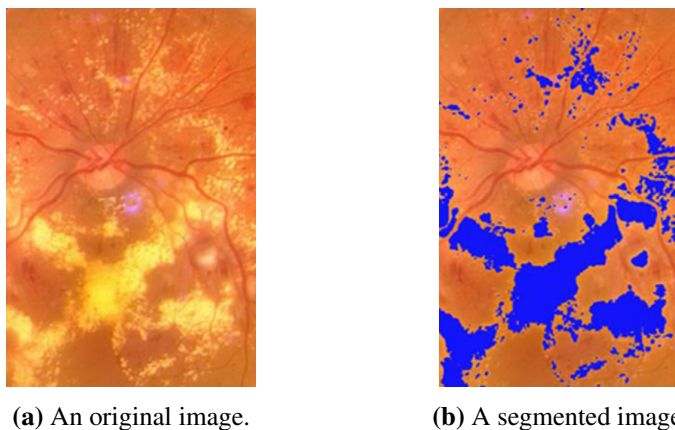


Figure 2.4: An example of a region-based segmentation task for the detection of diabetic retinopathy lesions, namely hard exudates, and for monitoring its progression in fundus images [37]. (a) Represents the original image containing lesions (yellow regions) that are to be segmented. (b) Represents the segmented image and it can be seen that the lesions have been successfully identified and segmented (blue regions) by the method.

adjacent regions based on the detection of variations in the colour or textural appearance [36]. It is not necessary for the number of regions to be previously known. However, the boundaries of different regions may not be identified accurately if the boundaries are not well defined. In other words, the segmentation will be successful only if all the boundaries that form closed curves are accurately detected. Figure 2.5 shows an example of a boundary-based method.

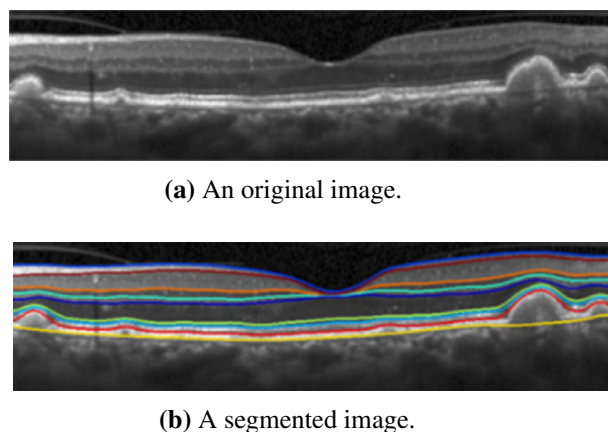


Figure 2.5: An example of a boundary-based segmentation task for the detection of various retinal layer boundaries in OCT images for AMD [38]. (a) Represents a cross-section image of the retina that is to be segmented for a patient with AMD. (b) Represents the segmentation results for the image and each line in the image separates each layer from the other.

The classification and segmentation are closely related to each other. Depending

upon the task to be achieved, the techniques used for creating an image classification system could be borrowed for building an image segmentation system, and vice versa. For example, the classification techniques can be used to classify objects or regions of interest within an image so that they can be segmented based on their similarity. This is the same with segmentation techniques; they could also be used to segment the image into regions, then based on some measurements derived from the segmented regions or the identification of a region of interest the image could be classified into a predetermined category.

Given a computer vision task to solve an image classification or segmentation problem, primarily image details must be accurately measured in a way that conveys the essential information that presents within the image. One way to facilitate the accomplishment of the task in question is to use texture. Texture can be present in a wide range of images captured from different sources such as natural, microscopic, x-ray, aerial, etc. The following section, 2.3, presents the role of texture in computer vision and medical image analysis applications.

2.3 Texture Role in Computer Vision and Medical Applications

Vision is an important part of the human body as the vast majority of information observed about the surroundings is through eyesight. At least 50% of our brain is devoted to understanding and processing visual information [39]. Similarly, texture representation i.e.: texture feature extraction is also a fundamental element for building computer vision systems. This is because it allows these systems to perceive and understand their surroundings and lets them perform the tasks that they have been built for. Examples of important tasks include building a computer vision system to assist in diagnosing various diseases in medicine such as detecting normal and abnormal areas within images. Other examples of computer vision applications include creating facial or object recognition systems to recognise certain faces or objects appear within images.

The fundamental step, however, in creating a successful computer vision system for medical image analysis is to first characterise the perceived qualities of the texture appearing in images. In medicine, images of normal and abnormal tissue regions may appear textured due to various absorption coefficients of healthy and pathological tissues or cells [39]. Texture is considered to be one of the fundamental and powerful characteristics of many different kinds of digital images, especially medical images.

It is used by clinicians in image interpretation as it helps them in performing tasks such as creating links between the textural visual appearance patterns and particular pathologies present within the images.

The texture of images is rich with very important information describing complex patterns. These can be distinguished visually by appearance, structure, arrangement, colour, brightness, size, shape and so on [11, 40]. However, the texture by definition is unlike colour. This is because it refers to the spatial distribution and organisation of pixel intensity level variations, e.g.: changes in colour levels and a set of basic local conspicuous features [32]. These include edges, crossings, corners, etc., the essential micro-structures in natural images and the elementary units of pre-attentive texture discrimination perception of the human visual system [41]. These various features and pixel intensity variations are reflecting the scenes or objects that are being imaged. Texture regions may comply to some statistical properties, demonstrating repetitive local patterns that may appear perfectly regular, purely random or a mixture in between, with some level of variability in their relative appearance and locations [30].

Texture analysis and understanding is one of the most challenging problems in the computer vision area and has been an intensive research subject from the early 1960's [42]. This has led to the development of a wide variety of techniques to help in recognising various textures appearing in digital data such as images or videos. This is perhaps due to two main reasons [32]. Firstly, the importance of the role that texture plays in several computer vision applications and an important example of an application area that includes medical image analysis. Secondly, its significance in understanding how the perception of human vision works to discriminate various textures. The following section 2.4 provides the various categories of image texture representation techniques in computer vision.

2.4 Categories of Image Texture Representation

In computer vision, the overall objective of image texture representation or feature extraction is to convert texture images into machine readable formats e.g.: feature vectors that describe the fundamental properties of texture images. This is to facilitate the accomplishment of subsequent computer vision tasks such as image classification or segmentation. As texture by definition is a spatial and organisational phenomenon, texture representation techniques cannot only be based on a single pixel value, hence they generally require the analysis of various texture patterns over a number of local

neighbourhood pixel values [32]. A common procedure in texture representation techniques usually starts with converting a texture image or a certain texture area within an image into a number of local features. As texture properties are typically translationally invariant, the procedure is usually followed by applying a random aggregation operation such as max or sum of local features [32]. This final operation generates a global texture representation for an entire texture image or a certain texture area within an image. This final global texture representation is typically estimated by a histogram, which constructs the feature vector that forms the basis of solving the image texture analysis task, such as classification or segmentation. Figure 2.6 shows an illustrative example of the aforementioned procedure usually employed in several texture representation techniques.

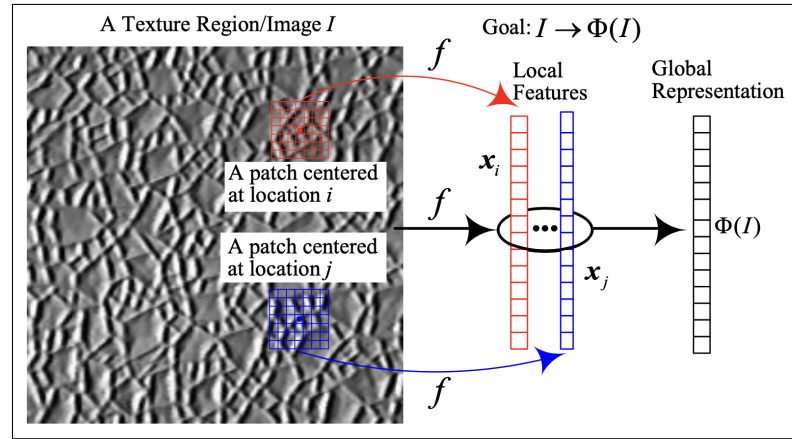


Figure 2.6: An illustrative example of a common procedure normally utilised in many texture representation techniques [32]. The procedure usually involves transforming a texture image or a particular texture region within an image into a number of local features extracted from several locations. It is then followed by an aggregation operation such as a sum of local features to form a global texture representation, i.e.: a feature vector for an entire texture image or a particular region of interest within a texture image. This final global texture representation is typically estimated by a histogram, which constructs the feature vector that forms the basis of solving the image texture analysis task, such as classification or segmentation.

Broadly, the techniques for image texture representation could be divided into two main categories based on their roles in measuring and describing the image texture content. These are hand-engineered and learned texture representation techniques. The following subsections, 2.4.1 and 2.4.2, introduce and review each category in detail along with some examples for the well-established and notable methods that belong to each one of these categories.

2.4.1 Hand-engineered Category

A traditional way to categorise the texture representation methods in the hand-engineered category is to divide them into five different groups, these being geometrical or structural, statistical, model based, signal processing and local texture descriptor methods [36,39]. These various groups are described below along with some examples of the most well-known methods of each group as well as the merits and demerits for each particular texture analysis group.

2.4.1.1 Geometrical or Structural

Approaches that fall under the group description of geometrical or structural methods are based on the assumption that image texture is composed of a number of texture elements or primitives [43]. These are arranged according to certain rules, which involve organising the spatial location of primitives within the image. What is referred to by the texture primitives or elements here is that the existence of texture regions or patterns within the image share uniform characteristics such as grey levels and appearance [36,44]. Hence, texture analysis approaches here depend upon the structural properties of primitives existing in image texture. For measuring image texture using structural methods, usually the texture elements and their spatial location rules need to be defined [36,45].

Texture primitives could be recognised and identified directly from image texture. Primitives present in image texture can be viewed in their simplest form as any of the following, dots, points, arrows, triangles, etc. [44]. Further different forms of primitives may also include a group of connected pixels that all share similar edge direction, or all have the same intensity values such as identical grey values in greyscale textural images [43]. Various possible kinds of more complex primitives could also be extracted by utilising one or more image processing techniques. This could be achieved by applying simple image thresholding techniques, morphological operations such as opening or closing, connected components analysis, filtering operations such as Laplacian of Gaussian (*LoG*) and so on [43,46]. A typical approach to extract the primitives from grey level textural images is given by Algorithm 1. Once the primitives have been successfully identified, the analysis can then be succeeded by one of the following two ways for describing texture.

One way is to calculate statistical measurements over the extracted primitives such

Algorithm 1 Texture Primitives Extraction**Input:** A grey level textural image (x,y).**Output:** A binary image with texture primitives extracted.

- 1: Apply a *LoG* filter to the textural image (x,y) utilising a *LoG* function. The two-dimensional *LoG* function centred on zero and with Gaussian standard deviation σ has the form: $LoG(x,y) = -\frac{1}{\pi\sigma^4} \left[1 - \frac{x^2+y^2}{2\sigma^2} \right] e^{-\frac{(x^2+y^2)}{2\sigma^2}}$.
- 2: Choose the pixels in the filtered image that are on a local peak. If the magnitude of a pixel in the filtered image is greater than six or more of its eight closest neighbours, that pixel is said to be on a local peak. This produces a binary image.
- 3: Conduct a connected component analysis on the binary image generated exploiting eight nearest neighbours. Every single connected component, consequently, describes a texture primitive.

as direction, region size, orientation, etc., and then to use these as texture descriptions [44]. This can be achieved using the Voronoi tessellation technique which defines the local spatial distributions of primitives that are reflected in the shapes of Voronoi polygons from which the statistical measurements can be derived. Examples of utilising this technique are presented in these works [36, 44]. The alternative way is by the inference of the placement rule directly by using, for example, a tree grammar. Then, the terminal symbols of the specified grammar describe the primitives while image texture is described as a string in the language defined by the grammar. This method of texture analysis is described in this work [47].

Structural approaches have several advantages. For example, they have the power to emphasise the shape aspects of various patterns present in texture images [43]. They also provide good representative descriptions of texture images that can be used for further analysis, namely texture generation, as well as recognition tasks such as segmentation or classification [36, 45]. However, their weaknesses are that they can provide powerful texture descriptions only if they are used with binary images, artificial textures and uniform textures with regular patterns rather than natural texture images [36, 43]. This is because the descriptions can be poorly defined with the presence of irregularity in natural texture images due to the great variability of both texture primitives and their placement rules and no clear distinction between them [45]. Hence, many real texture images may violate the assumption that texture images are composed of well-defined texture primitives [48]. As a consequence, structural approaches are considered of limited practical utility and among the least commonly applied techniques in solving image texture analysis problems [48, 49].

2.4.1.2 Statistical

This class of texture representation methods does not attempt to understand and capture explicitly the hierarchical structure and shape aspects of primitives present in texture images. This is because it considers the texture of images as spatial relationships and distributions of pixel intensity levels variations, such as changes in grey level values, in greyscale texture images [36,43]. This property is considered as one of the main defining qualities of image texture [36]. Texture description based on the statistical measure is, therefore, one of the early methods proposed in computer vision literature [36].

Simple statistical quantitative measures based on first-order statistics, such as the statistical moments, namely the mean, variance, and skewness based on raw image pixel intensity values distribution to represent and quantify image texture contents are generally inadequate. Figure 2.7 demonstrates an illustrative example of two simulated tumour images. These images represent two different visual texture appearances, namely rough and smooth tumours. The pixel intensity value distributions of both images are identical. Hence, discriminating between these images using the aforementioned statistical moments based on the distributions of image pixel intensity values only cannot be achieved, as in this case the statistical measurements will be identical for both images. However, they are different in the spatial relationship and organisation of the pixel intensity values and this precisely defines which texture details are being encoded [12]. Hence, image texture representation techniques that consider the relative position of pixel intensity values with respect to each other in the image are specifically well suited for measuring image texture characteristics.

The most notable and widely used approaches in the statistical category are based on second-order statistics of Grey Level Differences (GLD) described by Weszka et al. [50] and Grey Level Co-occurrence Matrices (GLCM) described by Haralick et al. [51]. These approaches extract the texture measurements by considering the spatial relationship and organisation of pixel pairs with respect to each other in the image.

The GLCM approach measures image texture by calculating the joint probability densities of pairs of neighbouring pixels having particular grey level values. In other words, the analysis involves building a two dimensional matrix (M). The rows (i) and columns (j) of the matrix M represent the number of times pairs of pixels have been neighbours. These pairs of neighbouring pixels are separated by a predefined distance d such as 1, 2, 3 and 4 pixels at a predefined angle α° such as 0° for the nearest horizontal direction neighbour pixel, 45° for the nearest right diagonal neighbour pixel, 90° for the nearest vertical direction neighbour pixel and 135° for the nearest left diagonal

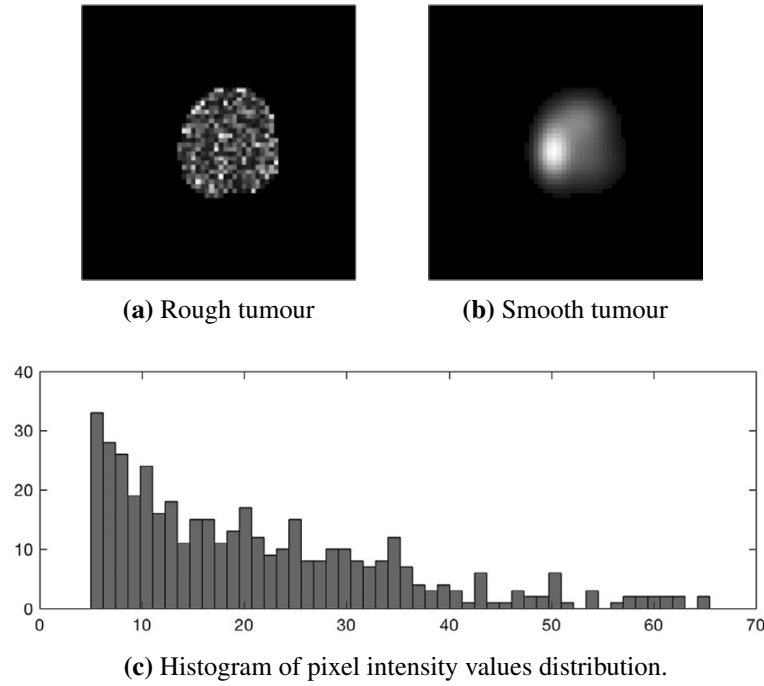


Figure 2.7: An illustrative example of two simulated tumour images that demonstrate two different textural appearances, namely rough and smooth tumours that share a comparable pixel intensity value distribution [12]. (a) Represents a rough tumour texture appearance. (b) Shows a smooth tumour texture appearance. (c) Illustrates the frequency distribution of pixel intensity values of the images of the simulated tumours (a) and (b). It can be clearly observed that the histogram is identical for both images.

neighbour pixel. It is more convenient to use a symmetric matrix M in counting the occurrences of neighbouring pairs of grey levels [50]. This means the order of value pairs is ignored. Figure 2.8 illustrates a simple example of GLCM approach using a 4 x 4 greyscale image.

The GLCM approach reveals specific textural features and characteristics of images such as homogeneity, contrast, etc. For measuring the various features and characteristics present in image texture, Haralick et al. [51] proposed a wide variety of statistical measures that can be computed from the extracted spatial neighbouring matrices M_{a° of grey levels. Examples of these measures are the angular second moment, which quantifies the homogeneity or uniformity of the image; the contrast, which quantifies the amount of local variations present in texture images and the correlation, which quantifies the grey levels linear dependencies in the image. The following equations 2.1, 2.2 and 2.3 demonstrate how these measures are mathematically computed [36, 50, 51]. Additional statistical measures and details about deriving the measurements can also be found in [51].

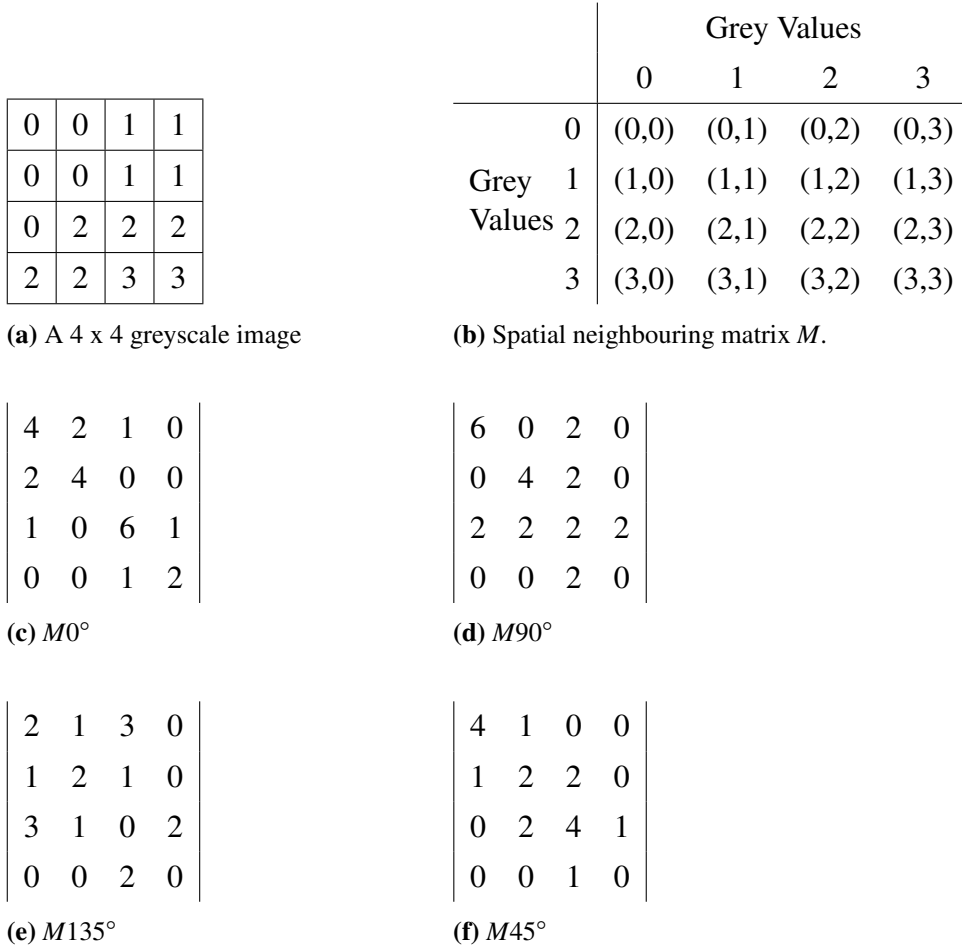


Figure 2.8: Illustration example of the application of GLCM approach on a greyscale image from [51]. (a) Shows an example of a 4 x 4 image with four discrete grey intensity values namely 0, 1, 2 and 3. (b) Represents an example of a general two dimensional matrix form (M) of grey levels spatial neighbouring for a greyscale image with discrete grey levels namely 0, 1, 2 and 3. The elements (i, j) in row i and column j of the matrix M , e.g.: (0,0), (0,1) and so on, denote the general neighbouring of the grey values of potential pairs of pixels. (c)-(f) Represent spatial neighbouring matrices Ma° that calculate the number of occurrences of neighbouring pairs of pixels separated by a single pixel at four different angles a° namely 0° , 90° , 135° and 45° . These four matrices show the number of times pairs of pixels having particular grey levels have been neighbours.

$$\text{Angular Second Moment} = \sum_i \sum_j Ma^\circ(i, j)^2 \quad (2.1)$$

$$\text{Contrast} = \sum_i \sum_j (i - j)^2 Ma^\circ(i, j) \quad (2.2)$$

$$Correlation = \frac{\sum_i \sum_j (i - \mu_x)(j - \mu_y) Ma^\circ(i, j)}{\sigma_x \sigma_y} \quad (2.3)$$

Where $Ma^\circ(i, j)$ denotes the $(i, j)^{th}$ element of the given spatial neighbouring matrix Ma° , and μ_x and σ_x are the mean and the standard deviation of the row sums of matrix Ma° and μ_y and σ_y are similar statistics of the column sums.

The GLD approach, on the other hand, is fairly similar to the GLCM approach. However, the difference between them is that instead of directly using the grey levels of the pair of pixels, the absolute differences values between pairs of grey levels are computed. Specifically, the GLD measures image texture by estimating the probability density of absolute differences values between pairs of grey levels [50]. For example, if the greyscale image has m grey levels, this would give an m -element vector whose elements are calculated by taking the absolute differences of all potential pairs of grey levels separated by a distance d at an angle a° , and counting the number of times the difference values occur. Weszka et al. [50] proposed a number of statistical measures that can be used to extract texture features from the computed m -element vector such as the mean, contrast and other measures which can be found in [50].

Due to the advantages of the GLCM and GLD approaches, such as their simplicity and ease to compute, they have been used in a wide variety of computer vision applications. Examples of employing the GLCM and GLD approaches to solve various computer vision tasks and applications include retinal image classification [52], face detection [53], aerial image classification for such as vegetation communities and terrain [50,51,54], characterising images of healthy and pathological tissues in the human brain [55, 56], detection of lung diseases in thin-section computed tomographic (CT) images [57] and many more applications [40].

Despite their applicability in a wide variety of problems, they have a number of limitations. Most importantly, when measuring image texture using either the GLCM or GLD approach, there is no well-established way to determine how far the pixels should be separated apart and at which angle [58]. Conventionally, when the GLCM approach is used, there is a set of twenty spatial neighbouring matrices of grey levels calculated [40]. These matrices are computed from different pairs of neighbouring pixels separated by various distances ranging from one to five pixels at four different angles, namely horizontally, vertically, and two different diagonal directions.

Nevertheless, this would result in generating very large spatial neighbouring matrices as the grey levels normally range from 0 to 255 in real greyscale texture images. Consequently, computing these various matrices using different distances and directions would be computationally very expensive. This issue, however, could be mitigated by applying colour quantisation technique on the greyscale image to reduce the number of distinct grey levels values such as to 32 or 42 grey levels [58]. While this technique enables efficient computation of the matrices, it can however introduce change or loss of essential details present in the image. Another important issue with the GLCM or GLD approaches also includes having significantly correlated measures due to the repetitive calculations process using different distances and directions on the same image [54]. Hence, the measurements derived may not be suitable for solving the image analysis problem in hand.

2.4.1.3 Model Based

This class of texture representation methods attempts to understand texture images by constructing an image model and using it for texture description [36]. The use of a constructed image model is not only limited to describing or measuring image texture but also it can be used for further analysis tasks such as texture synthesis to generate synthetic texture images. Once the image model is constructed, its parameters are then estimated and used for the image texture analysis task in hand such as image classification or segmentation [45]. The estimated parameters of the image model capture the fundamental perceived qualities present in image texture such as the roughness. Among the most widely used techniques for modelling texture are those based on Markov Random Field (MRF) models and fractals models [39, 59].

Methods based on MRF are based on the assumption that the intensity value at each particular pixel in the textured image depends on the intensity values of only its neighbouring pixels (Markovian property) [36]. These models capture and model contextual details locally and spatially in textured images by identifying the local interactions between the neighbouring pixels in terms of the conditional probabilities [36]. Modelling image texture using MRF models is a probabilistic process which is based on the fact that randomness plays a major role in predicting future occurrences. For example, the likelihood that a particular pixel is in a given state is only specified by probabilities for states of neighbouring pixels [45, 60]. The arrangement of neighbouring pixels for a given pixel can be defined in different ways. These can be first order neighbours which are the four connected pixels neighbours and second order neighbours which

are the eight connected pixels neighbours [36]. From these neighbourhoods, groups of neighbours which form cliques are normally used for calculating the conditional probabilities. A number of studies have utilised MRF to solve various image analysis problems such as texture generation [61], image texture classification [62, 63], image texture segmentation [64, 65] and many more.

Despite the ability of the MRF to provide relatively good representations of various texture images and their applicability to solve a wide variety of image texture analysis problems, they have a number of limitations. Firstly, measuring image texture utilising random field based models such as MRF is considered to be an optimisation problem [58]. This is because when the MRF model is applied to the texture image, the process involves utilising an estimation algorithm to estimate the values of the parameters that define and model the textural properties of the texture. However, one of the main concerns associated with this process is the high computational complexity due to the estimations process involved in defining the values of the models' parameters [58]. Another clear drawback of the MRF models is the sensitivity to almost any variations in image texture such as changes in illumination, orientation, etc. [32].

Approaches based on fractal models, on the other hand, assume that textured images of natural surfaces have a statistical quality of coarseness or roughness and self-similarity across various scales [36]. The appearance of fractals can be as curves or geometric figures that have the same structure at different scales [66]. Fractals are useful in modelling various structures appearing in textured images in which similar patterns recur at either smaller or larger scales. They are also useful in describing partly random or chaotic structures. The first attempt to explore the existence of fractals in the natural world was investigated by Mandelbrot [67]. Mandelbrot [67] proposed the first general fractal geometry framework for studying regular and irregular objects [36, 58].

There are two different kinds of fractals, the first is self-similar fractal and the second is self-affine fractal [58]. The main characteristic of a self-similar fractal is that its appearance will be the same whether statistically or exactly, as well as to its zoomed in or out version if all axes are rescaled similarly by the same magnification factor [66]. The self-affine fractal on the other hand changes in its zoomed in or out version as the scaling is different in each of the axes [68]. An important statistical quantity that provides a global description of fractals in texture images is the fractal dimension (FD) measure. The FD measure is related to the number of replicated fractals (N) and the ratio of magnification factors (r). It is estimated by the following equation 2.4.

$$FD = \frac{\log N}{\log(1/r)} \quad (2.4)$$

This FD measure gives the degree of roughness for texture surfaces and its value in the range of $(0 \leq FD \leq 2)$. A large value of FD measure indicates a rougher texture surface. For example, a FD value of 0 indicates a point, a FD value of 1 indicates a smooth curve and a FD value of 2 indicates a completely filled rectangle [69]. Any other FD values in between 0 and 2 may represent any fractals that take irregular patterns or shapes. Synthetic or man-made fractals may have integer FD values, while other fractals in nature may have fractional FD values. Figure 2.9 demonstrates some basic examples of fractal shapes in two dimensional surfaces and their corresponding FD values.

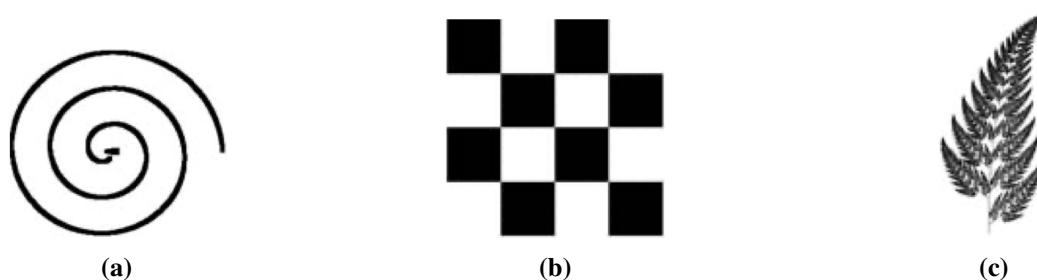


Figure 2.9: Basic examples of fractal shapes [69]. (a) Represents a smooth spiral curve with $FD = 1$. (b) Shows a checkerboard with $FD = 2$. (c) Illustrates a fern leaf or frond with $FD \approx 1.7$.

It should be recalled that the FD measure is based on the number of replicated fractals; however, in most natural texture images, this number is normally unknown due to the large quantity of variabilities and complexities in real images. Therefore, this measure may be more appropriate for deterministic fractals appearing in synthetic or man-made texture images, since the number of replicated fractals is normally known in those images. A further downside of the FD measure is also that most of the real texture surfaces may not be completely self-similar, whether statistically or visually. Therefore, the single value of FD measured on its own does not provide a sufficient description of image texture [69].

2.4.1.4 Signal Processing

The category of signal processing methods performs a frequency analysis of image texture similar to the way the human brain does, as psychophysical research suggests [36, 70, 71]. Physiological experiments performed on cats and monkeys, which have a visual system the same as the human, demonstrate that the visual systems in these animals decompose visual images into a number of filtered images [49, 72, 73]. Motivated by these findings, this category of image analysis is found to be appropriate to apply to texture images due to the properties of texture patterns such as frequencies, orientations and so on [36]. Figure 2.10 demonstrates a common conventional system setup for measuring textured images using signal processing methods.

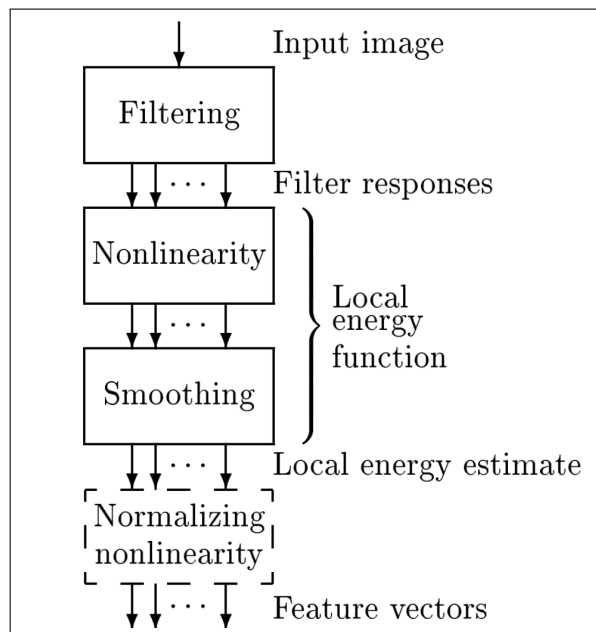


Figure 2.10: A typical conventional system setup of the texture feature extraction process using signal processing methods [49]. The first step involves the application of filtering operation (local linear transform). In this phase, the textured image is convolved with a filter, or a bank of filters (a set of filters) producing the preliminary features. The process is then followed by a local energy function comprising nonlinearity and smoothing operations. The nonlinearity operation here is performed by applying a nonlinear transformation to rectify individual initial features (filter responses). The rectification process here denotes to the transformation of negative amplitudes to positive amplitudes. Examples of nonlinearity operations used are the magnitude $|\cdot|$ and the squaring $(\cdot)^2$. The smoothing operation on the other hand is usually accomplished by rectangular or Gaussian filters. The final operation (normalising nonlinearity) is not usually used, though it has the same functionality as the nonlinearity operation. The results of local energy function elements here will provide a set of so-called local energy estimates that quantify and measure certain local texture properties. These final measurements represent the feature vectors that will form the basis for solving the image analysis problem in hand.

A number of different versions of filtering methods along with comparisons between their performances are given in this comparative study [74]. Among the most popular and widely used filtering methods are Gabor filters [75] and Leung and Malik filter bank (bank of LM filters) [76]. Gabor filters can be generally regarded as edge and bar (line) detectors, and are orientation and scale tuneable, and measurements derived from these filters in a given texture region are often used to characterise the underlying texture details [32, 77]. A two-dimensional Gabor function is made up of a sinusoidal plane wave modulated by a two-dimensional Gaussian envelope at a specific frequency and orientation [36, 75]. The Gabor filter in the spatial domain is, therefore, given by the following equation 2.5:

$$f(x, y) = \exp\left(-\frac{1}{2}\left[\frac{x^2}{\sigma_x^2} + \frac{y^2}{\sigma_y^2}\right]\right) \cos(2\pi u_0 x + \phi) \quad (2.5)$$

Where the values σ_x and σ_y are the space constants of the Gaussian envelope along the x and y directions, respectively, and u_0 and ϕ are the frequency and phase of the sinusoidal plane wave along the x direction, i.e.: the 0° orientation. The Gabor filter at any arbitrary orientation, θ_0 , can be obtained using equation 2.5 via a rigid rotation of the x and y coordinate system by θ_0 .

The Gabor filter is a frequency and orientation selective filter, and this is more explicit in its frequency domain representation [36, 75]. When the phase $\phi = 0$, the Fourier transform of the Gabor filter in equation 2.5 is real-valued and given by the following equation 2.6:

$$F(u, v) = A \left(\exp\left(-\frac{1}{2}\left[\frac{(u-u_0)^2}{\sigma_u^2} + \frac{v^2}{\sigma_v^2}\right]\right) + \exp\left(-\frac{1}{2}\left[\frac{(u+u_0)^2}{\sigma_u^2} + \frac{v^2}{\sigma_v^2}\right]\right) \right) \quad (2.6)$$

Where $A = 2\pi\sigma_x\sigma_y$, $\sigma_u = 1/(2\pi\sigma_x)$ and $\sigma_v = 1/(2\pi\sigma_y)$. The Fourier domain representation given in equation 2.6 determines the amount by which the filter modulates or modifies each frequency element of the input image [75].

Characterising complex patterns within texture images based on Gabor filters is usually accomplished using a bank of Gabor filters and it is defined by the values of its parameters including orientations and frequencies. Various settings for tuning and selecting the values of the parameters have been proposed in the literature, and the banks of filters generated by these settings work well in practice. Further details about obtaining the Gabor features as well as the parameters' tuning settings and selections can be accessed in these studies [32, 66, 75, 77, 78]. A number of previous works have adopted

Gabor features to solve a number of image analysis problems. For example, image texture segmentation and classification [75, 79, 80], image recognition [81–83], medical image registration [84, 85], motion tracking [86], and many more problems [77].

However, according to experimental studies in [87, 88], Gabor features are generally prone to fail under the presence of variations in scale and rotation [32]. Furthermore, Gabor filters are non-orthogonal and hence this implies that there is redundant or correlated information in the filter responses (Gabor features) [77]. Nevertheless, Gabor filters can capture structural texture features over a wider range of scales as well as multiple orientations [32]. It has also been demonstrated in a recent comparison study [87] that for large datasets with variations in illumination conditions, Gabor filters as a pre-processing step could serve as an efficient texture analysis algorithm to facilitate capturing stable texture features with reasonable robustness [32, 39, 89].

The bank of LM filters approach [76], on the other hand, pioneered addressing the issue of classifying various texture images under variations in viewing angles or directions and changes in illumination conditions [32]. This filtering approach is mainly developed for extracting texture features and it comprises a combination of spot, bar and edge filters at a range of various scales and multiple orientations. Nevertheless, this filtering approach may be criticised on one main ground, which is its limitation to the task of classifying a novel texture image based on a set of previously registered texture images under previously known imaging parameters [90]. Indeed, the applicability of this approach is very limited in several practical applications since details about the imaging conditions, such as illumination and viewing geometry, may be unavailable.

2.4.1.5 Local Texture Descriptors

The overall objective of texture representation techniques that fall under the category of local texture descriptors is to produce local texture representations, i.e.: appearance texture measurements of relatively small texture patterns that are dissimilar from their surrounding or immediate neighbourhood patterns. The local texture representations are typically robust and effective under several challenging image texture conditions. These include differences in illuminations, scale, rotation and perhaps other difficult imaging conditions. This category of texture representation can be divided further into two subcategories based on the method of measuring the texture of the images. These constitute either a sparse local texture descriptor, which means only certain pixels or locations of interest are visited or a dense local texture descriptor, which means every single pixel of the texture image to be measured is visited [32].

Sparse local texture descriptors: In this type of local texture descriptor, the process of measuring image texture in a sparse manner starts with designing a region detector that is capable of stably and reliably identifying a sparse set of areas of interest under different imaging conditions. A typical practice in this approach is that the identified set of locations of interest undergo a geometric normalisation [32]. The process is then followed by applying one or more local texture descriptors to encode the image texture contents. Early studies to introduce the sparse local texture descriptors to texture recognition include works by Lazebnik et al. [90, 91], which are then followed by Zhang et al. [88]. A number of different region detectors and local texture descriptors have been proposed in the literature and these outstanding surveys [92–94] provide comprehensive reviews and comparisons between their performances.

The total number of texture features derived from a set of interesting regions in a sparse way is significantly lower than the number of image texture pixels which can provide several advantages. For example, this ends up with a reliable way of measuring image texture as well as a neatly packed feature space facilitating solving several image texture analysis tasks such as classification or segmentation. Nevertheless, the sparse based texture representation techniques are generally inappropriate for many image texture analysis problems for several reasons [32]. More importantly, the region of interest detectors typically generate a set of sparse outputs; however, this may cause missing of several important texture patterns. Another major concern with the set of sparse outputs is that it may not be sufficient to produce robust statistical representations from relatively small texture images. Moreover, there are several problems associated with the repeatability of region of interest detectors, the lack of stability of orientation estimation and the stability of the detected regions [32, 93]. Because of the aforementioned limitations, the sparse local texture descriptors are among the least commonly utilised texture representations techniques in solving various image texture analysis problems.

Dense local texture descriptors: This type of local texture descriptor on the other hand extracts local texture features densely from every single pixel which can provide a sufficient and comprehensive statistical characterisation of texture images. Among the commonly utilised techniques to quantify image texture using a dense local texture descriptor based on a nonparametric dense local texture transformation [58, 95]. A nonparametric dense local texture transformation is a dense local texture description that considers the relative ordering, differences and organisation of the values of pixel intensity, rather than the values of pixel intensity themselves during the derivation of

the texture measurements [58, 95]. This category of dense local texture descriptors is considered to be one of the most popular and widely used texture representation techniques for many image texture analysis tasks, including classification and segmentation [32, 39]. Examples of noticeable, compact and efficient approaches that belong to this category include the Local Binary Pattern (LBP) descriptor of Ojala et al. [24, 96, 97] and the Binary Robust Independent Elementary Features (BRIEF) descriptor of Calonder et al. [98, 99].

The basic idea of the original LBP texture descriptor of Ojala et al. [96, 97] is based on the assumption that a two dimensional phenomenon of texture image, e.g.: a greyscale texture image, has two locally orthogonal complementary properties [39]. The first property is the spatial structure (local patterns) while the latter property is the strength of the patterns (local contrast). In the case of a greyscale texture image, the local patterns are estimated from each pixel in the image based on a fixed scale of a 3×3 neighbourhood block of pixels and use the value of the central pixel as a threshold value. Figure 2.11, demonstrates an illustrative example of deriving local texture measurements based on the basic idea of the original LBP texture descriptor. Figure 2.12 shows an example of the application of the LBP descriptor on a real texture data. An image demonstrating retinal blood vessels texture of a human eye with its corresponding LBP image and the histogram of LBP patterns are demonstrated.

The local pattern details by definition are independent of the greyscale levels, but the local contrast information is not [39]. Likewise, the local contrast measurements are not affected by changes in rotations, however, the local pattern details are sensitive by default [39]. Hence, relying on a pure greyscale invariant texture descriptor may waste very useful texture details. Motivated by these factors, the two different properties complement each other in such a very advantageous way and can provide robust local texture measurements.

A key advantage of the original LBP texture descriptor methodology includes capturing extremely fine-grained texture details from texture images. However, giving the ability to capture only very tiny texture structures at such a very small scale can present a major drawback to the original LBP texture descriptor. This is because capturing different sizes of texture patterns or structures at varying scales is not possible as the LBP methodology is only based on a fixed scale of a 3×3 neighbourhood block of pixels.

Nevertheless, several years following the original proposal of LBP texture descriptor methodology, the LBP has been revisited by Ojala et al. [24] proposing an enhanced

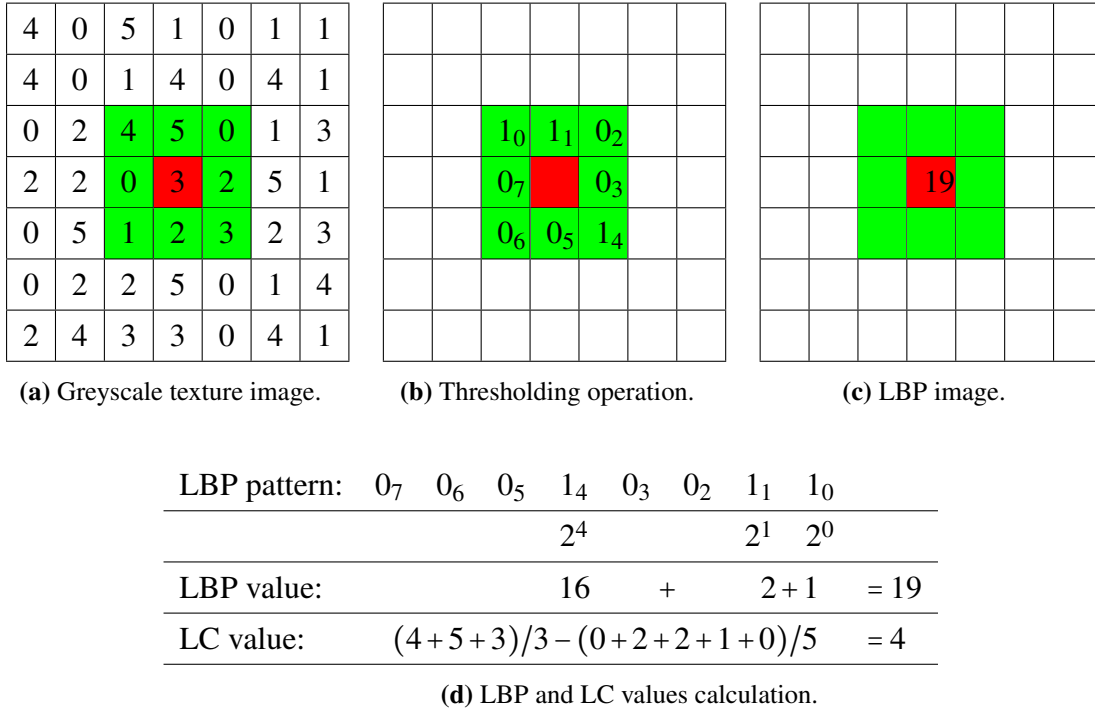
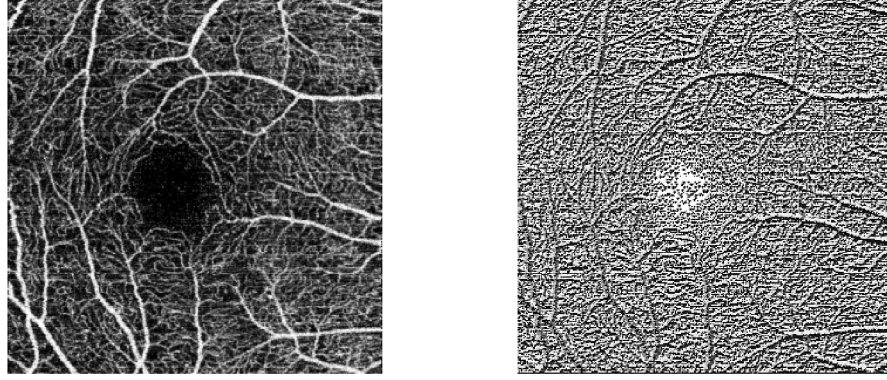


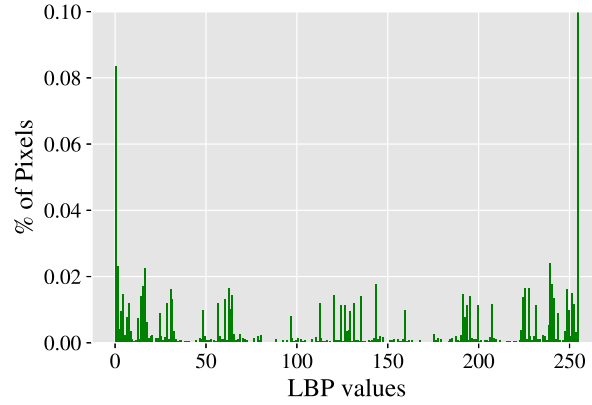
Figure 2.11: An illustrative example of extracting local texture features based on the original LBP texture descriptor using a greyscale texture image. (a) Shows an input greyscale texture image. For illustration purposes, the process here involves extracting a single local texture pattern and local contrast (LC) using 8 pixel neighbourhood (highlighted in green) surrounding a central pixel (highlighted in red) from the middle area of the image, though this can be from anywhere and can be based on the entire image or on certain regions within the image. (b) Demonstrates the thresholding operation to generate a set of 8 binary digit (LBP patterns) that describe the local texture area. It can start from any pixel in the neighbourhood block but here it starts at the top left in a clockwise manner. Any pixel intensity value in this neighbourhood that is greater than or equal to the central pixel value is given the value “1”, or “0” otherwise. This gives an 8-bit binary number and there is a total number of $2^8 = 256$ potential combinations of LBP patterns that can be identified. In this example, the identified LBP pattern is (00010011). The process is then followed by transforming the LBP pattern into a decimal number (LBP value). (c) Represents the LBP image where each LBP value of the identified local pattern is assigned to its local position (the central pixel on which the measurements were performed). (d) Demonstrates the way of calculating the LBP and LC values. The LC value is measured by subtracting the average of a neighbourhood block of pixel values that is lower than the central pixel value from the average of a neighbourhood block of those pixel values greater than or equivalent to the central pixel value. When all thresholded neighbourhood blocks of pixels have been given the same values, such as all having the value of “1’s” or “0’s”, the LC value is set to zero. In certain situations where a complete greyscale invariance description is not required, the availability of the supplement measure (LC value) can enhance the accuracy.

extension in a more universal revised form that can handle adjustable sizes of neighbourhood pixels. In contrast to its original methodology, this extension puts no limits



(a) An input texture image

(b) An output LBP image



(c) A histogram of LBP patterns distribution.

Figure 2.12: An application of the original LBP methodology on real texture data. (a) Shows an input texture image of retinal blood vessels of a human eye. (b) Demonstrates its corresponding LBP image. (c) Represents the histogram of LBP patterns distribution (number of pixels that share same LBP values).

on the neighbourhood size or on the number of sampling pixels. Hence, this extension provides the capacity to capture not only small scale but also large scale texture patterns or structures that may be the dominant texture features. To handle measuring texture patterns at varying scales, Ojala et al. [24] introduced two parameters, namely p and r , where $p > 1$ and $r > 0$ to the original LBP texture descriptor methodology so as to construct a generic $LBP_{p,r}$ texture descriptor, as follows:

1. The parameter p controls the number of sampling pixels in an evenly spaced circularly symmetric neighbourhood to be considered. Consequently, it removes the dependency on only a fixed square neighbourhood block of pixels.

2. The parameter r defines the circle radius of the circularly symmetrical neighbourhood of pixels which in other words specify the distance between the central pixel and the neighbourhood of p sampling pixels. Hence, this parameter allows the measurement of different texture patterns or structures at various scales.

The enhanced version of $LBP_{p,r}$ texture descriptor measures the image texture as follows. Given a two dimensional greyscale image (x,y) , the grey level values g of p individual sampling pixels can, therefore, be denoted as g_n at (x_n, y_n) , where $n = (0, 1, 2, 3, \dots, p-1)$, and the grey level value of any arbitrary single central pixel can be symbolised as g_c at (x_c, y_c) . When the coordinate of the central pixel g_c in the two dimensional image at (x_c, y_c) is $(0,0)$, the coordinates of all p sampling pixels g_n at (x_n, y_n) are then estimated by $(-r \sin(2\pi n/p), r \cos(2\pi n/p))$. If any of the p individual sampling pixels g_n does not fall accurately within the centre of a pixel in the image, its location is then estimated by bilinear interpolation [24, 39]. Figure 2.13 demonstrates a visualisation of circularly symmetrical neighbour sets with varying (p, r) parameters used to construct $LBP_{p,r}$ patterns.

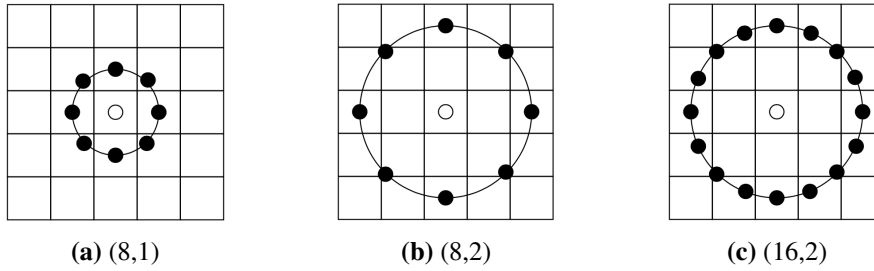


Figure 2.13: Visualisation of three different local circularly symmetrical neighbour sets with different (p, r) parameters [39]. (a) Represents $(8,1)$, (b) shows $(8,2)$ and (c) illustrates $(16,2)$ of varying (p, r) parameters. The locations of any sampling points of pixels in the neighbourhood are bilinearly interpolated if they are not exactly located in the centre of a pixel.

Estimating the values and coordinates of all p sampling pixels can be accomplished in any ordering direction, e.g.: a clockwise or an anticlockwise manner. Additionally, it may start from any location in the circularly symmetric neighbourhood of p sampling pixels. For example, the starting sampling pixel, i.e.: g_0 , can be assigned to be the pixel located to the right or the left of central pixel g_c . However, the selected direction of ordering technique as well as the location of the starting sampling pixel g_0 must be kept consistent.

Nevertheless, once the values and coordinates of all p sampling pixels g_n at (x_n, y_n)

are estimated, the $LBP_{p,r}$ texture descriptor typically characterises the texture of images by considering only the signs of difference between the grey level values of the central pixel g_c and the neighbourhood of p individual sampling pixels g_n instead of their exact grey level values, such that $s(g_0 - g_c), s(g_1 - g_c), \dots, s(g_{p-1} - g_c)$. In doing so, this makes the $LBP_{p,r}$ texture descriptor by definition even more robust against any greyscale monotonic transformation due to, for example, uneven illumination. The individual signs of differences are then typically passed through a thresholding operation $s(x)$, i.e.: a binary test step, as defined by the following function 2.7.

$$s(x) = \begin{cases} 1 & \text{if } x \geq 0 \\ 0 & \text{Otherwise} \end{cases} \quad (2.7)$$

The thresholding operation $s(x)$ given in function 2.7 constructs different p bit binary numbers or binary strings, i.e.: various local binary patterns. Nevertheless, the individual binary numbers, i.e.: 0 and 1, in the local binary patterns of different regions visited, i.e.: different central pixels, are typically individually weighted by powers of two, i.e.: 2^n and summed to convert the binary strings into decimal representations. The resulting decimal representations are then typically used to label the individual regions, i.e.: individual central pixels, that are being visited and measured. The mathematical expression of the generic $LBP_{p,r}$ texture descriptor for characterising the textural appearance around any random region, i.e.: any arbitrary central pixel g_c at (x_c, y_c) in the various two dimensional images can, therefore, be formally defined by the following equation 2.8.

$$LBP_{p,r}(x_c, y_c) = \sum_{n=0}^{n=p-1} s(g_n - g_c) 2^n \quad (2.8)$$

In practice, the generic $LBP_{p,r}$ texture descriptor given in equation 2.8 can generate 2^p potential combinations of $LBP_{p,r}$ patterns, i.e.: 2^p potentially distinct decimal values. These different possible $LBP_{p,r}$ patterns typically measure specific spatial structure of local texture features, e.g.: corners, edges and so on, see Figure 2.14, that may appear in the texture of various images.

While the generic $LBP_{p,r}$ texture descriptor is invariant to changes in illumination, it can, however, be very sensitive to any orientation variations in the texture of images. This is because when the orientation of an image changes, the values and coordinates of all p sampling pixels g_n at (x_n, y_n) will correspondingly change along the perimeter of the circularly symmetric neighbourhood. When the location of the starting sampling

pixel, i.e.: g_0 , is allocated to be the pixel positioned to the right of central pixel g_c , rotating a specific $LBP_{p,r}$ pattern certainly results in a different decimal representation or value. However, this case does not apply to $LBP_{p,r}$ patterns that are all 0s or 1s as these patterns will always be the same no matter if the rotation of the texture image changes at any angle.

Nevertheless, the rotation invariant uniform $LBP_{p,r}^{2riu}$ texture descriptor version of Ojala et al. [24] can alleviate the sensitivity to any rotation changes as well as add an extra level of tolerance capacity to any illumination variations in texture images. This is because it combines two different versions of $LBP_{p,r}$ texture descriptor, namely the rotation invariant $LBP_{p,r}^{ri}$ and the uniform $LBP_{p,r}^{2u}$ texture descriptors. The rotation invariant $LBP_{p,r}^{ri}$ texture descriptor, as the name suggests, can provide the advantage of being very robust with respect to any changes in image rotation. The effect of image rotation is removed in the $LBP_{p,r}^{ri}$ texture descriptor by mapping, i.e.: circularly rotating, every $LBP_{p,r}$ pattern into its minimum representation. Consequently, the mathematical expression of the $LBP_{p,r}^{ri}$ texture descriptor to estimate the rotation invariant local texture features around any random regions, i.e.: any arbitrary central pixels g_c at (x_c, y_c) from the texture of images is formally defined by the following equation 2.9.

$$LBP_{p,r}^{ri}(x_c, y_c) = \min\{ROR(LBP_{p,r}(x_c, y_c), n) | n = (0, 1, 2, 3, \dots, p-1)\} \quad (2.9)$$

The $ROR(LBP_{p,r}(x_c, y_c), n)$ function given in the previous equation 2.9 performs a circular bit-wise right shift, i.e.: a right rotation, on the p bit binary numbers or binary strings, i.e.: the $LBP_{p,r}$ patterns, by n steps. In other words, it simply corresponds to rotating the neighbourhood of p sampling pixels in a clockwise direction several steps so as the minimal number of the least significant bit i.e.: the bit furthest to the right in the $LBP_{p,r}$ pattern, starting from g_0 , is 1. For example, given several $LBP_{p,r}$ patterns with $p = 8$ bit binary numbers, e.g.: 00000010, 00000100, and 00001000, are all mapped to the minimum $LBP_{p,r}$ pattern, i.e.: 00000001, by 1, 2 and 3 steps respectively.

The uniform $LBP_{p,r}^{2u}$ texture descriptor, on the other hand, can provide numerous advantages including statistical robustness and stabilities of the uniform local texture features derived, i.e.: the uniform $LBP_{p,r}^{2u}$ patterns. As such the uniform $LBP_{p,r}^{2u}$ patterns are demonstrated to be less hampered by and more resistant to image noise, as evidenced by numerous previous studies [24, 39, 100]. The uniform $LBP_{p,r}^{2u}$ texture descriptor works by calculating the number of bitwise pattern transitions from 1 to 0 or

vice versa in the constructed $LBP_{p,r}$ patterns. The uniformity pattern measure of the $LBP_{p,r}^{2u}$ texture descriptor is formally defined by the following equation 2.10.

$$u(LBP_{p,r}) = |s(g_{p-1} - g_c) - s(g_0 - g_c)| + \sum_{n=1}^{n=p-1} |s(g_n - g_c) - s(g_{n-1} - g_c)| \quad (2.10)$$

Based on the uniformity pattern measure $u(LBP_{p,r})$ given in the previous equation 2.10, the $LBP_{p,r}$ pattern is considered as a uniform $LBP_{p,r}^{2u}$ pattern if the value of the uniformity pattern measure, i.e.: the number of bitwise pattern transitions, is at most two. For example, the following $LBP_{p,r}$ patterns 00000000 has zero transitions, 00000001 has one transition and 00111000 has two transitions, which are all considered as uniform $LBP_{p,r}^{2u}$ patterns since they comprise at most two bitwise 1/0 or 0/1 changes. However, as regards the following $LBP_{p,r}$ patterns, 11000101 has four transitions, 01010011 has five transitions and 01101010 has six transitions, which are not considered as uniform $LBP_{p,r}^{2u}$ patterns since they include more than two bitwise 1/0 or 0/1 changes. Various local texture patterns are captured by the $LBP_{p,r}^{2u}$ texture descriptor and these include curves, flat areas, edges, spots, line ends and so on. Figure 2.14 demonstrates some examples of local texture structures or patterns captured by the $LBP_{p,r}^{2u}$ texture descriptor with 8 neighbourhood of pixels.

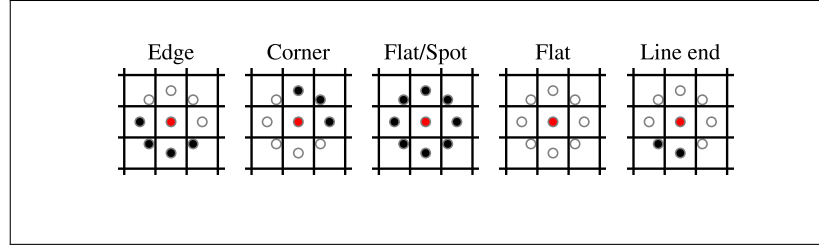


Figure 2.14: Visualisation of different local texture structures or patterns detected by the $LBP_{p,r}^{2u}$ texture descriptor with 8 neighbourhood of pixels [39]. In these neighbourhoods, bit values of ones and zeros in the identified uniform $LBP_{p,r}^{2u}$ patterns are represented in black and white circles while the red circles denote the central pixels.

Given the outstanding advantages, e.g.: statistical stabilities and robustness with respect to image noise that the previously mentioned texture descriptors, i.e.: the $LBP_{p,r}^{ri}$ and the $LBP_{p,r}^{2u}$ can provide, the $LBP_{p,r}^{2riu}$ can, therefore, be viewed as a very powerful texture descriptor. Nevertheless, the mathematical expression of the $LBP_{p,r}^{2riu}$ texture descriptor to estimate rotation invariant uniform local texture features around any random region, i.e.: any arbitrary central pixel at (x_c, y_c) in the various two dimensional

images, is formally expressed by the following equation 2.11.

$$LBP_{p,r}^{2riu}(x_c, y_c) = \begin{cases} \sum_{n=0}^{n=p-1} s(g_n - g_c) & \text{if } u(LBP_{p,r}) \leq 2 \\ p+1 & \text{Otherwise} \end{cases} \quad (2.11)$$

By definition, only $p+1$ rotation invariant uniform local binary patterns, i.e.: rotation invariant uniform $LBP_{p,r}^{2riu}$ patterns, can occur in a circularly symmetric neighbourhood of p sampling pixels. The $LBP_{p,r}^{2riu}$ texture descriptor given in equation 2.11 allocates a distinctive integer value or label starting from 0 to p for every single rotation invariant uniform $LBP_{p,r}^{2riu}$ pattern captured. These individual labels correspond to the number of ones, i.e.: “1s” bits, in the rotation invariant uniform $LBP_{p,r}^{2riu}$ patterns, while the non-uniform $LBP_{p,r}^{2riu}$ patterns are all together grouped under an assorted label, i.e.: a single integer value given by $p+1$. Figure 2.15 demonstrates an excellent visualisation of all potential rotation invariant uniform $LBP_{p,r}^{2riu}$ patterns that can occur in a circularly symmetric neighbourhood of p sampling pixels with $p = 8$.

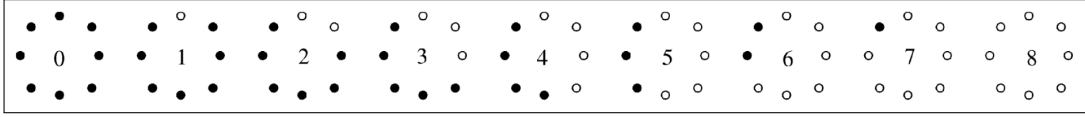


Figure 2.15: Visualisation of all potential rotation invariant uniform circular patterns or structures that comprises unique spatial transitions detected by the rotation invariant uniform $LBP_{p,r}^{2riu}$ texture descriptor with 8 neighbourhood of pixels [24]. Within these rotation invariant uniform circular patterns, bit values of zeros and ones are demonstrated in black and white circles. All distinct values for rotation invariant uniform $LBP_{p,r}^{2riu}$ patterns are denoted inside each neighbourhood ($0 \Rightarrow 8$) while all other non-uniform $LBP_{p,r}^{2riu}$ patterns, when they occur, will be grouped under the value of 9

In Figure 2.15, all possible distinctive output values or labels that starting from 0 to 8 for every single rotation invariant uniform $LBP_{p,r}^{2riu}$ pattern are given inside each circularly symmetric neighbourhood of eight sampling pixels. However, all other non-uniform $LBP_{p,r}^{2riu}$ patterns are grouped together under a single integer value of $p+1$ i.e.: 9. The rotation invariant uniform $LBP_{p,r}^{2riu}$ patterns function as shapes for microstructures appear in examined surface textures [24]. For example, patterns with a value of 0 denotes bright spots, 8 indicates flat areas or dark spots and $1 \Rightarrow 7$ suggest edges of variable negative and positive curvatures [24]. Consequently, the $LBP_{p,r}^{2riu}$ texture descriptor can generate $p+2$ distinctive output labels or values in total. These different values also typically quantify specific spatial structure of local texture features, e.g.: corners, edges and so on, see Figure 2.14, which may appear in the texture of various

images.

The enhanced or generic form of $LBP_{p,r}$ texture descriptor including other versions of it such as the rotation invariant uniform $LBP_{p,r}^{2riu}$ texture descriptor attained an established position and have been widely exploited in a broad range of computer vision applications. Examples of most notable ones include facial image analysis [101, 102], image and video retrieval [103, 104], forest environment modelling [105], pedestrian detection [106], visual characterisation and inspection [107, 108], motion analysis and recognition [109, 110], aerial and biomedical image analysis [111, 112], remote sensing [113] and many more [95]. Generally, in all situations such as when large or limited training data sets are available with rotation variations and illumination related changes, the rotation invariant uniform $LBP_{p,r}^{2riu}$ texture descriptor version can serve as an effective and efficient method to capture well representative texture features [32].

The BRIEF descriptor methodology of Calonder et al. [98, 99], on the other hand, shares the same general concept of the enhanced $LBP_{p,r}$ texture descriptor to form the representations as binary strings on the basis of performing pairwise comparisons based on a predefined small set of sampling pixels. However, there are several differences between them. Unlike the $LBP_{p,r}$ texture descriptor, the BRIEF descriptor methodology was originally proposed for image matching and it comprises two key components. The first component is the utilisation of a region detector. This is to mark a certain sparse set of keypoint locations or interesting regions. The second component is the application of a descriptor. This is to generate descriptions on the basis of pixels' intensity difference binary tests. These descriptions are obtained from a number of image patches of size $S \times S$ pixels extracted around each keypoint or interesting region detected after applying a Gaussian smoothing over the patches to reduce the noise sensitivity.

Another difference includes the spatial arrangement techniques of the sampling points of pixels for performing the binary tests to generate the description. The sampling points techniques in the $LBP_{p,r}$ texture descriptor are only based on equally spaced circularly symmetrical neighbourhood of pixels, while in the BRIEF descriptor they can involve one of five different sampling strategies, which can be random or regular. Figure 2.16 demonstrates five different options of sampling points techniques for selecting the binary test locations in the BRIEF descriptor. Experimental evaluation conducted by Calonder et al. [98] shows that the random sampling generally performs better than the symmetrical.

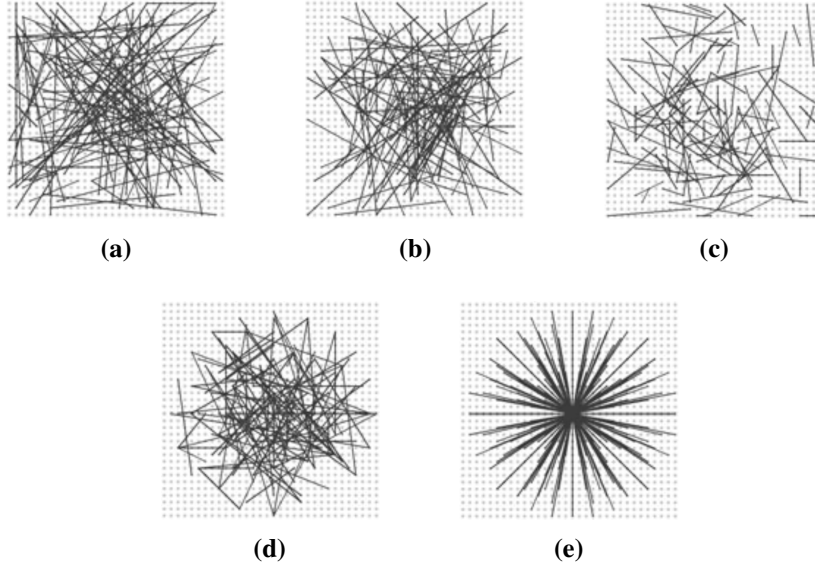


Figure 2.16: Visualisation of five different sampling points locations strategies that define a set of binary tests using the BRIEF descriptor [98]. (a)-(d) show random sampling strategies while (e) illustrates a symmetrical and regular sampling strategy.

Consequently, the main steps involved in the original BRIEF descriptor methodology can be summarised as follows. It starts with marking keypoints or regions using a region detector. It is then followed by smoothing the image patches of size $S \times S$ pixels, which are sampled around each interest keypoint. The final process is then creating a bitstring out of binary tests responses. These binary tests are conducted within every smoothed image patch based on a predefined set of n pixel pairs selected at symmetrical or random locations as explained earlier in Figure 2.16. For instance, the intensities of a given pixel pair that are arranged based a certain sampling strategy in the smoothed image patch are compared in such a way that if the intensity value of one pixel is less than the other one then the binary test result is set to '1', else it is set to '0'. This process of pixel intensity comparison is applied for all n location pixel pairs located within the smoothed image patch to generate an n -dimensional bitstring that defines the final output of the BRIEF descriptor. Different values of n can be considered, which define the set of location pixel pairs or the set of binary tests. In the original BRIEF descriptor of Calonder et al. [98], the following different values of n tests, namely 128, 256 and 512, have been used and demonstrated in general quite good compromises between storage efficiency, speed and recognition rate.

Although the original BRIEF descriptor was not essentially designed to be rotationally invariant, empirical evaluation experiments results utilising six different test

data sets conducted by Calonder et al. [98,99] demonstrate that it can tolerate insignificant amounts of rotation. Furthermore, the noise sensitivity of the original BRIEF descriptor to uneven illumination is controlled with a smoothing operation applied on every image patch. This is because the BRIEF descriptor only takes into account the relative values of pixels' intensities when comparing the pixel pairs. Therefore, it is noise sensitive as any minor changes to the pixel's intensities, due to for instance, illumination variations, may cause the pixels' pairwise test responses to change from '1' to '0' or vice versa [58]. Consequently, the smoothing operation can increase the repeatability and stability of the BRIEF descriptor and hence, make it more robust against any illumination related changes [58,98,99]. As a result, under some special situations such as for a data set with illumination variations but no particularly significant rotation changes, the BRIEF descriptor can serve as an effective and efficient texture representation technique to solve various image texture analysis tasks.

However, the basic idea of the BRIEF descriptor is based on keypoints locations or interesting regions detection which is then followed by a characterisation of every keypoint or interesting region detected. Therefore, this local descriptor is used in a sparse manner similar to that of Lazechnik et al. [90,91]. However, as mentioned earlier at the beginning of this subsection, the sparse based representation techniques are demonstrated to be very complex as well as to have the potential to miss several important texture patterns or elements due to their sparse scheme. Nevertheless, the original BRIEF descriptor methodology has been modified and utilised in a dense manner in a wide variety of computer vision tasks such as classification and segmentation and demonstrated better and more remarkable results compared to other well established texture representation techniques such as the GLCM, GLD and LBP approaches. Noticeable recent works include using the BRIEF features for texture classification and segmentation tasks of retinal images such as those ones by Mohammad et al. [114,115] and Morris and Mohammad [116].

There are a few modifications of the original BRIEF descriptor methodology that have been introduced in these works [114,114,116]. The modified version of the $BRIEF_{S,n}$ texture descriptor relies on adjusting two important parameters, namely S and n . The value of S regulates the size of image patches P , i.e.: $S \times S$ pixel dimension, and the value of n controls the number of n sampling pixels, i.e.: n sampling pixel pair set, to be considered within the individual image patches P . Once these values, i.e.: S and n are defined, the $BRIEF_{S,n}$ texture descriptor typically quantifies the texture of images by considering only the signs of difference between the grey level values of the

n sampling pixel pair set instead of their exact grey level values. The individual signs of differences within every image patch P of size $S \times S$ pixels are then typically passed through a thresholding test operation $\tau(P : X, Y)$, i.e.: a binary test step, as defined by the following function 2.12.

$$\tau(P : X, Y) = \begin{cases} 1 & \text{if } (P(X) - P(Y)) > A \text{ threshold value} \\ 0 & \text{Otherwise} \end{cases} \quad (2.12)$$

Where $P(X)$ and $P(Y)$ are the grey level values of n pixel pairs within the image patch P that are ordered at symmetrical or random locations X and Y as previously illustrated in Figure 2.16. The threshold value, on the other hand, is estimated based on the image noise level, i.e.: noise standard deviation (σ). As in previous studies [58, 114, 116], the noise standard deviation (σ) is calculated through blurring the image using a Gaussian filter. The Gaussian filter is estimated by using the following two-dimensional Gaussian function 2.13:

$$G(x, y) = \frac{1}{2\pi\sigma^2} e^{-\frac{(x^2+y^2)}{2\sigma^2}} \quad (2.13)$$

Where x and y are the distances from the origin in the horizontal and vertical axes, respectively, and σ is the standard deviation of the Gaussian distribution. The process is then followed by subtracting the filtered image from the original image. The resultant image is subsequently anticipated to only include the noise signal. The noise standard deviation (σ) is, consequently, estimated from the resultant image.

Nevertheless, the thresholding test operation $\tau(P : X, Y)$ given in function 2.12 constructs different n bit binary numbers or binary strings, i.e.: various local binary patterns. The individual binary numbers, i.e.: 0 and 1, in the local binary patterns of different regions visited, i.e.: different image patches P , are typically individually weighted by powers of two, i.e.: 2^{i-1} where $(1 \leq i \leq n)$, and summed to convert the binary strings into decimal representations. The resulting decimal representations are then typically used to label the individual regions, i.e.: individual image patches P , that are being visited and measured. The mathematical expression of the $BRIEF_{S,n}$ texture descriptor for characterising the textural appearance around any random region, i.e.: any arbitrary image patch P in the two dimensional images can, therefore, be formally defined by the following equation 2.14.

$$BRIEF_{S,n}P = \sum_{1 \leq i \leq n} \tau(P : X_i, Y_i) 2^{i-1} \quad (2.14)$$

In practice, the $BRIEF_{S,n}$ texture descriptor given in equation 2.14 can generate 2^n potential combinations of $BRIEF_{S,n}$ patterns, i.e.: 2^n potentially distinct decimal values. These different possible $BRIEF_{S,n}$ patterns typically measure the specific spatial structure of local texture features that may appear in the texture of various images. These measurements form the basis of solving the image texture analysis task such as classification or segmentation.

2.4.2 Learned Category

Texture representation techniques under the learned category are based on the so-called “deep learning”. Deep learning can be regarded as a part of a wider computer science discipline, specifically the machine learning field that deals with the constructions of computational statistics and algorithms motivated primarily by the neural structure and function of the central nervous system (CNS) of the biological brain (whether a human or another animal) named Artificial Neural Networks (ANN) [117]. The ANN algorithms are also mainly supported by the fact that the brain is the sole real existing operational instance of such an extremely proficient pattern recognition system [118].

The main building blocks for ANN algorithms are the artificial neurons. Figure 2.17 shows the typical structure of a simple artificial neuron model. This artificial neuron model can be viewed as a computational node or unit in which all n inputs data values $\{x_1, \dots, x_n\}$ are individually weighted by n weights $\{w_1, \dots, w_n\}$, then summed. The process is then followed by passing the result of the weighted sum through an activation function, sometimes termed a transfer function, to determine the final output y of the neuron.

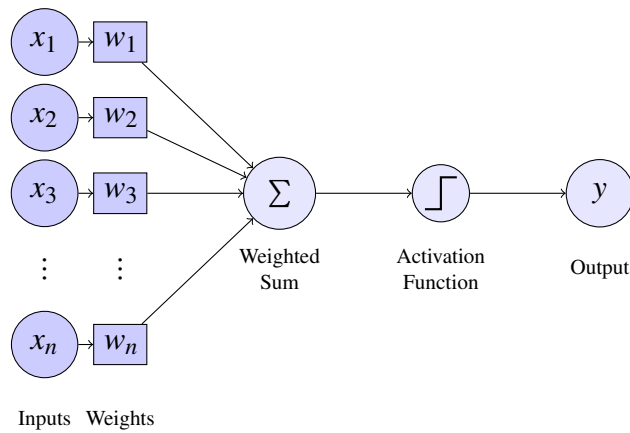


Figure 2.17: A typical structure of a simple artificial neuron model.

Formally, the artificial neuron performs the following calculation given by equation 2.15:

$$z = b + \sum_{i=1}^n w_i x_i \quad (2.15)$$

Where w_i and x_i are the weights associated with individual inputs data values, respectively, and b is a constant known as a bias and it should be weighted too with w_0 . The final output y of the artificial neuron is, therefore, determined by the following equation 2.15:

$$y = T(z) \quad (2.16)$$

Where $T()$ is the activation function. The task of activation function is typically to perform a simple mapping of the final output of artificial neurons and the resulting values may have the range between 0 to 1 or 0 to infinity. Different activation functions can be employed, and these include a sigmoid activation function, a tanh activation function, and a rectified linear activation function, usually known as a rectified linear activation unit (ReLU) [117]. Mathematically, these different activation functions are defined by the following equations 2.17, 2.18 and 2.19, respectively:

$$T_{sigmoid}(z) = \frac{1}{1 + e^{-z}} \quad (2.17)$$

$$T_{tanh}(z) = \frac{e^z - e^{-z}}{e^z + e^{-z}} \quad (2.18)$$

$$T_{ReLU}(z) = \begin{cases} z & \text{if } z > 0 \\ 0 & \text{Otherwise} \end{cases} \quad (2.19)$$

The choice of the activation function is largely dependent upon the problem type in hand. For instance, the sigmoid activation function is normally utilised with solving binary classification tasks. A classic structure of ANN algorithms comprises a network of artificial neurons and they are typically organised in the form of multiple layers [118]. These multiple layers are generally structured e.g.: an input layer followed by intermediate or hidden layers and the final layer of the intermediate layers is normally referred to as an output layer. With multiple hidden or intermediate layers, an ANN algorithm can be considered as a deep learning algorithm, hence the term “deep learning”.

A typical example of a deep learning algorithm is the feed forward deep artificial neural network or a multiple-layer neural network, referred to as a multilayer perceptron (MLP) [117]. Figure 2.18 displays an illustrative example of representing a textured image that contains a person to be recognised using a deep learning algorithm. The multiple learning levels in the context of learned texture representations by the means of deep learning algorithms is demonstrated. Visualisations of various texture representations, such as edges and corners that are learnt in every single hidden layer are also given.

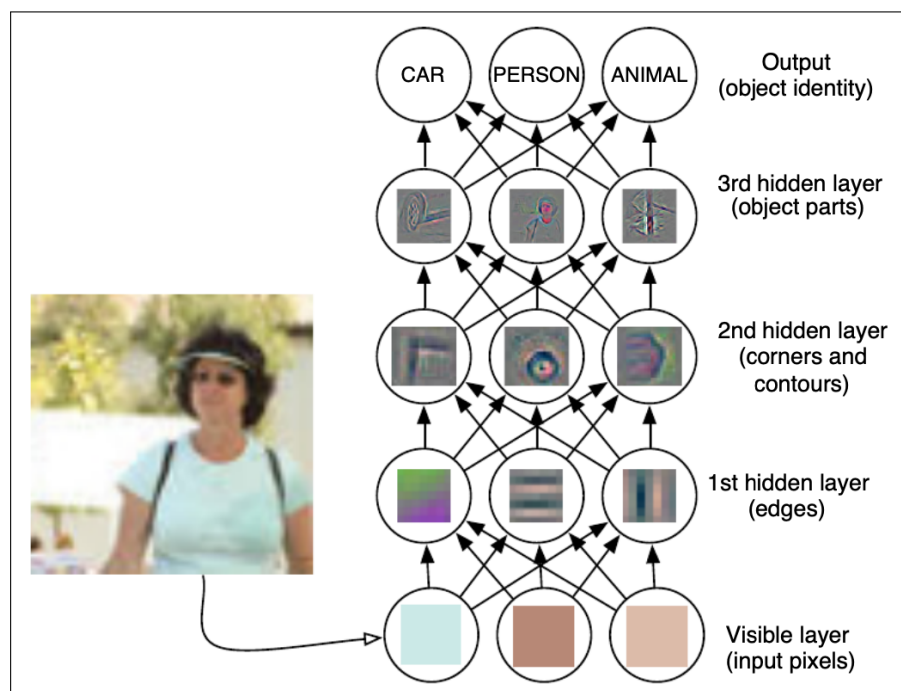


Figure 2.18: An explanatory instance of a deep learning algorithm applied on a textured image that contains a person [117]. The task of this algorithm is to recognise the identity of objects, namely animal, person or car, which may appear in an input textured image. The algorithm takes pixel intensity values as inputs through the input or visible layer. It is then followed by three middle or hidden layers that learn increasingly more complicated texture representations. For instance, the first hidden layer identifies very simple texture representations, namely edges, by comparing the variations in the brightness of neighbouring pixels. The subsequent hidden layers recognise higher texture representations, such as extended contours, in the second hidden layer and whole parts of certain objects in the third hidden layer, based on representations learnt from previous layers. The final layer is the output layer that produces the recognised object identity such as animal, person or car.

There are numerous types of deep learning algorithms, however, deep convolutional networks also usually known as convolutional neural networks, CNN or ConvNets for short, are among the quintessential examples and the most widely used algorithms for image texture analysis and representations takes [32]. In particular, the CNN algorithms are considered as a specialised category of ANN algorithms that have been remarkably successful in a wide variety of practical computer vision applications that involve processing data with a grid like topology [117]. For instance, a two dimensional texture image, which can be seen as a two dimensional matrix or grid of pixel values. The CNN algorithms specifically became popular after the major breakthrough point in 2012 with a special type of CNN algorithm developed by Krizhevsky et al. [119], usually referred to as AlexNet, that accomplished a record-breaking accuracy in an image classification task using a highly challenging data set [32, 117, 120].

Nevertheless, since the image data sets used in this thesis are relatively small and represent a very specific domain, namely medical images, and the fact that there is no a pre-trained deep learning model on a similar domain to be found, the deep learning algorithms and their applications were concisely reviewed here as these have not been touched upon in depth in this research project. However, some of the basic background that is perhaps useful and necessary for understanding deep learning algorithms and applications have been demonstrated in Appendix A, Section A.1. A comprehensive review of deep learning algorithms is, however, beyond the scope of the research presented in this thesis. Consequently, readers are referred to these outstanding surveys and books [32, 117, 120–129] for further details about the various deep learning technologies and applications.

2.5 Classification Approaches

There are a wide variety of classification schemes which can be employed to solve image texture analysis problems. These usually fall under two different classification categories. The first category includes the utilisation of machine learning classification algorithms and the latter category involves the use of distance similarity measure metrics. Each category is reviewed in the following two subsections 2.5.1 and 2.5.2.

2.5.1 Machine Learning Algorithms for Classification

A number of machine learning algorithms are possible to use for performing classifications. However, among the most commonly used classifiers are the Support Vector Machine (SVM) and K-Nearest Neighbour (KNN) [32]. The KNN and SVM classifiers are widely used in texture and medical image analysis methods and both have been demonstrated to perform fairly well, with satisfactorily representative texture features. Every single classifier is reviewed below.

2.5.1.1 Support Vector Machine (SVM)

The Support Vector Machine (SVM) is a type of extremely powerful and highly flexible statistical modelling method that was first established around the mid-1960s by Vladimir Vapnik [130–132]. In the following years, the SVM has evolved significantly and currently is considered as one of the most effective machine learning algorithms available [130]. The main theory behind the original development of SVM was principally for the setting of mere classification modelling problems.

Given a training data set X comprises n sample-class label pairs (x_i, y_i) , where $i = (1, 2, 3, \dots, n)$ and $x_i \in R^d$, where R^d denotes the feature space with d dimensions and $y_i \in \{-1, +1\}$, the SVM classifier learns in what way to separate the different classes (positive and negative) of samples by constructing a decision boundary known as a separating hyperplane. Figure 2.19 visualises the separating hyperplane that separates positive and negative data samples in a linearly separable classification problem.

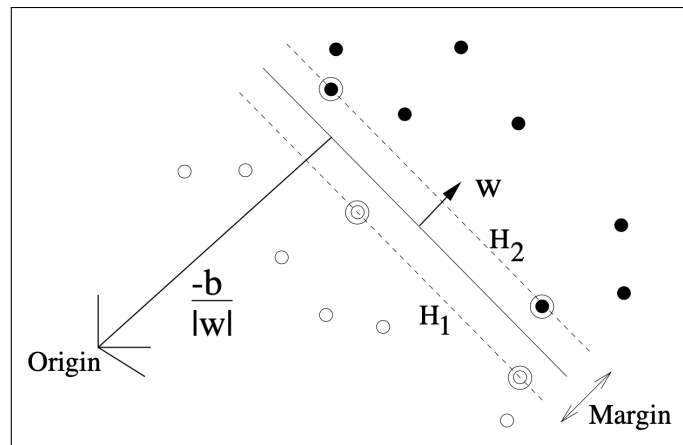


Figure 2.19: The separating hyperplane (middle line between two dashed lines H_1 & H_2) of an SVM classifier that separates two different classes in a linear separable case [133]. The area between the two dashed lines H_1 & H_2 is called the margin. The data samples positioned on the margin sides (two dashed lines H_1 & H_2) are called the support vectors.

Any data samples x_i that lie on the separating hyperplane given in Figure 2.19 should satisfy the following equation 2.20:

$$\mathbf{w} \cdot \mathbf{x} + b = 0 \quad (2.20)$$

Where \mathbf{w} is a vector normal to the hyperplane, \cdot is the dot-product, \mathbf{x} is the input feature vector, and b is a constant. The parameter $\frac{b}{\|\mathbf{w}\|}$ is the perpendicular distance from the hyperplane to the origin and $\|\mathbf{w}\|$ is the length of the vector \mathbf{w} .

Let Distance^+ be the shortest distance between the nearest positive data sample and the separating hyperplane and Distance^- be the shortest distance between the nearest negative data sample and the separating hyperplane. The margin of the separating hyperplane can, therefore, be defined as $(\text{Distance}^+ + \text{Distance}^-)$. For the linearly separable classification problem, the main goal of SVM is simply to find the separating hyperplane with the largest margin. This can be formulated by the following decision function given by equation 2.21:

$$D(\mathbf{x}) = \text{sign}(\mathbf{w} \cdot \mathbf{x} + b) \quad (2.21)$$

With the vector \mathbf{w} and the constant b , the following criteria should be satisfied for all training data samples:

$$\mathbf{w} \cdot \mathbf{x}_i + b \geq +1 \text{ if } y_i = +1 \quad (2.22)$$

$$\mathbf{w} \cdot \mathbf{x}_i + b \leq -1 \text{ if } y_i = -1 \quad (2.23)$$

These two criteria can be combined into the following set of inequalities such that:

$$y_i(\mathbf{w} \cdot \mathbf{x}_i + b) - 1 \geq 0 \forall i \quad (2.24)$$

Consider some data samples that satisfy the equality given in equation 2.22 and lie on the hyperplane \mathbf{H}_1 which is given by the following equation 2.25:

$$\mathbf{w} \cdot \mathbf{x}_i + b = 1 \quad (2.25)$$

With normal \mathbf{w} and perpendicular distance from the origin $\frac{|1-b|}{\|\mathbf{w}\|}$. Likewise, consider some data samples that satisfy the equality given in equation 2.23 and lie on the hyperplane \mathbf{H}_2 which is given by the following equation 2.26:

$$\mathbf{w} \cdot \mathbf{x}_i + b = -1 \quad (2.26)$$

With normal \mathbf{w} , and perpendicular distance from the origin $\frac{|-1-b|}{\|\mathbf{w}\|}$. Consequently, $\text{Distance}^+ = \text{Distance}^- = \frac{1}{\|\mathbf{w}\|}$ and the margin is simply given by $\frac{2}{\|\mathbf{w}\|}$. It should be noted that the hyperplanes \mathbf{H}_1 and \mathbf{H}_2 that define the margin sides are parallel, i.e.: they have the same normal, and no data samples fall between them. As the SVM finds the separating hyperplane that has the largest margin, the optimal separating hyperplane with the maximal margin is, therefore, determined by minimising $\|\mathbf{w}\|^2$:

$$\min_{\mathbf{w}} \|\mathbf{w}\|^2 \quad (2.27)$$

$$\text{Subject to } y_i(\mathbf{w} \cdot \mathbf{x}_i + b) \geq 1 \forall i \quad (2.28)$$

However, it would be hard to assume that all data sets used in most real-world classification problems could be perfectly separated by a straight separating hyperplane. To handle situations like this, a tuning penalty parameter called simply C was introduced to construct a soft margin hyperplane [133–135]. Roughly speaking, the value of C defines how “strict” the margin will be, hence defining the number of violations of the margin allowed.

Nevertheless, when the different classes of samples are not completely separable, motivated by the findings of Boser et al. [136] which provide an extension to the linear nature of the SVM classifier to produce nonlinear classification boundaries, Cortes and Vapnik [134] proposed further enhancements to the soft margin hyperplane to accommodate additional challenging situations by the means of introducing a “kernel function” [130, 137]. The application of kernel function allows the SVM classifier to construct extremely flexible decisions for the classification task of interest, hence this generalisation is usually referred to as a “kernel trick”.

Broadly, the kernel function establishes a measure of similarity or distance between the new data samples and the support vectors. Because the distance measure is a linear combination of the input data samples in the linear SVM, the dot product is the kernel function used for the linear SVM. Nevertheless, other kernels can also be employed instead of the dot product which transform the input feature space into higher dimensions. Among the popular kernels are the Radial Basis Function (*rbf*) and the Polynomial (*poly*) [133, 135]. The *poly* kernel allows for creating curved separating lines in the feature space while the *rbf* kernel is very local and can construct complex

regions. Given x_i training data vectors and x_j hypothetical test points to classify, the *poly* and *rbf* kernel functions are briefly expressed by the following equations 2.30 and 2.29, respectively:

$$K_{poly}(x_i, x_j) = (1 + x_i x_j)^d \quad (2.29)$$

$$K_{rbf}(x_i, x_j) = e^{-\gamma(x_i - x_j)^2} \quad (2.30)$$

Where d is the degree of the polynomial, $\gamma = \frac{1}{2\sigma^2}$ which controls the width of the Gaussian, and σ is the standard deviation.

Nevertheless, the theoretical underpinning behind the SVM classifier along with a comprehensive description of how it works in solving a classification predictive modelling problem are given in Appendix A, Section A.2. However, it is worth mentioning that the SVM classifier demonstrated to be less sensitive to the class imbalance problems compared to other machine learning classification algorithms [138, 139]. This is because the classification boundaries, i.e.: the separating hyperplanes, between the different classes are typically estimated based on only a small number of support vectors, i.e.: data samples. Consequently, the SVM classifier is expected to continue to provide valuable insights into the increasing amounts, variations in class sizes, and diversity of both medical and industrial data sets [137].

2.5.1.2 K-Nearest Neighbour (KNN)

The K-Nearest Neighbour (KNN) is one of the most fundamental and simple non-parametric statistical modelling methods, initially developed by Fix and Hodges [140] around the early 1950s [141, 142]. In particular, Fix and Hodges [140] jointly made a primary contribution to the KNN classifier methodology by developing the first formulation of the nearest neighbour rule that is the first fundamental component of the KNN classifier [142]. Following its original formulation, it became widely known in the pattern recognition communities as the k nearest neighbour vote rule [141]. The general idea of this voting rule is that a new data sample is classified as belonging to the class represented by the nearby k neighbours' majority vote in the training data set, hence the term "K-Nearest Neighbour (KNN)" [130, 141].

To illustrate the notion of the KNN classifier, let it be assumed that a data sample domain, X , is endowed with a distance metric function D . Such that $D: X \times X \rightarrow R$ is a distance metric function which returns the distance between any two data samples

(x, x') of X . For instance, if $X = R^n$, where n is the number of dimensions, then D can be the Euclidean distance metric, which is given by equation 2.31:

$$D_{euclidean}(x, x') = \sqrt{\sum_{i=1}^n (x_i - x'_i)^2} \quad (2.31)$$

Let S be a set of training data samples such that $S = \{(x_1, y_1), \dots, (x_m, y_m)\}$. For every data sample $x \in X$, let $\{z_1(x), \dots, z_m(x)\}$ be a reordering of $\{1, \dots, m\}$ based on their distance to the data sample x , $D(x, x_i)$. That is, $\forall i < m, D(x, x_{z_i(x)}) \leq D(x, x_{z_{i+1}(x)})$. The rule for the KNN classifier to solve a binary classification problem with a number K can, therefore, be formally defined by the following Algorithm 2:

Algorithm 2 KNN Classifier

Input: A set of data samples $S = \{(x_1, y_1), \dots, (x_m, y_m)\}$

Output: For every data sample $x \in X$, return the majority label among $\{y_{z_i(x)} : i \leq K\}$

While the Euclidean distance function is the most commonly used metric with the KNN classifier, other distance metrics are also available. These include Manhattan and Chebyshev distance functions, which are given by the following equations 2.32 and 2.33, respectively:

$$D_{manhattan}(x, x') = \sum_{i=1}^n |x_i - x'_i| \quad (2.32)$$

$$D_{chebyshev}(x, x') = \max_{i=1 \text{ to } n} |x_i - x'_i| \quad (2.33)$$

Nevertheless, the theoretical foundation behind the KNN classifier along with a description of how it works in solving a classification predictive modelling problem are given in Appendix A, Section A.3. However, the advantages of the KNN classifier should not be underestimated and specifically those derived from its simplicity and interpretability [143]. This is because the KNN classifier has been demonstrated to perform fairly excellently with fairly well representative features, key to the retention of its popularity across various domains. With this in mind, it is therefore expected that one can easily achieve outstanding classification results given that the KNN classifier is a very simple and transparent classifier that is specifically suited to apply in certain important domains, such as medical applications, since interpreting and investigating the classification decisions or results are always a very important matter.

2.5.2 Similarity Measure Metrics

There are numerous possible discrimination measures which could be employed for quantifying similarities or performing classifications in predictive modelling tasks such as an image texture classification or a texture region localisation [24, 32, 39]. These include histogram metrics such as intersection distance similarity measure [144] and correlation distance similarity measure [145]. Other nonparametric statistical tests are also possible to use as discrimination measures. For instance, there are several notable goodness-of-fit statistics that can be used, such as the chi-square χ^2 statistic [32, 102, 146] and the log-likelihood statistic [24, 39].

A key advantage of the aforementioned nonparametric statistical tests is that they do not require any assumptions to be made about the distributions of texture features [24, 39]. Hence, these provide robustness against any possible erroneous results that may occur due to incorrect assumptions that might potentially be made about the feature distributions [24]. Other advantages of nonparametric statistical tests include that they do not require a large number of training data sets since there is no statistical or learning stage involved, hence, the availability of a few data samples is generally adequate for quantifying similarities or performing classifications. Therefore, these statistical tests can be more appropriate for situations when collecting large training data sets is very expensive or hard to find and requires domain experts.

Of the above-mentioned discrimination measures, the most commonly used in texture classification problems are the chi-square χ^2 statistic and the histogram intersection distance similarity metric [39, 102]. The log-likelihood statistic works generally well in most situations, however sometimes it can be unstable when used with very small sized samples. This is because with small sized samples, the distribution of the histogram is more likely to include several zeros, which in turn means the logarithm is undefined [39].

Conversely, the chi-square χ^2 statistic generally works better with small sized samples compared to other discrimination metrics measures [39]. Furthermore, the histogram intersection distance similarity metric provides an equivalent performance to the chi-square χ^2 statistic but at a remarkably smaller computational overhead [39]. Consequently, the chi-square χ^2 statistic and the histogram intersection distance similarity metric are reviewed in the following sub-subsections 2.5.2.1 and 2.5.2.2 and along with brief descriptions of how they are usually utilised and interpreted in classification or predictive modelling situations.

2.5.2.1 Chi-square χ^2 Distance Similarity Metric

The chi-square χ^2 , sometimes known as the chi-square χ^2 distance similarity metric, has been extensively employed in a wide variety of image texture analysis tasks such as face recognition, texture segmentation, image retrieval and many more [39, 58, 102, 146]. Since the final output of most texture representation techniques are typically estimated by a histogram that accumulates various texture features, the chi-square χ^2 statistic is typically computed by comparing a pair of histograms, namely sample and model histograms. Statistically, the chi-square χ^2 statistic is therefore formally expressed by the following equation 2.34:

$$\chi^2(SH, MH) = \sum_{b=1}^n \frac{(SH_b - MH_b)^2}{(SH_b + MH_b)} \quad (2.34)$$

Where the (SH) and the (MH) are the sample and the model histograms respectively while the (n) is the total number of histogram bins. Hence, based on the above equation, the chi-square χ^2 statistic estimates the similarity by taking the squared difference of every individual bin count value of the SH and the MH , divided by the sum of every individual bin count value of the SH and the MH . The output of the chi-square χ^2 statistic is a single distance value, i.e.: a match value. A very small distance value indicates higher similarity, and a very large distance value indicates higher dissimilarity. Hence, when measuring the similarities in solving predictive modelling tasks such as an image texture classification or a texture region localisation, predicting the class of a new sample is typically achieved by measuring the distance, i.e.: comparing the new sample histogram SH with all known model histograms MH and then assigning the new sample to the class of the model that gives the smallest distance value, i.e.: minimum value.

2.5.2.2 Intersection Distance Similarity Metric

Similar to the chi-square χ^2 statistic, the histogram intersection distance similarity metric has also been extensively utilised in a wide variety of image texture analysis tasks such as face recognition, image matching and many more [39, 89, 102, 147]. The histogram intersection distance similarity metric can provide almost an equivalent accuracy to the chi-square χ^2 statistic but with a remarkably much smaller computational overhead. Hence, when the computational efficiency is of an important matter such as

real time applications, the histogram intersection distance similarity metric can serve as a great choice. Just as the chi-square χ^2 statistic, the histogram intersection metric is typically calculated by matching a pair of histograms, namely sample and model histograms. The histogram intersection metric (*Intersection*) is then formally defined mathematically by the following equation 2.35.

$$Intersection(SH, MH) = \sum_{b=1}^n \min(SH_b, MH_b) \quad (2.35)$$

Where the (n) is the total number of histogram bins, while the (SH) and the (MH) are the sample and the model histograms, respectively. The histogram intersection metric measures the similarity by employing a *min* function that compares every individual bin count value of the SH and the MH and returns the minimum one, i.e.: the smallest value. The result of the intersection of the SH with the MH is the number of bins which represent certain features from the MH that have corresponding bins of the same type of features in the SH . A higher value of the distance metric indicates the more accurate the match is, i.e.: a higher similarity, and a very small value of the distance metric indicates a higher dissimilarity. The histogram intersection metric can be normalised by the number of bin count values of the MH to obtain a fractional similarity value, i.e.: match value, between 0 and 1 [147]. Hence, the histogram intersection match value (*IMV*) is then computed statistically by the following equation 2.36:

$$IMV(SH, MH) = \frac{\sum_{b=1}^n \min(SH_b, MH_b)}{\sum_{b=1}^n MH_b} \quad (2.36)$$

Where the (SH) and the (MH) are the sample and the model histograms respectively, and the (n) is the total number of histogram bins. Subsequently, when measuring the similarities in solving predictive modelling tasks such as an image texture classification or a texture region localisation, predicting the class of a new sample is typically achieved by measuring the distance, i.e.: comparing the new sample histogram SH with all known model histograms MH and then assigning the new sample to the class of the model that gives the largest distance value, i.e.: maximum value.

2.6 Feature Selection and Reduction

Machine learning classification algorithms are often susceptible to the widely known problem associated with high dimensional data, i.e.: the number of features exceeds the number of samples, specifically the curse of dimensionality issue [143, 148]. Hence,

as the number of texture features increases, the more degradation in the performance of a given machine learning classification algorithm. Nevertheless, there are some certain situations in which texture representation techniques are specifically designed to provide extremely small and well compacted texture features. However, partially related or completely unrelated texture features can have a huge and negative influence on the kind of performance that can be achieved.

To deal with such situations like the above-mentioned, feature selection and reduction or decorrelation techniques are often applied as a data pre-processing step or as part of the texture analysis task to simplify and obtain more meaningful data representations that contribute most to the prediction or are most relevant to the target task [148, 149]. Broadly, the typical overall objective of these techniques is to transform or carefully select the most appropriate subset of low dimensional data representations that are highly relevant to the task out of the original high dimensional data representations. With reduced sets of data representations, tasks such as classification or segmentation can often achieve better performances and readily interpretable results at significantly reduced computational costs [148].

Furthermore, partially relevant or noisy individual features can have an equivalent influence of individual relevant features on classification or segmentation tasks [143, 148]. For example, in the case of the KNN classifier, every single individual feature contributes to the final predictions. Consequently, they can negatively impact on the accuracy of the classifier. A further aspect includes the fact that the greater number of features used to describe different data samples, the greater the chance that the features appear similar to each other on average [143, 148]. This fact is illustrated in Figure 2.20. Based on the demonstrative example in Figure 2.20, it can be seen that the resolution of similarity measures can be poorer in the twenty dimensional space, i.e.: twenty features compared to the five dimensional space, i.e.: five features.

Broadly, current research on feature selection and reduction approaches is divided into two different folds [143, 148]. The first fold is typically explored under the category of dimensionality reduction techniques while the second fold is usually investigated under the category of feature selection techniques. Hence, the first category involves investigating methods that carefully “transform” the original features into a completely new reduced set of features while the latter category is more focused on exploring methods that precisely “select” a subset of the original features. These two different categories are discussed in more detail in the following subsections 2.6.1 and 2.6.2.

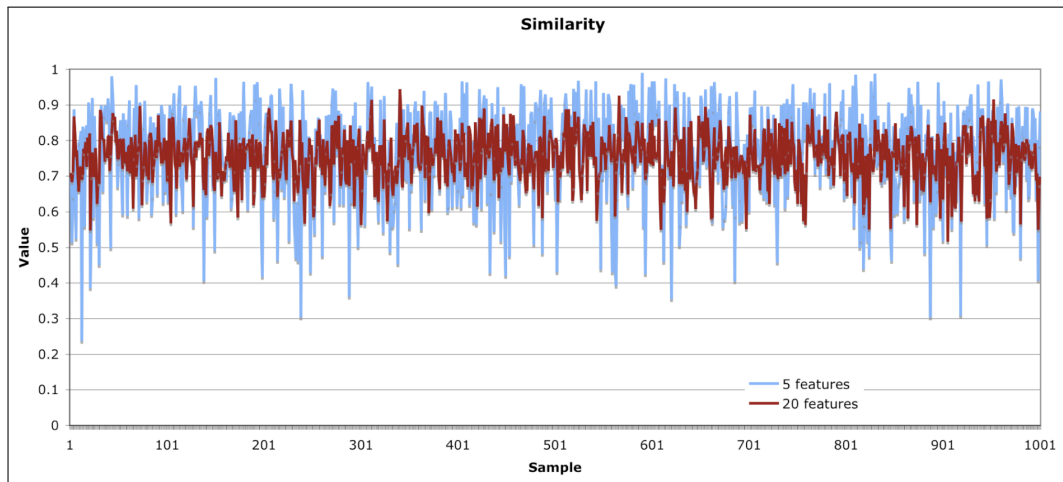


Figure 2.20: An illustrative plot that demonstrates the similarity values of randomly generated data samples described by five and by twenty different features [148]. The more features used to describe various data samples the more likely the features are to appear similar to each other on average. It can be clearly observed that the variance of similarity values with twenty features is much lower compared to that with five features.

2.6.1 Dimensionality Reduction Techniques

There are a wide variety of dimensionality reduction techniques. However, among the most dominant and popular techniques employed in the vast majority of scientific disciplines including computer science is Principal Components Analysis (*PCA*) [130, 148, 150]. Generally, the origin of *PCA* methodology can be traced back to Pearson [151] or perhaps even Cauchy [152], or Jordan [153] including many other researchers [154–156]; however the present formalisation of *PCA* is ultimately attributed to Hotelling [157] who made a substantial contribution to *PCA* methodology by inventing the currently well-known term “principal components” [150]. The principal components (*PCs*) of the *PCA* technique are defined as linear combinations of the original features that capture the most potential variance [130]. Such that the first *PC* is described as the linear combination of the features that capture the most variability of all possible linear combinations. The following *PCs* are then derived such that these linear combinations capture the most remaining variance as well as uncorrelated with all previous *PCs*.

Formally, estimating the *PCs* in the *PCA* technique comprises the following steps. As the *PCA* technique does not consider the relationships between different classes in classification tasks when summarising the variance, let D be a data matrix that comprises an N data samples and an F features. Hence, the $N \times F$ data matrix D can be

written as follows:

$$D_{N \times F} = \begin{bmatrix} x_{(11)} & x_{(12)} & \cdots & x_{(1F)} \\ x_{(21)} & x_{(22)} & \cdots & x_{(2F)} \\ \vdots & \vdots & \vdots & \vdots \\ x_{(N1)} & x_{(N2)} & \cdots & x_{(NF)} \end{bmatrix}$$

Where x denotes the feature values. This data matrix D is then transposed, i.e.: flipped over its diagonal, to produce the transpose of data matrix D that is denoted by D^T . The transposed data matrix D^T can, therefore, be written as follows:

$$D_{F \times N}^T = \begin{bmatrix} x_{(11)} & x_{(12)} & \cdots & x_{(1N)} \\ x_{(21)} & x_{(22)} & \cdots & x_{(2N)} \\ \vdots & \vdots & \vdots & \vdots \\ x_{(F1)} & x_{(F2)} & \cdots & x_{(FN)} \end{bmatrix}$$

Once the transposed data matrix D^T is constructed, the following step is to compute the covariance matrix Σ using the data matrix D and its transpose form, i.e.: data matrix D^T . The covariance matrix Σ can, therefore, be estimated by the following equation 2.37:

$$\Sigma = D^T D N^{-1} = \frac{1}{N} \sum_{i=1}^N x_{(i)}^T x_{(i)} \quad (2.37)$$

The resultant covariance matrix Σ has the dimensions of $F \times F$. Once the covariance matrix Σ is constructed, the following step is to estimate the *PCs*. The *PCs* are found by computing the individual eigenvectors ϕ and corresponding eigenvalues λ of the computed covariance matrix Σ . Let the total variance (*TV*) in the original data be estimated as the sum of all F eigenvalues λ of the estimated covariance matrix Σ which is given by the following equation 2.38:

$$TV = \sum_{j=1}^F \lambda_j \quad (2.38)$$

Hence, the proportion of the variance (PV_i) that the i^{th} eigenvector ϕ is accounted for can be estimated by the following equation 2.39:

$$PV_i = \frac{\lambda_i}{\sum_{j=1}^F \lambda_j} \quad (2.39)$$

Nevertheless, the individual F eigenvalues λ are sorted in descending order, i.e.: arranged such that $(\lambda_j \geq \lambda_{j+1})$. Then, a set Φ of K eigenvectors ϕ , where $\Phi = [\phi_1, \phi_2, \dots, \phi_K]$ and typically $K < F$, of the computed covariance matrix Σ which have the K largest eigenvalues λ is selected to reduce the dimensions of original data. As such the eigenvector ϕ_1 with the greatest eigenvalue λ_1 represents the first *PC* or direction of maximum variation. The eigenvector ϕ_2 with the second greatest eigenvalue λ_2 represents the second *PC* or direction of the next maximum variation that is orthogonal to the previous *PC* and so on.

However, the K eigenvectors ϕ corresponding to the K largest eigenvalues λ are typically selected based on a predefined proportion of the total variance, e.g.: 95 for 95%, that one desires to retain. Consequently, the set Φ of K eigenvectors ϕ that retains a certain proportion, e.g.: 95% of the total variance of the original data can be constructed based on the sum of the proportion of the variance (PV_i) accounted for by individual K eigenvectors ϕ that have the K largest eigenvalues λ as follows in 2.40:

$$\sum_{i=1}^K PV_i \geq 95 \quad (2.40)$$

Once the K eigenvectors ϕ that have the K largest eigenvalues λ are selected which explain the previously defined proportion, i.e.: 95 for 95% of the variance exhibited in the original data, the selected set Φ of K eigenvectors ϕ constructs the set of *PCs* that will be used to create the new transformed features in place of the original features. The final step in the *PCA* technique is, therefore, the projection of the original data into a new subspace of reduced features via matrix multiplication of the original data with the selected set Φ of K eigenvectors ϕ . Hence, this ultimate step constructs the new transformed set of reduced features.

To illustrate the notion of the *PCA* technique, consider the two dimensional data set in the example demonstrated in Figure 2.21a. This data set comprises a set of two highly correlated features used to assess or classify the segmentation quality of cells in a living organism and a categorical response, namely as being poorly segmented or well segmented [130]. For simplifying the explanation of this predictive modelling problem, the two different features are denoted as Feature 1 and Feature 2 in the scatter plot of Figure 2.21a. These two features quantify two different classes of segmentation quality demonstrated as orange colour filled circles (●) for Class 1, indicating

imperfectly segmented cells, and blue colour filled squares (■) for Class 2, indicating excellently segmented cells, in the scatter plot of Figure 2.21a.

Given the high correlation that is nearly 0.93 between the original features, one could infer that the values of Feature 1 and Feature 2 intercorrelate strongly, meaning that they both measure highly redundant details about the cells and that a single feature or a linear combination of these features could be used as a substitute of the original two features [130]. Nevertheless, the correlation in this predictive modelling problem can be addressed by applying the *PCA* technique to transform the original features into two *PCs* that are orthogonal to one another. The result of this transformation is demonstrated in the scatter plot of Figure 2.21b, which represents a rotation version of the original features about the axis of greatest variation. The 1st *PC* describes 97% of the variance, while the 2nd *PC* describes 3%. Consequently, since the 1st *PC* describes the vast majority of details about the cells, it is potentially sensible to remove the 2nd *PC* and only use the 1st *PC* for the predictive modelling problem [130].

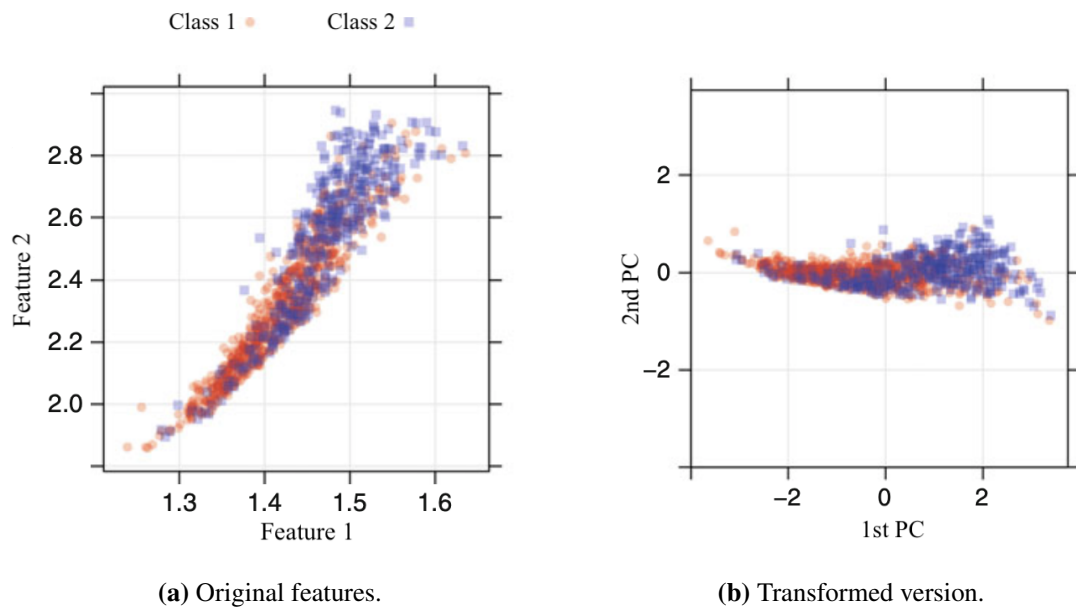


Figure 2.21: An application example of the *PCA* technique to address two highly correlated features used in a predictive modelling task for classifying the segmentation quality of cells in a living organism [130]. (a) Represents the distribution of the original features. The two different features, Feature 1 and Feature 2, can provide an indication of which cells that are imperfectly segmented as Class 1 (●) or excellently segmented as Class 2 (■). (b) Shows the distribution of the transformed version of the original features after applying the *PCA* technique in which two *PCs* are derived in place of the original features. This transformation can be seen as a rotation of the original features about the axis of greatest variation. The 1st *PC* describes 97% of the variance, while the 2nd *PC* describes 3%.

An important aspect of *PCA* that has led it to retain its wide popularity among various domains as a dimensionality reduction technique is its impressive capability to create new features, i.e.: *PCs* that are uncorrelated [130]. As such, if there are two features that are perfectly correlated, then including both features does not provide any additional details or benefit to solving the task of interest. This is because one of the features is already determined by the other, hence, one of them can be safely removed or a linear combination of these features can be used instead. Given this key advantage, several classification schemes can specifically benefit from the features being uncorrelated. For instance, certain classification schemes, e.g.: those employing or relying on similarity distance measures including the KNN classifier typically prefer the features to be uncorrelated, i.e.: free of redundant features or at least with a very low correlation [130, 143].

As stated earlier in section 2.6, the more features used to describe things the more likely the features are to appear similar to each other on average, see Figure 2.20. Furthermore, including irrelevant features in solving the task of interest can be computationally expensive as well as negatively impacting on the accuracy of the classification scheme employed [143]. Consequently, the *PCA* can be seen as a powerful technique that produces a new set of features with desirable characteristics, i.e.: uncorrelated features that perhaps facilitate finding the most appropriate solutions as well as improving the features stability for the predictive modelling task in hand, such as classification.

Although the *PCA* technique can provide a new set of features with fairly desirable characteristics, it must be employed with profound understanding and caution [130]. This is mainly because the *PCA* technique notably seeks to explore and understand the variance of features set without being entirely concerned about any further details regarding the underlying features, i.e.: measurement units or distributions, as well as the predictive modelling task objectives, i.e.: prediction outputs or classes. Therefore, the application of the *PCA* technique without appropriate guidance can produce a new set of features, i.e.: *PCs* which summarise certain characteristics of the original features, but which may unfortunately be irrelevant to the original structure of the features, hence to the ultimate objective of the predictive modelling task in hand.

Since the *PCA* technique seeks to find linear combinations of original features that maximise variance, it will instinctively be anticipated that it will summarise features of greater variation [130]. For instance, consider a situation when the underlying features represent values that are measured on different scales or units, for example, consider a case of using demographic features, namely income level, e.g.: in dollars, and height,

e.g.: in feet [130]. Subsequently, the first few *PCs* will concentrate mainly on summarising the features of higher scale, namely the income level, while the last *PCs* will ultimately summarise features of lower variance, namely the height. Such that the first few *PC* weights will be larger for the higher variance features. When taking the aforementioned aspects into account, it becomes clear that the *PCA* technique works mainly by focusing only on summarising the structure of the features by bearing in mind their measurement units or scales instead of considering the important relationships between the features themselves for the modelling task in hand

In most situations, data sets may include various features that are measured in terms of different units or scales. Nevertheless, there are a number of popular data transformation techniques, namely data centring and scaling techniques that can be applied to the original features prior to applying the *PCA* technique to avoid summarising the units or scales details of the original features. Data centring and scaling techniques are among the most commonly used data transformation techniques that provide the *PCA* technique with the opportunity to summarise and discover the underlying relationships in the features without being manipulated by the original units or scales of the feature measurement.

A further important property about the *PCA* technique is that it does not take into account the overall objective of the predictive modelling problem or the relationships between class labels in classification tasks when summarising the variance [130, 148]. Hence, since the *PCA* technique is blind to the class label relationships, it is normally considered as an unsupervised technique [130, 148]. Nevertheless, when solving a predictive modelling problem such as a classification task and when the modelling relationship between the features and classes is related to the features' variability, then the newly constructed set of features, i.e.: *PCs*, after applying the *PCA* technique, can provide an effective and appropriate relationship between the new features and the target class, hence facilitating solving the predictive modelling problem in hand [130].

A typical approach when applying the *PCA* technique to address the correlation or reduce the dimension of features is to retain 95% of the variance which is a common percentage widely selected when employing the *PCA* technique. Other values of variance percentages are also possible. These are typically determined by a statistically rigorous method, such as employing a cross validation strategy, e.g.: a resampling technique that involves experimenting with a set of different values of variance percentages to retain. The *PCA* technique has been applied across various domains to

facilitate solving a wide variety of image texture analysis tasks including classification and segmentation, for instance, aerial image classification tasks, such as those that classify vegetation communities [54] and medical image analysis tasks, such as retinal image classification [158–160] and many more applications [161].

2.6.2 Feature Selection Techniques

Most feature selection techniques follow a different approach compared to the previously mentioned dimensionality reduction techniques that ‘transform’ the original set of features into a new reduced set of features. In particular, the feature selection techniques tend primarily to discard or remove some of the features that provide uninformative or redundant details about the predictive modelling task in hand. This is typically accomplished by carefully ‘selecting’ a subset of features out of the original set of features for the purpose of mainly increasing accuracy [130, 143].

This is typically accomplished by incorporating a search strategy for investigating the most appropriate features subset from the original features. This is usually conducted by precisely exploring a number of different potential effective candidates, i.e.: feature subsets, and then determining the most successful starting point subset of features to use with the task of interest [143]. The feature selection techniques can be steered with evaluation criteria, e.g.: the prediction accuracy estimates or performance estimates that act as a guide in the search or the feature selection process [143, 162]. Consequently, the overall objectives of the feature selection techniques are to compare the determined candidates of features subsets, assess their suitability to the task of interest and ultimately find the most suitable subset of features that maximises the performance estimates to achieve the best possible accuracy.

Generally, there are a wide variety of feature selection techniques that can be employed; however, perhaps the simplest and most straightforward approach is that of exploiting the performance of the classification scheme to lead the search or the feature selection process. Specifically, the classification scheme, e.g.: a machine learning classifier or a similarity distance metric is enclosed in the feature selection or search procedure to ‘select’ a subset of most relevant features [143, 163]. This is typically conducted by utilising a cross validation strategy, e.g.: a resampling technique to generate a number of different candidates of feature subsets. The search process is then followed by estimating the performance or the predictive accuracy of the classification scheme applied to every single subset of features generated through the resampling technique. The subset of features that maximises or provides the best predictive accuracy is then

selected. The merit of the selected feature subset is the generalisation accuracy it holds as evaluated using the resampling technique on the original features [143].

Broadly, a wide variety of feature selection techniques can be employed; however, perhaps the simplest and most straightforward approach is that of exploiting the performance of the classification scheme to lead the search or the feature selection process. Specifically, there are two different types of common search strategies for feature selection techniques. The first search strategy is the forward feature selection while the latter search strategy is the backward feature selection [130, 143, 164]. Given a feature set $X = \{x_1, x_2, x_3, \dots, x_n\}$, the overall objective of these search strategies is to find the best feature subset $S = \{x_1, x_2, x_3, \dots, x_m\}$ and typically $m < n$. That is, S optimises an objective function $F(S)$, ideally maximising the performance estimates to achieve the best possible accuracy.

The forward feature selection strategy begins with selecting no features, i.e.: an empty set $S_0 = \{\emptyset\}$, and then sequentially assesses all the possibilities, choosing only a single feature x^+ that optimises the value of the objective function $F(S_m)$, where $S_m = \{x^+\}$. The process is then followed by selecting the best of previous possibilities, e.g.: $S_m = \{x^+\}$, and then considering the possibilities by choosing the previously selected feature plus one more, i.e.: $S_{m+1} = \{S_m + x^+\}$, etc.

The backward feature selection strategy, on the other hand, begins by selecting all original features, i.e.: $S_m = \{X\}$, and then sequentially considers the possibilities by deleting a single feature x^- that optimises or results in the smallest decrease in the value of the objective function $F(S_{m-1})$ when deleted, where $S_{m-1} = \{S_m - x^-\}$. The process is then followed by selecting the best of previous possibilities, e.g.: $S_{m-1} = \{S_m - x^-\}$, and then considering the possibilities by removing the previously removed feature plus one more, i.e.: $S_{m-2} = \{S_{m-1} - x^-\}$, etc.

The aforementioned search strategies typically terminate when selecting or removing a feature, hence they may not produce an enhancement in the classification performance [143]. These search strategies are together considered as greedy strategies and as a consequence cannot guarantee the discovery or the determination of the best relevant feature subset for the task under consideration [143, 149]. Therefore, more advanced and sophisticated search strategies should be considered to improve the way of investigating the original set of features. Nevertheless, Reunanen [162] warned that the more rigorous the search strategies are, the more possible they may overfit the original set of features and hence generate a biased subset of features [143].

2.7 Fundamental Part in Image Texture Analysis Tasks

As demonstrated so far, the construction of a computer vision system for image texture analysis tasks such as classification or segmentation typically comprises several components that employ specific techniques to accomplish certain tasks. In classification problems, for instance, the components can include employing a texture representation technique, a feature selection or reduction technique, a classification scheme, etc. However, the fundamental component that plays a major role behind the potential success in solving various image texture classification problems is the texture representation technique used to derive the texture measurements or features.

While the classification scheme employed to perform texture classification is notably an important matter, since the good design of texture features can be wasted when selecting a poor classification scheme, but no classification scheme can survive with poor design of texture features [165]. Consequently, additional consideration needs to be made particularly for selecting the most appropriate texture representation technique that meets certain requirements related to the texture characteristics or conditions of the images used such as unstable illuminations, orientation variations, etc., so as to facilitate accomplishing the task in question effectively.

Recall that texture analysis and understanding is one of the most challenging and active research problems in computer vision and pattern recognition that has been an intensive research subject as well as witnessing rapid progress since the early 1960s [42]. As a result, this has led to several developments of a wide variety of choices of robust texture representation techniques that can be utilised to assist in recognising various textures appearing in digital data, such as images or videos that are captured under various imaging conditions such as different viewpoints, lighting, etc. The most notable and widely used texture representation techniques, including those hand-engineered and learned, have been reviewed in this chapter, section 2.4, along with highlighting their effectiveness when utilised to solve image texture analysis tasks in the presence of various potentially difficult imaging situations. However, due to significant progress in the area of texture analysis and understanding over the last few years, it is impossible to list and review every single texture representation technique along with their merits and demerits and how they perform under various challenging situations such as changes in illuminations and orientations of texture images.

Nevertheless, there are a number of outstanding surveys and comparative studies have been conducted to compare various texture representation techniques, including

those hand-engineered and learned, to assess and compare their performance and effectiveness for image texture analysis tasks such as classification and segmentation. Examples of comparisons between hand-engineered texture representation techniques include comparative studies conducted by Weszka et al. [50] and Connors and Harlow [166]. These studies compared several texture representation techniques including those approaches from the statistical category and together determined that the GLCM approach performs best compared to other approaches [74]. A further comparative study conducted by Du Buf et al. [167], aimed to compare several hand-engineered texture representation techniques including those approaches from the statistical, model based and signal processing categories; however, they reported that all approaches demonstrated roughly the same performance [74].

A further comparative study was conducted by Ojala et al. [97] to compare the performance of several hand-engineered texture representation techniques from various categories including signal processing and local texture descriptor methods [74]. They determined that texture representation techniques from the local texture descriptor category are among the ones that perform best, while other techniques, particularly those from the signal processing category, demonstrated generally poor performance [74]. An additional comparative study was conducted by Randen et al. [74] to evaluate the performance of various hand-engineered texture representation techniques from the statistical and signal processing categories. An equivalent conclusion to that of the comparative study performed by Du Buf et al. [167] was also reached [58].

A recent outstanding survey was conducted by Liu et al. [32] to compare various texture representation techniques from the hand-engineered and learned categories. They concluded that the performances vary between the hand-engineered and learned texture representation techniques and that this can be largely attributed to several factors including the size and imaging conditions of texture images. They also noted one of the main limitations of learned texture representation techniques, i.e.: approaches based on CNN algorithms, is that of being very sensitive to image degradations caused by illumination variations and rotation changes [32]. Despite the typical advantages of the learned texture representation techniques, namely that the texture features are automatically learned from the data rather than manually crafted, Liu et al. [32] emphasised that hand-engineered texture representation techniques still have merits that should not be underestimated. In particular, Liu et al. [32] observed that local texture descriptor methods, e.g.: the $LBP_{p,r}$ texture descriptor, demonstrated great robustness in very challenging situations, such as when real-time computation is very important,

when only a limited size of labelled texture images can be made available and when robustness to image degradations, e.g.: illumination changes, etc., is required [168].

As demonstrated so far, numerous texture representation techniques, including hand-engineered and learned, have been reviewed and compared in several comparative studies and surveys and different conclusions have been reached [74]. The reasons for the contradicting conclusions can be attributed to several factors. Among the most important ones include the diversity of texture images, the variations of experimental setups, and the various texture representation techniques and classification schemes employed [74]. Despite the significant progress that has been made over the past decades, regardless of whether exploring hand-engineered or learned texture representation techniques, the research in texture analysis and understanding has not yet been capable to develop and accomplish a single 'general purpose' texture representation technique that can be deployed in almost any domain no matter what the types of imaging conditions of texture images are, or the resources available. While this can be attributed to numerous reasons, among the most important ones include the unavailability of large scale labelled texture data sets, the diversity and complexity of textures especially those appearing in medical images representing certain characteristics requiring domain experts, constraints related to resource limited situations, and so on.

Consequently, there are a number of important aspects that should be considered before solving any image texture analysis problem such as classification or segmentation. Ojala and Pietikäinen [165] highlighted some of the most important properties that must be taken into account when selecting or developing texture representation techniques and these properties are summarised by the following points:

1. **Robustness with respect to illumination variations:** This property is particularly important for situations like solving medical image texture analysis problems since the potential presence of unstable imaging conditions, e.g.: changes in lighting or illumination, are quite common. Therefore, the sensitivity of the texture representation technique to illumination variations, e.g.: changes in grey level values of greyscale textural images, can be crucial for accomplishing the task of interest effectively.
2. **Robustness with respect to rotation changes:** The property of rotation invariant is also very important. In some situations, it is desirable to have a texture representation technique that can cope when the rotation of texture images

varies with respect to the viewpoint. This is because in most image texture analysis situations, the availability of details about rotations are rarely obtainable.

3. **Robustness with respect to the spatial scale variance:** Sometimes, it is desirable to be able to analyse or classify various texture patterns that appear at various spatial scales. Consider the case of a classification problem where unknown objects to be identified in texture images appear in different sizes from that of training data sets. Hence, having a texture representation technique that can cope with these variations can be very helpful in solving the classification problem successfully.
4. **Robustness with respect to the size of data samples:** Some texture representation techniques perform differently depending on the data set size available. For instance, learned texture representation techniques generally perform better as the size of data sets increase; however, hand-engineered texture representation techniques have been demonstrated to produce effective performance with the availability of limited numbers of data sets [32]. Hence, employing the most appropriate texture representation technique to the task under consideration while bearing in mind the size of data set needed or necessary to help generate good descriptions of texture content can be crucial to solving the task of interest effectively.
5. **Robustness with respect to computational complexity:** Some texture representation techniques are very computationally expensive and hence cannot be deployed in real time applications with limited resources such as real time visual inspection systems and retrieval of huge databases. Hence, when real time is an important matter, it is always desirable to have a texture representation technique that provides a good compromise between producing good texture descriptions while remaining computationally inexpensive, hence, suitable to be applied in real time applications with limited resource situations.
6. **Robustness with respect to parameters:** Most texture representation techniques typically have several built-in parameters that are related to the process of extracting texture features. Finding the right values of the parameters can be sometimes challenging, although the parameters can be tuned by employing a cross validation strategy, e.g.: a resampling technique that involves experimenting with different values of the parameters. Nevertheless, the parameters of a texture representation technique that can be easily tuned such that given a set of parameters values, which were determined by a cross validation strategy, can

also be applied to a wide range of various texture images, is always desirable.

While the aforementioned properties are all very important, the need for every single given property is largely dictated by the image texture analysis problem under consideration [165]. As such, complementing texture representation techniques with additional unnecessary properties such as invariance to rotation or illumination changes can have a significant impact on accomplishing the task of interest. Consider cases when details about the changes are already available or very important and closely related to the task under consideration. For example, the illumination in industrial visual inspection systems can be precisely controlled and hence adding details about the changes in illumination can not only have a crucial impact on achieving the task successfully but also may introduce additional unnecessary computational cost that can affect the deployment of these texture representation techniques in other real time applications.

2.8 Evaluation Measures and Resampling Strategies

Given an image texture analysis problem such as classification, the performance is often measured by employing a number of different evaluation measures and resampling strategies. The most widely utilised evaluation measures and resampling strategies are presented in the following two subsections, 2.8.1 and 2.8.2.

2.8.1 Evaluation Measures

Evaluation measures in classification problems are fundamental components and play a crucial role in assessing the quality and effectiveness of various methods constructed to perform certain classification tasks [139, 169, 170]. As such, selecting inappropriate evaluation measures to quantify the performance of a classification system may potentially lead to inaccurate and misleading results. While a wide variety of evaluation measures have been defined in the literature, the most widely used in classification task situations are accuracy, sensitivity, specificity, precision, recall and the area under the Receiver Operating Characteristic curve (ROC curve).

In a binary classification situation, the class of a very high identification importance is usually denoted as a positive class while the other class is indicated as a negative class. For instance, in diagnostic classification systems, a positive class can mean the subject has a disease while a negative class can mean the subject does not have a disease or is healthy depending upon the task. Nevertheless, given a binary classification

predictive modelling problem, the classification outcomes are typically grouped into four different categories. These various categories are represented in the confusion matrix given in Table 2.1. The true positive (TP) indicates the subject was correctly predicted as belonging to the positive class and the false positive (FP) implies that the subject was incorrectly predicted as belonging to the positive class, while it actually belongs the negative class. Likewise, the true negative (TN) suggests the subject was accurately predicted as belonging to the negative class and the false negative (FN) means the subject was wrongly predicted as belonging to the negative class, while it actually belongs the positive class. While the confusion matrix demonstrated in Table 2.1 is constructed based on the binary classification case, constructing a confusion matrix for a multiclass classification problem is also possible.

Table 2.1: Confusion matrix.

		Predicted	
		Positive	Negative
Actual	Positive	True Positive (TP)	False Negative (FN)
	Negative	False Positive (FP)	True Negative (TN)

The previously mentioned evaluation measures, namely the accuracy, the sensitivity, the specificity, the precision, the recall and the Receiver Operating Characteristic curve (ROC curve) are typically estimated based on this confusion matrix. Every single evaluation measure is explained in detail below along with highlighting the fundamental insight that can be obtained from each one with respect to the performance. Specifying the point at which each one should be used to evaluate the performance of classification application is also given. The evaluation measures are summarised as follows:

1. **Accuracy:** The accuracy measure is the most widely used and simplest measure to quantify the overall performance in classification predictive modelling tasks. It is typically estimated as the degree of correct predictions of a classifier. Mathematically, the accuracy is computed as the sum of all correct predictions divided by the sum of all correct and incorrect predictions as given by the following equation 2.41.

$$Accuracy = \frac{(TP + TN)}{(TP + TN + FP + FN)} \quad (2.41)$$

While the accuracy measure is widely used across various classification tasks,

classification results estimated based on the accuracy can be generally considered inappropriate for certain classification situations, especially when employed with imbalanced class data sets. This is because a classifier can simply achieve a high accuracy by only predicting the dominant class, hence misleading results. To remedy this issue, alternative measures such as the sensitivity, specificity, precision and recall are commonly used to get more insight about the performance with class imbalance situations. This is because these measures primarily focus on a single class to evaluate the classification performance.

2. **Sensitivity:** The sensitivity measure is usually used to quantify how well the prediction or classification performs on the positive class data samples. The sensitivity measure is also sometimes known as the True Positive Rate (TPR). The sensitivity is calculated as the total number of correct predictions of the positive class data samples divided by the sum of all correct and incorrect predictions of the data samples that actually belong to the positive class as measured by the following equation 2.42.

$$Sensitivity = \frac{(TP)}{(TP + FN)} \quad (2.42)$$

3. **Specificity:** The specificity measure is, on the other hand, usually employed to measure how well the prediction or classification performs on the negative class data samples. The specificity measure is also sometimes referred to as the True Negative Rate (TNR). The specificity is estimated as the total number of correct predictions of the negative class data samples divided by the sum of all correct and incorrect predictions of the data samples that actually belong to the negative class as quantified by the following equation 2.43.

$$Specificity = \frac{(TN)}{(TN + FP)} \quad (2.43)$$

4. **Precision:** The precision measure is usually used to quantify the proportion of data samples classified as belonging to the positive class that actually belong to the positive class. The precision measure can be thought of as a measure of exactness and it is also occasionally known as the Positive Predictive Value (PPV) [171]. The precision is measured as the total number of correct predictions of the positive class data samples divided by the sum of all correct and incorrect predictions belonging to the positive class as calculated by the following equation 2.44.

$$Precision = \frac{(TP)}{(TP + FP)} \quad (2.44)$$

5. **Recall:** The recall measure is typically used to determine the proportion of data samples that are correctly classified as belonging to the positive class. The recall measure can be thought of as a measure of completeness and it is the same as the sensitivity measure and the TPR [171].
6. **The Receiver Operating Characteristic curve (ROC curve):** The ROC curve is a popular evaluation tool used in binary classification situations with imbalanced data sets and the area under the ROC curve (AUC) is typically measured to determine the classification performance as a single value performance score [171]. The ROC curve provides a summary of the relative trade-off between the benefits of the TPR, i.e.: the sensitivity or recall, and the costs of the False Positive Rate (FPR), cf. equation 2.45 or $1 - \text{specificity}$, i.e.: the proportion of data samples that are incorrectly predicted to be positive out of all negative data samples [139, 171]. In classification predictive modelling tasks, data samples are typically assigned probabilistic scores as class predictions based on a score threshold value. The score threshold value is typically applied to construct a decision point for the class predictions as such to discriminate between predicted data samples as either belonging to the positive or negative class. A default score threshold value is usually 0.5 for normalised probabilities or scores of predicted data samples, hence predicted scores that are below the threshold value are assigned to the negative class or the positive class otherwise. By changing the score threshold value, various class predictions can be obtained. Every different score threshold value produces a different pair of measurements, namely the TPR and the FPR. By connecting these different measurements, the ROC curve is constructed such that the TPR is on the y-axis and the FPR is on the x-axis, as depicted in Figure 2.22.

$$FPR = \frac{FP}{(TN + FP)} = 1 - \text{Specificity} \quad (2.45)$$

A classification scheme with a perfect discriminative power is one that has $TPR = 1$ and $FPR = 0$. The perfect classification scheme, i.e.: Ideal Model, illustrated with an arrow in Figure 2.22, is the one represented by a curve that aligns with the top-most left i.e.: bows up to the top-most left of the plot. Consequently, the ROC curve of a good classification scheme should be located as

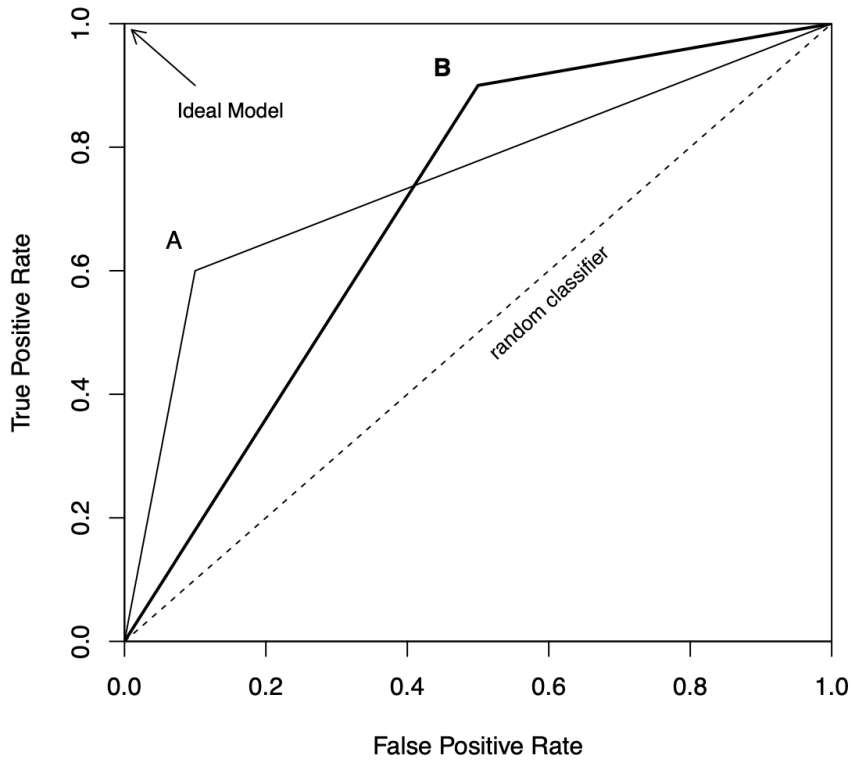


Figure 2.22: The ROC curves of three different classifiers, namely A, B and random classifiers [171].

close as possible to the upper left corner of the plot. However, the classification scheme that cannot discriminate between the different classes and only makes a random guess, e.g.: the random classifier displayed as a dashed line in Figure 2.22, should reside along the main diagonal, i.e.: the dashed line stretched from the bottom left to the top right of the plot. This dashed line is constructed by connecting the different measurements, namely the TPR and the FPR such that the $TPR = 0$ and the $FPR = 0$ indicating that every single data sample is predicted as belong to the negative class, and the $TPR = 1$ and the $FPR = 1$ indicating that every single data sample is predicted as belonging to the positive class [139]. Nevertheless, the ROC curve by itself does not provide a single performance score, which inspires the introduction of the AUC measure. The AUC measure provides a single measure for determining which classification scheme is best on average and yet, it is not biased to the minority class [171]. As such, the classifier with a perfect classification skill, i.e.: the Ideal Model, would have an AUC score = 1.0 while the classifier with a random guessing skill, i.e.: the random classifier, would have an AUC score = 0.5.

While the above-mentioned evaluation measures are among the most frequently used, several evaluation measures were also devised in the literature for evaluating various classification tasks that involve utilising either balanced or imbalanced data sets. For comprehensive details and comparisons of various evaluation measures, readers are referred to the following outstanding surveys and books [139, 169–171].

2.8.2 Resampling Strategies

There are a wide variety of resampling techniques; however, the most common technique is the cross-validation strategy [130]. The popularity of the cross-validation strategy is mainly driven by its simplicity to perform and its ability to produce appropriate estimates of the classification method performance that generally have a lower bias. There are several variants of the cross-validation strategy; however, they all generally operate in a similar manner, such that a subset of data samples is utilised to train the classification method and the remaining data samples are used to evaluate the effectiveness of the classification method. This procedure can be repeated several times and the outcomes are accumulated and summarised with the mean and the standard deviation measures. These measures are normally used to understand the effectiveness of the classification method with respect to the change in values of the parameters, the generalisation on previously unseen data samples, etc.

The central difference between the various cross-validation strategies, however, is the manner of choosing the subset of data samples. A typical version of the cross-validation strategy is that the data set is randomly separated into different k folds, i.e.: subsets of approximately identical size [130]. The steps involved in this strategy are summarised by the following Algorithm 3. An illustrative example of cross-validation strategy with $k = 3$ is also depicted in Figure 2.23.

To account for the potential difference in class proportion when separating or resampling a data set under class imbalanced situations, a stratified random sampling technique is usually applied [130, 172]. The stratified random sampling technique is another variant of cross-validation strategy and typically resampling is performed within subcategories, i.e.: the classes. Algorithm 4 summarises the steps involved in this resampling technique.

A different variant of cross-validation strategy includes a leave-one-out cross-validation (LOOCV) technique [130]. This is a special type of resampling technique since every single data sample is given the opportunity to contribute to evaluating the performance of classification method, such that the value of k is set as the same as the

Algorithm 3 K Folds Cross-Validation Strategy

Input: A data set S comprises n sample-label pairs $S = \{(x_1, y_1), \dots, (x_n, y_n)\}$; A model.

Output: Overall performance estimate = $Mean \pm std$.

- 1: Select the value of k ; $k < n$.
- 2: Separate the data set randomly into different k folds of approximately equal size.
- 3: Select all folds as the training set except the first fold as the test set.
- 4: Train a model on the training set and validate on the test set.
- 5: Estimate the outcomes based on evaluation measures, e.g.: accuracy, AUC, etc.
- 6: Return the first fold to the whole data set and replace it with the second fold.
- 7: Train again on the whole data set excluding the second held out fold.
- 8: Estimate the outcomes and repeat the same procedure with all subsequent k folds.
- 9: Summarise evaluation estimates of the k folds with the mean and the standard deviation (std) measures.

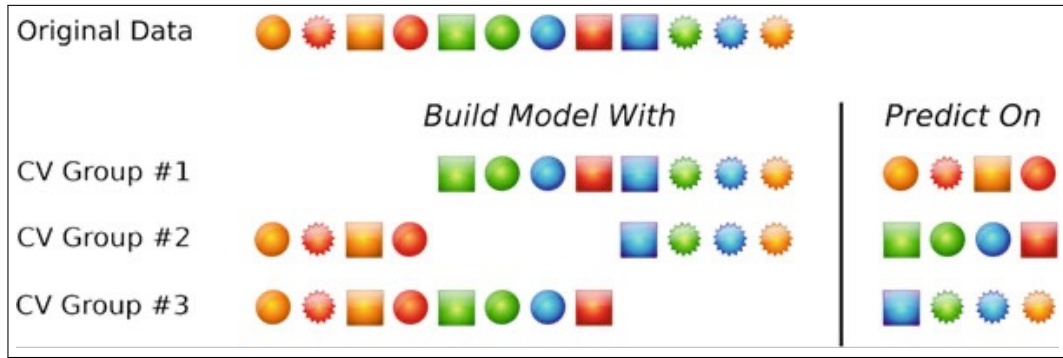


Figure 2.23: A visualisation of three folds cross-validation strategy [130]. The original data set comprises twelve data samples represented with various symbols and are distributed into three different groups, i.e.: subsets or folds. For every single cross-validation (CV) Group, i.e.: cross-validation fold, the model or the classification method is built, i.e.: trained on the original data set excluding the fold held out in which the predictions are performed on. Evaluation measures, such as accuracy, AUC and so on are estimated from every single held out fold. The overall performance of the classification method is then summarised based on the mean and standard deviation measures of the accuracy or AUC measures obtained from every single CV Group. In practice, the number of individual data samples in the held out folds can vary; however, in most situations the size of held out folds is approximately equivalent.

total number of data samples, hence every single data sample is used as a held out fold only once. This type of resampling technique is illustrated in Algorithm 5.

A further version of cross-validation strategy involves an n repeated k fold cross-validation technique [130]. As the name suggests, this technique replicates the procedure in Figure 2.23 several times depending on the value of n . For instance, if the cross-validation strategy with $k = 3$ that is depicted in Figure 2.23 is repeated by setting

Algorithm 4 Stratified K Folds Cross-Validation Strategy

Input: A data set S comprises n sample-label pairs $S = \{(x_1, y_1), \dots, (x_n, y_n)\}$; A model.

Output: Overall performance estimate = $Mean \pm std$.

- 1: Select the value of k ; $k < n$.
 - 2: Separate the data set into k folds. Each fold should include a comparable proportion of samples of each class.
 - 3: Select all folds as the training set except the first fold as the test set.
 - 4: Train a model on the training set and validate on the test set.
 - 5: Estimate the outcomes based on evaluation measures, e.g.: accuracy, AUC, etc.
 - 6: Return the first fold to the whole data set and replace it with the second fold.
 - 7: Train again on the whole data set excluding the second held out fold.
 - 8: Estimate the outcomes and repeat the same procedure with all subsequent k folds.
 - 9: Summarise evaluation estimates of the k folds with the mean and the standard deviation (std) measures.
-

Algorithm 5 Leave-One-Out Cross-Validation (LOOCV) Strategy

Input: A data set S comprises n sample-label pairs $S = \{(x_1, y_1), \dots, (x_n, y_n)\}$; A model.

Output: Overall performance estimate = $Mean \pm std$

- 1: Select the value of k ; $k = n$
 - 2: Select one sample as the test set and the remaining $k - 1$ samples as the training set
 - 3: Train a model on the training set and validate on the test set.
 - 4: Estimate the outcomes based on evaluation measures, e.g.: accuracy, AUC, etc.
 - 5: Return the first sample to the whole data set and replace it with the second sample.
 - 6: Train again on the whole data set excluding the second sample held out.
 - 7: Estimate the outcomes and repeat the same procedure with all subsequent k samples.
 - 8: Summarise evaluation estimates of the k folds with the mean and the standard deviation (std) measures.
-

$n = 10$, this constructs 30 different held out folds that would be used to measure the classification method effectiveness.

There is no formal rule in selecting the number of folds, i.e.: the value of k ; however, the typical choices include $k = 5$ or $k = 10$ [130, 173]. Empirical evaluation results using these values, namely $k = 5$ or $k = 10$, have been demonstrated to produce performance estimates that do not suffer from either extremely high bias, e.g.: overestimate of performance estimates, or from very high variance, e.g.: very high change in performance estimates [173].

From a practical perspective, as the value of k increases, the more computationally

burdensome it can become [130]. When this aspect is taken into account, it becomes clear that the LOOCV technique is the most computationally expensive among other variants of cross-validation strategy. This is because the LOOCV technique requires training as many classification methods as data samples in the original data set and for each trained classification method a single data sample is used as a held out fold at a time.

Nevertheless, Molinaro et al. [174] demonstrated that the LOOCV technique and the typical version of cross-validation strategy that involves random sampling, such as the example depicted in Figure 2.23 but with $k = 10$, both yielded the smallest bias as well as producing comparable evaluation estimates. Therefore, the typical version of cross-validation strategy with $k = 10$ can be more attractive from a computational efficiency perspective [130]. While the previously mentioned resampling strategies are among the most common strategies employed, several alternative strategies have been devised in the literature. For further comprehensive illustrations, examples and comparisons, readers are referred to the following excellent books and comparative studies [130, 172–175].

2.9 Chapter Conclusion

This chapter provided a comprehensive technical background for the various computer vision domains and techniques used to automate the analysis of image texture. The chapter started by providing explanations of the various computer vision tasks usually applied in medical image analysis applications. However, the focus was merely on image classification and segmentation tasks, as these fall within the domain of the research presented in this thesis. This was then followed by a presentation of the various techniques used for image texture representation, i.e.: texture feature extraction. Following this, the various classification approaches or schemes such as distance similarity measure metrics and the machine learning classification algorithms were presented. Subsequently, feature selection and decorrelation techniques were then described with highlighting of their potential benefits to improve the classification performance as well as to find the most appropriate texture representation. The chapter then concluded by demonstrating the various evaluation measures and resampling strategies that could be employed to quantify the performance of methods developed to perform a particular computer vision task such as classification.

Chapter 3

Application Domain, Data Sets and Related Works

3.1 Chapter Introduction

This chapter covers the related background of the application domain of the work undertaken in this thesis. The chapter commences by presenting brief details about the human eye. This is then followed by explanations about the anatomy and physiology of the retina, the fundamental component of the human eye since it is responsible for visual recognition. Details with regards to the most common eye conditions affecting the retina are then presented with a special focus on the disease of interest for the work presented in this thesis, namely AMD disease. Various retinal imaging modalities are then reviewed, highlighting the pros and cons of every single imaging technique. Subsequently, comprehensive explanations about the OCTA image data sets utilised in this thesis are given. Finally, the most recent and notable OCTA image data analysis studies related to AMD disease are selectively reviewed.

3.2 The Human Eye

The human body comprises five key sensory organs, namely the nose to smell, the ears to hear, the tongue to taste, the skin to touch and the eyes to see. However, the human eye is by far the fundamental sensory organ of the human body. This is because it provides the sense of sight that allows us to realise and understand the nearby environment more than we can with any of the other four sensory organs. As such nearly 80% of the information perceived from the outside world comes through the

visual system by the means of the vision sense, allowing us to observe the surrounding world in the form of images that we experience [176, 177]. Being able to perceive the nearby environment through the sense of sight can facilitate numerous aspects of human life, including performing normal daily life activities such as driving, walking, reading, differentiating shapes or objects, distinguishing colours, recognising faces, etc.

The human eye comprises three main layers: internal, intermediate and external, as demonstrated in Figure 3.1. The internal layer formed by the retina is the fundamental sensory element of the eye [178]. The intermediate layer is composed of two main parts, namely the anterior part that is formed by the iris and the ciliary body, and the posterior part that is formed by the choroid. The external layer is constructed of two different elements, namely the sclera and the cornea. Other important elements of the eye include the optic nerve, the fovea, the pupil and the lens, among others, see Figure 3.1.

Nevertheless, no part of the human eye has been as clinically and scientifically important as the retina in the most recent years, as such forming a major research field of its own in ophthalmology [118]. In particular, retinal conditions including AMD disease are given special intensive and predominant consideration with common understanding that the conditions of the retina are among the main leading causes of harsh vision loss and blindness among various populations at a global level. The following subsections 3.2.1 and 3.2.2 provide some basic details about the anatomy and physiology of the retina as well as the most common eye conditions affecting the retina.

3.2.1 Anatomy and Physiology of The Retina

The retina is not only the most essential part of the human eye but also it is considered one of the most fruitful areas for studying the human brain [179]. The retina is considered an embryological part of the central nervous system; however, it is readily accessible to investigate and can be examined with relative simplicity by both clinicians and scientists [179]. Furthermore, nearly 80% of almost all sensory information perceived by humans is believed to be of retinal origin and hence this suggests the major significance of the retinal function for the human capacity to perceive and interact with surrounding environments [179].

The retina has the appearance of a very thin transparent tissue layer that lines the interior or the back of the eye [180]. Figure 3.2 demonstrates a cross section view

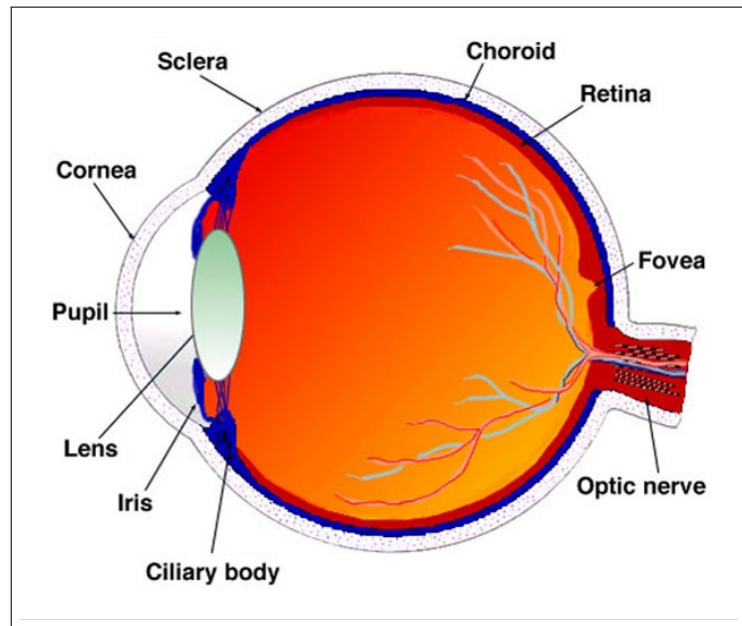


Figure 3.1: A cross section view illustrating the anatomy of the human eye [178]. The human eye comprises three main layers: the internal, the intermediate and the external. The internal layer is formed by the retina. The intermediate layer is constructed by three different components, specifically the iris, the ciliary body and the choroid. The external layer is composed by two different elements, namely the sclera and cornea. Other important elements of the eye include the fovea, the pupil, the lens and the optic nerve that connects the eye to the brain.

captured under light microscopy that illustrates the anatomy of the retina. Clinically, the retina is also composed of a number of further different layers. For instance, the cross-sectional image of the retina demonstrated in Figure 3.2 shows ten different retinal layers that are fairly evident. However, closer investigation of these ten layers may disclose that they are not totally different layers [181]. They are in fact formed by only four different layers, namely a layer of pigmented epithelium and three other different layers of neuronal cell bodies between which processes and synapses are performed, see Figure 3.2A.

The retina is an important component of the eye since it is the site that allows the transformation of incoming light energy into a neural signal that is appropriate for further analysis and processing in the visual cortex of the brain [180, 181]. As such it forms a fundamental element in the visual route, the pathway where all visual information observed from the nearby environment reaches the brain for understanding and interpretation [181]. Consequently, it can be considered as a major part or an extension of the human brain. Thus, dictated by this major role of the retina, the various

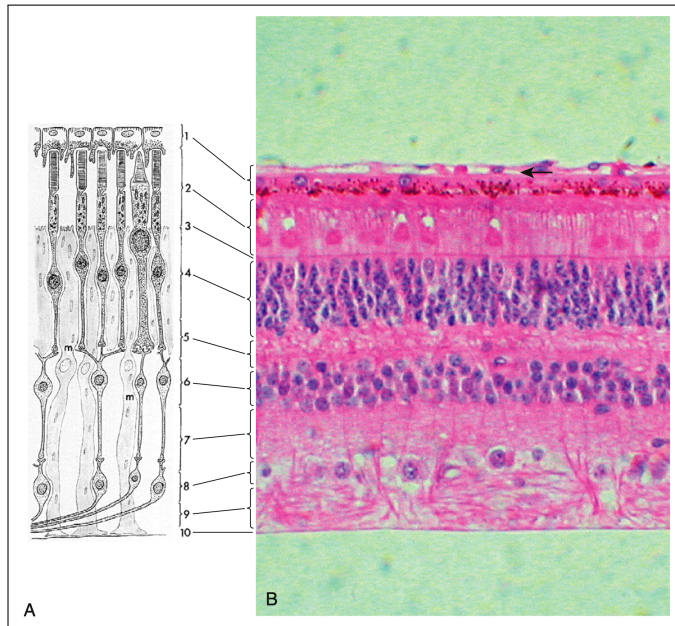


Figure 3.2: A cross section view illustrating the anatomy of the retina [181]. (A) Shows a diagram representation for the various layers of the retina. (B) Demonstrates a micrograph of same area including the inner area of choroid layer with the choriocapillaris indicated by a black arrow. The choroid layer is of fundamental importance for delivering a steady supply of oxygen and nourishment to the retina to ensure appropriate visual function. For both images A and B, the various retinal layers are labelled from numbers from 1 to 10 based on the retinal layer order. (1) The retinal pigment epithelial (RPE) layer. (2) The photoreceptor layer. (3) The external limiting membrane. (4) The outer nuclear layer. (5) The outer plexiform layer. (6) The inner nuclear layer. (7) The inner plexiform layer. (8) The ganglion cell layer. (9) The nerve fibre layer. (10) The internal limiting membrane.

diseases affecting either the eye or the brain can be together observable from the retinal layer [180]. Example of serious ocular disorders that affect the retina include the macular degeneration, e.g.: AMD disease and glaucoma disease that are ranked as the first and third most significant causes of vision damage among numerous populations in the developed world [180]. There are also numerous systemic diseases that affect the retina, including diabetic retinopathy (DR), a complication of diabetes, among others. The following subsection 3.2.2 reviews the most common eye complications affecting the retina with a special concentration on the disease of interest for the research presented in this thesis, namely AMD disease, which is categorised as the most damaging eye disorder among developed countries.

3.2.2 Common Eye Conditions

There are several significant ocular diseases that manifest themselves in the retina. In this section, brief overviews of the most dominant eye diseases that can be relatively easily studied, diagnosed and detected through imaging the retinal layer of the eye are given. These eye diseases are AMD, DR and glaucoma.

3.2.2.1 Age-related Macular Degeneration (AMD)

Age-related Macular Degeneration (AMD) is considered as one of the most serious and damaging eye conditions and comprises one of the key causes of vision loss among elderly populations in developed countries as well as the cause of an increasing global health problem [1, 2, 118, 180–184]. Several factors are generally attributed as the popular risks and pathophysiological mechanisms underlying the development of AMD disease, including genetics, smoking and ageing [182–184]. While these various risk factors seem to elucidate the ambiguity behind AMD, their role is yet to be seen as a major cause of it.

Nevertheless, the multifaceted interrelationship between these factors may imply the involvement of many if not all of them in AMD. However, sadly this has not yet evidently been fully understood or confirmed [181, 184]. Given this difficulty and the uncertainty of the underlying reason for this damaging disease, the number of people with AMD at a worldwide level was estimated to be approximately 196 million in 2020, while its global prevalence is anticipated to escalate rapidly to nearly 288 million by 2040 [118, 184, 185].

Beyond the above mentioned, AMD is also regarded as a multifactorial and degenerative ocular disease that detrimentally affects various major parts of the eye including the retinal layers, the choroid as well as the macula region that is the fundamental functional centre of the retina as it is responsible for most of our central, high resolution and colour vision [3, 182, 183]. AMD is clinically characterised into two main types, namely wet AMD and dry AMD [3]. Clinical indicators of early-stage AMD disease include drusen and the presence of abnormalities in the RPE layer, while late-stage of AMD disease can be neovascular (also typically known as exudative or wet) or non-neovascular (usually recognised as non-exudative, atrophic, or dry) [3].

Neovascular or wet AMD disease is characterised by the presence of a common, vision-threatening complication of AMD called choroidal neovascularisation (CNV); this involves the growth of abnormal blood vessels [3]. The CNV perforates the

Bruch's membrane that is the innermost layer of the choroid layer and grows into the subretinal layers starting beneath the RPE layer causing detachment of the RPE layer from the Bruch's membrane as well as serious damage to other retinal layers, causing profound visual impairment [183].

Atrophic or dry AMD disease is also known as geographic atrophy, which includes outer retinal thinning and is typically characterised by damage of retinal pigment epithelial cells, underlying choroidal capillaries and overlying photoreceptors [3]. Dry AMD is the more common subtype and is associated with gradual vision loss, whereas wet AMD is linked to a more acute presentation [3]. Figure 3.3 demonstrates two different visual fields seen by two people, one with healthy vision and the other one with AMD disease including visualisations of the typical hallmarks of AMD disease.

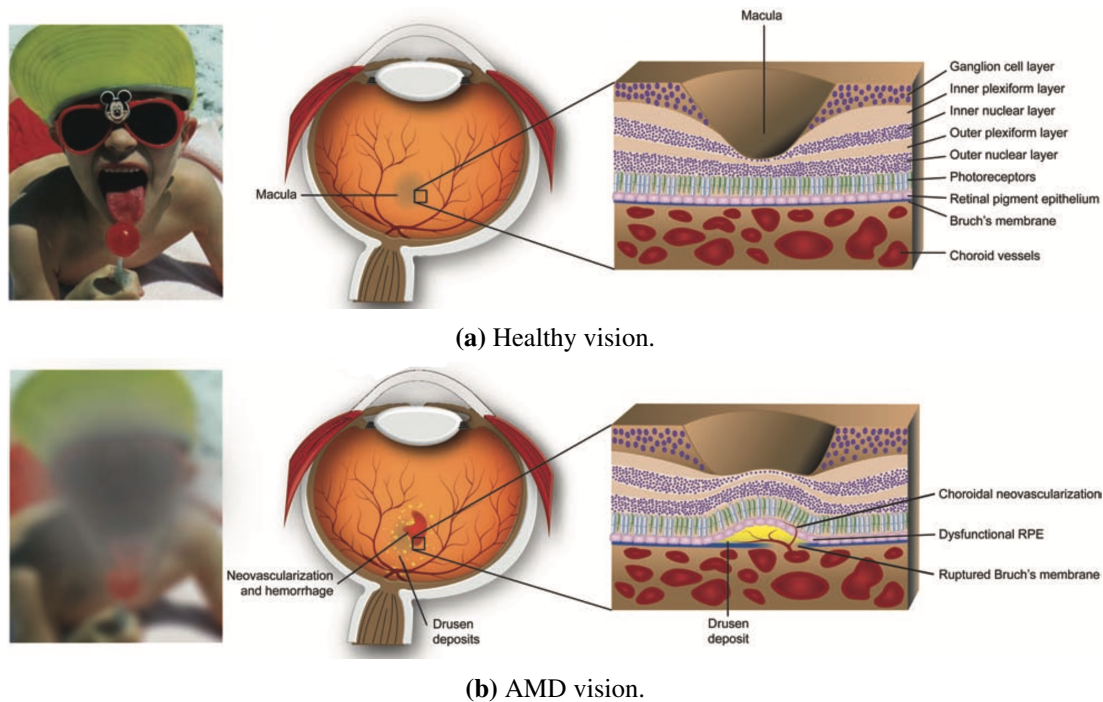


Figure 3.3: Demonstration of two different visual fields seen by two people, one with healthy vision and the other one with AMD disease [186]. (a) Shows a visual field seen by a person with healthy vision, a diagram of a healthy human eye and a diagram illustrating a cross-section view of a healthy eye captured through the macula region demonstrating the anatomical healthy structure of the retinal layers as well as the choroid layer. (b) Demonstrates a visual field seen by a person with AMD disease, a diagram of a human eye with AMD disease depicting the deposits of drusen, i.e.: the yellow spots and the choroidal neovascularisation (CNV), i.e.: red area; and finally a diagram illustrating a cross-section view of an AMD eye captured through the macula region demonstrating how the anatomical structure of the retinal layers as well as the choroid layer are disrupted by AMD disease.

Unfortunately, the pathophysiology of the AMD disease remains largely unknown and there are no clear warning early indications that can be linked to it. However, it should be noted that wet AMD can be successfully treated by clinical interventions with intravitreal injections to stop the vision from getting worse, while the current treatment for dry AMD is regular examinations to prevent progression to wet AMD. Unfortunately, there is no definitive or effective cure found at present that can provide a full recovery to the original vision for those patients diagnosed with either types of AMD disease [181, 184].

However, special dietary supplements such as high doses of vitamins including C and E, among others may lower the chances of vision from getting worse or at least prevent the potentially rapid progression to the advanced form of AMD disease for those patients diagnosed with dry AMD [181, 187, 188]. Consequently, early discovery and treatment are critical, and quick diagnosis has been associated with better results [4]. Early detection of areas related to CNV lesions and distinction between subjects with wet AMD and dry AMD are consequently prioritised in terms of effort and healthcare resources. Clinical trials are also continuing to seek improved imaging mechanisms and treatment modalities [181].

3.2.2.2 Diabetic Retinopathy (DR)

Diabetic Retinopathy (DR) is one of the most common complications of a well-known systemic and chronic disease, specifically diabetes mellitus, and is ranked as the second most common source of vision impairment among working age populations in the developed world and recognised as a worldwide epidemic [118, 180]. One in ten adults aged 20 to 79 years, or 537 million people, are estimated by the International Diabetes Federation (IDF) to have diabetes [189]. By 2030, this figure is expected to reach 643 million, and by 2045, it will reach 783 million [189]. Fortunately, there is abundant evidence that vision impairment and visual loss of patients diagnosed with DR disease can be successfully prevented through annual screening, keeping blood sugar under control, early diagnosis, etc. [180, 188, 190]. This is in contrast to AMD disease, the pathophysiology of which remains, unfortunately, largely unknown and there are no clear or early warning signs or symptoms associated with it.

3.2.2.3 Glaucoma

Among other major ocular diseases that act on the retina is glaucoma [180]. It is also categorised as one of the leading causes of visual impairments worldwide [58,

191]. It is recognised as being the third most significant ocular disease tending to cause blindness in the developed world. Clinically, it is defined as a permanent optic neuropathy that causes gradual damage to the optic nerve that connects the eye to the brain, and the ganglion cell layer of the retina. This can result in losing central vision and ultimately visual field loss as well [58, 191]. Unlike wet AMD disease that progresses very rapidly, i.e.: over a few months or even weeks, resulting in vision loss, the glaucoma generally tends to progress slowly over many years. Because of this, most patients with glaucoma only realise by chance that they have the disease, e.g.: during a routine vision examination. Due to this, it can lead to impaired vision if not treated or diagnosed early.

3.3 Retinal Vasculature Imaging Modalities

As demonstrated so far, the retina can be very vulnerable to both organ specific and systemic diseases. Consequently, imaging the retinal vasculature, i.e.: the network of retinal blood vessels, is crucial in facilitating the detection and diagnosis of the various eye diseases in a good and timely manner. To enable this, a number of retinal imaging modalities have been developed. Examples of common imaging techniques include the fundus imaging techniques, e.g.: the Fluorescein Angiography (FA) and the Indocyanine Green Angiography (IGA), the Optical Coherence Tomography (OCT) imaging technique and the Optical Coherence Tomography Angiography (OCTA) imaging technique. Section 3.3 discusses these various imaging techniques, including highlighting the advantages and disadvantages of each imaging technique.

3.3.1 Fundus

Broadly, fundus imaging is the procedure in which a two dimensional image set is acquired using reflected light of the three dimensional retinal semi-transparent tissues projected onto the imaging plane [180]. Consequently, any imaging technique that results in a two dimensional image set, where the intensities of image set characterise only the quantity of a reflected amount of light, is considered as fundus imaging technique. Because the fundus camera is generally considered quite safe as well as cost effective at characterising retinal abnormalities, it has continued to be the primary technique of retinal imaging.

Nevertheless, the fundus camera is capable of providing a number of different fundus imaging techniques for imaging important retinal landmarks including the retinal vasculature. Among the most popular fundus imaging techniques usually used for clinical retinal vascular imaging are Fluorescein Angiography (FA) and Indocyanine Green Angiography (IGA). FA and IGA are both invasive fundus imaging techniques that require intravenous administration of dye and the imaging time can take up to 30 minutes [7, 192–196]. They have been the gold standard imaging techniques for evaluating and visualising clinical vascular including the retinal blood circulation [7, 197, 198]. This is because they can provide a decent dynamic visualisation of the vascular anatomy and blood flow with a wide field of view [7]. Figure 3.4 provides two different images of a human eye with wet AMD disease captured by the FA and IGA imaging techniques. As such in some situations where the dye leaks out of incompetent vessels, this is a useful clinical sign of pathologic processes that is often used as an indication of abnormal blood vessels [197].

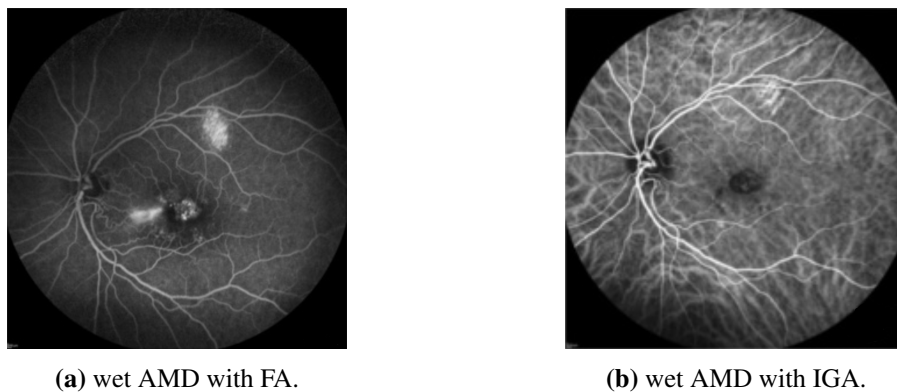


Figure 3.4: Visualising images of abnormal retinal blood vessels appearance of a human eye as captured using two different fundus imaging techniques, namely FA and IGA [7]. (a) Shows wet AMD with FA imaging technique and (b) displays wet AMD with IGA imaging technique.

Nevertheless, while the above mentioned two fundus imaging techniques have been the criterion standard imaging techniques for a relatively long time due to their advantages such as cost effectiveness, reasonable safety and capacity to provide relatively sufficient imaging resolution of retinal vasculature, they both suffer from several disadvantages. For instance, although the patterns of dye leakage are typically used as a clinical indication of vascular pathologies or anatomical anomalies e.g.: vascular permeability, it may, however, obscure other serious retinal vascular pathologies e.g.: CNV areas [7, 197].

Furthermore, the localisation of the lesions through the various retinal layers as

well as the size delineation of CNV regions can be extremely challenging due to not only the dye leakage but also because neither of the imaging techniques are depth resolved [7]. Although they enabled improved imaging of retinal blood vessels, it became apparent that not all blood vessels of the various retinal layers were being imaged [198]. Consequently, it is not normally possible to trace the abnormalities of retinal vasculature through retinal layers by segmenting the various retinal vascular layers with FA or IGA.

The FA and IGA fundus imaging techniques also have further major disadvantages that may restrict their widespread utility. Due to the invasive and time-consuming nature of both imaging techniques, they are not desirable to be utilised on a day-to-day clinical routine basis in such busy situations. Although they are generally considered to be quite safe to use, they may cause numerous serious complications and side effects that are potentially life threatening. Among the most frequent side effects with the dye injections with utilising the FA imaging technique are those varying from nausea or vomiting to allergic reactions, e.g.: hives, itching and in rare situations anaphylaxis, i.e.: severe allergic reaction that may include the patient feeling faint, difficulty in breathing, etc. that can cause death [7, 197, 199]. A further severe complication of dye injection that can occur using the FA imaging technique is extravasation, i.e.: the leakage of a fluid under the skin [199]. This can be very painful and may result in a number of uncomfortable symptoms that may involve sloughing of the skin, although this may happen only in rare circumstances [199].

Besides the aforementioned severe complications and side effects that may occur, utilising the IGA and FA imaging techniques are also contraindicated in pregnancy, particularly those in the first trimester as well as those with kidney problems [7, 200, 201]. There are also some published and unpublished stories reporting the death of some patients shortly after intravenous of dye injection using the FA imaging technique [199]. Although the reasons behind these deaths were unclear, they could potentially be due to severe allergic reactions, among others. The exact cause of death in every case has not been reported or confirmed and hence, it may be coincidental [199]. Nevertheless, severe pulmonary edema, i.e.: a serious condition caused by excess of watery fluid fill in the lungs, after utilising the FA imaging technique has also been reported [199].

Basic details and examples about the textural appearance of retinal vasculature in IGA and FA images have been demonstrated; however, full details about understanding and interpreting the IGA and FA images of the human eye under various ocular

conditions are beyond the scope of research presented in this thesis. Hence, readers are referred to these outstanding papers [7, 198, 199, 202] for additional details with regards to images interpretations as well as comparisons with other well established imaging techniques including OCT and OCTA.

Nevertheless, patients who need regular follow up examinations or those who cannot tolerate repeated intravenous dye injections due to concerns about the potential side effects and complications previously mentioned, imaging techniques that are accompanied with features such as speed, non-invasiveness and capacity to clearly visualise the various retinal vascular layers and choroidal vascular are always profoundly desirable. Examples of such outstanding imaging techniques that are complemented with these exceptional features include OCT and OCTA. The following subsections 3.3.2 and 3.3.3 provide comprehensive descriptions of important details about OCT and OCTA imaging techniques respectively.

3.3.2 Optical Coherence Tomography (OCT)

The optical coherence tomography (OCT) imaging technique was originally developed in 1991 by Huang et al. [203]. The OCT imaging technique is completely different from the aforementioned fundus imaging techniques, i.e.: FA and IGA, which are dye based and also require highly skilled photographers and interpreters [199,204]. Briefly, the OCT imaging technique works by scanning a beam of light on the anterior eye or the retina to measure the depth of a certain ocular tissue structure as well as quantifying how much this tissue structure scatters or reflects light [202]. This measurement of scanning procedure is known as an axial scan or an A-scan. The cross-sectional OCT image is typically produced by successively obtaining several A-scans as the light beam is scanned in the transverse direction.

The OCT imaging technique generated an enormous revolution in the field of ophthalmology by allowing a three dimensional, rapid, easy, safe, noninvasive and quantitative evaluation as well as visualisation of the structure of various retinal layers, including other major parts of the eye, e.g.: the fovea and optic disc at a microscopic level [197, 203–208]. With the OCT imaging technology, visualising the posterior of the human eye, including the internal cross-sectional microstructure of tissues in real time have been successfully made possible in a contact free manner [205, 209]. Figure 3.5 shows the appearance of diseased and healthy cross-sectional tomographic images of two different human eyes. Detachments and disruptions of various retinal layer thicknesses can be clearly observed. These retinal layer changes are among the

major characteristics for identifying CNV areas of AMD disease in OCT images.

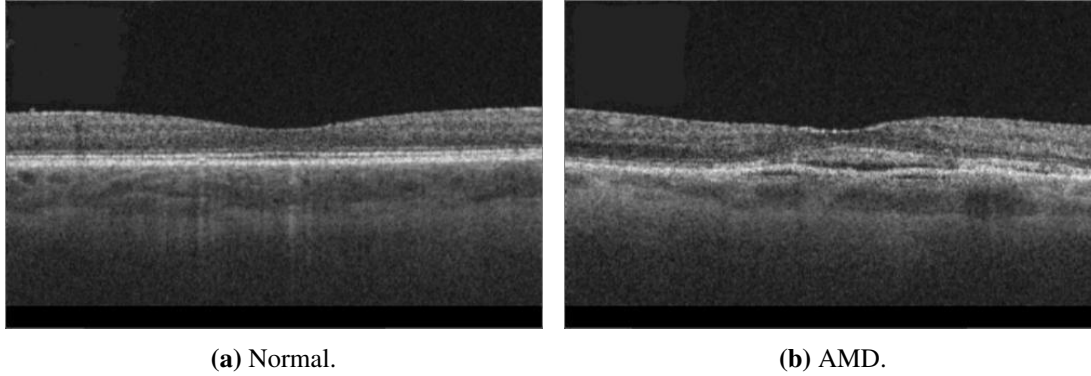


Figure 3.5: Visualising the textural appearance of cross-sectional tomographic images of two different human eyes with different conditions captured using the OCT imaging technique. (a) Represents a healthy cross-sectional structure of the retinal layers. (b) Demonstrates a disrupted and abnormal cross-sectional structure of retinal layers due to AMD disease.

The OCT imaging technique has also been successfully utilised and applied in a wide variety of ophthalmic studies. These include imaging and evaluating the human anterior eye [206], the layered structure of the retina [207], measuring the retinal thickness [210] and many more applications [209]. Nevertheless, this wide applicability and investigation of its utility had not continued for long before it became apparent that the characteristics of cross-sectional tomographic images of OCT imaging technique were inadequate since they provide poor visualisation about the structure of retinal vasculature [204]. Specifically, OCT can only provide cross-sectional tomographic images that represent the thickness of retinal vasculature layers, rather than the whole vasculature network of retinal and choroidal layers themselves.

Motivated by the great imaging capabilities that the OCT imaging technique can provide, such as three dimensionality, rapidity, ease and safety of imaging as well as its noninvasive nature, despite the previously mentioned limitations, improvements have continued to evolve significantly and rapidly in speed, resolution as well as imaging depth [197]. This rapid progress has led to the introduction of the OCTA imaging technique that is an advanced extension form of the conventional cross-sectional OCT imaging technique. The following subsection 3.3.3 provides details about the OCTA imaging technique.

3.3.3 Optical Coherence Tomography Angiography (OCTA)

The Optical Coherence Tomography Angiography imaging technique, sometimes known as (OCT) Angiography or OCTA for short is an extraordinary retinal vasculature imaging technique. While this imaging technique is a few years old i.e.: roughly a little more than ten years, its first introduction into clinical use was in 2014 [22]. Despite being a very recent retinal vascular imaging technique, it has brought about an enormous shift not only in evaluating and quantifying the structure of retinal and choroidal vasculature but also in diagnosing and understanding various retinal and choroidal vasculature pathologies.

In particular, the OCTA imaging technique allowed the visualisation of extremely fine details concerning the retinal and choroidal blood vessels in an unprecedented manner. It is a functional extension of the conventional OCT imaging technique but with an additional capacity to precisely visualise very tiny details of retinal and choroidal vasculature at a micro level [202, 211–222]. This is accomplished by employing a motion contrast scanning technology to characterise and distinguish between static and moving elements in retinal and choroidal blood vessels. Nevertheless, important details about the OCTA imaging technique and how it works as well as comparisons with other angiography gold standard imaging techniques, e.g.: the FA, IGA and OCT, are comprehensively illustrated in Appendix B, Section B.1.

Motivated by the significantly negative impact of AMD disease in the elderly population and the outstanding imaging features and capabilities that the OCTA imaging technique can deliver, these two elements, namely AMD and OCTA, are among the major subjects of research presented in this thesis. Hence, the following section, 3.4, provides comprehensive details about the characteristics and the size of OCTA image data sets utilised in this research project including information about the conditions of various subjects, e.g.: healthy and different AMD types that the OCTA image data sets represented.

3.4 Description of OCTA Image Data Sets

The work presented in this thesis makes use of OCTA image data sets that are captured from a 3×3 mm field of view that is centred around the fovea region. The dimensions of the OCTA images are 320×320 pixels. The motivations of using the OCTA image data sets with the 3×3 mm field of view are not only because they have been demonstrated to provide better resolution of ocular vascular texture appearance, but also since they

can reveal important ocular vascular texture details that cannot be seen on conventional dye-based images, e.g.: the FA and IGA images, as investigated across a wide variety of studies [7, 197].

The study also utilises the automatically projected and segmented OCTA image data sets that show the typical ocular vascular texture appearance at four distinct retinal and choroidal depth level slabs or layers. Specifically, the OCTA images of the superficial inner retina, the deep inner retina, the outer retina and the choriocapillaris layers are obtained. The depth levels of OCTA images that show the various retinal and choroidal layers are unaltered and purely used as extracted directly by the default defined settings of ocular tissue depth levels measurements and segmentations of the OCTA imaging technique used, which is the ZEISS AngioPlex. This is to avoid the additional complexity of manual manipulations of adjusting and segmenting the OCTA images.

Moreover, the step of manual annotating or delineating of vascular pathologies regions, e.g.: CNV areas in the retinal and choroidal OCTA images, were not performed in this research. While the manual annotating and adjustments of the imaging depth levels may provide OCTA images that perhaps demonstrate the best possible view of regions of important vascular pathologies, e.g.: CNV areas, so as to be precisely delineated and measured, the addition of such manual steps would also make the automated analysis of OCTA images less user-friendly, more labour-intensive and would ultimately introduce bias. Consequently, these additional manual steps can lead to misleading measurements about ocular vasculature, hence potential errors in diagnosis results.

The OCTA image data sets used in this research project are provided by two different hospitals, namely the Manchester Royal Eye Hospital and the Moorfields Eye Hospital. Comprehensive descriptions of the OCTA image data sets of both individual hospitals are given in the following two subsections, 3.4.1 and 3.4.2 for the Manchester and the Moorfields hospitals, respectively.

3.4.1 Manchester Royal Eye Hospital

The Manchester Royal Eye Hospital OCTA image data set comprises various subjects with healthy and late stage of AMD, i.e.: wet AMD, eyes. The number of healthy eyes involved in this study is 33, while the number of wet AMD eyes is 23. Hence, the number of OCTA images of every single healthy ocular vascular tissue layer is 33 while the number of OCTA images of every single wet AMD ocular vascular tissue

layer is 23. Table 3.1 provides a detailed description of the number of OCTA images that represent the individual retinal and choroidal vascular layers comprised in the Manchester OCTA image data set. Figure 3.6 demonstrates the textural appearance of the individual retinal and choroidal vascular layers, namely the superficial inner retina, the deep inner retina, the outer retina and the choriocapillaris layers of randomly selected healthy and wet AMD eyes.

Table 3.1: Summary of the total number of images in the OCTA image data set provided by Manchester Royal Eye Hospital.

Subjects	Ocular Vascular Tissue Layers				Total
	Superficial inner retina	Deep inner retina	Outer retina	Choriocapillaris	
Healthy	33	33	33	33	132
Wet AMD	23	23	23	23	92

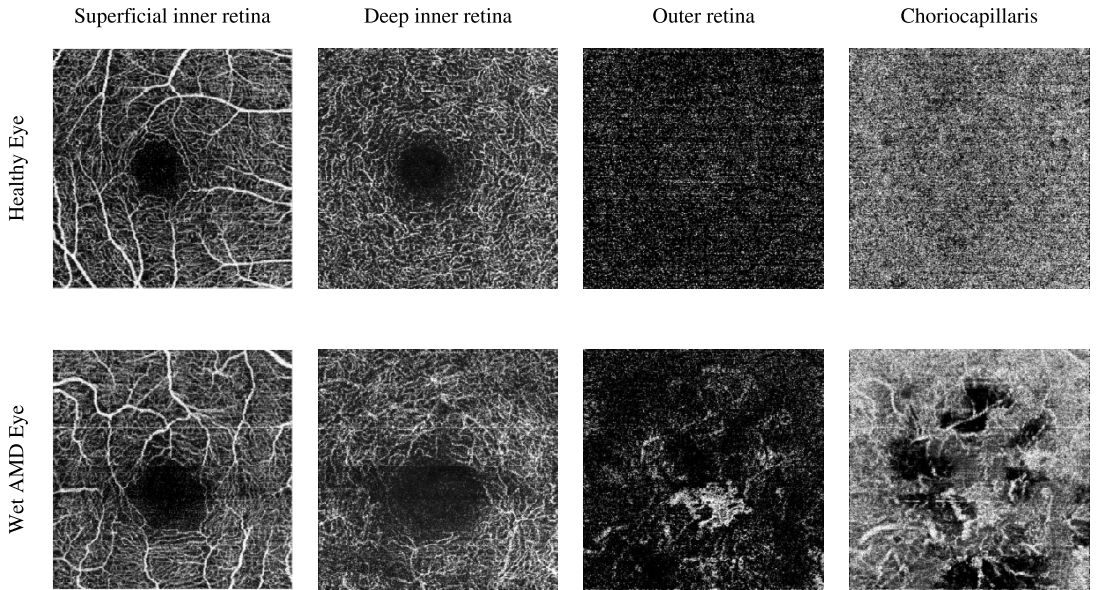


Figure 3.6: Visualising the various retinal and choroidal vascular layers of two randomly selected eyes with different ocular conditions, specifically healthy and wet AMD eyes from the Manchester Royal Eye Hospital OCTA image data set. The OCTA images in the upper row demonstrate the textural appearance of the individual retinal and choroidal vascular layers, namely the superficial inner retina, the deep inner retina, the outer retina and the choriocapillaris layers of a healthy eye. The OCTA images in the lower row, on the other hand, display the textural appearance of the same retinal and choroidal vascular layers but for an eye with wet AMD condition.

3.4.2 Moorfields Eye Hospital

The Moorfields Eye Hospital OCTA image data set includes numerous subjects with different types of AMD disease, i.e.: dry AMD and wet AMD, eyes. Other subjects with secondary CNV that share similar abnormal vascular characteristics of wet AMD disease are also included. They are denoted as secondary CNV because the causes of CNV regions are due to ophthalmic vascular pathologies other than AMD disease. The numbers of dry AMD, wet AMD and secondary CNV eyes involved in this study are 79, 166 and 25, respectively. Consequently, the total number of OCTA images of every single dry AMD ocular vascular tissue layer is 79, the total number of OCTA images of every single wet AMD ocular vascular tissue layer is 166 and the total number of OCTA images of every single secondary CNV ocular vascular tissue layer is 25. Table 3.2 provides a comprehensive description about the number of OCTA images that represent the individual retinal and choroidal vascular layers comprised in the Moorfields OCTA image data set. Figure 3.7 demonstrates the textural appearance of the individual retinal and choroidal vascular layers, namely the superficial inner retina, the deep inner retina, the outer retina and the choriocapillaris layers of randomly selected dry AMD and wet AMD eyes.

Table 3.2: Summary of the total number of images in the OCTA image data set provided by Moorfields Eye Hospital.

Subjects	Ocular Vascular Tissue Layers				Total
	Superficial inner retina	Deep inner retina	Outer retina	Choriocapillaris	
Wet AMD	166	166	166	166	664
Dry AMD	79	79	79	79	316
Secondary CNV	25	25	25	25	100

Interpreting and understanding OCTA image data under various ocular vascular conditions including AMD disease are typically performed using the above en face two dimensional OCTA images that are demonstrated in Figure 3.6 and Figure 3.7. Given the fine details about the individual ocular vascular tissue layers that the OCTA images can provide, identifying the presentation of CNV areas in AMD patients was part of the initial application of the OCTA imaging technique [18]. This is because it allows the defining and conducting of several qualitative and quantitative measures that can help in distinguishing healthy eyes among other eyes with various ocular vascular abnormalities including AMD disease. The following section 3.5 provides a comprehensive review of the numerous previous attempts to establish standardised qualitative

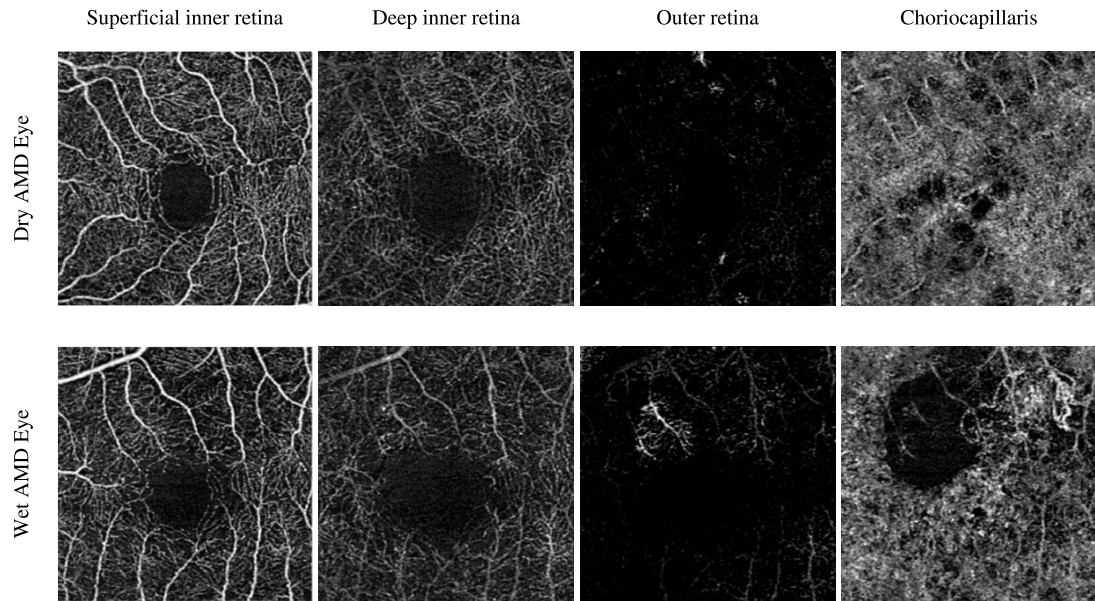


Figure 3.7: Demonstrating the various retinal and choroidal vascular layers of two randomly selected eyes with different ocular conditions, specifically dry AMD and wet AMD eyes, from the Moorfields Eye Hospital OCTA image data set. The OCTA images of the uppermost row demonstrate the textural appearance of the individual retinal and choroidal vascular layers namely the superficial inner retina, the deep inner retina, the outer retina and the choriocapillaris layers of a dry eye; the lowermost row displays the OCTA images for an eye with a wet AMD disease.

and quantitative measures as well as other studies that endeavour to develop and automate image texture analysis tasks, e.g.: image classification or image segmentation to analyse the textural appearance of OCTA images in the context of AMD disease.

3.5 Related Works

Since the first introduction of the OCTA imaging technique for use in daily clinical practice in 2014, there has been a huge surge in research interest towards using OCTA image data across numerous studies endeavouring to interpret, understand and quantify the textural appearance of OCTA images in the context of various ophthalmic vascular conditions including AMD disease [22]. Due to extensive research towards the analysis of OCTA image data since 2014, it may be impossible to list all previous related studies. As of January 2021, there have been over 3660 publications when only searching for “OCT + angiography” and “OCT angiography” in the PubMed search engine,

while in 2020 alone there have been over 1000 publications [22].

However, as the AMD disease is one of the major subjects of research presented in this thesis, only notable OCTA image data analysis studies related to AMD disease are selectively reviewed. Nonetheless, various OCTA image data analysis studies related to AMD disease can be grouped into two broad categories, namely conventional approaches and automated approaches. The following subsections 3.5.2 and 3.5.1 provide comprehensive details about the various approaches related to each category.

3.5.1 Conventional Approaches

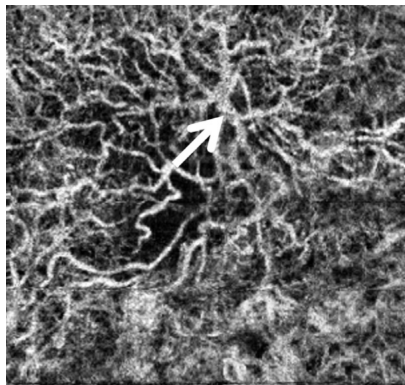
The previous methods for interpreting and understanding OCTA image data in the context of AMD disease that fall under the category of conventional approaches can be generally classified further into two main groups, namely qualitative analysis and quantitative analysis. These different conventional approaches typically attempt to propose various qualitative or quantitative measures based on certain morphological characteristics of the CNV areas that can be visually observed or statistically quantified from the textural appearance of OCTA images. Comprehensive details about the advantages and disadvantages related to the various previous studies, as well as the overall objectives of each individual approach, e.g.: qualitative analysis or quantitative analysis, are presented in the following sub-subsections 3.5.1.1 and 3.5.1.2.

3.5.1.1 Qualitative Analysis

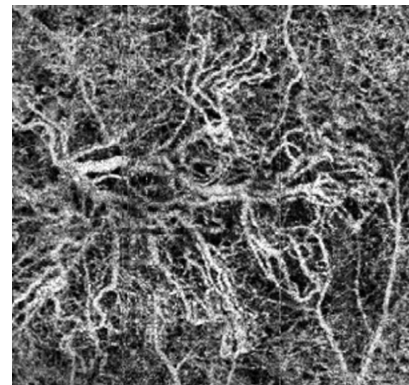
Performing qualitative analysis on OCTA image data is one of the early studies to detect ocular vascular pathologies in the context of AMD disease. The qualitative OCTA image analysis approaches generally attempt to visually establish standardised patterns for the CNV areas. This is typically accomplished by suggesting various qualitative features based on certain morphological characteristics of the CNV areas that can be visually observed from the textural appearance of OCTA images. Examples of notable works include the studies conducted by Kuehlewein et al. [8] and Sulzbacher et al. [9], among others [13–18].

The qualitative features used to describe the structures or textural arrangements of CNV regions suggested by Kuehlewein et al. [8] include defining three distinct terms of structural forms namely the “medusa”, the “sea fan” and the “indistinct” patterns. The term medusa pattern is typically used to describe the textural appearance of OCTA image that shows a large thick central abnormal blood vessel trunk with abnormal blood

vessels branched in various directions. However, if more than 90% of the abnormal blood vessels are branched in a single direction from a large thick central blood vessel trunk, the term sea fan pattern is used instead as a description. The term indistinct pattern, however, is typically used to describe the absence of distinct abnormal blood vessels or lack of clear detail about the textural appearance of vascular abnormalities, i.e.: CNV areas in OCTA images. The work conducted by Kuehlewein et al. [8] is based on two dimensional OCTA images that demonstrate the textural appearance of vascular in the choriocapillaris layer. Examples of OCTA images that show the textural appearance of these various qualitative features or patterns of CNV regions are given in Figure 3.8.



(a) A CNV lesion with a medusa pattern.



(b) A CNV lesion with a sea fan pattern.

Figure 3.8: Samples of OCTA images that show the textural appearance of two different qualitative features or patterns of CNV regions as suggested by Kuehlewein et al. [8]. (a) Represents an OCTA image that shows a CNV lesion with medusa pattern. The large thick central blood vessel trunk is indicated by a white arrow. (b) Demonstrates an OCTA image that visualises a CNV lesion with sea fan pattern.

The work conducted by Sulzbacher et al. [9], on the other hand, attempted to propose a new classification scheme for the wet AMD disease by establishing several specific vascular morphological patterns or qualitative features for describing the CNV regions. The qualitative features suggested in their classification scheme include a loose-net configuration (LN) pattern, a dense-net configuration (DN) pattern, a mixed type of DN and LN patterns and an unidentifiable CNV pattern. The LN pattern is typically used to describe the presence of individual blood vessels of large diameter within the CNV lesion that are perceptible and well defined with low branching index demonstrating no growing of capillary.

The DN pattern, on the other hand, is used to describe a high signal intensity of vascular network with a dense capillary branching, i.e.: a region of vascular flow that

bears a resemblance to a fine netlike pattern within the CNV lesion. The mixed type of pattern is typically used to describe a situation of CNV lesion that comprises a ratio of approximately 50% of CNV regions with a LN pattern and approximately 50% of CNV regions with a DN pattern. The unidentifiable CNV pattern, as the name suggests, it is used to describe situations when the CNV regions can neither be visually perceived in the outer retina nor in the choriocapillaris layers. The work conducted by Sulzbacher et al. [9] is based on two dimensional OCTA images that demonstrate the textural appearance of vascular in the outer retina and the choriocapillaris layers. Examples of OCTA images that show the textural appearance of the aforementioned different qualitative features or patterns of CNV regions are given in Figure 3.9.

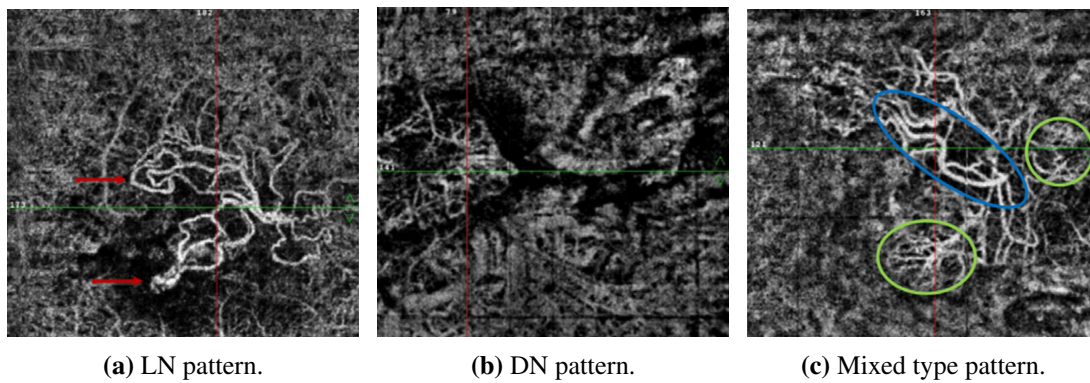


Figure 3.9: Samples of OCTA images that show the textural appearance of three different qualitative features or patterns of CNV regions as suggested by Sulzbacher et al. [9]. (a) Represents an OCTA image that shows a CNV lesion with LN pattern. The two red arrows indicate perceptible new blood vessels anastomosing, i.e.: forming connections that are normally branching or diverging, at the edge of the CNV lesion. (b) Demonstrates an OCTA image that visualises a CNV lesion with DN pattern. The region of CNV lesion with DN pattern is surrounded by a dark halo area, i.e.: located approximately around the crossing green and red lines. (c) Shows an OCTA image that presents a CNV lesion with a mixed type pattern that comprises both LN and DN patterns. The area of CNV lesion that contains the LN pattern is specified by a blue elongated circle while the areas of CNV lesions that comprise the DN pattern are indicated by green circles.

While numerous studies [8,9,14–18,223] have attempted to create consistent qualitative features for identifying and describing the presentation of CNV regions in AMD disease, the suggested classification schemes, criteria, and assessments are typically performed merely by means of inferential personal judgments. However, purely relying on the above-mentioned qualitative features for detecting areas of CNV lesions can be inappropriate for several reasons. For instance, the identification of various qualitative features visually can vary among clinicians or researchers. In addition, interpreting

and confirming their visual appearance in the texture of OCTA images generally tends to be largely subjective in nature. Consequently, this may lead to unreliable measurements of CNV lesions and hence, misleading diagnosis results.

3.5.1.2 Quantitative Analysis

Nevertheless, to alleviate the matter of potential variations between various clinicians and facilitate establishing standardised methodologies for interpreting the texture of OCTA images, quantitative measures have been widely employed across several AMD based OCTA image analysis related studies. Among remarkable OCTA image analysis studies related to AMD disease that are based on quantitative features include the works conducted by Kuehlewein et al. [224], Al-Sheikh et al. [225] and many others [18, 223, 226–228]. The overall objective of utilising quantitative measures is generally attributed to seeking additional rigorous consistency in analysing the texture of OCTA images. As such, several simple mathematical formulas or feature extraction operations have been employed to acquire quantitative measurements of CNV regions in patients with AMD disease from the texture of OCTA images. Examples of quantitative operations typically employed to quantify areas of CNV lesions include the blood vessel density (BVD) measure and the fractal dimension (FD) measure, among other quantitative measures [18, 224, 228].

The BVD measure is typically used to estimate the proportion of the region occupied by blood vessels to the whole region of a CNV lesion based on merely pixel intensity values [17, 18, 224, 225, 228]. It is normally computed over two dimensional greyscale OCTA images that are transformed into binary images using a thresholding operation that is manually fine-tuned to best visualise abnormal vascular networks, e.g.: CNV lesions [18]. Manual adjustments of the imaging depth levels of the OCTA imaging technique are usually required [18, 224, 225]. As such to provide OCTA images that reveal the best possible view of the regions of important vascular pathologies, e.g.: CNV areas, so as to allow performance of precise delineation and quantification. This BVD measure can provide details of variations in region size of CNV lesions before and after treatments [18, 224].

The FD measure, on the other hand, is related to the number of replicated patterns and the ratio of magnification factors. Specifically, it is estimated based on how many repeated patterns of an equal scale are required to enclose a certain blood vessel structure [225, 228]. This measure is typically used to assess the architecture of an abnormal vascular network as it provides an estimate of the degree of vascular lesion

pattern complexity, i.e.: details of the texture roughness of an abnormal blood vessel [225]. It is normally calculated over two dimensional greyscale OCTA images that are transformed into binarised and skeletonised images using thresholding and skeletonisation operations that are manually fine-tuned to best visualise abnormal vascular networks, e.g.: CNV lesions [18, 225]. The skeletonisation operation is related to the process of reducing certain foreground regions in binary images to enhance the representation while preserving most of the underlying structure of regions present in the original images. Manual adjustments of the imaging depth levels of the OCTA imaging technique are also usually required [18, 224, 225]. As such to provide OCTA images that reveal the best possible view of the regions of important vascular pathologies, e.g.: CNV areas, so that to facilitate performing precise delineation as well as quantification over the regions of interest.

The FD measure can take any value in the range of 0 to 2 such that ($0 \leq \text{FD} \leq 2$). A large value of FD measure indicates an increased complexity of vascular lesion pattern i.e.: a rougher texture of vascular lesion [225]. If the value of FD measure is 0 that may indicate the appearance of a point, while the value of 1 may suggest the presence of a smooth curve and the value of 2 may refer to the existence of a filled rectangle [69]. Any other FD measure values that fall between 0 and 2 may represent the existence of any irregular vascular texture patterns or shapes. The changes of the FD measure values are usually used as indicators for assessing improvements in the pattern complexity of the CNV lesion regions before and after treatments [225].

The ability to quantitatively estimate ocular vascular changes in OCTA images due to abnormalities, e.g.: CNV lesions in AMD disease, has been demonstrated to enhance AMD detection as well as to provide several advantages. For instance, it can provide great opportunities including not only the acquisition of greater insight into understanding details about the spatial progression of CNV lesions over a certain period but also to allow evaluating their structural information in response to treatments [18]. Nevertheless, when assessing the previously mentioned approaches that utilise quantitative measures as clinical diagnostic techniques for evaluating and monitoring patients with AMD disease, they suffer from several limitations. For example, most of the previous techniques require manually delineating for the boundaries of the CNV lesions regions so as to be measured [18, 223]. However, this is a very laborious task to perform that would rather constrain the applicability of such approaches that require outlining regions of interest manually in such busy clinic situations. Additionally, this is not a trivial task to perform given the complexities and significant variations

in the textural appearance of CNV lesions in OCTA images among various patients as well as different ocular vascular layers.

An additional important limitation associated with previous approaches includes the necessity of manual steps for adjusting the imaging depth levels of the OCTA imaging technique to allow capturing OCTA images with the best possible view of details of regions of vascular pathologies, e.g.: CNV areas. Besides the involvement of manual steps being very time consuming and potentially introducing bias, the adjustments of the imaging depth levels can be an extremely challenging task. This is because the textural appearance of vascular details varies significantly among various ocular vascular layers and this is largely attributed to the nature of how abnormal blood vessels grow. As the CNV lesions typically grow by perforating the Bruch's membrane that is the deepest part of the choroid layer and progress into other subretinal layers, vascular details can appear more obvious in certain layers than others [183]. Hence, capturing OCTA images that include precise and comprehensive localisation information about CNV areas can be impossible to achieve.

A further downside associated with the previous approaches is the application of morphological transformations, e.g.: a skeletonisation operation or applying a simple thresholding operation to the OCTA images [18, 225]. While the application of these techniques is believed to enhance the vascular networks appearance in OCTA images, they may cause undesirable changes to the underlying structural arrangement of vascular texture in the OCTA images. Furthermore, the quantitative operations, e.g.: the BVD and the FD measures for evaluating the regions of CNV lesions suggested by the previous approaches are manually performed. Consequently, they are not ideal to be employed in clinics with large populations as they are very laborious to compute on every single patient visit.

Although some basic quantitative OCTA related measures, e.g.: the BVD and the FD measures, have been made possible and can be provisionally estimated directly from OCTA images with certain pathologies, e.g.: AMD disease, even with such simple quantitative measurements they can be inaccurate if they are not calculated rigorously [22, 229, 230]. A major reason for this is due to the potential presence of image artifacts, i.e.: noise, such as uneven illumination in OCTA images [222, 231]. This can cause major distortion to the textural appearance of CNV regions in OCTA images. Consider a case with the presence of significant uneven illumination of CNV regions in OCTA images. While the textural appearance of CNV regions in the OCTA images may appear different, the CNV regions may, however, share the same distribution of

pixel intensity values as the case previously illustrated in Figure 2.7. Therefore, relying on simple statistical quantitative measures including the BVD measure that is based on raw image pixel intensity values distribution to quantify the texture contents of OCTA image, i.e.: the CNV regions, can be inadequate and misleading.

Likewise, the FD measure can also be inaccurate for quantifying the areas of CNV lesions in OCTA images. This is because the FD measure values in OCTA images typically take fractional FD measure values, while synthetic or man-made images may have integer FD measure values. Recall that the FD measure is based on the number of replicated fractals or patterns; however, in most natural texture images including OCTA images, this number is normally unknown due to the large quantity of variabilities and complexities in real images. Consequently, this FD measure may be more appropriate for deterministic patterns that appear in synthetic or man-made texture images, since the number of replicated patterns is normally well-known in those images.

As the OCTA is an emerging imaging technique, OCTA image data may also involve other image artifacts, e.g.: orientation changes to the texture of OCTA images [25, 27, 202, 222]. The severity of these potential image artifacts i.e.: illumination and orientation changes can vary among OCTA images from being negligible to prevalent [22]. Equally important, evaluating OCTA image data visually and manually can also be indefensible due to limited resources. This issue is particularly critical for the OCTA imaging technique as it produces high resolution image data that typically require additional effort to examine and evaluate.

Given the previously mentioned limitations with previous approaches, automating the ways of quantifying and analysing the textural appearance of OCTA images for patients with AMD disease is therefore of a profound priority to be enabled. Besides, automation of OCTA image analysis can allow effective validation of OCTA image data to be performed so that they can reach their highest potential in the clinic, the automation of OCTA image analysis can also provide several advantages. For example, this can allow performing a rapid evaluation of abnormal vascular regions, e.g.: the CNV lesions, specifically on every single patient visit to the clinic or the hospital. Consequently, this can provide effective assessments of AMD patients who need regular follow-up examinations to be performed as well as early identification of those patients who are in extreme need of urgent observation or treatment to be effectively recognised in a suitable timely manner. Hence, this in turn can allow accomplishing both smooth and rapid streamlined workflow in busy clinical settings.

The following subsection 3.5.2 provides comprehensive details about the various

advances and most recent works that attempt to automate the task of analysing OCTA images in the context of AMD disease.

3.5.2 Automated Approaches

Fortunately, rapid developments in the OCTA imaging technique are proceeding simultaneously with improvements in automating various tasks of analysing the texture of OCTA images, e.g.: classification and segmentation [22]. This rapid progress in the automation of various OCTA image analysis tasks are mainly steered by the introduction of various advanced computer vision and AI systems that are constructed with carefully selected specialised and sophisticated techniques including texture representation, deep learning, pattern recognition and machine learning algorithms [22]. Techniques based on computer vision and AI systems are among the most important approaches in the field of computer science as they are exploited across numerous domains ranging from academia, medicine, business and industry, among others [22].

Nevertheless, medical diagnostic imaging is one of the domains that has particularly benefited the most from the developments and improvements of various computer vision and AI systems [22], such as the numerous computer vision and AI systems accomplishing state-of-the-art performance in various extremely challenging image texture analysis tasks. These tasks include performing feature extraction, pattern recognition, classification and segmentation and many more in medical image data that are captured by numerous imaging modalities such as X-ray, Magnetic Resonance Imaging (MRI), Computed Tomography (CT), OCTA, OCT, FA, IGA and many other imaging techniques [22, 232].

Extensive research in exploring computer vision and AI systems has already revealed that these systems demonstrated feasibility in various medical domains, including radiology and pathology, that have remarkable similarities to ophthalmology [118]. This is because these various medical domains are equally deeply embedded into the diagnostic medical imaging that is the most prominent application of computer vision and AI systems in healthcare as evidenced by several studies [22, 118, 233]. Figure 3.10 illustrates the proportion of computer vision and AI systems that are applied into diagnostic medical imaging data in comparison to other diagnostic medical related data on the PubMed search engine [233].

From Figure 3.10, it can be clearly perceived that diagnostic medical imaging holds the highest proportion. Hence, this confirms diagnostic medical imaging as the most prominent domain for the application of computer vision and AI systems to automate

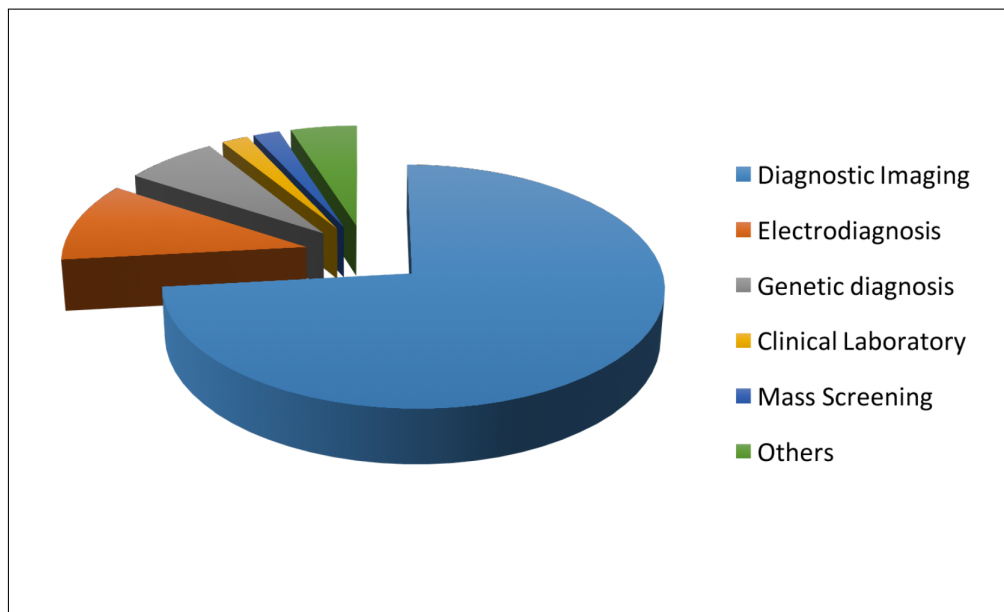


Figure 3.10: Illustrating the proportion of computer vision and AI systems that are applied into diagnostic medical imaging data in comparison to other diagnostic medical related data on the PubMed search engine [233].

various medical image understanding and analysis tasks. This can be greatly appreciated, and this is due to the nature of medical images, as they usually appear very complex and high-volume which makes them challenging to be interpreted visually [233]. The application of computer vision and AI systems in diagnostic medical imaging data is also anticipated to further expand as various imaging modalities, e.g.: OCTA imaging technique, rapidly improve [118].

Nevertheless, while numerous studies [118, 159, 160, 234–242] endeavour to automate identifying AMD disease, most of them are concerned with automating the analysis of images produced by the OCT, FA and IGA imaging techniques, rather than the novel OCTA imaging technique. However, the OCT, FA and IGA imaging techniques are not designed to generate high resolution images of individual ocular vascular layers and hence may fail to visualise or distinguish the abnormalities associated with the AMD disease. Likewise, automated AMD detection approaches based on the OCT, FA and IGA images are carefully developed with specialised measures and methods that are particularly suited to the characteristics of those images. Hence, they may not be appropriate or applicable for analysing OCTA images of AMD disease. Consequently, developing specialised automated image texture analysis approaches for AMD detection based on the characteristics of OCTA images is necessary.

Although there are numerous studies [8, 9, 14–18, 223–228] endeavouring to quantify and identify AMD disease in OCTA images, studies concerning specifically the automation of AMD detection in the context of OCTA image data have been significantly lacking until now. Nevertheless, recent works to automate OCTA image texture analysis tasks in the presence of AMD disease broadly fall into two main categories, namely image segmentation and image classification tasks. Comprehensive details about the merits and demerits related to the various previous studies as well as the overall objectives of every individual task, e.g.: segmentation or classification, are given in the following sub-subsections 3.5.2.1 and 3.5.2.2.

3.5.2.1 Image Segmentation

As previously seen with the conventional quantitative operations, e.g.: BVD and FD measures for evaluating the regions of CNV lesions, they typically require precise manual tissue and blood vessels segmentation or delineation as an initial step. However, with the presence of potentially significant image artifacts, e.g.: changes in illumination and rotation, and complex vascular patterns, e.g.: variations in shape, location, and size in the OCTA images of various ocular vascular layers between different patients, the capacity of manually segmenting the areas of CNV lesions effectively may exceed the clinician's ability [10]. Hence, measurements of CNV lesions derived based on manual delineating of the boundaries of CNV areas via conventional quantitative approaches may potentially be misleading.

Motivated by the potential issues mentioned above, accurate automated segmentation and quantification of CNV lesions is extremely necessary. This is not only because it can ensure the extraction of robust and less biased measurements of areas of CNV lesions, but also can provide several advantages to clinicians. For instance, it can allow them to gain more insight into understanding details about the CNV lesions in AMD disease. Specifically, it would be extremely useful in the diagnosis of CNV lesions, the evaluation of the therapeutic effectiveness of various treatments, speeding up the clinic workflow and so on [10]. Consequently, these matters call for the profound necessity for robust and reliable automated segmentation methods that are capable of accurately identifying regions of CNV lesions in OCTA images.

The overall aim, however, of automating the analysis of OCTA image texture by the mean of image segmentation is typically to partition the OCTA image into multiple disjoint regions in order to simplify and transform the complex representation of an OCTA image into a new representation that is more interpretable and understandable,

i.e.: highlighting important regions, e.g.: CNV areas, to make it clearly observable. It might also potentially help for further analysis to be performed or for more information to be obtained using the segmented regions of interest, such as the areas of CNV lesions. As such, various segmented regions, i.e.: CNV areas in the segmented OCTA image, may comprise a certain appearance or characteristics such as texture, colour, etc that are potentially heterogeneous or homogeneous with other regions, e.g.: healthy vascular areas or areas of CNV lesions. Based on the similarities or dissimilarities of segmented regions, OCTA images may perhaps be more measurable or understandable.

Notably, image segmentation problems are among the most challenging image texture analysis tasks among computer vision and AI-assisted medical image analysis applications. This is essentially because prior knowledge or details about the regions of interest, e.g.: CNV areas that are to be segmented, are typically required, however, these details may not be always evidently apparent. Examples of these details include the number of various regions, e.g.: CNV areas, objects, types of textures that exist in the textured image and so on. While it may not be necessary to know these details, being aware of them is the only way to tell if the various segmented areas, e.g.: CNV regions or healthy vascular regions in the OCTA image, share similarity with each other or if each area, e.g.: a CNV region, is distinct from another region, e.g.: a healthy vascular region, in the segmented image.

As demonstrated in Chapter 2, specifically in subsection 2.2.2, image segmentation tasks are typically further grouped into two broad categories, namely region-based and boundary-based, depending upon the task to be achieved. Nevertheless, most previous attempts to automate the analysis of OCTA image texture by means of image segmentation are region-based. In the region-based approaches, the overall objective is to detect the areas, e.g.: CNV regions, that have a uniform textural appearance or colour. The process then typically may involve merging or combining the detected areas, e.g.: CNV regions, with each other based on their similarity.

The region-based approaches have the advantage that the boundaries of the areas, e.g.: CNV regions, are usually roughly closed. Hence, areas identified with different texture appearance or colour may be well defined and separated. However, the region-based approaches have some disadvantages. This is because it may be sometimes necessary to define a set of values of parameters before segmenting the image, e.g.: the OCTA image, such as a similarity threshold value, number of distinct regions, e.g.: CNV regions and so on. Nonetheless, among notable recent studies to automate the

task of segmenting and quantifying areas of CNV lesions in OCTA images for patients diagnosed with AMD disease are the works by Jia et al. [6], Liu et al. [10], Zhang et al. [243] and Taibouni et al. [244].

The automated segmentation approach proposed by Jia et al. [6] is among the early attempts to analysis OCTA images with a view to automate detecting and quantifying regions of CNV lesions by the means of segmentation. Their segmentation scheme is based on two dimensional greyscale OCTA images of the deep inner retinal and the outer retinal layers that are captured from a $3 \times 3 \text{ mm}$ field of view that is centred around the fovea region. The OCTA images of these two different retinal layers are extracted by manually adjusting the imaging depth levels of the OCTA imaging technique to acquire OCTA images that reveal the best possible view of the regions of interest, e.g.: CNV areas. A total number of 10 eyes comprising 5 eyes diagnosed with wet AMD disease and 5 eyes normal controls were involved in their study.

The segmentation procedure of Jia et al. [6] starts by applying a 30×30 -pixel Gaussian filter to an OCTA image of the deep inner retinal layer to produce a binary OCTA image of large deep inner retinal vessel map. This filtering step is aimed at removing any potential blood flow projections from the blood vessels of the superficial retinal layer to the outer retinal layer. The result of this filtering operation is a new OCTA image of the deep inner retinal layer that contains only large blood vessels projections while most small deep inner retinal blood vessels are removed. The segmentation technique is then followed by subtracting the filtered OCTA image of the deep inner retinal layer from the OCTA image of outer retinal layer. This produces a new OCTA image of the outer retinal layer that contains no large blood vessel projections. A 10×10 -pixel Gaussian filter is then applied to the newly generated OCTA image of the outer retinal layer to produce a binary OCTA image of the outer retinal flow map. This filtering step is intended to remove any potential remaining blood flow projections to obtain a clean map of the outer retinal layer as it is a typically avascular layer, i.e.: shows no blood vessels. The final resultant OCTA image of the outer retinal layer is then anticipated to demonstrate a clear map of the CNV region, where further analysis can be performed such as measuring the size of CNV area.

The automated segmentation scheme proposed by Liu et al. [10], on the other hand, is built upon the work by Jia et al. [6], introducing further enhancements to allow accurate recognition of CNV areas. Their segmentation scheme is based on two dimensional greyscale OCTA images of the deep inner retinal and the outer retinal layers that are captured from a $3 \times 3 \text{ mm}$ field of view that is centred around the fovea region, as

in the work by Jia et al. [6]. The imaging depth levels of the OCTA imaging technique were also manually adjusted during extraction of the OCTA images of the two different retinal layers. This is to obtain OCTA images that reveal the best possible view of the regions of interest, e.g.: CNV areas. A total number of 7 eyes from 7 participants diagnosed with wet AMD disease were involved in their study. Their segmentation scheme assumes that the CNV region occupied a large portion of the OCTA image.

Broadly, the segmentation procedure by Liu et al. [10] starts with a pre-processing step that involves applying a 20×20 -pixel Gaussian filter to an OCTA image of the deep inner retinal layer. This is then followed by subtracting the filtered OCTA image of the deep inner retinal layer from an OCTA image of the outer retinal layer. This is to produce a clean OCTA image of the outer retinal layer that better highlights the CNV region, since most large, deep inner retinal blood vessels are removed. However, the resulting OCTA image may still contain minor, bright discrete noise regions, i.e.: very small areas of blood flow projections. To eliminate these potential noise regions and define a clear map of the CNV area, a context-aware saliency model based on orientation, brightness, and location information is applied. This produces a saliency map of the CNV area that is further improved by a post-processing step through applying non-linear filtering, thresholding, and morphological operations to acquire a clean outline or boundary of the CNV area to be measured. The CNV area is then estimated based on the proportion of flow pixels located within the boundary of CNV lesions.

A later study was conducted by Zhang et al. [243] to propose an automated segmentation algorithm to identify CNV lesions and quantify the size of CNV regions in OCTA images. Their segmentation scheme is based on two dimensional greyscale OCTA images of the outer retinal layers captured from 3×3 mm and 6×6 mm field of views centred around the fovea region. During extraction of the OCTA images of the outer retinal layers, a semi-automated segmentation procedure was employed. This was performed by incorporating manual corrections to the imaging depth levels of the OCTA imaging technique. This is to ensure accurate segmentation and detection of the OCTA images revealing the best possible visualisation of the relevant retinal layer that distinctly show useful and important details, i.e.: regions of CNV lesion. A total number of 27 eyes from 23 subjects diagnosed with AMD disease were involved in their study.

The automated segmentation algorithm of Zhang et al. [243] briefly follows six main steps. It starts by taking the OCTA image of the outer retinal layer as an input and enhances the contrast and brightness by applying an adaptive thresholding method,

i.e.: different threshold values for different image regions. This generates a contrast enhanced OCTA image that is smoothed by applying a Gaussian filter. The smoothed OCTA image is further processed by applying a thresholding operation to generate a binary OCTA image. A morphological dilation operation is then applied on the generated binary OCTA image to detect the contour or boundary of the CNV areas. The area size of the CNV lesion is finally estimated based on the proportion of pixels that occupy the CNV region that is bounded by the boundary line. Their study demonstrated that when using OCTA images captured with $3 \times 3 \text{ mm}$ field of view, it is possible to obtain reliable measurements of CNV regions via the automated algorithm. However, this is in contrast with OCTA images that are captured with $6 \times 6 \text{ mm}$ field of view, as this in turn made it a challenge for the automated algorithm to quantify the correct size of the CNV regions.

A recent study was conducted by Taibouni et al. [244] to design an automated quantification and segmentation algorithm for distinguishing various shapes, sizes, and locations of regions of CNV lesions in the context of AMD disease based on OCTA images. Their segmentation scheme is based on two dimensional greyscale OCTA images of the outer retinal layers that are captured from a $3 \times 3 \text{ mm}$ field of view that is centred around the macula region. The OCTA images of the outer retinal layers are obtained by manually amending the imaging depth levels if the automated segmentation of the OCTA imaging technique for the relevant retinal layers was not satisfying to ensure the acquisition of OCTA images that reveal the best possible view of the regions of interest, e.g.: CNV areas. A total number of 54 eyes from 54 patients diagnosed with wet AMD disease were involved in their study.

The patients involved in the study of Taibouni et al. [244] were also further divided into two different categories based on the topology appearance of CNV lesions in OCTA images. The OCTA images that show densely crowded networks of CNV lesions with no noticeable branching patterns are grouped under category 1. However, the OCTA images that demonstrate networks of CNV lesions with noticeable separate branching patterns are grouped under category 2. A different segmentation algorithm was created for every single category. Nevertheless, two common steps were involved with the two different segmentation algorithms. The first step included the contrast enhancement operations as well as median filtering operations. These operations are intended to separate areas of CNV lesions from noise to clearly discriminate the outlines of CNV regions. The second step comprises the necessity of the clinicians' interactions to manually select a single or several markers on the OCTA images to suggest the

location of CNV lesions that are to be segmented and measured. Several quantitative measures based merely on pixel intensity value disputations have been used in their study to quantify areas of CNV lesions, e.g.: the BVD measure, to estimate the proportion of the region occupied by blood vessels to the whole region of a CNV lesion. The algorithm developed for the group of patients in category 2 that have noticeable separate branching patterns of CNV lesions broadly demonstrated better performance compared to the algorithm designed for the group of patients in category 1.

Previous automated segmentation algorithms [6, 10, 243, 244] have been demonstrated to provide several advantages for clinicians. These include allowing rapid and accurate detection and quantification for areas of CNV lesions in AMD patients to be performed. They can also reduce the interactions of clinicians in interpreting, delineating and understating complex OCTA images of various retinal vascular layers for various patients with AMD disease. Despite previous attempts [6, 10, 243, 244] to automate the analysis of OCTA images by means of image segmentation being potentially clinically beneficial, being soundly innovative and having provided some advantages to clinicians, they do, however, suffer from numerous limitations. Examples of these include situations where several patients diagnosed with AMD disease were excluded from the automated analysis in most previous studies [10, 243]. On some occasions, various patients diagnosed with AMD disease were separated into several different groups and distinct automated segmentation algorithms developed based on the topology appearance of the areas or the texture areas characteristics of CNV lesions [244].

There are several motivations for exclusion of some patients or separation of them into different groups based on the topology of CNV areas in previous studies [10, 243, 244]. These can include a situation where the trained graders were potentially unable to identify or confirm the presence of CNV regions in OCTA images. Another potential reason may be that the areas of CNV lesions were not very perceptible or fully contained within the OCTA images. The well-defined presence of CNV areas in OCTA images is crucial in enabling the successful automated analysis of OCTA images by means of image segmentation. As such to allow precise quantifications to be performed over the regions of interest, i.e.: areas of CNV lesions.

Nevertheless, most previous automated segmentation approaches [6, 10, 243, 244] also require assistance from clinicians who are domain experts to manually amend the imaging depth levels of the OCTA imaging technique. This is to ensure production of OCTA images that show the best possible details of regions of CNV lesions. While the amendment of the depth levels of the OCTA imaging technique may be beneficial, it

may however, introduce bias. Consequently, the previously mentioned limitations can be a major barrier that would rather limit making the most of the features delivered by the OCTA imaging technique, such as the automated segmentation of various vascular retinal layers. Likewise, the clinical applicability and utility of almost all previous automated segmentation approaches [6, 10, 243, 244] designed for evaluating patients diagnosed with AMD disease can be inappropriate and misleading. Hence, these automated segmentation approaches [6, 10, 243, 244] cannot be integrated into daily clinical practices as their overall objectives, e.g.: reducing the burden on the clinicians, ensuring to capture reliable and consistence measurements of CNV lesions and so on, are nearly all violated.

3.5.2.2 Image Classification

In computer vision and AI-assisted medical image texture analysis applications, the task of an image or a texture classification follows a slightly different approach to that in the image segmentation tasks. Specifically, the overall objective is typically to assign an entire image or a particular texture region within an image as belonging to a class of a predefined set of categories in the training samples. The classification task can be conducted as a binary classification problem, such as classifying a whole image as diseased or healthy. An additional example of a binary classification problem includes the task of localising a texture region within an image as being inside or outside a given texture class, e.g.: a healthy or a diseased texture region. The classification task can also be performed as a multiclass classification problem, such as classifying different images from healthy subjects among other subjects with various ocular diseases, e.g.: AMD, DR and glaucoma. Nevertheless, comprehensive details including general examples about a range of image classification tasks are given in Chapter 2, specifically in subsection 2.2.1.

While there are several attempts [6, 10, 243, 244] to automate the analysis of OCTA image texture in the context of AMD disease by means of image segmentation, studies that concern automating the task of image classification in OCTA images with AMD disease are unfortunately significantly lacking until present. This is not only because the OCTA imaging technique is new and there are only a few labelled OCTA image data sets with AMD disease that can be made available, but also the opposite classes, i.e.: healthy subjects that are profoundly necessary for enabling the image classification tasks, are extremely hard to obtain. These two aspects are very crucial behind the success in creating various computer vision and AI-assisted medical image texture

analysis systems by the means of image classification. Nevertheless, among the outstanding recent works to automate the task of image classification in OCTA images for patients diagnosed with AMD disease are the studies by Vaghefi et al. [245] and Wang et al. [246].

The study conducted by Vaghefi et al. [245] is aimed at exploring the feasibility of combining various ocular vascular image data sets as produced from multiple different ocular vascular imaging modalities in comparison to only relying on a single ocular vascular image data set generated from a single ocular vascular imaging modality in solving retinal image analysis and understanding tasks. Specifically, this is to investigate whether the detection accuracy of dry AMD could be enhanced in this way. The various ocular vascular imaging modalities employed in their study include the OCTA, the OCT and the standard colour fundus photography (CFP) imaging techniques. The standard CFP imaging technique visualises the ocular vasculature in a manner similar to those previously mentioned fundus imaging techniques, i.e.: the FA and the IGA. However, the main difference is that the CFP imaging technique does not involve the injection of a contrast agent, i.e.: dye. Instead, the retina is typically illuminated by only white light and then examined merely in full colour, hence the name “colour fundus photography” [58].

Before diving into the description of the automated retinal image analysis work for the diagnosis of dry AMD proposed by Vaghefi et al. [245], a brief overview about the participants enrolled and data sets utilised in their study are firstly given. A total number of 75 participants were involved in the study, distributed into three different groups based on their age and eye condition. The first group includes 20 young healthy (YH) subjects, the second group involves 21 old healthy (OH) subjects, and finally the third group comprises 34 patients diagnosed with dry AMD. Only a single eye of each individual participant underwent several different eye scan examinations, specifically the CFP, the OCT, and the OCTA imaging techniques.

The automated retinal image analysis in the study of Vaghefi et al. [245] was performed based on participants not individual images to avoid data leakage between the training and testing data sets. None of the participants were excluded in their study due to, for example, having any existing posterior eye diseases, e.g.: glaucoma, low image quality and so on that may affect the appearance of retinal or choroidal vasculature in the various images captured. The OCTA, OCT, and CFP image data sets are used in their raw form and there was no pre-processing step involved prior to conducting the

image analysis. As the OCTA image data set comprises several images from the various retinal and choroidal layers, e.g.: images of the outer retina and choriocapillaris layers, the images of individual layers are identified and extracted in an automated manner without any manual assistance.

Nevertheless, the automated retinal image analysis for the diagnosis of dry AMD proposed by Vaghefi et al. [245] is accomplished by means of developing different automated image classification methods based on so-called “deep learning” technology. Particularly, various automated image classification methods are developed through experimenting with numerous different design strategies of learned texture representation techniques, e.g.: CNN models. These are achieved by utilising the various ocular vascular image data sets generated to train several different designs of CNN models. This is then followed by evaluating the performance of the individual designs of CNN models to identify the best overall performing design of CNN model that can detect dry AMD cases more accurately.

The general investigation strategy followed by the study of Vaghefi et al. [245] comprises experimenting with specifically three different designs of CNN models. The first design involves training three separate single modality-based CNN models on every single ocular vascular image data set as produced from every single imaging modality, namely the CFP, the OCT, and the OCTA imaging techniques respectively. The second design comprises training two separate dual modality-based CNN models on two different ocular vascular image data sets combined. These combined data sets are generated by combining two different retinal image data sets as produced from two different imaging modalities, namely the OCT + the OCTA and the OCT + the CFP imaging techniques, respectively. The third design includes training one multimodality-based CNN model on multimodal ocular vascular image data sets that are generated by merging together the different retinal image data sets produced from the three different imaging modalities, namely the OCT + the OCTA + the CFP imaging techniques. Multiclass image classification tasks, i.e.: classifying individual participants as belonging to one of the following three classes, namely young healthy (YH), old healthy (OH) and dry AMD, are conducted in all three previous steps of investigation.

The evaluation results of various methods developed by Vaghefi et al. [245] demonstrated that each imaging modality can be more appropriate for classifying certain categories. For example, both single modality-based CNN models based on the CFP data

set alone and the OCTA data set alone are almost equally revealed to be the most sensitive in identifying dry AMD cases. However, the single modality-based CNN model that is based on the OCT data set alone has been demonstrated to be more sensitive to ageing, i.e.: detecting the YH and OH groups more accurately rather than identifying the eye condition. Nevertheless, the evaluation of three different designs of CNN models related to exploitation of the OCTA data set show that the single modality-based CNN model trained on the OCTA data set alone can achieve an overall diagnostic accuracy of 91%. The dual modality-based CNN model trained on the OCT + the OCTA data sets demonstrates an overall diagnostic accuracy of 96%. The multimodality-based CNN model trained on the OCT + the OCTA + the CFP data sets demonstrates near perfect diagnostic accuracy result as of 99%.

A summary of the evaluation results for the multiclass image classification tasks performed by the various CNN models that are specifically concerning to exploit OCTA data set as proposed by Vaghefi et al. [245] is given in Table 3.3. Particularly, the evaluation results demonstrate the performance of various CNN models that are based on the OCTA data set alone, the combination of the OCTA + the OCT data sets and the merging of the OCT + the OCTA + the CFP data sets, respectively. From the evaluation results in Table 3.3, it can be clearly observed that as more image data from different imaging modalities are combined, the performance greatly improves for detecting both ageing, i.e.: YH or OH, as well as the eye condition, i.e.: dry AMD disease.

Table 3.3: A summary of the multiclass image classification results of the various CNN models proposed by Vaghefi et al. [245].

Design of CNN Model	Evaluation Measures	Age and Eye Condition		
		YH	OH	Dry AMD
CNN Model based on OCTA	Sensitivity / recall	95%	83%	97%
	Specificity	99%	96%	76%
	Accuracy	91%		
CNN Model based on OCTA+OCT	Sensitivity / recall	100%	95%	92%
	Specificity	97%	94%	98%
	Accuracy	96%		
CNN Model based on OCTA+OCT+CFP	Sensitivity / recall	100%	99%	100%
	Specificity	100%	100%	99%
	Accuracy	99%		

A very recent and outstanding study was conducted by Wang et al. [246] for the

identification of areas associated with CNV lesions in OCTA images for patients diagnosed with late stage of AMD disease, i.e.: wet AMD. Recall that the tasks of image classification and image segmentation are closely related to each other as previously described in Chapter 2, specifically in subsection 2.2.2. As such, the various techniques used to solve image classification tasks can also be borrowed for solving image segmentation tasks, and vice versa. Nevertheless, the work conducted by Wang et al. [246] integrates both image analysis tasks, namely classification and segmentation, in a single algorithm by exploiting deep learning technologies. Specifically, they developed a single algorithm based on two learned texture representation techniques, i.e.: two CNN models. The two CNN models perform complimentary tasks, and together construct a robust algorithm for classifying and segmenting areas of CNV lesions. Broadly, the algorithm starts first with the task of classifying input OCTA images based on the presence or absence of regions associated with the CNV lesions, and then, if areas of CNV lesions are present, the following task is to segment the areas of CNV lesions that appear within the OCTA images.

Prior to outlining the algorithm proposed by Wang et al. [246], details about the eye conditions of participants, the OCTA image data sets and the pre-processing steps involved in their study are given. A total number of 607 eyes comprising 117 eyes diagnosed as CNV cases and 490 eyes as non-CNV control cases were involved in their study. The CNV cases comprise several eyes diagnosed by retinal specialists with CNV lesions due to wet AMD disease and CNV secondary to wet AMD disease. The eyes with secondary CNV lesions share similar abnormal vascular characteristics of wet AMD disease. The non-CNV control cases comprise several eyes with various conditions including healthy eyes as well as eyes diagnosed with other retinal vascular pathologies including dry AMD, DR, among others.

All participants with CNV and non-CNV eyes in the study of Wang et al. [246] underwent several eye scan examinations using only the OCTA imaging technique. The field of view of scanning area was set to 3×3 mm centred around the fovea region. Diverse and information-rich OCTA image data sets including OCTA images of the inner and outer retina with different depth levels as well as volumetric OCTA image data cubes of the outer retinal vasculature were collected and used in their study. The three-dimensional OCTA outer retinal volumes were separated into several two dimensional OCTA images with distinct depth levels to facilitate feeding them into the two dimensional CNN model employed.

Nevertheless, the number of OCTA images used in the work of Wang et al. [246]

is 1,676 in total involving several OCTA images from repeat and regular follow-up eye examinations that are captured from same macular area which is centred on the fovea. The various OCTA images obtained from follow-up eye examinations were treated as unique cases. This is because the textural appearance of CNV lesions in the OCTA images is significantly different between various visits of patients to the clinic for the OCTA imaging sessions. None of the OCTA images were excluded due to, for example, low image quality that could affect the textural appearance of retinal or choroidal vasculature in the various OCTA images captured.

Additionally, different pre-processing steps were performed in the study by Wang et al. [246] on the various OCTA image data sets utilised. These include manual modifications of the imaging depth levels of the OCTA imaging technique during extraction of the OCTA images. Furthermore, various regions of interest, i.e.: areas of CNV lesions in the OCTA images of the outer retinal layer, were manually segmented by experienced clinicians to use as ground truth to train the algorithm for performing the segmentation task. Additionally, the application of layer subtraction operations on the OCTA images, e.g.: images captured from the superficial retinal layers which are subtracted from images acquired from the deeper retinal layers, was also performed. This is to construct clean OCTA images of the outer retinal layers that typically contain no large blood vessel projections and better highlight the CNV regions.

Generally, the outline of the proposed automated CNV lesions identification and segmentation algorithm of Wang et al. [246] is as follows. As the algorithm consists of two distinct CNN models, they are jointly trained on the diverse OCTA data sets to perform two integrated tasks. Specifically, these are to classify the OCTA images as either containing CNV lesion or being CNV lesion free, and to segment the areas of CNV lesions if present in the OCTA images. Consequently, the algorithm performs two image analysis tasks, namely a binary image classification in the OCTA images, i.e.: CNV vs non-CNV, and an image segmentation on the detected areas related to CNV lesions in the OCTA images, respectively.

The overall task of the first CNN model in the algorithm of Wang et al. [246] is to identify whether the areas of CNV lesions are present in the input OCTA images based on a CNV size cut-off threshold value or otherwise classify the input OCTA images as non-CNV, i.e.: CNV-free. The CNV size cut-off threshold value of an area of CNV lesion was estimated based on maximising the detection sensitivity in the training OCTA data sets. The OCTA images with areas of CNV lesions that are smaller than a physical area of $0.004 \text{ mm} \times 0.004 \text{ mm}$, i.e.: approximately equivalent to a pixel area

of 7×7 in an OCTA image, are not considered to comprise regions of CNV lesions. If the CNV lesions are present, the process is then followed by localising the areas of CNV lesions within the input OCTA images and generating blood vessel masks corresponding to the locations of CNV lesions. However, the main task of the second CNN model is to perform a pixel-wise blood vessel segmentation over the blood vessel masks generated through the first CNN model. Overall, the ultimate outputs of the entire automated diagnosis algorithm are segmented OCTA images that comprise only segmented areas associated with the CNV lesions.

The automated OCTA image analysis algorithm developed by Wang et al. [246] was evaluated based on the individual eyes rather than the individual OCTA images. As such, no single eye was included in both training and testing the algorithm developed, i.e.: the OCTA image data sets used for training and testing the algorithm are all from totally different eyes. Nevertheless, the training OCTA image data set involves massively diverse and information-rich OCTA image data sets with a wide variety of representations. These include original and manually depth level adjusted OCTA images of the inner and outer retina, the manually annotated OCTA images of the outer retinal layer that demonstrate the segmented areas of CNV lesions, the OCTA images of outer retina processed by layer subtraction operations and volumetric OCTA image data cubes of the outer retina. As such, every single eye may have numerous different representations of OCTA image data in the training OCTA image data set. The training OCTA image data set involves 764 OCTA images with different representations acquired from 67 CNV eyes and 802 OCTA images with different representations obtained from 430 non-CNV eyes.

However, the testing OCTA image data set used to assess the performance of the algorithm developed by Wang et al. [246] on previously unseen OCTA image data comprises a single OCTA image of every single eye involved. Specifically, a single OCTA image of the outer retinal layer of every single eye was involved. The OCTA images of the outer retinal layer were selectively chosen as the testing OCTA image data set since it was anticipated to include certain vascular characteristics that normally cause confusion in solving various related OCTA image data analysis problems, e.g.: segmentation and classification. Similarly, the use of OCTA images of the outer retinal layer in the evaluation of the algorithm is also because it is the layer into which the CNV lesions typically grow. The areas of CNV lesions also usually appear to be more noticeable in the outer retinal layer among other retinal layers. In total, the testing OCTA image data set involves 50 OCTA images captured from 50 CNV eyes and

60 OCTA images acquired from 60 non-CNV eyes. Although the number of OCTA images used in the testing OCTA image data set was significantly smaller than the training OCTA data set, the number of eyes in the training and the testing OCTA image data set was comparable. Additionally, the various eyes used in the evaluation are all selected randomly to avoid introducing any potential bias.

The evaluation results from an image classification perspective demonstrated that the automated algorithm developed by Wang et al. [246] was able to achieve a promising classification performance on the testing OCTA image data set as the sensitivity and the specificity measures were 100% and 95%, respectively. This clearly indicates that the automated algorithm successfully accomplished the first objective task, i.e.: performing an image classification in the OCTA images to differentiate between CNV vs non-CNV cases, as there were no cases of misdiagnosis related to CNV lesions on the selected testing OCTA image data set. Additionally, the overall classification performance was estimated based on the AUC measure and demonstrated a reliable diagnostic performance that has a near perfect classification result of 99%.

From an image segmentation perspective, the automated algorithm proposed by Wang et al. [246] was able to achieve such an encouraging segmentation performance on the classified OCTA images as to have detectable regions of CNV lesions from the testing OCTA image data set. Specifically, the segmentation accuracy of the automated algorithm on the various OCTA images with regions associated with CNV lesions was evaluated based on the Intersection Over Union (IOU) measure. The IOU measure is related to dividing the area of overlap between the manually and the automatically segmented regions by the area of union of both regions. A higher value of IOU measure, i.e.: over 0.50, indicates a good segmentation accuracy, while a low value of IOU measure suggests a poor segmentation accuracy. Nevertheless, the overall segmentation performance of the automated algorithm was 0.88 ± 0.10 as estimated based on the mean value of IOU measures obtained from the individual segmented OCTA images that were classified to have detectable regions of CNV lesions. Additionally, the automated segmentation scheme proposed by Liu et al. [10] was also evaluated on the same testing OCTA image data set and achieved a mean value of IOU measures, of 0.61 ± 0.23 .

The previously described automated diagnosis and classification algorithms [245, 246] were demonstrated to provide several advantages. For instance, they can reduce the burden of clinicians in busy clinical situations. Furthermore, they can also be less prone and influenced by individual human factors that may result in diagnosis errors

due to, for example, bias, tiredness, attitude, depression, among others. Additionally, they may provide the opportunity for various vascular imaging modalities, e.g.: the OCTA imaging technique to reach their highest potential in the clinic. With the utilisation of automated diagnosis methods, possible further insights into understanding deep details related to various eye conditions, e.g.: AMD disease, can be gained by extensively exploiting imaging data captured through various imaging techniques including OCTA.

An example of how such an important opportunity may arise includes revealing the capacity of a particular imaging data to reveal very important and crucial details that are potentially useful for identifying and diagnosing a certain eye condition, e.g.: AMD disease. The work by Vaghefi et al. [245] is a true, tested example of this as their automated diagnosis algorithm suggested that OCT, OCTA and CFP imaging modalities are inherently sensitive to various aspects of ocular conditions including AMD disease as well as ageing. Specifically, OCT imaging technique was found to be more sensitive to ageing, while CFP and OCTA imaging techniques were found to be more appropriate for identifying vascular pathologies related to AMD disease. However, these details would not have been feasible to identify visually as they became evident only after performing the automated analysis on various ocular vascular image data sets acquired from different imaging modalities, namely OCT, OCTA and CFP imaging techniques.

Likewise, the automated diagnosis algorithm proposed by Wang et al. [246] was demonstrated to provide enhanced solutions and techniques for improving patient care that were potentially very useful for evaluating and monitoring patients with AMD disease. For instance, the transition for the task of segmenting areas of CNV lesions from a manual to an automated approach can expand the amount of information available during patient monitoring within a very short time as well as with limited resources. As more imaging data accumulates, the automated diagnosis may also reveal crucial markers of CNV lesions that are potentially related to the progression or the prognosis which could have been previously unknown [246]. The manual tracing and outlining of areas associated with CNV lesions for every single patient would not be feasible. Hence, automated diagnosis by the means of joining two tasks, namely classification and segmentation in a single algorithm, can provide clinicians with a fundamental capability in case they desire to monitor or identify new and possibly better biomarkers associated with CNV lesions in the clinic.

Despite rapid progress and improvements witnessed across various domains, including medical imaging, automated medical image texture analysis and diagnosis algorithms based on deep learning techniques have not always kept pace. While the previously discussed algorithms proposed by Wang et al. [246] and Vaghefi et al. [245] to automate the diagnosis of OCTA images in the context of AMD disease can provide several advantages, sound innovative and accomplish the essential tasks for which they were intended, they suffer from numerous limitations. Notably, the evaluation of all previous attempts [245, 246] was conducted based on only very small, labelled data sets instead of performing the evaluation rigorously. The evaluation of the automated diagnosis algorithms has always been ideally performed through using large labelled data sets or potentially based on a statistically rigorous method, such as employing a cross validation strategy. Consequently, the generalisability of these automated algorithms [245, 246] have not been sufficiently proved, hence, the results are empirical.

As the previous automated algorithms proposed by Wang et al. [246] and Vaghefi et al. [245] are together based on deep learning techniques, i.e.: CNN models, evaluating both algorithms using large data sets or employing a cross validation strategy may also be infeasible. The lack of or insufficient steps taken in evaluating previous automated algorithms [245, 246] can be attributed to numerous factors. Among the most important is the unavailability of large scale and labelled OCTA image data sets, which are usually extremely difficult and expensive to obtain since the OCTA imaging technique has only recently been introduced. Additionally, the utilisation of a cross validation strategy to allow a rigorous evaluation can be a very computationally intensive operation. This is because the training and testing are typically conducted numerous times and hence can be an extremely tedious investigation task.

Notably, the evaluation step is always considered a critical phase in the development of various computer vision and AI-assisted medical image texture analysis algorithms. When performed rigorously, it can help to reduce the potential risks for the algorithms developed to overfitting or underfitting the data that to be analysed. The overfitting refers to the case when the algorithm performs well on the training data set but has a poor generalisation to the unseen data set. The underfitting refers to the case when the algorithm performs poor on the training data set and has a poor generalisation to the unseen data set. Nevertheless, the current common trend in developing automated image texture analysis techniques, including medical image diagnosis algorithms, have been based on introducing deeper and more complicated architectures of deep CNN models.

Despite the current trend being to develop deeper and more complicated architectures of deep CNN models for automating medical image texture analysis tasks, e.g.: classification or segmentation, they typically require tremendously large, labelled image data sets as well as special hardware, e.g.: power hungry GPUs [32]. Consequently, automated diagnosis algorithms based on deep learning techniques may not be appropriate to deploy on certain domains. For instance, the domain of medical diagnostic imaging when only limited resources can be made available. This can include the availability of only a limited number of skilled clinicians that can label or annotate novel image data sets, e.g.: OCTA images. Hence, this can present a major barrier towards the collection of OCTA image data sets that represent a particular ocular disease, e.g.: AMD disease, at a sufficient size that is appropriate to train and test deep CNN models.

Nevertheless, several measures have been taken in the studies by Wang et al. [246] and Vaghefi et al. [245] to tackle the matter of inadequate size of OCTA image data sets that represent the classes of interests, e.g.: AMD disease and healthy, so that it can be distinguished by exploiting deep learning techniques. For example, the work by Vaghefi et al. [245] addressed the matter by combining various retinal image data sets generated from three different imaging modalities, specifically OCT, OCTA and CFP imaging techniques. These various retinal image data sets allowed a multiclass image classification to be performed to differentiate between YH, OH and dry AMD disease subjects accurately by means of deep learning techniques.

The work of Wang et al. [246], on the other hand, tackled the matter by combining several OCTA images of eyes with various conditions including healthy eyes as well as various eyes diagnosed with other retinal vascular pathologies including dry AMD, DR, among others. These diverse OCTA images with various ocular conditions were used as the control cases and labelled together under the single name, non-CNV class. The opposite class comprises numerous OCTA images with CNV lesions due to wet AMD disease and CNV secondary to wet AMD disease and grouped together under the single name, CNV class. These diverse OCTA image data sets allowed performance of a binary image classification to accurately distinguish only subjects with CNV related lesions, i.e.: selectively differentiating only CNV cases from non-CNV cases.

While the various actions taken by the studies of Vaghefi et al. [245] and Wang et al. [246] facilitated identifying the subjects with AMD disease with a limited number of labelled OCTA image data sets, they involved numerous serious limitations. The automated algorithm proposed by Vaghefi et al. [245] demonstrates a superior diagnostic

accuracy as more different and diverse retinal image data sets from various imaging modalities are combined. Likewise with the automated algorithm proposed by Wang et al. [246], since identifying only CNV cases in OCTA images was only achievable when diverse OCTA images with various ocular conditions were used. From a feature engineering perspective, however, it is always desirable or perhaps necessary to have a set of robust representative features that characterises the textural appearance of an image representing the class or object of interest. This can be a car, a horse, a disease and so on, depending upon the image texture analysis task in hand. Nevertheless, having diverse and messy retinal images with different texture appearances that are perhaps not relevant or that do not represent a single factual ocular condition can be inappropriate and misleading.

Together, the studies by Vaghefi et al. [245] and Wang et al. [246] were demonstrated to be great examples of situations where only small OCTA data sets are available and that made both training and testing the deep CNN models employed in the automated retinal image analysis algorithms extremely challenging. The automated algorithm of Vaghefi et al. [245] can be an impractical technique for the diagnosis of dry AMD disease. This is because diagnosing every single patient visiting the clinic based on several images acquired from numerous ocular vascular imaging modalities is time consuming as well as requiring massively expensive resources including skilled photographers and different imaging techniques, e.g.: OCTA, OCT and CFP.

Furthermore, the basis on which the decision was made in the automated algorithm of Wang et al. [246] for the various OCTA images as being free of CNV lesions was not adequately justified. This is because the textural appearance of various OCTA images that fall under the class of non-CNV is significantly different from one ocular condition to another. For instance, the textural appearance of OCTA images captured from the healthy eyes normally show a uniform texture appearance in almost all retinal and choroidal layers that is significantly different from other eyes involved with different ocular conditions, e.g.: dry AMD, DR, among others. Additionally, it is not clear which ocular condition has contributed most to identifying accurately the OCTA images as being either CNV or non-CNV cases.

Moreover, identifying OCTA images with CNV lesions by the automated algorithm of Wang et al. [246] is only based on the presence of a noticeable CNV region. As the CNV lesions typically grow by perforating the Bruch's membrane that is the deepest part of the choroid layer and by progressing into other subretinal layers, vascular details of CNV regions can appear more obvious in certain layers than others. Hence, when

the regions of CNV lesions are not easily perceptible in the OCTA images, the OCTA images may be identified as non-CNV cases.

These previous issues are also amplified by the fact that the automated algorithm of Wang et al. [246] is also based on performing several pre-processing steps over the OCTA images used. These include manually adjusting the imaging depth levels of the OCTA imaging technique to allow capturing OCTA images with the best possible view of details within CNV areas. Furthermore, manually segmenting areas of CNV lesions in the OCTA images was also involved. Processing the various OCTA images through the layer subtraction operations was conducted. The application of these complex pre-processing steps in the OCTA images used may not only cause changes of important vascular details but also may be subject to human influence, e.g.: potential bias, attitude and so on.

As demonstrated so far, the OCTA imaging technique has served as an excellent example of a critical situation, since only limited image data sets can be made available despite the advantages of its various features over other imaging techniques, e.g.: OCT, FA, IGA, among others. This is because it is just a few years old and there is only a small number OCTA image data sets currently available that represent certain ocular conditions including AMD disease as well as healthy, as evidenced by several studies [6, 10, 25–27, 243–246]. Despite the various measures taken to tackle the limited size of OCTA image data sets available by several studies including the works by Wang et al. [246] and Vaghefi et al. [245], these works taken together are considered to be only proof of concept studies which would rather require conducting further investigation and validation when much larger labelled OCTA image data sets are available. Nevertheless, the most appropriate automated algorithm to diagnose and monitor patients with AMD disease, considering the current limitations with the OCTA imaging technique, would be the algorithm that can produce effective performance with the availability of limited numbers of labelled OCTA data sets.

3.6 Chapter Conclusion

The chapter provided a comprehensive summary of the related background of the application domain of the work presented in this thesis. It started by presenting brief details about the human eye. This was then followed by descriptions of the structure and physiology of the retina, the fundamental component of the human eye since it is

accountable for visual recognition. Afterwards, details with regards to the most common ocular conditions affecting the retina were presented. However, a special focus was given to AMD disease since it is the disease of interest for the whole work presented in this thesis. The various ocular vascular imaging modalities, e.g.: OCTA, OCT, FA, among others, were then reviewed. The advantages and disadvantages associated with every single imaging technique were also highlighted. Then, comprehensive descriptions about the various OCTA image data sets utilised in this thesis were given, including highlighting of the novelty of the OCTA image data sets used as produced by the novel OCTA imaging technique without any alterations or modifications, i.e.: in their raw form. Finally, the most recent and outstanding OCTA image data analysis studies related to AMD disease were selectively reviewed. The various studies reviewed were grouped into two broad categories, namely conventional approaches and automated approaches, and the merits and demerits of individual approaches were demonstrated.

Chapter 4

Classification Algorithm Based on Whole-Local Texture Features

4.1 Chapter Introduction

This chapter presents a fully automated OCTA image classification algorithm for the diagnosis of AMD disease based on whole-local texture features. The chapter begins by providing details about the motivations of enabling the automated analysis of OCTA images in the context of AMD disease by means of whole image classification. Additionally, the justifications of making the various choices including performing the analysis on the entire OCTA image of individual retinal and choroidal layers, selecting certain local texture descriptors as texture representation techniques, and choosing specific machine learning algorithms for conducting the image classification task, among other choices to be considered in the automated algorithm, are also provided. Afterwards, the outline of the automated algorithm, including the manner of extracting the local texture features from whole OCTA images and the way of classifying the various OCTA images with lesions related to AMD disease as well as healthy, are also given. Finally, comprehensive evaluation of the automated classification algorithm proposed, including performance comparison of the evaluation results, are also presented.

4.2 Motivation

A wide variety of studies have been conducted, irrespective of exploring image segmentation approaches [6, 10, 243, 244] or image classification approaches [245, 246], to enable the analysis of OCTA images in the context of AMD disease in an automated

manner. Despite numerous previous attempts [6, 10, 243–246], several limitations and issues attributed to several factors have been encountered. These factors can be associated with the OCTA image data or potentially the manner of analysing OCTA image data. Examples of these factors may include the lack of large, high-quality, and carefully labelled OCTA image data sets. Additionally, there is a risk of potential image artifacts, e.g.: illumination and orientation variations that can be present in various OCTA images. The severity of these image artifacts appears to vary among different OCTA images from negligible to prevalent [22].

Furthermore, the dependency on manual assistance was necessary in nearly all previous studies [6, 10, 243–246]. The necessities of manual involvements have been different across various automated image analysis algorithms proposed by previous studies [6, 10, 243–246]. These may include the need to manually adjust the imaging depth levels of the OCTA imaging technique. This is to allow the capture of high quality OCTA images that show the most detailed view of regions of CNV lesions. Another potential necessity may be manual annotation or delineation of important vascular pathologies, e.g.: CNV areas. This is to facilitate achieving certain objectives such as to conduct precise quantification over the regions of interest, i.e.: areas of CNV lesions, to train the OCTA image analysis algorithm on the areas of CNV lesions so that they can be segmented or identified, among numerous objectives.

Nevertheless, details about the various advantages and limitations of previous related studies [6, 10, 243–246] have already been comprehensively discussed from various perspectives in Chapter 3, specifically in section 3.5. However, when taking all the previously discussed factors into consideration, it becomes clear that they unfortunately have negatively impacted the accomplishment of automated analysis of OCTA image in the context of AMD disease in nearly all previous studies [6, 10, 243–246]. As such, a wide variety of automated image analysis algorithms for the diagnosis of AMD disease based on the OCTA images was constructed and achieved state-of-the-art performance, but with unfortunately questionable utilities. This is also amplified by the significant hurdle that still remains with the OCTA imaging technique, which is the lack of specific diagnostic criteria for OCTA image data in the presence of various retinal diseases including AMD disease [22].

Consequently, the work presented in this chapter seeks to tackle the various limitations confronted as well as to improve upon the previously reviewed attempts [6, 10, 243–246]. Specifically, this is to enable the construction of a reliable and fully automated OCTA image analysis algorithm that can accurately diagnose as well as

quantify AMD disease presentation in OCTA images. In seeking to achieve this fundamental goal, i.e.: building a reliable fully automated OCTA image analysis algorithm for AMD disease detection, several choices and measures have been carefully made. These are summarised by the following points, which include the rationales behind each consideration.

- **Enable a fully automated OCTA image analysis for AMD detection by the means of whole image classification.**

The main motivations for performing the OCTA image analysis by the means of whole image classification rather than image segmentation can be divided into two categories. Firstly, AMD disease suffers the absence of a standardised diagnostic criterion based on the novel OCTA image data [22]. As the OCTA is a new emerging imaging technique, identifying standardised biomarkers associated with AMD disease based OCTA image data have not yet been established despite significant progress in OCTA image analysis related to AMD disease studies [22, 246]. While this issue is linked to several factors, it can be mainly attributed to the nature of how the CNV lesions normally grow. This is because the CNV lesions typically grow by perforating the Bruch's membrane that is the deepest part of the choroid layer and by progressing into other subretinal layers. Therefore, important details about vascular pathologies, i.e.: areas of CNV lesions, can appear more perceptible in certain ocular vascular layers than others. Hence, defining standardised biomarkers related to the appearance of CNV regions based on a single OCTA image of any of the individual retinal or choroidal layers can be extremely challenging to accomplish.

Secondly, the OCTA images of various retinal and choroidal layers typically demonstrate blood vessels that are very thin and small, i.e.: at a pixel scale. As such with very small as well as dimly lit blood vessels, it can be very difficult for the human eye to distinguish which pixels exactly correspond to true blood flow through the vessels [246]. Consequently, the task of manually annotating and delineating areas of CNV lesions in the individual OCTA images of various retinal and choroidal layers to train and validate an automated image segmentation algorithm can be very challenging, even if the manual annotation was performed by highly skilled clinicians, as this task is highly subjective in nature. Likewise, inconsistencies between both the manually segmented regions by the expert clinicians and the automated segmented regions by the automated image segmentation algorithm may lead to significant variations when assessing the performance of the image segmentation task [246]. As such, it is difficult to tell whether the manually segmented regions by skilled clinicians or the automated

segmented regions by the automated image segmentation algorithm are the most accurate [246].

Consequently, quantitative measures based on manually or automated segmented regions as well as comparisons between outcomes from such regions may potentially be misleading. When taking all the previously mentioned aspects into account, it becomes clear that facilitating the automated analysis of OCTA image data for AMD detection by the means of whole image classification can be the most sensible approach. As such it can minimise the potential risk of the diagnosis results to be influenced by human factors, e.g.: bias, attitude and so on, due to the need of manual assistance as evident in previous studies [6, 10, 243, 244].

- **Use the OCTA images of four distinct retinal and choroidal layers in their raw form.**

The four different retinal and choroidal layers utilised are specifically the superficial inner retina, the deep inner retina, the outer retina and the choriocapillaris. The OCTA images of these various ocular vascular layers are extracted in a pure manner as previously described in Chapter 3, specifically section 3.4. As such, through exploiting the default defined settings of ocular tissue depth level measurements and segmentations of the OCTA imaging technique. Most previous studies [6, 10, 243–246] performed the analysis on the OCTA images of manually adjusted depth levels of various ocular vascular layers including the outer retina and the choriocapillaris layers. This is because vascular pathologies, e.g.: areas of CNV lesions, tend to appear more perceptible in the OCTA images of the outer retina and the choriocapillaris layers. The OCTA images of the superficial inner retina and the deep inner retina, on the other hand, are not typically used. However, they may have only been utilised when performing pre-processing steps, e.g.: layer subtraction operations as demonstrated by several studies [5, 6, 10, 246]. This is to construct clean OCTA images of certain ocular vascular layers, e.g.: the outer retinal layers, that typically would contain no large blood vessel projections but would only clearly exhibit the areas of CNV lesions.

Therefore, the use of OCTA images of the four different retinal and choroidal layers in their raw form exactly as extracted automatically by the OCTA imaging technique without also employing any pre-processing or manual assistance steps can provide several advantages. For example, it may assist identification of the most predictive ocular vascular layer, which includes the most important information related to the vascular pathologies of interest, e.g.: CNV lesions. Additionally, it may help to identify other novel ocular vascular abnormalities in the OCTA images of the superficial inner retina

and the deep inner retina, despite the fact that they do not display perceptible vascular abnormalities, nor are typically used in diagnosing areas of CNV lesions. As the main task is to automate the analysis of the OCTA images for AMD disease detection, this can also facilitate the construction of a purely data-driven diagnosis technique.

Additionally, the use of OCTA images of four different retinal and choroidal layers would be especially beneficial to ophthalmologists in situations when the characteristics of AMD disease in the various OCTA images appear to be more extremely complex in certain layers than others. As such, this can make relying on OCTA images of certain individual retinal or choroidal layers potentially misleading. This is because when the textural appearance of OCTA images appear very complex, it can make acquiring accurate measurements about areas of vascular pathologies, e.g.: regions of CNV lesions, extremely hard to obtain. Despite the several attempts to alleviate this issue by employing various procedures including the manual assistance steps, e.g.: adjusting the imaging depth levels of the OCTA imaging technique and the pre-processing steps, e.g.: layer subtraction operations, among other procedures. However, all these procedures have been demonstrated as highly challenging to accomplish, can cause undesirable changes to vascular details in the OCTA images and misleading diagnosis results, among numerous issues, as evident in numerous previous studies [6, 10, 243–246].

- **Employ dense local texture descriptors as texture representation techniques.**

Recall that the construction of computer vision and AI-assisted diagnosis systems for medical image texture analysis tasks such as classification or segmentation typically comprises several components that employ specific techniques to accomplish the task of interest. In solving medical image classification problems, for instance, the various components may include employing a texture representation technique, a feature selection or reduction technique, a classification scheme, etc. However, the fundamental element among the previously mentioned components that plays a crucial role behind the potential success in solving various image texture classification problems is the texture representation technique utilised to derive the texture measurements or features. Similarly important is finding the most appropriate texture representation technique, which is largely dependent on certain properties or requirements dictated by the image texture analysis problem under consideration.

The different properties can be related to various factors including the imaging conditions of texture images or the resources available, among others. Nonetheless, essential details of the most important properties must be taken into account when developing or selecting texture representation techniques. Additionally, specifying the

points at which every single property should be considered prior to quantifying the texture of images have already been comprehensively discussed from six different aspects in Chapter 2, specifically in section 2.7. The various aspects discussed include the property of robustness with respect to illumination or rotation variations in the texture of images and the property of robustness with respect to the size of image data sets available, among other important properties.

These various aspects, therefore, assist in decisions of whether or not a certain property should be considered in solving various image texture analysis problems, e.g.: classification and segmentation. As such, providing criteria to define or find the optimal texture representation technique based on the characteristics of the image texture data to be measured. However, when considering every single property in turn, it becomes obvious that employing the dense local texture descriptors as texture representation techniques for the OCTA image data are among the most sensible choices. The rationales behind making this choice, i.e.: employing the dense local texture descriptors to measure the texture of OCTA images for AMD disease recognition, can be justified by two main aspects.

The first aspect is that the OCTA is a newly emerging imaging technique and there is currently a significant lack of available OCTA image data sets that represent the ocular disease of interest, i.e.: AMD, including the healthy condition at a sufficient size to enable a reliable automated analysis of OCTA images. This matter has been a common issue with nearly all previous related studies [6, 10, 243–246]. As such, this has made validating approaches proposed by previous studies [6, 10, 243–246] as well as acquiring reliable and robust measurements associated with the textural appearance of AMD disease in the texture of various OCTA images extremely challenging.

Nevertheless, the matter of availability of only a limited size of labelled image data sets is not a new issue to the domain of medical image texture analysis. Noticing and highlighting the significance of this matter has already been demonstrated across numerous studies including the excellent comprehensive and collaborative review of Ching et al. [247] and the recent outstanding survey of Liu et al. [32]. In particular, these two outstanding studies both agreed and demonstrated that the availability of only a limited size of labelled image data sets can be a major barrier towards exploiting certain texture representation techniques, e.g.: approaches based on deep learning algorithms, to solve a wide variety of image texture analysis problems including image classification and image segmentation.

Specifically, the review conducted by Ching et al. [247] was mainly intended to examine the application of deep learning technologies in biology and medicine. They noted, however, that exploiting learned texture representation techniques, i.e.: approaches based on deep learning algorithms, for the diagnosis of the DR disease based on fundus images was achievable only after large and labelled fundus image data sets that included more than 80,000 images became available [247, 248]. Likewise, the survey conducted by Liu et al. [32] mainly aimed to compare various texture representation techniques from the hand-engineered and the learned texture representation categories. However, they observed that in comparison to the learned texture representation techniques, e.g.: approaches based on CNN algorithms, the dense local texture descriptors, which fall under the hand-engineered category, e.g.: the $LBP_{p,r}$ texture descriptor, demonstrated great robustness in several very challenging situations. These include when real-time computation is very important and more importantly when only a limited size of labelled texture image data sets can be made available, among numerous extremely difficult situations [32, 168].

The second aspect, on the other hand, is that the OCTA image data is notably affected by variations in illumination as well as rotation as illustrated in appendix B, section B.1. Notably, neither the illumination can be controlled, nor the rotation details can be accessible with the OCTA imaging technique. Therefore, special consideration needs to be made specifically to selecting the most appropriate texture representation techniques that are insensitive to these variations. This would allow the generation of reliable and robust texture features that are invariant against illumination and rotation changes. Consequently, this can facilitate effective accomplishment of the image analysis task. Nonetheless, a wide variety of texture representation techniques are proposed in the literature, including techniques from the hand-engineered and the learned texture representation categories. However, the most notable texture representation techniques that belong to each category were selectively reviewed and comprehensively discussed in Chapter 2, specifically in subsections 2.4.1 and 2.4.2 respectively. The merits and demerits with every single texture representation technique were also given.

Nevertheless, when evaluating the various texture representation techniques previously described in subsections 2.4.1 and 2.4.2, irrespective of whether hand-engineered or learned, for quantifying the texture of OCTA images, not every single texture representation technique can provide robustness with respect to the illumination and orientation changes in the OCTA image data. Likewise, the individual texture representation techniques previously described can only provide limited robustness. As such, there is

not yet a single 'general purpose' texture representation technique that can be deployed in almost any domain no matter what the types of imaging conditions of texture images are, or the resources and size of image data sets available. Nevertheless, comprehensive details including comparisons based on several outstanding surveys and notable comparative studies [32, 50, 74, 97, 166, 167] that have been conducted to evaluate various texture representation techniques under various challenging situations, have already been demonstrated in Chapter 3, specifically in section 2.7.

Nonetheless, when taking all the previously mentioned aspects into account, it becomes evident that the dense local texture descriptors are again among the most sensible choices to be employed in this research project. However, there are numerous dense local texture descriptors proposed in the literature including the various notable descriptors reviewed in Chapter 2, subsection 2.4.1.5. Nevertheless, the illumination and rotation invariant uniform $LBP_{p,r}^{2riu}$ texture descriptor version of Ojala et al. [24] is particularly anticipated to serve as an effective and efficient choice. This is because it holds all the essential properties, i.e.: invariant against illumination and rotation changes that are necessary for measuring the texture of various OCTA images. It also has the capability to generate discriminative texture features without being hampered by the size of the image data sets available, either small or large [32]. Hence, the $LBP_{p,r}^{2riu}$ texture descriptor has the most potential to capture well representative texture features associated with the AMD disease from the texture of OCTA images.

Additionally, several research studies including that of Liu et al. [32] also observed the great robustness of the $LBP_{p,r}^{2riu}$ texture descriptor across various very challenging situations including illumination, rotation changes in several image texture analysis tasks, e.g.: classification and segmentation [168]. Furthermore, recall that the OCTA imaging technique generates OCTA images that demonstrate blood vessels and flows in a monochrome display, i.e.: in colour over a greyscale. Hence, this would also make the $LBP_{p,r}^{2riu}$ texture descriptor particularly well suited to measuring the texture of OCTA images. This is because the $LBP_{p,r}^{2riu}$ texture descriptor was also essentially developed for quantifying monochrome texture images [39]. It also holds numerous benefits, and these include being free of complex parameters to tune, low computational complexity, among other advantages.

Consequently, the previously mentioned outstanding features that accompany the $LBP_{p,r}^{2riu}$ texture descriptor provide the motivations as well as making it extremely attractive to employ for quantifying the textural appearance of AMD disease in OCTA images. However, as there are a few studies, namely the works by Wang et al. [246]

and Vaghefi et al. [245] that concern automation of the analysis of OCTA images for AMD disease detection by means of image classification, a further two dense local texture descriptors are also selectively employed. These are the generic version of $LBP_{p,r}$ texture descriptor of Ojala et al. [24] and the enhanced version of $BRIEF_{S,n}$ texture descriptor of Morris and Mohammad [116].

The rationales behind selectively choosing these two additional, different texture descriptors, namely the $LBP_{p,r}$ and the $BRIEF_{S,n}$ besides the $LBP_{p,r}^{2riu}$ are due to both sharing certain characteristics and features in common with the $LBP_{p,r}^{2riu}$ texture descriptor. These include requiring no complex parameters to tune, low computational complexity and not being foiled by the size of image data set. Additionally, the $LBP_{p,r}$ and the $BRIEF_{S,n}$ texture descriptors together can tolerate uneven illumination in the same way as the $LBP_{p,r}^{2riu}$ texture descriptor. Moreover, the $BRIEF_{S,n}$ texture descriptor also demonstrates capacity to tolerate insignificant amounts of rotation changes [98, 99]. The $LBP_{p,r}$ and the $BRIEF_{S,n}$ texture descriptors have also been employed in numerous previous studies [33, 58, 114, 116, 158–160], which concern solving medical image texture analysis problems that are comparable to research presented in this thesis. Consequently, the utilisation of the $LBP_{p,r}$ and the $BRIEF_{S,n}$ texture descriptors can allow an excellent validation for the choice of the $LBP_{p,r}^{2riu}$ texture descriptor due to the significant lack of studies related to the work presented in this thesis.

- **Extract whole-local texture features densely from the entire OCTA image to measure the textural appearance of AMD disease.**

There are several main motivations for extracting the whole local texture features densely from the entire OCTA image without targeting any particular region in the OCTA image to measure the textural appearance of AMD disease. Firstly, the OCTA imaging technique provides a rich-image data that shows important ocular vascular texture details from a very small area around the macular region that is near the centre of the retina. Specifically, the OCTA images typically demonstrate a 3×3 mm field of view centred around the fovea region where the regions of vascular pathologies, e.g.: areas of CNV lesions, normally grow and can appear more noticeable. However, the regions of CNV lesions are not restricted to a specific location within the fovea region and hence can appear anywhere in the OCTA images. Additionally, the textural appearance and locations of CNV regions in the different OCTA images vary among various retinal and choroidal layers and they appear more obvious in certain layers than in others.

The above-mentioned details are also amplified by the lack of specific diagnostic criteria for OCTA image data in the presence of various retinal diseases including AMD disease [22]. Furthermore, there is also strong evidence to demonstrate that it is problematic for the human eye to recognise textural information that is related to the spectral properties, e.g.: spectral reflectance, of an image [23]. Consequently, there is no adequate justification to rely solely on specific areas to quantify the textural appearance of AMD disease in any of the different OCTA images of the various retinal and choroidal layers. Performing the automated image classification for AMD disease recognition based on whole-local texture features that are extracted densely from the entire OCTA image can, therefore, be more clinically beneficial. As such, it can take care of both areas of CNV lesions that can be visually perceived as well as other areas that potentially may not be easily perceptible by the human eye.

- **Utilise machine learning algorithms as the classification schemes for accomplishing the OCTA image classification task in an automated manner.**

There are a wide variety of classification schemes or approaches that can be employed for performing the image classification task in an automated manner. These various classification schemes typically fall under two broad classification categories, namely the similarity measure metrics and the machine learning classification algorithms. Comprehensive details about these two different categories, including examples of notable classification schemes that belong to each category, however, have already been given in Chapter 2, specifically in section 2.5. Nevertheless, the similarity measure metrics, e.g.: the chi-square χ^2 statistic and the histogram intersection distance similarity metrics, are generally appropriate for performing image classifications in situations when there are only a few, potentially one training image data sample per class. However, from an image classification perspective, a typical problem in medical image texture analysis is to have a few, perhaps only two different classes and several training image data samples per class. With that in mind, machine learning classification algorithms are, therefore, more desirable for accomplishing the image classification task.

With the utilisation of machine learning classification algorithms, it can allow rigorous statistical or learning techniques to be performed over the complex and diverse training image data samples of different classes, e.g.: dry AMD, wet AMD and healthy. As such, allowing the machine learning classification algorithms to distinguish as yet unseen image data samples based on the diversity and variety of image data samples

utilised in the training. Taking that into consideration, two different machine learning algorithms are consequently employed namely the SVM and the KNN classifiers. The motivations of selectively employing these two different classifiers have already been given in Chapter 2, specifically in subsection 2.5.1. Nevertheless, the SVM classifier is considered as among the most sophisticated machine learning classification algorithms while the KNN classifier is deemed as among the simplest ones. The utilisation of these two different classifiers, therefore, can allow an effective evaluation to be performed over the texture measurements derived from the OCTA image data for quantifying AMD disease. This is because the image classification is conducted and evaluated based on two different classification settings, i.e.: sophisticated via the SVM classifier and simple via the KNN classifier.

The following section 4.3 provides comprehensive details about the proposed algorithm including the various steps involved. Section 4.4, on the other hand, delivers the results of the extensive evaluation performed over the algorithm developed. The evaluation is conducted based on the various OCTA image data sets previously given in Chapter 3, in section 3.4.

4.3 Proposed Algorithm

The framework of the automated OCTA image texture analysis algorithm proposed for AMD disease detection by the means of image classification involves two main steps. The first step is the local texture feature extraction while the second step is the classification. Figure 4.1 demonstrates a brief overview of the analysis pipeline that is followed by the automated OCTA image classification algorithm proposed. The two steps involved are comprehensively explained in the following subsections 4.3.1 and 4.3.2, respectively.

4.3.1 Local Texture Feature Extraction

The overall objective of the local texture feature extraction step is to only measure the textural appearance of various OCTA images in the presence of different ocular conditions, dry AMD, wet AMD and healthy. There are two different texture descriptors evaluated in this step, namely the $LBP_{p,r}$ and the $BRIEF_{S,n}$, besides the $LBP_{p,r}^{riu}$ texture descriptor that is selectively proposed to measure the texture of various OCTA images in this research project. However, the theoretical underpinnings behind these

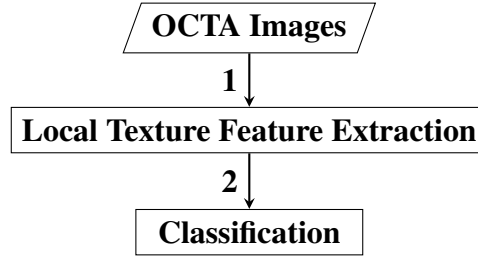


Figure 4.1: Outline of the automated OCTA image texture analysis algorithm that is proposed for AMD disease detection by the means of image classification. The analysis procedure begins with taking the OCTA images as an input where the local texture features extraction step takes place first to quantify the textural appearance of OCTA images. Following this step, the classification is then performed over the extracted local texture features that quantify the various OCTA images to classify them based on the ocular conditions they represent e.g.: dry AMD, wet AMD and healthy.

three different texture descriptors, i.e.: the $LBP_{p,r}$, the $LBP_{p,r}^{2riu}$ and the $BRIEF_{S,n}$, were comprehensively illustrated in Chapter 2, specifically in subsubsection 2.4.1.5. Nevertheless, the $LBP_{p,r}$ and the $LBP_{p,r}^{2riu}$ texture descriptors generally work in a comparable manner in estimating various local texture features or patterns, e.g.: bright or dark spots, flat areas, edges and so on, see Figure 2.14 in Chapter 2, from texture images. This is because the $LBP_{p,r}^{2riu}$ texture descriptor is a functional extension version of the generic $LBP_{p,r}$ texture descriptor. Consequently, details about how the local texture features are estimated from the texture of various OCTA images are commenced with the $LBP_{p,r}$ and the $LBP_{p,r}^{2riu}$ texture descriptors, followed by the $BRIEF_{S,n}$ texture descriptor, respectively.

Recall that the generic $LBP_{p,r}$ texture descriptor, including other versions of it such as the $LBP_{p,r}^{2riu}$ texture descriptor, typically relies on fine-tuning two different and important parameters, namely p and r , where $p > 1$ and $r > 0$. The parameter p is responsible for regulating the number of sampling pixels in an evenly spaced circularly symmetric neighbourhood centred around a single central pixel. The parameter r , on the other hand, specifies the circle radius i.e.: the distance between the central pixel and the neighbourhood of p sampling pixels. Nevertheless, the values of these p sampling pixels including the value of the single central pixel are all utilised with both the $LBP_{p,r}$ and the $LBP_{p,r}^{2riu}$ texture descriptors to characterise the local texture features or patterns that appear in the texture of different OCTA images.

As the OCTA imaging technique generates two-dimensional greyscale OCTA images of various ocular vascular layers, the values of p individual sampling pixels and

the single central pixel represent the grey levels g . Given a two dimensional greyscale OCTA image (x, y) , the grey level values of p individual sampling pixels can, therefore, be denoted as g_n at (x_n, y_n) , where $n = (0, 1, 2, 3, \dots, p-1)$, and the grey level value of any arbitrary single central pixel can be symbolised as g_c at (x_c, y_c) . When the coordinate of the central pixel g_c in the two dimensional OCTA image at (x_c, y_c) is $(0, 0)$, the coordinates of all p sampling pixels g_n at (x_n, y_n) are then estimated by $(-r \sin(2\pi n/p), r \cos(2\pi n/p))$. If any of the p individual sampling pixels g_n does not fall accurately within the centre of a pixel in the OCTA image, its location is then estimated by bilinear interpolation.

Estimating the values and coordinates of all p sampling pixels can be accomplished in any ordering direction, e.g.: a clockwise or an anticlockwise manner. Additionally, it may start from any location in the circularly symmetric neighbourhood of p sampling pixels. For example, the starting sampling pixel, i.e.: g_0 , can be assigned to be the pixel located to the right or the left of central pixel g_c . However, the selected direction of ordering technique as well as the location of the starting sampling pixel g_0 must be kept consistent. In this study, therefore, the location of starting sampling pixel, i.e.: g_0 , is always assigned to be the pixel situated to the right of central pixel g_c . Moreover, the ordering direction is conducted in a clockwise manner for all regions or pixels visited in the OCTA image as well as any subsequent OCTA images that will be measured.

Nevertheless, once the values and coordinates of all p sampling pixels g_n at (x_n, y_n) are estimated, the $LBP_{p,r}$ and the $LBP_{p,r}^{2riu}$ texture descriptors typically characterise the texture of OCTA images by considering only the signs of difference between the grey level values of the central pixel g_c and the neighbourhood of p individual sampling pixels g_n instead of their exact grey level values, such that $s(g_0 - g_c), s(g_1 - g_c), \dots, s(g_{p-1} - g_c)$. The individual signs of differences are then typically passed through a thresholding operation $s(x)$, i.e.: a binary test step, as defined by function 2.7 in Chapter 2, subsection 2.4.1.5.

The thresholding operation $s(x)$ given in function 2.7 constructs different p bit binary numbers or binary strings, i.e.: various local binary patterns. Nevertheless, the individual binary numbers, i.e.: 0 and 1, in the local binary patterns of different regions visited, i.e.: different central pixels, are typically individually weighted by powers of two, i.e.: 2^n and summed to convert the binary strings into decimal representations. The resulting decimal representations are then typically used to label the individual regions, i.e.: individual central pixels, that are being visited and measured. Describing the textural appearance around any random region, i.e.: any arbitrary central pixel at

(x_c, y_c) in the various two dimensional OCTA images based on the generic $LBP_{p,r}$ texture descriptor can, therefore, be formally defined by equation 2.8 in Chapter 2, subsubsection 2.4.1.5.

In practice, the generic $LBP_{p,r}$ texture descriptor given in equation 2.8 can generate 2^p potential combinations of $LBP_{p,r}$ patterns, i.e.: 2^p potentially distinct decimal values. These different possible $LBP_{p,r}$ patterns typically measure specific spatial structure of local texture features, e.g.: corners, edges and so on, see Figure 2.14 in Chapter 2, that may appear in the texture of various images. In this study, however, the generic $LBP_{p,r}$ texture descriptor is applied densely to every single region, i.e.: every single pixel, of the various OCTA images constructing different combinations of $LBP_{p,r}$ patterns. Nevertheless, the different local texture features measured by the generic $LBP_{p,r}$ texture descriptor are estimated by a single histogram for every single OCTA image. Every single histogram is constructed with approximately 2^p bin discrete distributions of different decimal values, corresponding to all potential individual $LBP_{p,r}$ patterns.

The estimated histograms of individual OCTA images, therefore, construct the feature vectors that form the basis of accomplishing the automated analysis of OCTA image texture analysis by means of image classification. Figures 4.2, 4.3 and 4.4 demonstrate illustrative examples of different OCTA images of four ocular vascular layers with their corresponding encoded texture structures, i.e.: the $LBP_{p,r}$ images, and the feature vectors, i.e.: histograms, for three different eyes with different conditions, namely healthy, dry AMD and wet AMD, respectively. In each figure, the texture of each OCTA image was empirically measured with $r = 1$ and $p = 8$, specifically to demonstrate how the $LBP_{p,r}$ texture descriptor quantifies the presence of each different eye condition in the OCTA images.

While the generic $LBP_{p,r}$ texture descriptor is invariant to changes in illumination, it can, however, be very sensitive to any orientation variations in the texture of images. This is because when the orientation of an image changes, the values and coordinates of all p sampling pixels g_n at (x_n, y_n) will correspondingly change along the perimeter of the circularly symmetric neighbourhood. As the location of the starting sampling pixel, i.e.: g_0 , is always allocated to be the pixel positioned to the right of central pixel g_c , rotating a specific $LBP_{p,r}$ pattern certainly results in a different decimal representation or value. However, this case does not apply to $LBP_{p,r}$ patterns that are all 0s or 1s as these patterns will always be the same no matter if the rotation of the texture image changes at any angle.

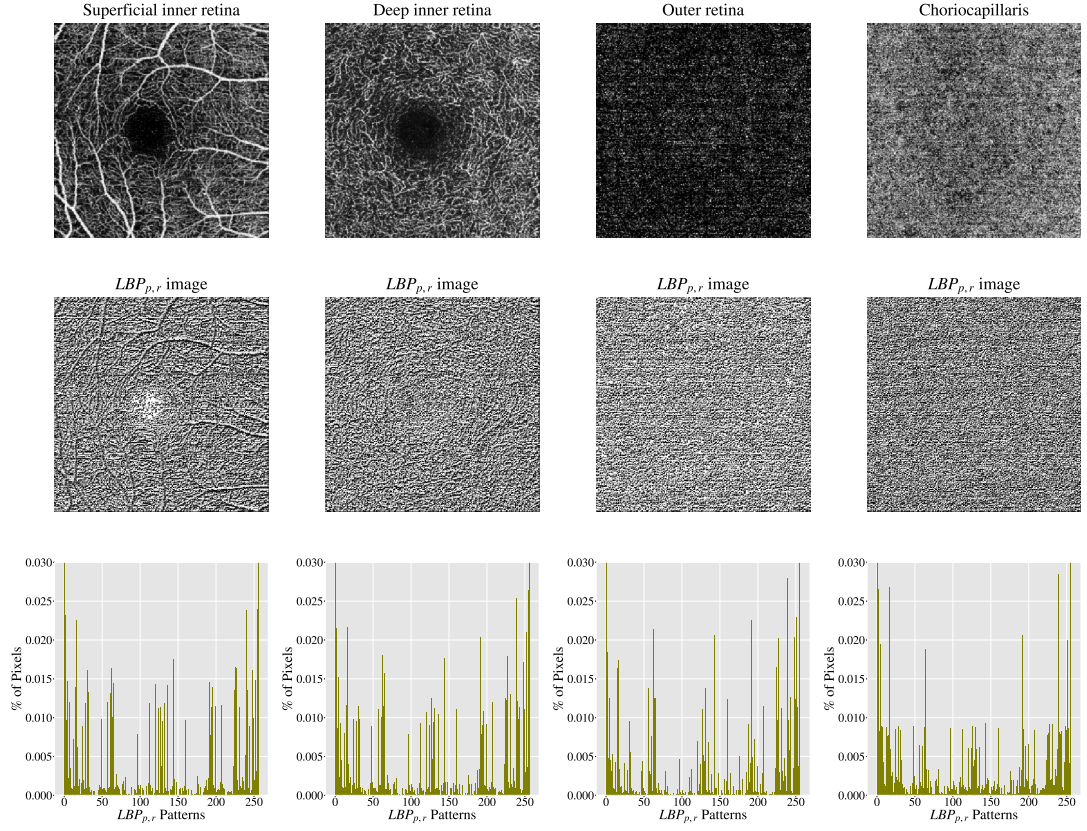


Figure 4.2: The top row visualises different OCTA images of four ocular vascular layers, namely the superficial inner retina, the deep inner retina, the outer retina and the choriocapillaris layers for a healthy eye. The middle row shows the corresponding encoded texture structure, i.e.: the $LBP_{p,r}$ image, of every single OCTA image. The bottom row illustrates the feature vectors, i.e.: histograms, that accumulate the various local texture features, i.e.: $LBP_{p,r}$ patterns, as obtained by the $LBP_{p,r}$ texture descriptor from the texture of individual OCTA images. The % of Pixels in the individual histograms of each OCTA image denotes the proportion of regions, i.e.: the percentage of pixels, visited and measured that share the same $LBP_{p,r}$ patterns.

Nevertheless, the $LBP_{p,r}^{2riu}$ texture descriptor version can alleviate the sensitivity to any rotation changes as well as add an extra level of tolerance capacity to any illumination variations in texture images. This is because it combines two different versions of $LBP_{p,r}$ texture descriptor, namely the rotation invariant $LBP_{p,r}^{ri}$ and the uniform $LBP_{p,r}^{2u}$. The theoretical underpinnings related to these two different texture descriptors, i.e.: the $LBP_{p,r}^{ri}$ and the $LBP_{p,r}^{2u}$ were, however, comprehensively illustrated in Chapter 2, specifically in subsubsection 2.4.1.5. Nonetheless, the rotation invariant $LBP_{p,r}^{ri}$ texture descriptor, as the name suggests, can provide the advantage of being very robust with respect to any changes in image rotation. The effect of image rotation is removed

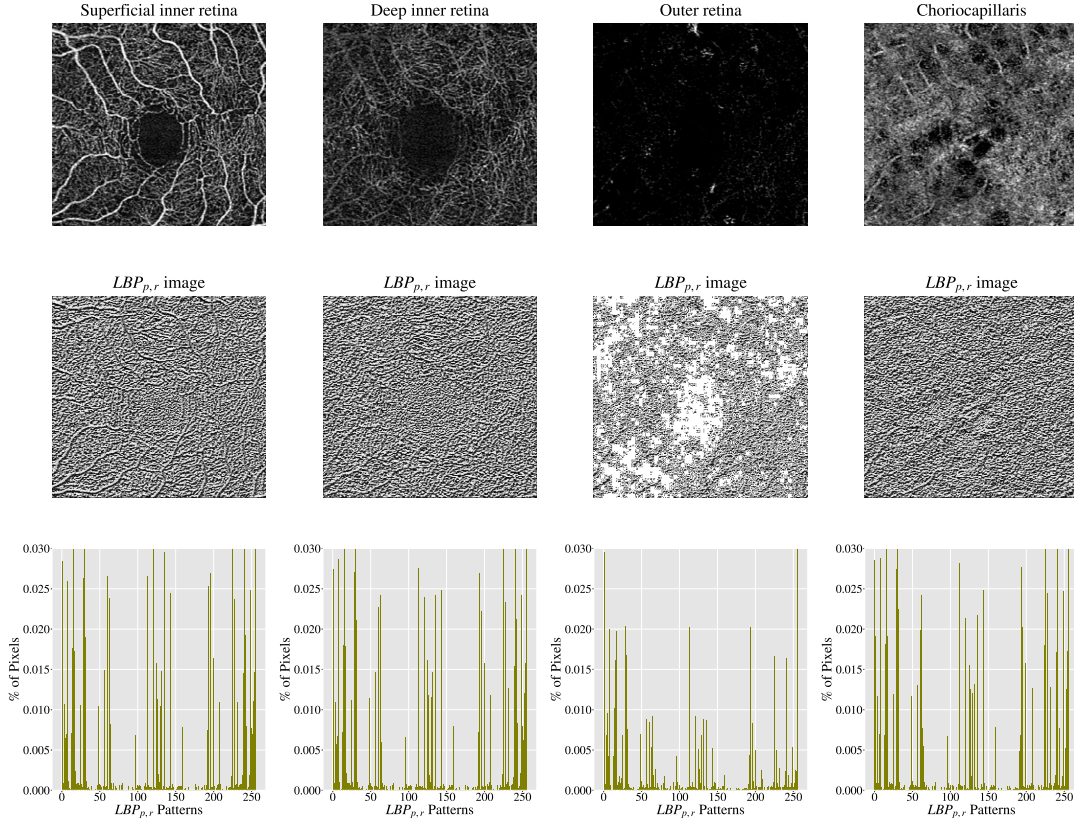


Figure 4.3: The topmost row demonstrates different OCTA images of four ocular vascular layers, namely the superficial inner retina, the deep inner retina, the outer retina and the choriocapillaris layers for an eye with dry AMD. The middle row shows the corresponding encoded texture structure, i.e.: the $LBP_{p,r}$ image, of every single OCTA image. The bottom row illustrates the feature vectors, i.e.: histograms, that accumulate the various local texture features, i.e.: $LBP_{p,r}$ patterns, as captured by the $LBP_{p,r}$ texture descriptor from the texture of individual OCTA images. The % of Pixels in the individual histograms of each OCTA image denotes the proportion of regions, i.e.: the percentage of pixels, visited and measured that share the same $LBP_{p,r}$ patterns.

in the $LBP_{p,r}^{ri}$ texture descriptor by mapping, i.e.: circularly rotating, every $LBP_{p,r}$ pattern into its minimum representation. Consequently, the $LBP_{p,r}^{ri}$ texture descriptor to estimate the rotation invariant local texture features around any random regions, i.e.: any arbitrary central pixels at (x_c, y_c) from the texture of different OCTA images is formally given by equation 2.9 in Chapter 2, subsection 2.4.1.5.

The $ROR(LBP_{p,r}(x_c, y_c), n)$ function given in the previous equation 2.9 performs a circular bit-wise right shift, i.e.: a right rotation, on the p bit binary numbers or binary strings, i.e.: the $LBP_{p,r}$ patterns, by n steps. In other words, it simply corresponds to rotating the neighbourhood of p sampling pixels in a clockwise direction several

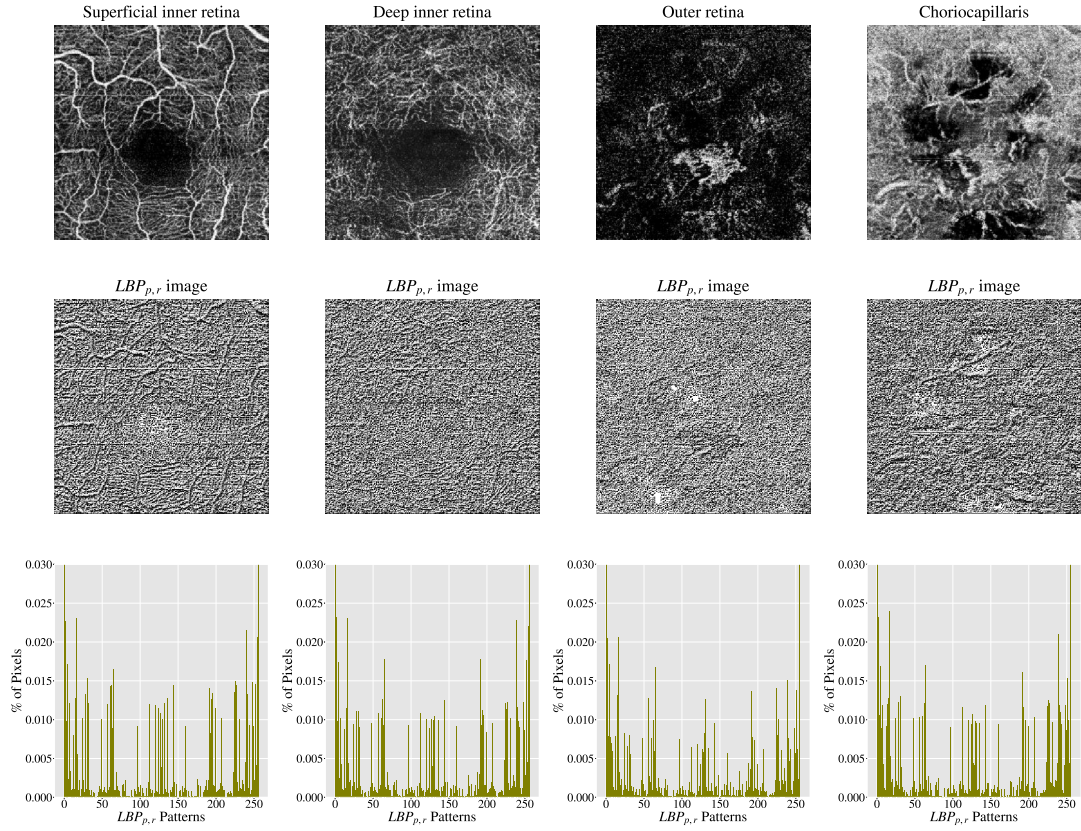


Figure 4.4: The uppermost row displays different OCTA images of four ocular vascular layers, namely the superficial inner retina, the deep inner retina, the outer retina and the choriocapillaris layers for an eye with wet AMD. The middle row shows the corresponding encoded texture structure, i.e.: the $LBP_{p,r}$ image, of every single OCTA image. The bottom row demonstrates the feature vectors, i.e.: histograms, that accumulate the various local texture features, i.e.: $LBP_{p,r}$ patterns, as detected by the $LBP_{p,r}$ texture descriptor from the texture of individual OCTA images. The % of Pixels in the individual histograms of each OCTA image denotes the proportion of regions, i.e.: the percentage of pixels, visited and measured that share the same $LBP_{p,r}$ patterns.

steps so as the minimal number of the least significant bit i.e.: the bit furthest to the right in the $LBP_{p,r}$ pattern, starting from g_0 , is 1. For example, given several $LBP_{p,r}$ patterns with $p = 8$ bit binary numbers, e.g.: 00000010, 00000100, and 00001000, are all mapped to the minimum $LBP_{p,r}$ pattern, i.e.: 00000001, by 1,2 and 3 steps respectively.

The uniform $LBP_{p,r}^{2u}$ texture descriptor, on the other hand, can provide numerous advantages including statistical robustness and stabilities of the uniform local texture features derived, i.e.: the uniform $LBP_{p,r}^{2u}$ patterns. As such the uniform $LBP_{p,r}^{2u}$ patterns are demonstrated to be less hampered by and more resistant to image noise, as

evidenced by numerous previous studies [24, 39, 100]. The uniform $LBP_{p,r}^{2u}$ texture descriptor works by calculating the number of bitwise pattern transitions from 1 to 0 or vice versa in the constructed $LBP_{p,r}$ patterns. The uniformity pattern measure of the $LBP_{p,r}^{2u}$ texture descriptor is formally defined by equation 2.10 in Chapter 2, subsubsection 2.4.1.5.

Based on the uniformity pattern measure $u(LBP_{p,r})$ given in the previous equation 2.10, the $LBP_{p,r}$ pattern is considered as a uniform $LBP_{p,r}^{2u}$ pattern if the value of the uniformity pattern measure, i.e.: the number of bitwise pattern transitions, is at most two. For example, the following $LBP_{p,r}$ patterns 00000000 has zero transitions, 00000001 has one transition and 00111000 has two transitions, which are all considered as uniform $LBP_{p,r}^{2u}$ patterns since they comprise at most two bitwise 1/0 or 0/1 changes. However, as regards the following $LBP_{p,r}$ patterns, 11000101 has four transitions, 01010011 has five transitions and 01101010 has six transitions, which are not considered as uniform $LBP_{p,r}^{2u}$ patterns since they include more than two bitwise 1/0 or 0/1 changes.

Given the outstanding advantages, e.g.: statistical stabilities and robustness with respect to image noise that the previously mentioned texture descriptors, i.e.: the $LBP_{p,r}^{ri}$ and the $LBP_{p,r}^{2u}$ can provide, the $LBP_{p,r}^{2riu}$ can, therefore, be viewed as a very powerful texture descriptor. Nevertheless, the $LBP_{p,r}^{2riu}$ texture descriptor to estimate rotation invariant uniform local texture features around any random region, i.e.: any arbitrary central pixel at (x_c, y_c) in the various two dimensional OCTA images, is formally expressed by equation 2.11 in Chapter 2, subsubsection 2.4.1.5.

By definition, only $p + 1$ rotation invariant uniform local binary patterns, i.e.: rotation invariant uniform $LBP_{p,r}^{2riu}$ patterns, can occur in a circularly symmetric neighbourhood of p sampling pixels. The $LBP_{p,r}^{2riu}$ texture descriptor given in equation 2.11 allocates a distinctive integer value or label starting from 0 to p for every single rotation invariant uniform $LBP_{p,r}^{2riu}$ pattern captured. These individual labels correspond to the number of ones, i.e.: “1s” bits, in the rotation invariant uniform $LBP_{p,r}^{2riu}$ patterns, while the non-uniform $LBP_{p,r}^{2riu}$ patterns are all together grouped under an assorted label, i.e.: a single integer value given by $p + 1$. Figure 2.15, in Chapter 2, demonstrates an excellent visualisation of all potential rotation invariant uniform $LBP_{p,r}^{2riu}$ patterns that can occur in a circularly symmetric neighbourhood of p sampling pixels with $p = 8$. In Figure 2.15, all possible distinctive output values or labels that starting from 0 to 8 for every single rotation invariant uniform $LBP_{p,r}^{2riu}$ pattern are given inside each circularly symmetric neighbourhood of eight sampling pixels. However, all other non-uniform

$LBP_{p,r}^{2riu}$ patterns are grouped together under a single integer value of $p+1$ i.e.: 9.

Consequently, the $LBP_{p,r}^{2riu}$ texture descriptor can generate $p+2$ distinctive output labels or values in total. These different values also typically quantify specific spatial structure of local texture features, e.g.: corners, edges and so on, see Figure 2.14 in Chapter 2, which may appear in the texture of various images. In this study, however, the $LBP_{p,r}^{2riu}$ texture descriptor is applied densely to every single region, i.e.: every single pixel, of the various OCTA images constructing different rotation invariant uniform $LBP_{p,r}^{2riu}$ patterns. Nevertheless, the different local texture features measured by the $LBP_{p,r}^{2riu}$ texture descriptor are estimated by a single histogram for every single OCTA image. Every single histogram is constructed with approximately $p+2$ bin discrete distributions of different labels or values, corresponding to all potential individual rotation invariant uniform as well as non-uniform $LBP_{p,r}^{2riu}$ patterns.

The estimated histograms of individual OCTA images, therefore, construct the feature vectors that form the basis of accomplishing the automated analysis of OCTA image texture analysis by means of image classification. Figures 4.5, 4.6 and 4.7 demonstrate illustrative examples of different OCTA images of four ocular vascular layers with their corresponding encoded texture structures, i.e.: the $LBP_{p,r}^{2riu}$ images and the feature vectors, i.e.: histograms, for three different eyes with different conditions, namely healthy, dry AMD and wet AMD, respectively. In each figure, the texture of each OCTA image was empirically measured with $r=1$ and $p=8$, specifically to demonstrate how the $LBP_{p,r}^{2riu}$ texture descriptor quantifies the presence of each different eye condition in the OCTA images.

The $BRIEF_{S,n}$ texture descriptor, on the other hand, also relies on fine-tuning two important parameters, namely S and n . The value of S regulates the size of image patches P , i.e.: $S \times S$ pixel dimension, and the value of n controls the number of n sampling pixels, i.e.: n sampling pixel pair set, to be considered within the individual image patches P . Once these values, i.e.: S and n are defined, the $BRIEF_{S,n}$ texture descriptor typically quantifies the texture of OCTA images by considering only the signs of difference between the grey level values of the n sampling pixel pair set instead of their exact grey level values. The individual signs of differences within every image patch P of size $S \times S$ pixels are then typically passed through a thresholding test operation $\tau(P: X, Y)$, i.e.: a binary test step, as defined by function 2.12 in Chapter 2, subsubsection 2.4.1.5.

Where $P(X)$ and $P(Y)$ are the grey level values of n pixel pairs within the image patch P that are ordered at symmetrical or random locations X and Y as previously

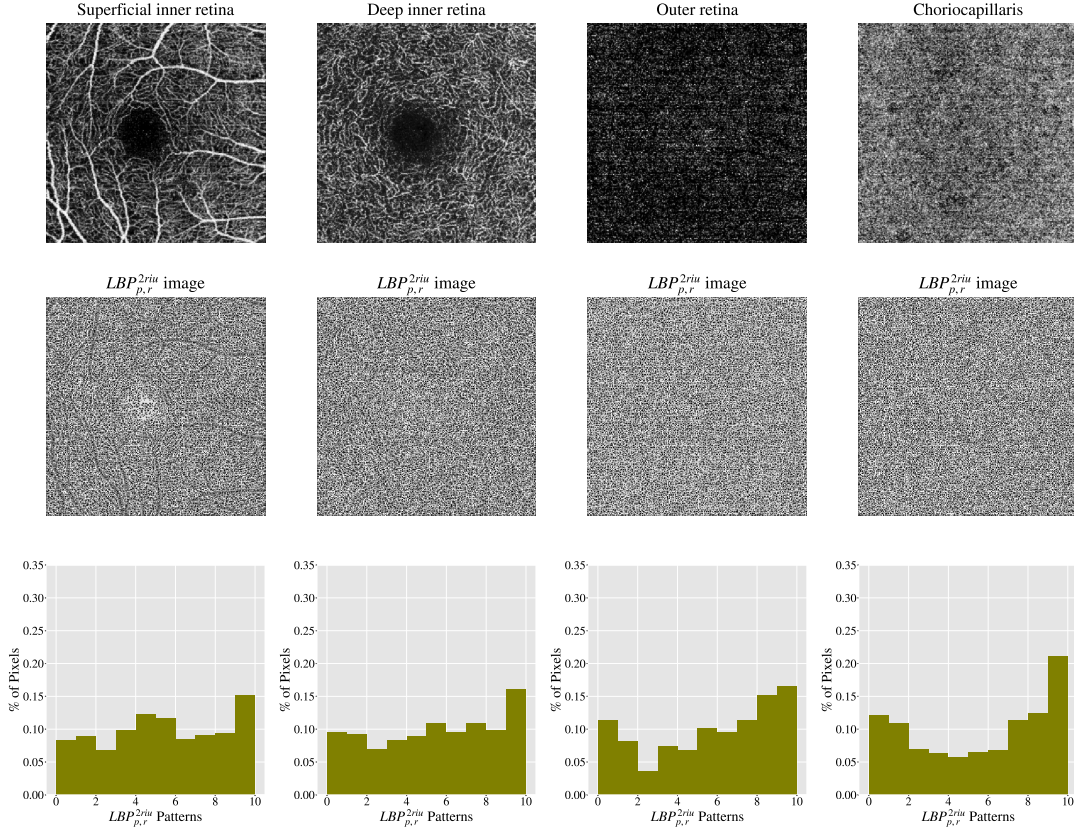


Figure 4.5: The top row visualises different OCTA images of four ocular vascular layers, namely the superficial inner retina, the deep inner retina, the outer retina and the choriocapillaris layers for a healthy eye. The middle row shows the corresponding encoded texture structure, i.e.: the $LBP^{2riu}_{p,r}$ image, of every single OCTA image. The bottom row illustrates the feature vectors, i.e.: histograms, that accumulate the various local texture features, i.e.: $LBP^{2riu}_{p,r}$ patterns, as obtained by the $LBP^{2riu}_{p,r}$ texture descriptor from the texture of individual OCTA images. The % of Pixels in the individual histograms of each OCTA image denotes the proportion of regions, i.e.: the percentage of pixels, visited and measured that share the same $LBP^{2riu}_{p,r}$ patterns.

illustrated in Chapter 2, see Figure 2.16. In this study, however, the locations of n pixel pairs, i.e.: X and Y , are organised randomly based on the sampling strategy in Figure 2.16a, as in previous studies [58, 114, 116]. This type of random sampling strategy can allow the locations of n pixel pairs, i.e.: X and Y , to be equally distributed over the image patch P . The binary tests can, therefore, lie near the border of image patch P . Important local texture regions or elements, e.g.: CNV areas can, therefore, have the potential to be visited and measured no matter where they may appear in the various OCTA images.

The threshold value, on the other hand, is estimated based on the image noise level,

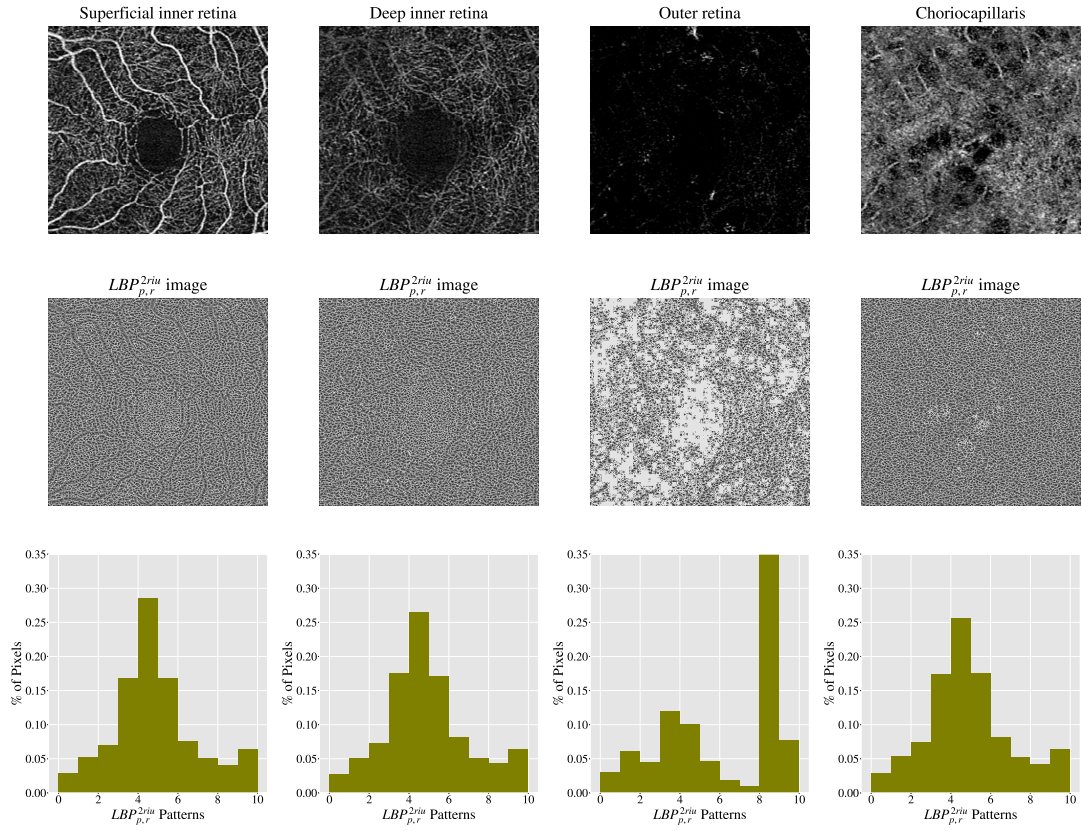


Figure 4.6: The topmost row demonstrates different OCTA images of four ocular vascular layers, namely the superficial inner retina, the deep inner retina, the outer retina and the choriocapillaris layers for an eye with dry AMD. The middle row shows the corresponding encoded texture structure, i.e.: the $LBP_{p,r}^{2riu}$ image, of every single OCTA image. The bottom row illustrates the feature vectors, i.e.: histograms, that accumulate the various local texture features, i.e.: $LBP_{p,r}^{2riu}$ patterns, as captured by the $LBP_{p,r}^{2riu}$ texture descriptor from the texture of individual OCTA images. The % of Pixels in the individual histograms of each OCTA image denotes the proportion of regions, i.e.: the percentage of pixels, visited and measured that share the same $LBP_{p,r}^{2riu}$ patterns.

i.e.: noise standard deviation (σ). As in previous studies [58, 114, 116], the noise standard deviation (σ) is calculated through blurring an OCTA image using a Gaussian filter. The process is then followed, subtracting the filtered OCTA image from the original OCTA image. The resultant image is subsequently anticipated to only include the noise signal. The noise standard deviation (σ) is, consequently, estimated from the resultant image. In this study, the threshold value is set to three times the noise standard deviation (3σ). This threshold value, i.e.: 3σ , demonstrates good classification performance, while higher threshold values, e.g.: 4σ showed a slight drop in classification accuracy as investigated by Mohammad [58]. As the OCTA image data are in

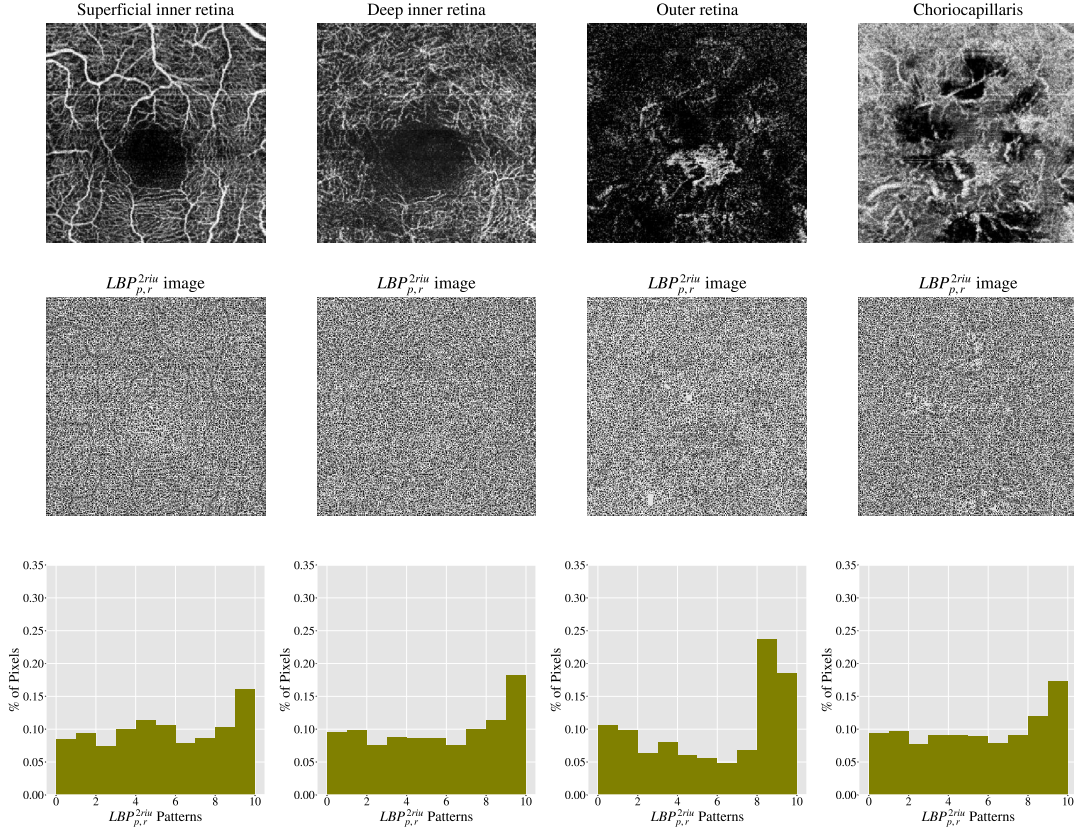


Figure 4.7: The uppermost row displays different OCTA images of four ocular vascular layers namely the superficial inner retina, the deep inner retina, the outer retina and the choriocapillaris layers for an eye with wet AMD. The middle row shows the corresponding encoded texture structure, i.e.: the $LBP_{p,r}^{2riu}$ image, of every single OCTA image. The bottom row demonstrates the feature vectors, i.e.: histograms, that accumulate the various local texture features, i.e.: $LBP_{p,r}^{2riu}$ patterns, as detected by the $LBP_{p,r}^{2riu}$ texture descriptor from the texture of individual OCTA images. The % of Pixels in the individual histograms of each OCTA image denotes the proportion of regions, i.e.: the percentage of pixels, visited and measured that share the same $LBP_{p,r}^{2riu}$ patterns.

greyscale colour, the threshold value (3σ) roughly speaking corresponds to a grey level value in the range of four to six [58].

Nevertheless, the thresholding test operation $\tau(P : X, Y)$ given in function 2.12 constructs different n bit binary numbers or binary strings, i.e.: various local binary patterns. The individual binary numbers, i.e.: 0 and 1, in the local binary patterns of different regions visited, i.e.: different image patches P , are typically individually weighted by powers of two, i.e.: 2^{i-1} where $(1 \leq i \leq n)$, and summed to convert the binary strings into decimal representations. The resulting decimal representations are then typically used to label the individual regions, i.e.: individual image patches P ,

that are being visited and measured. Characterising the textural appearance around any random region, i.e.: any arbitrary image patch P in the various two dimensional OCTA images based on the $BRIEF_{S,n}$ texture descriptor can, therefore, be formally defined by equation 2.14 in Chapter 2, subsection 2.4.1.5.

In practice, the $BRIEF_{S,n}$ texture descriptor given in equation 2.14 can generate 2^n potential combinations of $BRIEF_{S,n}$ patterns, i.e.: 2^n potentially distinct decimal values. These different possible $BRIEF_{S,n}$ patterns typically measure the specific spatial structure of local texture features that may appear in the texture of various images. In this study, however, the $BRIEF_{S,n}$ texture descriptor is applied densely to every single region, i.e.: acquiring a patch P from every single pixel, of the various OCTA images constructing different combinations of $BRIEF_{S,n}$ patterns. Nevertheless, the different local texture features measured by the $BRIEF_{S,n}$ texture descriptor are estimated by a single histogram for every single OCTA image. Every single histogram is constructed with approximately 2^n bin discrete distributions to accumulate the different decimal values, corresponding to all potential individual $BRIEF_{S,n}$ patterns.

The estimated histograms of individual OCTA images, therefore, construct the feature vectors that form the basis of accomplishing the automated analysis of OCTA image texture analysis by means of image classification. Figures 4.8, 4.9 and 4.10 demonstrate illustrative examples of different OCTA images of four ocular vascular layers with their corresponding encoded texture structures, i.e.: the $BRIEF_{S,n}$ images, and the feature vectors, i.e.: histograms, for three different eyes with different conditions, namely healthy, dry AMD and wet AMD, respectively. In each figure, the texture of each OCTA image was empirically measured with $S = 5$ and $n = 8$, specifically to demonstrate how the $BRIEF_{S,n}$ texture descriptor quantifies the presence of every different eye condition in the OCTA images.

From a feature engineering perspective, the local texture feature extraction step described earlier can be viewed as a very powerful phase. This is because, technically, it employs two different approaches on the OCTA image texture patterns, namely a structural approach and a statistical approach. The structural approach is achieved by characterising the micro-structures that appear in the texture of OCTA images, e.g.: edges, corners, lines and so on, as detected through the $LBP_{p,r}^{2riu}$, the $LBP_{p,r}$ and the $BRIEF_{S,n}$ texture descriptors. The statistical approach, on the other hand, is accomplished by estimating the distribution of various local texture features or patterns, i.e.: the micro-structures, in histograms, constructing the feature vectors that form the basis of undertaking the automated analysis of OCTA image texture analysis by means of

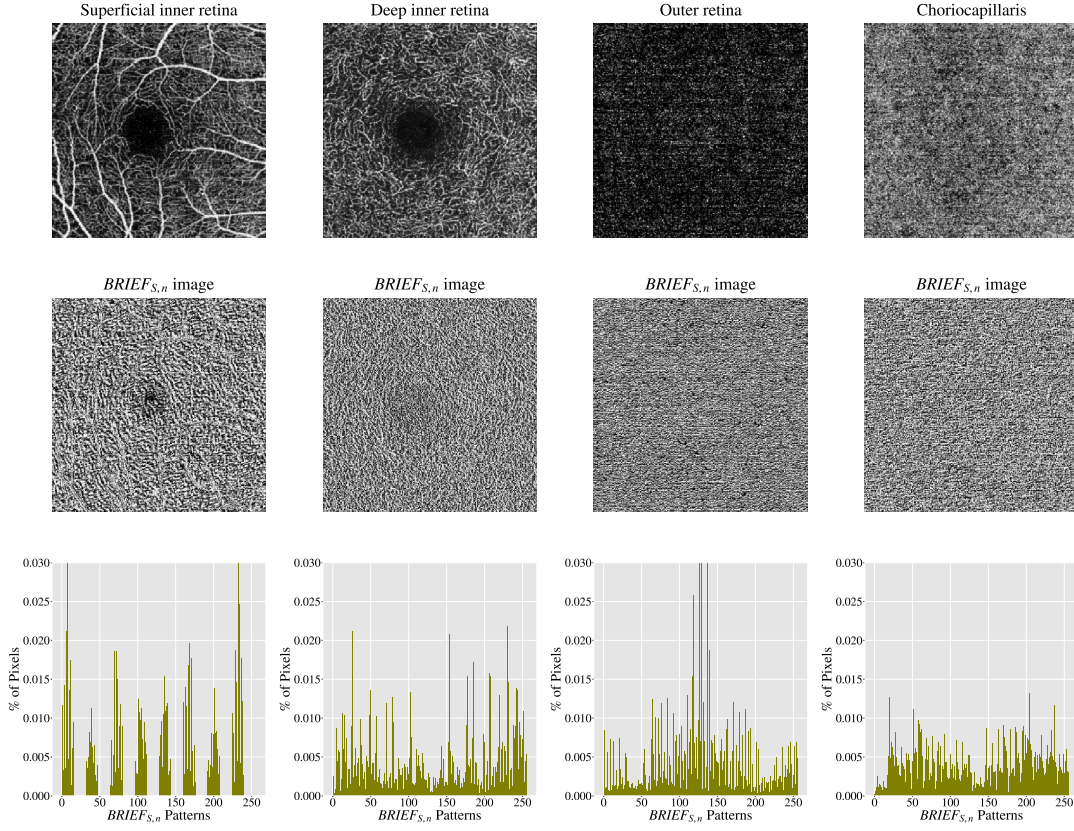


Figure 4.8: The top row visualises different OCTA images of four ocular vascular layers, namely the superficial inner retina, the deep inner retina, the outer retina and the choriocapillaris layers for a healthy eye. The middle row shows the corresponding encoded texture structure, i.e.: the $BRIEF_{S,n}$ image, of every single OCTA image. The bottom row illustrates the feature vectors, i.e.: histograms, that accumulate the various local texture features, i.e.: $BRIEF_{S,n}$ patterns, as obtained by the $BRIEF_{S,n}$ texture descriptor from the texture of individual OCTA images. The % of Pixels in the individual histograms of each OCTA image denotes the proportion of regions, i.e.: the percentage of pixels, visited and measured that share the same $BRIEF_{S,n}$ patterns.

image classification.

4.3.2 Classification

Once the feature vectors of individual OCTA images are constructed, the overall objective of the classification step is to classify the different eyes as belonging to one of the different predefined classes of eye conditions, e.g.: healthy, wet AMD or CNV and dry AMD or non-CNV. To achieve this, two different machine learning classification algorithms, namely the SVM and the KNN classifiers are employed and tested

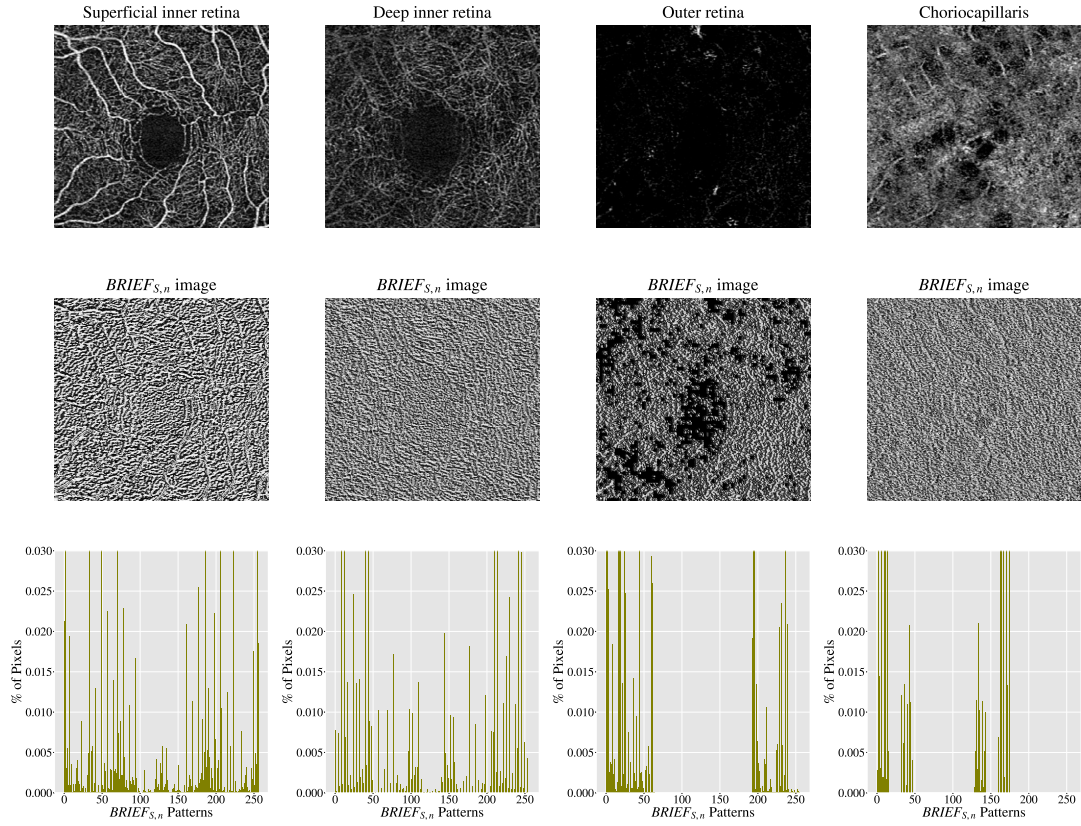


Figure 4.9: The topmost row demonstrates different OCTA images of four ocular vascular layers, namely the superficial inner retina, the deep inner retina, the outer retina and the choriocapillaris layers for an eye with dry AMD. The middle row shows the corresponding encoded texture structure, i.e.: the $BRIEF_{S,n}$ image, of every single OCTA image. The bottom row illustrates the feature vectors, i.e.: histograms, that accumulate the various local texture features, i.e.: $BRIEF_{S,n}$ patterns, as captured by the $BRIEF_{S,n}$ texture descriptor from the texture of individual OCTA images. The % of Pixels in the individual histograms of each OCTA image denotes the proportion of regions, i.e.: the percentage of pixels, visited and measured that share the same $BRIEF_{S,n}$ patterns.

for the task of image classification. The main motivations behind selectively choosing these two different classifiers have already been given at the beginning of this chapter, section 4.2.

A hyper-parameter search was conducted for the KNN and the SVM classifiers. This is accomplished by defining a search space as a grid of hyper-parameter values and then every location on the grid is evaluated individually via a cross-validation strategy. The space of hyper-parameters for the KNN classifier was empirically searched by varying the value of K nearest neighbours with $k = \{1, 3, 5, 7, 9\}$ as well as changing the distance metrics using Euclidean, Manhattan and Chebyshev distance functions.

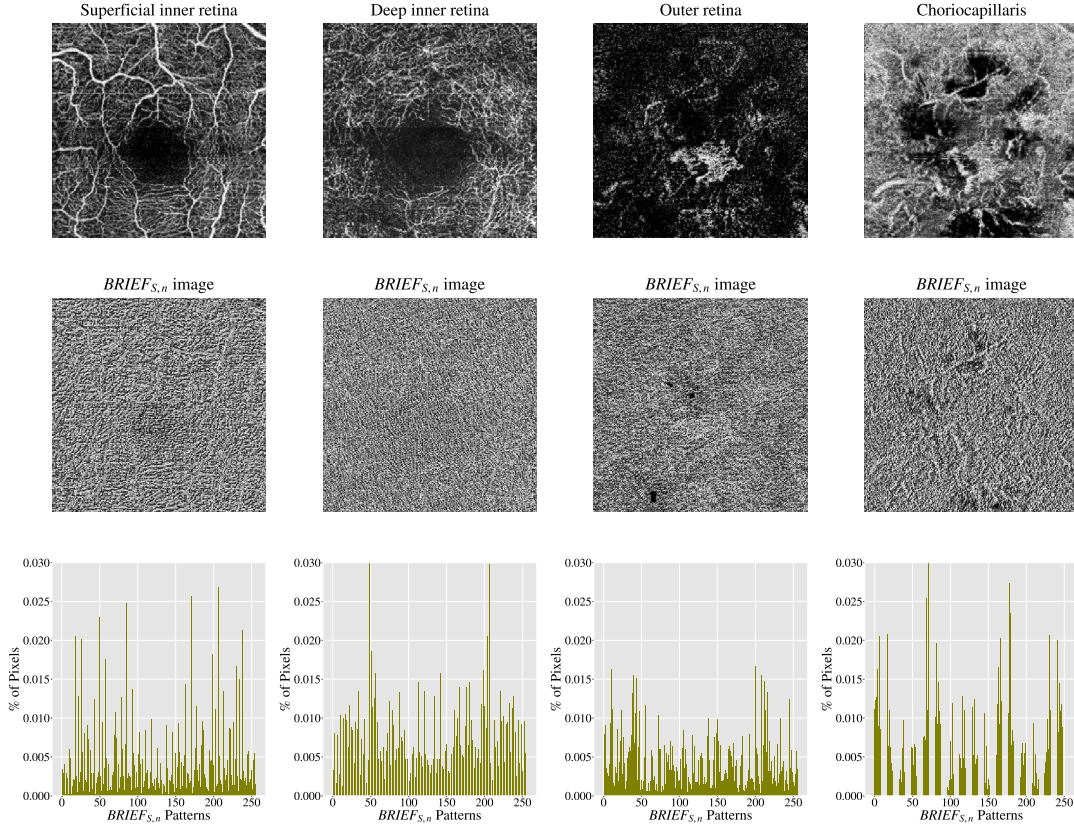


Figure 4.10: The uppermost row displays different OCTA images of four ocular vascular layers, namely the superficial inner retina, the deep inner retina, the outer retina and the choriocapillaris layers for an eye with wet AMD. The middle row shows the corresponding encoded texture structure, i.e.: the $BRIEF_{S,n}$ image, of every single OCTA image. The lowermost row demonstrates the feature vectors, i.e.: histograms, that accumulate the various local texture features, i.e.: $BRIEF_{S,n}$ patterns, as detected by the $BRIEF_{S,n}$ texture descriptor from the texture of individual OCTA images. The % of Pixels in the individual histograms of each OCTA image denotes the proportion of regions, i.e.: the percentage of pixels, visited and measured that share the same $BRIEF_{S,n}$ patterns.

The space of hyper-parameters for the SVM classifier was also empirically explored by changing the value of the penalty parameter C where $C = \{0.1, 1, 5, 10, 50, 100\}$ along with varying the kernel functions using linear, Radial Basis Function (*rbf*) and Polynomial (*poly*) kernels. As the *rbf* and the *poly* kernel functions are explored, the γ and the d parameters are also fine-tuned with different values where $\gamma = \{0.00001, 0.0001, 0.001, 0.01, 0.1, 1\}$ and $d = \{2, 3, 4, 5, 6, 7, 8, 9\}$. The optimal hyper-parameter combinations for the different classifiers that facilitate accomplishing the best classification performance as assessed via a cross-validation strategy are then finally selected. The following section 4.4 provides a comprehensive evaluation

of the algorithm proposed.

4.4 Experimental Evaluation and Results

The evaluation of the algorithm proposed was conducted on the diverse OCTA image data sets previously described in Chapter 3, section 3.4. Nevertheless, the evaluation was performed as a binary image classification problem on the individual OCTA image data sets of the two different eye hospitals, namely Manchester Royal Eye Hospital and Moorfields Eye Hospital. The Manchester Royal Eye Hospital OCTA image data set comprises a small number of OCTA images representing two different eye conditions, namely from 33 healthy eyes and 23 wet AMD eyes, see Table 3.1 in Chapter 3, subsection 3.4.1. Hence, the binary image classification performed on Manchester Royal Eye Hospital OCTA image data set was conducted as healthy versus wet AMD.

The Moorfields Eye Hospital OCTA image data set, on the other hand, includes a much larger number of OCTA images demonstrating three different eye conditions, specifically from 79 dry AMD eyes, 166 wet AMD eyes and 25 secondary CNV eyes, see Table 3.2 in Chapter 3, subsection 3.4.2. Therefore, the binary image classification performed on Moorfields Eye Hospital OCTA image data set was conducted as dry AMD versus wet AMD. However, as the secondary CNV images share similar abnormal vascular characteristics of wet AMD images, a further binary image classification on the Moorfields Eye Hospital data set was also conducted, specifically CNV (wet AMD plus secondary CNV) versus non-CNV (dry AMD).

For all experiments conducted, the binary image classifications were performed as follows:

1. Based on individual feature vectors extracted from OCTA images of every separate ocular vascular layer, namely the superficial inner retina, the deep inner retina, the outer retina and the choriocapillaris layers, respectively. In this manner, the classification is performed solely based on the individual ocular vascular layer for every single eye.
2. Based on concatenating two feature vectors extracted from two OCTA images of the ocular vascular layers. These are (1) the superficial and the deep inner retina layers, (2) the superficial inner and the outer retina layers, (3) the superficial inner and the choriocapillaris layers, (4) the deep inner and the outer retina layers, (5) the deep inner retina and the choriocapillaris layers, and (6) the outer

retina and the choriocapillaris layers that are both typically used for diagnosing AMD disease. The concatenated two feature vectors generated from the various two layers construct a global feature vector for every individual eye. Consequently, the classification is performed based on the global feature vectors constructed for the individual eyes.

3. Based on concatenating three feature vectors extracted from three OCTA images of the ocular vascular layers. These are (1) the superficial, the deep inner and the outer retina layers, (2) the superficial, the deep inner retina and the choriocapillaris layers, (3) the superficial inner, the outer retina and the choriocapillaris layers and (4) the deep inner, the outer retina and the choriocapillaris layers. The concatenated three feature vectors generated from the various three layers construct a global feature vector for every individual eye. Consequently, the classification is performed based on the global feature vectors constructed for the individual eyes.
4. Based on concatenating all feature vectors extracted from all OCTA images of all ocular vascular layers constructing a global feature vector for every individual eye. Hence, the classification is performed based on the individual eyes not the individual ocular vascular layers.

There are several motivations for performing the binary image classifications in these ways. Performing the binary image classification on every OCTA image of each separate ocular vascular layer may potentially help to identify the most predictive ocular vascular layer with the most information describing the vascular abnormalities related to AMD disease, e.g.: areas of CNV regions. Additionally, it may help to identify other novel ocular vascular abnormalities associated with AMD disease in the OCTA images of certain ocular vascular layers, e.g.: the superficial inner retina and the deep inner retina, even though they do not typically display perceptible vascular abnormalities, e.g.: areas of CNV lesions, nor are typically used in current clinical practice for diagnosing areas of CNV lesions in AMD disease.

Recall that the textural appearance of vascular pathologies related to AMD disease can appear more perceptible in certain ocular vascular layers than others. Hence, conducting the binary image classification based on concatenating two feature vectors extracted from two OCTA images of various ocular vascular layers, based on concatenating three feature vectors extracted from three OCTA images of different ocular vascular layers, and based on concatenating all feature vectors extracted from the OCTA images of all ocular vascular layers, may potentially assist in identifying if there is

any complementary relationship between the various features arising from the different ocular vascular layers. Additionally, it may also help to exploit such information to address the large within-class variation issue as well as enhance the detection of AMD disease.

However, the Manchester Royal Eye Hospital and the Moorfields Eye Hospital OCTA data sets are all imbalanced. As such, the number of eyes involved in the OCTA data sets for each class of eye condition, e.g.: healthy, wet AMD, and dry AMD, are unequal. Nonetheless, since all individual classes of eye conditions, e.g.: healthy, wet AMD, and dry AMD, are very important to identify, the following evaluation strategies for the algorithm developed were conducted on the OCTA image data sets of both hospitals:

1. Use the stratified K folds cross-validation strategy with the value of $K = 10$ to split the OCTA image data sets into 10 stratified folds, i.e.: 10 stratified training and testing sets. This means every single training and testing set is created by preserving the number of samples, i.e.: OCTA images, of each class i.e.: healthy, wet AMD and dry AMD. The main motivation of setting the value of $K = 10$ is that, as evidenced by empirical evaluation results when using the value of $K = 10$, this is demonstrated to produce performance estimates that do not suffer from either extremely high bias, e.g.: overestimate of performance estimates, or from very high variance, e.g.: very high change in performance estimates [173]. These details, however, have already been comprehensively discussed and justified in Chapter 2, subsection 2.8.2. Nevertheless, this type of resampling technique can allow ensuring a reliable evaluation of the predictive performance for the proposed algorithm as well as limitation of the overfitting problem.
2. Compute the area under the ROC curve (AUC) score and this is to provide equal weight for both different classes of eye conditions in the binary classification problems i.e.: healthy vs wet AMD, dry AMD vs wet AMD and CNV vs non-CNV.

These evaluation strategies would give an accurate measure of insight into overall performance as well as ensuring enhanced validation for the algorithm developed. Besides the above mentioned evaluation strategies, the performance of the algorithm was also tested on the individual three texture descriptors, namely the $LBP_{p,r}^{2riu}$, the $LBP_{p,r}$ and the $BRIEF_{S,n}$ previously described in the local texture feature extraction step of the algorithm, section 4.3.1.

Additionally, the various parameters of the three different texture descriptors, i.e.: (p and r) for the $LBP_{p,r}^{2riu}$ and the $LBP_{p,r}$ and (S and n) for the $BRIEF_{S,n}$, were empirically fine-tuned with different values. The same values of parameters were used in the evaluation of all classification experiments. This is to facilitate fair and consistent evaluations. As the texture descriptors, i.e.: the $LBP_{p,r}^{2riu}$, the $LBP_{p,r}$ and the $BRIEF_{S,n}$, were individually fine-tuned with different combinations of parameters, the various values of parameters tested are denoted in the subscripts, i.e.: in place of p , r , S and n , of individual texture descriptors.

The motivation for undertaking the aforementioned evaluation procedures can be justified in two ways. Firstly, this can allow a comprehensive evaluation and validation of the texture descriptor proposed, i.e.: the $LBP_{p,r}^{2riu}$, for quantifying AMD textural appearance in OCTA images in comparison to other comparable texture descriptors, i.e. the $LBP_{p,r}$ and the $BRIEF_{S,n}$. Secondly, this may facilitate the identification of the optimal ocular vascular specific parameters of the different texture descriptors employed, i.e.: the $LBP_{p,r}^{2riu}$, the $LBP_{p,r}$ and the $BRIEF_{S,n}$, that may help to acquire decent and rich texture representations for AMD disease in OCTA images. As such this may facilitate automating the image classification task with at least near perfect results that are close to human capabilities.

As the evaluation involved employing the stratified $K = 10$ folds cross-validation strategy and computing the AUC scores, the mean AUC scores along with the standard deviations were estimated. Hence, the overall performance of the algorithm is estimated based on the mean AUC scores \pm standard deviations using the two different machine learning classifiers, specifically the KNN and the SVM previously illustrated in the classification step of the algorithm, see section 4.3.2.

Besides the above mentioned, cross-corpora experiments were also conducted. As the wet AMD is common in both OCTA image data sets, the cross-corpora experiments were performed by training the classifiers on one of the OCTA image data sets and then testing them on the other OCTA image data sets (as external validation) to demonstrate the generalisation performance. Specifically, the classifier trained on the Manchester OCTA image data set to solve the healthy versus wet AMD classification task is tested on the wet AMD cases of the Moorfields OCTA image data set. Likewise, the classifier trained on the Moorfields OCTA image data set to solve the dry AMD versus wet AMD classification task is tested on the wet AMD cases of the Manchester OCTA image data set.

As only the Manchester OCTA image data set contains healthy eyes, the same

healthy data set is used to train the classifier for solving the Manchester healthy versus Moorfields wet AMD classification task and then test the trained classifier on the wet AMD cases of the Manchester OCTA image data set. Likewise, as only the Moorfields OCTA image data set involves dry AMD eyes, the same dry AMD data set is used to train the classifier for solving the Moorfields dry AMD versus Manchester wet AMD classification task and then to test the trained classifier on the wet AMD cases of the Moorfields OCTA image data set.

The following two subsections 4.4.1 and 4.4.2 present the evaluation results of the algorithm proposed on both OCTA image data sets of the Manchester Royal Eye Hospital and the Moorfields Eye Hospital, respectively. The evaluation results of the cross-corpora experiments conducted are summarised in subsection 4.4.3.

4.4.1 Manchester Royal Eye Hospital

This subsection provides the analysis results of the automated classification algorithm proposed on the Manchester Royal Eye Hospital OCTA image data set for solving only a binary image classification task, i.e.: healthy vs wet AMD. The evaluation of the classification algorithm is performed in order based on the conducting of classification experiments. As such, it starts with the individual ocular vascular layers, namely the superficial inner retina layer, the deep inner retina layer, the outer retina layer and the choriocapillaris layer, respectively. This is then followed by layer combination namely by concatenating two feature vectors extracted from two OCTA images of various ocular vascular layers as well as concatenating all feature vectors extracted from the OCTA images of all ocular vascular layers.

4.4.1.1 Superficial Inner Retina Layer

The algorithm was firstly applied to the OCTA images of the superficial inner retina layer. Table 4.1 illustrates the classification results that demonstrate the diagnostic ability of the algorithm on the OCTA images of this retinal layer.

Although the OCTA images of the superficial inner retina layer do not usually show any perceptible vascular pathologies, i.e.: areas of CNV lesions, related to AMD disease, the evaluation results in Table 4.1 show that the automated classification algorithm can successfully detect some differences between the normal and abnormal vascular texture in the OCTA images of the superficial inner retina layer. However, the

Table 4.1: A summary of classification results (mean AUC scores \pm standard deviations) that measure the performance of the automated classification algorithm that is based on whole-local texture features for solving the healthy vs wet AMD classification task, on the OCTA images of the superficial inner retina layer.

Descriptor	KNN Classifier		SVM Classifier	
	Best Parameters	AUC \pm std	Best Parameters	AUC \pm std
$LBP_{4,1}^{2riu}$	$D^{k=3}_{euclidean}$	0.89 \pm 0.05	$K^{C=100, \gamma=1}_{rbf}$	0.83 \pm 0.19
$LBP_{4,1}$	$D^{k=3}_{euclidean}$	0.86 \pm 0.06	$K^{C=10}_{linear}$	0.86 \pm 0.20
$BRIEF_{4,4}$	$D^{k=7}_{chebyshev}$	0.59 \pm 0.08	$K^{C=100, \gamma=1}_{rbf}$	0.53 \pm 0.12
$LBP_{8,2}^{2riu}$	$D^{k=9}_{euclidean}$	0.81 \pm 0.10	$K^{C=10}_{linear}$	0.70 \pm 0.24
$LBP_{8,2}$	$D^{k=5}_{manhattan}$	0.85 \pm 0.06	$K^{C=10}_{linear}$	0.86 \pm 0.24
$BRIEF_{5,8}$	$D^{k=3}_{euclidean}$	0.51 \pm 0.10	$K^{C=1, d=6}_{poly}$	0.54 \pm 0.10
$LBP_{12,3}^{2riu}$	$D^{k=3}_{chebyshev}$	0.77 \pm 0.08	$K^{C=50, \gamma=1}_{rbf}$	0.70 \pm 0.21
$LBP_{12,3}$	$D^{k=5}_{manhattan}$	0.80 \pm 0.08	$K^{C=100, \gamma=1}_{rbf}$	0.81 \pm 0.15
$BRIEF_{6,12}$	$D^{k=7}_{chebyshev}$	0.65 \pm 0.06	$K^{C=50, d=4}_{poly}$	0.59 \pm 0.12
$LBP_{16,4}^{2riu}$	$D^{k=7}_{manhattan}$	0.77 \pm 0.08	$K^{C=100, \gamma=0.01}_{rbf}$	0.66 \pm 0.05
$LBP_{16,4}$	$D^{k=7}_{euclidean}$	0.78 \pm 0.08	$K^{C=10}_{linear}$	0.78 \pm 0.15
$BRIEF_{7,16}$	$D^{k=9}_{chebyshev}$	0.60 \pm 0.16	$K^{C=100, d=3}_{poly}$	0.55 \pm 0.13

$BRIEF_{S,n}$ texture descriptor was not capable of producing robust local texture descriptions as the performance was always close to random guessing skill, i.e.: mean AUC scores ≈ 0.55 , in both classification settings, i.e.: with the SVM and the KNN classifiers. Nevertheless, the $LBP_{p,r}^{2riu}$ and the $LBP_{p,r}$ texture descriptors generally demonstrated to facilitate the attainment of a satisfactory classification performance in all classification experiments. Based on the classification results given in Table 4.1, however, the best overall performance was succeeded with the $LBP_{4,1}^{2riu}$ texture descriptor based on a KNN classifier with $D^{k=3}_{euclidean}$ accomplishing a mean AUC score and a standard deviation = 0.89 \pm 0.05.

4.4.1.2 Deep Inner Retina Layer

The automated classification algorithm was then applied on the OCTA images of the deep inner retina layer. Table 4.2 displays the classification results that illustrate the diagnostic capability of the algorithm on the OCTA images of this retinal layer.

Similar to the OCTA images of the superficial inner retina layer, the OCTA images of the deep inner retina layer do not typically display any perceptible vascular pathologies, i.e.: regions of CNV lesions, related to AMD disease. However, the evaluation results in Table 4.2 demonstrate that the automated classification algorithm can

Table 4.2: A summary of classification results (mean AUC scores \pm standard deviations) that measure the performance of the automated classification algorithm that is based on whole-local texture features for solving the healthy vs wet AMD classification task, on the OCTA images of the deep inner retina layer.

Descriptor	KNN Classifier		SVM Classifier	
	Best Parameters	AUC \pm std	Best Parameters	AUC \pm std
$LBP_{4,1}^{2riu}$	$D_{manhattan}^{k=9}$	0.94 ± 0.06	$K_{rbf}^{C=100, \gamma=1}$	0.90 ± 0.06
$LBP_{4,1}$	$D_{chebyshev}^{k=9}$	0.91 ± 0.08	$K_{rbf}^{C=100, \gamma=1}$	0.92 ± 0.19
$BRIEF_{4,4}$	$D_{euclidean}^{k=1}$	0.61 ± 0.14	$K_{rbf}^{C=10, \gamma=1}$	0.60 ± 0.17
$LBP_{8,2}^{2riu}$	$D_{euclidean}^{k=5}$	0.91 ± 0.03	$K_{rbf}^{C=1, \gamma=0.001}$	0.82 ± 0.09
$LBP_{8,2}$	$D_{chebyshev}^{k=7}$	0.91 ± 0.06	$K_{linear}^{C=10}$	0.91 ± 0.04
$BRIEF_{5,8}$	$D_{chebyshev}^{k=5}$	0.58 ± 0.06	$K_{rbf}^{C=1, \gamma=0.0001}$	0.54 ± 0.07
$LBP_{12,3}^{2riu}$	$D_{euclidean}^{k=3}$	0.90 ± 0.06	$K_{linear}^{C=1}$	0.87 ± 0.21
$LBP_{12,3}$	$D_{manhattan}^{k=9}$	0.91 ± 0.04	$K_{rbf}^{C=1, \gamma=0.001}$	0.92 ± 0.25
$BRIEF_{6,12}$	$D_{euclidean}^{k=5}$	0.56 ± 0.11	$K_{poly}^{C=100, d=4}$	0.54 ± 0.11
$LBP_{16,4}^{2riu}$	$D_{euclidean}^{k=3}$	0.96 ± 0.04	$K_{rbf}^{C=1, \gamma=1}$	0.95 ± 0.03
$LBP_{16,4}$	$D_{euclidean}^{k=7}$	0.95 ± 0.04	$K_{linear}^{C=10}$	0.95 ± 0.05
$BRIEF_{7,16}$	$D_{chebyshev}^{k=7}$	0.69 ± 0.04	$K_{rbf}^{C=100, \gamma=1}$	0.59 ± 0.10

effectively identify dissimilarities between the normal and abnormal vascular texture appearance in the OCTA images of the deep inner retina layer. The $BRIEF_{S,n}$ texture descriptor, however, was not capable of producing robust local texture descriptions as the classification performance was almost constantly close to random guessing, i.e.: mean AUC scores ≈ 0.55 , in both classification settings, i.e.: with the SVM and the KNN classifiers. Nevertheless, the $LBP_{p,r}^{2riu}$ and the $LBP_{p,r}$ texture descriptors mostly showed to enable the achievement of good and comparable classification results in all classification experiments. However, based on the classification results given in Table 4.2, the best overall performance was accomplished with the $LBP_{16,4}^{2riu}$ texture descriptor based on a KNN classifier with $D_{euclidean}^{k=3}$ achieving a mean AUC score and a standard deviation = 0.96 ± 0.04 .

4.4.1.3 Outer Retina Layer

The automated classification algorithm was subsequently applied to the OCTA images of the outer retina layer. Table 4.3 presents the classification results that demonstrate the diagnostic skill of the algorithm on the OCTA images of the retinal layer.

In contrast to the OCTA images of the superficial inner retina layer and the deep

Table 4.3: A summary of classification results (mean AUC scores \pm standard deviations) that measure the performance of the automated classification algorithm that is based on whole-local texture features for solving the healthy vs wet AMD classification task, on the OCTA images of the outer retina layer.

Descriptor	KNN Classifier		SVM Classifier	
	Best Parameters	AUC \pm std	Best Parameters	AUC \pm std
$LBP_{4,1}^{2riu}$	$D^{k=3}_{euclidean}$	0.99 \pm 0.00	$K^{C=1}_{linear}$	0.99 \pm 0.00
$LBP_{4,1}$	$D^{k=3}_{euclidean}$	0.99 \pm 0.00	$K^{C=1}_{linear}$	0.99 \pm 0.00
$BRIEF_{4,4}$	$D^{k=3}_{euclidean}$	0.76 \pm 0.08	$K^{C=1}_{linear}$	0.72 \pm 0.15
$LBP_{8,2}^{2riu}$	$D^{k=3}_{euclidean}$	0.99 \pm 0.00	$K^{C=1}_{linear}$	0.99 \pm 0.00
$LBP_{8,2}$	$D^{k=3}_{euclidean}$	0.99 \pm 0.00	$K^{C=1}_{linear}$	0.99 \pm 0.00
$BRIEF_{5,8}$	$D^{k=7}_{manhattan}$	0.62 \pm 0.07	$K^{C=1, \gamma=0.0001}_{rbf}$	0.54 \pm 0.08
$LBP_{12,3}^{2riu}$	$D^{k=3}_{euclidean}$	0.99 \pm 0.00	$K^{C=1}_{linear}$	0.99 \pm 0.00
$LBP_{12,3}$	$D^{k=3}_{euclidean}$	0.99 \pm 0.00	$K^{C=1}_{linear}$	0.99 \pm 0.00
$BRIEF_{6,12}$	$D^{k=9}_{manhattan}$	0.71 \pm 0.13	$K^{C=1, d=3}_{poly}$	0.62 \pm 0.16
$LBP_{16,4}^{2riu}$	$D^{k=3}_{euclidean}$	0.99 \pm 0.00	$K^{C=1}_{linear}$	0.99 \pm 0.00
$LBP_{16,4}$	$D^{k=3}_{euclidean}$	0.99 \pm 0.00	$K^{C=1}_{linear}$	0.99 \pm 0.00
$BRIEF_{7,16}$	$D^{k=9}_{chebyshev}$	0.77 \pm 0.07	$K^{C=1, d=2}_{poly}$	0.61 \pm 0.14

inner retina layer, the OCTA images of the outer retina layer typically exhibit perceptible signs of vascular pathologies, i.e.: areas of CNV lesions, associated with AMD disease. However, the areas of CNV lesions in the OCTA images of outer retina layer may not be fully visualised, possibly due to the nature of how the CNV lesions normally grow. As the CNV lesions typically grow by perforating the Bruch's membrane that is the deepest part of the choroid layer and by progressing into other subretinal layers, some parts of CNV regions may appear more perceptible in certain ocular vascular layers than others. Nevertheless, the evaluation results in Table 4.3 demonstrate that the automated classification algorithm achieved outstanding classification results. As such the algorithm can successfully identify dissimilarities between the normal and abnormal vascular texture appearance in the OCTA images of the outer retina layer with nearly no misclassification cases, i.e.: with almost no incorrect predictions.

The $BRIEF_{S,n}$ texture descriptor was not capable of producing robust local texture descriptions from the OCTA images of the superficial inner retina and the deep inner retina layers as evidenced by previous results, see Tables 4.2 and 4.1. This is in contrast with the OCTA images of the outer retina layer, with which the $BRIEF_{S,n}$ texture descriptor demonstrated to allow quite good improvements in classification performance. As such, in some classification experiments, i.e.: using the SVM and the

KNN classifiers, the classification results using the $BRIEF_{S,n}$ texture descriptor generally outperformed the random guessing skill, i.e.: mean AUC scores over 0.75. Yet, the best overall performance was accomplished with the $LBP_{p,r}^{2riu}$ as well as the $LBP_{p,r}$ texture descriptors irrespective of which values of parameters are used. Both encouraged the attainment of a mean AUC score and a standard deviation = 0.99 ± 0.00 with both classifiers, i.e.: the KNN using $D_{euclidean}^{k=3}$ and the SVM using $K_{linear}^{C=1}$.

4.4.1.4 Choriocapillaris Layer

Following the application of the automated classification algorithm to the previous ocular vascular layers, the algorithm was afterward applied to the OCTA images of the choriocapillaris layer. Table 4.4 presents the classification results that demonstrate the diagnostic skill of the classification algorithm on the OCTA images of this choroidal layer.

Table 4.4: A summary of classification results (mean AUC scores \pm standard deviations) that measure the performance of the automated classification algorithm that is based on whole-local texture features for solving the healthy vs wet AMD classification task, on the OCTA images of choriocapillaris layer.

Descriptor	KNN Classifier		SVM Classifier	
	Best Parameters	AUC \pm std	Best Parameters	AUC \pm std
$LBP_{4,1}^{2riu}$	$D_{chebyshev}^{k=3}$	0.93 ± 0.08	$K_{poly}^{C=50,d=2}$	0.94 ± 0.08
$LBP_{4,1}$	$D_{chebyshev}^{k=3}$	0.97 ± 0.04	$K_{linear}^{C=1}$	0.97 ± 0.06
$BRIEF_{4,4}$	$D_{chebyshev}^{k=3}$	0.78 ± 0.08	$K_{rbf}^{C=100,\gamma=1}$	0.81 ± 0.08
$LBP_{8,2}^{2riu}$	$D_{euclidean}^{k=3}$	0.87 ± 0.05	$K_{rbf}^{C=100,\gamma=1}$	0.88 ± 0.05
$LBP_{8,2}$	$D_{manhattan}^{k=1}$	0.94 ± 0.06	$K_{linear}^{C=1}$	0.93 ± 0.06
$BRIEF_{5,8}$	$D_{manhattan}^{k=5}$	0.77 ± 0.10	$K_{linear}^{C=100}$	0.82 ± 0.10
$LBP_{12,3}^{2riu}$	$D_{manhattan}^{k=5}$	0.93 ± 0.03	$K_{linear}^{C=10}$	0.94 ± 0.04
$LBP_{12,3}$	$D_{manhattan}^{k=7}$	0.95 ± 0.02	$K_{linear}^{C=1}$	0.95 ± 0.03
$BRIEF_{6,12}$	$D_{chebyshev}^{k=9}$	0.81 ± 0.10	$K_{rbf}^{C=100,\gamma=1}$	0.69 ± 0.19
$LBP_{16,4}^{2riu}$	$D_{manhattan}^{k=9}$	0.95 ± 0.02	$K_{linear}^{C=10}$	0.97 ± 0.03
$LBP_{16,4}$	$D_{manhattan}^{k=1}$	0.96 ± 0.02	$K_{linear}^{C=1}$	0.96 ± 0.03
$BRIEF_{7,16}$	$D_{chebyshev}^{k=3}$	0.84 ± 0.09	$K_{rbf}^{C=100,\gamma=1}$	0.83 ± 0.11

The OCTA images of the choriocapillaris layer are analogous to the OCTA images of the outer retina layer in being known to typically display noticeable marks of vascular pathologies, i.e.: areas of CNV lesions, associated with AMD disease. However, the areas of CNV lesions in the OCTA images of choriocapillaris may not be fully visualised, as was the case with the OCTA images of the outer retina layer. This is mainly

due to the nature of how CNV lesions normally grow. The CNV lesions typically grow by perforating the Bruch's membrane, that is the deepest part of the choroid layer, and by progressing into other subretinal layers. Hence, some parts of CNV regions may be more distinguishable in certain ocular vascular layers than in others. Nevertheless, the evaluation results in Table 4.4 demonstrate that the automated classification algorithm was able to achieve great classification results. As such the algorithm successfully identified dissimilarities between the normal and abnormal vascular texture appearance in the OCTA images of the choriocapillaris layer with a few misclassification cases.

Similar to the case with the OCTA images of the outer retina layer, the $BRIEF_{S,n}$ texture descriptor was capable of generating local texture descriptions from the OCTA images of the choriocapillaris layer that adequately facilitated a slight improvement in the classification performance compared to its poor results in previous ocular vascular layers, see Tables 4.1 and 4.2. Based on the classification results given in Table 4.4, however, the best overall performance was accomplished with the $LBP_{16,4}^{2riu}$ texture descriptor achieving a mean AUC score and a standard deviation = 0.97 ± 0.03 based on the SVM classifier with $K_{linear}^{C=10}$.

4.4.1.5 Layer Combination

After evaluating the automated classification algorithm on the OCTA images of ocular vascular layers individually, the performance of the algorithm was subsequently assessed on classifying the various eyes via layer combination. Specifically, this is accomplished by conducting the binary image classification based on concatenating two feature vectors extracted from two OCTA images of the different ocular vascular layers, based on concatenating three feature vectors extracted from three OCTA images of the various ocular vascular layers and based on concatenating all feature vectors extracted from the OCTA images of all ocular vascular layers. It should be recalled that the classification performance of the algorithm was assessed based on the individual eyes, not the individual OCTA images of various ocular vascular layers.

Tables 4.5, 4.6, 4.7, 4.8, 4.9 and 4.10 present the classification results that demonstrate the diagnostic skill of the classification algorithm to classify the different eyes when concatenating two feature vectors extracted from two OCTA images of the different ocular vascular layers. These are the superficial and the deep inner retina, the superficial inner and the outer retina, the superficial inner retina and the choriocapillaris, the deep inner and the outer retina, the deep inner retina and the choriocapillaris,

and the outer retina and the choriocapillaris layers, respectively.

Table 4.5: A summary of classification results (mean AUC scores \pm standard deviations) that measure the performance of the automated classification algorithm that is based on whole-local texture features for solving the healthy vs wet AMD classification task, based on concatenating two feature vectors extracted from the OCTA images of the superficial and the deep retina layers.

Descriptor	KNN Classifier		SVM Classifier	
	Best Parameters	AUC \pm std	Best Parameters	AUC \pm std
$LBP_{4,1}^{2riu}$	$D^{k=5}_{manhattan}$	0.93 ± 0.06	$K^{C=1}_{linear}$	0.94 ± 0.03
$LBP_{4,1}$	$D^{k=3}_{euclidean}$	0.91 ± 0.08	$K^{C=1,d=2}_{poly}$	0.93 ± 0.07
$BRIEF_{4,4}$	$D^{k=3}_{manhattan}$	0.56 ± 0.08	$K^{C=10,d=4}_{poly}$	0.54 ± 0.11
$LBP_{8,2}^{2riu}$	$D^{k=1}_{euclidean}$	0.83 ± 0.08	$K^{C=50,d=2}_{poly}$	0.89 ± 0.09
$LBP_{8,2}$	$D^{k=5}_{manhattan}$	0.90 ± 0.06	$K^{C=50,d=6}_{poly}$	0.93 ± 0.06
$BRIEF_{5,8}$	$D^{k=7}_{chebyshev}$	0.54 ± 0.07	$K^{C=50,\gamma=0.01}_{rbf}$	0.51 ± 0.06
$LBP_{12,3}^{2riu}$	$D^{k=1}_{euclidean}$	0.86 ± 0.06	$K^{C=50,d=5}_{poly}$	0.91 ± 0.07
$LBP_{12,3}$	$D^{k=5}_{manhattan}$	0.90 ± 0.03	$K^{C=100,d=2}_{poly}$	0.93 ± 0.05
$BRIEF_{6,12}$	$D^{k=7}_{euclidean}$	0.50 ± 0.07	$K^{C=1,\gamma=0.0001}_{rbf}$	0.51 ± 0.08
$LBP_{16,4}^{2riu}$	$D^{k=5}_{manhattan}$	0.93 ± 0.04	$K^{C=10}_{linear}$	0.75 ± 0.10
$LBP_{16,4}$	$D^{k=5}_{euclidean}$	0.92 ± 0.07	$K^{C=1}_{linear}$	0.88 ± 0.10
$BRIEF_{7,16}$	$D^{k=5}_{chebyshev}$	0.53 ± 0.13	$K^{C=1}_{linear}$	0.52 ± 0.15

Table 4.6: A summary of classification results (mean AUC scores \pm standard deviations) that measure the performance of the automated classification algorithm that is based on whole-local texture features for solving the healthy vs wet AMD classification task, based on concatenating two feature vectors extracted from the OCTA images of the superficial and the outer retina layers.

Descriptor	KNN Classifier		SVM Classifier	
	Best Parameters	AUC \pm std	Best Parameters	AUC \pm std
$LBP_{4,1}^{2riu}$	$D^{k=1}_{euclidean}$	0.96 ± 0.05	$K^{C=1}_{linear}$	0.97 ± 0.02
$LBP_{4,1}$	$D^{k=1}_{euclidean}$	0.95 ± 0.06	$K^{C=1}_{linear}$	0.94 ± 0.04
$BRIEF_{4,4}$	$D^{k=3}_{euclidean}$	0.52 ± 0.08	$K^{C=1,d=5}_{poly}$	0.51 ± 0.11
$LBP_{8,2}^{2riu}$	$D^{k=3}_{euclidean}$	0.96 ± 0.06	$K^{C=1}_{linear}$	0.95 ± 0.22
$LBP_{8,2}$	$D^{k=1}_{euclidean}$	0.96 ± 0.02	$K^{C=1}_{linear}$	0.95 ± 0.02
$BRIEF_{5,8}$	$D^{k=1}_{euclidean}$	0.51 ± 0.08	$K^{C=50,d=6}_{poly}$	0.50 ± 0.10
$LBP_{12,3}^{2riu}$	$D^{k=1}_{euclidean}$	0.95 ± 0.02	$K^{C=1}_{linear}$	0.90 ± 0.10
$LBP_{12,3}$	$D^{k=1}_{euclidean}$	0.94 ± 0.01	$K^{C=1}_{linear}$	0.95 ± 0.22
$BRIEF_{6,12}$	$D^{k=7}_{manhattan}$	0.63 ± 0.16	$K^{C=1,\gamma=0.001}_{rbf}$	0.55 ± 0.15
$LBP_{16,4}^{2riu}$	$D^{k=1}_{euclidean}$	0.98 ± 0.02	$K^{C=1}_{linear}$	0.90 ± 0.10
$LBP_{16,4}$	$D^{k=1}_{euclidean}$	0.95 ± 0.02	$K^{C=1}_{linear}$	0.96 ± 0.02
$BRIEF_{7,16}$	$D^{k=5}_{euclidean}$	0.50 ± 0.11	$K^{C=1}_{linear}$	0.51 ± 0.12

Table 4.7: A summary of classification results (mean AUC scores \pm standard deviations) that measure the performance of the automated classification algorithm that is based on whole-local texture features for solving the healthy vs wet AMD classification task, based on concatenating two feature vectors extracted from the OCTA images of the superficial and the choriocapillaris retina layers.

Descriptor	KNN Classifier		SVM Classifier	
	Best Parameters	AUC \pm std	Best Parameters	AUC \pm std
$LBP_{4,1}^{2riu}$	$D^{k=9}_{euclidean}$	0.90 ± 0.04	$K^{C=1,d=3}_{poly}$	0.92 ± 0.04
$LBP_{4,1}$	$D^{k=9}_{euclidean}$	0.90 ± 0.05	$K^{C=1,d=3}_{poly}$	0.91 ± 0.05
$BRIEF_{4,4}$	$D^{k=7}_{manhattan}$	0.71 ± 0.08	$K^{C=100,d=3}_{poly}$	0.63 ± 0.16
$LBP_{8,2}^{2riu}$	$D^{k=5}_{manhattan}$	0.88 ± 0.04	$K^{C=1,d=4}_{poly}$	0.90 ± 0.05
$LBP_{8,2}$	$D^{k=5}_{euclidean}$	0.89 ± 0.03	$K^{C=100,d=2}_{poly}$	0.90 ± 0.05
$BRIEF_{5,8}$	$D^{k=9}_{manhattan}$	0.64 ± 0.06	$K^{C=10,d=5}_{poly}$	0.68 ± 0.11
$LBP_{12,3}^{2riu}$	$D^{k=3}_{manhattan}$	0.88 ± 0.06	$K^{C=100,d=6}_{poly}$	0.93 ± 0.06
$LBP_{12,3}$	$D^{k=3}_{manhattan}$	0.94 ± 0.04	$K^{C=100,d=6}_{poly}$	0.93 ± 0.04
$BRIEF_{6,12}$	$D^{k=5}_{manhattan}$	0.63 ± 0.13	$K^{C=50,d=5}_{poly}$	0.66 ± 0.13
$LBP_{16,4}^{2riu}$	$D^{k=5}_{manhattan}$	0.92 ± 0.06	$K^{C=1}_{linear}$	0.86 ± 0.19
$LBP_{16,4}$	$D^{k=5}_{euclidean}$	0.93 ± 0.06	$K^{C=1}_{linear}$	0.93 ± 0.05
$BRIEF_{7,16}$	$D^{k=5}_{chebyshev}$	0.66 ± 0.12	$K^{C=1}_{linear}$	0.55 ± 0.14

Table 4.8: A summary of classification results (mean AUC scores \pm standard deviations) that measure the performance of the automated classification algorithm that is based on whole-local texture features for solving the healthy vs wet AMD classification task, based on concatenating two feature vectors extracted from two OCTA images, namely the deep and the outer retina layers.

Descriptor	KNN Classifier		SVM Classifier	
	Best Parameters	AUC \pm std	Best Parameters	AUC \pm std
$LBP_{4,1}^{2riu}$	$D^{k=1}_{euclidean}$	0.97 ± 0.02	$K^{C=1}_{linear}$	0.96 ± 0.02
$LBP_{4,1}$	$D^{k=1}_{euclidean}$	0.94 ± 0.05	$K^{C=1}_{linear}$	0.95 ± 0.22
$BRIEF_{4,4}$	$D^{k=1}_{euclidean}$	0.57 ± 0.12	$K^{C=100,d=2}_{poly}$	0.62 ± 0.11
$LBP_{8,2}^{2riu}$	$D^{k=1}_{euclidean}$	0.94 ± 0.02	$K^{C=1}_{linear}$	0.96 ± 0.00
$LBP_{8,2}$	$D^{k=1}_{euclidean}$	0.97 ± 0.07	$K^{C=1}_{linear}$	0.95 ± 0.22
$BRIEF_{5,8}$	$D^{k=9}_{euclidean}$	0.57 ± 0.08	$K^{C=1,d=6}_{poly}$	0.57 ± 0.07
$LBP_{12,3}^{2riu}$	$D^{k=3}_{euclidean}$	0.95 ± 0.02	$K^{C=1}_{linear}$	0.94 ± 0.22
$LBP_{12,3}$	$D^{k=1}_{euclidean}$	0.96 ± 0.06	$K^{C=1}_{linear}$	0.95 ± 0.07
$BRIEF_{6,12}$	$D^{k=9}_{manhattan}$	0.60 ± 0.13	$K^{C=1,d=5}_{poly}$	0.54 ± 0.16
$LBP_{16,4}^{2riu}$	$D^{k=1}_{euclidean}$	0.98 ± 0.01	$K^{C=1}_{linear}$	0.96 ± 0.04
$LBP_{16,4}$	$D^{k=1}_{euclidean}$	0.97 ± 0.03	$K^{C=1}_{linear}$	0.90 ± 0.10
$BRIEF_{7,16}$	$D^{k=3}_{chebyshev}$	0.61 ± 0.10	$K^{C=10}_{linear}$	0.51 ± 0.15

Tables 4.11, 4.12, 4.13 and 4.14, on the other hand, exhibit the classification results

Table 4.9: A summary of classification results (mean AUC scores \pm standard deviations) that measure the performance of the automated classification algorithm that is based on whole-local texture features for solving the healthy vs wet AMD classification task, based on concatenating two feature vectors extracted from the OCTA images of the deep retina and the choriocapillaris layers.

Descriptor	KNN Classifier		SVM Classifier	
	Best Parameters	AUC \pm std	Best Parameters	AUC \pm std
$LBP_{4,1}^{2riu}$	$D_{euclidean}^{k=9}$	0.94 ± 0.05	$K_{poly}^{C=1,d=3}$	0.95 ± 0.06
$LBP_{4,1}$	$D_{chebyshev}^{k=9}$	0.94 ± 0.05	$K_{poly}^{C=1,d=3}$	0.94 ± 0.06
$BRIEF_{4,4}$	$D_{euclidean}^{k=3}$	0.69 ± 0.08	$K_{poly}^{C=50,d=2}$	0.70 ± 0.12
$LBP_{8,2}^{2riu}$	$D_{euclidean}^{k=5}$	0.91 ± 0.06	$K_{poly}^{C=10,d=3}$	0.95 ± 0.06
$LBP_{8,2}$	$D_{manhattan}^{k=7}$	0.93 ± 0.05	$K_{poly}^{C=100,d=6}$	0.96 ± 0.05
$BRIEF_{5,8}$	$D_{manhattan}^{k=3}$	0.74 ± 0.10	$K_{poly}^{C=50,d=5}$	0.76 ± 0.10
$LBP_{12,3}^{2riu}$	$D_{manhattan}^{k=5}$	0.95 ± 0.04	$K_{poly}^{C=50,d=5}$	0.97 ± 0.04
$LBP_{12,3}$	$D_{manhattan}^{k=7}$	0.97 ± 0.02	$K_{poly}^{C=100,d=6}$	0.97 ± 0.02
$BRIEF_{6,12}$	$D_{manhattan}^{k=3}$	0.65 ± 0.11	$K_{poly}^{C=50,d=6}$	0.67 ± 0.11
$LBP_{16,4}^{2riu}$	$D_{manhattan}^{k=5}$	0.97 ± 0.03	$K_{linear}^{C=10}$	0.91 ± 0.20
$LBP_{16,4}$	$D_{manhattan}^{k=5}$	0.98 ± 0.01	$K_{linear}^{C=1}$	0.88 ± 0.28
$BRIEF_{7,16}$	$D_{chebyshev}^{k=3}$	0.61 ± 0.09	$K_{linear}^{C=1}$	0.50 ± 0.15

Table 4.10: A summary of classification results (mean AUC scores \pm standard deviations) that measure the performance of the automated classification algorithm that is based on whole-local texture features for solving the healthy vs wet AMD classification task, based on concatenating two feature vectors extracted from the OCTA images of the outer retina and the choriocapillaris layers.

Descriptor	KNN Classifier		SVM Classifier	
	Best Parameters	AUC \pm std	Best Parameters	AUC \pm std
$LBP_{4,1}^{2riu}$	$D_{manhattan}^{k=5}$	0.99 ± 0.03	$K_{linear}^{C=1}$	0.98 ± 0.04
$LBP_{4,1}$	$D_{euclidean}^{k=3}$	0.97 ± 0.04	$K_{linear}^{C=1}$	0.98 ± 0.03
$BRIEF_{4,4}$	$D_{chebyshev}^{k=5}$	0.72 ± 0.13	$K_{linear}^{C=100}$	0.76 ± 0.13
$LBP_{8,2}^{2riu}$	$D_{euclidean}^{k=3}$	0.96 ± 0.02	$K_{linear}^{C=1}$	0.95 ± 0.12
$LBP_{8,2}$	$D_{euclidean}^{k=3}$	0.96 ± 0.02	$K_{linear}^{C=1}$	0.95 ± 0.12
$BRIEF_{5,8}$	$D_{chebyshev}^{k=7}$	0.71 ± 0.08	$K_{poly}^{C=10,d=3}$	0.64 ± 0.20
$LBP_{12,3}^{2riu}$	$D_{euclidean}^{k=3}$	0.99 ± 0.04	$K_{linear}^{C=1}$	0.97 ± 0.03
$LBP_{12,3}$	$D_{euclidean}^{k=3}$	0.96 ± 0.02	$K_{linear}^{C=1}$	0.97 ± 0.02
$BRIEF_{6,12}$	$D_{manhattan}^{k=9}$	0.76 ± 0.05	$K_{linear}^{C=50}$	0.64 ± 0.19
$LBP_{16,4}^{2riu}$	$D_{euclidean}^{k=3}$	1.00 ± 0.00	$K_{linear}^{C=1}$	0.95 ± 0.12
$LBP_{16,4}$	$D_{euclidean}^{k=3}$	0.98 ± 0.03	$K_{linear}^{C=1}$	0.97 ± 0.02
$BRIEF_{7,16}$	$D_{chebyshev}^{k=5}$	0.73 ± 0.10	$K_{poly}^{C=10,d=2}$	0.71 ± 0.10

that show the diagnostic capability of the classification algorithm when concatenating

three feature vectors extracted from three OCTA images of the various ocular vascular layers. These are the superficial, the deep inner and the outer retina, the superficial, the deep inner retina and the choriocapillaris, the superficial inner, the outer retina and the choriocapillaris, and the deep inner, the outer retina and the choriocapillaris layers, respectively.

Table 4.11: A summary of classification results (mean AUC scores \pm standard deviations) that measure the performance of the automated classification algorithm that is based on whole-local texture features for solving the healthy vs wet AMD classification task, based on concatenating three feature vectors extracted from the OCTA images of the superficial inner, the deep inner and the outer retina layers.

Descriptor	KNN Classifier		SVM Classifier	
	Best Parameters	AUC \pm std	Best Parameters	AUC \pm std
$LBP_{4,1}^{2riu}$	$D^{k=1}_{euclidean}$	0.97 ± 0.02	$K^{C=1}_{linear}$	0.94 ± 0.12
$LBP_{4,1}$	$D^{k=1}_{euclidean}$	0.97 ± 0.05	$K^{C=1}_{linear}$	0.95 ± 0.12
$BRIEF_{4,4}$	$D^{k=1}_{chebyshev}$	0.59 ± 0.08	$K^{C=10,d=3}_{poly}$	0.64 ± 0.11
$LBP_{8,2}^{2riu}$	$D^{k=3}_{euclidean}$	0.97 ± 0.06	$K^{C=1}_{linear}$	0.97 ± 0.04
$LBP_{8,2}$	$D^{k=3}_{euclidean}$	0.95 ± 0.02	$K^{C=1}_{linear}$	0.97 ± 0.01
$BRIEF_{5,8}$	$D^{k=3}_{chebyshev}$	0.51 ± 0.06	$K^{C=1,d=2}_{poly}$	0.50 ± 0.07
$LBP_{12,3}^{2riu}$	$D^{k=3}_{euclidean}$	0.97 ± 0.03	$K^{C=1}_{linear}$	0.96 ± 0.02
$LBP_{12,3}$	$D^{k=1}_{euclidean}$	0.95 ± 0.06	$K^{C=1}_{linear}$	0.96 ± 0.03
$BRIEF_{6,12}$	$D^{k=3}_{manhattan}$	0.60 ± 0.15	$K^{C=1}_{linear}$	0.53 ± 0.13
$LBP_{16,4}^{2riu}$	$D^{k=3}_{euclidean}$	0.98 ± 0.01	$K^{C=1}_{linear}$	0.95 ± 0.03
$LBP_{16,4}$	$D^{k=1}_{euclidean}$	0.97 ± 0.05	$K^{C=1}_{linear}$	0.95 ± 0.12
$BRIEF_{7,16}$	$D^{k=5}_{manhattan}$	0.50 ± 0.07	$K^{C=1,\gamma=0.01}_{rbf}$	0.51 ± 0.09

Table 4.15 shows the classification results when concatenating all feature vectors extracted from the OCTA images of all ocular vascular layers.

Combining the various OCTA images of ocular vascular layers with different eye conditions, i.e.: healthy and wet AMD, can be quite challenging to differentiate even for highly skilled ophthalmologists. This is because the textural vascular appearance in the various OCTA images usually appear significantly different among various ocular vascular layers. With the presence of an eye condition, i.e.: wet AMD disease, the OCTA images of certain ocular vascular layers, e.g.: the superficial inner retina and the deep inner retina layers, typically demonstrate a relatively uniform textural vascular appearance that is comparable to healthy. However, the OCTA images of the outer retina and the choriocapillaris layers with wet AMD disease usually show random textural vascular appearance that is dramatically different from healthy.

Despite these diversities and difficulties, the evaluation results previously presented

Table 4.12: A summary of classification results (mean AUC scores \pm standard deviations) that measure the performance of the automated classification algorithm that is based on whole-local texture features for solving the healthy vs wet AMD classification task, based on concatenating three feature vectors extracted from the OCTA images of the superficial, the deep inner retina and the choriocapillaris layers.

Descriptor	KNN Classifier		SVM Classifier	
	Best Parameters	AUC \pm std	Best Parameters	AUC \pm std
$LBP_{4,1}^{2riu}$	$D_{chebyshev}^{k=3}$	0.95 ± 0.05	$K_{poly}^{C=1,d=2}$	0.96 ± 0.04
$LBP_{4,1}$	$D_{manhattan}^{k=3}$	0.96 ± 0.06	$K_{linear}^{C=1}$	0.96 ± 0.05
$BRIEF_{4,4}$	$D_{manhattan}^{k=1}$	0.63 ± 0.09	$K_{poly}^{C=10,d=3}$	0.55 ± 0.10
$LBP_{8,2}^{2riu}$	$D_{manhattan}^{k=5}$	0.88 ± 0.08	$K_{poly}^{C=10,d=3}$	0.93 ± 0.08
$LBP_{8,2}$	$D_{manhattan}^{k=3}$	0.92 ± 0.07	$K_{rbf}^{C=1,\gamma=0.01}$	0.88 ± 0.10
$BRIEF_{5,8}$	$D_{manhattan}^{k=5}$	0.70 ± 0.10	$K_{poly}^{C=10,d=2}$	0.65 ± 0.11
$LBP_{12,3}^{2riu}$	$D_{manhattan}^{k=3}$	0.93 ± 0.06	$K_{poly}^{C=10,d=3}$	0.92 ± 0.07
$LBP_{12,3}$	$D_{manhattan}^{k=3}$	0.97 ± 0.02	$K_{linear}^{C=10}$	0.95 ± 0.03
$BRIEF_{6,12}$	$D_{manhattan}^{k=5}$	0.50 ± 0.10	$K_{poly}^{C=10,d=3}$	0.52 ± 0.12
$LBP_{16,4}^{2riu}$	$D_{manhattan}^{k=5}$	0.96 ± 0.02	$K_{linear}^{C=10}$	0.93 ± 0.07
$LBP_{16,4}$	$D_{manhattan}^{k=5}$	0.98 ± 0.02	$K_{linear}^{C=50}$	0.97 ± 0.03
$BRIEF_{7,16}$	$D_{manhattan}^{k=5}$	0.57 ± 0.10	$K_{poly}^{C=10,d=3}$	0.54 ± 0.11

Table 4.13: A summary of classification results (mean AUC scores \pm standard deviations) that measure the performance of the automated classification algorithm that is based on whole-local texture features for solving the healthy vs wet AMD classification task, based on concatenating three feature vectors extracted from the OCTA images of the superficial inner, the outer retina and the choriocapillaris layers.

Descriptor	KNN Classifier		SVM Classifier	
	Best Parameters	AUC \pm std	Best Parameters	AUC \pm std
$LBP_{4,1}^{2riu}$	$D_{euclidean}^{k=3}$	0.96 ± 0.05	$K_{linear}^{C=1}$	0.95 ± 0.06
$LBP_{4,1}$	$D_{euclidean}^{k=3}$	0.95 ± 0.04	$K_{linear}^{C=1}$	0.96 ± 0.03
$BRIEF_{4,4}$	$D_{euclidean}^{k=3}$	0.54 ± 0.11	$K_{linear}^{C=50}$	0.53 ± 0.13
$LBP_{8,2}^{2riu}$	$D_{euclidean}^{k=3}$	0.96 ± 0.07	$K_{linear}^{C=1}$	0.95 ± 0.12
$LBP_{8,2}$	$D_{euclidean}^{k=1}$	0.95 ± 0.05	$K_{linear}^{C=1}$	0.90 ± 0.10
$BRIEF_{5,8}$	$D_{euclidean}^{k=1}$	0.61 ± 0.07	$K_{poly}^{C=10,d=3}$	0.59 ± 0.13
$LBP_{12,3}^{2riu}$	$D_{euclidean}^{k=3}$	0.96 ± 0.02	$K_{linear}^{C=1}$	0.90 ± 0.10
$LBP_{12,3}$	$D_{euclidean}^{k=1}$	0.96 ± 0.04	$K_{linear}^{C=1}$	0.95 ± 0.12
$BRIEF_{6,12}$	$D_{manhattan}^{k=5}$	0.71 ± 0.12	$K_{poly}^{C=10,d=3}$	0.65 ± 0.14
$LBP_{16,4}^{2riu}$	$D_{euclidean}^{k=3}$	0.97 ± 0.02	$K_{linear}^{C=1}$	0.97 ± 0.04
$LBP_{16,4}$	$D_{euclidean}^{k=1}$	0.96 ± 0.03	$K_{linear}^{C=1}$	0.96 ± 0.02
$BRIEF_{7,16}$	$D_{chebyshev}^{k=5}$	0.61 ± 0.11	$K_{poly}^{C=10,d=3}$	0.60 ± 0.06

show that the automated classification algorithm can successfully detect differences

Table 4.14: A summary of classification results (mean AUC scores \pm standard deviations) that measure the performance of the automated classification algorithm that is based on whole-local texture features for solving the healthy vs wet AMD classification task, based on concatenating three feature vectors extracted from the OCTA images of the deep inner, the outer retina and the choriocapillaris layers.

Descriptor	KNN Classifier		SVM Classifier	
	Best Parameters	AUC \pm std	Best Parameters	AUC \pm std
$LBP_{4,1}^{2riu}$	$D^{k=1}_{manhattan}$	0.97 ± 0.06	$K^{C=1}_{linear}$	0.89 ± 0.10
$LBP_{4,1}$	$D^{k=3}_{euclidean}$	0.96 ± 0.07	$K^{C=1}_{linear}$	0.90 ± 0.10
$BRIEF_{4,4}$	$D^{k=5}_{manhattan}$	0.65 ± 0.10	$K^{C=10,d=3}_{poly}$	0.66 ± 0.14
$LBP_{8,2}^{2riu}$	$D^{k=3}_{euclidean}$	0.97 ± 0.05	$K^{C=1}_{linear}$	0.96 ± 0.04
$LBP_{8,2}$	$D^{k=5}_{euclidean}$	0.96 ± 0.04	$K^{C=1}_{linear}$	0.97 ± 0.03
$BRIEF_{5,8}$	$D^{k=5}_{manhattan}$	0.69 ± 0.10	$K^{C=10,d=3}_{poly}$	0.71 ± 0.14
$LBP_{12,3}^{2riu}$	$D^{k=3}_{euclidean}$	0.96 ± 0.06	$K^{C=1}_{linear}$	0.90 ± 0.10
$LBP_{12,3}$	$D^{k=1}_{euclidean}$	0.95 ± 0.03	$K^{C=1}_{linear}$	0.94 ± 0.02
$BRIEF_{6,12}$	$D^{k=5}_{manhattan}$	0.64 ± 0.11	$K^{C=10,d=3}_{poly}$	0.54 ± 0.14
$LBP_{16,4}^{2riu}$	$D^{k=3}_{euclidean}$	0.98 ± 0.03	$K^{C=10}_{linear}$	0.95 ± 0.12
$LBP_{16,4}$	$D^{k=1}_{euclidean}$	0.97 ± 0.07	$K^{C=1}_{linear}$	0.95 ± 0.12
$BRIEF_{7,16}$	$D^{k=5}_{manhattan}$	0.64 ± 0.11	$K^{C=10,d=2}_{poly}$	0.63 ± 0.13

Table 4.15: A summary of classification results (mean AUC scores \pm standard deviations) that measure the performance of the automated classification algorithm that is based on whole-local texture features for solving the healthy vs wet AMD classification task, based on concatenating all feature vectors extracted from the OCTA images of all ocular vascular layers.

Descriptor	KNN Classifier		SVM Classifier	
	Best Parameters	AUC \pm std	Best Parameters	AUC \pm std
$LBP_{4,1}^{2riu}$	$D^{k=3}_{euclidean}$	0.98 ± 0.03	$K^{C=1}_{linear}$	0.95 ± 0.12
$LBP_{4,1}$	$D^{k=1}_{euclidean}$	0.98 ± 0.02	$K^{C=1}_{linear}$	0.94 ± 0.12
$BRIEF_{4,4}$	$D^{k=1}_{chebyshev}$	0.60 ± 0.09	$K^{C=50}_{linear}$	0.60 ± 0.14
$LBP_{8,2}^{2riu}$	$D^{k=3}_{euclidean}$	0.98 ± 0.05	$K^{C=1}_{linear}$	0.89 ± 0.10
$LBP_{8,2}$	$D^{k=3}_{euclidean}$	0.98 ± 0.03	$K^{C=1}_{linear}$	0.98 ± 0.01
$BRIEF_{5,8}$	$D^{k=9}_{chebyshev}$	0.61 ± 0.12	$K^{C=50,\gamma=0.01}_{rbf}$	0.57 ± 0.09
$LBP_{12,3}^{2riu}$	$D^{k=3}_{euclidean}$	0.99 ± 0.03	$K^{C=1}_{linear}$	0.94 ± 0.22
$LBP_{12,3}$	$D^{k=1}_{euclidean}$	0.98 ± 0.04	$K^{C=1}_{linear}$	0.90 ± 0.10
$BRIEF_{6,12}$	$D^{k=9}_{manhattan}$	0.60 ± 0.14	$K^{C=50}_{linear}$	0.55 ± 0.14
$LBP_{16,4}^{2riu}$	$D^{k=3}_{euclidean}$	0.98 ± 0.05	$K^{C=1}_{linear}$	0.85 ± 0.16
$LBP_{16,4}$	$D^{k=1}_{euclidean}$	0.98 ± 0.04	$K^{C=1}_{linear}$	0.90 ± 0.10
$BRIEF_{7,16}$	$D^{k=5}_{manhattan}$	0.58 ± 0.12	$K^{C=100}_{linear}$	0.53 ± 0.12

between the normal and abnormal vascular texture via layer combination. While the

$BRIEF_{S,n}$ texture descriptor was not able to produce representative local texture features suitable for classification, the $LBP_{p,r}^{2riu}$ and the $LBP_{p,r}$ texture descriptors generally demonstrated great capacity to generate robust texture features as evidenced by the classification results in all previous experiments.

For solving the healthy vs wet AMD classification task via layer combination, however, the best classification performance was achieved when concatenating two feature vectors extracted from the OCTA images of the outer retina and the choriocapillaris layers. This was accomplished by employing the KNN classifier with $D_{euclidean}^{k=3}$ using the $LBP_{p=16,r=4}^{2riu}$ texture descriptor achieving a mean AUC score and a standard deviation = 1.00 ± 0.00 .

4.4.2 Moorfields Eye Hospital

This subsection provides the analysis results of the automated classification algorithm proposed on the Moorfields Eye Hospital OCTA image data set for solving two binary image classification tasks, i.e.: dry AMD vs wet AMD and CNV vs non-CNV. The evaluation of the classification algorithm is performed in order, i.e.: on the superficial inner retina, the deep inner retina, the outer retina, and the choriocapillaris layers, respectively. This is then followed by layer combination, namely by concatenating two feature vectors extracted from two OCTA images of the different ocular vascular layers, concatenating three feature vectors extracted from three OCTA images of the various ocular vascular layers and concatenating all feature vectors extracted from the OCTA images of all ocular vascular layers.

4.4.2.1 Superficial Inner Retina Layer

The classification algorithm was firstly evaluated to differentiate dry AMD from wet AMD cases on the OCTA images of the superficial inner retina layer. Table 4.16 presents the classification results that demonstrate the diagnostic ability of the classification algorithm on the OCTA images of this retinal layer to solve the dry AMD vs wet AMD classification task.

The OCTA images of the superficial inner retina layer do not typically demonstrate any perceptible vascular pathologies related to dry AMD or wet AMD. Nevertheless, the evaluation results in Table 4.16 show that the automated classification algorithm can distinguish some differences between dry AMD and wet AMD texture appearance in the OCTA images of the superficial inner retina layer. Generally, the classification

Table 4.16: A summary of classification results (mean AUC scores \pm standard deviations) that measure the performance of the automated classification algorithm that is based on whole-local texture features for solving the dry AMD vs wet AMD classification task, on the OCTA images of the superficial inner retina layer.

Descriptor	KNN Classifier		SVM Classifier	
	Best Parameters	AUC \pm std	Best Parameters	AUC \pm std
$LBP_{4,1}^{2riu}$	$D^{k=7}_{chebyshev}$	0.62 ± 0.04	$K^{C=1}_{linear}$	0.71 ± 0.06
$LBP_{4,1}$	$D^{k=5}_{manhattan}$	0.57 ± 0.06	$K^{C=50}_{linear}$	0.65 ± 0.10
$BRIEF_{4,4}$	$D^{k=5}_{chebyshev}$	0.54 ± 0.04	$K^{C=10,d=2}_{poly}$	0.51 ± 0.06
$LBP_{8,2}^{2riu}$	$D^{k=9}_{chebyshev}$	0.59 ± 0.03	$K^{C=50}_{linear}$	0.68 ± 0.09
$LBP_{8,2}$	$D^{k=9}_{chebyshev}$	0.59 ± 0.06	$K^{C=1,\gamma=0.001}_{rbf}$	0.61 ± 0.06
$BRIEF_{5,8}$	$D^{k=5}_{euclidean}$	0.53 ± 0.08	$K^{C=50}_{linear}$	0.50 ± 0.08
$LBP_{12,3}^{2riu}$	$D^{k=9}_{manhattan}$	0.62 ± 0.06	$K^{C=10,\gamma=0.1}_{rbf}$	0.65 ± 0.10
$LBP_{12,3}$	$D^{k=9}_{euclidean}$	0.58 ± 0.05	$K^{C=1,\gamma=0.001}_{rbf}$	0.66 ± 0.05
$BRIEF_{6,12}$	$D^{k=1}_{euclidean}$	0.57 ± 0.06	$K^{C=50,d=3}_{poly}$	0.55 ± 0.06
$LBP_{16,4}^{2riu}$	$D^{k=5}_{euclidean}$	0.57 ± 0.08	$K^{C=50}_{linear}$	0.65 ± 0.13
$LBP_{16,4}$	$D^{k=9}_{chebyshev}$	0.56 ± 0.03	$K^{C=10,\gamma=0.01}_{rbf}$	0.59 ± 0.10
$BRIEF_{7,16}$	$D^{k=7}_{euclidean}$	0.51 ± 0.05	$K^{C=50}_{linear}$	0.53 ± 0.07

results with the $BRIEF_{S,n}$ texture descriptor were demonstrated to be among the worst. However, the best overall classification performance was achieved with the $LBP_{4,1}^{2riu}$ texture descriptor based on the SVM classifier with $K^{C=1}_{linear}$ accomplishing a mean AUC score and a standard deviation = 0.71 ± 0.06 .

The classification algorithm was then evaluated on the OCTA images of the superficial inner retina layer, but for the task of distinguishing CNV from non-CNV cases. Table 4.17 presents the classification results that demonstrate the diagnostic ability of the algorithm on the OCTA images of the superficial inner retina layer to solve the CNV vs non-CNV classification task.

Again, similar to the findings in Table 4.16, the evaluation results in Table 4.17 show that the automated classification algorithm can distinguish some dissimilarities between non-CNV, i.e.: dry AMD, and CNV, i.e.: wet AMD plus secondary CNV, texture appearance in the OCTA images of the superficial inner retina layer. While the classification results with the $BRIEF_{S,n}$ texture descriptor were proved to be the worst, the $LBP_{p,r}^{2riu}$ and the $LBP_{p,r}$ texture descriptors both enabled the achievement of fairly good enhancements in classification performance. Nonetheless, the best overall classification performance was achieved with the $LBP_{8,2}^{2riu}$ texture descriptor based on the SVM classifier with $K^{C=1}_{linear}$ accomplishing a mean AUC score and a standard deviation = 0.70 ± 0.05 .

Table 4.17: A summary of classification results (mean AUC scores \pm standard deviations) that measure the performance of the automated classification algorithm that is based on whole-local texture features for solving the CNV vs non-CNV classification task, on the OCTA images of the superficial inner retina layer.

Descriptor	KNN Classifier		SVM Classifier	
	Best Parameters	AUC \pm std	Best Parameters	AUC \pm std
$LBP_{4,1}^{2riu}$	$D_{chebyshev}^{k=5}$	0.61 ± 0.02	$K_{linear}^{C=50}$	0.66 ± 0.09
$LBP_{4,1}$	$D_{manhattan}^{k=3}$	0.61 ± 0.02	$K_{linear}^{C=50}$	0.60 ± 0.06
$BRIEF_{4,4}$	$D_{chebyshev}^{k=7}$	0.50 ± 0.05	$K_{rbf}^{C=1, \gamma=0.001}$	0.51 ± 0.06
$LBP_{8,2}^{2riu}$	$D_{euclidean}^{k=3}$	0.61 ± 0.05	$K_{linear}^{C=1}$	0.70 ± 0.05
$LBP_{8,2}$	$D_{manhattan}^{k=1}$	0.57 ± 0.02	$K_{linear}^{C=50}$	0.58 ± 0.06
$BRIEF_{5,8}$	$D_{euclidean}^{k=5}$	0.52 ± 0.04	$K_{rbf}^{C=10, \gamma=0.001}$	0.53 ± 0.12
$LBP_{12,3}^{2riu}$	$D_{manhattan}^{k=9}$	0.54 ± 0.04	$K_{linear}^{C=50}$	0.62 ± 0.07
$LBP_{12,3}$	$D_{euclidean}^{k=7}$	0.58 ± 0.06	$K_{linear}^{C=50}$	0.59 ± 0.04
$BRIEF_{6,12}$	$D_{chebyshev}^{k=3}$	0.53 ± 0.06	$K_{poly}^{C=50, d=3}$	0.51 ± 0.06
$LBP_{16,4}^{2riu}$	$D_{chebyshev}^{k=5}$	0.57 ± 0.07	$K_{linear}^{C=1}$	0.59 ± 0.09
$LBP_{16,4}$	$D_{euclidean}^{k=5}$	0.55 ± 0.03	$K_{linear}^{C=50}$	0.57 ± 0.07
$BRIEF_{7,16}$	$D_{euclidean}^{k=9}$	0.50 ± 0.02	$K_{rbf}^{C=10, \gamma=0.01}$	0.53 ± 0.13

4.4.2.2 Deep Inner Retina Layer

Following evaluation of the classification algorithm on the OCTA images of the superficial inner retina layer, the classification algorithm then was examined in discriminating dry AMD from wet AMD cases on the OCTA images of the deep inner retina layer. Table 4.18 illustrates the classification results that show the diagnostic capability of the algorithm on the OCTA images of this retinal layer to solve the dry AMD vs wet AMD classification task.

Like the OCTA images of the superficial inner retina layer, the OCTA images of the deep inner retina layer also do not normally show any noticeable vascular pathologies related to the various types of AMD disease, e.g.: dry AMD and wet AMD. However, the evaluation results in Table 4.18 demonstrate that the automated classification algorithm can recognise variations between dry AMD and wet AMD texture appearance in the OCTA images of the deep inner retina layer. Broadly, the classification results accomplished with the $BRIEF_{S,n}$ texture descriptor were very poor compared to using the $LBP_{p,r}^{2riu}$ and the $LBP_{p,r}$ texture descriptors. Nevertheless, the best overall classification performance was achieved with the $LBP_{16,4}^{2riu}$ texture descriptor based on the SVM classifier with $K_{linear}^{C=1}$ accomplishing a mean AUC score and a standard deviation $= 0.75 \pm 0.04$.

Table 4.18: A summary of classification results (mean AUC scores \pm standard deviations) that measure the performance of the automated classification algorithm that is based on whole-local texture features for solving the dry AMD vs wet AMD classification task, on the OCTA images of the deep inner retina layer.

Descriptor	KNN Classifier		SVM Classifier	
	Best Parameters	AUC \pm std	Best Parameters	AUC \pm std
$LBP_{4,1}^{2riu}$	$D^{k=9}_{euclidean}$	0.62 ± 0.06	$K^{C=10,d=2}_{poly}$	0.62 ± 0.07
$LBP_{4,1}$	$D^{k=9}_{chebyshev}$	0.62 ± 0.06	$K^{C=1,\gamma=0.001}_{rbf}$	0.69 ± 0.01
$BRIEF_{4,4}$	$D^{k=1}_{manhattan}$	0.51 ± 0.05	$K^{C=1,\gamma=0.001}_{rbf}$	0.51 ± 0.06
$LBP_{8,2}^{2riu}$	$D^{k=9}_{manhattan}$	0.64 ± 0.04	$K^{C=50,\gamma=0.001}_{rbf}$	0.62 ± 0.08
$LBP_{8,2}$	$D^{k=9}_{euclidean}$	0.63 ± 0.07	$K^{C=1,\gamma=0.001}_{rbf}$	0.64 ± 0.08
$BRIEF_{5,8}$	$D^{k=9}_{chebyshev}$	0.51 ± 0.04	$K^{C=1,\gamma=0.001}_{rbf}$	0.53 ± 0.07
$LBP_{12,3}^{2riu}$	$D^{k=7}_{manhattan}$	0.63 ± 0.06	$K^{C=50}_{linear}$	0.70 ± 0.02
$LBP_{12,3}$	$D^{k=5}_{manhattan}$	0.63 ± 0.05	$K^{C=50}_{linear}$	0.66 ± 0.07
$BRIEF_{6,12}$	$D^{k=1}_{chebyshev}$	0.56 ± 0.07	$K^{C=1,d=4}_{poly}$	0.53 ± 0.06
$LBP_{16,4}^{2riu}$	$D^{k=3}_{chebyshev}$	0.66 ± 0.07	$K^{C=1}_{linear}$	0.75 ± 0.04
$LBP_{16,4}$	$D^{k=7}_{manhattan}$	0.62 ± 0.05	$K^{C=50}_{linear}$	0.68 ± 0.03
$BRIEF_{7,16}$	$D^{k=1}_{manhattan}$	0.52 ± 0.02	$K^{C=1,\gamma=0.01}_{rbf}$	0.53 ± 0.04

Subsequently, the classification algorithm was evaluated on the OCTA images of the deep inner retina layer, but for the task of differentiating CNV from non-CNV subjects. Table 4.19 demonstrates the classification results that reveal the diagnostic ability of the classification algorithm on the OCTA images of the deep inner retina layer to solve the CNV vs non-CNV classification task.

Analogous to the findings in Table 4.18, the evaluation results in Table 4.19 also demonstrate that the automated classification algorithm can discriminate some variations between non-CNV, i.e.: dry AMD, and CNV, i.e.: wet AMD plus secondary CNV, texture appearance in the OCTA images of the deep inner retina layer. The classification results achieved with the $BRIEF_{S,n}$ texture descriptor were, however, very poor in all classification experiments. Nevertheless, the $LBP_{p,r}^{2riu}$ and the $LBP_{p,r}$ texture descriptors both again showed to enable slight improvements in classification performance. Nonetheless, the best overall classification performance was achieved with the $LBP_{12,3}^{2riu}$ texture descriptor using the SVM classifier with $K^{C=1}_{linear}$ accomplishing a mean AUC score and a standard deviation = 0.72 ± 0.03 .

Table 4.19: A summary of classification results (mean AUC scores \pm standard deviations) that measure the performance of the automated classification algorithm that is based on whole-local texture features for solving the CNV vs non-CNV classification task, on the OCTA images of the deep inner retina layer.

Descriptor	KNN Classifier		SVM Classifier	
	Best Parameters	AUC \pm std	Best Parameters	AUC \pm std
$LBP_{4,1}^{2riu}$	$D^{k=3}_{euclidean}$	0.58 ± 0.05	$K^{C=50}_{linear}$	0.66 ± 0.08
$LBP_{4,1}$	$D^{k=5}_{manhattan}$	0.62 ± 0.04	$K^{C=1, \gamma=0.01}_{rbf}$	0.66 ± 0.05
$BRIEF_{4,4}$	$D^{k=1}_{chebyshev}$	0.53 ± 0.04	$K^{C=50, d=3}_{poly}$	0.54 ± 0.03
$LBP_{8,2}^{2riu}$	$D^{k=3}_{euclidean}$	0.63 ± 0.05	$K^{C=50}_{linear}$	0.67 ± 0.03
$LBP_{8,2}$	$D^{k=5}_{chebyshev}$	0.63 ± 0.05	$K^{C=1, \gamma=0.001}_{rbf}$	0.64 ± 0.06
$BRIEF_{5,8}$	$D^{k=3}_{euclidean}$	0.50 ± 0.04	$K^{C=10, d=4}_{poly}$	0.52 ± 0.02
$LBP_{12,3}^{2riu}$	$D^{k=3}_{euclidean}$	0.61 ± 0.04	$K^{C=1}_{linear}$	0.72 ± 0.03
$LBP_{12,3}$	$D^{k=3}_{manhattan}$	0.64 ± 0.03	$K^{C=50}_{linear}$	0.68 ± 0.06
$BRIEF_{6,12}$	$D^{k=5}_{euclidean}$	0.50 ± 0.04	$K^{C=50}_{linear}$	0.52 ± 0.04
$LBP_{16,4}^{2riu}$	$D^{k=5}_{euclidean}$	0.67 ± 0.05	$K^{C=10}_{linear}$	0.69 ± 0.02
$LBP_{16,4}$	$D^{k=3}_{euclidean}$	0.63 ± 0.05	$K^{C=1, \gamma=0.01}_{rbf}$	0.64 ± 0.09
$BRIEF_{7,16}$	$D^{k=7}_{euclidean}$	0.52 ± 0.01	$K^{C=50}_{linear}$	0.51 ± 0.04

4.4.2.3 Outer Retina Layer

Following assessment of the classification algorithm on the OCTA images of the superficial and deep inner retinal layers, the algorithm was then examined in separating dry AMD from wet AMD subjects based on the OCTA images of the outer retina layer. Table 4.20 illustrates the classification results that show the diagnostic capability of the classification algorithm on the OCTA images of this retinal layer to solve the dry AMD vs wet AMD classification task.

While the OCTA images of the outer retina layer normally demonstrate noticeable vascular abnormalities related to dry AMD and wet AMD diseases, which can be clearly distinguishable from normal ocular vascular texture appearance, visually differentiating diverse texture vascular pathologies, e.g.: dry AMD and wet AMD diseases, from each other in the OCTA images of the outer retina layer can be extremely challenging. As such it is not uncommon for clinicians to request a second opinion due to the significant pattern variations between individuals, and the fact that dry AMD and wet AMD diseases may appear similar causing difficulties in the interpretation process [10, 27]. Nonetheless, the evaluation results in Table 4.20 illustrate that the automated classification algorithm can identify distinctions between dry AMD and wet

Table 4.20: A summary of classification results (mean AUC scores \pm standard deviations) that measure the performance of the automated classification algorithm that is based on whole-local texture features for solving the dry AMD vs wet AMD classification task, on the OCTA images of the outer retina layer.

Descriptor	KNN Classifier		SVM Classifier	
	Best Parameters	AUC \pm std	Best Parameters	AUC \pm std
$LBP_{4,1}^{2riu}$	$D^{k=9}_{manhattan}$	0.70 ± 0.05	$K^{C=50}_{linear}$	0.77 ± 0.03
$LBP_{4,1}$	$D^{k=7}_{manhattan}$	0.74 ± 0.02	$K^{C=50}_{linear}$	0.81 ± 0.03
$BRIEF_{4,4}$	$D^{k=7}_{chebyshev}$	0.68 ± 0.05	$K^{C=50,d=2}_{poly}$	0.69 ± 0.06
$LBP_{8,2}^{2riu}$	$D^{k=3}_{manhattan}$	0.75 ± 0.05	$K^{C=50}_{linear}$	0.82 ± 0.03
$LBP_{8,2}$	$D^{k=5}_{manhattan}$	0.77 ± 0.05	$K^{C=50}_{linear}$	0.81 ± 0.03
$BRIEF_{5,8}$	$D^{k=7}_{euclidean}$	0.65 ± 0.06	$K^{C=50}_{linear}$	0.67 ± 0.07
$LBP_{12,3}^{2riu}$	$D^{k=5}_{manhattan}$	0.77 ± 0.05	$K^{C=50}_{linear}$	0.82 ± 0.02
$LBP_{12,3}$	$D^{k=3}_{manhattan}$	0.76 ± 0.03	$K^{C=1}_{linear}$	0.81 ± 0.06
$BRIEF_{6,12}$	$D^{k=5}_{manhattan}$	0.64 ± 0.07	$K^{C=1,d=3}_{poly}$	0.66 ± 0.07
$LBP_{16,4}^{2riu}$	$D^{k=9}_{manhattan}$	0.76 ± 0.02	$K^{C=1}_{linear}$	0.83 ± 0.03
$LBP_{16,4}$	$D^{k=5}_{manhattan}$	0.73 ± 0.04	$K^{C=50}_{linear}$	0.80 ± 0.04
$BRIEF_{7,16}$	$D^{k=5}_{manhattan}$	0.60 ± 0.06	$K^{C=1,d=3}_{poly}$	0.65 ± 0.07

AMD texture appearance in the OCTA images of the outer retina layer. While the classification results with the $BRIEF_{S,n}$ texture descriptor proved to be among the worst, the $LBP_{p,r}^{2riu}$ and the $LBP_{p,r}$ texture descriptors both were capable of boosting classification performance. The best overall classification performance, yet, was accomplished with the $LBP_{16,4}^{2riu}$ texture descriptor utilising the SVM classifier with $K^{C=1}_{linear}$ achieving a mean AUC score and a standard deviation = 0.83 ± 0.03 .

The classification algorithm was subsequently assessed on the OCTA images of the outer retina layer, however, for the task of separating CNV from non-CNV cases. Table 4.21 displays the classification results that show the diagnostic ability of the classification algorithm on the OCTA images of the outer retina layer to solve the CNV vs non-CNV classification task.

Like the previous classification task, i.e.: dry AMD vs wet AMD, performed on the OCTA images of the outer retina layer, visually distinguishing non-CNV from CNV lesions in the OCTA images of the outer retina layer is also tremendously challenging [10, 27]. However, the evaluation results in Table 4.21 demonstrate that the automated classification algorithm can recognise differences between non-CNV and CNV texture appearance in the OCTA images of the outer retina layer. The classification results with the $BRIEF_{S,n}$ texture descriptor were among the worst. Nevertheless, the $LBP_{p,r}^{2riu}$ and the $LBP_{p,r}$ texture descriptors both generally showed to facilitate the

Table 4.21: A summary of classification results (mean AUC scores \pm standard deviations) that measure the performance of the automated classification algorithm that is based on whole-local texture features for solving the CNV vs non-CNV classification task, on the OCTA images of the outer retina layer.

Descriptor	KNN Classifier		SVM Classifier	
	Best Parameters	AUC \pm std	Best Parameters	AUC \pm std
$LBP_{4,1}^{2riu}$	$D_{manhattan}^{k=9}$	0.71 ± 0.04	$K_{rbf}^{C=10, \gamma=0.01}$	0.75 ± 0.04
$LBP_{4,1}$	$D_{manhattan}^{k=9}$	0.73 ± 0.04	$K_{rbf}^{C=10, \gamma=0.001}$	0.79 ± 0.02
$BRIEF_{4,4}$	$D_{euclidean}^{k=9}$	0.64 ± 0.04	$K_{poly}^{C=1, d=2}$	0.67 ± 0.05
$LBP_{8,2}^{2riu}$	$D_{manhattan}^{k=9}$	0.76 ± 0.04	$K_{linear}^{C=1}$	0.80 ± 0.03
$LBP_{8,2}$	$D_{manhattan}^{k=9}$	0.77 ± 0.04	$K_{linear}^{C=1}$	0.79 ± 0.03
$BRIEF_{5,8}$	$D_{manhattan}^{k=9}$	0.64 ± 0.05	$K_{linear}^{C=50}$	0.66 ± 0.06
$LBP_{12,3}^{2riu}$	$D_{manhattan}^{k=9}$	0.77 ± 0.04	$K_{linear}^{C=1}$	0.80 ± 0.03
$LBP_{12,3}$	$D_{manhattan}^{k=9}$	0.78 ± 0.04	$K_{linear}^{C=1}$	0.80 ± 0.03
$BRIEF_{6,12}$	$D_{manhattan}^{k=9}$	0.62 ± 0.06	$K_{rbf}^{C=10, \gamma=0.001}$	0.66 ± 0.09
$LBP_{16,4}^{2riu}$	$D_{manhattan}^{k=5}$	0.77 ± 0.04	$K_{linear}^{C=1}$	0.82 ± 0.03
$LBP_{16,4}$	$D_{manhattan}^{k=9}$	0.76 ± 0.06	$K_{linear}^{C=1}$	0.81 ± 0.03
$BRIEF_{7,16}$	$D_{manhattan}^{k=3}$	0.60 ± 0.05	$K_{rbf}^{C=10, \gamma=0.01}$	0.67 ± 0.07

achievement of very promising classification performance. The best overall classification performance, still, was achieved with the $LBP_{16,4}^{2riu}$ texture descriptor using the SVM classifier with $K_{linear}^{C=1}$ accomplishing a mean AUC score and a standard deviation $= 0.82 \pm 0.03$.

4.4.2.4 Choriocapillaris Layer

Following the evaluation of the classification algorithm on the OCTA images of individual previous retinal layers, the classification algorithm was then examined in separating dry AMD from wet AMD subjects using the OCTA images of the choriocapillaris layer. Table 4.22 illustrates the classification results that show the diagnostic capacity of the classification algorithm on the OCTA images of this choroidal layer to solve the dry AMD vs wet AMD classification task.

The OCTA images of the choriocapillaris layer are similar to the OCTA images of the outer retina layer in that they normally demonstrate noticeable areas of vascular abnormalities relating to dry AMD and wet AMD diseases, which can be clearly distinguishable from normal ocular vascular texture appearance. However, visually differentiating the appearance of diverse texture vascular pathologies related to dry AMD and wet AMD diseases from each other in the OCTA images of the choriocapillaris layer can also be enormously challenging [10,27]. However, the evaluation results

Table 4.22: A summary of classification results (mean AUC scores \pm standard deviations) that measure the performance of the automated classification algorithm that is based on whole-local texture features for solving the dry AMD vs wet AMD classification task, on the OCTA images of the choriocapillaris layer.

Descriptor	KNN Classifier		SVM Classifier	
	Best Parameters	AUC \pm std	Best Parameters	AUC \pm std
$LBP_{4,1}^{2riu}$	$D^{k=3}_{euclidean}$	0.76 ± 0.04	$K_{rbf}^{C=50, \gamma=0.01}$	0.81 ± 0.02
$LBP_{4,1}$	$D^{k=9}_{chebyshev}$	0.75 ± 0.02	$K_{rbf}^{C=1, \gamma=0.01}$	0.74 ± 0.04
$BRIEF_{4,4}$	$D^{k=3}_{chebyshev}$	0.55 ± 0.01	$K_{rbf}^{C=50, \gamma=0.1}$	0.52 ± 0.05
$LBP_{8,2}^{2riu}$	$D^{k=9}_{chebyshev}$	0.79 ± 0.03	$K_{linear}^{C=1}$	0.82 ± 0.02
$LBP_{8,2}$	$D^{k=9}_{chebyshev}$	0.77 ± 0.02	$K_{linear}^{C=10}$	0.79 ± 0.01
$BRIEF_{5,8}$	$D^{k=5}_{manhattan}$	0.54 ± 0.05	$K_{rbf}^{C=10, \gamma=0.001}$	0.55 ± 0.03
$LBP_{12,3}^{2riu}$	$D^{k=3}_{euclidean}$	0.78 ± 0.04	$K_{rbf}^{C=50, \gamma=0.1}$	0.83 ± 0.01
$LBP_{12,3}$	$D^{k=9}_{euclidean}$	0.79 ± 0.04	$K_{linear}^{C=1}$	0.81 ± 0.02
$BRIEF_{6,12}$	$D^{k=3}_{chebyshev}$	0.52 ± 0.04	$K_{poly}^{C=1, d=2}$	0.53 ± 0.04
$LBP_{16,4}^{2riu}$	$D^{k=9}_{euclidean}$	0.77 ± 0.02	$K_{linear}^{C=1}$	0.82 ± 0.02
$LBP_{16,4}$	$D^{k=5}_{euclidean}$	0.76 ± 0.03	$K_{linear}^{C=1}$	0.79 ± 0.03
$BRIEF_{7,16}$	$D^{k=5}_{chebyshev}$	0.52 ± 0.03	$K_{poly}^{C=10, d=2}$	0.56 ± 0.02

in Table 4.22 prove that the automated classification algorithm can recognise dissimilarities between dry AMD and wet AMD texture appearance in the OCTA images of choriocapillaris layer. Generally, the classification results achieved with the $BRIEF_{S,n}$ texture descriptor were very poor compared to using the $LBP_{p,r}^{2riu}$ and the $LBP_{p,r}$ texture descriptors. The best overall classification performance yet was accomplished with the $LBP_{12,3}^{2riu}$ texture descriptor employing the SVM classifier with $K_{rbf}^{C=50, \gamma=0.1}$ attaining a mean AUC score and a standard deviation = 0.83 ± 0.01 .

The algorithm was next evaluated on the OCTA images of the choriocapillaris layer, but for the task of distinguishing CNV from non-CNV cases. Table 4.23 presents the classification results that summarise the diagnostic skill of the classification algorithm on the OCTA images of this choroidal layer to solve the CNV vs non-CNV classification task.

Like the previous classification task, i.e.: dry AMD vs wet AMD, conducted on the OCTA images of the choriocapillaris layer, visually distinguishing non-CNV from CNV lesions in the OCTA images of the choriocapillaris layer can also be massively challenging [10, 27]. Nevertheless, the evaluation results in Table 4.23 show that the automated classification algorithm can identify dissimilarities between non-CNV and

Table 4.23: A summary of classification results (mean AUC scores \pm standard deviations) that measure the performance of the automated classification algorithm that is based on whole-local texture features for solving the CNV vs non-CNV classification task, on the OCTA images of the choriocapillaris layer.

Descriptor	KNN Classifier		SVM Classifier	
	Best Parameters	AUC \pm std	Best Parameters	AUC \pm std
$LBP_{4,1}^{2riu}$	$D^{k=3}_{euclidean}$	0.71 ± 0.05	$K_{linear}^{C=50}$	0.78 ± 0.02
$LBP_{4,1}$	$D^{k=5}_{euclidean}$	0.72 ± 0.05	$K_{rbf}^{C=50,\gamma=0.01}$	0.67 ± 0.09
$BRIEF_{4,4}$	$D^{k=1}_{manhattan}$	0.55 ± 0.05	$K_{linear}^{C=50}$	0.53 ± 0.06
$LBP_{8,2}^{2riu}$	$D^{k=7}_{chebyshev}$	0.75 ± 0.04	$K_{rbf}^{C=50,\gamma=0.1}$	0.80 ± 0.02
$LBP_{8,2}$	$D^{k=3}_{euclidean}$	0.75 ± 0.04	$K_{linear}^{C=50}$	0.79 ± 0.03
$BRIEF_{5,8}$	$D^{k=3}_{euclidean}$	0.54 ± 0.02	$K_{rbf}^{C=10,\gamma=0.001}$	0.52 ± 0.05
$LBP_{12,3}^{2riu}$	$D^{k=7}_{manhattan}$	0.73 ± 0.03	$K_{rbf}^{C=10,\gamma=0.1}$	0.80 ± 0.03
$LBP_{12,3}$	$D^{k=7}_{manhattan}$	0.74 ± 0.04	$K_{rbf}^{C=50,\gamma=0.1}$	0.78 ± 0.05
$BRIEF_{6,12}$	$D^{k=3}_{euclidean}$	0.55 ± 0.06	$K_{poly}^{C=1,d=4}$	0.55 ± 0.05
$LBP_{16,4}^{2riu}$	$D^{k=7}_{chebyshev}$	0.75 ± 0.04	$K_{linear}^{C=1}$	0.81 ± 0.04
$LBP_{16,4}$	$D^{k=5}_{euclidean}$	0.73 ± 0.03	$K_{linear}^{C=50}$	0.79 ± 0.02
$BRIEF_{7,16}$	$D^{k=1}_{manhattan}$	0.52 ± 0.04	$K_{linear}^{C=50}$	0.55 ± 0.03

CNV texture appearance in the OCTA images of the choriocapillaris layer. The classification results accomplished with the $BRIEF_{S,n}$ texture descriptor were, however, extremely poor in all classification experiments. Nonetheless, the $LBP_{p,r}^{2riu}$ and the $LBP_{p,r}$ texture descriptors both again proved to enable some improvements in classification performance. The best overall classification performance yet was also reached with the $LBP_{16,4}^{2riu}$ texture descriptor using the SVM classifier with $K_{linear}^{C=1}$ accomplishing a mean AUC score and a standard deviation = 0.81 ± 0.04 .

4.4.2.5 Layer Combination

The classification algorithm was then evaluated in discriminating dry AMD from wet AMD subjects via layer combination. This is accomplished by conducting the binary image classification based on concatenating two feature vectors extracted from two OCTA images of the various ocular vascular layers, based on concatenating three feature vectors extracted from three OCTA images of the different ocular vascular layers and based on concatenating all feature vectors extracted from the OCTA images of all ocular vascular layers. It also should be recalled that the classification performance of the classification algorithm was evaluated based on the individual eyes, not the individual OCTA images of ocular vascular layers.

The following Tables 4.24, 4.25, 4.26, 4.27, 4.28 and 4.29 summarise the classification results that demonstrate the diagnostic capability of the classification algorithm when concatenating two feature vectors extracted from the OCTA images of two various ocular vascular layers. These being the superficial and the deep inner retina, the superficial inner and the outer retina, the superficial inner retina and the choriocapillaris, the deep inner and the outer retina, the deep inner retina and the choriocapillaris, and the outer retina and the choriocapillaris layers, respectively.

Table 4.24: A summary of classification results (mean AUC scores \pm standard deviations) that measure the performance of the automated classification algorithm that is based on whole-local texture features for solving the dry AMD vs wet AMD classification task, based on concatenating two feature vectors extracted from the OCTA images of the superficial and the deep retina layers.

Descriptor	KNN Classifier		SVM Classifier	
	Best Parameters	AUC \pm std	Best Parameters	AUC \pm std
$LBP_{4,1}^{2riu}$	$D^{k=3}_{euclidean}$	0.64 ± 0.06	$K^{C=1,d=2}_{poly}$	0.71 ± 0.09
$LBP_{4,1}$	$D^{k=3}_{euclidean}$	0.61 ± 0.06	$K^{C=1,d=3}_{poly}$	0.68 ± 0.09
$BRIEF_{4,4}$	$D^{k=3}_{manhattan}$	0.50 ± 0.03	$K^{C=1,d=2}_{poly}$	0.50 ± 0.05
$LBP_{8,2}^{2riu}$	$D^{k=3}_{chebyshev}$	0.61 ± 0.04	$K^{C=1,d=3}_{poly}$	0.64 ± 0.11
$LBP_{8,2}$	$D^{k=3}_{chebyshev}$	0.62 ± 0.06	$K^{C=1,d=3}_{poly}$	0.65 ± 0.06
$BRIEF_{5,8}$	$D^{k=3}_{euclidean}$	0.50 ± 0.06	$K^{C=1,d=3}_{poly}$	0.51 ± 0.07
$LBP_{12,3}^{2riu}$	$D^{k=3}_{euclidean}$	0.56 ± 0.03	$K^{C=1,d=2}_{poly}$	0.64 ± 0.09
$LBP_{12,3}$	$D^{k=3}_{manhattan}$	0.60 ± 0.04	$K^{C=1,d=2}_{poly}$	0.62 ± 0.05
$BRIEF_{6,12}$	$D^{k=1}_{chebyshev}$	0.50 ± 0.03	$K^{C=1,d=2}_{poly}$	0.51 ± 0.05
$LBP_{16,4}^{2riu}$	$D^{k=5}_{euclidean}$	0.57 ± 0.04	$K^{C=1,d=3}_{poly}$	0.62 ± 0.08
$LBP_{16,4}$	$D^{k=7}_{manhattan}$	0.61 ± 0.05	$K^{C=10,d=2}_{poly}$	0.60 ± 0.04
$BRIEF_{7,16}$	$D^{k=3}_{euclidean}$	0.50 ± 0.04	$K^{C=1,d=2}_{poly}$	0.51 ± 0.03

Tables 4.30, 4.31, 4.32 and 4.33, on the other hand, demonstrate the classification results that show the diagnostic capability of the classification algorithm when concatenating three feature vectors extracted from the OCTA images of three different ocular vascular layers. These are the superficial, the deep inner and the outer retina, the superficial, the deep inner retina and the choriocapillaris, the superficial inner, the outer retina and the choriocapillaris, and the deep inner, the outer retina and the choriocapillaris layers, respectively.

Table 4.34 presents the classification results when concatenating all feature vectors extracted from the OCTA images of all ocular vascular layers.

Nevertheless, combining the various OCTA images of ocular vascular layers and performing the task of classifying the two different eye conditions, i.e.: dry AMD vs

Table 4.25: A summary of classification results (mean AUC scores \pm standard deviations) that measure the performance of the automated classification algorithm that is based on whole-local texture features for solving the dry AMD vs wet AMD classification task, based on concatenating two feature vectors extracted from the OCTA images of the superficial and the outer retina layers.

Descriptor	KNN Classifier		SVM Classifier	
	Best Parameters	AUC \pm std	Best Parameters	AUC \pm std
$LBP_{4,1}^{2riu}$	$D^{k=3}_{manhattan}$	0.71 ± 0.03	$K^{C=1,d=3}_{poly}$	0.71 ± 0.04
$LBP_{4,1}$	$D^{k=3}_{euclidean}$	0.70 ± 0.05	$K^{C=10}_{linear}$	0.71 ± 0.06
$BRIEF_{4,4}$	$D^{k=3}_{chebyshev}$	0.60 ± 0.04	$K^{C=1,d=3}_{poly}$	0.63 ± 0.06
$LBP_{8,2}^{2riu}$	$D^{k=3}_{euclidean}$	0.70 ± 0.03	$K^{C=1,d=3}_{poly}$	0.73 ± 0.05
$LBP_{8,2}$	$D^{k=3}_{manhattan}$	0.73 ± 0.05	$K^{C=1}_{linear}$	0.73 ± 0.05
$BRIEF_{5,8}$	$D^{k=3}_{euclidean}$	0.58 ± 0.06	$K^{C=10}_{linear}$	0.60 ± 0.06
$LBP_{12,3}^{2riu}$	$D^{k=3}_{euclidean}$	0.72 ± 0.04	$K^{C=1}_{linear}$	0.72 ± 0.05
$LBP_{12,3}$	$D^{k=3}_{manhattan}$	0.74 ± 0.05	$K^{C=1}_{linear}$	0.73 ± 0.06
$BRIEF_{6,12}$	$D^{k=3}_{manhattan}$	0.58 ± 0.06	$K^{C=1,d=3}_{poly}$	0.61 ± 0.07
$LBP_{16,4}^{2riu}$	$D^{k=5}_{euclidean}$	0.70 ± 0.03	$K^{C=10}_{linear}$	0.71 ± 0.04
$LBP_{16,4}$	$D^{k=7}_{manhattan}$	0.72 ± 0.03	$K^{C=10}_{linear}$	0.72 ± 0.05
$BRIEF_{7,16}$	$D^{k=5}_{euclidean}$	0.57 ± 0.05	$K^{C=10,d=3}_{poly}$	0.60 ± 0.06

Table 4.26: A summary of classification results (mean AUC scores \pm standard deviations) that measure the performance of the automated classification algorithm that is based on whole-local texture features for solving the dry AMD vs wet AMD classification task, based on concatenating two feature vectors extracted from the OCTA images of the superficial retina and the choriocapillaris retina layers.

Descriptor	KNN Classifier		SVM Classifier	
	Best Parameters	AUC \pm std	Best Parameters	AUC \pm std
$LBP_{4,1}^{2riu}$	$D^{k=3}_{manhattan}$	0.74 ± 0.03	$K^{C=10}_{linear}$	0.76 ± 0.05
$LBP_{4,1}$	$D^{k=3}_{manhattan}$	0.70 ± 0.05	$K^{C=1,\gamma=0.1}_{rbf}$	0.74 ± 0.06
$BRIEF_{4,4}$	$D^{k=3}_{chebyshev}$	0.50 ± 0.05	$K^{C=10}_{linear}$	0.49 ± 0.05
$LBP_{8,2}^{2riu}$	$D^{k=3}_{chebyshev}$	0.71 ± 0.05	$K^{C=1,d=2}_{poly}$	0.75 ± 0.06
$LBP_{8,2}$	$D^{k=3}_{manhattan}$	0.71 ± 0.04	$K^{C=10}_{linear}$	0.75 ± 0.05
$BRIEF_{5,8}$	$D^{k=3}_{manhattan}$	0.50 ± 0.05	$K^{C=1,d=3}_{poly}$	0.53 ± 0.07
$LBP_{12,3}^{2riu}$	$D^{k=3}_{manhattan}$	0.68 ± 0.04	$K^{C=10}_{linear}$	0.74 ± 0.07
$LBP_{12,3}$	$D^{k=3}_{manhattan}$	0.69 ± 0.04	$K^{C=10}_{linear}$	0.74 ± 0.06
$BRIEF_{6,12}$	$D^{k=3}_{manhattan}$	0.52 ± 0.07	$K^{C=1,d=3}_{poly}$	0.51 ± 0.08
$LBP_{16,4}^{2riu}$	$D^{k=5}_{manhattan}$	0.72 ± 0.04	$K^{C=1}_{linear}$	0.73 ± 0.03
$LBP_{16,4}$	$D^{k=3}_{manhattan}$	0.69 ± 0.04	$K^{C=10,\gamma=0.01}_{rbf}$	0.70 ± 0.05
$BRIEF_{7,16}$	$D^{k=5}_{chebyshev}$	0.51 ± 0.06	$K^{C=1}_{linear}$	0.50 ± 0.04

wet AMD, can be enormously challenging to accomplish even for highly skilled ophthalmologists. This is because the textural vascular appearance in the various OCTA

Table 4.27: A summary of classification results (mean AUC scores \pm standard deviations) that measure the performance of the automated classification algorithm that is based on whole-local texture features for solving the dry AMD vs wet AMD classification task, based on concatenating two feature vectors extracted from the OCTA images of the deep and the outer retina layers.

Descriptor	KNN Classifier		SVM Classifier	
	Best Parameters	AUC \pm std	Best Parameters	AUC \pm std
$LBP_{4,1}^{2riu}$	$D^{k=3}_{chebyshev}$	0.70 ± 0.04	$K^{C=1,d=3}_{poly}$	0.72 ± 0.05
$LBP_{4,1}$	$D^{k=3}_{manhattan}$	0.70 ± 0.03	$K^{C=1,d=3}_{poly}$	0.72 ± 0.04
$BRIEF_{4,4}$	$D^{k=3}_{euclidean}$	0.60 ± 0.03	$K^{C=1,d=3}_{poly}$	0.63 ± 0.06
$LBP_{8,2}^{2riu}$	$D^{k=3}_{manhattan}$	0.72 ± 0.03	$K^{C=1,d=3}_{poly}$	0.75 ± 0.05
$LBP_{8,2}$	$D^{k=3}_{manhattan}$	0.74 ± 0.04	$K^{C=1,\gamma=0.1}_{rbf}$	0.73 ± 0.05
$BRIEF_{5,8}$	$D^{k=3}_{chebyshev}$	0.54 ± 0.07	$K^{C=1,d=2}_{poly}$	0.59 ± 0.09
$LBP_{12,3}^{2riu}$	$D^{k=3}_{manhattan}$	0.72 ± 0.03	$K^{C=10}_{linear}$	0.72 ± 0.05
$LBP_{12,3}$	$D^{k=3}_{manhattan}$	0.74 ± 0.04	$K^{C=1,\gamma=0.1}_{rbf}$	0.73 ± 0.05
$BRIEF_{6,12}$	$D^{k=3}_{manhattan}$	0.60 ± 0.03	$K^{C=1,d=3}_{poly}$	0.62 ± 0.05
$LBP_{16,4}^{2riu}$	$D^{k=3}_{manhattan}$	0.70 ± 0.03	$K^{C=1}_{linear}$	0.71 ± 0.04
$LBP_{16,4}$	$D^{k=5}_{manhattan}$	0.73 ± 0.05	$K^{C=10,\gamma=0.01}_{rbf}$	0.72 ± 0.06
$BRIEF_{7,16}$	$D^{k=5}_{manhattan}$	0.58 ± 0.05	$K^{C=10,d=2}_{poly}$	0.56 ± 0.06

Table 4.28: A summary of classification results (mean AUC scores \pm standard deviations) that measure the performance of the automated classification algorithm that is based on whole-local texture features for solving the dry AMD vs wet AMD classification task, based on concatenating two feature vectors extracted from the OCTA images of the deep retina and the chorio-capillaris layers.

Descriptor	KNN Classifier		SVM Classifier	
	Best Parameters	AUC \pm std	Best Parameters	AUC \pm std
$LBP_{4,1}^{2riu}$	$D^{k=3}_{chebyshev}$	0.73 ± 0.04	$K^{C=1,\gamma=0.1}_{rbf}$	0.76 ± 0.05
$LBP_{4,1}$	$D^{k=3}_{manhattan}$	0.70 ± 0.04	$K^{C=10}_{linear}$	0.75 ± 0.06
$BRIEF_{4,4}$	$D^{k=3}_{chebyshev}$	0.50 ± 0.06	$K^{C=1,d=3}_{poly}$	0.51 ± 0.06
$LBP_{8,2}^{2riu}$	$D^{k=3}_{manhattan}$	0.74 ± 0.04	$K^{C=1,d=2}_{poly}$	0.77 ± 0.05
$LBP_{8,2}$	$D^{k=3}_{euclidean}$	0.73 ± 0.03	$K^{C=1,d=2}_{poly}$	0.75 ± 0.04
$BRIEF_{5,8}$	$D^{k=1}_{chebyshev}$	0.50 ± 0.05	$K^{C=1,\gamma=0.1}_{rbf}$	0.50 ± 0.06
$LBP_{12,3}^{2riu}$	$D^{k=3}_{euclidean}$	0.75 ± 0.06	$K^{C=1,d=3}_{poly}$	0.78 ± 0.06
$LBP_{12,3}$	$D^{k=3}_{manhattan}$	0.74 ± 0.04	$K^{C=1,\gamma=0.1}_{rbf}$	0.75 ± 0.05
$BRIEF_{6,12}$	$D^{k=1}_{euclidean}$	0.53 ± 0.06	$K^{C=1,d=3}_{poly}$	0.50 ± 0.06
$LBP_{16,4}^{2riu}$	$D^{k=5}_{euclidean}$	0.70 ± 0.03	$K^{C=10,d=3}_{poly}$	0.74 ± 0.04
$LBP_{16,4}$	$D^{k=5}_{euclidean}$	0.72 ± 0.04	$K^{C=1,d=2}_{poly}$	0.73 ± 0.05
$BRIEF_{7,16}$	$D^{k=3}_{chebyshev}$	0.50 ± 0.04	$K^{C=10,\gamma=0.1}_{rbf}$	0.51 ± 0.05

Table 4.29: A summary of classification results (mean AUC scores \pm standard deviations) that measure the performance of the automated classification algorithm that is based on whole-local texture features for solving the dry AMD vs wet AMD classification task, based on concatenating the two feature vectors extracted from the OCTA images of the outer retina and the choriocapillaris layers.

Descriptor	KNN Classifier		SVM Classifier	
	Best Parameters	AUC \pm std	Best Parameters	AUC \pm std
$LBP_{4,1}^{2riu}$	$D_{manhattan}^{k=3}$	0.69 ± 0.07	$K_{linear}^{C=1}$	0.71 ± 0.06
$LBP_{4,1}$	$D_{manhattan}^{k=5}$	0.67 ± 0.07	$K_{linear}^{C=10}$	0.71 ± 0.07
$BRIEF_{4,4}$	$D_{euclidean}^{k=5}$	0.60 ± 0.06	$K_{linear}^{C=10}$	0.64 ± 0.07
$LBP_{8,2}^{2riu}$	$D_{manhattan}^{k=3}$	0.71 ± 0.06	$K_{poly}^{C=10,d=3}$	0.76 ± 0.08
$LBP_{8,2}$	$D_{manhattan}^{k=3}$	0.74 ± 0.06	$K_{poly}^{C=10,d=3}$	0.76 ± 0.05
$BRIEF_{5,8}$	$D_{euclidean}^{k=5}$	0.59 ± 0.06	$K_{poly}^{C=10,d=2}$	0.62 ± 0.07
$LBP_{12,3}^{2riu}$	$D_{manhattan}^{k=3}$	0.73 ± 0.06	$K_{poly}^{C=10,d=3}$	0.77 ± 0.06
$LBP_{12,3}$	$D_{manhattan}^{k=3}$	0.75 ± 0.05	$K_{rbf}^{C=10,\gamma=0.01}$	0.76 ± 0.05
$BRIEF_{6,12}$	$D_{manhattan}^{k=5}$	0.59 ± 0.06	$K_{poly}^{C=10,d=2}$	0.60 ± 0.06
$LBP_{16,4}^{2riu}$	$D_{manhattan}^{k=3}$	0.72 ± 0.04	$K_{rbf}^{C=10,\gamma=0.01}$	0.74 ± 0.05
$LBP_{16,4}$	$D_{manhattan}^{k=5}$	0.76 ± 0.05	$K_{linear}^{C=1}$	0.75 ± 0.05
$BRIEF_{7,16}$	$D_{chebyshev}^{k=1}$	0.53 ± 0.06	$K_{poly}^{C=1,d=2}$	0.59 ± 0.09

Table 4.30: A summary of classification results (mean AUC scores \pm standard deviations) that measure the performance of the automated classification algorithm that is based on whole-local texture features for solving the dry AMD vs wet AMD classification task, based on concatenating three feature vectors extracted from the OCTA images of the superficial inner, the deep inner and the outer retina layers.

Descriptor	KNN Classifier		SVM Classifier	
	Best Parameters	AUC \pm std	Best Parameters	AUC \pm std
$LBP_{4,1}^{2riu}$	$D_{manhattan}^{k=5}$	0.74 ± 0.04	$K_{poly}^{C=10,d=3}$	0.77 ± 0.05
$LBP_{4,1}$	$D_{euclidean}^{k=3}$	0.72 ± 0.03	$K_{poly}^{C=10,d=3}$	0.75 ± 0.05
$BRIEF_{4,4}$	$D_{euclidean}^{k=3}$	0.52 ± 0.05	$K_{poly}^{C=1,d=3}$	0.57 ± 0.07
$LBP_{8,2}^{2riu}$	$D_{manhattan}^{k=5}$	0.73 ± 0.04	$K_{poly}^{C=10,d=3}$	0.79 ± 0.07
$LBP_{8,2}$	$D_{manhattan}^{k=5}$	0.77 ± 0.04	$K_{poly}^{C=10,d=3}$	0.77 ± 0.04
$BRIEF_{5,8}$	$D_{chebyshev}^{k=5}$	0.53 ± 0.06	$K_{linear}^{C=50}$	0.55 ± 0.07
$LBP_{12,3}^{2riu}$	$D_{manhattan}^{k=5}$	0.73 ± 0.04	$K_{poly}^{C=10,d=3}$	0.76 ± 0.06
$LBP_{12,3}$	$D_{manhattan}^{k=5}$	0.75 ± 0.06	$K_{poly}^{C=10,d=3}$	0.75 ± 0.06
$BRIEF_{6,12}$	$D_{manhattan}^{k=5}$	0.57 ± 0.04	$K_{poly}^{C=10,d=3}$	0.61 ± 0.06
$LBP_{16,4}^{2riu}$	$D_{manhattan}^{k=7}$	0.72 ± 0.05	$K_{poly}^{C=1,d=2}$	0.75 ± 0.04
$LBP_{16,4}$	$D_{manhattan}^{k=5}$	0.74 ± 0.05	$K_{poly}^{C=1,d=3}$	0.73 ± 0.04
$BRIEF_{7,16}$	$D_{euclidean}^{k=5}$	0.56 ± 0.03	$K_{poly}^{C=10,d=2}$	0.60 ± 0.05

Table 4.31: A summary of classification results (mean AUC scores \pm standard deviations) that measure the performance of the automated classification algorithm that is based on whole-local texture features for solving the dry AMD vs wet AMD classification task, based on concatenating three feature vectors extracted from the OCTA images of the superficial, the deep inner retina and the choriocapillaris layers.

Descriptor	KNN Classifier		SVM Classifier	
	Best Parameters	AUC \pm std	Best Parameters	AUC \pm std
$LBP_{4,1}^{2riu}$	$D^{k=5}_{chebyshev}$	0.78 ± 0.03	$K^{C=10,d=3}_{poly}$	0.79 ± 0.06
$LBP_{4,1}$	$D^{k=5}_{manhattan}$	0.76 ± 0.04	$K^{C=10,d=2}_{poly}$	0.78 ± 0.05
$BRIEF_{4,4}$	$D^{k=5}_{chebyshev}$	0.50 ± 0.04	$K^{C=50}_{linear}$	0.51 ± 0.05
$LBP_{8,2}^{2riu}$	$D^{k=5}_{euclidean}$	0.74 ± 0.05	$K^{C=1,d=2}_{poly}$	0.78 ± 0.06
$LBP_{8,2}$	$D^{k=3}_{euclidean}$	0.75 ± 0.03	$K^{C=1,\gamma=0.1}_{rbf}$	0.77 ± 0.04
$BRIEF_{5,8}$	$D^{k=1}_{chebyshev}$	0.50 ± 0.05	$K^{C=50}_{linear}$	0.50 ± 0.07
$LBP_{12,3}^{2riu}$	$D^{k=3}_{manhattan}$	0.73 ± 0.06	$K^{C=1}_{linear}$	0.77 ± 0.06
$LBP_{12,3}$	$D^{k=3}_{euclidean}$	0.74 ± 0.04	$K^{C=1,d=2}_{poly}$	0.76 ± 0.04
$BRIEF_{6,12}$	$D^{k=5}_{euclidean}$	0.50 ± 0.07	$K^{C=10,d=3}_{poly}$	0.50 ± 0.06
$LBP_{16,4}^{2riu}$	$D^{k=5}_{manhattan}$	0.71 ± 0.04	$K^{C=10,d=2}_{poly}$	0.74 ± 0.06
$LBP_{16,4}$	$D^{k=7}_{manhattan}$	0.73 ± 0.04	$K^{C=10,d=3}_{poly}$	0.72 ± 0.05
$BRIEF_{7,16}$	$D^{k=5}_{chebyshev}$	0.51 ± 0.06	$K^{C=10,d=2}_{poly}$	0.50 ± 0.05

Table 4.32: A summary of classification results (mean AUC scores \pm standard deviations) that measure the performance of the automated classification algorithm that is based on whole-local texture features for solving the dry AMD vs wet AMD classification task, based on concatenating three feature vectors extracted from the OCTA images of the superficial inner, the outer retina and the choriocapillaris layers.

Descriptor	KNN Classifier		SVM Classifier	
	Best Parameters	AUC \pm std	Best Parameters	AUC \pm std
$LBP_{4,1}^{2riu}$	$D^{k=5}_{euclidean}$	0.72 ± 0.04	$K^{C=10,d=3}_{poly}$	0.75 ± 0.05
$LBP_{4,1}$	$D^{k=5}_{manhattan}$	0.72 ± 0.05	$K^{C=10,d=3}_{poly}$	0.75 ± 0.06
$BRIEF_{4,4}$	$D^{k=1}_{euclidean}$	0.57 ± 0.06	$K^{C=50}_{linear}$	0.62 ± 0.08
$LBP_{8,2}^{2riu}$	$D^{k=5}_{manhattan}$	0.71 ± 0.05	$K^{C=10,d=3}_{poly}$	0.76 ± 0.08
$LBP_{8,2}$	$D^{k=3}_{manhattan}$	0.76 ± 0.06	$K^{C=10,d=3}_{poly}$	0.78 ± 0.05
$BRIEF_{5,8}$	$D^{k=5}_{manhattan}$	0.53 ± 0.03	$K^{C=50}_{linear}$	0.56 ± 0.06
$LBP_{12,3}^{2riu}$	$D^{k=5}_{manhattan}$	0.72 ± 0.06	$K^{C=10,d=3}_{poly}$	0.77 ± 0.07
$LBP_{12,3}$	$D^{k=5}_{manhattan}$	0.77 ± 0.05	$K^{C=10,d=3}_{poly}$	0.77 ± 0.05
$BRIEF_{6,12}$	$D^{k=5}_{manhattan}$	0.61 ± 0.05	$K^{C=50}_{linear}$	0.62 ± 0.06
$LBP_{16,4}^{2riu}$	$D^{k=7}_{manhattan}$	0.71 ± 0.04	$K^{C=1,d=3}_{poly}$	0.76 ± 0.06
$LBP_{16,4}$	$D^{k=5}_{manhattan}$	0.75 ± 0.07	$K^{C=1,d=2}_{poly}$	0.76 ± 0.04
$BRIEF_{7,16}$	$D^{k=3}_{manhattan}$	0.59 ± 0.04	$K^{C=10}_{linear}$	0.60 ± 0.05

Table 4.33: A summary of classification results (mean AUC scores \pm standard deviations) that measure the performance of the automated classification algorithm that is based on whole-local texture features for solving the dry AMD vs wet AMD classification task, based on concatenating three feature vectors extracted from the OCTA images of the deep inner, the outer retina and the choriocapillaris layers.

Descriptor	KNN Classifier		SVM Classifier	
	Best Parameters	AUC \pm std	Best Parameters	AUC \pm std
$LBP_{4,1}^{2riu}$	$D_{manhattan}^{k=3}$	0.73 ± 0.04	$K_{poly}^{C=10,d=3}$	0.77 ± 0.06
$LBP_{4,1}$	$D_{manhattan}^{k=3}$	0.72 ± 0.04	$K_{poly}^{C=10,d=3}$	0.76 ± 0.06
$BRIEF_{4,4}$	$D_{chebyshev}^{k=5}$	0.57 ± 0.05	$K_{linear}^{C=50}$	0.62 ± 0.07
$LBP_{8,2}^{2riu}$	$D_{manhattan}^{k=5}$	0.75 ± 0.04	$K_{poly}^{C=10,d=3}$	0.80 ± 0.06
$LBP_{8,2}$	$D_{manhattan}^{k=5}$	0.78 ± 0.04	$K_{poly}^{C=10,d=3}$	0.79 ± 0.04
$BRIEF_{5,8}$	$D_{chebyshev}^{k=5}$	0.55 ± 0.06	$K_{linear}^{C=50}$	0.57 ± 0.06
$LBP_{12,3}^{2riu}$	$D_{manhattan}^{k=5}$	0.73 ± 0.04	$K_{poly}^{C=10,d=3}$	0.78 ± 0.06
$LBP_{12,3}$	$D_{manhattan}^{k=5}$	0.76 ± 0.04	$K_{poly}^{C=10,d=3}$	0.78 ± 0.04
$BRIEF_{6,12}$	$D_{manhattan}^{k=5}$	0.58 ± 0.04	$K_{poly}^{C=10,d=3}$	0.60 ± 0.05
$LBP_{16,4}^{2riu}$	$D_{manhattan}^{k=7}$	0.71 ± 0.03	$K_{poly}^{C=1,d=2}$	0.74 ± 0.04
$LBP_{16,4}$	$D_{manhattan}^{k=3}$	0.70 ± 0.05	$K_{poly}^{C=1,d=3}$	0.73 ± 0.05
$BRIEF_{7,16}$	$D_{chebyshev}^{k=3}$	0.55 ± 0.03	$K_{linear}^{C=10}$	0.60 ± 0.04

Table 4.34: A summary of classification results (mean AUC scores \pm standard deviations) that measure the performance of the automated classification algorithm that is based on whole-local texture features for solving the dry AMD vs wet AMD classification task, based on concatenating all feature vectors extracted from the OCTA images of all ocular vascular layers.

Descriptor	KNN Classifier		SVM Classifier	
	Best Parameters	AUC \pm std	Best Parameters	AUC \pm std
$LBP_{4,1}^{2riu}$	$D_{manhattan}^{k=7}$	0.75 ± 0.05	$K_{linear}^{C=100}$	0.78 ± 0.05
$LBP_{4,1}$	$D_{manhattan}^{k=5}$	0.74 ± 0.03	$K_{linear}^{C=100}$	0.77 ± 0.05
$BRIEF_{4,4}$	$D_{chebyshev}^{k=3}$	0.52 ± 0.03	$K_{linear}^{C=10}$	0.56 ± 0.09
$LBP_{8,2}^{2riu}$	$D_{manhattan}^{k=7}$	0.76 ± 0.05	$K_{linear}^{C=100}$	0.79 ± 0.04
$LBP_{8,2}$	$D_{manhattan}^{k=7}$	0.77 ± 0.04	$K_{linear}^{C=100}$	0.78 ± 0.05
$BRIEF_{5,8}$	$D_{chebyshev}^{k=5}$	0.54 ± 0.06	$K_{linear}^{C=100}$	0.56 ± 0.06
$LBP_{12,3}^{2riu}$	$D_{manhattan}^{k=5}$	0.76 ± 0.05	$K_{linear}^{C=100}$	0.78 ± 0.05
$LBP_{12,3}$	$D_{manhattan}^{k=7}$	0.78 ± 0.04	$K_{linear}^{C=100}$	0.77 ± 0.05
$BRIEF_{6,12}$	$D_{euclidean}^{k=5}$	0.56 ± 0.06	$K_{rbf}^{C=10,\gamma=0.001}$	0.61 ± 0.04
$LBP_{16,4}^{2riu}$	$D_{manhattan}^{k=7}$	0.74 ± 0.05	$K_{linear}^{C=100}$	0.77 ± 0.05
$LBP_{16,4}$	$D_{manhattan}^{k=7}$	0.78 ± 0.05	$K_{linear}^{C=100}$	0.77 ± 0.05
$BRIEF_{7,16}$	$D_{euclidean}^{k=5}$	0.54 ± 0.06	$K_{rbf}^{C=10,\gamma=0.001}$	0.61 ± 0.05

images can appear significantly different as well as very similar among various ocular vascular layers. As such, occasionally, the vascular pathologies related to dry AMD

and wet AMD disease may appear similar to each other as well as being more obvious in certain layers than others. For example, with the presence of an eye condition, i.e.: dry AMD or wet AMD disease, the OCTA images of certain ocular vascular layers, e.g.: the superficial inner retina and the deep inner retina layers, typically demonstrate quite uniform textural vascular appearance that is comparable to dry AMD, wet AMD as well as healthy.

However, the OCTA images of the outer retina and the choriocapillaris layers with wet AMD and dry AMD, usually show random textural vascular appearance that is comparable to each other but dramatically different from healthy. Despite these diversities and difficulties, the previous evaluation results demonstrate that the automated classification algorithm can identify dissimilarities between dry AMD and wet AMD vascular texture via combining the feature vectors extracted from the various OCTA images of ocular vascular layers. While the classification results with the $BRIEF_{S,n}$ texture descriptor showed to be very poor in all classification experiments, the $LBP_{p,r}^{2riu}$ and the $LBP_{p,r}$ texture descriptors both revealed the capacity to facilitate achieving reasonable classification results.

Broadly, for solving the dry AMD vs wet AMD classification task via layer combination, however, the best classification performance was achieved when concatenating three feature vectors extracted from the OCTA images of the deep inner, the outer retina and the choriocapillaris layers. This was accomplished by utilising the SVM classifier with $K_{poly}^{C=10,d=3}$ using the $LBP_{8,2}^{2riu}$ texture descriptor achieving a mean AUC score and a standard deviation = 0.80 ± 0.06 .

Finally, the classification algorithm was evaluated on classifying the various eyes via layer combination; however, for the task of discriminating CNV from non-CNV cases. Tables 4.35, 4.36, 4.37, 4.38, 4.39 and 4.40 show the classification results of the classification algorithm after concatenating two feature vectors extracted from the OCTA images of two various ocular vascular layers. These are the superficial and the deep inner retina, the superficial inner and the outer retina, the superficial inner retina and the choriocapillaris, the deep inner and the outer retina, the deep inner retina and the choriocapillaris, and the outer retina and the choriocapillaris layers, respectively.

Tables 4.41, 4.42, 4.43 and 4.44, on the other hand, demonstrate the classification results of the classification algorithm when concatenating three feature vectors extracted from three OCTA images of various ocular vascular layers. Specifically, the superficial, the deep inner and the outer retina, the superficial, the deep inner retina and the choriocapillaris, the superficial inner, the outer retina and the choriocapillaris, and

Table 4.35: A summary of classification results (mean AUC scores \pm standard deviations) that measure the performance of the automated classification algorithm that is based on whole-local texture features for solving the CNV vs non-CNV classification task, based on concatenating two feature vectors extracted from the OCTA images of the superficial and the deep retina layers.

Descriptor	KNN Classifier		SVM Classifier	
	Best Parameters	AUC \pm std	Best Parameters	AUC \pm std
$LBP_{4,1}^{2riu}$	$D_{manhattan}^{k=5}$	0.62 ± 0.06	$K_{poly}^{C=10,d=3}$	0.68 ± 0.04
$LBP_{4,1}$	$D_{manhattan}^{k=5}$	0.64 ± 0.05	$K_{poly}^{C=10,d=3}$	0.67 ± 0.06
$BRIEF_{4,4}$	$D_{manhattan}^{k=5}$	0.51 ± 0.05	$K_{poly}^{C=1,d=2}$	0.50 ± 0.06
$LBP_{8,2}^{2riu}$	$D_{euclidean}^{k=5}$	0.61 ± 0.04	$K_{poly}^{C=10,d=3}$	0.67 ± 0.07
$LBP_{8,2}$	$D_{euclidean}^{k=5}$	0.65 ± 0.04	$K_{poly}^{C=10,d=2}$	0.67 ± 0.05
$BRIEF_{5,8}$	$D_{euclidean}^{k=5}$	0.50 ± 0.04	$K_{linear}^{C=1}$	0.50 ± 0.05
$LBP_{12,3}^{2riu}$	$D_{euclidean}^{k=5}$	0.60 ± 0.04	$K_{poly}^{C=10,d=3}$	0.67 ± 0.08
$LBP_{12,3}$	$D_{manhattan}^{k=5}$	0.62 ± 0.06	$K_{linear}^{C=50}$	0.64 ± 0.07
$BRIEF_{6,12}$	$D_{manhattan}^{k=1}$	0.51 ± 0.04	$K_{poly}^{C=10,d=2}$	0.50 ± 0.05
$LBP_{16,4}^{2riu}$	$D_{euclidean}^{k=3}$	0.64 ± 0.03	$K_{poly}^{C=1,d=3}$	0.66 ± 0.06
$LBP_{16,4}$	$D_{manhattan}^{k=3}$	0.63 ± 0.04	$K_{poly}^{C=1,d=2}$	0.65 ± 0.06
$BRIEF_{7,16}$	$D_{manhattan}^{k=5}$	0.50 ± 0.04	$K_{poly}^{C=1,d=2}$	0.51 ± 0.06

Table 4.36: A summary of classification results (mean AUC scores \pm standard deviations) that measure the performance of the automated classification algorithm that is based on whole-local texture features for solving the CNV vs non-CNV classification task, based on concatenating two feature vectors extracted from the OCTA images of the superficial and the outer retina layers.

Descriptor	KNN Classifier		SVM Classifier	
	Best Parameters	AUC \pm std	Best Parameters	AUC \pm std
$LBP_{4,1}^{2riu}$	$D_{manhattan}^{k=3}$	0.70 ± 0.04	$K_{poly}^{C=10,d=3}$	0.74 ± 0.05
$LBP_{4,1}$	$D_{euclidean}^{k=5}$	0.71 ± 0.06	$K_{linear}^{C=50}$	0.74 ± 0.05
$BRIEF_{4,4}$	$D_{chebyshev}^{k=5}$	0.60 ± 0.06	$K_{poly}^{C=1,d=2}$	0.62 ± 0.06
$LBP_{8,2}^{2riu}$	$D_{manhattan}^{k=5}$	0.74 ± 0.04	$K_{poly}^{C=10,d=3}$	0.79 ± 0.06
$LBP_{8,2}$	$D_{manhattan}^{k=3}$	0.77 ± 0.05	$K_{linear}^{C=50}$	0.78 ± 0.04
$BRIEF_{5,8}$	$D_{euclidean}^{k=5}$	0.58 ± 0.05	$K_{poly}^{C=1,d=2}$	0.63 ± 0.06
$LBP_{12,3}^{2riu}$	$D_{manhattan}^{k=5}$	0.75 ± 0.04	$K_{poly}^{C=10,d=3}$	0.78 ± 0.05
$LBP_{12,3}$	$D_{manhattan}^{k=3}$	0.77 ± 0.05	$K_{linear}^{C=50}$	0.77 ± 0.05
$BRIEF_{6,12}$	$D_{manhattan}^{k=5}$	0.62 ± 0.04	$K_{poly}^{C=10,d=2}$	0.65 ± 0.05
$LBP_{16,4}^{2riu}$	$D_{manhattan}^{k=5}$	0.71 ± 0.03	$K_{poly}^{C=1,d=3}$	0.73 ± 0.04
$LBP_{16,4}$	$D_{manhattan}^{k=5}$	0.75 ± 0.04	$K_{linear}^{C=10}$	0.76 ± 0.05
$BRIEF_{7,16}$	$D_{chebyshev}^{k=3}$	0.61 ± 0.03	$K_{poly}^{C=10,d=2}$	0.63 ± 0.04

the deep inner, the outer retina and the choriocapillaris layers, respectively.

Table 4.37: A summary of classification results (mean AUC scores \pm standard deviations) that measure the performance of the automated classification algorithm that is based on whole-local texture features for solving the CNV vs non-CNV classification task, based on concatenating two feature vectors extracted from the OCTA images of the superficial retina and the chorio-capillaris layers.

Descriptor	KNN Classifier		SVM Classifier	
	Best Parameters	AUC \pm std	Best Parameters	AUC \pm std
$LBP_{4,1}^{2riu}$	$D^{k=5}_{manhattan}$	0.68 ± 0.06	$K^{C=10,d=3}_{poly}$	0.71 ± 0.07
$LBP_{4,1}$	$D^{k=5}_{manhattan}$	0.69 ± 0.07	$K^{C=10,d=3}_{poly}$	0.71 ± 0.06
$BRIEF_{4,4}$	$D^{k=1}_{chebyshev}$	0.50 ± 0.04	$K^{C=10}_{linear}$	0.51 ± 0.06
$LBP_{8,2}^{2riu}$	$D^{k=5}_{euclidean}$	0.70 ± 0.05	$K^{C=10,d=3}_{poly}$	0.75 ± 0.06
$LBP_{8,2}$	$D^{k=5}_{manhattan}$	0.74 ± 0.05	$K^{C=10,d=2}_{poly}$	0.74 ± 0.05
$BRIEF_{5,8}$	$D^{k=1}_{chebyshev}$	0.50 ± 0.05	$K^{C=1,d=2}_{poly}$	0.50 ± 0.06
$LBP_{12,3}^{2riu}$	$D^{k=5}_{euclidean}$	0.69 ± 0.05	$K^{C=10}_{linear}$	0.74 ± 0.06
$LBP_{12,3}$	$D^{k=5}_{manhattan}$	0.72 ± 0.04	$K^{C=1,d=2}_{poly}$	0.74 ± 0.05
$BRIEF_{6,12}$	$D^{k=5}_{euclidean}$	0.54 ± 0.06	$K^{C=1,d=3}_{poly}$	0.52 ± 0.06
$LBP_{16,4}^{2riu}$	$D^{k=3}_{euclidean}$	0.68 ± 0.04	$K^{C=1,d=2}_{poly}$	0.70 ± 0.03
$LBP_{16,4}$	$D^{k=7}_{manhattan}$	0.67 ± 0.06	$K^{C=1,d=2}_{poly}$	0.70 ± 0.05
$BRIEF_{7,16}$	$D^{k=3}_{chebyshev}$	0.51 ± 0.04	$K^{C=10,d=3}_{poly}$	0.52 ± 0.05

Table 4.38: A summary of classification results (mean AUC scores \pm standard deviations) that measure the performance of the automated classification algorithm that is based on whole-local texture features for solving the CNV vs non-CNV classification task, based on concatenating two feature vectors extracted from the OCTA images of the deep and the outer retina layers.

Descriptor	KNN Classifier		SVM Classifier	
	Best Parameters	AUC \pm std	Best Parameters	AUC \pm std
$LBP_{4,1}^{2riu}$	$D^{k=3}_{chebyshev}$	0.72 ± 0.04	$K^{C=50}_{linear}$	0.74 ± 0.04
$LBP_{4,1}$	$D^{k=3}_{euclidean}$	0.70 ± 0.05	$K^{C=50}_{linear}$	0.73 ± 0.05
$BRIEF_{4,4}$	$D^{k=5}_{chebyshev}$	0.60 ± 0.06	$K^{C=10}_{linear}$	0.59 ± 0.09
$LBP_{8,2}^{2riu}$	$D^{k=5}_{manhattan}$	0.74 ± 0.05	$K^{C=10,d=3}_{poly}$	0.79 ± 0.07
$LBP_{8,2}$	$D^{k=5}_{manhattan}$	0.75 ± 0.04	$K^{C=10,d=3}_{poly}$	0.77 ± 0.05
$BRIEF_{5,8}$	$D^{k=5}_{manhattan}$	0.58 ± 0.06	$K^{C=1,d=3}_{poly}$	0.62 ± 0.07
$LBP_{12,3}^{2riu}$	$D^{k=5}_{manhattan}$	0.73 ± 0.05	$K^{C=10,d=3}_{poly}$	0.78 ± 0.06
$LBP_{12,3}$	$D^{k=5}_{manhattan}$	0.75 ± 0.05	$K^{C=50}_{linear}$	0.77 ± 0.05
$BRIEF_{6,12}$	$D^{k=1}_{manhattan}$	0.57 ± 0.06	$K^{C=50}_{linear}$	0.63 ± 0.08
$LBP_{16,4}^{2riu}$	$D^{k=3}_{manhattan}$	0.72 ± 0.05	$K^{C=1,d=2}_{poly}$	0.75 ± 0.07
$LBP_{16,4}$	$D^{k=7}_{euclidean}$	0.71 ± 0.4	$K^{C=1,d=3}_{poly}$	0.72 ± 0.05
$BRIEF_{7,16}$	$D^{k=3}_{manhattan}$	0.54 ± 0.08	$K^{C=1,d=2}_{poly}$	0.53 ± 0.07

Table 4.45 provides the classification results when concatenating all feature vectors extracted from the OCTA images of all ocular vascular layers.

Table 4.39: A summary of classification results (mean AUC scores \pm standard deviations) that measure the performance of the automated classification algorithm that is based on whole-local texture features for solving the CNV vs non-CNV classification task, based on concatenating two feature vectors extracted from the OCTA images of the deep retina and the choriocapillaris layers.

Descriptor	KNN Classifier		SVM Classifier	
	Best Parameters	AUC \pm std	Best Parameters	AUC \pm std
$LBP_{4,1}^{2riu}$	$D_{chebyshev}^{k=5}$	0.71 ± 0.07	$K_{poly}^{C=10,d=3}$	0.72 ± 0.06
$LBP_{4,1}$	$D_{manhattan}^{k=5}$	0.71 ± 0.07	$K_{poly}^{C=10,d=3}$	0.71 ± 0.06
$BRIEF_{4,4}$	$D_{manhattan}^{k=1}$	0.54 ± 0.05	$K_{poly}^{C=10,d=3}$	0.50 ± 0.08
$LBP_{8,2}^{2riu}$	$D_{euclidean}^{k=5}$	0.73 ± 0.06	$K_{poly}^{C=10,d=3}$	0.74 ± 0.06
$LBP_{8,2}$	$D_{euclidean}^{k=5}$	0.73 ± 0.05	$K_{linear}^{C=10}$	0.73 ± 0.06
$BRIEF_{5,8}$	$D_{manhattan}^{k=1}$	0.50 ± 0.04	$K_{rbf}^{C=1,\gamma=0.1}$	0.50 ± 0.06
$LBP_{12,3}^{2riu}$	$D_{euclidean}^{k=5}$	0.69 ± 0.06	$K_{poly}^{C=1,d=3}$	0.74 ± 0.08
$LBP_{12,3}$	$D_{manhattan}^{k=5}$	0.76 ± 0.04	$K_{poly}^{C=10,d=2}$	0.75 ± 0.06
$BRIEF_{6,12}$	$D_{manhattan}^{k=1}$	0.50 ± 0.05	$K_{rbf}^{C=10,\gamma=0.1}$	0.50 ± 0.04
$LBP_{16,4}^{2riu}$	$D_{euclidean}^{k=3}$	0.71 ± 0.06	$K_{poly}^{C=1,d=3}$	0.72 ± 0.09
$LBP_{16,4}$	$D_{euclidean}^{k=5}$	0.74 ± 0.05	$K_{poly}^{C=10,d=2}$	0.73 ± 0.08
$BRIEF_{7,16}$	$D_{manhattan}^{k=5}$	0.50 ± 0.07	$K_{rbf}^{C=10,\gamma=0.1}$	0.51 ± 0.09

Table 4.40: A summary of classification results (mean AUC scores \pm standard deviations) that measure the performance of the automated classification algorithm that is based on whole-local texture features for solving the CNV vs non-CNV classification task, based on concatenating the two feature vectors extracted from the OCTA images of the outer retina and the choriocapillaris layers.

Descriptor	KNN Classifier		SVM Classifier	
	Best Parameters	AUC \pm std	Best Parameters	AUC \pm std
$LBP_{4,1}^{2riu}$	$D_{manhattan}^{k=5}$	0.73 ± 0.03	$K_{poly}^{C=10,d=3}$	0.75 ± 0.04
$LBP_{4,1}$	$D_{manhattan}^{k=5}$	0.74 ± 0.05	$K_{poly}^{C=10,d=3}$	0.75 ± 0.05
$BRIEF_{4,4}$	$D_{manhattan}^{k=5}$	0.64 ± 0.05	$K_{rbf}^{C=1,\gamma=0.01}$	0.65 ± 0.05
$LBP_{8,2}^{2riu}$	$D_{manhattan}^{k=3}$	0.78 ± 0.03	$K_{poly}^{C=10,d=3}$	0.82 ± 0.04
$LBP_{8,2}$	$D_{manhattan}^{k=3}$	0.80 ± 0.04	$K_{poly}^{C=10,d=3}$	0.80 ± 0.04
$BRIEF_{5,8}$	$D_{chebyshev}^{k=5}$	0.59 ± 0.03	$K_{rbf}^{C=1,\gamma=0.01}$	0.63 ± 0.06
$LBP_{12,3}^{2riu}$	$D_{manhattan}^{k=3}$	0.80 ± 0.04	$K_{poly}^{C=10,d=3}$	0.81 ± 0.04
$LBP_{12,3}$	$D_{manhattan}^{k=3}$	0.80 ± 0.05	$K_{poly}^{C=10,d=3}$	0.80 ± 0.04
$BRIEF_{6,12}$	$D_{euclidean}^{k=5}$	0.58 ± 0.03	$K_{rbf}^{C=1,\gamma=0.01}$	0.61 ± 0.04
$LBP_{16,4}^{2riu}$	$D_{manhattan}^{k=5}$	0.79 ± 0.04	$K_{poly}^{C=10,d=3}$	0.79 ± 0.04
$LBP_{16,4}$	$D_{manhattan}^{k=5}$	0.80 ± 0.04	$K_{poly}^{C=10,d=3}$	0.79 ± 0.04
$BRIEF_{7,16}$	$D_{chebyshev}^{k=5}$	0.57 ± 0.05	$K_{rbf}^{C=1,\gamma=0.01}$	0.59 ± 0.05

Table 4.41: A summary of classification results (mean AUC scores \pm standard deviations) that measure the performance of the automated classification algorithm that is based on whole-local texture features for solving the CNV vs non-CNV classification task, based on concatenating three feature vectors extracted from the OCTA images of the superficial inner, the deep inner and the outer retina layers.

Descriptor	KNN Classifier		SVM Classifier	
	Best Parameters	AUC \pm std	Best Parameters	AUC \pm std
$LBP_{4,1}^{2riu}$	$D^{k=3}_{euclidean}$	0.71 ± 0.05	$K^{C=10,d=3}_{poly}$	0.75 ± 0.06
$LBP_{4,1}$	$D^{k=5}_{manhattan}$	0.73 ± 0.05	$K^{C=10,d=3}_{poly}$	0.75 ± 0.05
$BRIEF_{4,4}$	$D^{k=5}_{euclidean}$	0.58 ± 0.05	$K^{C=1,d=2}_{poly}$	0.61 ± 0.06
$LBP_{8,2}^{2riu}$	$D^{k=3}_{euclidean}$	0.75 ± 0.06	$K^{C=10,d=3}_{poly}$	0.80 ± 0.07
$LBP_{8,2}$	$D^{k=5}_{manhattan}$	0.79 ± 0.05	$K^{C=50}_{linear}$	0.79 ± 0.04
$BRIEF_{5,8}$	$D^{k=5}_{euclidean}$	0.53 ± 0.06	$K^{C=1,\gamma=0.1}_{rbf}$	0.60 ± 0.09
$LBP_{12,3}^{2riu}$	$D^{k=5}_{manhattan}$	0.74 ± 0.05	$K^{C=10,d=3}_{poly}$	0.78 ± 0.06
$LBP_{12,3}$	$D^{k=5}_{manhattan}$	0.79 ± 0.05	$K^{C=50}_{linear}$	0.78 ± 0.05
$BRIEF_{6,12}$	$D^{k=3}_{manhattan}$	0.54 ± 0.03	$K^{C=1,d=2}_{poly}$	0.59 ± 0.06
$LBP_{16,4}^{2riu}$	$D^{k=5}_{euclidean}$	0.72 ± 0.04	$K^{C=1,d=3}_{poly}$	0.75 ± 0.05
$LBP_{16,4}$	$D^{k=3}_{manhattan}$	0.76 ± 0.04	$K^{C=10}_{linear}$	0.77 ± 0.03
$BRIEF_{7,16}$	$D^{k=3}_{euclidean}$	0.53 ± 0.03	$K^{C=10,d=2}_{poly}$	0.56 ± 0.04

Table 4.42: A summary of classification results (mean AUC scores \pm standard deviations) that measure the performance of the automated classification algorithm that is based on whole-local texture features for solving the CNV vs non-CNV classification task, based on concatenating three feature vectors extracted from the OCTA images of the superficial, the deep inner retina and the choriocapillaris layers.

Descriptor	KNN Classifier		SVM Classifier	
	Best Parameters	AUC \pm std	Best Parameters	AUC \pm std
$LBP_{4,1}^{2riu}$	$D^{k=5}_{euclidean}$	0.73 ± 0.07	$K^{C=10,d=2}_{poly}$	0.75 ± 0.06
$LBP_{4,1}$	$D^{k=5}_{manhattan}$	0.70 ± 0.06	$K^{C=10,d=3}_{poly}$	0.73 ± 0.06
$BRIEF_{4,4}$	$D^{k=1}_{chebyshev}$	0.51 ± 0.02	$K^{C=50}_{linear}$	0.50 ± 0.06
$LBP_{8,2}^{2riu}$	$D^{k=5}_{manhattan}$	0.74 ± 0.06	$K^{C=10,d=3}_{poly}$	0.77 ± 0.05
$LBP_{8,2}$	$D^{k=5}_{manhattan}$	0.74 ± 0.05	$K^{C=1,d=2}_{poly}$	0.75 ± 0.06
$BRIEF_{5,8}$	$D^{k=1}_{manhattan}$	0.51 ± 0.07	$K^{C=1,d=3}_{poly}$	0.50 ± 0.07
$LBP_{12,3}^{2riu}$	$D^{k=5}_{euclidean}$	0.66 ± 0.05	$K^{C=10}_{linear}$	0.73 ± 0.08
$LBP_{12,3}$	$D^{k=5}_{manhattan}$	0.75 ± 0.04	$K^{C=1,d=2}_{poly}$	0.75 ± 0.05
$BRIEF_{6,12}$	$D^{k=5}_{manhattan}$	0.50 ± 0.05	$K^{C=10,d=2}_{poly}$	0.50 ± 0.04
$LBP_{16,4}^{2riu}$	$D^{k=3}_{euclidean}$	0.65 ± 0.06	$K^{C=1}_{linear}$	0.72 ± 0.07
$LBP_{16,4}$	$D^{k=5}_{manhattan}$	0.74 ± 0.05	$K^{C=10,d=2}_{poly}$	0.73 ± 0.05
$BRIEF_{7,16}$	$D^{k=5}_{euclidean}$	0.50 ± 0.06	$K^{C=1,d=2}_{poly}$	0.50 ± 0.05

Table 4.43: A summary of classification results (mean AUC scores \pm standard deviations) that measure the performance of the automated classification algorithm that is based on whole-local texture features for solving the CNV vs non-CNV classification task, based on concatenating three feature vectors extracted from the OCTA images of the superficial inner, the outer retina and the choriocapillaris layers.

Descriptor	KNN Classifier		SVM Classifier	
	Best Parameters	AUC \pm std	Best Parameters	AUC \pm std
$LBP_{4,1}^{2riu}$	$D^{k=5}_{euclidean}$	0.74 ± 0.04	$K^{C=10,d=3}_{poly}$	0.76 ± 0.05
$LBP_{4,1}$	$D^{k=5}_{manhattan}$	0.75 ± 0.05	$K^{C=10,d=3}_{poly}$	0.78 ± 0.06
$BRIEF_{4,4}$	$D^{k=5}_{euclidean}$	0.57 ± 0.04	$K^{C=10,\gamma=0.1}_{rbf}$	0.61 ± 0.06
$LBP_{8,2}^{2riu}$	$D^{k=5}_{manhattan}$	0.78 ± 0.05	$K^{C=10,d=3}_{poly}$	0.81 ± 0.06
$LBP_{8,2}$	$D^{k=3}_{manhattan}$	0.79 ± 0.05	$K^{C=10,d=3}_{poly}$	0.80 ± 0.05
$BRIEF_{5,8}$	$D^{k=5}_{euclidean}$	0.60 ± 0.05	$K^{C=1,d=3}_{poly}$	0.64 ± 0.06
$LBP_{12,3}^{2riu}$	$D^{k=5}_{manhattan}$	0.82 ± 0.04	$K^{C=10,d=3}_{poly}$	0.81 ± 0.04
$LBP_{12,3}$	$D^{k=5}_{manhattan}$	0.79 ± 0.04	$K^{C=10,d=3}_{poly}$	0.80 ± 0.04
$BRIEF_{6,12}$	$D^{k=5}_{euclidean}$	0.58 ± 0.04	$K^{C=1,\gamma=0.1}_{rbf}$	0.60 ± 0.04
$LBP_{16,4}^{2riu}$	$D^{k=3}_{manhattan}$	0.72 ± 0.03	$K^{C=1,d=3}_{poly}$	0.74 ± 0.04
$LBP_{16,4}$	$D^{k=7}_{manhattan}$	0.72 ± 0.04	$K^{C=10,d=2}_{poly}$	0.77 ± 0.05
$BRIEF_{7,16}$	$D^{k=3}_{euclidean}$	0.56 ± 0.05	$K^{C=10,\gamma=0.01}_{rbf}$	0.60 ± 0.07

Table 4.44: A summary of classification results (mean AUC scores \pm standard deviations) that measure the performance of the automated classification algorithm that is based on whole-local texture features for solving the CNV vs non-CNV classification task, based on concatenating three feature vectors extracted from the OCTA images of the deep inner, the outer retina and the choriocapillaris layers.

Descriptor	KNN Classifier		SVM Classifier	
	Best Parameters	AUC \pm std	Best Parameters	AUC \pm std
$LBP_{4,1}^{2riu}$	$D^{k=5}_{manhattan}$	0.74 ± 0.04	$K^{C=10,d=3}_{poly}$	0.76 ± 0.05
$LBP_{4,1}$	$D^{k=5}_{manhattan}$	0.76 ± 0.04	$K^{C=10,d=3}_{poly}$	0.78 ± 0.05
$BRIEF_{4,4}$	$D^{k=1}_{euclidean}$	0.64 ± 0.06	$K^{C=1}_{linear}$	0.66 ± 0.05
$LBP_{8,2}^{2riu}$	$D^{k=5}_{manhattan}$	0.78 ± 0.05	$K^{C=10,d=3}_{poly}$	0.81 ± 0.06
$LBP_{8,2}$	$D^{k=5}_{manhattan}$	0.81 ± 0.03	$K^{C=10,d=3}_{poly}$	0.80 ± 0.04
$BRIEF_{5,8}$	$D^{k=5}_{chebyshev}$	0.56 ± 0.02	$K^{C=1,\gamma=0.01}_{rbf}$	0.58 ± 0.08
$LBP_{12,3}^{2riu}$	$D^{k=5}_{manhattan}$	0.78 ± 0.06	$K^{C=10,d=3}_{poly}$	0.81 ± 0.05
$LBP_{12,3}$	$D^{k=5}_{manhattan}$	0.82 ± 0.03	$K^{C=10,d=3}_{poly}$	0.81 ± 0.04
$BRIEF_{6,12}$	$D^{k=3}_{euclidean}$	0.58 ± 0.05	$K^{C=1,\gamma=0.1}_{rbf}$	0.60 ± 0.05
$LBP_{16,4}^{2riu}$	$D^{k=7}_{manhattan}$	0.77 ± 0.05	$K^{C=1,d=2}_{poly}$	0.80 ± 0.04
$LBP_{16,4}$	$D^{k=3}_{manhattan}$	0.81 ± 0.03	$K^{C=1,d=3}_{poly}$	0.80 ± 0.04
$BRIEF_{7,16}$	$D^{k=3}_{chebyshev}$	0.55 ± 0.04	$K^{C=1,\gamma=0.01}_{rbf}$	0.95 ± 0.06

Table 4.45: A summary of classification results (mean AUC scores \pm standard deviations) that measure the performance of the automated classification algorithm that is based on whole-local texture features for solving the CNV vs non-CNV classification task, based on concatenating all feature vectors extracted from the OCTA images of all ocular vascular layers.

Descriptor	KNN Classifier		SVM Classifier	
	Best Parameters	AUC \pm std	Best Parameters	AUC \pm std
$LBP_{4,1}^{2riu}$	$D^{k=7}_{manhattan}$	0.75 ± 0.03	$K^{C=100}_{linear}$	0.77 ± 0.04
$LBP_{4,1}$	$D^{k=7}_{manhattan}$	0.76 ± 0.04	$K^{C=100}_{linear}$	0.77 ± 0.04
$BRIEF_{4,4}$	$D^{k=3}_{chebyshev}$	0.58 ± 0.05	$K^{C=100, \gamma=0.01}_{rbf}$	0.61 ± 0.04
$LBP_{8,2}^{2riu}$	$D^{k=7}_{manhattan}$	0.78 ± 0.04	$K^{C=100}_{linear}$	0.80 ± 0.05
$LBP_{8,2}$	$D^{k=5}_{manhattan}$	0.81 ± 0.04	$K^{C=100}_{linear}$	0.80 ± 0.04
$BRIEF_{5,8}$	$D^{k=7}_{euclidean}$	0.59 ± 0.05	$K^{C=10}_{linear}$	0.61 ± 0.06
$LBP_{12,3}^{2riu}$	$D^{k=7}_{manhattan}$	0.79 ± 0.03	$K^{C=100}_{linear}$	0.80 ± 0.04
$LBP_{12,3}$	$D^{k=7}_{manhattan}$	0.81 ± 0.03	$K^{C=100}_{linear}$	0.79 ± 0.04
$BRIEF_{6,12}$	$D^{k=7}_{euclidean}$	0.56 ± 0.05	$K^{C=1, \gamma=0.001}_{rbf}$	0.60 ± 0.06
$LBP_{16,4}^{2riu}$	$D^{k=7}_{manhattan}$	0.81 ± 0.05	$K^{C=100}_{linear}$	0.80 ± 0.04
$LBP_{16,4}$	$D^{k=7}_{manhattan}$	0.80 ± 0.03	$K^{C=100}_{linear}$	0.78 ± 0.04
$BRIEF_{7,16}$	$D^{k=7}_{chebyshev}$	0.59 ± 0.03	$K^{C=1, \gamma=0.001}_{rbf}$	0.60 ± 0.04

Similar to the challenges previously mentioned when combining the various OCTA images of ocular vascular layers and performing the task of classifying the two different eye conditions, i.e.: dry AMD vs wet AMD, the CNV vs non-CNV classification task can also be enormously challenging to accomplish even for highly skilled ophthalmologists. Despite the various difficulties that can be encountered, the previous evaluation results demonstrate that the automated classification algorithm can identify dissimilarities between CNV and non-CNV vascular texture via combining the various OCTA images of ocular vascular layers. The classification results with the $BRIEF_{S,n}$ texture descriptor were, however, among the worst. Nevertheless, the $LBP_{p,r}^{2riu}$ and the $LBP_{p,r}$ texture descriptors both indicated to facilitate the attainment of a satisfactory classification performance.

For solving the CNV vs non-CNV classification task via layer combination, however, the best classification performance was achieved when concatenating three feature vectors extracted from the OCTA images of the deep inner, the outer retina and the choriocapillaris layers. This was accomplished by employing the KNN classifier with $D^{k=5}_{manhattan}$ using the $LBP_{12,3}$ texture descriptor achieving a mean AUC score and a standard deviation = 0.82 ± 0.03 .

The following subsection 4.4.3 provides the results of the cross-corpora experiments conducted.

4.4.3 Cross-Corpora Experiments

Recall that the wet AMD is common in both OCTA image data sets. Hence, the cross-corpora experiments are accomplished by training the classifiers on one of the OCTA image data sets and then testing them on the other OCTA image data sets (as external validation) to demonstrate the generalisation performance. Specifically, the classifiers trained on the Manchester OCTA image data set to solve the healthy versus wet AMD classification task are tested on the wet AMD cases of the Moorfields OCTA image data set. Similarly, the classifiers trained on the Moorfields OCTA image data set to solve the dry AMD versus wet AMD classification task are tested on the wet AMD cases of the Manchester OCTA image data set.

The various classifiers are trained using the optimal components, i.e.: best parameter combinations of the various local texture descriptors and best hyper-parameter combinations of the different classifiers that facilitated improving the classification performance as identified in the various classification experiments conducted in subsections 4.4.1 and 4.4.2. In case there are several optimal components reported in the previous experiments performed, which give comparable classification performance, the best components that provide the highest sensitivity scores are selected and reported.

Table 4.46 provides the results (sensitivity scores) of evaluating the classifiers trained on the Manchester OCTA image data set for the healthy versus wet AMD classification task to distinguish the wet AMD cases of the Moorfields OCTA image data set. Table 4.47 delivers the results (sensitivity scores) of assessing the classifiers trained on the Moorfields OCTA image data set for the dry AMD versus wet AMD classification task to discriminate the wet AMD cases of the Manchester OCTA image data set.

As only the Manchester OCTA image data set contains healthy eyes, the same healthy data set is used to train the classifier for solving the Manchester healthy versus Moorfields wet AMD classification task and then test the trained classifier on the wet AMD cases of the Manchester OCTA image data set. Likewise, as only the Moorfields OCTA image data set involves dry AMD eyes, the same dry AMD data set is used to train the classifier for solving the Moorfields dry AMD versus Manchester wet AMD classification task and then test the trained classifier on the wet AMD cases of the Moorfields OCTA image data set.

Table 4.48 provides the results (sensitivity scores) of evaluating the classifiers trained on the OCTA image data set for the Manchester healthy versus Moorfields

Table 4.46: The evaluation results (sensitivity scores) of the classifiers trained on the OCTA image data set for the Manchester healthy versus Manchester wet AMD classification task to distinguish the wet AMD cases of Moorfields OCTA image data set.

Ocular Vascular Layers	Descriptor	Classifier	Sensitivity score
Superficial inner retina layer	$LBP_{4,1}^{2riu}$	KNN ($D_{euclidean}^{k=3}$)	0.31
Deep inner retina layer	$LBP_{16,4}^{2riu}$	KNN ($D_{euclidean}^{k=3}$)	0.21
Outer retina layer	$LBP_{16,4}^{2riu}$	KNN ($D_{euclidean}^{k=3}$)	0.99
Choriocapillaris layer	$LBP_{16,4}^{2riu}$	SVM ($K_{linear}^{C=10}$)	0.90
Superficial + Deep	$LBP_{4,1}^{2riu}$	SVM ($K_{linear}^{C=1}$)	0.40
Superficial + Outer	$LBP_{16,4}^{2riu}$	KNN ($D_{euclidean}^{k=1}$)	0.94
Superficial + Choriocapillaris	$LBP_{12,3}$	KNN ($D_{manhattan}^{k=3}$)	0.60
Deep + Outer	$LBP_{16,4}^{2riu}$	KNN ($D_{euclidean}^{k=1}$)	0.82
Deep + Choriocapillaris	$LBP_{16,4}$	KNN ($D_{manhattan}^{k=5}$)	0.69
Outer + Choriocapillaris	$LBP_{16,4}^{2riu}$	KNN ($D_{euclidean}^{k=3}$)	1.00
Superficial + Deep + Outer	$LBP_{16,4}^{2riu}$	KNN ($D_{euclidean}^{k=3}$)	0.95
Superficial + Deep + Choriocapillaris	$LBP_{16,4}$	KNN ($D_{manhattan}^{k=5}$)	0.95
Superficial + Outer + Choriocapillaris	$LBP_{16,4}^{2riu}$	KNN ($D_{euclidean}^{k=3}$)	0.97
Deep + Outer + Choriocapillaris	$LBP_{16,4}^{2riu}$	KNN ($D_{euclidean}^{k=3}$)	0.97
All ocular vascular layers	$LBP_{12,3}^{2riu}$	KNN ($D_{euclidean}^{k=3}$)	0.98

wet AMD classification task to distinguish the wet AMD cases of the Manchester OCTA image data set. Table 4.49 delivers the results (sensitivity scores) of assessing the classifiers trained on OCTA image data set for the Moorfields dry AMD versus Manchester wet AMD classification task to discriminate the wet AMD cases of the Moorfields OCTA image data set.

The following section 4.5 provides discussion and performance comparison of the evaluation results of the automated OCTA image classification algorithm proposed for the diagnosis of AMD disease based on whole-local texture features.

4.5 Discussion and Performance Comparison

This section provides a comprehensive description of the significance of the findings. The performance of the automated classification algorithm on the previous binary OCTA image classification tasks, i.e.: healthy vs wet AMD, dry AMD vs wet AMD and CNV vs non-CNV, using the OCTA image data sets of the Manchester and Moorfields hospitals have been encouraging. As such, the algorithm was able to find novel

Table 4.47: The evaluation results (sensitivity scores) of the classifiers trained on the OCTA image data set for the Moorfields dry AMD versus Moorfields wet AMD classification task to distinguish the wet AMD cases of Manchester OCTA image data set.

Ocular Vascular Layers	Descriptor	Classifier	Sensitivity score
Superficial inner retina layer	$LBP_{4,1}^{2riu}$	SVM ($K_{linear}^{C=1}$)	0.96
Deep inner retina layer	$LBP_{16,4}^{2riu}$	SVM ($K_{linear}^{C=1}$)	0.96
Outer retina layer	$LBP_{16,4}^{2riu}$	SVM ($K_{linear}^{C=1}$)	1.00
Choriocapillaris layer	$LBP_{12,3}^{2riu}$	SVM ($K_{rbf}^{C=50, \gamma=0.1}$)	1.00
Superficial + Deep	$LBP_{4,1}^{2riu}$	SVM ($K_{poly}^{C=1, d=2}$)	0.96
Superficial + Outer	$LBP_{12,3}$	KNN ($D_{manhattan}^{k=3}$)	1.00
Superficial + Choriocapillaris	$LBP_{4,1}^{2riu}$	SVM ($K_{linear}^{C=10}$)	1.00
Deep + Outer	$LBP_{8,2}^{2riu}$	SVM ($K_{poly}^{C=1, d=3}$)	1.00
Deep + Choriocapillaris	$LBP_{12,3}^{2riu}$	SVM ($K_{poly}^{C=1, d=3}$)	1.00
Outer + Choriocapillaris	$LBP_{12,3}^{2riu}$	SVM ($K_{poly}^{C=10, d=3}$)	1.00
Superficial + Deep + Outer	$LBP_{8,2}^{2riu}$	SVM ($K_{poly}^{C=10, d=3}$)	1.00
Superficial + Deep + Choriocapillaris	$LBP_{4,1}^{2riu}$	SVM ($K_{poly}^{C=10, d=3}$)	1.00
Superficial + Outer + Choriocapillaris	$LBP_{8,2}$	SVM ($K_{poly}^{C=10, d=3}$)	1.00
Deep + Outer + Choriocapillaris	$LBP_{8,2}^{2riu}$	SVM ($K_{poly}^{C=10, d=3}$)	1.00
All ocular vascular layers	$LBP_{8,2}^{2riu}$	SVM ($K_{linear}^{C=100}$)	1.00

variations in the various ocular vascular layers, e.g.: the superficial inner retina and the deep inner retina layers, with different eye conditions, e.g.: dry AMD, wet AMD including healthy, that are not typically used by clinicians in the diagnosis of vascular pathologies, e.g.: CNV and non-CNV lesions related to AMD disease.

Tables 4.50, 4.51 and 4.52 provide summaries of best classification results as achieved on the individual binary OCTA image classification tasks previously conducted, namely healthy vs wet AMD, dry AMD vs wet AMD and CNV vs non-CNV, respectively. The optimal components, e.g.: best local texture descriptors and best classifiers, for solving the various binary OCTA image classification tasks in the context of AMD disease, i.e.: healthy vs wet AMD, dry AMD vs wet AMD and CNV vs non-CNV, which facilitated improving the classification performance, are also given.

At a quick glance over the summary of best classification results presented in Tables 4.50, 4.51 and 4.52, broadly, the best local texture descriptor is the $LBP_{p,r}^{2riu}$ texture descriptor in most binary classification problems, i.e.: healthy vs wet AMD, dry AMD vs wet AMD and CNV vs non-CNV. However, the best classification scheme varies among the different binary classification problems. In most classification settings, the

Table 4.48: The evaluation results (sensitivity scores) of the classifiers trained on the OCTA image data set for the Manchester healthy versus Moorfields wet AMD classification task to distinguish the wet AMD cases of Manchester OCTA image data set.

Ocular Vascular Layers	Descriptor	Classifier	Sensitivity score
Superficial inner retina layer	$LBP_{4,1}^{2riu}$	KNN ($D_{euclidean}^{k=3}$)	0.13
Deep inner retina layer	$LBP_{16,4}^{2riu}$	KNN ($D_{euclidean}^{k=3}$)	0.09
Outer retina layer	$LBP_{16,4}^{2riu}$	KNN ($D_{euclidean}^{k=3}$)	0.43
Choriocapillaris layer	$LBP_{16,4}^{2riu}$	SVM ($K_{linear}^{C=10}$)	1.00
Superficial + Deep	$LBP_{4,1}^{2riu}$	SVM ($K_{linear}^{C=1}$)	0.17
Superficial + Outer	$LBP_{16,4}^{2riu}$	KNN ($D_{euclidean}^{k=1}$)	0.39
Superficial + Choriocapillaris	$LBP_{12,3}$	KNN ($D_{manhattan}^{k=3}$)	0.52
Deep + Outer	$LBP_{16,4}^{2riu}$	KNN ($D_{euclidean}^{k=1}$)	0.39
Deep + Choriocapillaris	$LBP_{16,4}$	KNN ($D_{manhattan}^{k=5}$)	0.48
Outer + Choriocapillaris	$LBP_{16,4}^{2riu}$	KNN ($D_{euclidean}^{k=3}$)	0.91
Superficial + Deep + Outer	$LBP_{16,4}^{2riu}$	KNN ($D_{euclidean}^{k=3}$)	0.30
Superficial + Deep + Choriocapillaris	$LBP_{16,4}$	KNN ($D_{manhattan}^{k=5}$)	0.35
Superficial + Outer + Choriocapillaris	$LBP_{16,4}^{2riu}$	KNN ($D_{euclidean}^{k=3}$)	0.65
Deep + Outer + Choriocapillaris	$LBP_{16,4}^{2riu}$	KNN ($D_{euclidean}^{k=3}$)	0.78
All ocular vascular layers	$LBP_{12,3}^{2riu}$	KNN ($D_{euclidean}^{k=3}$)	0.78

optimal classifier for the dry AMD vs wet AMD and CNV vs non-CNV classification tasks is the SVM classifier. The optimal classifier for the healthy vs wet AMD classification task, however, is the KNN classifier in most classification settings.

Nevertheless, based on the individual binary classification problems, it can be clearly observed that the most predictive ocular vascular layer for solving the two different binary OCTA image classification tasks, i.e.: healthy vs wet AMD and CNV vs non-CNV, is the outer retina layer. In solving the healthy vs wet AMD classification task, the automated OCTA image classification algorithm performed outstandingly. As such the classification algorithm was able to accomplish a perfect classification performance, i.e.: a mean AUC score and a standard deviation = 1.00 ± 0.00 , using the $LBP_{16,4}^{2riu}$ texture descriptor and the KNN classifier with ($D_{euclidean}^{k=3}$). This was achieved when concatenating two feature vectors extracted from two OCTA images of the outer retina and the choriocapillaris layers.

For the CNV vs non-CNV classification task, on the other hand, the automated OCTA image classification algorithm performed reasonably as demonstrated in the classification results in Table 4.52. As such the algorithm was able to achieve a mean

Table 4.49: The evaluation results (sensitivity scores) of the classifiers trained on the OCTA image data set for the Moorfields dry AMD versus Manchester wet AMD classification task to distinguish the wet AMD cases of Moorfields OCTA image data set.

Ocular Vascular Layers	Descriptor	Classifier	Sensitivity score
Superficial inner retina layer	$LBP_{4,1}^{2riu}$	SVM ($K_{linear}^{C=1}$)	0.10
Deep inner retina layer	$LBP_{16,4}^{2riu}$	SVM ($K_{linear}^{C=1}$)	0.10
Outer retina layer	$LBP_{16,4}^{2riu}$	SVM ($K_{linear}^{C=1}$)	0.30
Choriocapillaris layer	$LBP_{12,3}^{2riu}$	SVM ($K_{rbf}^{C=50, \gamma=0.1}$)	0.40
Superficial + Deep	$LBP_{4,1}^{2riu}$	SVM ($K_{poly}^{C=1, d=2}$)	0.08
Superficial + Outer	$LBP_{12,3}$	KNN ($D_{manhattan}^{k=3}$)	0.18
Superficial + Choriocapillaris	$LBP_{4,1}^{2riu}$	SVM ($K_{linear}^{C=10}$)	0.21
Deep + Outer	$LBP_{8,2}^{2riu}$	SVM ($K_{poly}^{C=1, d=3}$)	0.20
Deep + Choriocapillaris	$LBP_{12,3}^{2riu}$	SVM ($K_{poly}^{C=1, d=3}$)	0.20
Outer + Choriocapillaris	$LBP_{12,3}^{2riu}$	SVM ($K_{poly}^{C=10, d=3}$)	0.42
Superficial + Deep + Outer	$LBP_{8,2}^{2riu}$	SVM ($K_{poly}^{C=10, d=3}$)	0.22
Superficial + Deep + Choriocapillaris	$LBP_{4,1}^{2riu}$	SVM ($K_{poly}^{C=10, d=3}$)	0.23
Superficial + Outer + Choriocapillaris	$LBP_{8,2}$	SVM ($K_{poly}^{C=10, d=3}$)	0.24
Deep + Outer + Choriocapillaris	$LBP_{8,2}^{2riu}$	SVM ($K_{poly}^{C=10, d=3}$)	0.27
All ocular vascular layers	$LBP_{8,2}^{2riu}$	SVM ($K_{linear}^{C=100}$)	0.43

Table 4.50: A summary of best classification results (mean AUC scores \pm standard deviations) as achieved by the automated OCTA image classification algorithm proposed for solving the healthy vs wet AMD classification task based on whole-local texture features.

Ocular Vascular Layers	Optimal Descriptors	Optimal Classifiers	AUC \pm std
Superficial inner retina layer	$LBP_{4,1}^{2riu}$	KNN ($D_{euclidean}^{k=3}$)	0.89 \pm 0.05
Deep inner retina layer	$LBP_{16,4}^{2riu}$	KNN ($D_{euclidean}^{k=3}$)	0.96 \pm 0.04
Outer retina layer	$LBP_{all\ values}^{2riu} / LBP_{all\ values}$	KNN ($D_{euclidean}^{k=3}$) / SVM ($K_{linear}^{C=1}$)	0.99 \pm 0.00
Choriocapillaris layer	$LBP_{16,4}^{2riu}$	SVM ($K_{linear}^{C=10}$)	0.97 \pm 0.03
Superficial + Deep	$LBP_{4,1}^{2riu}$	SVM ($K_{linear}^{C=1}$)	0.94 \pm 0.03
Superficial + Outer	$LBP_{16,4}^{2riu}$	KNN ($D_{euclidean}^{k=1}$)	0.98 \pm 0.02
Superficial + Choriocapillaris	$LBP_{12,3}$	KNN ($D_{manhattan}^{k=3}$)	0.94 \pm 0.04
Deep + Outer	$LBP_{16,4}^{2riu}$	KNN ($D_{euclidean}^{k=1}$)	0.98 \pm 0.01
Deep + Choriocapillaris	$LBP_{16,4}$	KNN ($D_{manhattan}^{k=5}$)	0.98 \pm 0.01
Outer + Choriocapillaris	$LBP_{16,4}^{2riu}$	KNN ($D_{euclidean}^{k=3}$)	1.00 \pm 0.00
Superficial + Deep + Outer	$LBP_{16,4}^{2riu}$	KNN ($D_{euclidean}^{k=3}$)	0.98 \pm 0.01
Superficial + Deep + Choriocapillaris	$LBP_{16,4}$	KNN ($D_{manhattan}^{k=5}$)	0.98 \pm 0.02
Superficial + Outer + Choriocapillaris	$LBP_{16,4}^{2riu}$	KNN ($D_{euclidean}^{k=3}$)	0.97 \pm 0.02
Deep + Outer + Choriocapillaris	$LBP_{16,4}^{2riu}$	KNN ($D_{euclidean}^{k=3}$)	0.98 \pm 0.03
All ocular vascular layers	$LBP_{12,3}^{2riu}$	KNN ($D_{euclidean}^{k=3}$)	0.99 \pm 0.03

Table 4.51: A summary of best classification results (mean AUC scores \pm standard deviations) as achieved by the automated OCTA image classification algorithm proposed for solving the dry AMD vs wet AMD classification task based on whole-local texture features.

Ocular Vascular Layers	Optimal Descriptors	Optimal Classifiers	AUC \pm std
Superficial inner retina layer	$LBP_{4,1}^{2riu}$	SVM ($K_{linear}^{C=1}$)	0.71 ± 0.06
Deep inner retina layer	$LBP_{16,4}^{2riu}$	SVM ($K_{linear}^{C=1}$)	0.75 ± 0.04
Outer retina layer	$LBP_{16,4}^{2riu}$	SVM ($K_{linear}^{C=1}$)	0.83 ± 0.03
Choriocapillaris layer	$LBP_{12,3}^{2riu}$	SVM ($K_{rbf}^{C=50, \gamma=0.1}$)	0.83 ± 0.01
Superficial + Deep	$LBP_{4,1}^{2riu}$	SVM ($K_{poly}^{C=1, d=2}$)	0.71 ± 0.09
Superficial + Outer	$LBP_{12,3}$	KNN ($D_{manhattan}^{k=3}$)	0.74 ± 0.05
Superficial + Choriocapillaris	$LBP_{4,1}^{2riu}$	SVM ($K_{linear}^{C=10}$)	0.76 ± 0.05
Deep + Outer	$LBP_{8,2}^{2riu}$	SVM ($K_{poly}^{C=1, d=3}$)	0.75 ± 0.05
Deep + Choriocapillaris	$LBP_{12,3}^{2riu}$	SVM ($K_{poly}^{C=1, d=3}$)	0.78 ± 0.06
Outer + Choriocapillaris	$LBP_{12,3}^{2riu}$	SVM ($K_{poly}^{C=10, d=3}$)	0.77 ± 0.06
Superficial + Deep + Outer	$LBP_{8,2}^{2riu}$	SVM ($K_{poly}^{C=10, d=3}$)	0.79 ± 0.07
Superficial + Deep + Choriocapillaris	$LBP_{4,1}^{2riu}$	SVM ($K_{poly}^{C=10, d=3}$)	0.79 ± 0.06
Superficial + Outer + Choriocapillaris	$LBP_{8,2}$	SVM ($K_{poly}^{C=10, d=3}$)	0.78 ± 0.05
Deep + Outer + Choriocapillaris	$LBP_{8,2}^{2riu}$	SVM ($K_{poly}^{C=10, d=3}$)	0.80 ± 0.06
All ocular vascular layers	$LBP_{8,2}^{2riu}$	SVM ($K_{linear}^{C=100}$)	0.79 ± 0.04

AUC score and a standard deviation = 0.82 ± 0.03 using the $LBP_{16,4}^{2riu}$ texture descriptor and the SVM classifier with ($K_{linear}^{C=1}$) given the great difficulties to distinguish the abnormalities, i.e.: CNV and non-CNV lesions in the OCTA images. This is mainly due to the extreme similarities between the patterns of vascular pathologies, i.e.: CNV and non-CNV lesions, in the OCTA images. A comparable performance was also achieved using the $LBP_{12,3}$ texture descriptor and the KNN classifier with ($D_{manhattan}^{k=5}$) when concatenating three feature vectors extracted from three OCTA images of various ocular vascular layers. These are the deep inner, the outer retina and the choriocapillaris layers.

Nevertheless, based on the summary of best classification results in Table 4.51, the most predictive ocular vascular layer, with rich details about vascular pathologies related to dry AMD and wet AMD disease, which can be the most appropriate for solving the dry AMD vs wet AMD classification task, is the choriocapillaris layer closely followed by the outer retina layer. Likewise, differentiating the vascular pathologies related to dry AMD and wet AMD disease from each other is also quite challenging due to the great similarities between vascular patterns of dry AMD and wet AMD in the OCTA images.

Table 4.52: A summary of best classification results (mean AUC scores \pm standard deviations) as achieved by the automated OCTA image classification algorithm proposed for solving the CNV vs non-CNV classification task based on whole-local texture features.

Ocular Vascular Layers	Optimal Descriptors	Optimal Classifiers	AUC \pm std
Superficial inner retina layer	$LBP_{8,2}^{2riu}$	SVM ($K_{linear}^{C=1}$)	0.70 \pm 0.05
Deep inner retina layer	$LBP_{12,3}^{2riu}$	SVM ($K_{linear}^{C=1}$)	0.72 \pm 0.03
Outer retina layer	$LBP_{16,4}^{2riu}$	SVM ($K_{linear}^{C=1}$)	0.82 \pm 0.03
Choriocapillaris layer	$LBP_{16,4}^{2riu}$	SVM ($K_{linear}^{C=1}$)	0.81 \pm 0.04
Superficial + Deep	$LBP_{4,1}^{2riu}$	SVM ($K_{poly}^{C=10,d=3}$)	0.68 \pm 0.04
Superficial + Outer	$LBP_{8,2}^{2riu}$	SVM ($K_{poly}^{C=10,d=3}$)	0.79 \pm 0.06
Superficial + Choriocapillaris	$LBP_{8,2}^{2riu}$	SVM ($K_{poly}^{C=10,d=3}$)	0.75 \pm 0.06
Deep + Outer	$LBP_{8,2}^{2riu}$	SVM ($K_{poly}^{C=10,d=3}$)	0.79 \pm 0.07
Deep + Choriocapillaris	$LBP_{12,3}$	KNN ($D_{manhattan}^{k=5}$)	0.76 \pm 0.04
Outer + Choriocapillaris	$LBP_{8,2}^{2riu}$	SVM ($K_{poly}^{C=10,d=3}$)	0.82 \pm 0.04
Superficial + Deep + Outer	$LBP_{8,2}^{2riu}$	SVM ($K_{poly}^{C=10,d=3}$)	0.80 \pm 0.07
Superficial + Deep + Choriocapillaris	$LBP_{8,2}^{2riu}$	SVM ($K_{poly}^{C=10,d=3}$)	0.77 \pm 0.05
Superficial + Outer + Choriocapillaris	$LBP_{12,3}^{2riu}$	KNN ($D_{manhattan}^{k=5}$)	0.82 \pm 0.04
Deep + Outer + Choriocapillaris	$LBP_{12,3}$	KNN ($D_{manhattan}^{k=5}$)	0.82 \pm 0.03
All ocular vascular layers	$LBP_{12,3}$	KNN ($D_{manhattan}^{k=7}$)	0.81 \pm 0.03

Despite identification of variations between dry AMD and wet AMD in the OCTA images being very difficult, the classification algorithm was able to achieve reasonable classification results, i.e.: mean AUC scores \pm standard deviations = 0.83 ± 0.01 and 0.83 ± 0.03 on the choriocapillaris and the outer retina layers, respectively. The optimal texture descriptors and classifiers for classifying dry AMD from wet AMD cases are the $LBP_{12,3}^{2riu}$ and the SVM with ($K_{rbf}^{C=50,\gamma=0.1}$) for the OCTA images of the choriocapillaris layer and the $LBP_{16,4}^{2riu}$ and the SVM with ($K_{linear}^{C=1}$) for the OCTA images of the outer retina layer.

From the cross-corpora experiments perspective, however, the classifiers trained on the Manchester OCTA image data set for solving the healthy vs wet AMD classification task to distinguish the wet AMD cases of the Moorfields OCTA image data set, generally, demonstrated good generalisation performance. In some situations, a near perfect sensitivity score, i.e.: 0.99, was accomplished on the outer retina layer and a perfect sensitivity score, i.e.: 1.00, was achieved when concatenating two feature vectors extracted from two OCTA images of the outer retina and the choriocapillaris layers. On the other hand, the classifiers trained on the Moorfields OCTA image data set for solving the dry AMD vs wet AMD classification task to distinguish the wet

AMD cases of the Manchester OCTA image data set, broadly, showed perfect generalisation scores in most classification situations.

While there are numerous studies [6, 10, 243, 244] concerning the analysis of OCTA images in the context of AMD disease in an automated manner, these studies are all based on image segmentation rather than image classification. Although there are a few studies [245, 246] that aim to automate the analysis of OCTA images in the context of AMD disease by the means of image classification, these studies are based on specialised deep learning technologies that require large OCTA data sets, require OCTA images that are manually depth levels adjusted to get the best possible view of vascular abnormalities, and so on. Comprehensive details with regard to these works including the pros and cons have already been discussed in Chapter 3, specifically subsection 3.5.2.2. Hence, comparing the results of these works with the optimal classification results given in Tables 4.50, 4.51 and 4.52 or applying these works to the current OCTA image data sets can, therefore, be misleading.

4.6 Chapter Conclusion

This chapter presented a fully automated OCTA image classification algorithm for the diagnosis of AMD disease based on whole-local texture features. The chapter started by providing details about the motivations of enabling the automated analysis of OCTA images in the context of AMD disease by means of whole image classification. Furthermore, the justifications for making the various selections comprising conducting the analysis on the entire OCTA image of individual retinal and choroidal layers, selecting certain local texture descriptors as texture representation techniques, and selectively picking certain machine learning algorithms for accompanying the various OCTA image classification tasks, among other choices considered in the automated algorithm, are also provided. Afterwards, the outline of the automated classification algorithm, including the manner of extracting the local texture features from whole OCTA images and the way of classifying the various OCTA images with different ocular conditions including AMD disease as well as healthy, are also illustrated. Finally, comprehensive evaluation of the automated classification algorithm proposed, including performance comparison of the evaluation results, are also given.

Chapter 5

Classification Algorithm Based on Reduced-Local Texture Features

5.1 Chapter Introduction

This chapter provides a fully automated OCTA image classification algorithm for the diagnosis of AMD disease based on reduced-local texture features. The chapter begins by providing details about the motivation for enabling the automated analysis of OCTA images in the context of AMD disease by means of whole image classification using only a reduced set of local texture features. The justification for the decision to employ the dimensionality reduction technique, i.e.: the *PCA* technique, to transform the original features, i.e.: whole-local texture features, into a new much smaller set of transformed local texture features, i.e.: reduced-local texture features, is also provided. Additionally, comprehensive descriptions of the steps involved in the automated classification algorithm are also given. These include details about the methods of extracting the local texture features from the whole OCTA image, the manners of applying the *PCA* technique to decorrelate the local texture features extracted and the ways of performing the classification on the various OCTA images of different ocular conditions including dry AMD and wet AMD as well as healthy. Finally, comprehensive evaluation of the automated classification algorithm proposed in this chapter, including performance comparisons of optimum results obtained from the automated classification algorithm proposed in Chapter 4, are also given.

5.2 Motivation

Recall that the texture representation phase, i.e.: the local texture feature extraction step, always plays a crucial role behind successfully accomplishing various image texture analysis problems such as classification or segmentation. Specifically, the design or choice of a decent local texture feature extraction method can be wasted when selecting a poor classification scheme and likewise the design or choice of a poor local texture feature method cannot survive even when choosing a sophisticated classification scheme. Similar importance, the high dimensional and highly correlated aspects of the local texture features can also have a critical impact on the performance of the machine learning classification algorithms, e.g.: the KNN and the SVM classifiers, that are used for solving image texture analysis problems, e.g.: classification.

Inspired by the importance of the local texture feature extraction step as well as the outstanding classification results achieved by the automated classification algorithm proposed in Chapter 4, this chapter explores the potential of improving the classification performance by attempting to design a domain specific and well-representative reduced set of local texture features. To explore the possibility of achieving this, exploiting the dimensionality reduction techniques, e.g.: the *PCA* technique, after extracting the local texture features from the texture of OCTA images, is investigated. The motivations of designing a reduced set of local texture features to enable the automated analysis of OCTA images in the context of AMD disease by the means of whole image classification as well as selectively employing the *PCA* technique to generate the set of reduced-local texture features are justified under the following two bullet points.

- **Enable a fully automated OCTA image analysis for AMD detection by the means of whole image classification based on reduced-local texture features.**

The design of a reduced set of local texture features to measure normal vascular and abnormal vascular appearance due to AMD disease in the OCTA images was mainly motivated by the fact that when the number of sampling points increase, i.e.: (p and r) for the $LBP_{p,r}^{2riu}$ and the $LBP_{p,r}$ texture descriptors and (S and n) for the $BRIEF_{S,n}$ texture descriptor, the dimensionality of the local texture features that are constructed by these texture descriptors also increase. The possible negative impacts of having high dimensional feature space, i.e.: staggeringly numerous local texture features, that measure certain conditions or classes can, however, comprise introducing correlation or redundancies between local texture features of various classes or conditions to be

distinguished between. As such, the more local texture features that represent a certain class, the more chance of becoming very sparse and less discriminative, hence potentially less relevant to the class of interest. Comprehensive details in this regard, however, have already been discussed across various aspects in Chapter 2, specifically section 2.6.

Nevertheless, as the analysis of the OCTA images is performed without targeting any specific area in the OCTA image, i.e.: based on the entire OCTA image, utilising the whole local texture features extracted for performing the image classification task can also be inadequate. This is because the OCTA images with AMD disease comprise vascular regions of both healthy as well as AMD disease related lesions, e.g.: non-CNV and CNV. Consequently, some of the local texture features extracted from the OCTA images that represent only the healthy condition may be correlated with some of the local texture features obtained from the OCTA images that represent the AMD conditions, e.g.: dry or wet AMD disease. Hence, this may introduce some redundancies in the local texture features that describe and quantify the individual eye conditions, i.e.: healthy and dry or wet AMD disease. Nonetheless, redundant or correlated local texture features that measure different classes of eye conditions, e.g.: healthy and dry or wet AMD disease, can dramatically impact the performance of the classification scheme used, hence accomplishing the image classification task in hand successfully.

When taking these details into account, it becomes obvious that the techniques which can transform a large number of dimensions in the feature space, i.e.: the original local texture features, into a reduced set of local texture features but which comprises the essence of important details highly relevant to solving the task of interest, are profoundly desirable. The construction of new low dimensional features, i.e.: reduced-local texture features, in the sense that they are more predictive of the outcomes and are very closely related to solving the task of interest, can also be extremely beneficial from a feature engineering perspective. As such the reduced-local texture features may not only help to eliminate the risk of potential overfitting and perhaps improve the performance of solving various image texture analysis tasks such as classification but also can help accomplishing the classification task at significantly reduced computational costs.

- **Exploiting the dimensionality reduction techniques, i.e.: the PCA technique, to generate the set of reduced-local texture features.**

Several techniques can be employed for the task of reducing the number of local

texture features extracted from the texture of OCTA images. These techniques are typically grouped under two broad categories, namely dimensionality reduction and feature selection. Important details including examples with respect to the two different categories have already been given and comprehensively discussed across various aspects in Chapter 2, section 2.6. Nevertheless, the main motivation for selectively exploiting the *PCA* technique that fall under the category of dimensionality reduction techniques is to investigate whether eliminating the redundancy or correlation between the local texture features extracted from the texture of OCTA images of different eye conditions, e.g.: dry AMD, wet AMD and healthy, can improve the classification performance. As such, the *PCA* technique can address the high dimensional and highly correlated aspects of local texture features in an interpretable fashion while maintaining most of the important information in the original feature space.

If the classification relationship between the local texture features and the individual classes of interest, i.e.: dry AMD, wet AMD and healthy, is linked to the variability of local texture features, then the decorrelated or reduced-local texture features, after applying the *PCA* technique, may potentially provide an effective and appropriate relationship with the individual target classes to be discriminated, hence facilitating an effective solution to the image classification problem in hand. This fundamental aspect can make the automated OCTA image classification algorithm less biased since the *PCA* technique can help to eliminate or remove redundant local texture features. Other advantages of exploiting the *PCA* technique can include improving the accuracy of the classification algorithm as it may reduce the occurrence of misrepresentative local texture features. Besides these features, the application of *PCA* technique can also help to reduce the time taken for training the machine learning classification algorithms, e.g.: the SVM classifier, since the classifier makes use of feature vectors of much lower dimensionality, among other advantages, see Chapter 2, subsection 2.6.1.

5.3 Proposed Algorithm

The automated OCTA image texture analysis algorithm proposed in this chapter follows a comparable pipeline of the previous algorithm proposed in Chapter 4 but with an additional step of feature dimensionality reduction. Hence, the framework of the automated OCTA image texture analysis algorithm proposed for AMD disease detection by the means of image classification based on reduced-local texture features involves four main steps in total. The first step is the local texture feature extraction, the second

step is the data pre-processing, the third step is the feature dimensionality reduction, and the fourth step is the classification. Figure 5.1 demonstrates a brief overview of the analysis pipeline that is followed by the automated OCTA image classification algorithm proposed. The four different steps involved are comprehensively explained in the following subsections 5.3.1, 5.3.2, 5.3.3 and 5.3.4, respectively.

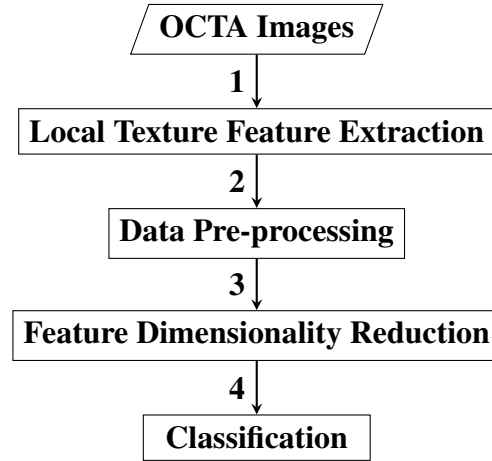


Figure 5.1: An outline of the automated OCTA image texture analysis algorithm that is proposed for AMD disease detection by the means of image classification based on reduced-local texture features. The analysis procedure begins with taking the OCTA images as an input where the local texture feature extraction step takes place first to quantify the textural appearance of OCTA images. A data pre-processing step is then followed, which involves applying data transformation techniques, specifically data centring and scaling techniques to the local texture features extracted. The following step is the feature dimensionality reduction that applies the *PCA* technique to decorrelate the extracted local texture features generating a representative and reduced set of local texture features. Finally, the classification step is followed to perform classifications using the reduced-local texture features which measure the various OCTA images to classify them based on the ocular conditions they represent, e.g.: dry AMD, wet AMD and healthy.

5.3.1 Local Texture Feature Extraction

The overall objective of the local texture feature extraction step is to measure the textural appearance of various OCTA images in the presence of different ocular conditions, dry AMD, wet AMD and healthy. The same three different texture descriptors, namely the $LBP_{p,r}^{2riu}$, the $LBP_{p,r}$ and the $BRIEF_{S,n}$, employed in the local texture feature extraction step of the previous classification algorithm proposed in Chapter 4 are also individually evaluated in this step. Recall that the classification algorithm proposed

in this chapter follows a comparable procedure of the local texture feature extraction step of the previous classification algorithm proposed in Chapter 4. Hence, the local texture features in this step are estimated from the texture of various OCTA images in a similar manner to that followed in the previous Chapter 4, see subsection 4.3.1. Consequently, the final outputs of this step are several histograms, i.e.: several feature vectors. These several feature vectors estimate or accumulate the distribution of all various local texture features or patterns, i.e.: whole-local texture features, that are detected in the individual OCTA images.

5.3.2 Data Pre-processing

Once the original feature vectors that comprise whole-local texture features of individual OCTA images with different ocular vascular conditions related to AMD disease and healthy are constructed in the previous step, see subsection 5.3.1, the task of data pre-processing step is to apply two different data transformation techniques, specifically data centring and scaling techniques to the whole-local texture features of original feature vectors. This is to ensure the individual local texture features of original feature vectors contribute equally to estimating the new reduced feature vectors in the following feature dimensionality reduction step 5.3.3.

The main motivation of employing these data transformation techniques is that the textural appearance varies between the diseased OCTA images. As such in some situations the textural appearance of vascular abnormalities appear to dominate the whole diseased OCTA images while in other situation appear very comparable to the healthy OCTA images. Therefore, transforming the whole-local texture features of original feature vectors to comparable scales can make the *PCA* technique less biased to the individual local texture features that have high range values during the process of estimating the reduced feature vectors. This aspect, however, has already been comprehensively discussed in Chapter 2, subsection 2.6.1.

As two data transformation techniques, i.e.: data centring and scaling techniques, will be applied on the original feature vectors, the entire original feature vectors that comprise whole-local texture features of individual OCTA images can, therefore, be written as an $N \times F$ data matrix D as follows:

$$D_{N \times F} = \begin{bmatrix} x_{(11)} & x_{(12)} & \cdots & x_{(1F)} \\ x_{(21)} & x_{(22)} & \cdots & x_{(2F)} \\ \vdots & \vdots & \vdots & \vdots \\ x_{(N1)} & x_{(N2)} & \cdots & x_{(NF)} \end{bmatrix}$$

Where x denotes the local texture features, the subscript N represents the total number of OCTA images, and the subscript F indicates the total number of local texture features. Hence, in the data matrix D , the N rows represent the different OCTA images, and the F columns demonstrate the various local texture features. As the data centring and scaling techniques, are applied, the mean μ and the standard deviation σ of individual columns, i.e.: individual F local texture features, are estimated from the data matrix D . Hence, the mean μ of each F local texture feature, i.e.: every single column in the data matrix D , can be mathematically computed by the following formula 5.1:

$$\mu_F = \frac{1}{N} \sum_{i=1}^N x_{(iF)} \quad (5.1)$$

The standard deviation σ of each F local texture feature, i.e.: every single column in the data matrix D , can therefore be mathematically calculated by the following formula 5.2:

$$\sigma_F = \sqrt{\frac{\sum_{i=1}^N (x_{(iF)} - \mu_F)^2}{N}} \quad (5.2)$$

Once the μ_F and σ_F of all F local texture features, i.e.: all different columns in the data matrix D , are estimated, every single $x_{(iF)}$ is substituted with $\frac{x_{(iF)} - \mu_F}{\sigma_F}$ in the original data matrix D . This process generates a standardised data matrix SD of the original data matrix D . Therefore, the standardised data matrix SD can be written as follows:

$$SD_{N \times F} = \begin{bmatrix} \frac{x_{(11)} - \mu_1}{\sigma_1} & \frac{x_{(12)} - \mu_2}{\sigma_2} & \cdots & \frac{x_{(1F)} - \mu_F}{\sigma_F} \\ \frac{x_{(21)} - \mu_1}{\sigma_1} & \frac{x_{(22)} - \mu_2}{\sigma_2} & \cdots & \frac{x_{(2F)} - \mu_F}{\sigma_F} \\ \vdots & \vdots & \vdots & \vdots \\ \frac{x_{(N1)} - \mu_1}{\sigma_1} & \frac{x_{(N2)} - \mu_2}{\sigma_2} & \cdots & \frac{x_{(NF)} - \mu_F}{\sigma_F} \end{bmatrix}$$

5.3.3 Feature Dimensionality Reduction

Once the standardised data matrix SD that comprise whole-local texture features of individual OCTA images with different ocular vascular conditions related to AMD disease and healthy is constructed in the previous step, see subsection 5.3.2, the task of the feature dimensionality reduction step is to decorrelate the individual local texture features of the original feature vectors by applying the *PCA* technique. The application of the *PCA* technique generates a new transformed set of reduced-local texture features, i.e.: new reduced feature vectors, that seek to capture the vast majority of the important information in the whole-local texture features of original feature vectors.

In this manner, a much smaller size of feature vectors can be utilised which provide reasonable fidelity to the original size. The reduced feature vectors are functions of the original feature vectors. Therefore, the whole-local texture features in the original feature vectors are yet required to generate the substitute ones, i.e.: the reduced feature vectors. However, the theoretical foundation and important properties of the *PCA* technique as well as illustrative examples have already been demonstrated in Chapter 2, subsection 2.6.1.

As the standardised data matrix SD is constructed, the typical initial step in the *PCA* technique is to transpose the data matrix SD , i.e.: flipped over its diagonal, to produce the transpose of data matrix SD that is denoted by SD^T . The transposed data matrix SD^T can, therefore, be written as follows:

$$SD_{F \times N}^T = \begin{bmatrix} x_{(11)} & x_{(12)} & \cdots & x_{(1N)} \\ x_{(21)} & x_{(22)} & \cdots & x_{(2N)} \\ \vdots & \vdots & \vdots & \vdots \\ x_{(F1)} & x_{(F2)} & \cdots & x_{(FN)} \end{bmatrix}$$

Once the transposed data matrix SD^T is constructed, the following step is to compute the covariance matrix Σ using the standardised data matrix SD and its transpose form, i.e.: data matrix SD^T . In the case of the standardised data, i.e.: with mean = zero and standard deviation = one, the covariance matrix Σ can, therefore, be estimated by equation 2.37 given in Chapter 2, subsection 2.6.1.

The resultant covariance matrix Σ has the dimensions of $F \times F$. Once the covariance matrix Σ is constructed, the following step is to estimate the principal components, i.e.: *PCs*. The *PCs* are found by computing the individual eigenvectors ϕ and corresponding eigenvalues λ of the computed covariance matrix Σ . Let the total variance (*TV*)

in the original data be estimated as the sum of all F eigenvalues λ of the estimated covariance matrix Σ which is given by equation 2.38 in Chapter 2, subsection 2.6.1. Hence, the proportion of the variance (PV_i) that the i^{th} eigenvector ϕ is accounted for can be estimated by equation 2.39 given in Chapter 2, subsection 2.6.1.

Nevertheless, the individual F eigenvalues λ are sorted in descending order, i.e.: arranged such that $(\lambda_j \geq \lambda_{j+1})$. Then, a set Φ of K eigenvectors ϕ , where $\Phi = [\phi_1, \phi_2, \dots, \phi_K]$ and typically $K < F$, of the computed covariance matrix Σ which have the K largest eigenvalues λ is selected to reduce the dimensions of original data. As such the eigenvector ϕ_1 with the greatest eigenvalue λ_1 represents the first *PC* or direction of maximum variation. The eigenvector ϕ_2 with the second greatest eigenvalue λ_2 represents the second *PC* or direction of the next maximum variation that is orthogonal to the previous *PC* and so on.

However, the K eigenvectors ϕ corresponding to the K largest eigenvalues λ are typically selected based on a predefined proportion of the total variance, e.g.: 95 for 95%, that one desires to retain. Consequently, the set Φ of K eigenvectors ϕ that retains a certain proportion, e.g.: 95% of the total variance of the original data can be constructed based on the sum of the proportion of the variance (PV_i) accounted for by individual K eigenvectors ϕ that have the K largest eigenvalues λ as follows in 5.3:

$$\sum_{i=1}^K PV_i \geq 95 \quad (5.3)$$

Once the K eigenvectors ϕ that have the K largest eigenvalues λ are selected which explain the previously defined proportion, i.e.: 95 for 95% of the variance exhibited in the original data, the selected set Φ of K eigenvectors ϕ constructs the set of *PCs* that will be used to create the new transformed features in place of the original local texture features in the original data. The final step in the *PCA* technique is, therefore, the projection of the original data into a new subspace of reduced features via matrix multiplication of the original data with the selected set Φ of K eigenvectors ϕ . This ultimate step constructs the new reduced feature vectors that comprise a new transformed set of reduced-local texture features which measure the individual OCTA images.

In this work, the new reduced feature vectors constructed in the feature dimensionality reduction step retained 95% of the variance exhibited in the original data which is a common percentage widely used when applying the *PCA* technique. As the various local texture features constructed by the three different texture descriptors, namely the $LBP_{p,r}^{2riu}$, the $LBP_{p,r}$ and the $BRIEF_{S,n}$ are all transformed into new reduced features,

the individual texture descriptors are denoted as the $LBP_{p,r}^{2riuPCA}$, the $LBP_{p,r}^{PCA}$ and the $BRIEF_{S,n}^{PCA}$, the additional superscript PCA reflecting the application of the PCA technique on the local texture features extracted. Hence, the newly reduced feature vectors that comprise reduced-local texture features, therefore, construct the final design of feature vectors that form the basis of accomplishing the automated analysis of OCTA image texture by means of image classification.

5.3.4 Classification

Once the newly reduced feature vectors of individual OCTA images are constructed, the overall objective of the classification step is to classify the different eyes as belonging to one of the different predefined classes of eye conditions, e.g.: healthy, wet AMD or CNV and dry AMD or non-CNV. To achieve this, two different machine learning classification algorithms, namely the SVM and the KNN classifiers, are employed and tested for the task of image classification. Like the classification step of the previous classification algorithm proposed in Chapter 4 that is illustrated in subsection 4.3.2, a hyper-parameter search was also conducted for the KNN and the SVM classifiers using the same hyper-parameter values. The optimal hyper-parameter combinations of the individual classifiers that enable achieving the best classification performance as evaluated via a cross-validation strategy are subsequently selected. The following section 5.4 provides a comprehensive evaluation of the classification algorithm proposed.

5.4 Experimental Evaluation and Results

The evaluation of the classification algorithm proposed in this chapter was conducted on the diverse OCTA image data sets previously described in Chapter 3, section 3.4. The evaluation procedure followed in this chapter is the same as the evaluation procedure conducted in Chapter 4, section 4.4. Consequently, the automated image analysis of the Manchester Royal Eye Hospital OCTA image data set is conducted as a binary image classification problem, i.e.: healthy versus wet AMD. The automated image analysis of the Moorfields Eye Hospital OCTA image data set, on the other hand, is conducted as two binary image classification problems, i.e.: dry AMD versus wet AMD and CNV (wet AMD plus secondary CNV) versus non-CNV (dry AMD).

Similar to the evaluation procedure followed in Chapter 4, section 4.4, the binary image classifications in this chapter were also performed in the following manners for

both OCTA image data sets of the Manchester Royal Eye Hospital and the Moorfields Eye Hospital:

1. Based on individual feature vectors extracted from OCTA images of every separate ocular vascular layer namely the superficial inner retina, the deep inner retina, the outer retina and the choriocapillaris layers, respectively. In this manner, the classification is performed solely based on the individual ocular vascular layer for every single eye.
2. Based on concatenating two feature vectors extracted from two OCTA images of the ocular vascular layers. These are (1) the superficial and the deep inner retina layers, (2) the superficial inner and the outer retina layers, (3) the superficial inner and the choriocapillaris layers, (4) the deep inner and the outer retina layers, (5) the deep inner retina and the choriocapillaris layers, and (6) the outer retina and the choriocapillaris layers that are both typically used for diagnosing AMD disease. The concatenated two feature vectors generated by the various two layers construct a global feature vector for every individual eye. Consequently, the classification is performed based on the global feature vectors constructed for the individual eyes.
3. Based on concatenating three feature vectors extracted from three OCTA images of the ocular vascular layers. These are (1) the superficial, the deep inner and the outer retina layers, (2) the superficial, the deep inner retina and the choriocapillaris layers, (3) the superficial inner, the outer retina and the choriocapillaris layers and (4) the deep inner, the outer retina and the choriocapillaris layers. The concatenated three feature vectors generated from the various three layers construct a global feature vector for every individual eye. Consequently, the classification is performed based on the global feature vectors constructed for the individual eyes.
4. Based on concatenating all feature vectors extracted from all OCTA images of all ocular vascular layers constructing a global feature vector for every individual eye. Hence, the classification is performed based on the individual eyes not the individual ocular vascular layers.

The performance of the classification algorithm proposed in this chapter is also tested on the individual three texture descriptors namely the $LBP_{p,r}^{2riuPCA}$, the $LBP_{p,r}^{PCA}$ and the $BRIEF_{S,n}^{PCA}$. The various parameters of the three different texture descriptors, i.e.: (p and r) for the $LBP_{p,r}^{2riuPCA}$ and the $LBP_{p,r}^{PCA}$, and (S and n) for the $BRIEF_{S,n}^{PCA}$, are also empirically fine-tuned with different values. Additionally, the same values of

parameters that were used in evaluating the previous classification algorithm proposed in Chapter 4 are also utilised in the evaluation of the classification algorithm proposed in this chapter in all classification experiments. Since the texture descriptors, i.e.: the $LBP_{p,r}^{2riuPCA}$, the $LBP_{p,r}^{PCA}$ and the $BRIEF_{S,n}^{PCA}$, are individually fine-tuned with different combinations of parameters, the various values of parameters tested are denoted in the subscripts, i.e.: in place of p , r , S and n , of individual texture descriptors.

Moreover, the same evaluation strategies, i.e.: employing the stratified $K = 10$ folds cross-validation strategy and computing the AUC scores, are also employed. As the evaluation involved employing the stratified $K = 10$ folds cross-validation strategy and measuring the AUC scores, the mean AUC scores along with the standard deviations are also estimated. Hence, the overall performance of the classification algorithm proposed in this chapter is estimated based on the mean AUC scores \pm standard deviations using the two different machine learning classifiers specifically the KNN and the SVM previously demonstrated in the classification step of the algorithm, see section 5.3.4.

Besides the above mentioned, cross-corpora experiments were also conducted. As the wet AMD is common in both OCTA image data sets, the cross-corpora experiments were performed by training the classifiers on one of the OCTA image data sets and then testing them on the other OCTA image data sets (as external validation) to demonstrate the generalisation performance. Specifically, the classifier trained on the Manchester OCTA image data set to solve the healthy versus wet AMD classification task is tested on the wet AMD cases of the Moorfields OCTA image data set. Likewise, the classifier trained on the Moorfields OCTA image data set to solve the dry AMD versus wet AMD classification task is tested on the wet AMD cases of the Manchester OCTA image data set.

As only the Manchester OCTA image data set contains healthy eyes, the same healthy data set is used to train the classifier for solving the Manchester healthy versus Moorfields wet AMD classification task and then to test the trained classifier on the wet AMD cases of the Manchester OCTA image data set. Likewise, as only the Moorfields OCTA image data set involves dry AMD eyes, the same dry AMD data set is used to train the classifier for solving the Manchester wet AMD versus Moorfields dry AMD classification task and then to test the trained classifier on the wet AMD cases of the Moorfields OCTA image data set.

The motivation for undertaking these evaluation procedures is to allow the accomplishment of fair and consistent comparison and evaluation of the two different automated image classification algorithms developed in this thesis. The following two

subsections 5.4.1 and 5.4.2 demonstrate the evaluation results of the classification algorithm proposed in this chapter on both OCTA image data sets of the Manchester Royal Eye Hospital and the Moorfields Eye Hospital, and subsection 5.4.3 summarises the evaluation results of the cross-corpora experiments conducted.

5.4.1 Manchester Royal Eye Hospital

This subsection provides the evaluation results of the automated classification algorithm proposed in this chapter on the Manchester Royal Eye Hospital OCTA image data set for solving only a binary image classification task, i.e.: healthy vs wet AMD. The evaluation of the classification algorithm is performed in order based on the conducting of classification experiments. As such, it starts with the individual ocular vascular layers namely the superficial inner retina layer, the deep inner retina layer, the outer retina layer and the choriocapillaris layer, respectively. This is then followed by layer combination namely by concatenating two feature vectors extracted from two OCTA images of the different ocular vascular layers, concatenating three feature vectors extracted from three OCTA images of the various ocular vascular layers and concatenating all feature vectors extracted from the OCTA images of all ocular vascular layers.

5.4.1.1 Superficial Inner Retina Layer

The classification algorithm was initially assessed on the OCTA images of the superficial inner retina layer. Table 5.1 shows the classification results that demonstrate the diagnostic capability of the classification algorithm on the OCTA images of this retinal layer.

While the OCTA images of the superficial inner retina layer do not typically display any perceptible vascular pathologies related to AMD disease, e.g.: regions of CNV lesions, the classification results in Table 5.1 do show that the automated classification algorithm can effectively distinguish differences between normal and pathological vascular texture in the OCTA images of the superficial inner retina layer. Nevertheless, the $BRIEF_{S,n}^{PCA}$ texture descriptor could not effectively generate robust local texture descriptions as the classification performance was always approximately nearby the random guessing skill, i.e.: mean AUC scores ≈ 0.55 , in both classification settings, i.e.: with the SVM and the KNN classifiers. This is in contrast to the $LBP_{p,r}^{2riuPCA}$ and the $LBP_{p,r}^{PCA}$ texture descriptors as both mostly demonstrated to enable the achievement

Table 5.1: A summary of classification results (mean AUC scores \pm standard deviations) that measure the performance of the automated classification algorithm that is based on reduced-local texture features for solving the healthy vs wet AMD classification task, on the OCTA images of superficial inner retina layer.

Descriptor	KNN Classifier		SVM Classifier	
	Best Parameters	AUC \pm std	Best Parameters	AUC \pm std
$LBP^{2riuPCA}_{4,1}$	$D^{k=3}_{euclidean}$	0.90 ± 0.06	$K^{C=100}_{linear}$	0.89 ± 0.06
$LBP^{PCA}_{4,1}$	$D^{k=7}_{manhattan}$	0.87 ± 0.03	$K^{C=100, \gamma=0.001}_{rbf}$	0.89 ± 0.05
$BRIEF^{PCA}_{4,4}$	$D^{k=1}_{chebyshev}$	0.51 ± 0.10	$K^{C=100, d=2}_{poly}$	0.52 ± 0.03
$LBP^{2riuPCA}_{8,2}$	$D^{k=7}_{manhattan}$	0.90 ± 0.02	$K^{C=100, \gamma=0.1}_{rbf}$	0.86 ± 0.07
$LBP^{PCA}_{8,2}$	$D^{k=5}_{chebyshev}$	0.82 ± 0.06	$K^{C=100, \gamma=0.01}_{rbf}$	0.82 ± 0.04
$BRIEF^{PCA}_{5,8}$	$D^{k=9}_{euclidean}$	0.51 ± 0.09	$K^{C=100, d=2}_{poly}$	0.52 ± 0.02
$LBP^{2riuPCA}_{12,3}$	$D^{k=5}_{manhattan}$	0.87 ± 0.06	$K^{C=50}_{linear}$	0.85 ± 0.08
$LBP^{PCA}_{12,3}$	$D^{k=5}_{manhattan}$	0.78 ± 0.02	$K^{C=1}_{linear}$	0.78 ± 0.06
$BRIEF^{PCA}_{6,12}$	$D^{k=3}_{chebyshev}$	0.58 ± 0.12	$K^{C=10, \gamma=0.001}_{rbf}$	0.60 ± 0.10
$LBP^{2riuPCA}_{16,4}$	$D^{k=7}_{manhattan}$	0.84 ± 0.08	$K^{C=10}_{linear}$	0.82 ± 0.09
$LBP^{PCA}_{16,4}$	$D^{k=3}_{manhattan}$	0.79 ± 0.09	$K^{C=1}_{linear}$	0.79 ± 0.11
$BRIEF^{PCA}_{7,16}$	$D^{k=3}_{chebyshev}$	0.56 ± 0.05	$K^{C=1, d=3}_{poly}$	0.53 ± 0.16

of a satisfactory classification performance in all classification experiments. The classification results given in Table 5.1, however, show that the best overall performance was accomplished with the $LBP^{2riuPCA}_{8,2}$ texture descriptor based on the KNN classifier with $D^{k=7}_{manhattan}$ achieving a mean AUC score and a standard deviation = 0.90 ± 0.02 .

5.4.1.2 Deep Inner Retina Layer

Nonetheless, the automated classification algorithm is then evaluated on the OCTA images of the deep inner retina layer. Table 5.2 exhibits the classification results that demonstrate the diagnostic skill of the classification algorithm on the OCTA images of this retinal layer.

In the same way as the OCTA images of the superficial inner retina layer, the OCTA images of the deep inner retina layer do not usually exhibit any noticeable vascular pathologies related to AMD disease, e.g.: areas of CNV lesions. Nevertheless, the evaluation results presented in Table 5.2 confirm that the automated classification algorithm can successfully recognise some variations between normal and abnormal vascular texture appearance in the OCTA images of the deep inner retina layer. Yet, the $BRIEF^{PCA}_{S,n}$ texture descriptor was not able to construct robust local texture descriptions as the classification performance was nearly always near the random guessing

Table 5.2: A summary of classification results (mean AUC scores \pm standard deviations) that measure the performance of the automated classification algorithm that is based on reduced-local texture features for solving the healthy vs wet AMD classification task, on the OCTA images of deep inner retina layer.

Descriptor	KNN Classifier		SVM Classifier	
	Best Parameters	AUC \pm std	Best Parameters	AUC \pm std
$LBP^{2riuPCA}_{4,1}$	$D^{k=3}_{chebyshev}$	0.93 ± 0.06	$K^{C=1, \gamma=0.1}_{rbf}$	0.93 ± 0.06
$LBP^{PCA}_{4,1}$	$D^{k=3}_{chebyshev}$	0.91 ± 0.06	$K^{C=50, \gamma=0.0001}_{rbf}$	0.92 ± 0.04
$BRIEF^{PCA}_{4,4}$	$D^{k=1}_{chebyshev}$	0.58 ± 0.17	$K^{C=100, \gamma=0.1}_{rbf}$	0.55 ± 0.19
$LBP^{2riuPCA}_{8,2}$	$D^{k=9}_{euclidean}$	0.92 ± 0.05	$K^{C=1}_{linear}$	0.94 ± 0.05
$LBP^{PCA}_{8,2}$	$D^{k=9}_{euclidean}$	0.91 ± 0.03	$K^{C=50, \gamma=0.001}_{rbf}$	0.92 ± 0.07
$BRIEF^{PCA}_{5,8}$	$D^{k=7}_{chebyshev}$	0.56 ± 0.10	$K^{C=1, \gamma=0.1}_{rbf}$	0.53 ± 0.16
$LBP^{2riuPCA}_{12,3}$	$D^{k=9}_{manhattan}$	0.91 ± 0.05	$K^{C=50, \gamma=0.001}_{rbf}$	0.94 ± 0.04
$LBP^{PCA}_{12,3}$	$D^{k=9}_{manhattan}$	0.94 ± 0.03	$K^{C=50, \gamma=0.01}_{rbf}$	0.94 ± 0.04
$BRIEF^{PCA}_{6,12}$	$D^{k=3}_{chebyshev}$	0.51 ± 0.04	$K^{C=1, d=3}_{poly}$	0.51 ± 0.02
$LBP^{2riuPCA}_{16,4}$	$D^{k=9}_{manhattan}$	0.94 ± 0.03	$K^{C=10}_{linear}$	0.95 ± 0.03
$LBP^{PCA}_{16,4}$	$D^{k=7}_{manhattan}$	0.89 ± 0.05	$K^{C=1, \gamma=0.001}_{rbf}$	0.89 ± 0.02
$BRIEF^{PCA}_{7,16}$	$D^{k=7}_{chebyshev}$	0.57 ± 0.06	$K^{C=10}_{linear}$	0.54 ± 0.11

skill, i.e.: mean AUC scores ≈ 0.55 , with both classifiers, i.e.: the SVM and the KNN. Nevertheless, the $LBP^{2riuPCA}_{p,r}$ and the $LBP^{PCA}_{p,r}$ texture descriptors mostly demonstrated to allow the attainment of good classification results that are fairly comparable in all classification experiments. However, the classification results presented in Table 5.2 show that the best overall performance was achieved with the $LBP^{2riuPCA}_{16,4}$ texture descriptor using the SVM classifier with $K^{C=10}_{linear}$ accomplishing a mean AUC score and a standard deviation = 0.95 ± 0.03 .

5.4.1.3 Outer Retina Layer

The automated classification algorithm was then applied to classifying the OCTA images of the outer retina layer. Table 5.3 provides the classification results that reveal the diagnostic skill of the classification algorithm on the OCTA images of this retinal layer.

Unlike the OCTA images of the superficial inner retina layer and the deep inner retina layer, the OCTA images of outer retina layer do typically demonstrate distinguishable marks of vascular pathologies associated with AMD disease, e.g.: regions of CNV lesions. Nonetheless, the areas of CNV lesions in the OCTA images of the outer retina layer may not usually be fully visualised or noticeable and hence, may

Table 5.3: A summary of classification results (mean AUC scores \pm standard deviations) that measure the performance of the automated classification algorithm that is based on reduced-local texture features for solving the healthy vs wet AMD classification task, on the OCTA images of outer retina layer.

Descriptor	KNN Classifier		SVM Classifier	
	Best Parameters	AUC \pm std	Best Parameters	AUC \pm std
$LBP_{4,1}^{2riuPCA}$	$D^{k=3}_{euclidean}$	0.99 \pm 0.00	$K^{C=1}_{linear}$	0.99 \pm 0.00
$LBP_{4,1}^{PCA}$	$D^{k=3}_{euclidean}$	0.99 \pm 0.00	$K^{C=1}_{linear}$	0.99 \pm 0.00
$BRIEF_{4,4}^{PCA}$	$D^{k=3}_{manhattan}$	0.72 \pm 0.06	$K^{C=100}_{linear}$	0.69 \pm 0.10
$LBP_{8,2}^{2riuPCA}$	$D^{k=9}_{manhattan}$	0.99 \pm 0.00	$K^{C=10}_{linear}$	0.99 \pm 0.00
$LBP_{8,2}^{PCA}$	$D^{k=3}_{euclidean}$	0.99 \pm 0.00	$K^{C=1}_{linear}$	0.99 \pm 0.00
$BRIEF_{5,8}^{PCA}$	$D^{k=5}_{euclidean}$	0.68 \pm 0.11	$K^{C=100, \gamma=0.001}_{rbf}$	0.77 \pm 0.09
$LBP_{12,3}^{2riuPCA}$	$D^{k=9}_{chebyshev}$	0.98 \pm 0.03	$K^{C=1}_{linear}$	0.99 \pm 0.03
$LBP_{12,3}^{PCA}$	$D^{k=3}_{euclidean}$	0.99 \pm 0.00	$K^{C=1}_{linear}$	0.99 \pm 0.00
$BRIEF_{6,12}^{PCA}$	$D^{k=9}_{chebyshev}$	0.75 \pm 0.01	$K^{C=10, \gamma=0.001}_{rbf}$	0.73 \pm 0.10
$LBP_{16,4}^{2riuPCA}$	$D^{k=9}_{chebyshev}$	0.98 \pm 0.04	$K^{C=10}_{linear}$	0.99 \pm 0.03
$LBP_{16,4}^{PCA}$	$D^{k=3}_{euclidean}$	0.99 \pm 0.00	$K^{C=1}_{linear}$	0.99 \pm 0.00
$BRIEF_{7,16}^{PCA}$	$D^{k=7}_{chebyshev}$	0.66 \pm 0.11	$K^{C=1}_{linear}$	0.76 \pm 0.14

perhaps be barely obvious due to the nature of how the CNV lesions normally grow. This is because the CNV lesions typically grow by perforating the Bruch's membrane, the deepest part of the choroid layer, and by progressing into other subretinal layers. Hence, some areas of CNV lesions may appear more observable in certain ocular vascular layers than others. Nevertheless, the evaluation results given in Table 5.3 proved that the automated classification algorithm accomplished outstanding classification results. As such, the classification algorithm can successfully identify dissimilarities between normal and abnormal vascular texture appearance in the OCTA images of the outer retina layer with extremely few misclassification cases, i.e.: with very few incorrect predictions.

While the $BRIEF_{S,n}^{PCA}$ texture descriptor was not able to construct robust local texture descriptions from the OCTA images of the superficial inner retina and the deep inner retina layers as evidenced by previous classification results, see Tables 5.2 and 5.1, it showed to enable quite good improvements in classification performance on the OCTA images of the outer retina layer. As such, in some situations, the classification performance using the $BRIEF_{S,n}^{PCA}$ texture descriptor was demonstrated to relatively outperform the random guessing skill, i.e.: mean AUC scores between 0.66 and 0.77. Nevertheless, the best overall performance was again accomplished with the $LBP_{all\ values}^{PCA}$ texture descriptor using the KNN classifier with $D^{k=3}_{euclidean}$ and the SVM

classifier with $K_{linear}^{C=1}$ as well as the $LBP_{p=4,8,r=1,2}^{2riuPCA}$ texture descriptor using the SVM classifier with $K_{linear}^{C=1}$ and the KNN classifiers with $D_{euclidean}^{k=3}$ using $(p = 4, r = 1)$ and $D_{manhattan}^{k=9}$ using $(p = 8, r = 2)$, and all accomplishing a mean AUC score and a standard deviation = 0.99 ± 0.00 .

5.4.1.4 Choriocapillaris Layer

Following the evaluation of the automated classification algorithm on the previous ocular vascular layers, the classification algorithm is subsequently assessed in classifying the OCTA images of the choriocapillaris layer. Table 5.4 gives the classification results that show the diagnostic ability of the classification algorithm on the OCTA images of the choroidal layer.

Table 5.4: A summary of classification results (mean AUC scores \pm standard deviations) that measure the performance of the automated classification algorithm that is based on reduced-local texture features for solving the healthy vs wet AMD classification task, on the OCTA images of choriocapillaris layer.

Descriptor	KNN Classifier		SVM Classifier	
	Best Parameters	AUC \pm std	Best Parameters	AUC \pm std
$LBP_{4,1}^{2riuPCA}$	$D_{euclidean}^{k=3}$	0.99 \pm 0.00	$K_{linear}^{C=1}$	0.99 \pm 0.00
$LBP_{4,1}^{PCA}$	$D_{manhattan}^{k=5}$	0.97 \pm 0.04	$K_{linear}^{C=10}$	0.98 \pm 0.03
$BRIEF_{4,4}^{PCA}$	$D_{manhattan}^{k=1}$	0.78 \pm 0.11	$K_{rbf}^{C=50, \gamma=0.01}$	0.79 \pm 0.09
$LBP_{8,2}^{2riuPCA}$	$D_{euclidean}^{k=5}$	0.84 \pm 0.07	$K_{linear}^{C=50}$	0.86 \pm 0.06
$LBP_{8,2}^{PCA}$	$D_{euclidean}^{k=5}$	0.95 \pm 0.04	$K_{linear}^{C=1}$	0.92 \pm 0.22
$BRIEF_{5,8}^{PCA}$	$D_{manhattan}^{k=5}$	0.88 \pm 0.08	$K_{rbf}^{C=50, \gamma=0.001}$	0.91 \pm 0.07
$LBP_{12,3}^{2riuPCA}$	$D_{chebyshev}^{k=5}$	0.92 \pm 0.04	$K_{rbf}^{C=10, \gamma=0.1}$	0.94 \pm 0.03
$LBP_{12,3}^{PCA}$	$D_{euclidean}^{k=5}$	0.99 \pm 0.01	$K_{linear}^{C=10}$	0.99 \pm 0.01
$BRIEF_{6,12}^{PCA}$	$D_{euclidean}^{k=5}$	0.85 \pm 0.06	$K_{linear}^{C=0}$	0.87 \pm 0.07
$LBP_{16,4}^{2riuPCA}$	$D_{euclidean}^{k=5}$	0.95 \pm 0.02	$K_{linear}^{C=1}$	0.95 \pm 0.04
$LBP_{16,4}^{PCA}$	$D_{manhattan}^{k=3}$	0.97 \pm 0.05	$K_{linear}^{C=10}$	0.97 \pm 0.04
$BRIEF_{7,16}^{PCA}$	$D_{chebyshev}^{k=5}$	0.90 \pm 0.05	$K_{rbf}^{C=10, \gamma=0.001}$	0.90 \pm 0.08

The OCTA images of the choriocapillaris layer are the same as the OCTA images of the outer retina layer in being known to typically demonstrate perceptible marks of vascular pathologies linked to AMD disease, e.g.: regions of CNV lesions. However, the areas of CNV lesions in the OCTA images of the choriocapillaris are not always entirely visualised or detectable either, and hence may perhaps be hardly obvious as is the case with the OCTA images of the outer retina layer. This is mainly due to the nature of how the CNV lesions normally develop. The CNV lesions typically grow by

perforating the Bruch's membrane that is the deepest part of the choroid layer and by progressing into other subretinal layers. Therefore, certain parts of CNV regions may appear to be more distinguishable in certain ocular vascular layers than in others. Nevertheless, the evaluation results in Table 5.4 proved that the automated classification algorithm was capable of accomplishing outstanding classification results. As such the algorithm effectively recognised variations between normal and abnormal vascular texture appearance in the OCTA images of the choriocapillaris layer with only very few misclassification cases.

Analogous to the situation with the OCTA images of the outer retina layer, the $BRIEF_{S,n}^{PCA}$ texture descriptor was also able to produce moderately good local texture descriptions from the OCTA images of the choriocapillaris layer that satisfactorily facilitated slight improvements in the classification performance compared to its poor classification results in previous ocular vascular layers, see Table 5.4. However, based on the classification results of the classification algorithm on the OCTA images of the choriocapillaris layer given in Table 5.4, the best overall performance was achieved with the $LBP_{4,1}^{2riuPCA}$ texture descriptor. As such, a mean AUC score and a standard deviation = 0.99 ± 0.00 , was accomplished, with the SVM classifier using $K_{linear}^{C=1}$ and the KNN classifier using $D_{euclidean}^{k=3}$.

5.4.1.5 Layer Combination

Following the evaluation of the automated classification algorithm on the OCTA images of ocular vascular layers individually, the performance of the algorithm was then assessed on classifying the various eyes via layer combination. This is accomplished by conducting the binary image classification based on concatenating two feature vectors extracted from the OCTA images of different ocular vascular layers, based on concatenating three feature vectors extracted from three OCTA images of the different ocular vascular layers and based on concatenating all feature vectors extracted from the OCTA images of all ocular vascular layers. It should be recalled that the classification performance of the classification algorithm is estimated based on classifying the individual eyes not the individual OCTA images of various ocular vascular layers.

Tables 5.5, 5.6, 5.7, 5.8, 5.9 and 5.10 summarise the classification results that show the diagnostic ability of the classification algorithm when concatenating two feature vectors extracted from the OCTA images of two various ocular vascular layers. These are the superficial and the deep inner retina, the superficial inner and the outer retina, the superficial inner retina and the choriocapillaris, the deep inner and the outer retina,

the deep inner retina and the choriocapillaris, and the outer retina and the choriocapillaris layers, respectively.

Table 5.5: A summary of classification results (mean AUC scores \pm standard deviations) that measure the performance of the automated classification algorithm that is based on reduced-local texture features for solving the healthy vs wet AMD classification task, based on concatenating two feature vectors extracted from the OCTA images of the superficial and the deep retina layers.

Descriptor	KNN Classifier		SVM Classifier	
	Best Parameters	AUC \pm std	Best Parameters	AUC \pm std
$LBP^{2riuPCA}_{4,1}$	$D^{k=3}_{euclidean}$	0.91 ± 0.04	$K^{C=10,d=3}_{poly}$	0.90 ± 0.04
$LBP^{PCA}_{4,1}$	$D^{k=3}_{euclidean}$	0.91 ± 0.07	$K^{C=1,d=2}_{poly}$	0.90 ± 0.19
$BRIEF^{PCA}_{4,4}$	$D^{k=3}_{manhattan}$	0.56 ± 0.07	$K^{C=10,d=3}_{poly}$	0.61 ± 0.10
$LBP^{2riuPCA}_{8,2}$	$D^{k=1}_{euclidean}$	0.90 ± 0.04	$K^{C=1}_{linear}$	0.92 ± 0.05
$LBP^{PCA}_{8,2}$	$D^{k=5}_{manhattan}$	0.90 ± 0.06	$K^{C=10}_{linear}$	0.84 ± 0.19
$BRIEF^{PCA}_{5,8}$	$D^{k=3}_{chebyshev}$	0.51 ± 0.07	$K^{C=1,d=2}_{poly}$	0.50 ± 0.09
$LBP^{2riuPCA}_{12,3}$	$D^{k=5}_{manhattan}$	0.88 ± 0.05	$K^{C=1,\gamma=0.1}_{rbf}$	0.92 ± 0.05
$LBP^{PCA}_{12,3}$	$D^{k=5}_{manhattan}$	0.90 ± 0.03	$K^{C=10,\gamma=0.1}_{rbf}$	0.88 ± 0.20
$BRIEF^{PCA}_{6,12}$	$D^{k=5}_{euclidean}$	0.50 ± 0.07	$K^{C=10,d=3}_{poly}$	0.51 ± 0.11
$LBP^{2riuPCA}_{16,4}$	$D^{k=3}_{euclidean}$	0.91 ± 0.03	$K^{C=10}_{linear}$	0.93 ± 0.05
$LBP^{PCA}_{16,4}$	$D^{k=3}_{manhattan}$	0.88 ± 0.06	$K^{C=1}_{linear}$	0.85 ± 0.10
$BRIEF^{PCA}_{7,16}$	$D^{k=5}_{chebyshev}$	0.50 ± 0.06	$K^{C=10,d=2}_{poly}$	0.53 ± 0.07

Tables 5.11, 5.12, 5.13 and 5.14, on the other hand, present the classification results that demonstrate the diagnostic skill of the classification algorithm when concatenating three feature vectors extracted from three OCTA images of various ocular vascular layers. Namely, the superficial, the deep inner and the outer retina, the superficial, the deep inner retina and the choriocapillaris, the superficial inner, the outer retina and the choriocapillaris, and the deep inner, the outer retina and the choriocapillaris layers, respectively.

Table 5.15 presents the classification results when concatenating all feature vectors extracted from the OCTA images of all ocular vascular layers.

Classifying the various OCTA images of ocular vascular layers with different eye conditions, e.g.: healthy and wet AMD, can be quite challenging to discriminate even for exceptionally skilled ophthalmologists. This is mainly because the textural vascular appearance in the various OCTA images usually appear significantly different among individual ocular vascular layers. With the presence of an eye condition, e.g.: wet AMD disease, the OCTA images of certain ocular vascular layers, e.g.: the superficial inner retina and the deep inner retina layers, usually display quite uniform

Table 5.6: A summary of classification results (mean AUC scores \pm standard deviations) that measure the performance of the automated classification algorithm that is based on reduced-local texture features for solving the healthy vs wet AMD classification task, based on concatenating two feature vectors extracted from the OCTA images of the superficial and the outer retina layers.

Descriptor	KNN Classifier		SVM Classifier	
	Best Parameters	AUC \pm std	Best Parameters	AUC \pm std
$LBP^{2riuPCA}_{4,1}$	$D^{k=1}_{euclidean}$	0.92 ± 0.03	$K^{C=1}_{linear}$	0.93 ± 0.06
$LBP^{PCA}_{4,1}$	$D^{k=1}_{euclidean}$	0.94 ± 0.05	$K^{C=1}_{linear}$	0.93 ± 0.06
$BRIEF^{PCA}_{4,4}$	$D^{k=3}_{euclidean}$	0.50 ± 0.08	$K^{C=1,d=3}_{poly}$	0.55 ± 0.10
$LBP^{2riuPCA}_{8,2}$	$D^{k=3}_{manhattan}$	0.93 ± 0.03	$K^{C=10,\gamma=0.01}_{rbf}$	0.94 ± 0.02
$LBP^{PCA}_{8,2}$	$D^{k=1}_{euclidean}$	0.94 ± 0.06	$K^{C=1}_{linear}$	0.93 ± 0.07
$BRIEF^{PCA}_{5,8}$	$D^{k=1}_{euclidean}$	0.50 ± 0.09	$K^{C=10,d=3}_{poly}$	0.51 ± 0.11
$LBP^{2riuPCA}_{12,3}$	$D^{k=3}_{manhattan}$	0.93 ± 0.04	$K^{C=10,\gamma=0.01}_{rbf}$	0.94 ± 0.03
$LBP^{PCA}_{12,3}$	$D^{k=1}_{euclidean}$	0.95 ± 0.04	$K^{C=1}_{linear}$	0.94 ± 0.03
$BRIEF^{PCA}_{6,12}$	$D^{k=5}_{manhattan}$	0.61 ± 0.16	$K^{C=10,d=2}_{poly}$	0.56 ± 0.15
$LBP^{2riuPCA}_{16,4}$	$D^{k=3}_{euclidean}$	0.90 ± 0.07	$K^{C=10}_{linear}$	0.90 ± 0.04
$LBP^{PCA}_{16,4}$	$D^{k=5}_{euclidean}$	0.94 ± 0.08	$K^{C=1}_{linear}$	0.93 ± 0.06
$BRIEF^{PCA}_{7,16}$	$D^{k=3}_{euclidean}$	0.52 ± 0.05	$K^{C=10,d=2}_{poly}$	0.55 ± 0.07

Table 5.7: A summary of classification results (mean AUC scores \pm standard deviations) that measure the performance of the automated classification algorithm that is based on reduced-local texture features for solving the healthy vs wet AMD classification task, based on concatenating two feature vectors extracted from the OCTA images of the superficial and the chorio-capillaris retina layers.

Descriptor	KNN Classifier		SVM Classifier	
	Best Parameters	AUC \pm std	Best Parameters	AUC \pm std
$LBP^{2riuPCA}_{4,1}$	$D^{k=3}_{euclidean}$	0.90 ± 0.09	$K^{C=1,\gamma=0.01}_{rbf}$	0.91 ± 0.07
$LBP^{PCA}_{4,1}$	$D^{k=5}_{euclidean}$	0.89 ± 0.06	$K^{C=1,d=3}_{poly}$	0.91 ± 0.06
$BRIEF^{PCA}_{4,4}$	$D^{k=1}_{chebyshev}$	0.72 ± 0.11	$K^{C=10,d=3}_{poly}$	0.69 ± 0.11
$LBP^{2riuPCA}_{8,2}$	$D^{k=5}_{chebyshev}$	0.85 ± 0.06	$K^{C=10,\gamma=0.01}_{rbf}$	0.89 ± 0.06
$LBP^{PCA}_{8,2}$	$D^{k=5}_{euclidean}$	0.89 ± 0.03	$K^{C=10,\gamma=0.1}_{rbf}$	0.88 ± 0.05
$BRIEF^{PCA}_{5,8}$	$D^{k=1}_{euclidean}$	0.71 ± 0.09	$K^{C=10,d=3}_{poly}$	0.66 ± 0.14
$LBP^{2riuPCA}_{12,3}$	$D^{k=3}_{manhattan}$	0.88 ± 0.05	$K^{C=10}_{linear}$	0.91 ± 0.06
$LBP^{PCA}_{12,3}$	$D^{k=3}_{manhattan}$	0.92 ± 0.07	$K^{C=10}_{linear}$	0.90 ± 0.06
$BRIEF^{PCA}_{6,12}$	$D^{k=5}_{manhattan}$	0.65 ± 0.12	$K^{C=10,d=3}_{poly}$	0.61 ± 0.15
$LBP^{2riuPCA}_{16,4}$	$D^{k=3}_{chebyshev}$	0.82 ± 0.04	$K^{C=1,\gamma=0.1}_{rbf}$	0.88 ± 0.03
$LBP^{PCA}_{16,4}$	$D^{k=3}_{euclidean}$	0.84 ± 0.02	$K^{C=10,\gamma=0.01}_{rbf}$	0.85 ± 0.06
$BRIEF^{PCA}_{7,16}$	$D^{k=5}_{euclidean}$	0.70 ± 0.05	$K^{C=1,d=3}_{poly}$	0.64 ± 0.04

Table 5.8: A summary of classification results (mean AUC scores \pm standard deviations) that measure the performance of the automated classification algorithm that is based on reduced-local texture features for solving the healthy vs wet AMD classification task, based on concatenating two feature vectors extracted from the OCTA images of the deep and the outer retina layers.

Descriptor	KNN Classifier		SVM Classifier	
	Best Parameters	AUC \pm std	Best Parameters	AUC \pm std
$LBP_{4,1}^{2riuPCA}$	$D^{k=1}_{euclidean}$	0.94 ± 0.02	$K^{C=1}_{linear}$	0.93 ± 0.06
$LBP_{4,1}^{PCA}$	$D^{k=1}_{euclidean}$	0.94 ± 0.03	$K^{C=1}_{linear}$	0.93 ± 0.02
$BRIEF_{4,4}^{PCA}$	$D^{k=1}_{euclidean}$	0.54 ± 0.10	$K^{C=10,d=2}_{poly}$	0.61 ± 0.11
$LBP_{8,2}^{2riuPCA}$	$D^{k=5}_{manhattan}$	0.94 ± 0.02	$K^{C=1}_{linear}$	0.93 ± 0.07
$LBP_{8,2}^{PCA}$	$D^{k=1}_{euclidean}$	0.93 ± 0.06	$K^{C=1}_{linear}$	0.92 ± 0.04
$BRIEF_{5,8}^{PCA}$	$D^{k=5}_{chebyshev}$	0.59 ± 0.07	$K^{C=1,d=3}_{poly}$	0.58 ± 0.04
$LBP_{12,3}^{2riuPCA}$	$D^{k=3}_{manhattan}$	0.94 ± 0.05	$K^{C=1,\gamma=0.1}_{rbf}$	0.93 ± 0.02
$LBP_{12,3}^{PCA}$	$D^{k=1}_{euclidean}$	0.95 ± 0.03	$K^{C=1}_{linear}$	0.93 ± 0.06
$BRIEF_{6,12}^{PCA}$	$D^{k=5}_{manhattan}$	0.58 ± 0.17	$K^{C=1,\gamma=0.01}_{rbf}$	0.53 ± 0.16
$LBP_{16,4}^{2riuPCA}$	$D^{k=5}_{manhattan}$	0.94 ± 0.02	$K^{C=10,\gamma=0.1}_{rbf}$	0.93 ± 0.03
$LBP_{16,4}^{PCA}$	$D^{k=3}_{euclidean}$	0.93 ± 0.06	$K^{C=10}_{linear}$	0.92 ± 0.05
$BRIEF_{7,16}^{PCA}$	$D^{k=3}_{manhattan}$	0.56 ± 0.10	$K^{C=10,\gamma=0.1}_{rbf}$	0.52 ± 0.09

Table 5.9: A summary of classification results (mean AUC scores \pm standard deviations) that measure the performance of the automated classification algorithm that is based on reduced-local texture features for solving the healthy vs wet AMD classification task, based on concatenating two feature vectors extracted from the OCTA images of the deep retina and the choriocapillaris layers.

Descriptor	KNN Classifier		SVM Classifier	
	Best Parameters	AUC \pm std	Best Parameters	AUC \pm std
$LBP_{4,1}^{2riuPCA}$	$D^{k=5}_{manhattan}$	0.92 ± 0.06	$K^{C=1,\gamma=0.1}_{rbf}$	0.91 ± 0.05
$LBP_{4,1}^{PCA}$	$D^{k=5}_{manhattan}$	0.93 ± 0.05	$K^{C=1,d=3}_{poly}$	0.92 ± 0.06
$BRIEF_{4,4}^{PCA}$	$D^{k=3}_{euclidean}$	0.70 ± 0.08	$K^{C=10,d=3}_{poly}$	0.68 ± 0.10
$LBP_{8,2}^{2riuPCA}$	$D^{k=5}_{chebyshev}$	0.93 ± 0.05	$K^{C=1}_{linear}$	0.92 ± 0.05
$LBP_{8,2}^{PCA}$	$D^{k=5}_{manhattan}$	0.92 ± 0.06	$K^{C=1,\gamma=0.01}_{rbf}$	0.89 ± 0.08
$BRIEF_{5,8}^{PCA}$	$D^{k=3}_{manhattan}$	0.75 ± 0.07	$K^{C=10,d=3}_{poly}$	0.77 ± 0.09
$LBP_{12,3}^{2riuPCA}$	$D^{k=5}_{manhattan}$	0.93 ± 0.02	$K^{C=10}_{linear}$	0.92 ± 0.02
$LBP_{12,3}^{PCA}$	$D^{k=5}_{manhattan}$	0.93 ± 0.04	$K^{C=10,\gamma=0.1}_{rbf}$	0.90 ± 0.10
$BRIEF_{6,12}^{PCA}$	$D^{k=3}_{manhattan}$	0.65 ± 0.11	$K^{C=10,d=3}_{poly}$	0.62 ± 0.10
$LBP_{16,4}^{2riuPCA}$	$D^{k=3}_{manhattan}$	0.92 ± 0.04	$K^{C=1,\gamma=0.1}_{rbf}$	0.94 ± 0.03
$LBP_{16,4}^{PCA}$	$D^{k=3}_{manhattan}$	0.92 ± 0.06	$K^{C=10,d=3}_{poly}$	0.92 ± 0.03
$BRIEF_{7,16}^{PCA}$	$D^{k=5}_{euclidean}$	0.69 ± 0.07	$K^{C=10,d=3}_{poly}$	0.66 ± 0.06

Table 5.10: A summary of classification results (mean AUC scores \pm standard deviations) that measure the performance of the automated classification algorithm that is based on reduced-local texture features for solving the healthy vs wet AMD classification task, based on concatenating two feature vectors extracted from the OCTA images of the outer retina and the choriocapillaris layers.

Descriptor	KNN Classifier		SVM Classifier	
	Best Parameters	AUC \pm std	Best Parameters	AUC \pm std
$LBP^{2riuPCA}_{4,1}$	$D^{k=5}_{manhattan}$	0.96 ± 0.05	$K^{C=1}_{linear}$	0.97 ± 0.11
$LBP^{PCA}_{4,1}$	$D^{k=3}_{euclidean}$	0.97 ± 0.03	$K^{C=1}_{linear}$	0.94 ± 0.04
$BRIEF^{PCA}_{4,4}$	$D^{k=5}_{chebyshev}$	0.70 ± 0.13	$K^{C=10,d=2}_{poly}$	0.70 ± 0.16
$LBP^{2riuPCA}_{8,2}$	$D^{k=5}_{euclidean}$	0.97 ± 0.03	$K^{C=1}_{linear}$	0.96 ± 0.04
$LBP^{PCA}_{8,2}$	$D^{k=5}_{euclidean}$	0.96 ± 0.03	$K^{C=1}_{linear}$	0.90 ± 0.10
$BRIEF^{PCA}_{5,8}$	$D^{k=3}_{manhattan}$	0.70 ± 0.06	$K^{C=10,d=3}_{poly}$	0.67 ± 0.16
$LBP^{2riuPCA}_{12,3}$	$D^{k=5}_{euclidean}$	0.97 ± 0.03	$K^{C=1,d=3}_{poly}$	0.96 ± 0.02
$LBP^{PCA}_{12,3}$	$D^{k=1}_{euclidean}$	0.96 ± 0.05	$K^{C=1}_{linear}$	0.95 ± 0.11
$BRIEF^{PCA}_{6,12}$	$D^{k=5}_{manhattan}$	0.72 ± 0.09	$K^{C=10,d=2}_{poly}$	0.58 ± 0.19
$LBP^{2riuPCA}_{16,4}$	$D^{k=5}_{euclidean}$	0.98 ± 0.03	$K^{C=1,\gamma=0.01}_{rbf}$	0.97 ± 0.03
$LBP^{PCA}_{16,4}$	$D^{k=1}_{euclidean}$	0.96 ± 0.05	$K^{C=1}_{linear}$	0.97 ± 0.05
$BRIEF^{PCA}_{7,16}$	$D^{k=5}_{chebyshev}$	0.69 ± 0.08	$K^{C=10,d=2}_{poly}$	0.69 ± 0.09

Table 5.11: A summary of classification results (mean AUC scores \pm standard deviations) that measure the performance of the automated classification algorithm that is based on reduced-local texture features for solving the healthy vs wet AMD classification task, based on concatenating three feature vectors extracted from the OCTA images of the superficial inner, the deep inner and the outer retina layers.

Descriptor	KNN Classifier		SVM Classifier	
	Best Parameters	AUC \pm std	Best Parameters	AUC \pm std
$LBP^{2riuPCA}_{4,1}$	$D^{k=1}_{euclidean}$	0.94 ± 0.05	$K^{C=1}_{linear}$	0.95 ± 0.06
$LBP^{PCA}_{4,1}$	$D^{k=1}_{euclidean}$	0.94 ± 0.08	$K^{C=1}_{linear}$	0.93 ± 0.10
$BRIEF^{PCA}_{4,4}$	$D^{k=1}_{chebyshev}$	0.59 ± 0.08	$K^{C=10,d=3}_{poly}$	0.64 ± 0.11
$LBP^{2riuPCA}_{8,2}$	$D^{k=5}_{euclidean}$	0.95 ± 0.06	$K^{C=1}_{linear}$	0.93 ± 0.05
$LBP^{PCA}_{8,2}$	$D^{k=3}_{euclidean}$	0.95 ± 0.10	$K^{C=1}_{linear}$	0.95 ± 0.22
$BRIEF^{PCA}_{5,8}$	$D^{k=3}_{chebyshev}$	0.50 ± 0.06	$K^{C=1,d=2}_{poly}$	0.50 ± 0.07
$LBP^{2riuPCA}_{12,3}$	$D^{k=3}_{manhattan}$	0.94 ± 0.04	$K^{C=10,d=3}_{poly}$	0.93 ± 0.05
$LBP^{PCA}_{12,3}$	$D^{k=1}_{euclidean}$	0.93 ± 0.06	$K^{C=1}_{linear}$	0.92 ± 0.08
$BRIEF^{PCA}_{6,12}$	$D^{k=3}_{manhattan}$	0.60 ± 0.15	$K^{C=1}_{linear}$	0.53 ± 0.13
$LBP^{2riuPCA}_{16,4}$	$D^{k=3}_{euclidean}$	0.93 ± 0.04	$K^{C=1,\gamma=0.01}_{rbf}$	0.94 ± 0.03
$LBP^{PCA}_{16,4}$	$D^{k=1}_{euclidean}$	0.96 ± 0.04	$K^{C=1}_{linear}$	0.95 ± 0.05
$BRIEF^{PCA}_{7,16}$	$D^{k=5}_{manhattan}$	0.50 ± 0.17	$K^{C=1,\gamma=0.01}_{rbf}$	0.50 ± 0.10

textural vascular appearance that is highly similar to healthy. Nevertheless, the OCTA

Table 5.12: A summary of classification results (mean AUC scores \pm standard deviations) that measure the performance of the automated classification algorithm that is based on reduced-local texture features for solving the healthy vs wet AMD classification task, based on concatenating three feature vectors extracted from the OCTA images of the superficial, the deep inner retina and the choriocapillaris layers.

Descriptor	KNN Classifier		SVM Classifier	
	Best Parameters	AUC \pm std	Best Parameters	AUC \pm std
$LBP_{4,1}^{2riuPCA}$	$D^{k=9}_{chebyshev}$	0.96 ± 0.02	$K_{rbf}^{C=1, \gamma=0.01}$	0.96 ± 0.03
$LBP_{4,1}^{PCA}$	$D^{k=9}_{euclidean}$	0.95 ± 0.02	$K_{rbf}^{C=1, \gamma=0.001}$	0.96 ± 0.03
$BRIEF_{4,4}^{PCA}$	$D^{k=9}_{chebyshev}$	0.57 ± 0.06	$K_{rbf}^{C=100, \gamma=0.01}$	0.58 ± 0.09
$LBP_{8,2}^{2riuPCA}$	$D^{k=5}_{manhattan}$	0.89 ± 0.06	$K_{rbf}^{C=50, \gamma=0.001}$	0.94 ± 0.07
$LBP_{8,2}^{PCA}$	$D^{k=7}_{euclidean}$	0.96 ± 0.05	$K_{rbf}^{C=10, \gamma=0.001}$	0.96 ± 0.06
$BRIEF_{5,8}^{PCA}$	$D^{k=5}_{euclidean}$	0.62 ± 0.12	$K_{rbf}^{C=100, \gamma=0.001}$	0.56 ± 0.08
$LBP_{12,3}^{2riuPCA}$	$D^{k=5}_{manhattan}$	0.95 ± 0.02	$K_{rbf}^{C=100, \gamma=0.001}$	0.96 ± 0.05
$LBP_{12,3}^{PCA}$	$D^{k=9}_{chebyshev}$	0.92 ± 0.08	$K_{linear}^{C=1}$	0.95 ± 0.07
$BRIEF_{6,12}^{PCA}$	$D^{k=1}_{manhattan}$	0.52 ± 0.10	$K_{poly}^{C=1, d=3}$	0.50 ± 0.11
$LBP_{16,4}^{2riuPCA}$	$D^{k=7}_{manhattan}$	0.97 ± 0.05	$K_{rbf}^{C=100, \gamma=0.001}$	0.96 ± 0.06
$LBP_{16,4}^{PCA}$	$D^{k=3}_{manhattan}$	0.84 ± 0.11	$K_{linear}^{C=1}$	0.72 ± 0.09
$BRIEF_{7,16}^{PCA}$	$D^{k=9}_{chebyshev}$	0.63 ± 0.09	$K_{rbf}^{C=1, \gamma=0.001}$	0.69 ± 0.10

Table 5.13: A summary of classification results (mean AUC scores \pm standard deviations) that measure the performance of the automated classification algorithm that is based on reduced-local texture features for solving the healthy vs wet AMD classification task, based on concatenating three feature vectors extracted from the OCTA images of the superficial inner, the outer retina and the choriocapillaris layers.

Descriptor	KNN Classifier		SVM Classifier	
	Best Parameters	AUC \pm std	Best Parameters	AUC \pm std
$LBP_{4,1}^{2riuPCA}$	$D^{k=3}_{euclidean}$	0.95 ± 0.07	$K_{linear}^{C=1}$	0.94 ± 0.04
$LBP_{4,1}^{PCA}$	$D^{k=3}_{euclidean}$	0.94 ± 0.08	$K_{linear}^{C=1}$	0.93 ± 0.06
$BRIEF_{4,4}^{PCA}$	$D^{k=3}_{euclidean}$	0.54 ± 0.11	$K_{linear}^{C=50}$	0.56 ± 0.12
$LBP_{8,2}^{2riuPCA}$	$D^{k=5}_{chebyshev}$	0.95 ± 0.07	$K_{linear}^{C=1}$	0.94 ± 0.03
$LBP_{8,2}^{PCA}$	$D^{k=1}_{euclidean}$	0.93 ± 0.04	$K_{linear}^{C=1}$	0.95 ± 0.12
$BRIEF_{5,8}^{PCA}$	$D^{k=1}_{euclidean}$	0.61 ± 0.07	$K_{poly}^{C=10, d=3}$	0.58 ± 0.14
$LBP_{12,3}^{2riuPCA}$	$D^{k=5}_{manhattan}$	0.95 ± 0.03	$K_{rbf}^{C=1, \gamma=0.01}$	0.95 ± 0.05
$LBP_{12,3}^{PCA}$	$D^{k=1}_{euclidean}$	0.93 ± 0.07	$K_{linear}^{C=1}$	0.95 ± 0.05
$BRIEF_{6,12}^{PCA}$	$D^{k=5}_{manhattan}$	0.71 ± 0.12	$K_{poly}^{C=10, d=3}$	0.65 ± 0.14
$LBP_{16,4}^{2riuPCA}$	$D^{k=5}_{euclidean}$	0.97 ± 0.03	$K_{rbf}^{C=1, \gamma=0.01}$	0.95 ± 0.05
$LBP_{16,4}^{PCA}$	$D^{k=1}_{euclidean}$	0.95 ± 0.08	$K_{linear}^{C=1}$	0.95 ± 0.12
$BRIEF_{7,16}^{PCA}$	$D^{k=5}_{chebyshev}$	0.61 ± 0.11	$K_{poly}^{C=10, d=3}$	0.62 ± 0.14

Table 5.14: A summary of classification results (mean AUC scores \pm standard deviations) that measure the performance of the automated classification algorithm that is based on reduced-local texture features for solving the healthy vs wet AMD classification task, based on concatenating three feature vectors extracted from the OCTA images of the deep inner, the outer retina and the choriocapillaris layers.

Descriptor	KNN Classifier		SVM Classifier	
	Best Parameters	AUC \pm std	Best Parameters	AUC \pm std
$LBP^{2riuPCA}_{4,1}$	$D^{k=3}_{manhattan}$	0.95 ± 0.04	$K^{C=1}_{linear}$	0.96 ± 0.05
$LBP^{PCA}_{4,1}$	$D^{k=3}_{euclidean}$	0.94 ± 0.05	$K^{C=1}_{linear}$	0.90 ± 0.09
$BRIEF^{PCA}_{4,4}$	$D^{k=5}_{manhattan}$	0.65 ± 0.10	$K^{C=10,d=3}_{poly}$	0.68 ± 0.11
$LBP^{2riuPCA}_{8,2}$	$D^{k=5}_{manhattan}$	0.95 ± 0.05	$K^{C=1}_{linear}$	0.94 ± 0.07
$LBP^{PCA}_{8,2}$	$D^{k=5}_{euclidean}$	0.94 ± 0.07	$K^{C=1}_{linear}$	0.95 ± 0.09
$BRIEF^{PCA}_{5,8}$	$D^{k=5}_{manhattan}$	0.69 ± 0.10	$K^{C=10,d=3}_{poly}$	0.73 ± 0.10
$LBP^{2riuPCA}_{12,3}$	$D^{k=5}_{euclidean}$	0.93 ± 0.05	$K^{C=1}_{linear}$	0.95 ± 0.06
$LBP^{PCA}_{12,3}$	$D^{k=1}_{euclidean}$	0.95 ± 0.06	$K^{C=1}_{linear}$	0.94 ± 0.05
$BRIEF^{PCA}_{6,12}$	$D^{k=5}_{manhattan}$	0.64 ± 0.11	$K^{C=10,d=3}_{poly}$	0.56 ± 0.13
$LBP^{2riuPCA}_{16,4}$	$D^{k=3}_{euclidean}$	0.95 ± 0.08	$K^{C=1}_{linear}$	0.94 ± 0.06
$LBP^{PCA}_{16,4}$	$D^{k=1}_{euclidean}$	0.97 ± 0.02	$K^{C=1}_{linear}$	0.90 ± 0.08
$BRIEF^{PCA}_{7,16}$	$D^{k=5}_{manhattan}$	0.64 ± 0.11	$K^{C=10,d=2}_{poly}$	0.60 ± 0.09

Table 5.15: A summary of classification results (mean AUC scores \pm standard deviations) that measure the performance of the automated classification algorithm that is based on reduced-local texture features for solving the healthy vs wet AMD classification task, based on concatenating all feature vectors extracted from the OCTA images of all ocular vascular layers.

Descriptor	KNN Classifier		SVM Classifier	
	Best Parameters	AUC \pm std	Best Parameters	AUC \pm std
$LBP^{2riuPCA}_{4,1}$	$D^{k=3}_{euclidean}$	0.94 ± 0.05	$K^{C=1}_{linear}$	0.93 ± 0.06
$LBP^{PCA}_{4,1}$	$D^{k=3}_{euclidean}$	0.94 ± 0.05	$K^{C=1}_{linear}$	0.93 ± 0.04
$BRIEF^{PCA}_{4,4}$	$D^{k=3}_{chebyshev}$	0.59 ± 0.08	$K^{C=100,d=3}_{poly}$	0.61 ± 0.10
$LBP^{2riuPCA}_{8,2}$	$D^{k=7}_{manhattan}$	0.94 ± 0.02	$K^{C=1}_{linear}$	0.93 ± 0.05
$LBP^{PCA}_{8,2}$	$D^{k=3}_{euclidean}$	0.96 ± 0.04	$K^{C=1,\gamma=0.001}_{rbf}$	0.97 ± 0.04
$BRIEF^{PCA}_{5,8}$	$D^{k=7}_{manhattan}$	0.51 ± 0.10	$K^{C=1}_{linear}$	0.62 ± 0.08
$LBP^{2riuPCA}_{12,3}$	$D^{k=7}_{euclidean}$	0.92 ± 0.06	$K^{C=1}_{linear}$	0.93 ± 0.04
$LBP^{PCA}_{12,3}$	$D^{k=7}_{euclidean}$	0.96 ± 0.06	$K^{C=1}_{linear}$	0.94 ± 0.04
$BRIEF^{PCA}_{6,12}$	$D^{k=3}_{manhattan}$	0.58 ± 0.11	$K^{C=1,d=3}_{poly}$	0.56 ± 0.10
$LBP^{2riuPCA}_{16,4}$	$D^{k=3}_{manhattan}$	0.98 ± 0.01	$K^{C=1}_{linear}$	0.97 ± 0.05
$LBP^{PCA}_{16,4}$	$D^{k=7}_{euclidean}$	0.79 ± 0.10	$K^{C=1}_{linear}$	0.89 ± 0.11
$BRIEF^{PCA}_{7,16}$	$D^{k=7}_{euclidean}$	0.52 ± 0.07	$K^{C=1}_{linear}$	0.61 ± 0.10

images of the outer retina and the choriocapillaris layers with wet AMD disease, typically demonstrate randomly disrupted textural vascular appearance that is dramatically

different from healthy.

Nevertheless, the previous classification results show that the automated classification algorithm can successfully distinguish dissimilarities between normal and abnormal vascular texture via combining the various OCTA images of ocular vascular layers. While the $BRIEF_{S,n}^{PCA}$ texture descriptor was not effective to construct representative local texture features that are appropriate for classification, both the $LBP_{p,r}^{2riuPCA}$ and the $LBP_{p,r}^{PCA}$ texture descriptors could generally produce robust local texture features as evidenced by the previous classification results.

For solving the healthy vs wet AMD classification task via layer combination, however, the best overall classification performance was attained when concatenating all feature vectors extracted from the OCTA images of all ocular vascular layers. This was achieved by using the $LBP_{16,4}^{2riuPCA}$ texture descriptor based on the KNN classifier with $D_{manhattan}^{k=3}$ accomplishing a mean AUC score and a standard deviation = 0.98 ± 0.01 .

5.4.2 Moorfields Eye Hospital

This subsection delivers the analysis results of the automated classification algorithm proposed in this chapter on the Moorfields Eye Hospital OCTA image data set for solving two different binary image classification tasks. These are dry AMD vs wet AMD and CNV vs non-CNV classification problems. The evaluation of the classification algorithm is started first on the individual ocular vascular layers namely the superficial inner retina layer, the deep inner retina layer, the outer retina layer and the choriocapillaris layer, respectively. This is then followed by layer combination namely by concatenating two feature vectors extracted from two OCTA images of the different ocular vascular layers, concatenating three feature vectors extracted from three OCTA images of the various ocular vascular layers and concatenating all feature vectors extracted from the OCTA images of all ocular vascular layers.

5.4.2.1 Superficial Inner Retina Layer

The classification algorithm is firstly evaluated on the OCTA images of the superficial inner retina layer to discriminate patients with dry AMD from wet AMD. Table 5.16 demonstrates the classification results that prove the diagnostic skill of the classification algorithm on the OCTA images of this retinal layer for solving the image classification problem of dry AMD vs wet AMD.

The OCTA images of the superficial inner retina layer do not typically exhibit any

Table 5.16: A summary of classification results (mean AUC scores \pm standard deviations) that measure the performance of the automated classification algorithm that is based on reduced-local texture features for solving the dry AMD vs wet AMD classification task, on the OCTA images of superficial inner retina layer.

Descriptor	KNN Classifier		SVM Classifier	
	Best Parameters	AUC \pm std	Best Parameters	AUC \pm std
$LBP_{4,1}^{2riuPCA}$	$D^{k=3}_{euclidean}$	0.67 ± 0.06	$K^{C=1}_{linear}$	0.74 ± 0.04
$LBP_{4,1}^{PCA}$	$D^{k=7}_{manhattan}$	0.62 ± 0.04	$K^{C=10}_{linear}$	0.71 ± 0.05
$BRIEF_{4,4}^{PCA}$	$D^{k=7}_{euclidean}$	0.52 ± 0.07	$K^{C=10}_{linear}$	0.51 ± 0.05
$LBP_{8,2}^{2riuPCA}$	$D^{k=7}_{euclidean}$	0.58 ± 0.07	$K^{C=1}_{linear}$	0.66 ± 0.11
$LBP_{8,2}^{PCA}$	$D^{k=5}_{chebyshev}$	0.61 ± 0.05	$K^{C=1, \gamma=0.001}_{rbf}$	0.62 ± 0.09
$BRIEF_{5,8}^{PCA}$	$D^{k=7}_{chebyshev}$	0.50 ± 0.02	$K^{C=1}_{linear}$	0.50 ± 0.06
$LBP_{12,3}^{2riuPCA}$	$D^{k=7}_{euclidean}$	0.55 ± 0.07	$K^{C=10, \gamma=0.001}_{rbf}$	0.66 ± 0.03
$LBP_{12,3}^{PCA}$	$D^{k=7}_{chebyshev}$	0.53 ± 0.06	$K^{C=50, \gamma=0.001}_{rbf}$	0.62 ± 0.05
$BRIEF_{6,12}^{PCA}$	$D^{k=7}_{euclidean}$	0.55 ± 0.06	$K^{C=10}_{linear}$	0.54 ± 0.06
$LBP_{16,4}^{2riuPCA}$	$D^{k=7}_{manhattan}$	0.58 ± 0.04	$K^{C=1}_{linear}$	0.63 ± 0.02
$LBP_{16,4}^{PCA}$	$D^{k=3}_{manhattan}$	0.55 ± 0.04	$K^{C=1}_{linear}$	0.58 ± 0.11
$BRIEF_{7,16}^{PCA}$	$D^{k=3}_{chebyshev}$	0.50 ± 0.02	$K^{C=1, \gamma=0.01}_{rbf}$	0.52 ± 0.05

observable vascular pathologies associated with dry or wet AMD disease. However, the evaluation results presented in Table 5.16 illustrate that the automated classification algorithm can discriminate some dissimilarities among dry AMD and wet AMD texture appearance in the OCTA images of the superficial inner retina layer. Broadly, the classification results with the $BRIEF_{S,n}^{PCA}$ texture descriptor were demonstrated to be the worst while with the $LBP_{p,r}^{2riuPCA}$ and the $LBP_{p,r}^{PCA}$ texture descriptors proved slightly better. Nevertheless, the best overall classification performance was achieved with the $LBP_{4,1}^{2riuPCA}$ texture descriptor using the SVM classifier with $K^{C=1}_{linear}$. As such accomplishing a mean AUC score and a standard deviation = 0.74 ± 0.04 .

The classification algorithm was subsequently assessed on the OCTA images of the superficial inner retina layer, however, for the task of differentiating subjects with CNV lesions from those with non-CNV lesions. Table 5.17 provides the classification results that show the diagnostic capability of the classification algorithm on the OCTA images of this retinal layer to solve the binary image classification problem i.e.: CNV vs non-CNV task.

Similar to the findings in Table 5.16, the evaluation results in Table 5.17 also illustrate that the automated classification algorithm can differentiate some dissimilarities between the textural appearance of non-CNV lesions related to dry AMD disease and CNV lesions associated with wet AMD and secondary CNV diseases, in the OCTA

Table 5.17: A summary of classification results (mean AUC scores \pm standard deviations) that measure the performance of the automated classification algorithm that is based on reduced-local texture features for solving the CNV vs non-CNV classification task, on the OCTA images of superficial inner retina layer.

Descriptor	KNN Classifier		SVM Classifier	
	Best Parameters	AUC \pm std	Best Parameters	AUC \pm std
$LBP_{4,1}^{2riuPCA}$	$D^{k=7}_{manhattan}$	0.66 ± 0.03	$K^{C=50,d=3}_{poly}$	0.62 ± 0.07
$LBP_{4,1}^{PCA}$	$D^{k=3}_{manhattan}$	0.59 ± 0.04	$K^{C=50,\gamma=0.01}_{rbf}$	0.62 ± 0.06
$BRIEF_{4,4}^{PCA}$	$D^{k=7}_{manhattan}$	0.52 ± 0.07	$K^{C=1,\gamma=0.001}_{rbf}$	0.51 ± 0.03
$LBP_{8,2}^{2riuPCA}$	$D^{k=7}_{chebyshev}$	0.61 ± 0.03	$K^{C=1,\gamma=0.1}_{rbf}$	0.66 ± 0.01
$LBP_{8,2}^{PCA}$	$D^{k=5}_{manhattan}$	0.58 ± 0.05	$K^{C=1,\gamma=0.01}_{rbf}$	0.61 ± 0.06
$BRIEF_{5,8}^{PCA}$	$D^{k=7}_{manhattan}$	0.54 ± 0.04	$K^{C=1,d=3}_{poly}$	0.53 ± 0.07
$LBP_{12,3}^{2riuPCA}$	$D^{k=3}_{manhattan}$	0.61 ± 0.04	$K^{C=10}_{linear}$	0.65 ± 0.04
$LBP_{12,3}^{PCA}$	$D^{k=7}_{chebyshev}$	0.60 ± 0.04	$K^{C=10,\gamma=0.001}_{rbf}$	0.63 ± 0.03
$BRIEF_{6,12}^{PCA}$	$D^{k=7}_{euclidean}$	0.51 ± 0.05	$K^{C=50,\gamma=0.001}_{rbf}$	0.52 ± 0.04
$LBP_{16,4}^{2riuPCA}$	$D^{k=7}_{manhattan}$	0.59 ± 0.03	$K^{C=1,d=4}_{poly}$	0.59 ± 0.07
$LBP_{16,4}^{PCA}$	$D^{k=5}_{euclidean}$	0.58 ± 0.04	$K^{C=1,d=3}_{poly}$	0.58 ± 0.05
$BRIEF_{7,16}^{PCA}$	$D^{k=3}_{manhattan}$	0.51 ± 0.06	$K^{C=1,d=4}_{poly}$	0.51 ± 0.05

images of the superficial inner retina layer. While the classification results with the $BRIEF_{S,n}^{PCA}$ texture descriptor were demonstrated to be the worst, the $LBP_{p,r}^{2riuPCA}$ and the $LBP_{p,r}^{PCA}$ texture descriptors both facilitated the attainment of relatively good improvements in classification performance. Nonetheless, the best overall classification performance was accomplished with the $LBP_{8,2}^{2riuPCA}$ texture descriptor utilising the SVM classifier with $K^{C=1,\gamma=0.1}_{rbf}$. As such, achieving a mean AUC score and a standard deviation = 0.66 ± 0.01 .

5.4.2.2 Deep Inner Retina Layer

Following assessment of the classification algorithm on the OCTA images of the superficial inner retina layer, the classification algorithm was then evaluated on the OCTA images of the deep inner retina layer for classifying subjects with dry AMD disease from those with wet AMD disease. Table 5.18 summarises the classification results that show the diagnostic skill of the classification algorithm on the OCTA images of this retinal layer to solve the dry AMD vs wet AMD image classification task.

Comparable to the OCTA images of the superficial inner retina layer, the OCTA images of the deep inner retina layer do not usually display any obvious ocular vascular pathologies related to the various types of AMD disease either, e.g.: dry AMD and

Table 5.18: A summary of classification results (mean AUC scores \pm standard deviations) that measure the performance of the automated classification algorithm that is based on reduced-local texture features for solving the dry AMD vs wet AMD classification task, on the OCTA images of deep inner retina layer.

Descriptor	KNN Classifier		SVM Classifier	
	Best Parameters	AUC \pm std	Best Parameters	AUC \pm std
$LBP_{4,1}^{2riuPCA}$	$D^{k=7}_{euclidean}$	0.62 ± 0.03	$K^{C=10}_{linear}$	0.59 ± 0.11
$LBP_{4,1}^{PCA}$	$D^{k=7}_{chebyshev}$	0.64 ± 0.05	$K^{C=1, \gamma=0.001}_{rbf}$	0.62 ± 0.05
$BRIEF_{4,4}^{PCA}$	$D^{k=3}_{chebyshev}$	0.50 ± 0.04	$K^{C=10, d=2}_{poly}$	0.52 ± 0.05
$LBP_{8,2}^{2riuPCA}$	$D^{k=7}_{chebyshev}$	0.63 ± 0.05	$K^{C=1, \gamma=0.1}_{rbf}$	0.72 ± 0.02
$LBP_{8,2}^{PCA}$	$D^{k=7}_{euclidean}$	0.62 ± 0.06	$K^{C=1, \gamma=0.001}_{rbf}$	0.68 ± 0.02
$BRIEF_{5,8}^{PCA}$	$D^{k=3}_{chebyshev}$	0.53 ± 0.06	$K^{C=1}_{linear}$	0.51 ± 0.04
$LBP_{12,3}^{2riuPCA}$	$D^{k=5}_{chebyshev}$	0.62 ± 0.04	$K^{C=1}_{linear}$	0.74 ± 0.05
$LBP_{12,3}^{PCA}$	$D^{k=3}_{chebyshev}$	0.62 ± 0.04	$K^{C=50, d=3}_{poly}$	0.69 ± 0.10
$BRIEF_{6,12}^{PCA}$	$D^{k=5}_{euclidean}$	0.56 ± 0.06	$K^{C=1}_{linear}$	0.51 ± 0.07
$LBP_{16,4}^{2riuPCA}$	$D^{k=7}_{manhattan}$	0.69 ± 0.05	$K^{C=1, \gamma=0.01}_{rbf}$	0.79 ± 0.03
$LBP_{16,4}^{PCA}$	$D^{k=7}_{manhattan}$	0.68 ± 0.07	$K^{C=1}_{linear}$	0.72 ± 0.04
$BRIEF_{7,16}^{PCA}$	$D^{k=3}_{manhattan}$	0.53 ± 0.05	$K^{C=1, d=2}_{poly}$	0.55 ± 0.06

wet AMD. Nevertheless, the evaluation results in Table 5.18 prove that the automated classification algorithm can distinguish some variations among the textural appearance of dry AMD and wet AMD in the OCTA images of the deep inner retina layer. Broadly, the classification results achieved with the $BRIEF_{S,n}^{PCA}$ texture descriptor are very poor compared to the $LBP_{p,r}^{2riuPCA}$ and the $LBP_{p,r}^{PCA}$ texture descriptors. As such the two latter texture descriptors both proved able to facilitate attaining slightly better classification performance. However, the best overall classification performance was achieved with the $LBP_{16,4}^{2riuPCA}$ texture descriptor exploiting the SVM classifier with $K^{C=1, \gamma=0.01}_{rbf}$. As such, accomplishing a mean AUC score and a standard deviation = 0.79 ± 0.03 .

Afterwards, the classification algorithm was assessed on the OCTA images of the deep inner retina layer but for the task of differentiating various patients with lesions related to CNV and non-CNV. Table 5.19 reveals the classification results that show the diagnostic capability of the classification algorithm on the OCTA images of this retinal layer to solving the CNV vs non-CNV classification task.

Like the findings in Table 5.18, the evaluation results in Table 5.19 also demonstrate that the automated classification algorithm can recognise some differences between the texture appearance of both CNV and non-CNV related lesions in the OCTA images of the deep inner retina layer. The classification results achieved with the $BRIEF_{S,n}^{PCA}$ texture descriptor are, however, very poor in all classification experiments. Nonetheless,

Table 5.19: A summary of classification results (mean AUC scores \pm standard deviations) that measure the performance of the automated classification algorithm that is based on reduced-local texture features for solving the CNV vs non-CNV classification task, on the OCTA images of the deep inner retina layer.

Descriptor	KNN Classifier		SVM Classifier	
	Best Parameters	AUC \pm std	Best Parameters	AUC \pm std
$LBP^{2riuPCA}_{4,1}$	$D^{k=7}_{chebyshev}$	0.59 ± 0.04	$K^{C=10,d=3}_{poly}$	0.62 ± 0.07
$LBP^{PCA}_{4,1}$	$D^{k=5}_{euclidean}$	0.64 ± 0.03	$K^{C=1,\gamma=0.1}_{rbf}$	0.66 ± 0.05
$BRIEF^{PCA}_{4,4}$	$D^{k=7}_{manhattan}$	0.52 ± 0.06	$K^{C=1,\gamma=0.001}_{rbf}$	0.50 ± 0.05
$LBP^{2riuPCA}_{8,2}$	$D^{k=5}_{manhattan}$	0.63 ± 0.04	$K^{C=1,\gamma=0.1}_{rbf}$	0.67 ± 0.02
$LBP^{PCA}_{8,2}$	$D^{k=7}_{manhattan}$	0.65 ± 0.05	$K^{C=10,d=3}_{poly}$	0.65 ± 0.04
$BRIEF^{PCA}_{5,8}$	$D^{k=7}_{euclidean}$	0.53 ± 0.05	$K^{C=1,\gamma=0.1}_{rbf}$	0.51 ± 0.05
$LBP^{2riuPCA}_{12,3}$	$D^{k=7}_{manhattan}$	0.64 ± 0.06	$K^{C=10,d=3}_{poly}$	0.67 ± 0.04
$LBP^{PCA}_{12,3}$	$D^{k=3}_{chebyshev}$	0.61 ± 0.05	$K^{C=10,\gamma=0.001}_{rbf}$	0.68 ± 0.05
$BRIEF^{PCA}_{6,12}$	$D^{k=3}_{chebyshev}$	0.51 ± 0.05	$K^{C=10,\gamma=0.1}_{rbf}$	0.54 ± 0.05
$LBP^{2riuPCA}_{16,4}$	$D^{k=3}_{manhattan}$	0.73 ± 0.05	$K^{C=10,d=3}_{poly}$	0.76 ± 0.03
$LBP^{PCA}_{16,4}$	$D^{k=5}_{chebyshev}$	0.53 ± 0.09	$K^{C=1}_{linear}$	0.52 ± 0.08
$BRIEF^{PCA}_{7,16}$	$D^{k=7}_{chebyshev}$	0.50 ± 0.02	$K^{C=1,d=4}_{poly}$	0.53 ± 0.02

the $LBP^{2riuPCA}_{p,r}$ and the $LBP^{PCA}_{p,r}$ texture descriptors both again demonstrated to allow some improvement in classification performance. However, the best overall classification performance was achieved with the $LBP^{2riuPCA}_{16,4}$ texture descriptor based on the SVM classifier with $K^{C=10,d=3}_{poly}$ accomplishing a mean AUC score and a standard deviation = 0.76 ± 0.03 .

5.4.2.3 Outer Retina Layer

The classification algorithm is then examined by separating patients with dry AMD from those with wet AMD in the OCTA images of the outer retina layer. Table 5.20 demonstrates the classification results that illustrate the diagnostic skill of the classification algorithm on the OCTA images of this retinal layer to solve the dry AMD vs wet AMD classification task.

The OCTA images of the outer retina layer do normally exhibit perceptible ocular vascular abnormalities related to dry or wet AMD disease. As such, the abnormalities can be clearly distinguishable from normal ocular vascular texture appearance. However, visually differentiating and examining diverse texture vascular appearance of different pathologies, e.g.: dry AMD and wet AMD, from each other in the OCTA images of the outer retina layer can be tremendously challenging. It is not uncommon

Table 5.20: A summary of classification results (mean AUC scores \pm standard deviations) that measure the performance of the automated classification algorithm that is based on reduced-local texture features for solving the dry AMD vs wet AMD classification task, on the OCTA images of outer retina layer.

Descriptor	KNN Classifier		SVM Classifier	
	Best Parameters	AUC \pm std	Best Parameters	AUC \pm std
$LBP_{4,1}^{2riuPCA}$	$D^{k=9}_{euclidean}$	0.68 ± 0.06	$K^{C=1}_{linear}$	0.75 ± 0.05
$LBP_{4,1}^{PCA}$	$D^{k=3}_{euclidean}$	0.73 ± 0.06	$K^{C=1}_{linear}$	0.79 ± 0.04
$BRIEF_{4,4}^{PCA}$	$D^{k=9}_{manhattan}$	0.66 ± 0.03	$K^{C=100}_{linear}$	0.68 ± 0.05
$LBP_{8,2}^{2riuPCA}$	$D^{k=3}_{euclidean}$	0.76 ± 0.05	$K^{C=1}_{linear}$	0.81 ± 0.04
$LBP_{8,2}^{PCA}$	$D^{k=9}_{manhattan}$	0.80 ± 0.03	$K^{C=10}_{linear}$	0.81 ± 0.03
$BRIEF_{5,8}^{PCA}$	$D^{k=9}_{euclidean}$	0.67 ± 0.06	$K^{C=10}_{linear}$	0.67 ± 0.06
$LBP_{12,3}^{2riuPCA}$	$D^{k=9}_{chebyshev}$	0.79 ± 0.05	$K^{C=1}_{linear}$	0.83 ± 0.03
$LBP_{12,3}^{PCA}$	$D^{k=7}_{euclidean}$	0.79 ± 0.08	$K^{C=1}_{linear}$	0.81 ± 0.04
$BRIEF_{6,12}^{PCA}$	$D^{k=5}_{euclidean}$	0.66 ± 0.04	$K^{C=10}_{linear}$	0.63 ± 0.06
$LBP_{16,4}^{2riuPCA}$	$D^{k=9}_{chebyshev}$	0.80 ± 0.05	$K^{C=50}_{linear}$	0.85 ± 0.02
$LBP_{16,4}^{PCA}$	$D^{k=3}_{euclidean}$	0.79 ± 0.05	$K^{C=10}_{linear}$	0.79 ± 0.05
$BRIEF_{7,16}^{PCA}$	$D^{k=9}_{euclidean}$	0.60 ± 0.05	$K^{C=10}_{linear}$	0.57 ± 0.06

for clinicians to request a second opinion in the diagnosis process. This is mainly due to the significant pattern variations between individuals, and the fact that the presentation of dry AMD and wet AMD in the various OCTA images can sometimes appear quite similar [10, 27].

Nonetheless, the evaluation results in Table 5.20 demonstrate that the automated classification algorithm can recognise dissimilarities among the textural appearance of dry AMD and wet AMD in the OCTA images of the outer retina layer. While the classification results with the $BRIEF_{S,n}^{PCA}$ texture descriptor proved to be the worst, the $LBP_{p,r}^{2riuPCA}$ and the $LBP_{p,r}^{PCA}$ texture descriptors both were capable of encouraging classification performance. Yet, the best overall classification performance was accomplished with the $LBP_{16,4}^{2riuPCA}$ texture descriptor based on the SVM classifier with $K^{C=50}_{linear}$ achieving a mean AUC score and a standard deviation = 0.85 ± 0.02 .

The algorithm is then evaluated on the OCTA images of the outer retina layer, but for the task of separating patients with CNV lesions from those with non-CNV lesions. Table 5.21 demonstrates the classification results that show the diagnostic skill of the classification algorithm on the OCTA images of this retinal layer to solve the image classification task of CNV vs non-CNV.

As was the case with the preceding classification task, i.e.: dry AMD vs wet AMD,

Table 5.21: A summary of classification results (mean AUC scores \pm standard deviations) that measure the performance of the automated classification algorithm that is based on reduced-local texture features for solving the CNV vs non-CNV classification task, on the OCTA images of outer retina layer.

Descriptor	KNN Classifier		SVM Classifier	
	Best Parameters	AUC \pm std	Best Parameters	AUC \pm std
$LBP_{4,1}^{2riuPCA}$	$D^{k=9}_{euclidean}$	0.71 ± 0.03	$K^{C=1}_{linear}$	0.76 ± 0.03
$LBP_{4,1}^{PCA}$	$D^{k=9}_{euclidean}$	0.71 ± 0.03	$K^{C=1}_{linear}$	0.73 ± 0.03
$BRIEF_{4,4}^{PCA}$	$D^{k=9}_{chebyshev}$	0.67 ± 0.04	$K^{C=100}_{linear}$	0.66 ± 0.05
$LBP_{8,2}^{2riuPCA}$	$D^{k=9}_{manhattan}$	0.76 ± 0.04	$K^{C=1}_{linear}$	0.81 ± 0.03
$LBP_{8,2}^{PCA}$	$D^{k=9}_{manhattan}$	0.79 ± 0.03	$K^{C=1}_{linear}$	0.80 ± 0.03
$BRIEF_{5,8}^{PCA}$	$D^{k=7}_{euclidean}$	0.66 ± 0.06	$K^{C=10}_{linear}$	0.65 ± 0.06
$LBP_{12,3}^{2riuPCA}$	$D^{k=7}_{manhattan}$	0.79 ± 0.03	$K^{C=1}_{linear}$	0.81 ± 0.03
$LBP_{12,3}^{PCA}$	$D^{k=3}_{euclidean}$	0.77 ± 0.05	$K^{C=1}_{linear}$	0.81 ± 0.03
$BRIEF_{6,12}^{PCA}$	$D^{k=5}_{euclidean}$	0.66 ± 0.05	$K^{C=10}_{linear}$	0.63 ± 0.06
$LBP_{16,4}^{2riuPCA}$	$D^{k=9}_{chebyshev}$	0.80 ± 0.02	$K^{C=1}_{linear}$	0.83 ± 0.03
$LBP_{16,4}^{PCA}$	$D^{k=3}_{euclidean}$	0.79 ± 0.04	$K^{C=1}_{linear}$	0.82 ± 0.04
$BRIEF_{7,16}^{PCA}$	$D^{k=7}_{euclidean}$	0.63 ± 0.07	$K^{C=1}_{linear}$	0.59 ± 0.09

on the OCTA images of the outer retina layer, visually differentiating between different lesions related to non-CNV and CNV in the OCTA images of the outer retina layer is also tremendously challenging [10, 27]. Nevertheless, the evaluation results in Table 5.21 demonstrate that the automated classification algorithm can distinguish variations among the textural appearance of non-CNV and CNV lesions in the OCTA images of the outer retina layer. The classification results with the $BRIEF_{S,n}^{PCA}$ texture descriptor were among the worst. However, the $LBP_{p,r}^{2riuPCA}$ and the $LBP_{p,r}^{PCA}$ texture descriptors both generally showed to enable very promising classification performance. The best overall classification performance was, however, accomplished with the $LBP_{16,4}^{2riuPCA}$ texture descriptor based on the SVM classifier with $K^{C=1}_{linear}$ achieving a mean AUC score and a standard deviation = 0.83 ± 0.03 .

5.4.2.4 Choriocapillaris Layer

Following the evaluation of the classification algorithm on the OCTA images of individual previous retinal layers, the classification algorithm is subsequently assessed on solving the task of distinguishing various patients with dry AMD and wet AMD in the OCTA images of the choriocapillaris layer. Table 5.22 demonstrates the classification results that illustrate the diagnostic ability of the classification algorithm on the OCTA images of this choroidal layer for the dry AMD vs wet AMD image classification task.

Table 5.22: A summary of classification results (mean AUC scores \pm standard deviations) that measure the performance of the automated classification algorithm that is based on reduced-local texture features for solving the dry AMD vs wet AMD classification task, on the OCTA images of choriocapillaris layer.

Descriptor	KNN Classifier		SVM Classifier	
	Best Parameters	AUC \pm std	Best Parameters	AUC \pm std
$LBP_{4,1}^{2riuPCA}$	$D^{k=7}_{manhattan}$	0.76 ± 0.03	$K_{rbf}^{C=10, \gamma=0.001}$	0.78 ± 0.02
$LBP_{4,1}^{PCA}$	$D^{k=3}_{euclidean}$	0.76 ± 0.03	$K_{rbf}^{C=1, \gamma=0.01}$	0.76 ± 0.03
$BRIEF_{4,4}^{PCA}$	$D^{k=5}_{euclidean}$	0.55 ± 0.04	$K_{rbf}^{C=1, \gamma=0.01}$	0.53 ± 0.07
$LBP_{8,2}^{2riuPCA}$	$D^{k=3}_{euclidean}$	0.79 ± 0.03	$K_{rbf}^{C=1, \gamma=0.001}$	0.82 ± 0.01
$LBP_{8,2}^{PCA}$	$D^{k=3}_{euclidean}$	0.78 ± 0.03	$K_{rbf}^{C=1, \gamma=0.01}$	0.81 ± 0.01
$BRIEF_{5,8}^{PCA}$	$D^{k=5}_{manhattan}$	0.55 ± 0.10	$K_{linear}^{C=10}$	0.54 ± 0.09
$LBP_{12,3}^{2riuPCA}$	$D^{k=7}_{chebyshev}$	0.79 ± 0.05	$K_{linear}^{C=1}$	0.83 ± 0.02
$LBP_{12,3}^{PCA}$	$D^{k=7}_{chebyshev}$	0.77 ± 0.02	$K_{linear}^{C=1}$	0.81 ± 0.02
$BRIEF_{6,12}^{PCA}$	$D^{k=7}_{chebyshev}$	0.57 ± 0.04	$K_{linear}^{C=1}$	0.56 ± 0.05
$LBP_{16,4}^{2riuPCA}$	$D^{k=7}_{euclidean}$	0.75 ± 0.03	$K_{linear}^{C=1}$	0.80 ± 0.02
$LBP_{16,4}^{PCA}$	$D^{k=7}_{manhattan}$	0.77 ± 0.02	$K_{linear}^{C=1}$	0.80 ± 0.03
$BRIEF_{7,16}^{PCA}$	$D^{k=7}_{chebyshev}$	0.58 ± 0.06	$K_{poly}^{C=1, d=2}$	0.55 ± 0.08

The OCTA images of the choriocapillaris layer are also the same as the OCTA images of the outer retina layer in exhibiting perceptible regions of vascular abnormalities related to dry AMD and wet AMD, which are normally very noticeable and significantly different from normal ocular vascular texture appearance. Nevertheless, visually distinguishing the textural appearance of assorted vascular pathologies related to dry AMD and wet AMD from each other in the OCTA images of the choriocapillaris layer can be massively challenging [10, 27]. The evaluation results in Table 5.22, however, prove that the automated classification algorithm can identify differences in the vascular textural appearance of the OCTA images of choriocapillaris layer between various subjects with dry AMD and wet AMD. The classification results with the $BRIEF_{S,n}^{PCA}$ texture descriptor proved to be the worst, the $LBP_{p,r}^{2riuPCA}$ and the $LBP_{p,r}^{PCA}$ texture descriptors both were capable to facilitate improving classification performance. The best overall classification performance is, however, accomplished with the $LBP_{12,3}^{2riuPCA}$ texture descriptor based on the SVM classifier with $K_{linear}^{C=1}$ achieving a mean AUC score and a standard deviation = 0.83 ± 0.02 .

The classification algorithm is afterwards assessed on the OCTA images of the choriocapillaris layer, but for distinguishing between patients with CNV and non-CNV lesions. Table 5.23 summarises the classification results that provide the diagnostic capability of the classification algorithm on the OCTA images of this choroidal layer

to solve the CNV vs non-CNV image classification task.

Table 5.23: A summary of classification results (mean AUC scores \pm standard deviations) that measure the performance of the automated classification algorithm that is based on reduced-local texture features for solving the CNV vs non-CNV classification task, on the OCTA images of choriocapillaris layer.

Descriptor	KNN Classifier		SVM Classifier	
	Best Parameters	AUC \pm std	Best Parameters	AUC \pm std
$LBP_{4,1}^{2riuPCA}$	$D^{k=3}_{euclidean}$	0.73 ± 0.06	$K_{rbf}^{C=10,\gamma=0.01}$	0.71 ± 0.05
$LBP_{4,1}^{PCA}$	$D^{k=7}_{manhattan}$	0.71 ± 0.02	$K_{rbf}^{C=50,\gamma=0.01}$	0.69 ± 0.08
$BRIEF_{4,4}^{PCA}$	$D^{k=3}_{chebyshev}$	0.56 ± 0.06	$K_{poly}^{C=10,d=2}$	0.55 ± 0.08
$LBP_{8,2}^{2riuPCA}$	$D^{k=3}_{euclidean}$	0.72 ± 0.05	$K_{rbf}^{C=50,\gamma=0.001}$	0.73 ± 0.04
$LBP_{8,2}^{PCA}$	$D^{k=7}_{chebyshev}$	0.75 ± 0.04	$K_{rbf}^{C=1,\gamma=0.01}$	0.74 ± 0.06
$BRIEF_{5,8}^{PCA}$	$D^{k=7}_{euclidean}$	0.54 ± 0.04	$K_{rbf}^{C=1,\gamma=0.001}$	0.54 ± 0.05
$LBP_{12,3}^{2riuPCA}$	$D^{k=7}_{manhattan}$	0.76 ± 0.04	$K_{rbf}^{C=10,\gamma=0.001}$	0.81 ± 0.02
$LBP_{12,3}^{PCA}$	$D^{k=3}_{euclidean}$	0.73 ± 0.03	$K_{rbf}^{C=1,\gamma=0.001}$	0.76 ± 0.04
$BRIEF_{6,12}^{PCA}$	$D^{k=3}_{chebyshev}$	0.55 ± 0.07	$K_{linear}^{C=1}$	0.53 ± 0.04
$LBP_{16,4}^{2riuPCA}$	$D^{k=7}_{chebyshev}$	0.74 ± 0.04	$K_{rbf}^{C=10,\gamma=0.01}$	0.80 ± 0.02
$LBP_{16,4}^{PCA}$	$D^{k=7}_{chebyshev}$	0.74 ± 0.05	$K_{poly}^{C=1,d=2}$	0.79 ± 0.03
$BRIEF_{7,16}^{PCA}$	$D^{k=3}_{euclidean}$	0.50 ± 0.04	$K_{linear}^{C=1}$	0.53 ± 0.03

Comparable to the previous classification task, i.e.: dry AMD vs wet AMD, conducted on the OCTA images of the choriocapillaris layer, visually distinguishing non-CNV from CNV lesions in the OCTA images of the choriocapillaris layer can also be extremely challenging [10, 27]. Nonetheless, the evaluation results in Table 5.23 prove that the automated classification algorithm can successfully recognise some dissimilarities between non-CNV and CNV lesions in the textural appearance of the OCTA images of the choriocapillaris layer. The classification results obtained with the $BRIEF_{S,n}^{PCA}$ texture descriptor were among the worst. Nevertheless, the $LBP_{p,r}^{2riuPCA}$ and the $LBP_{p,r}^{PCA}$ texture descriptors both indicated a good capacity to allow the attainment of promising classification performance. Yet, the best overall classification performance is also reached with the $LBP_{12,3}^{2riuPCA}$ texture descriptor based on the SVM classifier with $K_{rbf}^{C=10,\gamma=0.001}$ accomplishing a mean AUC score and a standard deviation $= 0.81 \pm 0.2$.

5.4.2.5 Layer Combination

The classification algorithm is then assessed on classifying the various patients with dry AMD and wet AMD via layer combination. This is accomplished by conducting

the binary image classification based on concatenating two feature vectors extracted from the OCTA images of the different ocular vascular layers, based on concatenating three feature vectors extracted from three OCTA images of the different ocular vascular layers and based on concatenating all feature vectors extracted from the OCTA images of all ocular vascular layers.

Tables 5.24, 5.25, 5.26, 5.27, 5.28 and 5.29 provide the classification results of the classification algorithm after concatenating two feature vectors extracted from the OCTA images of two different ocular vascular layers. Specifically, the superficial and the deep inner retina, the superficial inner and the outer retina, the superficial inner retina and the choriocapillaris, the deep inner and the outer retina, the deep inner retina and the choriocapillaris, and the outer retina and the choriocapillaris layers, respectively.

Table 5.24: A summary of classification results (mean AUC scores \pm standard deviations) that measure the performance of the automated classification algorithm that is based on reduced-local texture features for solving the dry AMD vs wet AMD classification task, based on concatenating two feature vectors extracted from the OCTA images of the superficial and the deep retina layers.

Descriptor	KNN Classifier		SVM Classifier	
	Best Parameters	AUC \pm std	Best Parameters	AUC \pm std
$LBP_{4,1}^{2riuPCA}$	$D^{k=5}_{manhattan}$	0.62 ± 0.03	$K^{C=1}_{linear}$	0.63 ± 0.06
$LBP_{4,1}^{PCA}$	$D^{k=5}_{euclidean}$	0.64 ± 0.05	$K^{C=10,d=3}_{poly}$	0.65 ± 0.05
$BRIEF_{4,4}^{PCA}$	$D^{k=3}_{manhattan}$	0.50 ± 0.04	$K^{C=1,d=2}_{poly}$	0.51 ± 0.06
$LBP_{8,2}^{2riuPCA}$	$D^{k=5}_{euclidean}$	0.61 ± 0.06	$K^{C=10}_{linear}$	0.64 ± 0.06
$LBP_{8,2}^{PCA}$	$D^{k=5}_{chebyshev}$	0.64 ± 0.05	$K^{C=1,\gamma=0.01}_{rbf}$	0.63 ± 0.05
$BRIEF_{5,8}^{PCA}$	$D^{k=3}_{euclidean}$	0.50 ± 0.07	$K^{C=10,d=2}_{poly}$	0.50 ± 0.06
$LBP_{12,3}^{2riuPCA}$	$D^{k=5}_{chebyshev}$	0.61 ± 0.05	$K^{C=1,d=3}_{poly}$	0.63 ± 0.05
$LBP_{12,3}^{PCA}$	$D^{k=5}_{euclidean}$	0.62 ± 0.05	$K^{C=10,d=2}_{poly}$	0.64 ± 0.06
$BRIEF_{6,12}^{PCA}$	$D^{k=1}_{chebyshev}$	0.51 ± 0.04	$K^{C=1,d=2}_{poly}$	0.50 ± 0.04
$LBP_{16,4}^{2riuPCA}$	$D^{k=3}_{chebyshev}$	0.60 ± 0.04	$K^{C=10,d=3}_{poly}$	0.62 ± 0.02
$LBP_{16,4}^{PCA}$	$D^{k=7}_{euclidean}$	0.61 ± 0.04	$K^{C=1,d=2}_{poly}$	0.63 ± 0.05
$BRIEF_{7,16}^{PCA}$	$D^{k=5}_{chebyshev}$	0.50 ± 0.03	$K^{C=10,d=2}_{poly}$	0.50 ± 0.05

Tables 5.30, 5.31, 5.32 and 5.33, on the other hand, reveal the classification results of the classification algorithm when concatenating three feature vectors extracted from three OCTA images of different ocular vascular layers. Namely, the superficial, the deep inner and the outer retina, the superficial, the deep inner retina and the choriocapillaris, the superficial inner, the outer retina and the choriocapillaris, and the deep inner, the outer retina and the choriocapillaris layers, respectively.

Table 5.25: A summary of classification results (mean AUC scores \pm standard deviations) that measure the performance of the automated classification algorithm that is based on reduced-local texture features for solving the dry AMD vs wet AMD classification task, based on concatenating two feature vectors extracted from the OCTA images of the superficial and the outer retina layers.

Descriptor	KNN Classifier		SVM Classifier	
	Best Parameters	AUC \pm std	Best Parameters	AUC \pm std
$LBP_{4,1}^{2riuPCA}$	$D^{k=5}_{euclidean}$	0.65 ± 0.05	$K^{C=10}_{linear}$	0.64 ± 0.06
$LBP_{4,1}^{PCA}$	$D^{k=5}_{manhattan}$	0.64 ± 0.03	$K^{C=10,d=3}_{poly}$	0.65 ± 0.04
$BRIEF_{4,4}^{PCA}$	$D^{k=3}_{chebyshev}$	0.62 ± 0.05	$K^{C=1,d=3}_{poly}$	0.64 ± 0.06
$LBP_{8,2}^{2riuPCA}$	$D^{k=5}_{manhattan}$	0.65 ± 0.05	$K^{C=10}_{linear}$	0.64 ± 0.09
$LBP_{8,2}^{PCA}$	$D^{k=5}_{manhattan}$	0.64 ± 0.05	$K^{C=10,d=3}_{poly}$	0.65 ± 0.05
$BRIEF_{5,8}^{PCA}$	$D^{k=5}_{euclidean}$	0.56 ± 0.06	$K^{C=10,\gamma=0.1}_{rbf}$	0.59 ± 0.06
$LBP_{12,3}^{2riuPCA}$	$D^{k=5}_{chebyshev}$	0.64 ± 0.05	$K^{C=1,d=3}_{poly}$	0.65 ± 0.08
$LBP_{12,3}^{PCA}$	$D^{k=5}_{manhattan}$	0.64 ± 0.04	$K^{C=1}_{linear}$	0.65 ± 0.04
$BRIEF_{6,12}^{PCA}$	$D^{k=5}_{manhattan}$	0.57 ± 0.06	$K^{C=1,d=3}_{poly}$	0.60 ± 0.07
$LBP_{16,4}^{2riuPCA}$	$D^{k=5}_{euclidean}$	0.65 ± 0.04	$K^{C=10,d=2}_{poly}$	0.64 ± 0.06
$LBP_{16,4}^{PCA}$	$D^{k=3}_{manhattan}$	0.66 ± 0.03	$K^{C=10}_{linear}$	0.65 ± 0.05
$BRIEF_{7,16}^{PCA}$	$D^{k=3}_{manhattan}$	0.56 ± 0.03	$K^{C=10,d=3}_{poly}$	0.59 ± 0.05

Table 5.26: A summary of classification results (mean AUC scores \pm standard deviations) that measure the performance of the automated classification algorithm that is based on reduced-local texture features for solving the dry AMD vs wet AMD classification task, based on concatenating two feature vectors extracted from the OCTA images of the superficial retina and the choriocapillaris retina layers.

Descriptor	KNN Classifier		SVM Classifier	
	Best Parameters	AUC \pm std	Best Parameters	AUC \pm std
$LBP_{4,1}^{2riuPCA}$	$D^{k=5}_{chebyshev}$	0.66 ± 0.04	$K^{C=10}_{linear}$	0.65 ± 0.06
$LBP_{4,1}^{PCA}$	$D^{k=5}_{manhattan}$	0.66 ± 0.03	$K^{C=10,d=3}_{poly}$	0.64 ± 0.05
$BRIEF_{4,4}^{PCA}$	$D^{k=3}_{chebyshev}$	0.51 ± 0.04	$K^{C=10,d=3}_{poly}$	0.50 ± 0.05
$LBP_{8,2}^{2riuPCA}$	$D^{k=5}_{euclidean}$	0.66 ± 0.05	$K^{C=1}_{linear}$	0.65 ± 0.06
$LBP_{8,2}^{PCA}$	$D^{k=5}_{manhattan}$	0.66 ± 0.03	$K^{C=10,d=2}_{poly}$	0.64 ± 0.04
$BRIEF_{5,8}^{PCA}$	$D^{k=5}_{euclidean}$	0.50 ± 0.06	$K^{C=10,d=2}_{poly}$	0.51 ± 0.05
$LBP_{12,3}^{2riuPCA}$	$D^{k=5}_{euclidean}$	0.66 ± 0.05	$K^{C=1,d=3}_{poly}$	0.64 ± 0.06
$LBP_{12,3}^{PCA}$	$D^{k=5}_{manhattan}$	0.66 ± 0.03	$K^{C=10}_{linear}$	0.64 ± 0.05
$BRIEF_{6,12}^{PCA}$	$D^{k=5}_{manhattan}$	0.53 ± 0.05	$K^{C=10,d=3}_{poly}$	0.52 ± 0.06
$LBP_{16,4}^{2riuPCA}$	$D^{k=3}_{euclidean}$	0.67 ± 0.03	$K^{C=1}_{linear}$	0.66 ± 0.05
$LBP_{16,4}^{PCA}$	$D^{k=7}_{manhattan}$	0.65 ± 0.04	$K^{C=1,d=2}_{poly}$	0.64 ± 0.04
$BRIEF_{7,16}^{PCA}$	$D^{k=5}_{chebyshev}$	0.50 ± 0.03	$K^{C=10,d=2}_{poly}$	0.51 ± 0.04

Table 5.27: A summary of classification results (mean AUC scores \pm standard deviations) that measure the performance of the automated classification algorithm that is based on reduced-local texture features for solving the dry AMD vs wet AMD classification task, based on concatenating two feature vectors extracted from the OCTA images of the deep and the outer retina layers.

Descriptor	KNN Classifier		SVM Classifier	
	Best Parameters	AUC \pm std	Best Parameters	AUC \pm std
$LBP_{4,1}^{2riuPCA}$	$D^{k=5}_{chebyshev}$	0.62 ± 0.04	$K_{rbf}^{C=1, \gamma=0.01}$	0.61 ± 0.05
$LBP_{4,1}^{PCA}$	$D^{k=5}_{manhattan}$	0.65 ± 0.03	$K_{poly}^{C=10, d=3}$	0.63 ± 0.04
$BRIEF_{4,4}^{PCA}$	$D^{k=5}_{chebyshev}$	0.62 ± 0.06	$K_{poly}^{C=1, d=3}$	0.64 ± 0.07
$LBP_{8,2}^{2riuPCA}$	$D^{k=5}_{manhattan}$	0.62 ± 0.05	$K_{rbf}^{C=10, \gamma=0.01}$	0.65 ± 0.05
$LBP_{8,2}^{PCA}$	$D^{k=5}_{manhattan}$	0.64 ± 0.03	$K_{poly}^{C=10, d=3}$	0.67 ± 0.04
$BRIEF_{5,8}^{PCA}$	$D^{k=5}_{euclidean}$	0.55 ± 0.04	$K_{poly}^{C=1, d=2}$	0.60 ± 0.07
$LBP_{12,3}^{2riuPCA}$	$D^{k=5}_{euclidean}$	0.62 ± 0.04	$K_{linear}^{C=1}$	0.65 ± 0.05
$LBP_{12,3}^{PCA}$	$D^{k=5}_{manhattan}$	0.64 ± 0.03	$K_{poly}^{C=10, d=3}$	0.63 ± 0.04
$BRIEF_{6,12}^{PCA}$	$D^{k=5}_{manhattan}$	0.62 ± 0.04	$K_{poly}^{C=1, d=3}$	0.63 ± 0.05
$LBP_{16,4}^{2riuPCA}$	$D^{k=3}_{manhattan}$	0.65 ± 0.04	$K_{rbf}^{C=1, \gamma=0.1}$	0.62 ± 0.03
$LBP_{16,4}^{PCA}$	$D^{k=5}_{manhattan}$	0.64 ± 0.05	$K_{poly}^{C=1, d=2}$	0.66 ± 0.03
$BRIEF_{7,16}^{PCA}$	$D^{k=7}_{euclidean}$	0.52 ± 0.05	$K_{poly}^{C=01, d=2}$	0.57 ± 0.06

Table 5.28: A summary of classification results (mean AUC scores \pm standard deviations) that measure the performance of the automated classification algorithm that is based on reduced-local texture features for solving the dry AMD vs wet AMD classification task, based on concatenating two feature vectors extracted from the OCTA images of the deep retina and the choriocapillaris layers.

Descriptor	KNN Classifier		SVM Classifier	
	Best Parameters	AUC \pm std	Best Parameters	AUC \pm std
$LBP_{4,1}^{2riuPCA}$	$D^{k=5}_{chebyshev}$	0.67 ± 0.05	$K_{rbf}^{C=10, \gamma=0.01}$	0.66 ± 0.06
$LBP_{4,1}^{PCA}$	$D^{k=5}_{manhattan}$	0.67 ± 0.04	$K_{rbf}^{C=1, \gamma=0.01}$	0.65 ± 0.05
$BRIEF_{4,4}^{PCA}$	$D^{k=3}_{chebyshev}$	0.51 ± 0.06	$K_{poly}^{C=1, d=3}$	0.50 ± 0.07
$LBP_{8,2}^{2riuPCA}$	$D^{k=5}_{manhattan}$	0.65 ± 0.04	$K_{rbf}^{C=1, \gamma=0.01}$	0.64 ± 0.04
$LBP_{8,2}^{PCA}$	$D^{k=5}_{manhattan}$	0.67 ± 0.05	$K_{rbf}^{C=10, \gamma=0.01}$	0.64 ± 0.04
$BRIEF_{5,8}^{PCA}$	$D^{k=1}_{chebyshev}$	0.50 ± 0.05	$K_{rbf}^{C=1, \gamma=0.01}$	0.50 ± 0.07
$LBP_{12,3}^{2riuPCA}$	$D^{k=3}_{chebyshev}$	0.63 ± 0.04	$K_{rbf}^{C=1, \gamma=0.01}$	0.68 ± 0.05
$LBP_{12,3}^{PCA}$	$D^{k=5}_{manhattan}$	0.63 ± 0.05	$K_{rbf}^{C=1, \gamma=0.1}$	0.63 ± 0.05
$BRIEF_{6,12}^{PCA}$	$D^{k=1}_{euclidean}$	0.53 ± 0.06	$K_{poly}^{C=10, d=3}$	0.50 ± 0.07
$LBP_{16,4}^{2riuPCA}$	$D^{k=3}_{manhattan}$	0.67 ± 0.05	$K_{rbf}^{C=10, \gamma=0.1}$	0.63 ± 0.03
$LBP_{16,4}^{PCA}$	$D^{k=3}_{manhattan}$	0.63 ± 0.04	$K_{rbf}^{C=1, \gamma=0.1}$	0.69 ± 0.04
$BRIEF_{7,16}^{PCA}$	$D^{k=3}_{euclidean}$	0.52 ± 0.07	$K_{poly}^{C=1, d=3}$	0.51 ± 0.05

Table 5.29: A summary of classification results (mean AUC scores \pm standard deviations) that measure the performance of the automated classification algorithm that is based on reduced-local texture features for solving the dry AMD vs wet AMD classification task, based on concatenating two feature vectors extracted from the OCTA images of the outer retina and the choriocapillaris layers.

Descriptor	KNN Classifier		SVM Classifier	
	Best Parameters	AUC \pm std	Best Parameters	AUC \pm std
$LBP_{4,1}^{2riuPCA}$	$D^{k=3}_{manhattan}$	0.73 ± 0.07	$K^{C=1}_{linear}$	0.72 ± 0.06
$LBP_{4,1}^{PCA}$	$D^{k=5}_{manhattan}$	0.67 ± 0.07	$K^{C=10}_{linear}$	0.71 ± 0.07
$BRIEF_{4,4}^{PCA}$	$D^{k=5}_{euclidean}$	0.60 ± 0.06	$K^{C=10}_{linear}$	0.64 ± 0.07
$LBP_{8,2}^{2riuPCA}$	$D^{k=3}_{chebyshev}$	0.70 ± 0.07	$K^{C=10,\gamma=0.01}_{rbf}$	0.71 ± 0.07
$LBP_{8,2}^{PCA}$	$D^{k=3}_{manhattan}$	0.70 ± 0.06	$K^{C=10,d=3}_{poly}$	0.71 ± 0.05
$BRIEF_{5,8}$	$D^{k=5}_{euclidean}$	0.59 ± 0.06	$K^{C=10,d=2}_{poly}$	0.62 ± 0.07
$LBP_{12,3}^{2riuPCA}$	$D^{k=5}_{chebyshev}$	0.71 ± 0.05	$K^{C=10,\gamma=0.01}_{rbf}$	0.74 ± 0.07
$LBP_{12,3}^{PCA}$	$D^{k=3}_{manhattan}$	0.71 ± 0.05	$K^{C=10,\gamma=0.01}_{rbf}$	0.70 ± 0.05
$BRIEF_{6,12}^{PCA}$	$D^{k=5}_{manhattan}$	0.59 ± 0.06	$K^{C=10,d=2}_{poly}$	0.60 ± 0.06
$LBP_{16,4}^{2riuPCA}$	$D^{k=5}_{euclidean}$	0.70 ± 0.03	$K^{C=1}_{linear}$	0.72 ± 0.06
$LBP_{16,4}^{PCA}$	$D^{k=5}_{manhattan}$	0.71 ± 0.05	$K^{C=1}_{linear}$	0.70 ± 0.06
$BRIEF_{7,16}^{PCA}$	$D^{k=1}_{chebyshev}$	0.53 ± 0.06	$K^{C=1}_{linear}$	0.58 ± 0.08

Table 5.30: A summary of classification results (mean AUC scores \pm standard deviations) that measure the performance of the automated classification algorithm that is based on reduced-local texture features for solving the dry AMD vs wet AMD classification task, based on concatenating three feature vectors extracted from the OCTA images of the superficial inner, the deep inner and the outer retina layers.

Descriptor	KNN Classifier		SVM Classifier	
	Best Parameters	AUC \pm std	Best Parameters	AUC \pm std
$LBP_{4,1}^{2riuPCA}$	$D^{k=5}_{manhattan}$	0.67 ± 0.03	$K^{C=1}_{linear}$	0.66 ± 0.08
$LBP_{4,1}^{PCA}$	$D^{k=3}_{euclidean}$	0.64 ± 0.03	$K^{C=10,d=3}_{poly}$	0.63 ± 0.05
$BRIEF_{4,4}^{PCA}$	$D^{k=3}_{euclidean}$	0.52 ± 0.05	$K^{C=1,d=3}_{poly}$	0.57 ± 0.07
$LBP_{8,2}^{2riuPCA}$	$D^{k=5}_{euclidean}$	0.68 ± 0.05	$K^{C=10,\gamma=0.01}_{rbf}$	0.69 ± 0.07
$LBP_{8,2}^{PCA}$	$D^{k=5}_{manhattan}$	0.67 ± 0.04	$K^{C=10,d=3}_{poly}$	0.70 ± 0.04
$BRIEF_{5,8}^{PCA}$	$D^{k=5}_{chebyshev}$	0.53 ± 0.06	$K^{C=50}_{linear}$	0.56 ± 0.06
$LBP_{12,3}^{2riuPCA}$	$D^{k=5}_{euclidean}$	0.67 ± 0.03	$K^{C=1}_{linear}$	0.64 ± 0.08
$LBP_{12,3}^{PCA}$	$D^{k=5}_{manhattan}$	0.68 ± 0.06	$K^{C=10,d=3}_{poly}$	0.69 ± 0.06
$BRIEF_{6,12}^{PCA}$	$D^{k=5}_{manhattan}$	0.57 ± 0.04	$K^{C=10,d=3}_{poly}$	0.61 ± 0.06
$LBP_{16,4}^{2riuPCA}$	$D^{k=7}_{manhattan}$	0.64 ± 0.04	$K^{C=1,\gamma=0.1}_{rbf}$	0.63 ± 0.06
$LBP_{16,4}^{PCA}$	$D^{k=7}_{manhattan}$	0.65 ± 0.03	$K^{C=1,d=2}_{poly}$	0.64 ± 0.05
$BRIEF_{7,16}^{PCA}$	$D^{k=3}_{chebyshev}$	0.52 ± 0.05	$K^{C=10}_{linear}$	0.54 ± 0.07

Table 5.31: A summary of classification results (mean AUC scores \pm standard deviations) that measure the performance of the automated classification algorithm that is based on reduced-local texture features for solving the dry AMD vs wet AMD classification task, based on concatenating three feature vectors extracted from the OCTA images of the superficial, the deep inner retina and the choriocapillaris layers.

Descriptor	KNN Classifier		SVM Classifier	
	Best Parameters	AUC \pm std	Best Parameters	AUC \pm std
$LBP_{4,1}^{2riuPCA}$	$D^{k=5}_{manhattan}$	0.75 ± 0.05	$K^{C=1}_{linear}$	0.76 ± 0.05
$LBP_{4,1}^{PCA}$	$D^{k=5}_{manhattan}$	0.76 ± 0.04	$K^{C=1, \gamma=0.01}_{rbf}$	0.76 ± 0.05
$BRIEF_{4,4}^{PCA}$	$D^{k=5}_{chebyshev}$	0.50 ± 0.02	$K^{C=50}_{linear}$	0.50 ± 0.04
$LBP_{8,2}^{2riuPCA}$	$D^{k=5}_{manhattan}$	0.73 ± 0.05	$K^{C=1, \gamma=0.01}_{rbf}$	0.76 ± 0.06
$LBP_{8,2}^{PCA}$	$D^{k=5}_{euclidean}$	0.77 ± 0.05	$K^{C=1, d=3}_{poly}$	0.71 ± 0.10
$BRIEF_{5,8}^{PCA}$	$D^{k=3}_{manhattan}$	0.50 ± 0.05	$K^{C=50, d=3}_{poly}$	0.51 ± 0.06
$LBP_{12,3}^{2riuPCA}$	$D^{k=5}_{euclidean}$	0.72 ± 0.06	$K^{C=1, \gamma=0.01}_{rbf}$	0.75 ± 0.05
$LBP_{12,3}^{PCA}$	$D^{k=5}_{chebyshev}$	0.61 ± 0.03	$K^{C=1, d=3}_{poly}$	0.58 ± 0.10
$BRIEF_{6,12}^{PCA}$	$D^{k=3}_{chebyshev}$	0.57 ± 0.06	$K^{C=10, \gamma=0.1}_{rbf}$	0.55 ± 0.08
$LBP_{16,4}^{2riuPCA}$	$D^{k=5}_{manhattan}$	0.75 ± 0.06	$K^{C=1, \gamma=0.01}_{rbf}$	0.76 ± 0.06
$LBP_{16,4}^{PCA}$	$D^{k=5}_{manhattan}$	0.56 ± 0.08	$K^{C=1}_{linear}$	0.52 ± 0.09
$BRIEF_{7,16}^{PCA}$	$D^{k=3}_{euclidean}$	0.60 ± 0.07	$K^{C=50, d=3}_{poly}$	0.57 ± 0.07

Table 5.32: A summary of classification results (mean AUC scores \pm standard deviations) that measure the performance of the automated classification algorithm that is based on reduced-local texture features for solving the dry AMD vs wet AMD classification task, based on concatenating three feature vectors extracted from the OCTA images of the superficial inner, the outer retina and the choriocapillaris layers.

Descriptor	KNN Classifier		SVM Classifier	
	Best Parameters	AUC \pm std	Best Parameters	AUC \pm std
$LBP_{4,1}^{2riuPCA}$	$D^{k=5}_{chebyshev}$	0.70 ± 0.05	$K^{C=10}_{linear}$	0.75 ± 0.06
$LBP_{4,1}^{PCA}$	$D^{k=5}_{manhattan}$	0.72 ± 0.05	$K^{C=10, d=3}_{poly}$	0.70 ± 0.06
$BRIEF_{4,4}^{PCA}$	$D^{k=1}_{euclidean}$	0.57 ± 0.06	$K^{C=50}_{linear}$	0.62 ± 0.08
$LBP_{8,2}^{2riuPCA}$	$D^{k=5}_{manhattan}$	0.74 ± 0.04	$K^{C=1, d=3}_{poly}$	0.70 ± 0.06
$LBP_{8,2}^{PCA}$	$D^{k=3}_{manhattan}$	0.70 ± 0.06	$K^{C=10, d=3}_{poly}$	0.75 ± 0.05
$BRIEF_{5,8}^{PCA}$	$D^{k=5}_{manhattan}$	0.53 ± 0.03	$K^{C=50}_{linear}$	0.54 ± 0.07
$LBP_{12,3}^{2riuPCA}$	$D^{k=5}_{euclidean}$	0.70 ± 0.04	$K^{C=1, d=3}_{poly}$	0.74 ± 0.07
$LBP_{12,3}^{PCA}$	$D^{k=5}_{manhattan}$	0.70 ± 0.05	$K^{C=10, d=3}_{poly}$	0.77 ± 0.05
$BRIEF_{6,12}^{PCA}$	$D^{k=5}_{manhattan}$	0.61 ± 0.05	$K^{C=50}_{linear}$	0.62 ± 0.06
$LBP_{16,4}^{2riuPCA}$	$D^{k=7}_{euclidean}$	0.73 ± 0.04	$K^{C=1}_{linear}$	0.70 ± 0.05
$LBP_{16,4}^{PCA}$	$D^{k=3}_{manhattan}$	0.71 ± 0.04	$K^{C=1, d=4}_{poly}$	0.70 ± 0.05
$BRIEF_{7,16}^{PCA}$	$D^{k=7}_{euclidean}$	0.54 ± 0.08	$K^{C=10}_{linear}$	0.60 ± 0.07

Table 5.33: A summary of classification results (mean AUC scores \pm standard deviations) that measure the performance of the automated classification algorithm that is based on reduced-local texture features for solving the dry AMD vs wet AMD classification task, based on concatenating three feature vectors extracted from the OCTA images of the deep inner, the outer retina and the choriocapillaris layers.

Descriptor	KNN Classifier		SVM Classifier	
	Best Parameters	AUC \pm std	Best Parameters	AUC \pm std
$LBP_{4,1}^{2riuPCA}$	$D^{k=3}_{euclidean}$	0.72 ± 0.05	$K^{C=10}_{linear}$	0.75 ± 0.06
$LBP_{4,1}^{PCA}$	$D^{k=3}_{manhattan}$	0.72 ± 0.04	$K^{C=10,d=3}_{poly}$	0.75 ± 0.06
$BRIEF_{4,4}^{PCA}$	$D^{k=5}_{chebyshev}$	0.57 ± 0.05	$K^{C=50}_{linear}$	0.62 ± 0.07
$LBP_{8,2}^{2riuPCA}$	$D^{k=5}_{chebyshev}$	0.74 ± 0.04	$K^{C=1,d=3}_{poly}$	0.72 ± 0.06
$LBP_{8,2}^{PCA}$	$D^{k=5}_{manhattan}$	0.72 ± 0.04	$K^{C=10,d=3}_{poly}$	0.74 ± 0.04
$BRIEF_{5,8}^{PCA}$	$D^{k=5}_{chebyshev}$	0.55 ± 0.06	$K^{C=50}_{linear}$	0.57 ± 0.06
$LBP_{12,3}^{2riuPCA}$	$D^{k=5}_{manhattan}$	0.72 ± 0.04	$K^{C=10,\gamma=0.01}_{rbf}$	0.79 ± 0.05
$LBP_{12,3}^{PCA}$	$D^{k=5}_{manhattan}$	0.76 ± 0.04	$K^{C=10,d=3}_{poly}$	0.78 ± 0.04
$BRIEF_{6,12}^{PCA}$	$D^{k=5}_{manhattan}$	0.58 ± 0.04	$K^{C=10,d=3}_{poly}$	0.60 ± 0.05
$LBP_{16,4}^{2riuPCA}$	$D^{k=7}_{euclidean}$	0.72 ± 0.03	$K^{C=10,d=2}_{poly}$	0.75 ± 0.07
$LBP_{16,4}^{PCA}$	$D^{k=3}_{manhattan}$	0.75 ± 0.05	$K^{C=1,d=3}_{poly}$	0.77 ± 0.06
$BRIEF_{7,16}^{PCA}$	$D^{k=3}_{chebyshev}$	0.53 ± 0.08	$K^{C=10}_{linear}$	0.58 ± 0.07

Table 5.34 gives the classification results when concatenating all feature vectors extracted from the OCTA images of all ocular vascular layers.

Table 5.34: A summary of classification results (mean AUC scores \pm standard deviations) that measure the performance of the automated classification algorithm that is based on reduced-local texture features for solving the dry AMD vs wet AMD classification task, based on concatenating all feature vectors extracted from the OCTA images of all ocular vascular layers.

Descriptor	KNN Classifier		SVM Classifier	
	Best Parameters	AUC \pm std	Best Parameters	AUC \pm std
$LBP_{4,1}^{2riuPCA}$	$D^{k=7}_{manhattan}$	0.77 ± 0.06	$K^{C=50,\gamma=0.001}_{rbf}$	0.79 ± 0.05
$LBP_{4,1}^{PCA}$	$D^{k=3}_{euclidean}$	0.77 ± 0.04	$K^{C=10,\gamma=0.001}_{rbf}$	0.79 ± 0.06
$BRIEF_{4,4}^{PCA}$	$D^{k=7}_{euclidean}$	0.54 ± 0.05	$K^{C=50,d=3}_{poly}$	0.58 ± 0.06
$LBP_{8,2}^{2riuPCA}$	$D^{k=7}_{euclidean}$	0.75 ± 0.03	$K^{C=50,\gamma=0.001}_{rbf}$	0.79 ± 0.00
$LBP_{8,2}^{PCA}$	$D^{k=7}_{euclidean}$	0.78 ± 0.07	$K^{C=1,\gamma=0.001}_{rbf}$	0.80 ± 0.06
$BRIEF_{5,8}^{PCA}$	$D^{k=7}_{euclidean}$	0.59 ± 0.06	$K^{C=1}_{linear}$	0.61 ± 0.07
$LBP_{12,3}^{2riuPCA}$	$D^{k=7}_{manhattan}$	0.73 ± 0.05	$K^{C=10,\gamma=0.001}_{rbf}$	0.79 ± 0.04
$LBP_{12,3}^{PCA}$	$D^{k=5}_{euclidean}$	0.69 ± 0.07	$K^{C=1,d=3}_{poly}$	0.71 ± 0.11
$BRIEF_{6,12}^{PCA}$	$D^{k=3}_{euclidean}$	0.52 ± 0.06	$K^{C=1}_{linear}$	0.58 ± 0.08
$LBP_{16,4}^{2riuPCA}$	$D^{k=7}_{euclidean}$	0.77 ± 0.02	$K^{C=10,\gamma=0.001}_{rbf}$	0.81 ± 0.01
$LBP_{16,4}^{PCA}$	$D^{k=7}_{manhattan}$	0.64 ± 0.07	$K^{C=1}_{linear}$	0.59 ± 0.12
$BRIEF_{7,16}^{PCA}$	$D^{k=3}_{euclidean}$	0.56 ± 0.06	$K^{C=1,d=3}_{poly}$	0.57 ± 0.06

Nevertheless, using the diverse OCTA images of ocular vascular layers to solve the task of classifying two different eye conditions, i.e.: dry AMD vs wet AMD, can be extremely challenging to achieve even for highly skilled ophthalmologists. This is because the textural vascular appearance of dry AMD and wet AMD in the various OCTA images of different ocular vascular layers can appear significantly different and very similar among the layers. As such, occasionally, the texture of vascular pathologies related to dry AMD and wet AMD may appear comparable to each other in the OCTA images of certain ocular vascular layers as well as being more obvious in certain layers than others. For example, with the presence of an eye condition e.g.: dry AMD or wet AMD, the OCTA images of certain ocular vascular layers, e.g.: the superficial inner retina and the deep inner retina layers, typically exhibit a relatively uniform textural vascular appearance that is hard to differentiate among various eye conditions e.g.: dry AMD, wet AMD including healthy.

Conversely, the OCTA images of the outer retina and the choriocapillaris layers with wet AMD and dry AMD usually demonstrate arbitrary textural vascular patterns that are comparable to each other but substantially dissimilar from healthy. Despite these diversities and difficulties, the evaluation results previously demonstrated prove that the automated classification algorithm can recognise some dissimilarities among the vascular texture of dry AMD and wet AMD in the individual eyes via layer combination. While the classification results with the $BRIEF_{S,n}^{PCA}$ texture descriptor showed to be very poor, the $LBP_{p,r}^{2riuPCA}$ and the $LBP_{p,r}^{PCA}$ texture descriptors both revealed the capacity to allow achieving a reasonable classification performance.

For solving the dry AMD vs wet AMD classification task via layer combination, however, the best overall classification performance was achieved when concatenating all feature vectors extracted from the OCTA images of all ocular vascular layers. This was accomplished using the $LBP_{16,4}^{2riuPCA}$ texture descriptor based on the SVM classifier with $K_{rbf}^{C=10, \gamma=0.001}$ achieving a mean AUC score and a standard deviation = 0.81 ± 0.01 .

Ultimately, the classification algorithm is then examined on classifying the various eyes via layer combination, however, for the task of discriminating between various subjects with CNV and non-CNV lesions. Tables 5.35, 5.36, 5.37, 5.38, 5.39 and 5.40 illustrate the classification results of the classification algorithm when concatenating two feature vectors extracted from the OCTA images of two different ocular vascular layers. These are the superficial and the deep inner retina, the superficial inner and the outer retina, the superficial inner retina and the choriocapillaris, the deep inner and the outer retina, the deep inner retina and the choriocapillaris, and the outer retina and the

choriocapillaris layers, respectively.

Table 5.35: A summary of classification results (mean AUC scores \pm standard deviations) that measure the performance of the automated classification algorithm that is based on reduced-local texture features for solving the CNV vs non-CNV classification task, based on concatenating two feature vectors extracted from the OCTA images of the superficial and the deep retina layers.

Descriptor	KNN Classifier		SVM Classifier	
	Best Parameters	AUC \pm std	Best Parameters	AUC \pm std
$LBP^{2riuPCA}_{4,1}$	$D^{k=5}_{manhattan}$	0.62 ± 0.06	$K^{C=1,d=3}_{poly}$	0.63 ± 0.06
$LBP^{PCA}_{4,1}$	$D^{k=5}_{manhattan}$	0.62 ± 0.05	$K^{C=10,d=3}_{poly}$	0.63 ± 0.06
$BRIEF^{PCA}_{4,4}$	$D^{k=5}_{manhattan}$	0.51 ± 0.05	$K^{C=1,d=2}_{poly}$	0.50 ± 0.06
$LBP^{2riuPCA}_{8,2}$	$D^{k=5}_{chebyshev}$	0.61 ± 0.07	$K^{C=1,\gamma=0.1}_{rbf}$	0.64 ± 0.06
$LBP^{PCA}_{8,2}$	$D^{k=5}_{euclidean}$	0.62 ± 0.04	$K^{C=10,d=2}_{poly}$	0.63 ± 0.05
$BRIEF^{PCA}_{5,8}$	$D^{k=5}_{euclidean}$	0.50 ± 0.04	$K^{C=1}_{linear}$	0.51 ± 0.05
$LBP^{2riuPCA}_{12,3}$	$D^{k=5}_{chebyshev}$	0.61 ± 0.05	$K^{C=1}_{linear}$	0.62 ± 0.06
$LBP^{PCA}_{12,3}$	$D^{k=5}_{manhattan}$	0.62 ± 0.06	$K^{C=1,d=2}_{poly}$	0.61 ± 0.07
$BRIEF^{PCA}_{6,12}$	$D^{k=1}_{manhattan}$	0.51 ± 0.04	$K^{C=10,d=2}_{poly}$	0.50 ± 0.05
$LBP^{2riuPCA}_{16,4}$	$D^{k=3}_{manhattan}$	0.65 ± 0.05	$K^{C=10,\gamma=0.1}_{rbf}$	0.62 ± 0.04
$LBP^{PCA}_{16,4}$	$D^{k=5}_{euclidean}$	0.61 ± 0.04	$K^{C=1,d=3}_{poly}$	0.62 ± 0.07
$BRIEF^{PCA}_{7,16}$	$D^{k=3}_{euclidean}$	0.50 ± 0.05	$K^{C=10}_{linear}$	0.51 ± 0.03

Table 5.36: A summary of classification results (mean AUC scores \pm standard deviations) that measure the performance of the automated classification algorithm that is based on reduced-local texture features for solving the CNV vs non-CNV classification task, based on concatenating two feature vectors extracted from the OCTA images of the superficial and the outer retina layers.

Descriptor	KNN Classifier		SVM Classifier	
	Best Parameters	AUC \pm std	Best Parameters	AUC \pm std
$LBP^{2riuPCA}_{4,1}$	$D^{k=5}_{manhattan}$	0.66 ± 0.05	$K^{C=1,\gamma=0.01}_{rbf}$	0.64 ± 0.04
$LBP^{PCA}_{4,1}$	$D^{k=5}_{euclidean}$	0.65 ± 0.06	$K^{C=1}_{linear}$	0.67 ± 0.05
$BRIEF^{PCA}_{4,4}$	$D^{k=5}_{chebyshev}$	0.60 ± 0.06	$K^{C=1,d=2}_{poly}$	0.62 ± 0.06
$LBP^{2riuPCA}_{8,2}$	$D^{k=5}_{manhattan}$	0.66 ± 0.05	$K^{C=10}_{linear}$	0.67 ± 0.05
$LBP^{PCA}_{8,2}$	$D^{k=3}_{manhattan}$	0.67 ± 0.05	$K^{C=10,d=3}_{poly}$	0.65 ± 0.04
$BRIEF^{PCA}_{5,8}$	$D^{k=5}_{euclidean}$	0.58 ± 0.05	$K^{C=1,d=2}_{poly}$	0.63 ± 0.06
$LBP^{2riuPCA}_{12,3}$	$D^{k=5}_{manhattan}$	0.64 ± 0.04	$K^{C=10}_{linear}$	0.66 ± 0.06
$LBP^{PCA}_{12,3}$	$D^{k=3}_{manhattan}$	0.65 ± 0.05	$K^{C=10}_{linear}$	0.68 ± 0.05
$BRIEF^{PCA}_{6,12}$	$D^{k=5}_{manhattan}$	0.62 ± 0.04	$K^{C=10,d=2}_{poly}$	0.65 ± 0.05
$LBP^{2riuPCA}_{16,4}$	$D^{k=3}_{manhattan}$	0.65 ± 0.03	$K^{C=1}_{linear}$	0.65 ± 0.06
$LBP^{PCA}_{16,4}$	$D^{k=3}_{euclidean}$	0.64 ± 0.05	$K^{C=1}_{linear}$	0.63 ± 0.04
$BRIEF^{PCA}_{7,16}$	$D^{k=5}_{euclidean}$	0.55 ± 0.08	$K^{C=1,d=2}_{poly}$	0.61 ± 0.04

Table 5.37: A summary of classification results (mean AUC scores \pm standard deviations) that measure the performance of the automated classification algorithm that is based on reduced-local texture features for solving the CNV vs non-CNV classification task, based on concatenating two feature vectors extracted from the OCTA images of the superficial retina and the choriocapillaris layers.

Descriptor	KNN Classifier		SVM Classifier	
	Best Parameters	AUC \pm std	Best Parameters	AUC \pm std
$LBP^{2riuPCA}_{4,1}$	$D^{k=5}_{manhattan}$	0.66 ± 0.06	$K^{C=1, \gamma=0.1}_{rbf}$	0.67 ± 0.06
$LBP^{PCA}_{4,1}$	$D^{k=5}_{manhattan}$	0.67 ± 0.07	$K^{C=10, d=3}_{poly}$	0.66 ± 0.06
$BRIEF^{PCA}_{4,4}$	$D^{k=1}_{chebyshev}$	0.50 ± 0.04	$K^{C=1, \gamma=0.01}_{rbf}$	0.50 ± 0.06
$LBP^{2riuPCA}_{8,2}$	$D^{k=5}_{euclidean}$	0.66 ± 0.06	$K^{C=1, \gamma=0.1}_{rbf}$	0.65 ± 0.05
$LBP^{PCA}_{8,2}$	$D^{k=5}_{manhattan}$	0.68 ± 0.05	$K^{C=10, d=2}_{poly}$	0.67 ± 0.06
$BRIEF^{PCA}_{5,8}$	$D^{k=1}_{chebyshev}$	0.50 ± 0.05	$K^{C=1, d=2}_{poly}$	0.51 ± 0.06
$LBP^{2riuPCA}_{12,3}$	$D^{k=5}_{euclidean}$	0.67 ± 0.06	$K^{C=10, \gamma=0.01}_{rbf}$	0.66 ± 0.06
$LBP^{PCA}_{12,3}$	$D^{k=5}_{manhattan}$	0.67 ± 0.04	$K^{C=1, d=2}_{poly}$	0.65 ± 0.05
$BRIEF^{PCA}_{6,12}$	$D^{k=5}_{euclidean}$	0.54 ± 0.06	$K^{C=1, d=3}_{poly}$	0.53 ± 0.05
$LBP^{2riuPCA}_{16,4}$	$D^{k=3}_{euclidean}$	0.67 ± 0.03	$K^{C=1, \gamma=0.1}_{rbf}$	0.66 ± 0.07
$LBP^{PCA}_{16,4}$	$D^{k=3}_{manhattan}$	0.67 ± 0.05	$K^{C=1, d=3}_{poly}$	0.65 ± 0.04
$BRIEF^{PCA}_{7,16}$	$D^{k=7}_{euclidean}$	0.53 ± 0.04	$K^{C=1, d=3}_{poly}$	0.52 ± 0.02

Table 5.38: A summary of classification results (mean AUC scores \pm standard deviations) that measure the performance of the automated classification algorithm that is based on reduced-local texture features for solving the CNV vs non-CNV classification task, based on concatenating two feature vectors extracted from the OCTA images of the deep and the outer retina layers.

Descriptor	KNN Classifier		SVM Classifier	
	Best Parameters	AUC \pm std	Best Parameters	AUC \pm std
$LBP^{2riuPCA}_{4,1}$	$D^{k=5}_{manhattan}$	0.67 ± 0.06	$K^{C=10, d=3}_{poly}$	0.66 ± 0.07
$LBP^{PCA}_{4,1}$	$D^{k=3}_{euclidean}$	0.67 ± 0.05	$K^{C=10}_{linear}$	0.65 ± 0.05
$BRIEF^{PCA}_{4,4}$	$D^{k=5}_{chebyshev}$	0.60 ± 0.06	$K^{C=10}_{linear}$	0.61 ± 0.06
$LBP^{2riuPCA}_{8,2}$	$D^{k=5}_{manhattan}$	0.64 ± 0.04	$K^{C=10}_{linear}$	0.69 ± 0.04
$LBP^{PCA}_{8,2}$	$D^{k=5}_{manhattan}$	0.65 ± 0.04	$K^{C=10, d=3}_{poly}$	0.67 ± 0.04
$BRIEF^{PCA}_{5,8}$	$D^{k=5}_{manhattan}$	0.58 ± 0.06	$K^{C=1, d=3}_{poly}$	0.62 ± 0.07
$LBP^{2riuPCA}_{12,3}$	$D^{k=5}_{manhattan}$	0.66 ± 0.05	$K^{C=10, d=3}_{poly}$	0.67 ± 0.05
$LBP^{PCA}_{12,3}$	$D^{k=5}_{manhattan}$	0.65 ± 0.05	$K^{C=1}_{linear}$	0.67 ± 0.05
$BRIEF^{PCA}_{6,12}$	$D^{k=1}_{manhattan}$	0.57 ± 0.06	$K^{C=10, \gamma=0.01}_{rbf}$	0.62 ± 0.08
$LBP^{2riuPCA}_{16,4}$	$D^{k=3}_{manhattan}$	0.64 ± 0.05	$K^{C=10, d=3}_{poly}$	0.63 ± 0.03
$LBP^{PCA}_{16,4}$	$D^{k=5}_{euclidean}$	0.67 ± 0.04	$K^{C=1}_{linear}$	0.65 ± 0.06
$BRIEF^{PCA}_{7,16}$	$D^{k=3}_{chebyshev}$	0.59 ± 0.05	$K^{C=1}_{linear}$	0.60 ± 0.04

Table 5.39: A summary of classification results (mean AUC scores \pm standard deviations) that measure the performance of the automated classification algorithm that is based on reduced-local texture features for solving the CNV vs non-CNV classification task, based on concatenating two feature vectors extracted from the OCTA images of the deep retina and the chorio-capillaris layers.

Descriptor	KNN Classifier		SVM Classifier	
	Best Parameters	AUC \pm std	Best Parameters	AUC \pm std
$LBP_{4,1}^{2riuPCA}$	$D^{k=3}_{euclidean}$	0.67 ± 0.03	$K_{rbf}^{C=10, \gamma=0.01}$	0.68 ± 0.05
$LBP_{4,1}^{PCA}$	$D^{k=5}_{manhattan}$	0.67 ± 0.07	$K_{poly}^{C=10, d=3}$	0.66 ± 0.06
$BRIEF_{4,4}^{PCA}$	$D^{k=1}_{manhattan}$	0.54 ± 0.05	$K_{poly}^{C=10, d=3}$	0.52 ± 0.08
$LBP_{8,2}^{2riuPCA}$	$D^{k=5}_{euclidean}$	0.69 ± 0.07	$K_{rbf}^{C=1, \gamma=0.1}$	0.67 ± 0.06
$LBP_{8,2}^{PCA}$	$D^{k=5}_{euclidean}$	0.64 ± 0.05	$K_{linear}^{C=10}$	0.65 ± 0.06
$BRIEF_{5,8}^{PCA}$	$D^{k=1}_{manhattan}$	0.51 ± 0.04	$K_{rbf}^{C=1, \gamma=0.01}$	0.52 ± 0.06
$LBP_{12,3}^{2riuPCA}$	$D^{k=5}_{manhattan}$	0.63 ± 0.07	$K_{linear}^{C=10}$	0.66 ± 0.07
$LBP_{12,3}^{PCA}$	$D^{k=5}_{manhattan}$	0.70 ± 0.04	$K_{poly}^{C=10, d=2}$	0.69 ± 0.06
$BRIEF_{6,12}^{PCA}$	$D^{k=1}_{manhattan}$	0.50 ± 0.05	$K_{rbf}^{C=10, \gamma=0.1}$	0.50 ± 0.04
$LBP_{16,4}^{2riuPCA}$	$D^{k=7}_{euclidean}$	0.67 ± 0.06	$K_{rbf}^{C=10, \gamma=0.1}$	0.65 ± 0.05
$LBP_{16,4}^{PCA}$	$D^{k=3}_{euclidean}$	0.68 ± 0.06	$K_{linear}^{C=1}$	0.64 ± 0.04
$BRIEF_{7,16}^{PCA}$	$D^{k=5}_{manhattan}$	0.50 ± 0.03	$K_{rbf}^{C=1, \gamma=0.1}$	0.51 ± 0.05

Table 5.40: A summary of classification results (mean AUC scores \pm standard deviations) that measure the performance of the automated classification algorithm that is based on reduced-local texture features for solving the CNV vs non-CNV classification task, based on concatenating two feature vectors extracted from the OCTA images of the outer retina and the chorio-capillaris layers.

Descriptor	KNN Classifier		SVM Classifier	
	Best Parameters	AUC \pm std	Best Parameters	AUC \pm std
$LBP_{4,1}^{2riuPCA}$	$D^{k=5}_{euclidean}$	0.70 ± 0.04	$K_{rbf}^{C=1, \gamma=0.1}$	0.73 ± 0.05
$LBP_{4,1}^{PCA}$	$D^{k=5}_{manhattan}$	0.70 ± 0.05	$K_{poly}^{C=10, d=3}$	0.70 ± 0.06
$BRIEF_{4,4}^{PCA}$	$D^{k=5}_{manhattan}$	0.64 ± 0.05	$K_{rbf}^{C=1, \gamma=0.01}$	0.65 ± 0.04
$LBP_{8,2}^{2riuPCA}$	$D^{k=5}_{manhattan}$	0.76 ± 0.04	$K_{rbf}^{C=10, \gamma=0.01}$	0.75 ± 0.04
$LBP_{8,2}^{PCA}$	$D^{k=3}_{manhattan}$	0.70 ± 0.04	$K_{poly}^{C=10, d=3}$	0.77 ± 0.06
$BRIEF_{5,8}^{PCA}$	$D^{k=5}_{chebyshev}$	0.59 ± 0.03	$K_{rbf}^{C=1, \gamma=0.01}$	0.63 ± 0.06
$LBP_{12,3}^{2riuPCA}$	$D^{k=5}_{manhattan}$	0.76 ± 0.04	$K_{rbf}^{C=10, \gamma=0.01}$	0.79 ± 0.03
$LBP_{12,3}^{PCA}$	$D^{k=3}_{manhattan}$	0.75 ± 0.05	$K_{poly}^{C=10, d=3}$	0.75 ± 0.04
$BRIEF_{6,12}^{PCA}$	$D^{k=5}_{euclidean}$	0.58 ± 0.03	$K_{rbf}^{C=1, \gamma=0.01}$	0.61 ± 0.04
$LBP_{16,4}^{2riuPCA}$	$D^{k=5}_{euclidean}$	0.74 ± 0.03	$K_{linear}^{C=10}$	0.76 ± 0.05
$LBP_{16,4}^{PCA}$	$D^{k=5}_{manhattan}$	0.78 ± 0.04	$K_{linear}^{C=10}$	0.70 ± 0.05
$BRIEF_{7,16}^{PCA}$	$D^{k=5}_{chebyshev}$	0.57 ± 0.05	$K_{linear}^{C=1}$	0.58 ± 0.05

Tables 5.41, 5.42, 5.43 and 5.44, on the other hand, present the classification results of the classification algorithm when concatenating three feature vectors extracted from three OCTA images of different ocular vascular layers. Specifically, the superficial, the deep inner and the outer retina, the superficial, the deep inner retina and the choriocapillaris, the superficial inner, the outer retina and the choriocapillaris, and the deep inner, the outer retina and the choriocapillaris layers, respectively.

Table 5.41: A summary of classification results (mean AUC scores \pm standard deviations) that measure the performance of the automated classification algorithm that is based on reduced-local texture features for solving the CNV vs non-CNV classification task, based on concatenating three feature vectors extracted from the OCTA images of the superficial inner, the deep inner and the outer retina layers.

Descriptor	KNN Classifier		SVM Classifier	
	Best Parameters	AUC \pm std	Best Parameters	AUC \pm std
$LBP_{4,1}^{2riuPCA}$	$D^{k=5}_{euclidean}$	0.71 ± 0.06	$K_{rbf}^{C=1, \gamma=0.01}$	0.72 ± 0.05
$LBP_{4,1}^{PCA}$	$D^{k=5}_{manhattan}$	0.70 ± 0.05	$K_{poly}^{C=10, d=3}$	0.72 ± 0.05
$BRIEF_{4,4}^{PCA}$	$D^{k=5}_{euclidean}$	0.58 ± 0.05	$K_{poly}^{C=1, d=2}$	0.61 ± 0.06
$LBP_{8,2}^{2riuPCA}$	$D^{k=5}_{euclidean}$	0.70 ± 0.06	$K_{linear}^{C=1}$	0.75 ± 0.06
$LBP_{8,2}^{PCA}$	$D^{k=5}_{manhattan}$	0.72 ± 0.05	$K_{linear}^{C=50}$	0.74 ± 0.04
$BRIEF_{5,8}^{PCA}$	$D^{k=5}_{euclidean}$	0.53 ± 0.06	$K_{rbf}^{C=1, \gamma=0.1}$	0.58 ± 0.11
$LBP_{12,3}^{2riuPCA}$	$D^{k=5}_{manhattan}$	0.76 ± 0.04	$K_{linear}^{C=1}$	0.77 ± 0.05
$LBP_{12,3}^{PCA}$	$D^{k=5}_{manhattan}$	0.73 ± 0.05	$K_{linear}^{C=50}$	0.75 ± 0.05
$BRIEF_{6,12}^{PCA}$	$D^{k=3}_{manhattan}$	0.54 ± 0.03	$K_{poly}^{C=1, d=2}$	0.59 ± 0.06
$LBP_{16,4}^{2riuPCA}$	$D^{k=3}_{euclidean}$	0.73 ± 0.05	$K_{linear}^{C=10}$	0.75 ± 0.06
$LBP_{16,4}^{PCA}$	$D^{k=7}_{manhattan}$	0.74 ± 0.07	$K_{linear}^{C=50}$	0.75 ± 0.04
$BRIEF_{7,16}^{PCA}$	$D^{k=5}_{manhattan}$	0.53 ± 0.05	$K_{poly}^{C=10, d=3}$	0.57 ± 0.07

Table 5.45 presents the classification results when concatenating all feature vectors extracted from the OCTA images of all ocular vascular layers.

Likewise, the potential challenges earlier described when solving the dry AMD vs wet AMD image classification task using the various OCTA images of ocular vascular layers can also be encountered when solving the CNV vs non-CNV image classification task, which is also enormously challenging to achieve even for highly skilled ophthalmologists. Despite the various difficulties that can be faced, the previous evaluation results confirm that the automated classification algorithm can recognise some variations between the vascular texture of CNV and non-CNV lesions in the individual eyes via combining the diverse OCTA images of ocular vascular layers. The classification results with the $BRIEF_{S,n}^{PCA}$ texture descriptor, however, proved to be very poor. Nevertheless, the $LBP_{p,r}^{2riuPCA}$ and the $LBP_{p,r}^{PCA}$ texture descriptors can both facilitate the

Table 5.42: A summary of classification results (mean AUC scores \pm standard deviations) that measure the performance of the automated classification algorithm that is based on reduced-local texture features for solving the CNV vs non-CNV classification task, based on concatenating three feature vectors extracted from the OCTA images of the superficial, the deep inner retina and the choriocapillaris layers.

Descriptor	KNN Classifier		SVM Classifier	
	Best Parameters	AUC \pm std	Best Parameters	AUC \pm std
$LBP_{4,1}^{2riuPCA}$	$D^{k=5}_{euclidean}$	0.72 ± 0.07	$K_{rbf}^{C=10,\gamma=0.01}$	0.73 ± 0.06
$LBP_{4,1}^{PCA}$	$D^{k=5}_{chebyshev}$	0.69 ± 0.06	$K_{rbf}^{C=1,\gamma=0.01}$	0.72 ± 0.07
$BRIEF_{4,4}^{PCA}$	$D^{k=5}_{chebyshev}$	0.51 ± 0.05	$K_{rbf}^{C=1,\gamma=0.01}$	0.50 ± 0.05
$LBP_{8,2}^{2riuPCA}$	$D^{k=5}_{manhattan}$	0.71 ± 0.05	$K_{linear}^{C=10}$	0.74 ± 0.05
$LBP_{8,2}^{PCA}$	$D^{k=5}_{manhattan}$	0.70 ± 0.05	$K_{poly}^{C=50,d=3}$	0.71 ± 0.05
$BRIEF_{5,8}^{PCA}$	$D^{k=3}_{euclidean}$	0.52 ± 0.07	$K_{poly}^{C=50,d=2}$	0.55 ± 0.10
$LBP_{12,3}^{2riuPCA}$	$D^{k=5}_{euclidean}$	0.67 ± 0.05	$K_{rbf}^{C=10,\gamma=0.01}$	0.72 ± 0.07
$LBP_{12,3}^{PCA}$	$D^{k=5}_{manhattan}$	0.61 ± 0.07	$K_{poly}^{C=50,d=2}$	0.61 ± 0.09
$BRIEF_{6,12}^{PCA}$	$D^{k=5}_{chebyshev}$	0.52 ± 0.06	$K_{poly}^{C=50,d=2}$	0.50 ± 0.06
$LBP_{16,4}^{2riuPCA}$	$D^{k=5}_{manhattan}$	0.67 ± 0.04	$K_{linear}^{C=1}$	0.72 ± 0.07
$LBP_{16,4}^{PCA}$	$D^{k=1}_{manhattan}$	0.58 ± 0.06	$K_{poly}^{C=1,d=2}$	0.51 ± 0.10
$BRIEF_{7,16}^{PCA}$	$D^{k=1}_{manhattan}$	0.50 ± 0.03	$K_{rbf}^{C=1,\gamma=0.01}$	0.50 ± 0.03

Table 5.43: A summary of classification results (mean AUC scores \pm standard deviations) that measure the performance of the automated classification algorithm that is based on reduced-local texture features for solving the CNV vs non-CNV classification task, based on concatenating three feature vectors extracted from the OCTA images of the superficial inner, the outer retina and the choriocapillaris layers.

Descriptor	KNN Classifier		SVM Classifier	
	Best Parameters	AUC \pm std	Best Parameters	AUC \pm std
$LBP_{4,1}^{2riuPCA}$	$D^{k=5}_{chebyshev}$	0.70 ± 0.05	$K_{rbf}^{C=1,\gamma=0.1}$	0.72 ± 0.05
$LBP_{4,1}^{PCA}$	$D^{k=5}_{manhattan}$	0.70 ± 0.05	$K_{poly}^{C=10,d=3}$	0.75 ± 0.06
$BRIEF_{4,4}^{PCA}$	$D^{k=5}_{euclidean}$	0.57 ± 0.04	$K_{rbf}^{C=10,\gamma=0.1}$	0.61 ± 0.06
$LBP_{8,2}^{2riuPCA}$	$D^{k=5}_{manhattan}$	0.77 ± 0.06	$K_{rbf}^{C=10,\gamma=0.01}$	0.78 ± 0.05
$LBP_{8,2}^{PCA}$	$D^{k=3}_{manhattan}$	0.76 ± 0.05	$K_{poly}^{C=10,d=3}$	0.77 ± 0.05
$BRIEF_{5,8}^{PCA}$	$D^{k=5}_{euclidean}$	0.60 ± 0.05	$K_{poly}^{C=1,d=3}$	0.64 ± 0.06
$LBP_{12,3}^{2riuPCA}$	$D^{k=5}_{manhattan}$	0.73 ± 0.04	$K_{rbf}^{C=10,\gamma=0.01}$	0.76 ± 0.05
$LBP_{12,3}^{PCA}$	$D^{k=5}_{manhattan}$	0.76 ± 0.05	$K_{poly}^{C=10,d=3}$	0.79 ± 0.04
$BRIEF_{6,12}^{PCA}$	$D^{k=3}_{euclidean}$	0.58 ± 0.04	$K_{rbf}^{C=1,\gamma=0.1}$	0.60 ± 0.05
$LBP_{16,4}^{2riuPCA}$	$D^{k=7}_{manhattan}$	0.70 ± 0.04	$K_{rbf}^{C=1,\gamma=0.01}$	0.75 ± 0.06
$LBP_{16,4}^{PCA}$	$D^{k=3}_{manhattan}$	0.74 ± 0.04	$K_{poly}^{C=1,d=3}$	0.75 ± 0.05
$BRIEF_{7,16}^{PCA}$	$D^{k=5}_{euclidean}$	0.58 ± 0.03	$K_{rbf}^{C=1,\gamma=0.1}$	0.60 ± 0.07

Table 5.44: A summary of classification results (mean AUC scores \pm standard deviations) that measure the performance of the automated classification algorithm that is based on reduced-local texture features for solving the CNV vs non-CNV classification task, based on concatenating three feature vectors extracted from the OCTA images of the deep inner, the outer retina and the choriocapillaris layers.

Descriptor	KNN Classifier		SVM Classifier	
	Best Parameters	AUC \pm std	Best Parameters	AUC \pm std
$LBP_{4,1}^{2riuPCA}$	$D^{k=5}_{euclidean}$	0.75 ± 0.04	$K_{rbf}^{C=10,\gamma=0.1}$	0.77 ± 0.04
$LBP_{4,1}^{PCA}$	$D^{k=5}_{manhattan}$	0.73 ± 0.04	$K_{poly}^{C=10,d=3}$	0.74 ± 0.05
$BRIEF_{4,4}^{PCA}$	$D^{k=1}_{euclidean}$	0.64 ± 0.06	$K_{linear}^{C=1}$	0.66 ± 0.05
$LBP_{8,2}^{2riuPCA}$	$D^{k=5}_{manhattan}$	0.78 ± 0.04	$K_{rbf}^{C=10,\gamma=0.01}$	0.79 ± 0.05
$LBP_{8,2}^{PCA}$	$D^{k=5}_{manhattan}$	0.79 ± 0.03	$K_{poly}^{C=10,d=3}$	0.77 ± 0.04
$BRIEF_{5,8}^{PCA}$	$D^{k=5}_{chebyshev}$	0.56 ± 0.02	$K_{rbf}^{C=1,\gamma=0.01}$	0.60 ± 0.05
$LBP_{12,3}^{2riuPCA}$	$D^{k=5}_{manhattan}$	0.79 ± 0.04	$K_{rbf}^{C=10,\gamma=0.01}$	0.80 ± 0.05
$LBP_{12,3}^{PCA}$	$D^{k=5}_{manhattan}$	0.78 ± 0.03	$K_{poly}^{C=10,d=3}$	0.77 ± 0.04
$BRIEF_{6,12}^{PCA}$	$D^{k=3}_{euclidean}$	0.58 ± 0.05	$K_{rbf}^{C=1,\gamma=0.1}$	0.60 ± 0.05
$LBP_{16,4}^{2riuPCA}$	$D^{k=7}_{euclidean}$	0.75 ± 0.06	$K_{rbf}^{C=1,\gamma=0.01}$	0.77 ± 0.05
$LBP_{16,4}^{PCA}$	$D^{k=3}_{manhattan}$	0.75 ± 0.07	$K_{poly}^{C=10,d=3}$	0.77 ± 0.03
$BRIEF_{7,16}^{PCA}$	$D^{k=3}_{chebyshev}$	0.62 ± 0.07	$K_{linear}^{C=10}$	0.63 ± 0.06

Table 5.45: A summary of classification results (mean AUC scores \pm standard deviations) that measure the performance of the automated classification algorithm that is based on reduced-local texture features for solving the CNV vs non-CNV classification task, based on concatenating all feature vectors extracted from the OCTA images of all ocular vascular layers.

Descriptor	KNN Classifier		SVM Classifier	
	Best Parameters	AUC \pm std	Best Parameters	AUC \pm std
$LBP_{4,1}^{2riuPCA}$	$D^{k=7}_{manhattan}$	0.76 ± 0.03	$K_{rbf}^{C=50,\gamma=0.01}$	0.79 ± 0.05
$LBP_{4,1}^{PCA}$	$D^{k=7}_{manhattan}$	0.79 ± 0.04	$K_{rbf}^{C=10,\gamma=0.01}$	0.80 ± 0.05
$BRIEF_{4,4}^{PCA}$	$D^{k=5}_{manhattan}$	0.57 ± 0.04	$K_{rbf}^{C=1,\gamma=0.001}$	0.62 ± 0.07
$LBP_{8,2}^{2riuPCA}$	$D^{k=5}_{manhattan}$	0.80 ± 0.05	$K_{rbf}^{C=50,\gamma=0.01}$	0.81 ± 0.05
$LBP_{8,2}^{PCA}$	$D^{k=7}_{manhattan}$	0.81 ± 0.04	$K_{rbf}^{C=10,\gamma=0.001}$	0.83 ± 0.05
$BRIEF_{5,8}^{PCA}$	$D^{k=3}_{euclidean}$	0.57 ± 0.03	$K_{poly}^{C=10,d=3}$	0.61 ± 0.06
$LBP_{12,3}^{2riuPCA}$	$D^{k=5}_{manhattan}$	0.80 ± 0.03	$K_{rbf}^{C=10,\gamma=0.01}$	0.81 ± 0.04
$LBP_{12,3}^{PCA}$	$D^{k=7}_{euclidean}$	0.73 ± 0.04	$K_{poly}^{C=1,d=3}$	0.74 ± 0.05
$BRIEF_{6,12}^{PCA}$	$D^{k=3}_{manhattan}$	0.54 ± 0.05	$K_{linear}^{C=1}$	0.56 ± 0.07
$LBP_{16,4}^{2riuPCA}$	$D^{k=7}_{euclidean}$	0.80 ± 0.03	$K_{rbf}^{C=10,\gamma=0.01}$	0.81 ± 0.03
$LBP_{16,4}^{PCA}$	$D^{k=3}_{euclidean}$	0.63 ± 0.09	$K_{poly}^{C=1,d=3}$	0.63 ± 0.11
$BRIEF_{7,16}^{PCA}$	$D^{k=7}_{chebyshev}$	0.60 ± 0.05	$K_{linear}^{C=1}$	0.60 ± 0.06

attainment of satisfactory classification results.

Nevertheless, for solving the CNV vs non-CNV classification task via layer combination, the best overall classification performance was achieved when concatenating all feature vectors extracted from the OCTA images of all ocular vascular layers. This was achieved using the $LBP_{8,2}^{PCA}$ texture descriptor based on the SVM classifier with $K_{rbf}^{C=10, \gamma=0.001}$ attaining a mean AUC score and a standard deviation = 0.83 ± 0.05 .

The next subsection 5.4.3 delivers the evaluation results of the different cross-corpora experiments conducted.

5.4.3 Cross-Corpora Experiments

Similar to the cross-corpora experiments conducted in Chapter 4, subsection 4.4.3, the various experiments conducted here are accomplished by training the classifiers on one of the OCTA image data sets and then testing them on the other OCTA image data sets (as external validation) to show the generalisation performance. In particular, the classifiers trained on the Manchester OCTA image data set to solve the healthy versus wet AMD classification task are tested on the wet AMD cases of the Moorfields OCTA image data set. Likewise, the classifiers trained on the Moorfields OCTA image data set to solve the dry AMD versus wet AMD classification task are tested on the wet AMD cases of the Manchester OCTA image data set.

Table 5.46 provides the evaluation results (sensitivity scores) of the classifiers trained on Manchester OCTA image data set for the healthy versus wet AMD classification task to distinguish the wet AMD cases of Moorfields OCTA image data set. Table 5.47 delivers the evaluation results (sensitivity scores) of the classifiers trained on Moorfields OCTA image data set for the dry AMD versus wet AMD classification task to discriminate the wet AMD cases of Manchester OCTA image data set.

Given the Moorfields OCTA image data set does not include healthy eyes, the same healthy OCTA image data set of Manchester is used to train the classifier for solving the Manchester healthy versus Moorfields wet AMD classification task and then to test the trained classifier on the wet AMD cases of the Manchester OCTA image data set. Similarly, given the Manchester OCTA image data set does not contain dry AMD eyes, the same dry AMD OCTA image data set of Moorfields is used to train the classifier for solving the Moorfields dry AMD versus Manchester wet AMD classification task and then to test the trained classifier on the wet AMD cases of the Moorfields OCTA image data set.

Table 5.48 delivers the evaluation results (sensitivity scores) of the classifiers trained on the OCTA image data set for the Manchester healthy versus Moorfields wet

Table 5.46: The evaluation results (sensitivity scores) of the classifiers trained on the OCTA image data set for the Manchester healthy versus Manchester wet AMD classification task to distinguish the wet AMD cases of Moorfields OCTA image data set.

Ocular Vascular Layers	Descriptor	Classifier	Sensitivity score
Superficial inner retina layer	$LBP_{8,2}^{2riuPCA}$	KNN ($D_{manhattan}^{k=7}$)	0.40
Deep inner retina layer	$LBP_{16,4}^{2riuPCA}$	SVM ($K_{linear}^{C=10}$)	0.42
Outer retina layer	$LBP_{16,4}^{PCA}$	KNN ($D_{euclidean}^{k=3}$)	0.81
Choriocapillaris layer	$LBP_{4,1}^{2riuPCA}$	SVM ($K_{linear}^{C=1}$)	0.60
Superficial + Deep	$LBP_{16,4}^{2riuPCA}$	SVM ($K_{linear}^{C=10}$)	0.36
Superficial + Outer	$LBP_{12,3}^{PCA}$	KNN ($D_{euclidean}^{k=1}$)	0.41
Superficial + Choriocapillaris	$LBP_{12,3}^{PCA}$	KNN ($D_{manhattan}^{k=3}$)	0.34
Deep + Outer	$LBP_{12,3}^{PCA}$	KNN ($D_{euclidean}^{k=1}$)	0.36
Deep + Choriocapillaris	$LBP_{16,4}^{2riuPCA}$	SVM ($K_{rbf}^{C=1, \gamma=0.1}$)	0.42
Outer + Choriocapillaris	$LBP_{16,4}^{2riuPCA}$	KNN ($D_{euclidean}^{k=5}$)	0.45
Superficial + Deep + Outer	$LBP_{16,4}^{PCA}$	KNN ($D_{euclidean}^{k=1}$)	0.40
Superficial + Deep + Choriocapillaris	$LBP_{16,4}^{2riuPCA}$	KNN ($D_{manhattan}^{k=7}$)	0.36
Superficial + Outer + Choriocapillaris	$LBP_{16,4}^{2riuPCA}$	KNN ($D_{euclidean}^{k=5}$)	0.47
Deep + Outer + Choriocapillaris	$LBP_{16,4}^{PCA}$	KNN ($D_{euclidean}^{k=1}$)	0.54
All ocular vascular layers	$LBP_{16,4}^{2riuPCA}$	KNN ($D_{manhattan}^{k=3}$)	0.57

AMD classification task to distinguish the wet AMD cases of the Manchester OCTA image data set. Table 5.49 provides the evaluation results (sensitivity scores) of the classifiers trained on the OCTA image data set for the Moorfields dry AMD versus Manchester wet AMD classification task to discriminate the wet AMD cases of the Moorfields OCTA image data set.

The following section 5.5 provides comprehensive discussion and performance comparison of the evaluation results of the two automated OCTA image classification algorithms proposed for the diagnosis of AMD disease that are based on whole-local texture features and reduced-local texture features.

5.5 Discussion and Performance Comparison

This section starts with a comprehensive discussion of the significance of classification findings obtained from the evaluation conducted in section 5.4 using the automated image classification algorithm that is based on reduced-local texture features. Tables 5.50, 5.51 and 5.52 provide a summary of optimal classification results based

Table 5.47: The evaluation results (sensitivity scores) of the classifiers trained on the OCTA image data set for the Moorfields dry AMD versus Moorfields wet AMD classification task to distinguish the wet AMD cases of Manchester OCTA image data set.

Ocular Vascular Layers	Descriptor	Classifier	Sensitivity score
Superficial inner retina layer	$LBP_{4,1}^{2riuPCA}$	SVM ($K_{linear}^{C=1}$)	0.91
Deep inner retina layer	$LBP_{16,4}^{2riuPCA}$	SVM ($K_{rbf}^{C=1,\gamma=0.01}$)	0.91
Outer retina layer	$LBP_{16,4}^{2riuPCA}$	SVM ($K_{linear}^{C=50}$)	1.00
Choriocapillaris layer	$LBP_{12,3}^{2riuPCA}$	SVM ($K_{linear}^{C=1}$)	0.96
Superficial + Deep	$LBP_{4,1}^{PCA}$	SVM ($K_{poly}^{C=10,d=3}$)	0.87
Superficial + Outer	$LBP_{16,4}^{PCA}$	KNN ($D_{manhattan}^{k=3}$)	0.96
Superficial + Choriocapillaris	$LBP_{16,4}^{2riuPCA}$	KNN ($D_{euclidean}^{k=3}$)	0.83
Deep + Outer	$LBP_{8,2}^{PCA}$	SVM ($K_{poly}^{C=10,d=3}$)	0.87
Deep + Choriocapillaris	$LBP_{16,4}^{PCA}$	SVM ($K_{rbf}^{C=1,\gamma=0.1}$)	0.91
Outer + Choriocapillaris	$LBP_{12,3}^{2riuPCA}$	SVM ($K_{rbf}^{C=10,\gamma=0.01}$)	1.00
Superficial + Deep + Outer	$LBP_{8,2}^{PCA}$	SVM ($K_{poly}^{C=10,d=3}$)	0.83
Superficial + Deep + Choriocapillaris	$LBP_{8,2}^{PCA}$	KNN ($D_{euclidean}^{k=5}$)	0.83
Superficial + Outer + Choriocapillaris	$LBP_{12,3}^{PCA}$	SVM ($K_{poly}^{C=10,d=3}$)	0.87
Deep + Outer + Choriocapillaris	$LBP_{12,3}^{2riuPCA}$	SVM ($K_{rbf}^{C=10,\gamma=0.01}$)	0.91
All ocular vascular layers	$LBP_{16,4}^{2riuPCA}$	SVM ($K_{rbf}^{C=10,\gamma=0.001}$)	0.87

on mean AUC scores as accomplished on the individual binary OCTA image classification tasks previously conducted, namely healthy vs wet AMD, dry AMD vs wet AMD and CNV vs non-CNV, respectively. The optimal components, e.g.: best local texture descriptors and best classifiers, which facilitate the improvement in classification performance for solving the various binary OCTA image classification tasks, i.e.: healthy vs wet AMD, dry AMD vs wet AMD and CNV vs non-CNV, are also summarised.

Broadly, the classification results of the automated classification algorithm on the previous binary OCTA image classification tasks, i.e.: healthy vs wet AMD, dry AMD vs wet AMD and CNV vs non-CNV, are encouraging as evident in Tables 5.50, 5.51 and 5.52. As such the classification algorithm revealed previously unknown abnormalities and variations in the texture of certain OCTA images. Specifically, it allowed the discovery of otherwise indiscernible differences in the texture of OCTA images of two different ocular vascular layers, i.e.: the superficial inner retina and the deep inner retina layers. Notably, these two layers are not typically used by clinicians in the diagnosis of vascular pathologies associated with AMD disease e.g.: CNV and non-CNV lesions.

Table 5.48: The evaluation results (sensitivity scores) of the classifiers trained on the OCTA image data set for the Manchester healthy versus Moorfields wet AMD classification task to distinguish the wet AMD cases of Manchester OCTA image data set.

Ocular Vascular Layers	Descriptor	Classifier	Sensitivity score
Superficial inner retina layer	$LBP_{8,2}^{2riuPCA}$	KNN ($D_{manhattan}^{k=7}$)	0.87
Deep inner retina layer	$LBP_{16,4}^{2riuPCA}$	SVM ($K_{linear}^{C=10}$)	0.91
Outer retina layer	$LBP_{16,4}^{PCA}$	KNN ($D_{euclidean}^{k=3}$)	1.00
Choriocapillaris layer	$LBP_{4,1}^{2riuPCA}$	SVM ($K_{linear}^{C=1}$)	1.00
Superficial + Deep	$LBP_{16,4}^{2riuPCA}$	SVM ($K_{linear}^{C=10}$)	0.87
Superficial + Outer	$LBP_{12,3}^{PCA}$	KNN ($D_{euclidean}^{k=1}$)	1.00
Superficial + Choriocapillaris	$LBP_{12,3}^{PCA}$	KNN ($D_{manhattan}^{k=3}$)	1.00
Deep + Outer	$LBP_{12,3}^{PCA}$	KNN ($D_{euclidean}^{k=1}$)	1.00
Deep + Choriocapillaris	$LBP_{16,4}^{2riuPCA}$	SVM ($K_{rbf}^{C=1, \gamma=0.1}$)	0.87
Outer + Choriocapillaris	$LBP_{16,4}^{2riuPCA}$	KNN ($D_{euclidean}^{k=5}$)	1.00
Superficial + Deep + Outer	$LBP_{16,4}^{PCA}$	KNN ($D_{euclidean}^{k=1}$)	1.00
Superficial + Deep + Choriocapillaris	$LBP_{16,4}^{2riuPCA}$	KNN ($D_{manhattan}^{k=7}$)	0.91
Superficial + Outer + Choriocapillaris	$LBP_{16,4}^{2riuPCA}$	KNN ($D_{euclidean}^{k=5}$)	0.91
Deep + Outer + Choriocapillaris	$LBP_{16,4}^{PCA}$	KNN ($D_{euclidean}^{k=1}$)	1.00
All ocular vascular layers	$LBP_{16,4}^{2riuPCA}$	KNN ($D_{manhattan}^{k=3}$)	1.00

The abnormalities in the OCTA images of the superficial and the deep inner retina layers may not always be easily perceptible. This is mainly due to the nature of how the CNV lesions normally develop. The CNV lesions typically grow by perforating the Bruch's membrane that is the deepest part of the choroid layer and by progressing into other subretinal layers. Therefore, certain parts of CNV regions may appear to be more distinguishable in certain ocular vascular layers than in others. Despite these difficulties, the classification algorithm successfully differentiated between various eye conditions, e.g.: dry AMD and wet AMD including healthy, based on the OCTA images of these layers.

At a quick glance at the classification results given in Tables 5.50, 5.51 and 5.52, it can be clearly observed that in most binary image classification tasks, the best AUC scores are achieved with the $LBP_{p,r}^{2riuPCA}$ texture descriptor. Based on the classification results of individual binary image classification tasks, however, the most predictive ocular vascular layers that comprise the most useful texture details describing the healthy ocular vascular as well as the different ocular vascular pathologies associated with AMD disease, e.g.: CNV and non-CNV lesions, vary among the three different binary

Table 5.49: The evaluation results (sensitivity scores) of the classifiers trained on the OCTA image data set for the Moorfields dry AMD versus Manchester wet AMD classification task to distinguish the wet AMD cases of Moorfields OCTA image data set.

Ocular Vascular Layers	Descriptor	Classifier	Sensitivity score
Superficial inner retina layer	$LBP_{4,1}^{2riuPCA}$	SVM ($K_{linear}^{C=1}$)	0.16
Deep inner retina layer	$LBP_{16,4}^{2riuPCA}$	SVM ($K_{rbf}^{C=1,\gamma=0.01}$)	0.11
Outer retina layer	$LBP_{16,4}^{2riuPCA}$	SVM ($K_{linear}^{C=50}$)	0.25
Choriocapillaris layer	$LBP_{12,3}^{2riuPCA}$	SVM ($K_{linear}^{C=1}$)	0.25
Superficial + Deep	$LBP_{4,1}^{PCA}$	SVM ($K_{poly}^{C=10,d=3}$)	0.16
Superficial + Outer	$LBP_{16,4}^{PCA}$	KNN ($D_{manhattan}^{k=3}$)	0.10
Superficial + Choriocapillaris	$LBP_{16,4}^{2riuPCA}$	KNN ($D_{euclidean}^{k=3}$)	0.19
Deep + Outer	$LBP_{8,2}^{PCA}$	SVM ($K_{poly}^{C=10,d=3}$)	0.11
Deep + Choriocapillaris	$LBP_{16,4}^{PCA}$	SVM ($K_{rbf}^{C=1,\gamma=0.1}$)	0.17
Outer + Choriocapillaris	$LBP_{12,3}^{2riuPCA}$	SVM ($K_{rbf}^{C=10,\gamma=0.01}$)	0.20
Superficial + Deep + Outer	$LBP_{8,2}^{PCA}$	SVM ($K_{poly}^{C=10,d=3}$)	0.11
Superficial + Deep + Choriocapillaris	$LBP_{8,2}^{PCA}$	KNN ($D_{euclidean}^{k=5}$)	0.12
Superficial + Outer + Choriocapillaris	$LBP_{12,3}^{PCA}$	SVM ($K_{poly}^{C=10,d=3}$)	0.13
Deep + Outer + Choriocapillaris	$LBP_{12,3}^{2riuPCA}$	SVM ($K_{rbf}^{C=10,\gamma=0.01}$)	0.14
All ocular vascular layers	$LBP_{16,4}^{2riuPCA}$	SVM ($K_{rbf}^{C=10,\gamma=0.001}$)	0.14

image classification tasks conducted.

For instance, the most predictive ocular vascular layers for the healthy vs wet AMD classification task are the outer retina and choriocapillaris layers. As such the classification algorithm performed outstandingly on these two different ocular vascular layers accomplishing a mean AUC score and a standard deviation = 0.99 ± 0.00 that is a near human-like classification performance. This is achieved with the $LBP_{4,1}^{2riuPCA}$ and the $LBP_{all\ values}^{PCA}$ texture descriptors for the outer retina layer and with the $LBP_{4,1}^{2riuPCA}$ texture descriptor for the choriocapillaris layer, irrespective of which classification schemes are employed. The classification performance, however, gradually drops among the various classification experiments conducted using the OCTA images of deep and superficial inner retina layers as well as via layer combination. In the various classification experiments performed, nevertheless, the mean AUC scores are all ≥ 0.90 .

While differentiating between the various ocular vascular pathologies related to dry AMD and wet AMD, e.g.: CNV vs non-CNV lesions, from each other in the various OCTA images is quite challenging as they might appear comparable, the classification

Table 5.50: A summary of best classification results (mean AUC scores \pm standard deviations) as achieved by the automated OCTA image classification algorithm proposed for solving the healthy vs wet AMD classification task based on reduced-local texture features.

Ocular Vascular Layers	Optimal Descriptors	Optimal Classifiers	AUC \pm std
Superficial inner retina layer	$LBP_{8,2}^{2riuPCA}$	KNN ($D_{manhattan}^{k=7}$)	0.90 \pm 0.02
Deep inner retina layer	$LBP_{16,4}^{2riuPCA}$	SVM ($K_{linear}^C=10$)	0.95 \pm 0.03
Outer retina layer	$LBP_{p=4,8,r=1,2}^{2riuPCA} / LBP_{all\ values}^{PCA}$	KNN ($D_{euclidean,manhattan}^{k=3,9}$) / SVM ($K_{linear}^C=1,10$)	0.99 \pm 0.00
Choriocapillaris layer	$LBP_{4,1}^{2riuPCA}$	KNN ($D_{euclidean}^{k=3}$) / SVM ($K_{linear}^C=1$)	0.99 \pm 0.00
Superficial + Deep	$LBP_{16,4}^{2riuPCA}$	SVM ($K_{linear}^C=10$)	0.93 \pm 0.05
Superficial + Outer	$LBP_{12,3}^{PCA}$	KNN ($D_{euclidean}^{k=1}$)	0.95 \pm 0.04
Superficial + Choriocapillaris	$LBP_{12,3}^{PCA}$	KNN ($D_{manhattan}^{k=3}$)	0.92 \pm 0.07
Deep + Outer	$LBP_{12,3}^{PCA}$	KNN ($D_{euclidean}^{k=1}$)	0.95 \pm 0.03
Deep + Choriocapillaris	$LBP_{16,4}^{2riuPCA}$	SVM ($K_{rbf}^C=1, \gamma=0.1$)	0.94 \pm 0.03
Outer + Choriocapillaris	$LBP_{16,4}^{2riuPCA}$	KNN ($D_{euclidean}^{k=5}$)	0.98 \pm 0.03
Superficial + Deep + Outer	$LBP_{16,4}^{PCA}$	KNN ($D_{euclidean}^{k=1}$)	0.96 \pm 0.04
Superficial + Deep + Choriocapillaris	$LBP_{16,4}^{2riuPCA}$	KNN ($D_{manhattan}^{k=7}$)	0.97 \pm 0.05
Superficial + Outer + Choriocapillaris	$LBP_{16,4}^{2riuPCA}$	KNN ($D_{euclidean}^{k=5}$)	0.97 \pm 0.03
Deep + Outer + Choriocapillaris	$LBP_{16,4}^{PCA}$	KNN ($D_{euclidean}^{k=1}$)	0.97 \pm 0.02
All ocular vascular layers	$LBP_{16,4}^{2riuPCA}$	KNN ($D_{manhattan}^{k=3}$) / SVM ($K_{linear}^C=1$)	0.98 \pm 0.01

Table 5.51: A summary of best classification results (mean AUC scores \pm standard deviations) as achieved by the automated OCTA image classification algorithm proposed for solving the dry AMD vs wet AMD classification task based on reduced-local texture features.

Ocular Vascular Layers	Optimal Descriptors	Optimal Classifiers	AUC \pm std
Superficial inner retina layer	$LBP_{4,1}^{2riuPCA}$	SVM ($K_{linear}^{C=1}$)	0.74 \pm 0.04
Deep inner retina layer	$LBP_{16,4}^{2riuPCA}$	SVM ($K_{rbf}^{C=1,\gamma=0.01}$)	0.79 \pm 0.03
Outer retina layer	$LBP_{16,4}^{2riuPCA}$	SVM ($K_{linear}^{C=50}$)	0.85 \pm 0.02
Choriocapillaris layer	$LBP_{12,3}^{2riuPCA}$	SVM ($K_{linear}^{C=1}$)	0.83 \pm 0.02
Superficial + Deep	$LBP_{4,1}^{PCA}$	SVM ($K_{poly}^{C=10,d=3}$)	0.65 \pm 0.05
Superficial + Outer	$LBP_{16,4}^{PCA}$	KNN ($D_{manhattan}^{k=3}$)	0.66 \pm 0.03
Superficial + Choriocapillaris	$LBP_{16,4}^{2riuPCA}$	KNN ($D_{euclidean}^{k=3}$)	0.67 \pm 0.03
Deep + Outer	$LBP_{8,2}^{PCA}$	SVM ($K_{poly}^{C=10,d=3}$)	0.67 \pm 0.04
Deep + Choriocapillaris	$LBP_{16,4}^{PCA}$	SVM ($K_{rbf}^{C=1,\gamma=0.1}$)	0.69 \pm 0.04
Outer + Choriocapillaris	$LBP_{12,3}^{2riuPCA}$	SVM ($K_{rbf}^{C=10,\gamma=0.01}$)	0.74 \pm 0.07
Superficial + Deep + Outer	$LBP_{8,2}^{PCA}$	SVM ($K_{poly}^{C=10,d=3}$)	0.70 \pm 0.04
Superficial + Deep + Choriocapillaris	$LBP_{8,2}^{PCA}$	KNN ($D_{euclidean}^{k=5}$)	0.77 \pm 0.05
Superficial + Outer + Choriocapillaris	$LBP_{12,3}^{PCA}$	SVM ($K_{poly}^{C=10,d=3}$)	0.77 \pm 0.05
Deep + Outer + Choriocapillaris	$LBP_{12,3}^{2riuPCA}$	SVM ($K_{rbf}^{C=10,\gamma=0.01}$)	0.79 \pm 0.05
All ocular vascular layers	$LBP_{16,4}^{2riuPCA}$	SVM ($K_{rbf}^{C=10,\gamma=0.001}$)	0.81 \pm 0.01

algorithm generally performed quite reasonably in the dry AMD vs wet AMD and the CNV vs non-CNV classification tasks. Based on the best classification results summarised in Tables 5.51 and 5.52, the most predictive ocular vascular layer for both classification tasks, i.e.: dry AMD vs wet AMD and CNV vs non-CNV, is the outer retina layer. As such the classification algorithm accomplished a mean AUC score and a standard deviation = 0.85 \pm 0.02 for the dry AMD and wet AMD classification task and a mean AUC score and a standard deviation = 0.83 \pm 0.03 for the CNV vs non-CNV classification task. These mean AUC scores are both achieved with the $LBP_{16,4}^{2riuPCA}$ texture descriptor based on the SVM classifier with ($K_{linear}^{C=50}$) for the dry AMD vs wet AMD classification task and ($K_{linear}^{C=1}$) for the CNV vs non-CNV classification task.

Nevertheless, the choriocapillaris layer is the second most predictive ocular vascular layer for the dry AMD vs wet AMD and CNV vs non-CNV classification tasks. As such the classification algorithm achieved a mean AUC score and a standard deviation = 0.83 \pm 0.02 for the dry AMD and wet AMD classification task and a mean AUC score and a standard deviation = 0.81 \pm 0.02 for the CNV vs non-CNV classification task. These mean AUC scores are both attained with the $LBP_{12,3}^{2riuPCA}$ texture descriptor based on the SVM classifier with ($K_{linear}^{C=1}$) for the dry AMD vs wet AMD classification

Table 5.52: A summary of best classification results (mean AUC scores \pm standard deviations) as achieved by the automated OCTA image classification algorithm proposed for solving the CNV vs non-CNV classification task based on reduced-local texture features.

Ocular Vascular Layers	Optimal Descriptors	Optimal Classifiers	AUC \pm std
Superficial inner retina layer	$LBP_{8,2}^{2riuPCA}$	SVM ($K_{rbf}^{C=1,\gamma=0.1}$)	0.66 ± 0.01
Deep inner retina layer	$LBP_{16,4}^{2riuPCA}$	SVM ($K_{poly}^{C=10,d=3}$)	0.76 ± 0.03
Outer retina layer	$LBP_{16,4}^{2riuPCA}$	SVM ($K_{linear}^{C=1}$)	0.83 ± 0.03
Choriocapillaris layer	$LBP_{12,3}^{2riuPCA}$	SVM ($K_{rbf}^{C=10,\gamma=0.001}$)	0.81 ± 0.02
Superficial + Deep	$LBP_{16,4}^{2riuPCA}$	KNN ($D_{manhattan}^{k=3}$)	0.65 ± 0.05
Superficial + Outer	$LBP_{12,3}^{PCA}$	SVM ($K_{linear}^{C=10}$)	0.68 ± 0.05
Superficial + Choriocapillaris	$LBP_{8,2}^{PCA}$	KNN ($D_{manhattan}^{k=5}$)	0.68 ± 0.05
Deep + Outer	$LBP_{8,2}^{2riuPCA}$	SVM ($K_{linear}^{C=10}$)	0.69 ± 0.04
Deep + Choriocapillaris	$LBP_{12,3}^{PCA}$	KNN ($D_{manhattan}^{k=5}$)	0.70 ± 0.04
Outer + Choriocapillaris	$LBP_{12,3}^{2riuPCA}$	SVM ($K_{rbf}^{C=10,\gamma=0.01}$)	0.79 ± 0.03
Superficial + Deep + Outer	$LBP_{12,3}^{2riuPCA}$	SVM ($K_{linear}^{C=1}$)	0.77 ± 0.05
Superficial + Deep + Choriocapillaris	$LBP_{8,2}^{2riuPCA}$	SVM ($K_{linear}^{C=10}$)	0.74 ± 0.05
Superficial + Outer + Choriocapillaris	$LBP_{12,3}^{PCA}$	SVM ($K_{poly}^{C=10,d=3}$)	0.79 ± 0.04
Deep + Outer + Choriocapillaris	$LBP_{12,3}^{2riuPCA}$	SVM ($K_{rbf}^{C=10,\gamma=0.01}$)	0.80 ± 0.05
All ocular vascular layers	$LBP_{8,2}^{PCA}$	SVM ($K_{rbf}^{C=10,\gamma=0.001}$)	0.85 ± 0.05

task and ($K_{rbf}^{C=10,\gamma=0.001}$) for the CNV vs non-CNV classification task.. However, the classification performance subsequently steadily drops, i.e.: mean AUC scores < 80 , with the remaining classification experiments conducted on the OCTA images of individual ocular vascular layers separately for the dry AMD vs wet AMD and CNV vs non-CNV classification tasks.

The classification experiment conducted based on layer combination by concatenating feature vectors extracted from the OCTA images of all ocular vascular layers for the CNV vs non-CNV classification task, on the other hand, demonstrated a slight improvement in the classification performance. As such, a mean AUC score and a standard deviation = 0.85 ± 0.05 was accomplished using the $LBP_{8,2}^{PCA}$ texture descriptor based on the SVM classifier with ($K_{rbf}^{C=10,\gamma=0.001}$). This is in contrast to the dry AMD vs wet AMD classification task, as the classification experiment conducted when concatenating feature vectors extracted from the OCTA images of all ocular vascular layers showed a slight decrease in the classification performance. Specifically, a mean AUC score and a standard deviation = 0.81 ± 0.01 was achieved using the $LBP_{16,4}^{2riuPCA}$ texture descriptor based on the SVM classifier with ($K_{rbf}^{C=10,\gamma=0.001}$).

Nonetheless, the best classification results of the classification algorithm proposed

in this chapter for solving the various OCTA image classification problems in the context of AMD disease, i.e.: healthy vs wet AMD, dry AMD vs wet AMD and CNV vs non-CNV, are compared with the best classification results of the classification algorithm proposed in Chapter 4 based on mean AUC scores \pm standard deviations. Tables 5.53, 5.54 and 5.55 provide comprehensive performance comparisons between the classification algorithms that are based on reduced-local texture features and whole-local texture features for solving the healthy vs wet AMD, the dry AMD vs wet AMD and the CNV vs non-CNV classification tasks, respectively.

Table 5.53: Performance comparison based on mean AUC scores \pm standard deviations of the two automated OCTA image classification algorithms proposed for solving the healthy vs wet AMD classification task based on whole-local texture features and reduced-local texture features.

Ocular Vascular Layers	Whole-Local Features	Reduced-Local Features
Superficial inner retina layer	0.89 ± 0.05	0.90 ± 0.02
Deep inner retina layer	0.96 ± 0.04	0.95 ± 0.03
Outer retina layer	0.99 ± 0.00	0.99 ± 0.00
Choriocapillaris layer	0.97 ± 0.03	0.99 ± 0.00
Superficial + Deep	0.94 ± 0.03	0.93 ± 0.05
Superficial + Outer	0.98 ± 0.02	0.95 ± 0.04
Superficial + Choriocapillaris	0.94 ± 0.04	0.92 ± 0.07
Deep + Outer	0.98 ± 0.01	0.95 ± 0.03
Deep + Choriocapillaris	0.98 ± 0.01	0.94 ± 0.03
Outer + Choriocapillaris	1.00 ± 0.00	0.98 ± 0.03
Superficial + Deep + Outer	0.98 ± 0.01	0.96 ± 0.04
Superficial + Deep + Choriocapillaris	0.98 ± 0.02	0.97 ± 0.05
Superficial + Outer + Choriocapillaris	0.97 ± 0.02	0.97 ± 0.03
Deep + Outer + Choriocapillaris	0.98 ± 0.03	0.97 ± 0.02
All ocular vascular layers	0.99 ± 0.03	0.98 ± 0.01

Broadly, the classification algorithm that is based on reduced-local texture features demonstrated best classification results in most classification experiments conducted on the individual OCTA images of the different ocular vascular layers as evident in the performance comparisons presented in Tables 5.53, 5.54 and 5.55. Based on the various binary classification tasks conducted on the individual OCTA images of different ocular vascular layers, however, the classification performance varies among the various classification algorithms. For the healthy vs wet AMD classification task,

Table 5.54: Performance comparison based on mean AUC scores \pm standard deviations of the two automated OCTA image classification algorithms proposed for solving the dry AMD vs wet AMD classification task based on whole-local texture features and reduced-local texture features.

Ocular Vascular Layers	Whole-Local Features	Reduced-Local Features
Superficial inner retina layer	0.71 ± 0.06	0.74 ± 0.04
Deep inner retina layer	0.75 ± 0.04	0.79 ± 0.03
Outer retina layer	0.83 ± 0.03	0.85 ± 0.02
Choriocapillaris layer	0.83 ± 0.01	0.83 ± 0.02
Superficial + Deep	0.71 ± 0.09	0.65 ± 0.05
Superficial + Outer	0.74 ± 0.05	0.66 ± 0.03
Superficial + Choriocapillaris	0.76 ± 0.05	0.67 ± 0.03
Deep + Outer	0.75 ± 0.05	0.67 ± 0.04
Deep + Choriocapillaris	0.78 ± 0.06	0.69 ± 0.04
Outer + Choriocapillaris	0.77 ± 0.06	0.74 ± 0.07
Superficial + Deep + Outer	0.79 ± 0.07	0.70 ± 0.04
Superficial + Deep + Choriocapillaris	0.79 ± 0.06	0.77 ± 0.05
Superficial + Outer + Choriocapillaris	0.78 ± 0.05	0.77 ± 0.05
Deep + Outer + Choriocapillaris	0.80 ± 0.06	0.79 ± 0.05
All ocular vascular layers	0.79 ± 0.04	0.81 ± 0.01

the classification algorithm that is based on reduced-local texture features performed better on the OCTA images of the superficial inner retina and choriocapillaris layers. Nevertheless, the classification algorithm that is based on whole-local texture features achieved a higher classification performance on the OCTA images of the deep inner retina layer. Both classification algorithms proposed, however, accomplished comparable classification scores, i.e.: mean AUC scores and standard deviations = 0.99 ± 0.00 , on the OCTA images of the outer retina layer.

With regards to the dry AMD vs wet AMD classification task, the classification algorithm that is based on reduced-local texture features demonstrated a much better classification performance in comparison to the classification algorithm that is based on whole-local texture features in almost all classification experiments performed on the individual OCTA images of the different ocular vascular layers except the OCTA images of the choriocapillaris layer, see Table 5.54. For the CNV vs non-CNV classification task, on the other hand, the classification algorithm that is based on whole-local texture features achieved the best classification performance on only the OCTA images

Table 5.55: Performance comparison based on mean AUC scores \pm standard deviations of the two automated OCTA image classification algorithms proposed for solving the CNV vs non-CNV classification task based on whole-local texture features and reduced-local texture features.

Ocular Vascular Layers	Whole-Local Features	Reduced-Local Features
Superficial inner retina layer	0.70 ± 0.05	0.66 ± 0.01
Deep inner retina layer	0.72 ± 0.03	0.76 ± 0.03
Outer retina layer	0.82 ± 0.03	0.83 ± 0.03
Choriocapillaris layer	0.81 ± 0.04	0.81 ± 0.02
Superficial + Deep	0.68 ± 0.04	0.65 ± 0.05
Superficial + Outer	0.79 ± 0.06	0.68 ± 0.05
Superficial + Choriocapillaris	0.75 ± 0.06	0.68 ± 0.05
Deep + Outer	0.79 ± 0.07	0.69 ± 0.04
Deep + Choriocapillaris	0.76 ± 0.04	0.70 ± 0.04
Outer + Choriocapillaris	0.82 ± 0.04	0.79 ± 0.03
Superficial + Deep + Outer	0.80 ± 0.07	0.77 ± 0.05
Superficial + Deep + Choriocapillaris	0.77 ± 0.05	0.74 ± 0.05
Superficial + Outer + Choriocapillaris	0.82 ± 0.04	0.79 ± 0.04
Deep + Outer + Choriocapillaris	0.82 ± 0.03	0.80 ± 0.05
All ocular vascular layers	0.81 ± 0.03	0.85 ± 0.05

of the superficial inner retina layer. Nevertheless, the classification algorithm that is based on reduced-local texture features accomplished better classification results in the OCTA images of nearly every single ocular vascular layer.

However, when performing the binary classification tasks based on layer combination, the classification algorithm that is based on whole-local texture features broadly showed better classification performance in most classification experiments. For example, a perfect classification performance, i.e.: a mean AUC score and a standard deviation = 1.00 ± 0.00 was accomplished when concatenating the feature vectors extracted from the OCTA images of the outer retina and the choriocapillaris layers for the healthy vs wet AMD classification task. Nevertheless, when concatenating the feature vectors extracted from the OCTA images of all ocular vascular layers, the classification algorithm that is based on reduced-local texture features generally revealed better performance for the dry AMD vs wet AMD and CNV vs non-CNV classification tasks. Specifically, mean AUC scores and standard deviations = 0.81 ± 0.01 and 0.85 ± 0.05 were achieved for the dry AMD vs wet AMD and CNV vs non-CNV classification

tasks, respectively.

As mentioned at the beginning of this Chapter when the classification relationship between the local texture features and the individual classes of interest, i.e.: dry AMD, wet AMD and healthy, is associated with the variability of local texture features. Then, employing the *PCA* technique can possibly establish a suitable relationship between the decorrelated or reduced-local texture features and the individual target classes to be differentiated. Figures 5.2, 5.3 and 5.4 demonstrate plots with bar charts that quantify the explained variance ratios of the individual *PCs* in the various binary classification tasks, namely the healthy vs wet AMD, dry AMD vs wet AMD and CNV vs non-CNV, respectively. These plots show the explained variance ratios of the individual *PCs* after applying the *PCA* technique on the feature vectors extracted from the OCTA images of various ocular vascular layers but only for the occasions in which the classification algorithm that is based on reduced-local texture features achieved better performance.

Looking at the plots in Figures 5.2, 5.3 and 5.4, broadly, the first K *PCs* almost always contain most of the variance exhibited in the original data. Given that the classification algorithm that is based on reduced-local texture features achieves better performance in these classification experiments, it indicates that these classification predictive modelling problems are related to the variability of original local texture features. Hence, the reduced-local texture features that retained 95% of the variance exhibited in the original local texture features proved to facilitate an effective solution to the various image classification problems at hand as well as alleviating the potential redundancies that can be present in the original local texture features.

From a cross-corpora experiments perspective, nevertheless, the classifiers trained on the Manchester OCTA image data set for solving the healthy vs wet AMD classification task to distinguish the wet AMD cases of the Moorfields OCTA image data set, broadly, showed reasonable generalisation performance. Specifically, the best generalisation performance that is a sensitivity score = 0.81 was accomplished on the OCTA images of the outer retina layer. The classifiers trained on the Moorfields OCTA image data set for solving the dry AMD vs wet AMD classification task to distinguish the wet AMD cases of the Manchester OCTA image data set, on the other hand, generally revealed perfect generalisation results, i.e.: sensitivity scores = 1.00, in the classification experiments conducted on the OCTA images of outer retina layers separately as well as via layer combination by concatenating feature vectors extracted from the OCTA images of the outer retina and choriocapillaris layers.

Nevertheless, classification results achieved by the two purely OCTA data-driven

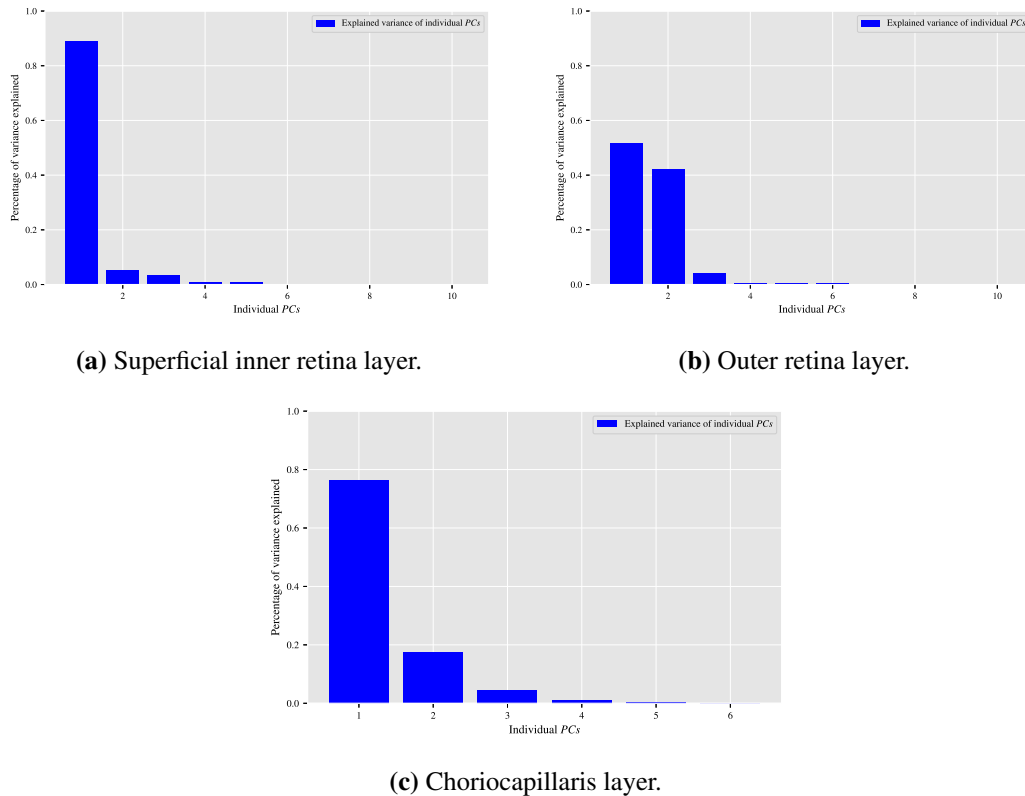


Figure 5.2: Plots of bar charts that demonstrate the percentage of variance explained by the individual PCs in the healthy vs wet AMD classification task for only the occasions in which the classification algorithm that is based on reduced-local texture features achieved better performance. (a) Demonstrates the explained variance ratios of the individual PCs after applying the PCA technique on the feature vectors extracted from the OCTA images of the superficial inner retina layer. (b) When applying the PCA technique on the feature vectors extracted from the OCTA images of the outer retina layer. (c) When applying the PCA technique on the feature vectors extracted from the OCTA images of the choriocapillaris layer.

classification algorithms developed in this thesis should not be underestimated. Specifically, the recognition of indiscernible variations in the texture of OCTA images of specific ocular vascular layers, i.e.: the superficial inner retina and the deep inner retina layers, which are not typically used for AMD disease detection. These significant findings are crucial in diagnosing regions of vascular pathologies related to AMD disease, e.g.: CNV and non-CNV lesions, based on the OCTA images. Finding areas of vascular abnormalities in the OCTA images of the superficial inner retina and the deep inner retina layers would be extremely beneficial for clinicians when the abnormalities would not be easily indicated in the OCTA images of the outer retina and the choriocapillaris layers that are typically used for diagnosing regions of vascular pathologies related to AMD disease.

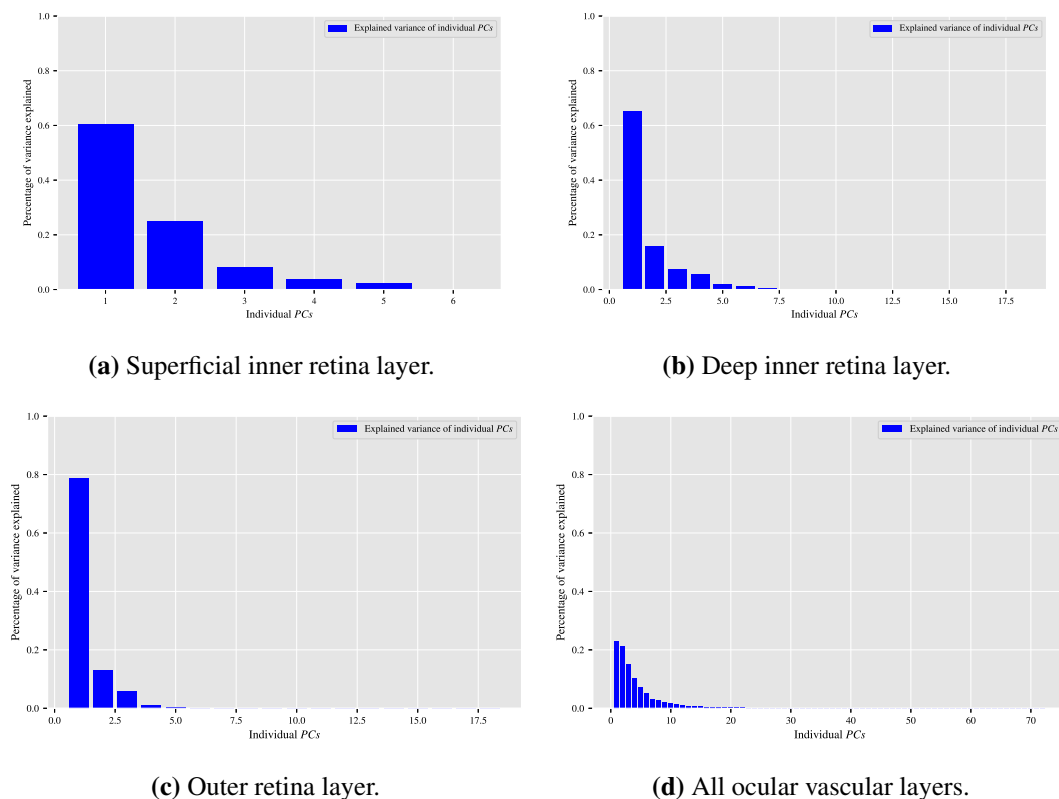


Figure 5.3: Visualising the percentage of variance explained by the individual *PCs* in the dry AMD vs wet AMD classification task for only the occasions in which the classification algorithm that is based on reduced-local texture features accomplished improved performance. (a) Reveals the explained variance ratios of the individual *PCs* when applying the *PCA* technique on the feature vectors extracted from the OCTA images of the superficial inner retina layer. (b) When applying the *PCA* technique on the feature vectors extracted from the OCTA images of the deep inner retina layer. (c) When applying the *PCA* technique on the feature vectors extracted from the OCTA images of the outer retina layer. (d) When applying the *PCA* technique on the combined feature vectors extracted by concatenating the features vectors of all ocular vascular layers.

Unlike the work by Wang et al. [246] that can only identify subjects with wet AMD disease based merely on visually perceptible areas of CNV lesions in the OCTA images of the outer retina layer, the work in this thesis enabled the discrimination between various subjects with different eye conditions including healthy and various stages of AMD disease, e.g.: dry AMD and wet AMD, in the OCTA images of various ocular vascular layers irrespective of whether areas of CNV lesions are clearly noticeable or not. This is due to the nature of how the CNV lesions normally develop as certain parts of CNV regions can appear more distinguishable in certain ocular vascular layers than in others.

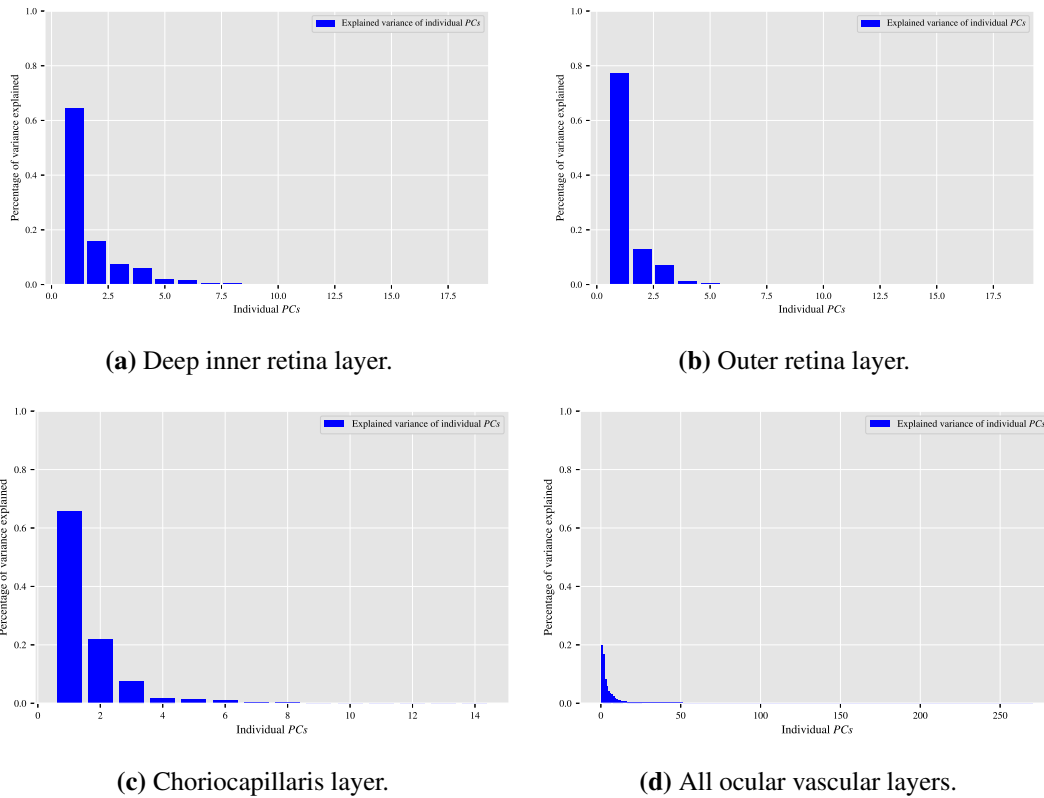


Figure 5.4: Visualising the percentage of variance explained by the individual *PCs* in the CNV vs non-CNV classification task for only the situations in which the classification algorithm that is based on reduced-local texture features demonstrated enhanced classification performance. (a) Shows the explained variance ratios of the individual *PCs* when applying the *PCA* technique on the feature vectors extracted from the OCTA images of the deep inner retina layer. (b) When applying the *PCA* technique on the feature vectors extracted from the OCTA images of the outer retina layer. (c) When applying the *PCA* technique on the feature vectors extracted from the OCTA images of the choriocapillaris layer. (d) When applying the *PCA* technique on the combined feature vectors extracted through concatenating the features vectors of all ocular vascular layers.

Merely from a wet AMD disease detection perspective, however, the optimal binary OCTA image classification task that facilitated the most accurate discrimination of wet AMD disease cases in the various OCTA images is the healthy vs wet AMD task. Table 5.56 summarises a further in-depth evaluation of the two different classification algorithms developed in this thesis on the optimal binary classification task, i.e.: healthy vs wet AMD, that greatly enhanced the accuracy of wet AMD disease detection in the different OCTA images. The two classification algorithms are evaluated using the best components, e.g.: best combinations of local texture descriptors and classifiers, summarised in Tables 4.50 and 5.50. The evaluation results in Table 5.56 are

estimated by employing different evaluation measures. These include accuracy, sensitivity or recall, specificity, precision, and AUC measures using stratified $K = 10$ folds cross-validation strategies. Hence, the evaluation results represent the mean scores \pm standard deviations of individual measures.

While the classification algorithm of Wang et al. [246] achieved a perfect sensitivity/recall score, i.e.: 1.00, it was evaluated based on only a single small OCTA image data set that is also manually depth levels adjusted to obtain OCTA images that clearly visualise areas of interest, i.e.: regions of CNV lesions. From both generalisation and practical validations perspectives, however, it is not entirely clear whether their classification algorithm would generalise well when confronted with previously unseen OCTA image data or not. This is because manually adjusting the depth levels of the OCTA imaging technique is largely subjective in nature and impractical to implement with every single patient visiting the clinic. Nevertheless, the two classification algorithms developed in this thesis are both evaluated based on cross-validation strategies as well as pure, i.e.: unaltered, much larger OCTA image data sets.

While both classification algorithms generally demonstrated very effective classification results, the classification algorithm that is based on reduced-local texture features broadly showed better classification performance in most binary classification experiments conducted on the individual OCTA images of different ocular vascular layers as evident in the evaluation results in Tables 5.53 and 5.56. The classification algorithm that is based on whole-local texture features, on the other hand, generally performed outstandingly in most binary classification experiments conducted via layer combination, see Tables 5.53 and 5.56.

5.6 Chapter Conclusion

This chapter provided a fully automated OCTA image classification algorithm for the diagnosis of AMD disease based on reduced-local texture features. The chapter started by providing details about the motivation of enabling the automated analysis of OCTA images in the context of AMD disease by means of whole image classification using only a reduced set of local texture features. The justification of making the choice of employing dimensionality reduction technique, i.e.: the *PCA* technique, to transform the original features, i.e.: whole-local texture features, into a new much smaller set of transformed local texture features, i.e.: reduced-local texture features, was also provided. Additionally, comprehensive descriptions of the various steps involved in the

Table 5.56: An in-depth evaluation of the two automated OCTA image classification algorithms proposed that are based on whole-local texture features and reduced-local texture features on the optimal binary classification task, i.e.: healthy vs wet AMD. The evaluation measures employed include mean accuracy, sensitivity or recall, specificity, precision, and AUC scores \pm standard deviations.

Ocular Vascular Layers	Evaluation Measures	Whole-Local Features	Reduced-Local Features
Superficial Inner Retina Layer	AUC	0.89 ± 0.05	0.90 ± 0.02
	Accuracy	0.82 ± 0.05	0.83 ± 0.05
	Sensitivity/Recall	1.00 ± 0.00	0.78 ± 0.10
	Specificity	0.83 ± 0.09	0.85 ± 0.10
	Precision	0.90 ± 0.07	0.92 ± 0.06
Deep Inner Retina Layer	AUC	0.96 ± 0.04	0.95 ± 0.03
	Accuracy	0.91 ± 0.05	0.88 ± 0.05
	Sensitivity/Recall	0.84 ± 0.10	0.90 ± 0.10
	Specificity	0.95 ± 0.06	0.90 ± 0.10
	Precision	1.00 ± 0.00	0.90 ± 0.07
Outer Retina Layer	AUC	0.99 ± 0.00	0.99 ± 0.00
	Accuracy	0.98 ± 0.02	1.00 ± 0.00
	Sensitivity/Recall	1.00 ± 0.00	1.00 ± 0.00

Continue on the next page

Table 5.56 – continued from previous page.

	Specificity	0.96 ± 0.05	0.99 ± 0.00
	Precision	0.97 ± 0.03	1.00 ± 0.00
Choriocapillaris layer	AUC	0.97 ± 0.03	0.99 ± 0.00
	Accuracy	0.94 ± 0.03	0.97 ± 0.03
	Sensitivity/Recall	1.00 ± 0.00	1.00 ± 0.00
	Specificity	0.88 ± 0.06	0.92 ± 0.06
	Precision	0.92 ± 0.05	0.96 ± 0.05
Superficial + Deep	AUC	0.94 ± 0.03	0.93 ± 0.05
	Accuracy	0.86 ± 0.08	0.85 ± 0.07
	Sensitivity/Recall	0.80 ± 0.09	0.85 ± 0.10
	Specificity	0.93 ± 0.06	0.82 ± 0.11
	Precision	0.95 ± 0.06	0.90 ± 0.07
Superficial + Outer	AUC	0.98 ± 0.02	0.95 ± 0.04
	Accuracy	0.94 ± 0.05	0.93 ± 0.04
	Sensitivity/Recall	0.98 ± 0.04	0.96 ± 0.04
	Specificity	0.89 ± 0.09	0.93 ± 0.08

Continue on the next page

Table 5.56 – continued from previous page.

	Precision	0.92 ± 0.06	0.96 ± 0.05
Superficial + Choriocapillaris	AUC	0.94 ± 0.04	0.92 ± 0.07
	Accuracy	0.85 ± 0.06	0.82 ± 0.10
	Sensitivity/Recall	0.89 ± 0.08	0.92 ± 0.06
	Specificity	0.91 ± 0.08	0.84 ± 0.09
	Precision	0.90 ± 0.06	0.81 ± 0.08
Deep + Outer	AUC	0.98 ± 0.01	0.95 ± 0.03
	Accuracy	0.98 ± 0.03	0.93 ± 0.05
	Sensitivity/Recall	1.00 ± 0.00	0.95 ± 0.07
	Specificity	0.96 ± 0.04	0.94 ± 0.08
	Precision	0.98 ± 0.03	0.93 ± 0.05
Deep + Choriocapillaris	AUC	0.98 ± 0.01	0.94 ± 0.03
	Accuracy	0.92 ± 0.04	0.90 ± 0.06
	Sensitivity/Recall	0.91 ± 0.08	0.90 ± 0.09
	Specificity	0.95 ± 0.06	0.95 ± 0.08

Continue on the next page

Table 5.56 – continued from previous page.

	Precision	0.96 ± 0.05	0.93 ± 0.04
Outer + Choriocapillaris	AUC	1.00 ± 0.00	0.98 ± 0.03
	Accuracy	1.00 ± 0.00	0.97 ± 0.03
	Sensitivity/Recall	1.00 ± 0.00	0.95 ± 0.04
	Specificity	1.00 ± 0.00	1.00 ± 0.00
	Precision	1.00 ± 0.00	1.00 ± 0.00
Superficial + Deep + Outer	AUC	0.98 ± 0.01	0.96 ± 0.04
	Accuracy	0.97 ± 0.03	0.93 ± 0.03
	Sensitivity/Recall	0.97 ± 0.04	0.98 ± 0.04
	Specificity	1.00 ± 0.00	0.80 ± 0.10
	Precision	0.98 ± 0.03	0.91 ± 0.06
Superficial + Deep + Choriocapillaris	AUC	0.98 ± 0.02	0.97 ± 0.05
	Accuracy	0.94 ± 0.05	0.90 ± 0.02
	Sensitivity/Recall	0.96 ± 0.04	0.90 ± 0.06
	Specificity	0.90 ± 0.06	0.93 ± 0.07

Continue on the next page

Table 5.56 – continued from previous page.

	Precision	0.94 ± 0.06	0.92 ± 0.06
Superficial + Outer + Choriocapillaris	AUC	0.97 ± 0.02	0.97 ± 0.03
	Accuracy	0.97 ± 0.04	0.92 ± 0.05
	Sensitivity/Recall	0.97 ± 0.04	0.89 ± 0.09
	Specificity	0.96 ± 0.06	0.97 ± 0.05
	Precision	0.98 ± 0.03	0.97 ± 0.04
Deep + Outer + Choriocapillaris	AUC	0.98 ± 0.03	0.97 ± 0.02
	Accuracy	0.95 ± 0.05	0.97 ± 0.04
	Sensitivity/Recall	0.92 ± 0.09	0.97 ± 0.07
	Specificity	1.00 ± 0.00	0.96 ± 0.04
	Precision	1.00 ± 0.00	0.96 ± 0.07
All ocular vascular layers	AUC	0.99 ± 0.03	0.98 ± 0.01
	Accuracy	0.99 ± 0.02	0.97 ± 0.03
	Sensitivity/Recall	0.98 ± 0.04	0.96 ± 0.04
	Specificity	1.00 ± 0.00	1.00 ± 0.00

Continue on the next page

Table 5.56 – continued from previous page.

	Precision	1.00 ± 0.00	0.99 ± 0.03
--	------------------	-----------------------------------	-----------------

automated classification algorithm were also given. These include details about the methods employed for extracting the local texture features from the whole OCTA image, the manner of applying the *PCA* technique to decorrelate the local texture features extracted and the ways of performing the classification on the various OCTA images with different ocular conditions including dry AMD and wet AMD as well as healthy. A comprehensive evaluation of the automated classification algorithm proposed in this chapter then followed. The chapter concluded with comparisons of optimum classification results obtained from the automated classification algorithm proposed. Performance comparisons with the previous classification algorithm proposed in Chapter 4 were also conducted.

Chapter 6

Localisation Algorithm Based on Local Texture Features

6.1 Chapter Introduction

This chapter presents a fully automated localisation algorithm for localising areas of CNV lesions related to AMD disease in the texture of OCTA images based on local texture features. The chapter commences with details about the motivation for exploring the potential to localise regions of CNV lesions in OCTA images using local texture features. Comprehensive descriptions of the various steps involved in the automated localisation algorithm are then given. An evaluation of the automated localisation algorithm on both OCTA image data sets, i.e.: the Manchester Royal Eye Hospital and the Moorfields Eye Hospital, then follows. The chapter concludes with discussions and performance comparisons about the localisation results obtained from the evaluation of the automated localisation algorithm proposed.

6.2 Motivation

Exploring image segmentation approaches to automate the analysis of OCTA images in the context of AMD disease has been extremely challenging in most previous attempts [6, 10, 243, 244]. Despite the analysis of OCTA images by means of image segmentation being potentially beneficial to clinicians, e.g.: reducing their burden of work and promoting consistent evaluation for patients with AMD disease, it does, however, entail numerous limitations. These include the requirement of domain experts to manually amend the imaging depth levels of the OCTA imaging technique as well as

to annotate the OCTA images. Another limitation may include the involvement of several pre-processing steps, e.g.: smoothing or filtering operations, across other major limitations. As such the previous limitations may not only introduce bias but also can cause changes of important details present in the OCTA image, among other potential serious disadvantages. Nevertheless, comprehensive details in this regard have already been discussed across various aspects in Chapter 3, specifically sub-subsection 3.5.2.1.

Motivated by the various challenges that may be encountered with automating the analysis of OCTA images by means of image segmentation, this chapter explores the potential for localising areas of CNV lesions associated with AMD disease. The main rationales behind selectively exploring the localisation approach instead of segmentation are mainly driven by the fact that parts of areas related to CNV lesions in the OCTA images can appear more noticeable in a particular ocular vascular layer than in others, i.e.: retinal or choroidal vascular layers. Additionally, the patterns or textural appearance and perceptibility of regions associated with CNV lesions vary significantly among different patients with wet AMD disease as evident in numerous previous studies [8, 9, 13–18]. As such the size and appearance of patterns related to CNV lesions in some situations can occur over nearly the entire OCTA image, see Figure 3.8 in Chapter 3. On some occasions, most regions of CNV lesions can also appear to be situated around a particular position within the OCTA image. This can be near the middle of the OCTA image or near either side, e.g.: left or right, of the OCTA image, see Figure 3.9 in Chapter 3.

Given the significant variations in the size and locations of areas related to CNV lesions in the OCTA images, establishing standardised biomarkers for AMD disease detection in the OCTA images by the means of image segmentation becomes extremely challenging. This is because visually identifying and annotating exact boundaries between areas related to healthy vascular and pathological vascular associated with CNV lesions, in order to use them for establishing an automated image segmentation approach, can be inconsistent and unfeasible to achieve. As the vascular details in the OCTA images are demonstrated in the form of very small and dimly lit vascular networks, i.e.: at a pixel scale, it can be enormously problematic for the human eye to discriminate which regions or pixels correspond to the exactly healthy or the pathological vascular. Therefore, the segmentation approach may excellently segment regions of CNV lesions in the testing set of OCTA image data, but may not generalise well in practice, i.e.: when confronted with a previously unseen OCTA image data set.

The above mentioned is also amplified by several factors related to the size and

quality of OCTA image data currently available. These include the lack of large, high-quality, carefully curated and annotated OCTA image data sets. Additionally, there is a high risk of numerous possible image artifacts related to the movements of the patient's eye or head. These movements can generate shearing deformation or gap defects, manifest as bright strips or horizontal and vertical bright lines in the OCTA images [22, 202, 222]. Additional potential image artifacts that can be present in the various OCTA images may include illumination and orientation variations. The severity of these image artifacts appears to vary among different OCTA images from negligible to prevalent. Consequently, the localisation approach can be useful, as the appearance of precise boundaries or even entire areas related to CNV lesions are typically not necessary. The localisation approach can also be clinically beneficial as it may help to localise CNV regions even if the OCTA images are affected by the previous image artifacts that often confound OCTA image analysis by means of image segmentation.

6.3 Proposed Algorithm

The automated localisation algorithm for localising areas of CNV lesions related to AMD disease in the texture of OCTA images comprises four main steps. These include densely partitioning a healthy OCTA image model and several samples of diseased OCTA images into overlapping patches and then extracting the local texture features from every single patch obtained from the healthy and diseased OCTA images. The similarity measure is then followed to quantify the similarity between every single patch in the diseased OCTA images with its corresponding patch in the healthy OCTA image model based on the local texture features extracted. The final step is the localisation where a bounding box is drawn around one patch which is indicated to be the most dissimilar part in the diseased OCTA images. Figure 6.1 shows a brief overview of the analysis pipeline that is followed by the automated localisation algorithm proposed. The four different steps involved are comprehensively described in the following subsections 6.3.1, 6.3.2, 6.3.3 and 6.3.4, respectively.

6.3.1 Partitioning OCTA Images into Overlapping Patches

For the first step towards achieving the localisation, a healthy OCTA image is randomly selected as a healthy model image of a single ocular vascular layer of interest. For example, the outer retina layer or the choriocapillaris layer, in which localising areas

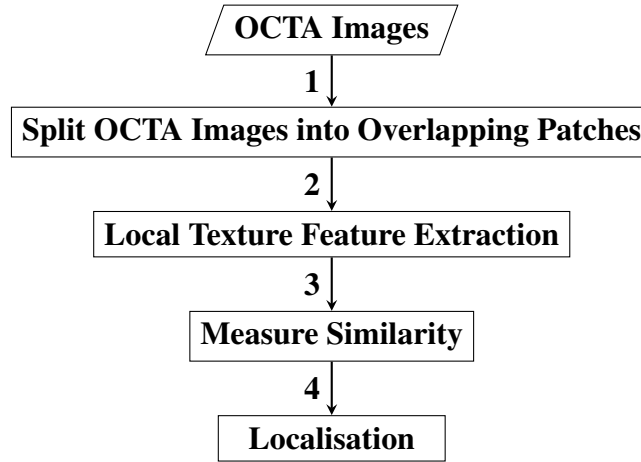


Figure 6.1: An outline of the automated localisation algorithm for localising areas of CNV lesions related to AMD disease in the texture of OCTA images based on local texture features. The analysis procedure commences by taking a healthy OCTA image model and several samples of diseased OCTA images as an input, followed by splitting the healthy and diseased OCTA images into overlapping patches. The local texture feature extraction step then takes place to measure the textural appearance of the extracted patches. The similarity measure step is then followed to measure the similarity between every single patch in the diseased OCTA images with its corresponding patch in the healthy OCTA image model using the local texture features. The final step is the localisation where a bounding box is drawn around a single patch that is indicated to be the most dissimilar part in the diseased OCTA images.

of CNV lesions in the diseased OCTA images will be conducted. Once this selection is made, the diseased OCTA images of the same ocular vascular layer are then fed into the algorithm for localising the vascular abnormalities, i.e.: areas of CNV lesions. To accomplish this, the selected healthy OCTA image model and diseased OCTA images are partitioned into numerous overlapping patches (P) of the same size $M \times M$ densely from every single pixel, starting from the top left to the bottom right of the OCTA images.

Given an OCTA image (x, y) with a width (W) and a height (H), the overlapping patches P are taken from $x = 0$ to W and $y = 0$ to H densely, i.e.: the patches P are captured from every single row and column in the OCTA image (x, y) . As the dimensions of the OCTA images are 320×320 pixels, three different patches P of various fixed sizes $M \times M$ are empirically individually explored. The various sizes of patches P explored include 120×120 , 100×100 and 80×80 pixels dimensions. The main rationale behind selecting these sizes is to explore the proper patch P size that can allow a compromise to be achieved between capturing good texture descriptions and reasonable estimates for the approximate locations of important areas related to CNV lesions

in the diseased OCTA images. As the OCTA images are 320×320 pixel dimension, the total number of potential patches P of size $M \times M$ that can be generated is formally defined by the following equation 6.1:

$$\text{Total Number of Patches } (TP) = (320 - M + 1)^2 \quad (6.1)$$

6.3.2 Local Texture Feature Extraction

Once the healthy OCTA image model and diseased OCTA images of the ocular vascular layer of interest are partitioned into overlapping patches P , the overall objective of the local texture feature extraction step is to measure the textural appearance of individual patches P captured from the healthy OCTA image model and diseased OCTA images. As the main task in this chapter is to identify the approximate locations of CNV lesions in the diseased OCTA images, the $LBP_{p,r}^{2riu}$ texture descriptor is selectively employed in this step. While its transformed form, i.e.: the $LBP_{p,r}^{2riuPCA}$ texture descriptor, broadly enabled the attainment of better classification results in some situations as evident in Chapter 5, the main motivation of using the $LBP_{p,r}^{2riu}$ texture descriptor is to deeply investigate the robustness of local texture features as constructed in their raw form and to gain more insight into their capability to accurately characterise the textural appearance of vascular details in the OCTA images.

The local texture features in this step are, therefore, estimated from the individual patches P captured from the healthy OCTA image model and diseased OCTA images in a similar manner to that followed in Chapter 4, see subsection 4.3.1. Specifically, utilising the $LBP_{p,r}^{2riu}$ texture descriptor to estimate the rotation invariant uniform local texture features around any random region, i.e.: any arbitrary central pixel at (x_c, y_c) in the various patches P captured is formally defined by equation 2.11 in Chapter 2, subsection 2.4.1.5. Recall that there are only $p + 1$ rotation invariant uniform $LBP_{p,r}^{2riu}$ patterns that can occur in a circularly symmetric neighbourhood of p sampling pixels. Hence, the $LBP_{p,r}^{2riu}$ texture descriptor given in equation 2.11 allocates a distinctive integer value or label starting from 0 to p for every single rotation invariant uniform $LBP_{p,r}^{2riu}$ pattern captured. These individual labels correspond to the number of ones, i.e.: “1s” bits, in the rotation invariant uniform $LBP_{p,r}^{2riu}$ patterns, while the non-uniform $LBP_{p,r}^{2riu}$ patterns are grouped all together under an assorted label, i.e.: a single integer value given by $p + 1$.

In this work, nevertheless, the $LBP_{p,r}^{2riu}$ texture descriptor is applied densely to every single region, i.e.: every single pixel, in the various patches P constructing numerous rotation invariant uniform $LBP_{p,r}^{2riu}$ patterns. Nevertheless, every single patch P is described by a histogram, i.e.: a feature vector, which estimates the distribution of all different local texture features as constructed by the $LBP_{p,r}^{2riu}$ texture descriptor. Every single histogram is created with approximately $p + 2$ bin discrete distributions of different labels or values, corresponding to all potential individual rotation invariant uniform as well as non-uniform $LBP_{p,r}^{2riu}$ patterns. The estimated histograms of individual patches P , consequently, form the basis of accomplishing the automated analysis of OCTA image texture to localise regions of CNV lesions.

Denote the various patches P captured as $(P^{healthy})$ and $(P^{diseased})$ for the healthy OCTA image model and the diseased OCTA images, respectively. The feature vectors of different patches $P^{healthy}$ and $P^{diseased}$ extracted can, therefore, be formally described by the following two equations 6.2 and 6.3, respectively:

$$P_v^{healthy} = \{b_1, b_2, b_3, \dots, b_n\} \quad (6.2)$$

$$P_v^{diseased} = \{b_1, b_2, b_3, \dots, b_n\} \quad (6.3)$$

Where $v = \{1, 2, 3, \dots, TP\}$ and TP is the total number of patches P captured from the individual OCTA images. The b denotes to the bin distributions that accumulate the distinct local texture features and n refers to the total number of different local texture features.

6.3.3 Similarity Measure

Once the feature vectors $P_v^{healthy}$ and $P_v^{diseased}$ of different patches $P^{healthy}$ and $P^{diseased}$ in the healthy OCTA image model and diseased OCTA images are estimated, every single patch $P^{diseased}$ in a diseased OCTA image is compared with its corresponding patch $P^{healthy}$ in the healthy OCTA image model for similarity based on their feature vectors. As there is only a single data sample per class, i.e.: one diseased patch $P^{diseased}$ and one healthy patch $P^{healthy}$, that will be compared at once for similarity in the localisation procedure, two different similarity measure metrics are independently employed and evaluated for accomplishing the localisation task. These are the chi-square χ^2 and the histogram intersection distance similarity metrics. Comprehensive review, including the motivation of selectively choosing these two similarity measure metrics, are given

in Chapter 2, specifically in subsection 2.5.2.

In this step, however, every single patch $P^{diseased}$ in the diseased OCTA image is labelled with its similarity value to the corresponding patch $P^{healthy}$ in the healthy OCTA image model. Given two different patches $P^{healthy}$ and $P^{diseased}$, the chi-square χ^2 statistic is formally estimated by comparing their feature vectors $P_v^{healthy}$ and $P_v^{diseased}$ as expressed by the following equation 6.4:

$$\chi^2(P_v^{diseased}, P_v^{healthy}) = \sum_{b=1}^n \frac{(P_b^{diseased} - P_b^{healthy})^2}{(P_b^{diseased} + P_b^{healthy})} \quad (6.4)$$

Where the n represents the total number of different local texture features, i.e.: the total number of histogram bins, the b refers to the individual bin distributions that accumulate the local texture features. Similar to the chi-square χ^2 statistic, the histogram intersection metric is typically calculated by comparing a pair of histograms, namely two feature vectors $P_v^{healthy}$ and $P_v^{diseased}$. The histogram intersection metric (*Intersection*) is, therefore, formally estimated by the following equation 6.5:

$$Intersection(P_v^{diseased}, P_v^{healthy}) = \sum_{b=1}^n \min(P_b^{diseased}, P_b^{healthy}) \quad (6.5)$$

Where the n is the total number of b histogram bins. The histogram intersection metric is typically normalised by the number of b bin count values of the $P_v^{healthy}$ to obtain a fractional similarity value, i.e.: match value, between 0 and 1. The histogram intersection match value (*IMV*) is, therefore, calculated mathematically by the following equation 6.6:

$$IMV(P_v^{diseased}, P_v^{healthy}) = \frac{\sum_{b=1}^n \min(P_b^{diseased}, P_b^{healthy})}{\sum_{b=1}^n P_b^{healthy}} \quad (6.6)$$

Recall that every single patch $P^{diseased}$ in the diseased OCTA image is labelled with its similarity value to the corresponding patch $P^{healthy}$ in the healthy OCTA image model using their feature vectors $P_v^{diseased}$ and $P_v^{healthy}$. Such that the $P_1^{diseased}$ is compared with the $P_1^{healthy}$, the $P_2^{diseased}$ is compared with the $P_2^{healthy}$, the $P_3^{diseased}$ is compared with the $P_3^{healthy}$ and so on. Let SV be a function that labels the different diseased patches $P^{diseased}$ with similarity values generated from the previous comparisons and d be the number of different diseased OCTA images in which the areas of CNV lesions will be localised. Hence, given a healthy OCTA image model and d diseased OCTA images, the results of different similarity comparisons can be mathematically

formalised by the following equation 6.7:

$$\text{Similarity Results}_d = \sum_{j=1}^v \{SV_j\} \quad (6.7)$$

Where the v denotes the total number of patches $P^{diseased}$ of the individual d diseased OCTA images that are compared with their corresponding patches $P^{healthy}$ of the healthy OCTA image model. If the chi-square χ^2 distance similarity metric is used, a very small value indicates higher similarity and a very large value indicates higher dissimilarity. When using the histogram intersection distance similarity metric, however, a higher value indicates a higher similarity, and a very small value indicates a higher dissimilarity.

6.3.4 Localisation

As the different patches $P^{diseased}$ in the diseased OCTA image are individually labelled with their similarity values to their corresponding patches $P^{healthy}$ in the healthy OCTA image model, the overall objective of this step is to draw a bounding box around the most dissimilar patch in the diseased OCTA image based on its similarity value. In case of employing the chi-square χ^2 distance similarity metric, the most dissimilar patch in the diseased OCTA image is the patch that yields the highest similarity value. Given a healthy OCTA image model, the localisation of the most dissimilar patch (MDP) based on the chi-square χ^2 distance similarity metric in the various d diseased OCTA images is accomplished by employing a max function on the different $\text{Similarity Results}_d$ as described by the following equation 6.8:

$$MDP_d^{\chi^2} = \max\{\text{Similarity Results}_d\} \quad (6.8)$$

Where the max function returns the maximum similarity value from the various $\text{Similarity Results}_d$. When the histogram intersection distance similarity metric is used, however, the MDP in the diseased OCTA image is the patch that yields the smallest similarity value. This is accomplished by employing a min function on the different $\text{Similarity Results}_d$ as given by the following equation 6.9:

$$MDP_d^{Intersection} = \min\{\text{Similarity Results}_d\} \quad (6.9)$$

Where the min function returns the minimum similarity value from the various $\text{Similarity Results}_d$.

6.4 Experimental Evaluation and Results

This section provides the evaluation results of the automated localisation algorithm proposed. The algorithm is assessed on both OCTA image data sets that are provided by the Manchester Royal Eye Hospital and the Moorfields Eye Hospital. As the OCTA images of the superficial inner retina and the deep inner retina layers do not typically show perceptible regions related to CNV lesions, the algorithm is merely applied on the OCTA images of the outer retina and the choriocapillaris layers. The $LBP_{p,r}^{2riu}$ texture descriptor is employed with empirically setting the values of its parameters to $p = 8$ and $r = 1$ in all localisation experiments. Additionally, the chi-square χ^2 and the histogram intersection distance similarity metrics are also individually evaluated for all localisation tasks.

The various OCTA images used are manual annotation-free, i.e.: there is no ground truth data in which OCTA images are precisely delineated around the boundaries of CNV areas. Nevertheless, the evaluation of the localisation algorithm is performed by employing an Intersection over Union (*IoU*) measure with a gold standard OCTA image data set that is determined by highly skilled clinicians. Specifically, the gold standard OCTA image data set is constructed by determining the approximate locations of CNV areas in the OCTA images using different sizes of patches P including 120×120 , 100×100 and 80×80 pixels dimensions.

The various sizes of patches P explored are all approximately positioned around the middle of CNV areas in the OCTA images as confirmed by the highly skilled clinicians. Hence, the overall performance or effectiveness of the localisation algorithm is assessed based on the *IoU* score. This is typically accomplished by dividing the area of intersection between the gold standard patch P^{gold} and automatically determined patch P^{auto} divided by the area of union of both patches P^{gold} and P^{auto} . The *IoU* measure can, therefore, be formally defined by the following equation 6.10:

$$\text{Intersection over Union (IoU)} = \frac{\text{Area of Intersection}}{\text{Area of Union}} = \frac{P^{gold} \cap P^{auto}}{P^{gold} \cup P^{auto}} \quad (6.10)$$

As the localisation algorithm involves randomly selecting a single OCTA image model that represents the healthy textural appearance of the ocular vascular layer of interest, the models of healthy OCTA images for the outer retina and the choriocapillaris layers are both visualised in Figure 6.2. The healthy OCTA image model of the choriocapillaris layer is used for localising regions of CNV lesions in the diseased

OCTA images of the choriocapillaris layer. The healthy OCTA image model of the outer retina layer is, on the other hand, utilised for localising regions of CNV lesions in the diseased OCTA images of the outer retina layer. These two different healthy models of OCTA images are both used in all experiments conducted on both hospitals' OCTA image data sets.

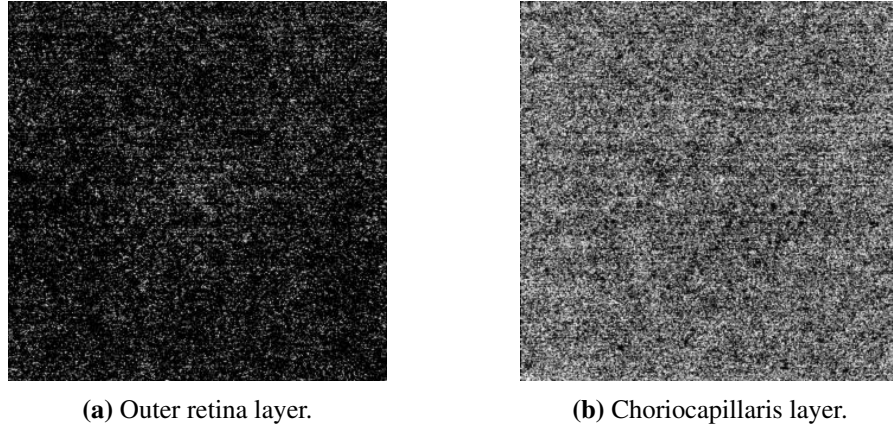


Figure 6.2: Two healthy models of OCTA images that show the typical textural appearance of the outer retina and the choriocapillaris layers. (a) Represents the healthy OCTA image model of the outer retina layer. (b) Demonstrates the healthy OCTA image model of the choriocapillaris layer.

6.4.1 Manchester and Moorfields Hospitals

This subsection presents the evaluation results of the localisation algorithm on the OCTA image data sets of Manchester and Moorfields hospitals. The localisation algorithm is applied to the diseased OCTA images of the outer retina and the choriocapillaris layers. A summary of evaluation results (mean *IoU* scores \pm standard deviations) that measure the performance of the localisation algorithm on the diseased OCTA images in both hospitals' data sets is given in Table 6.1. The results demonstrate the localisation capabilities of the algorithm when varying the sizes of patches P as well as employing either of the two different distance similarity metrics, i.e.: the chi-square χ^2 or the histogram intersection, as the similarity measure.

Based on the results given in Table 6.1, however, the best overall localisation performance is generally achieved when using the chi-square χ^2 distance similarity metric for both ocular vascular layers in both hospitals' data sets. While the localisation algorithm generally performed better when employing the chi-square χ^2 as the similarity

Table 6.1: A summary of evaluation results (mean IoU scores \pm standard deviations) that demonstrate the performance of the localisation algorithm on the diseased OCTA images of the outer retina and the choriocapillaris layers.

Hospital	Number of Images	Ocular Vascular Layers	Chi-square χ^2 Metric			Intersection Metric		
			120×120	100×100	80×80	120×120	100×100	80×80
Manchester	23	Outer retina layer	0.90 ± 0.04	0.79 ± 0.07	0.78 ± 0.06	0.41 ± 0.11	0.25 ± 0.04	0.26 ± 0.05
	23	Choriocapillaris layer	0.84 ± 0.11	0.73 ± 0.10	0.76 ± 0.08	0.44 ± 0.10	0.32 ± 0.08	0.14 ± 0.04
Moorfields	191	Outer retina layer	0.81 ± 0.07	0.65 ± 0.13	0.75 ± 0.06	0.30 ± 0.04	0.23 ± 0.09	0.27 ± 0.12
	191	Choriocapillaris layer	0.82 ± 0.05	0.74 ± 0.05	0.75 ± 0.06	0.43 ± 0.05	0.35 ± 0.04	0.26 ± 0.07

measure, all diseased OCTA images of both ocular vascular layers in which CNV areas are correctly localised when utilising the histogram intersection are also correctly localised when using the chi-square χ^2 in both hospitals' data sets. Additionally, the chi-square χ^2 distance similarity metric broadly demonstrated to provide more accurate estimates for the approximate locations of CNV regions in the diseased OCTA images of both ocular vascular layers in the various experiments conducted on both hospitals' data sets.

From the results in Table 6.1, it can be observed that the optimum patch P size is 120×120 pixels dimensions. This patch P size, broadly, enabled attaining a compromise between capturing decent texture descriptions and reasonable estimates for the approximate positions of areas related to CNV lesions in the various diseased OCTA images. Examples of properly localised CNV areas in the diseased OCTA images by the localisation algorithm when varying the similarity measures are demonstrated in Figures 6.3 and 6.4. Figure 6.3 shows the localisation results, i.e.: the red bounding boxes, on two different samples from the diseased OCTA images of the outer retina layer; Figure 6.4 displays the localisation results on two different examples from the diseased OCTA images of the choriocapillaris layer.

Figures 6.5 and 6.6 demonstrate situations of properly and improperly localised CNV areas in the diseased OCTA images by the localisation algorithm when changing the similarity measures. Figure 6.5 shows the localisation results, i.e.: the red bounding boxes, on two different samples from the diseased OCTA images of the outer retina layer. Figure 6.6 displays the localisation results, i.e.: the red bounding boxes, on two different examples from the diseased OCTA images of the choriocapillaris layer. Broadly, the CNV areas are perfectly localised by the localisation algorithm when utilising the chi-square χ^2 distance similarity metric, but imperfectly localised when using the histogram intersection distance similarity metric.

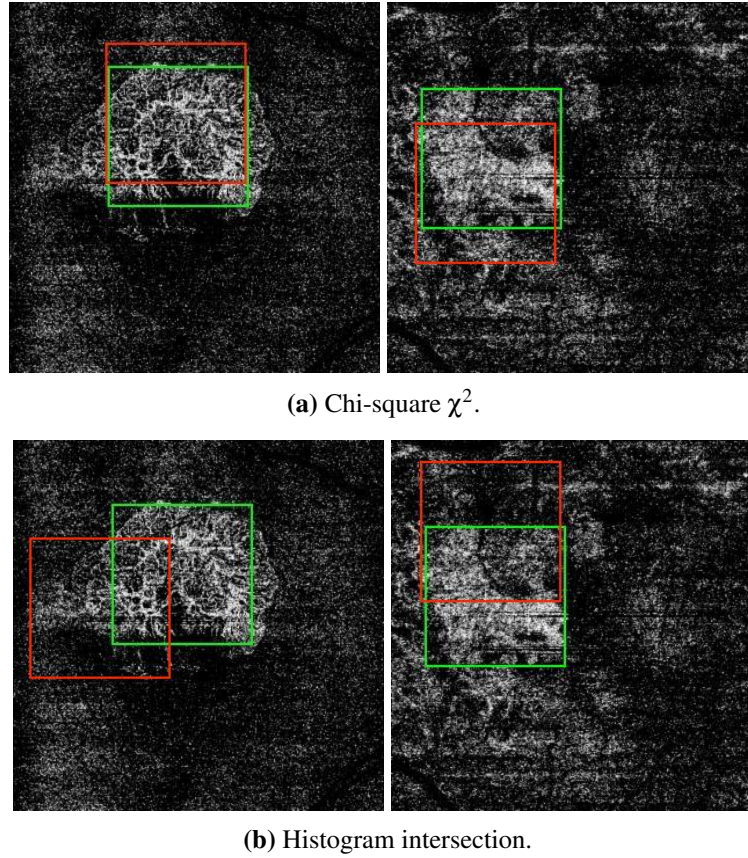
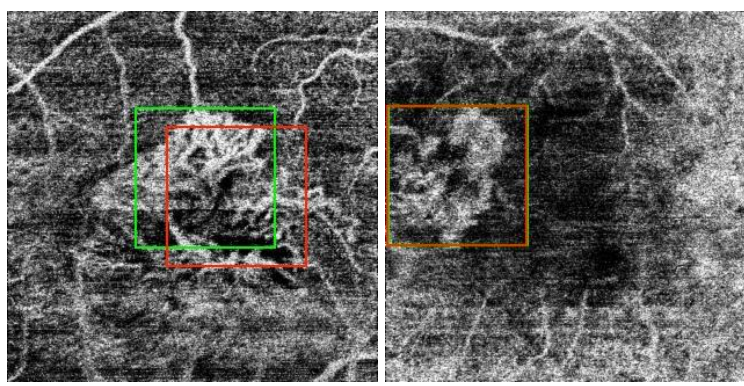
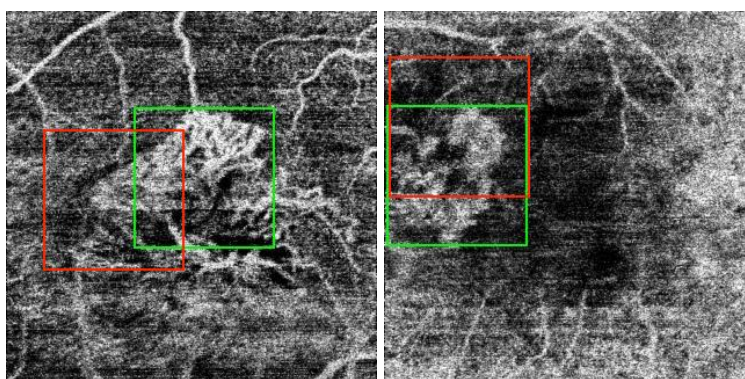


Figure 6.3: Two samples of diseased OCTA images of the outer retinal layer in which the CNV areas are more or less correctly localised by the localisation algorithm when varying the similarity measures. The gold standard patches P^{gold} are demonstrated as green bounding boxes and the automatically determined patches P^{auto} are indicated as red bounding boxes. (a) Shows the localisation results, i.e.: the red bounding boxes, when employing the chi-square χ^2 as the distance similarity metric in the algorithm. (b) Displays the localisation results, i.e.: the red bounding boxes, when utilising the histogram intersection as the similarity measure in the algorithm. It can be clearly observed that the chi-square χ^2 can provide slightly more accurate estimates for the approximate locations of CNV regions as the red bounding boxes are always situated near the middle of CNV areas.

6.5 Discussion and Performance Comparison

This section discusses the significance of the findings presented in this chapter. It also includes comparisons with previous related works as well as the works presented in Chapters 4 and 5. There are several key reasons why the evaluation results given in Table 6.1 show that the algorithm generally may not always be capable of precisely localising CNV areas in the diseased OCTA images of both ocular vascular layers in both hospitals' data sets. Firstly, the OCTA image data sets of both hospitals are used

(a) Chi-square χ^2 .

(b) Histogram intersection.

Figure 6.4: Two samples of diseased OCTA images of the choriocapillaris layer in which the locations of CNV areas are approximately correctly estimated by the localisation algorithm when changing the similarity measures. The gold standard patches P^{gold} are demonstrated as green bounding boxes and the automatically determined patches P^{auto} are indicated as red bounding boxes. (a) Displays the localisation results, i.e.: the red bounding boxes, when utilising the chi-square χ^2 as the distance similarity metric in the algorithm. (b) Exhibits the localisation results, i.e.: the red bounding boxes, when exploiting the histogram intersection as the similarity measure in the algorithm. From these results, it's clear that the chi-square χ^2 undoubtedly delivers slightly more precise approximations for the locations of CNV areas as the red bounding boxes are always positioned nearby the central of CNV areas.

in their raw form purely as extracted by the default settings of the OCTA imaging technique. Hence, the various diseased OCTA images used may not always clearly display regions related to CNV lesions. Examples of this situation for the diseased OCTA images of both ocular vascular layers is given in Figure 6.7. This is mainly due to the nature of how the CNV lesions typically grow. It starts by perforating the deepest part of the choroid layer and then may progress into other subretinal layers. Therefore, parts of CNV regions may appear to be more noticeable in certain depths of ocular vascular layers than in others.

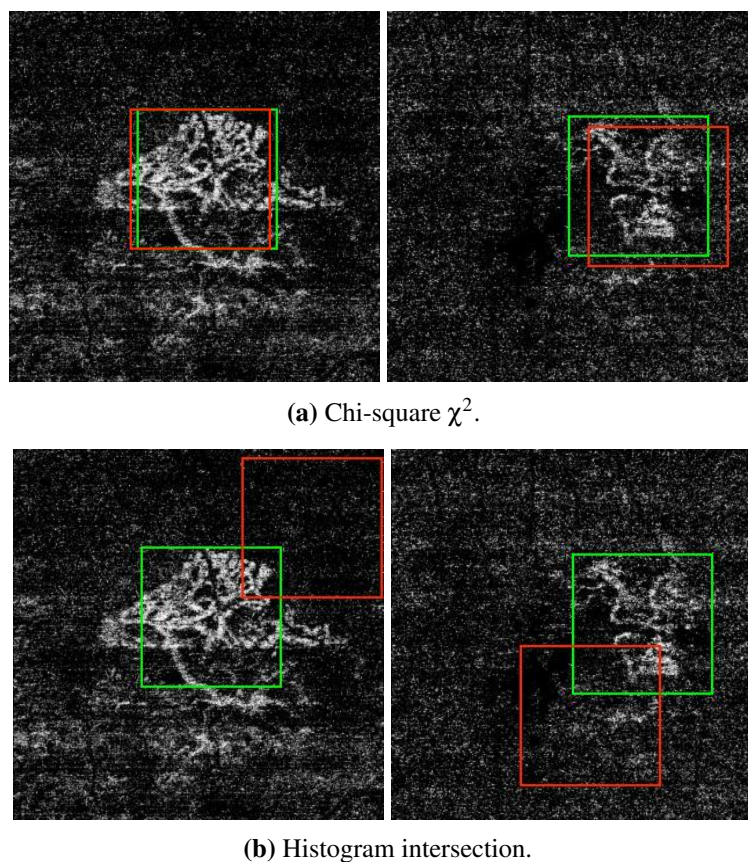
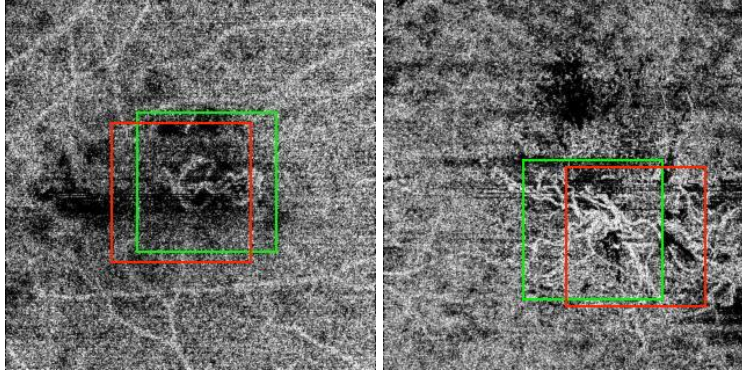
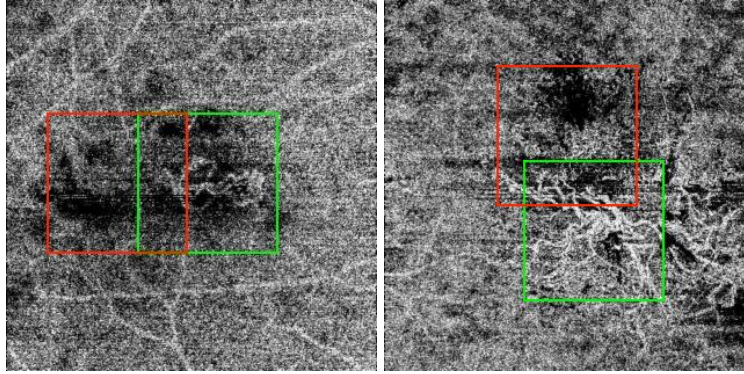


Figure 6.5: Samples of two different diseased OCTA images of the outer retinal layer in which the locations of CNV areas are properly and improperly estimated by the localisation algorithm when changing the similarity measures. The gold standard patches P^{gold} are demonstrated as green bounding boxes and the automatically determined patches P^{auto} are indicated as red bounding boxes. (a) Displays almost correct localisation results, i.e.: the red bounding boxes positioned about the centre of CNV regions, when using the chi-square χ^2 as the similarity measure in the algorithm. (b) Reveals more or less incorrect localisation results, i.e.: most of the CNV areas are situated out of the red bounding boxes, when employing the histogram intersection as the similarity measure in the algorithm.

Another major reason for the low performance of the localisation algorithm includes the presence of numerous challenging situations. For example, the textural appearance of CNV areas in the various diseased OCTA images usually appear in irregular patterns or forms. Hence, the CNV regions may appear everywhere in the diseased OCTA images and can dominate the whole diseased OCTA image. Additional difficult situations include the potential presentation of gap defects, manifest as dark strips or horizontal black lines in the diseased OCTA images. These defects are mainly due to movements of the patient's eye or head. Examples of the two previously mentioned challenging situations are given in Figures 6.8 and 6.9.

(a) Chi-square χ^2 .

(b) Histogram intersection.

Figure 6.6: Examples of two diseased OCTA images of the choriocapillaris layer in which the positions of CNV regions are correctly and incorrectly estimated by the localisation algorithm when varying the similarity measures. The gold standard patches P^{gold} are demonstrated as green bounding boxes and the automatically determined patches P^{auto} are indicated as red bounding boxes. (a) Presents approximately correct localisation results, i.e.: the red bounding boxes always positioned near the centre of CNV regions, when employing the chi-square χ^2 as the similarity measure in the algorithm. (b) Exhibits more or less incorrect localisation results, i.e.: most of the CNV regions are located out of the red bounding boxes, when utilising the histogram intersection as the similarity measure in the algorithm.

The aforementioned difficult situations may not only be challenging for the localisation algorithm proposed in this chapter but also can be extremely challenging for most previous algorithms [6, 10, 243, 244, 246] that analyse the OCTA images by the means of image segmentation. This is because most of these previous works mainly rely on the OCTA images that merely visualise CNV areas. This is accomplished by employing numerous preprocessing steps such as filtering or thresholding operations, manually adjusting the imaging depth levels of the OCTA imaging techniques, among others, that may not only change important vascular details but also can introduce bias. To the credit of the work presented in this thesis, these preprocessing steps were not

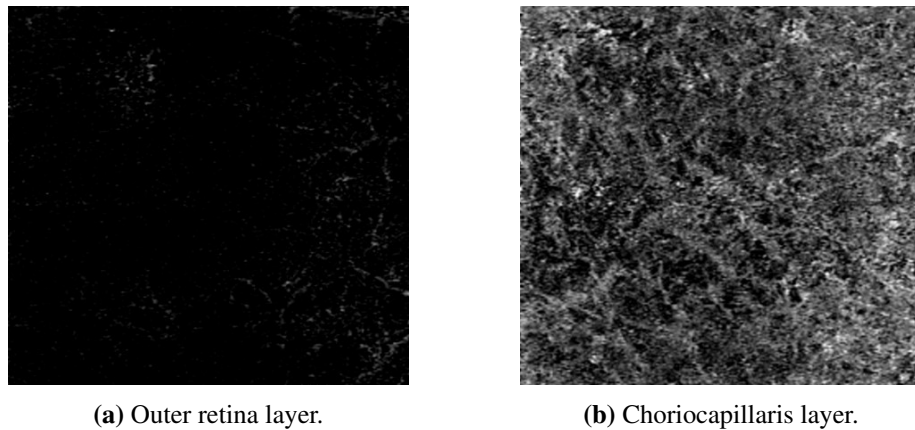


Figure 6.7: Examples of diseased OCTA images of the outer retina and the choriocapillaris layers that do not display perceptible regions associated with CNV lesions. (a) Illustrates a situation in the diseased OCTA image of the outer retina layer. (b) Presents a situation in the diseased OCTA image of the choriocapillaris layer.

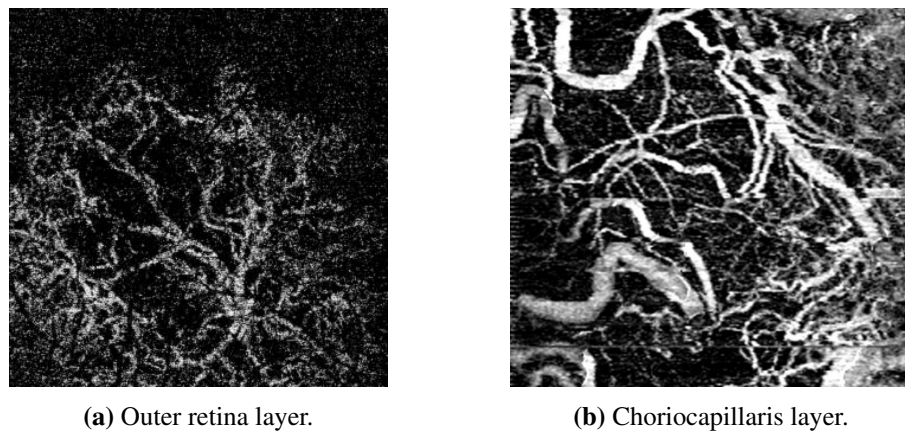


Figure 6.8: Examples of two challenging localisation situations where the CNV areas appear in irregular patterns and more or less dominate the whole OCTA image. (a) Shows a situation in the diseased OCTA image of the outer retina layer. (b) Exhibits a situation in the diseased OCTA image of the choriocapillaris layer.

applied on the OCTA image data sets used, nor was there any single OCTA image excluded due to not displaying perceivable CNV areas.

Broadly, the localisation algorithm did not allow the localisation of entire CNV regions in some situations. For example, the CNV areas may only be partially localised or some of the CNV regions may be located out of the bounding boxes, see Figure 6.6. Nevertheless, the usefulness of the localisation algorithm has been verified and evaluated across numerous difficult settings. As such it was demonstrated that the localisation algorithm can detect various important regions related to CNV lesions wherever they appear to be all positioned or concentrated around a certain region in

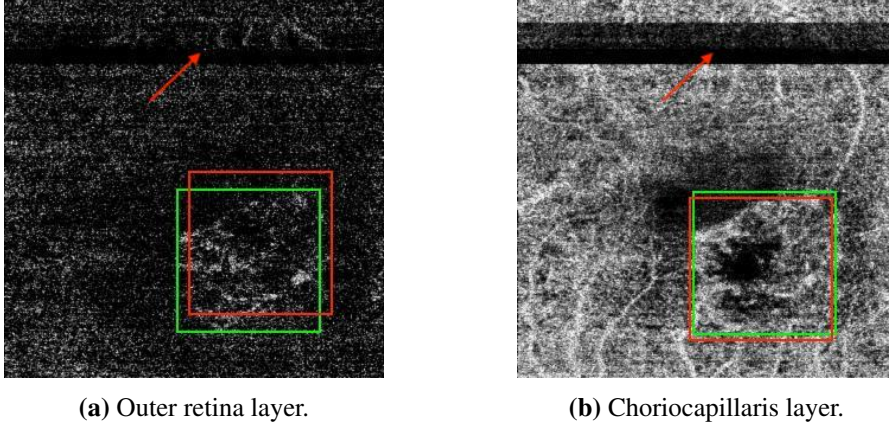


Figure 6.9: Two samples of challenging situations due to movements of the patient's eye or head. These movements generated shearing deformations or gap defects, manifest as dark strips or horizontal black lines in the diseased OCTA images. (a) Displays a situation in the diseased OCTA image of the outer retina layer. (b) Demonstrates a situation in the diseased OCT image of the choriocapillaris layer. The deformations are indicated in red arrows in both OCTA images. Despite these deformations having significantly changed the textural appearance of these diseased OCTA images, the algorithm has successfully localised the areas of CNV lesions. The gold standard patches P^{gold} are demonstrated as green bounding boxes and the automatically determined patches P^{auto} are indicated as red bounding boxes.

the diseased OCTA images of the outer retina and the choriocapillaris layers.

Additionally, the work in this chapter has also allowed an insightful evaluation of the usefulness of local texture features constructed by the $LBP_{p,r}^{2riu}$ texture descriptor that is used for measuring both the texture of a healthy vascular as well as the areas of CNV lesions which have a significantly different textural appearance in the OCTA images. The findings generally demonstrated that the $LBP_{p,r}^{2riu}$ texture descriptor has a key contribution to make towards the successful differentiation between both the appearance of normal and abnormal vascular in the texture of OCTA images. Consequently, this suggests that the localisation algorithm proposed in this chapter and the previous classification algorithms proposed in Chapters 4 and 5 all provide excellent modelling both the texture of a healthy vascular and the areas of CNV lesions.

6.6 Chapter Conclusion

This chapter presents a fully automated localisation algorithm for discriminating regions of CNV lesions associated with AMD disease in the texture of OCTA images based on local texture features. The chapter begins with descriptions of the motivation for investigating the potential to localise areas of CNV lesions in OCTA images using

local texture features. This is then followed by comprehensive descriptions of details with regards to the various steps involved in the automated localisation algorithm. An evaluation of the automated localisation algorithm on both OCTA image data sets, i.e.: the Manchester Royal Eye Hospital and the Moorfields Eye Hospital, is subsequently presented. Finally, the chapter concludes with discussions and performance comparisons of the localisation results obtained from the evaluation of the automated localisation algorithm proposed.

Chapter 7

Conclusion and Future Work

7.1 Chapter Introduction

This chapter concludes the whole work presented in this thesis. It starts by summarising the main findings, followed by drawing the conclusion. Afterwards, potential future works for further investigations to address the limitations are suggested.

7.2 Main Findings

The research presented in this thesis has produced numerous significant findings that can be extremely valuable to several fields of study. From the field of computer vision perspective, three different domain-specific and novel purely data-driven diagnostic techniques were developed to facilitate the identification of AMD disease in the context of OCTA image data in completely automated ways. Specifically, two automated image classification algorithms for AMD disease detection (see Chapters 4 and 5) and an automated localisation algorithm for identifying areas of CNV lesions in the texture of OCTA images (see Chapter 6) are developed.

The aforementioned diagnostic algorithms are developed by testing and exploiting several texture descriptors including the LBP^{2riu} , the $LBP^{2riuPCA}$ and the LBP^{PCA} . These texture descriptors are, broadly, revealed to generate robust local texture features that are suitable for analysing the texture of OCTA images for AMD disease detection by the means of whole image classification. As such, the feasibility of utilising these texture descriptors for AMD disease detection by the means of whole image classification is verified by testing different machine learning algorithms including the SVM and the KNN classifiers.

The LBP^{2riu} texture descriptor, on the other hand, has also demonstrated to allow producing local texture features that are suitable for discriminating regions of CNV lesions associated with AMD disease by the means of region localisation. The feasibility of using the produced local texture features for localising areas of CNV lesions in the OCTA images is verified by evaluating two different distance similarity metrics including the chi-square χ^2 and the histogram intersection.

From the field of ophthalmology perspective, however, the various diagnostic techniques developed facilitated the discovery of novel ocular vasculature texture variations between the various eye conditions related to AMD disease, including healthy, in the texture of OCTA images of two different retinal vascular layers. These different retinal vascular layers are the superficial inner retina and the deep inner retina layers. The significant findings are that these retinal vascular layers are not typically individually used or assessed by ophthalmologists, nor in previous attempts to automate the analysis of OCTA images for AMD disease detection. This is because the OCTA images of these retinal vascular layers may not always show the abnormalities related to AMD disease.

Nevertheless, the various techniques developed in this thesis have successfully identified and quantified the above-mentioned variations by applying supervised and unsupervised statistical pattern recognition techniques, e.g.: the LBP^{2riu} and the $LBP^{2riuPCA}$ texture descriptors, on the texture of OCTA images. Additional important findings are that the various diagnostic techniques developed can identify the ocular vascular abnormalities related to AMD disease in the raw OCTA images of the individual retinal and choroidal layers purely as extracted by the OCTA imaging technique.

7.3 Conclusion

The overall aim of this research was to automate ways of quantifying and finding evidence of AMD disease in the context of OCTA image data. To draw the final conclusion, the main research objectives formulated to achieve this overall aim, and the research hypotheses that are summarised in Chapter 1 are, therefore, reconsidered.

Research Objectives:

- **To explore ways to automate the analysis of OCTA image texture.** This objective is achieved in Chapter 2 by reviewing the typical computer vision tasks employed to assist in analysing the texture of medical images. Based on the exploration, automating the analysis of OCTA image texture by means of whole

image classification proved to be appropriate. This is because it may minimise the potential risk of the diagnosis results to be influenced by human factors, e.g.: bias, attitude and so on, due to the image segmentation techniques typically requiring manual assistance. As a result, quantitative measures based on manually or automated segmented regions as well as comparisons between outcomes from such regions may potentially be misleading.

- **To investigate texture representation techniques for measuring the texture of OCTA images.** This objective is accomplished in Chapter 2 by reviewing the most notable texture representation techniques. Based on the investigation, the dense local texture descriptors, e.g.: the $LBP_{p,r}$, the $LBP_{p,r}^{2riu}$ and the $BRIEF_{S,n}$ texture descriptors, appeared to be appropriate. This is because they typically require no complex parameters to tune, low computational complexity, not being foiled by the size of OCTA image data set, among other features as demonstrated in Chapter 2.
- **To identify the main characteristics of the OCTA image data and how these have been exploited by previous studies to diagnose AMD disease.** This objective is achieved in Chapter 3 by reviewing the most notable OCTA image data analysis studies related to AMD disease in general as well as studies concerning automating the analysis tasks. Based on the comprehensive review conducted in Chapter 3, it was found that the OCTA image data suffers from the lack of specific diagnostic criteria in the presence of various retinal diseases including AMD disease, despite numerous previous attempts for establishing standardised norms. Additionally, none of the conventional imaging modalities, e.g.: the OCT, the FA and the IGA, can provide comparable imaging capability to the OCTA imaging technique, nor can now be used in place of the OCTA for diagnosing various ocular vascular abnormalities including AMD disease.
- **To construct fully automated diagnosis algorithms that can accurately analyse the various OCTA images with different eye conditions related to AMD disease as well as healthy.** This objective is achieved in Chapters 4 and 5. Chapter 4 presents a fully automated OCTA image classification algorithm for the diagnosis of AMD disease based on whole-local texture features. Chapter 5 provides a fully automated OCTA image classification algorithm for the diagnosis of AMD disease based on reduced-local texture features. Broadly, the classification algorithm that is based on whole-local texture features exhibited better classification performance for the healthy vs wet AMD classification task.

However, the classification algorithm that is based on reduced-local texture features demonstrated improved classification performance for the dry AMD vs wet AMD and the CNV vs non-CNV classification tasks.

- **To create a fully automated diagnosis algorithm that can estimate the locations of abnormal ocular blood vessel areas, e.g.: regions of CNV lesions, in the texture of OCTA images.** This objective is achieved in Chapter 6. Chapter 6 presents a fully automated localisation algorithm for localising areas of CNV lesions related to AMD disease in the texture of OCTA images based on local texture features. Broadly, the best overall localisation performance of the localisation algorithm is achieved when employing the chi-square χ^2 distance similarity metric and utilising the patch P size of 120×120 pixels dimensions.

Research Hypotheses:

- **It is feasible to perform automated diagnosis for eye conditions, e.g.: AMD disease, using the OCTA image data in the raw form purely as extracted by the OCTA imaging technique.**

This research hypothesis is verified in Chapters 4, 5 and 6. As such, the possibilities to use the OCTA image data for automating the diagnosis of AMD disease are verified by conducting different automated image classification tasks in Chapters 4 and 5, and region localisation tasks in Chapter 6. From an image classification perspective, the classification algorithm proposed in Chapter 4, broadly, proved to perform excellently for the healthy vs wet AMD classification task. Specifically, a perfect classification performance, i.e.: a mean AUC score and a standard deviation = 1.00 ± 0.00 was accomplished when concatenating the feature vectors extracted from the OCTA images of the outer retina and the choriocapillaris layers.

However, the classification algorithm proposed in Chapter 5, generally demonstrated to perform better in solving the dry AMD vs wet AMD and the CNV vs non-CNV classification tasks. In particular, accomplishing mean AUC scores and standard deviations = 0.85 ± 0.02 when utilising the feature vectors extracted from the outer retina layer and 0.85 ± 0.05 when concatenating the feature vectors extracted from the OCTA images of all ocular vascular layers for the dry AMD vs wet AMD and the CNV vs non-CNV classification tasks, respectively. For comprehensive performance comparisons between the two classification algorithms in solving the various image classification problems, see Tables 5.53, 5.54 and 5.55 in Chapter 5.

From a region localisation perspective, however, the localisation algorithm proposed in Chapter 6, generally, showed to provide reasonable estimates for the approximate locations of CNV regions in the diseased OCTA images of the outer retina and the choriocapillaris layers. As such the best localisation performance, see Table 6.1 in Chapter 6, is always achieved when employing the chi-square χ^2 distance similarity metric and utilising the patch P size of 120×120 pixels dimensions. Consequently, the evaluation results given in Chapters 4, 5 and 6 confirm the validity of the previously stated research hypothesis.

- **There is a difference between the blood vessel patterns in the superficial inner retina and the deep inner retina layers of the diseased and healthy OCTA images.**

The validity of this research hypothesis is verified in Chapters 4 and 5 via utilising the OCTA images of the superficial inner retina and the deep inner retina layers in solving the various image classification tasks by the two image classification algorithms proposed in Chapters 4 and 5. For the healthy vs wet AMD classification task, the classification algorithm proposed in Chapter 5 accomplished mean AUC scores and standard deviations = 0.90 ± 0.02 when using the feature vectors extracted from the OCTA images of the superficial inner retina layer. The classification algorithm proposed in Chapter 4, on the other hand, achieved mean AUC scores and standard deviations = 0.96 ± 0.04 when exploiting the feature vectors obtained from the OCTA images of the deep inner retina layer.

For the dry AMD vs wet AMD classification task, the classification algorithm proposed in Chapter 5 attained mean AUC scores and standard deviations = 0.74 ± 0.04 when exploiting the feature vectors obtained from the OCTA images of the superficial inner retina layer and 0.79 ± 0.03 when utilising the feature vectors obtained from the OCTA images of the deep inner retina layer.

For the CNV vs non-CNV classification task, the classification algorithm proposed in Chapter 4 achieved mean AUC scores and standard deviations = 0.70 ± 0.05 when utilising the feature vectors obtained from the OCTA images of the superficial inner retina layer. The classification algorithm proposed in Chapter 5, on the other hand, attained mean AUC scores and standard deviations = 0.76 ± 0.03 when using the feature vectors obtained from the OCTA images of the deep inner retina layer.

The two image classification algorithms proposed in Chapters 4 and 5, generally, achieved better classification results in solving the various image classification tasks when utilising the feature vectors obtained from the OCTA images of other ocular

vascular layers. Nevertheless, the differences between the blood vessel patterns in the superficial inner retina and the deep inner retina layers of the diseased and healthy OCTA images have been demonstrated as evident in the performance comparisons given in Tables 5.53, 5.54 and 5.55 in Chapter 5.

Additionally, exploiting the OCTA images of the superficial inner retina and the deep inner retina layers in solving the CNV vs non-CNV classification task by concatenating the feature vectors obtained from the OCTA images of all ocular vascular layers demonstrated to boost the classification performance. Specifically, a mean AUC score and standard deviation 0.85 ± 0.05 was achieved. Consequently, the evaluation results presented in Chapters 4 and 5 prove the validity of the above stated research hypothesis.

The various diagnostic algorithms developed were rigorously evaluated based on diverse OCTA image data sets provided by two different hospitals, namely the Manchester Royal Eye Hospital and the Moorfields Eye Hospital. A hyper-parameter search was also conducted for the KNN and the SVM classifiers employed in the two classification algorithms proposed. Different distance similarity metrics including the chi-square χ^2 and the histogram intersection, and various sizes of patches P were also explored in the localisation algorithm. Overall, the evaluation results presented in Chapters 4, 5 and 6 demonstrate that the diagnostic algorithms presented in this thesis are useful, very effective and encouraging compared to other well-established techniques which perform OCTA image texture analysis tasks analogous to the analysis tasks presented in this thesis that mainly concern the detection of AMD disease.

7.4 Future Directions

While the diagnostic techniques developed in this thesis have generally accomplished the essential tasks for which they were intended, there are several ways in which they can be further enhanced, rigorously evaluated, and exploited. These are summarised as follows:

- The automated diagnostic classification algorithms demonstrated a great classification performance in differentiating healthy subjects from wet AMD patients in the various OCTA images. Therefore, exploiting these algorithms to distinguish healthy subjects from patients with another ocular disorder, e.g.: DR or glaucoma, would be of interest. To accomplish this, the attainment of carefully curated OCTA image data that represent DR or glaucoma condition disease is

required.

- Evaluating the automated diagnostic classification algorithms on more complex tasks would also be of interest. As such, it would be very clinically valuable if the variations between wet AMD patients could be quantified and discriminated. These are wet AMD patients with active CNV lesions that necessitate treatment and wet AMD patients with inactive CNV lesions which only can be observed. Hence, collocating carefully curated OCTA image data that represent these variations of wet AMD disease is required.
- The current OCTA image data sets that were used in this research project are smaller than the desired size. Hence, collecting a much larger OCTA image data set would allow full assessments to be conducted on the automated diagnostic algorithms developed.
- The localisation algorithm was evaluated based on the OCTA images of the outer retina and the choriocapillaris layers captured from patients with CNV lesions in their raw form. Hence, the low localisation performance was expected as the OCTA images may not always show the vascular abnormalities, i.e.: areas of CNV lesions. On some occasions, the CNV regions can also dominate the entire OCTA image. Consequently, assessing the localisation algorithm on carefully selected OCTA image data sets that show clearly the CNV lesions in the OCTA images of the outer retina and the choriocapillaris layers would be of interest. As such, this can allow a rigorous evaluation of the localisation algorithm to be performed to gain further insight into its ability in modelling both the normal and abnormal texture vascular appearance in the OCTA images.
- The recent dominant trend in developing automated image texture analysis techniques for medical image analysis and diagnosis tasks, e.g.: classification or segmentation, have been based on introducing deeper and more complicated architectures. Hence, exploring the performance of deep CNN models in similar tasks would be of interest. To enable this, the acquisition of highly curated OCTA image data sets that represent various eye conditions, e.g.: healthy and AMD disease, is necessary. Data augmentation techniques to increase the number of OCTA images are generally inappropriate and can be misleading. This is because they may distort the texture of OCTA image data in undesirable ways.

Bibliography

- [1] J. M. Colijn, G. H. Buitendijk, E. Prokofyeva, D. Alves, M. L. Cachulo, A. P. Khawaja, A. Cougnard-Gregoire, B. M. Merle, C. Korb, M. G. Erke *et al.*, “Prevalence of age-related macular degeneration in Europe: the past and the future,” *Ophthalmology*, vol. 124, no. 12, pp. 1753–1763, 2017.
- [2] R. R. Bourne, J. B. Jonas, S. R. Flaxman, J. Keeffe, J. Leasher, K. Naidoo, M. B. Parodi, K. Pesudovs, H. Price, R. A. White *et al.*, “Prevalence and causes of vision loss in high-income countries and in Eastern and Central Europe: 1990–2010,” *British Journal of Ophthalmology*, vol. 98, no. 5, pp. 629–638, 2014.
- [3] P. Mitchell, G. Liew, B. Gopinath, and T. Y. Wong, “Age-related macular degeneration,” *The Lancet*, vol. 392, no. 10153, pp. 1147–1159, 2018.
- [4] H. Mehta, A. Tufail, V. Daien, A. Y. Lee, V. Nguyen, M. Ozturk, D. Barthelmes, and M. C. Gillies, “Real-world outcomes in patients with neovascular age-related macular degeneration treated with intravitreal vascular endothelial growth factor inhibitors,” *Progress in Retinal and Eye Research*, vol. 65, pp. 127–146, 2018.
- [5] Y. Jia, S. T. Bailey, T. S. Hwang, S. M. McClintic, S. S. Gao, M. E. Pennesi, C. J. Flaxel, A. K. Lauer, D. J. Wilson, J. Hornegger *et al.*, “Quantitative optical coherence tomography angiography of vascular abnormalities in the living human eye,” *Proceedings of the National Academy of Sciences*, p. 201500185, 2015.
- [6] Y. Jia, S. T. Bailey, D. J. Wilson, O. Tan, M. L. Klein, C. J. Flaxel, B. Potsaid, J. J. Liu, C. D. Lu, M. F. Kraus *et al.*, “Quantitative optical coherence tomography angiography of choroidal neovascularization in age-related macular degeneration,” *Ophthalmology*, vol. 121, no. 7, pp. 1435–1444, 2014.

- [7] T. E. De Carlo, A. Romano, N. K. Waheed, and J. S. Duker, "A review of optical coherence tomography angiography (octa)," *International Journal of Retina and Vitreous*, vol. 1, no. 1, p. 5, 2015.
- [8] L. Kuehlewein, M. Bansal, T. L. Lenis, N. A. Iafe, S. R. Sadda, M. A. Bonini Filho, E. Talisa, N. K. Waheed, J. S. Duker, and D. Sarraf, "Optical coherence tomography angiography of type 1 neovascularization in age-related macular degeneration," *American Journal of Ophthalmology*, vol. 160, no. 4, pp. 739–748, 2015.
- [9] F. Sulzbacher, A. Pollreisz, A. Kaider, S. Kicking, S. Sacu, U. Schmidt-Erfurth, and V. E. S. Center, "Identification and clinical role of choroidal neovascularization characteristics based on optical coherence tomography angiography," *Acta Ophthalmologica*, vol. 95, no. 4, pp. 414–420, 2017.
- [10] L. Liu, S. S. Gao, S. T. Bailey, D. Huang, D. Li, and Y. Jia, "Automated choroidal neovascularization detection algorithm for optical coherence tomography angiography," *Biomedical Optics Express*, vol. 6, no. 9, pp. 3564–3576, 2015.
- [11] P. Simon and V. Uma, "Review of texture descriptors for texture classification," in *Data Engineering and Intelligent Computing*. Springer, 2018, pp. 159–176.
- [12] A. Depeursinge, J. Fageot, and O. S. Al-Kadi, "Chapter 1 - fundamentals of texture processing for biomedical image analysis: A general definition and problem formulation," in *Biomedical Texture Analysis*, A. Depeursinge, O. S. Al-Kadi, and J. Mitchell, Eds. Academic Press, 2017, pp. 1 – 27. [Online]. Available: <http://www.sciencedirect.com/science/article/pii/B9780128121337000016>
- [13] G. J. Coscas, M. Lupidi, F. Coscas, C. Cagini, and E. H. Souied, "Optical coherence tomography angiography versus traditional multimodal imaging in assessing the activity of exudative age-related macular degeneration: a new diagnostic challenge," *Retina*, vol. 35, no. 11, pp. 2219–2228, 2015.
- [14] A. El Ameen, S. Y. Cohen, O. Semoun, A. Miere, M. Srour, M. Quaranta-El Maftouhi, H. Oubraham, R. Blanco-Garavito, G. Querques, and E. H. Souied,

- “Type 2 neovascularization secondary to age-related macular degeneration imaged by optical coherence tomography angiography,” *Retina*, vol. 35, no. 11, pp. 2212–2218, 2015.
- [15] A. Miere, G. Querques, O. Semoun, V. Capuano, E. H. Souied *et al.*, “Optical coherence tomography angiography in early type 3 neovascularization,” *Retina*, vol. 35, no. 11, pp. 2236–2241, 2015.
- [16] A. Miere, G. Querques, O. Semoun, F. Amoroso, O. Zambrowski, T. Chapron, V. Capuano, and E. H. Souied, “Optical coherence tomography angiography changes in early type 3 neovascularization after anti-vascular endothelial growth factor treatment,” *Retina*, vol. 37, no. 10, pp. 1873–1879, 2017.
- [17] M. Choi, S. Ahn, C. Yun, and S.-W. Kim, “Quantitative oct angiography findings according to pattern classification of type 1 neovascularization exudative age-related macular degeneration,” *Eye*, pp. 1–10, 2021.
- [18] M. Lupidi, A. Cerquaglia, J. Chhablani, T. Fiore, S. R. Singh, F. Cardillo Piccolino, R. Corbucci, F. Coscas, G. Coscas, and C. Cagini, “Optical coherence tomography angiography in age-related macular degeneration: the game changer,” *European journal of ophthalmology*, vol. 28, no. 4, pp. 349–357, 2018.
- [19] P. J. Robinson, “Radiology’s achilles’ heel: error and variation in the interpretation of the röntgen image,” *The British Journal of Radiology*, vol. 70, no. 839, pp. 1085–1098, 1997, pMID: 9536897. [Online]. Available: <https://doi.org/10.1259/bjr.70.839.9536897>
- [20] G. Tourassi, S. Voisin, V. Paquit, and E. Krupinski, “Investigating the link between radiologists’ gaze, diagnostic decision, and image content,” *Journal of the American Medical Informatics Association*, vol. 20, no. 6, pp. 1067–1075, 06 2013. [Online]. Available: <https://doi.org/10.1136/amiajnl-2012-001503>
- [21] Z. A. Aziz, A. U. Wells, D. M. Hansell, G. A. Bain, S. J. Copley, S. R. Desai, S. M. Ellis, F. V. Gleeson, S. Grubnic, A. G. Nicholson, S. P. G. Padley, K. S. Pointon, J. H. Reynolds, R. J. H. Robertson, and M. B. Rubens, “Hrct diagnosis of diffuse parenchymal lung disease: inter-observer variation,” *Thorax*, vol. 59, no. 6, pp. 506–511, 2004. [Online]. Available: <https://thorax.bmj.com/content/59/6/506>

- [22] T. T. Hormel, T. S. Hwang, S. T. Bailey, D. J. Wilson, D. Huang, and Y. Jia, “Artificial intelligence in oct angiography,” *Progress in Retinal and Eye Research*, p. 100965, 2021.
- [23] G. D. Tourassi, “Journey toward computer-aided diagnosis: role of image texture analysis,” *Radiology*, vol. 213, no. 2, pp. 317–320, 1999.
- [24] T. Ojala, M. Pietikainen, and T. Maenpaa, “Multiresolution gray-scale and rotation invariant texture classification with local binary patterns,” *IEEE Transactions on pattern analysis and machine intelligence*, vol. 24, no. 7, pp. 971–987, 2002.
- [25] A. Alfahaid and T. Morris, “An automated age-related macular degeneration classification based on local texture features in optical coherence tomography angiography,” in *Medical Image Understanding and Analysis*, M. Nixon, S. Mahmoodi, and R. Zwigelaar, Eds. Cham: Springer International Publishing, 2018, pp. 189–200.
- [26] K. Balaskas, A. Alfahaid, H. Khalid, P. Sergouniotis, N. Pontikos, and P. A. Keane, “Machine learning for the automated interpretation of optical coherence tomography angiography for age-related macular degeneration,” *Investigative Ophthalmology & Visual Science*, vol. 60, no. 9, pp. 3095–3095, 2019.
- [27] A. Alfahaid, T. Morris, T. Cootes, P. A. Keane, H. Khalid, N. Pontikos, P. Sergouniotis, and K. Balaskas, “A hybrid machine learning approach using lbp descriptor and pca for age-related macular degeneration classification in octa images,” in *Medical Image Understanding and Analysis*, Y. Zheng, B. M. Williams, and K. Chen, Eds. Cham: Springer International Publishing, 2020, pp. 231–241.
- [28] R. Hartley and A. Zisserman, *Multiple view geometry in computer vision*. Cambridge university press, 2004.
- [29] J. Brownlee, “A gentle introduction to computer vision,” 2019, <https://machinelearningmastery.com/what-is-computer-vision/>, Accessed: 21-Jan-2020.
- [30] D. A. Forsyth and J. Ponce, *Computer vision: a modern approach*. Prentice Hall Professional Technical Reference, 2002.

- [31] S. J. Prince, *Computer vision: models, learning, and inference*. Cambridge University Press, 2012.
- [32] L. Liu, J. Chen, P. Fieguth, G. Zhao, R. Chellappa, and M. Pietikäinen, “From bow to cnn: Two decades of texture representation for texture classification,” *International Journal of Computer Vision*, vol. 127, no. 1, pp. 74–109, 2019.
- [33] M. A. Ali, T. Hurtut, T. Faucon, and F. Cheriet, “Glaucoma detection based on local binary patterns in fundus photographs,” in *Medical Imaging 2014: Computer-Aided Diagnosis*, vol. 9035. International Society for Optics and Photonics, 2014, p. 903531.
- [34] M. Peikari, M. J. Gangeh, J. Zubovits, G. Clarke, and A. L. Martel, “Triaging diagnostically relevant regions from pathology whole slides of breast cancer: A texture based approach,” *IEEE transactions on medical imaging*, vol. 35, no. 1, pp. 307–315, 2015.
- [35] J. Lauermann, M. Treder, M. Alnawaiseh, C. Clemens, N. Eter, and F. Alten, “Automated oct angiography image quality assessment using a deep learning algorithm,” *Graefe’s Archive for Clinical and Experimental Ophthalmology*, vol. 257, no. 8, pp. 1641–1648, 2019.
- [36] M. Tuceryan and A. K. Jain, “Texture analysis,” in *Handbook of pattern recognition and computer vision*. World Scientific, 1993, pp. 235–276.
- [37] C. Köse, U. ŞEvik, C. İKibaş, and H. Erdöl, “Simple methods for segmentation and measurement of diabetic retinopathy lesions in retinal fundus images,” *Computer methods and programs in biomedicine*, vol. 107, no. 2, pp. 274–293, 2012.
- [38] L. Fang, D. Cunefare, C. Wang, R. H. Guymer, S. Li, and S. Farsiu, “Automatic segmentation of nine retinal layer boundaries in oct images of non-exudative amd patients using deep learning and graph search,” *Biomedical Optics Express*, vol. 8, no. 5, pp. 2732–2744, 2017.
- [39] M. Pietikäinen, A. Hadid, G. Zhao, and T. Ahonen, *Computer vision using local binary patterns*. Springer Science & Business Media, 2011, vol. 40.
- [40] G. Castellano, L. Bonilha, L. Li, and F. Cendes, “Texture analysis of medical images,” *Clinical Radiology*, vol. 59, no. 12, pp. 1061 – 1069,

2004. [Online]. Available: <http://www.sciencedirect.com/science/article/pii/S000992600400265X>
- [41] B. Julesz, "Textons, the elements of texture perception, and their interactions," *Nature*, vol. 290, no. 5802, pp. 91–97, 1981.
- [42] B. Julesz, "Visual pattern discrimination," *IRE Transactions on Information Theory*, vol. 8, no. 2, pp. 84–92, February 1962.
- [43] R. M. Haralick, "Statistical and structural approaches to texture," *Proceedings of the IEEE*, vol. 67, no. 5, pp. 786–804, 1979.
- [44] M. Tuceryan and A. K. Jain, "Texture segmentation using voronoi polygons," *IEEE transactions on pattern analysis and machine intelligence*, vol. 12, no. 2, pp. 211–216, 1990.
- [45] A. Materka, M. Strzelecki *et al.*, "Texture analysis methods—a review," *Technical university of lodz, institute of electronics, COST B11 report, Brussels*, vol. 10, no. 1.97, p. 4968, 1998.
- [46] R. Fisher, S. Perkins, A. Walker, and E. Wolfart, "Hypermedia image processing reference," *Department of Artificial Intelligence, University of Edinburg, available on <http://www.cee.hw.uk>*, 1996.
- [47] K. S. Fu, *Syntactic pattern recognition and applications*. Prentice Hall, 1982.
- [48] T. R. Reed and J. H. Dubuf, "A review of recent texture segmentation and feature extraction techniques," *CVGIP: Image understanding*, vol. 57, no. 3, pp. 359–372, 1993.
- [49] T. Randen, "Filter and filter bank design for image texture recognition," PhD thesis, Norwegian University of Science and Technology, Stavanger College, 1997.
- [50] J. S. Weszka, C. R. Dyer, and A. Rosenfeld, "A comparative study of texture measures for terrain classification," *IEEE transactions on Systems, Man, and Cybernetics*, no. 4, pp. 269–285, 1976.
- [51] R. M. Haralick, K. Shanmugam, and I. H. Dinstein, "Textural features for image classification," *IEEE Transactions on systems, man, and cybernetics*, no. 6, pp. 610–621, 1973.

- [52] U. R. Acharya, E. Y.-K. Ng, J.-H. Tan, S. V. Sree, and K.-H. Ng, "An integrated index for the identification of diabetic retinopathy stages using texture parameters," *Journal of medical systems*, vol. 36, no. 3, pp. 2011–2020, 2012.
- [53] A. Eleyan and H. Demirel, "Co-occurrence based statistical approach for face recognition," in *2009 24th international symposium on computer and information sciences*. IEEE, 2009, pp. 611–615.
- [54] H. Murray, A. Lucieer, and R. Williams, "Texture-based classification of sub-antarctic vegetation communities on heard island," *International Journal of Applied Earth Observation and Geoinformation*, vol. 12, no. 3, pp. 138 – 149, 2010. [Online]. Available: <http://www.sciencedirect.com/science/article/pii/S0303243410000097>
- [55] S. Herlidou-Meme, J. Constans, B. Carsin, D. Olivie, P. Eliat, L. Nadal-Desbarats, C. Gondry, E. Le Rumeur, I. Idy-Peretti, and J. De Certaines, "Mri texture analysis on texture test objects, normal brain and intracranial tumors," *Magnetic resonance imaging*, vol. 21, no. 9, pp. 989–993, 2003.
- [56] V. A. Kovalev, M. Petrou, and Y. S. Bondar, "Texture anisotropy in 3-d images," *IEEE Transactions on Image Processing*, vol. 8, no. 3, pp. 346–360, 1999.
- [57] F. Chabat, G.-Z. Yang, and D. M. Hansell, "Obstructive lung diseases: texture classification for differentiation at ct," *Radiology*, vol. 228, no. 3, pp. 871–877, 2003.
- [58] S. Mohammad, "Textural measurements for retinal image analysis," PhD thesis, The University of Manchester, Manchester, UK, 2015.
- [59] R. Chellappa, R. Kashyap, and B. Manjunath, "Model-based texture segmentation and classification," in *Handbook of pattern recognition and computer vision*. World Scientific, 1993, pp. 277–310.
- [60] A. Blake and A. Zisserman, *Visual reconstruction*. MIT press, 1987.
- [61] G. R. Cross and A. K. Jain, "Markov random field texture models," *IEEE Transactions on Pattern Analysis and Machine Intelligence*, no. 1, pp. 25–39, 1983.
- [62] R. Chellappa and S. Chatterjee, "Classification of textures using gaussian markov random fields," *IEEE Transactions on Acoustics, Speech, and Signal Processing*, vol. 33, no. 4, pp. 959–963, 1985.

- [63] A. Khotanzad and R. L. Kashyap, "Feature selection for texture recognition based on image synthesis," *IEEE Transactions on Systems, Man, and Cybernetics*, vol. 17, no. 6, pp. 1087–1095, 1987.
- [64] F. S. Cohen and D. B. Cooper, "Simple parallel hierarchical and relaxation algorithms for segmenting noncausal markovian random fields," *IEEE Transactions on Pattern Analysis and Machine Intelligence*, no. 2, pp. 195–219, 1987.
- [65] C. W. Therrien, "An estimation-theoretic approach to terrain image segmentation," *Computer Vision, Graphics, and Image Processing*, vol. 22, no. 3, pp. 313–326, 1983.
- [66] M. Petrou and P. G. Sevilla, *Image processing: dealing with texture*. Wiley, 2006.
- [67] B. B. Mandelbrot, *The fractal geometry of nature*. WH freeman New York, 1983, vol. 173.
- [68] B. Mandelbrot, "Self-affine fractals and fractal dimension," *Physica Scripta*, vol. 32, no. 4, pp. 257–260, oct 1985. [Online]. Available: <https://doi.org/10.1088%2F0031-8949%2F32%2F4%2F001>
- [69] Y. Xu, H. Ji, and C. Fermüller, "Viewpoint invariant texture description using fractal analysis," *International Journal of Computer Vision*, vol. 83, no. 1, pp. 85–100, 2009.
- [70] F. W. Campbell and J. G. Robson, "Application of fourier analysis to the visibility of gratings," *The Journal of physiology*, vol. 197, no. 3, p. 551, 1968.
- [71] M. Georgeson, "Spatial fourier analysis and human vision," *Tutorial essays in psychology*, vol. 2, pp. 39–88, 1979.
- [72] S. G. Mallat, "Multifrequency channel decompositions of images and wavelet models," *IEEE Transactions on Acoustics, Speech, and Signal Processing*, vol. 37, no. 12, pp. 2091–2110, 1989.
- [73] D. H. Hubel and T. N. Wiesel, "Receptive fields, binocular interaction and functional architecture in the cat's visual cortex," *The Journal of physiology*, vol. 160, no. 1, pp. 106–154, 1962.

- [74] T. Randen and J. H. Husoy, "Filtering for texture classification: A comparative study," *IEEE Transactions on pattern analysis and machine intelligence*, vol. 21, no. 4, pp. 291–310, 1999.
- [75] A. K. Jain and F. Farrokhnia, "Unsupervised texture segmentation using gabor filters," in *1990 IEEE international conference on systems, man, and cybernetics conference proceedings*. IEEE, 1990, pp. 14–19.
- [76] T. Leung and J. Malik, "Representing and recognizing the visual appearance of materials using three-dimensional textons," *International journal of computer vision*, vol. 43, no. 1, pp. 29–44, 2001.
- [77] B. S. Manjunath and W.-Y. Ma, "Texture features for browsing and retrieval of image data," *IEEE Transactions on pattern analysis and machine intelligence*, vol. 18, no. 8, pp. 837–842, 1996.
- [78] T. S. Lee, "Image representation using 2d gabor wavelets," *IEEE Transactions on pattern analysis and machine intelligence*, vol. 18, no. 10, pp. 959–971, 1996.
- [79] A. C. Bovik, M. Clark, and W. S. Geisler, "Multichannel texture analysis using localized spatial filters," *IEEE transactions on pattern analysis and machine intelligence*, vol. 12, no. 1, pp. 55–73, 1990.
- [80] B. Manjunath and R. Chellappa, "A unified approach to boundary perception: edges, textures, and illusory contours," *IEEE Transactions on neural networks*, vol. 4, no. 1, pp. 96–108, 1993.
- [81] J. G. Daugman, "High confidence visual recognition of persons by a test of statistical independence," *IEEE transactions on pattern analysis and machine intelligence*, vol. 15, no. 11, pp. 1148–1161, 1993.
- [82] M. Lades, J. C. Vorbruggen, J. Buhmann, J. Lange, C. Von Der Malsburg, R. P. Wurtz, and W. Konen, "Distortion invariant object recognition in the dynamic link architecture," *IEEE Transactions on computers*, vol. 42, no. 3, pp. 300–311, 1993.
- [83] R. Chellappa, B. Manjunath, and C. Malsburg, "A feature based approach to face recognition," in *IEEE Conference on Computer Vision and Pattern Recognition*, 1992, pp. 373–378.

- [84] J. Liu, B. C. Vemuri, and J. L. Marroquín, "Local frequency representations for robust multimodal image registration," *IEEE transactions on medical imaging*, vol. 21, no. 5, pp. 462–469, 2002.
- [85] S. Liao and A. C. Chung, "Feature based nonrigid brain mr image registration with symmetric alpha stable filters," *IEEE transactions on medical imaging*, vol. 29, no. 1, pp. 106–119, 2009.
- [86] B. Manjunath, C. Shekhar, and R. Chellappa, "A new approach to image feature detection with applications," *Pattern Recognition*, vol. 29, no. 4, pp. 627–640, 1996.
- [87] U. Kandaswamy, S. A. Schuckers, and D. Adjero, "Comparison of texture analysis schemes under nonideal conditions," *IEEE Transactions on Image Processing*, vol. 20, no. 8, pp. 2260–2275, 2010.
- [88] J. Zhang, M. Marszałek, S. Lazebnik, and C. Schmid, "Local features and kernels for classification of texture and object categories: A comprehensive study," *International journal of computer vision*, vol. 73, no. 2, pp. 213–238, 2007.
- [89] W. Zhang, S. Shan, W. Gao, X. Chen, and H. Zhang, "Local gabor binary pattern histogram sequence (lgbphs): A novel non-statistical model for face representation and recognition," in *Tenth IEEE International Conference on Computer Vision (ICCV'05) Volume 1*, vol. 1. IEEE, 2005, pp. 786–791.
- [90] S. Lazebnik, C. Schmid, and J. Ponce, "A sparse texture representation using local affine regions," *IEEE Transactions on Pattern Analysis and Machine Intelligence*, vol. 27, no. 8, pp. 1265–1278, 2005.
- [91] S. Lazebnik, C. Schmid, and J. Ponce, "A sparse texture representation using affine-invariant regions," in *2003 IEEE Computer Society Conference on Computer Vision and Pattern Recognition, 2003. Proceedings.*, vol. 2. IEEE, 2003, pp. II–II.
- [92] K. Mikolajczyk and C. Schmid, "A performance evaluation of local descriptors," *IEEE transactions on pattern analysis and machine intelligence*, vol. 27, no. 10, pp. 1615–1630, 2005.

- [93] K. Mikolajczyk, T. Tuytelaars, C. Schmid, A. Zisserman, J. Matas, F. Schaf-falitzky, T. Kadir, and L. Van Gool, "A comparison of affine region detectors," *International journal of computer vision*, vol. 65, no. 1-2, pp. 43–72, 2005.
- [94] T. Tuytelaars and K. Mikolajczyk, *Local invariant feature detectors: a survey*. Now Publishers Inc, 2008.
- [95] D. Huang, C. Shan, M. Ardabilian, Y. Wang, and L. Chen, "Local binary pat-terns and its application to facial image analysis: a survey," *IEEE Transactions on Systems, Man, and Cybernetics, Part C (Applications and Reviews)*, vol. 41, no. 6, pp. 765–781, 2011.
- [96] T. Ojala, M. Pietikainen, and D. Harwood, "Performance evaluation of texture measures with classification based on kullback discrimination of distributions," in *Proceedings of 12th International Conference on Pattern Recognition*, vol. 1. IEEE, 1994, pp. 582–585.
- [97] T. Ojala, M. Pietikäinen, and D. Harwood, "A comparative study of texture mea-sures with classification based on featured distributions," *Pattern recognition*, vol. 29, no. 1, pp. 51–59, 1996.
- [98] M. Calonder, V. Lepetit, C. Strecha, and P. Fua, "Brief: Binary robust in-dependent elementary features," in *European conference on computer vision*. Springer, 2010, pp. 778–792.
- [99] M. Calonder, V. Lepetit, M. Ozuysal, T. Trzcinski, C. Strecha, and P. Fua, "Brief: Computing a local binary descriptor very fast," *IEEE transactions on pattern analysis and machine intelligence*, vol. 34, no. 7, pp. 1281–1298, 2011.
- [100] T. Ahonen, A. Hadid, and M. Pietikainen, "Face description with local binary patterns: Application to face recognition," *IEEE transactions on pattern analy-sis and machine intelligence*, vol. 28, no. 12, pp. 2037–2041, 2006.
- [101] A. Hadid, M. Pietikainen, and T. Ahonen, "A discriminative feature space for detecting and recognizing faces," in *Proceedings of the 2004 IEEE Computer Society Conference on Computer Vision and Pattern Recognition, 2004. CVPR 2004.*, vol. 2. IEEE, 2004, pp. II–II.

- [102] T. Ahonen, A. Hadid, and M. Pietikäinen, “Face recognition with local binary patterns,” in *Computer Vision - ECCV 2004*, T. Pajdla and J. Matas, Eds. Berlin, Heidelberg: Springer Berlin Heidelberg, 2004, pp. 469–481.
- [103] D. P. Huijsmans and N. Sebe, “Content-based indexing performance: size normalized precision, recall, generality evaluation,” in *Proceedings 2003 International Conference on Image Processing (Cat. No. 03CH37429)*, vol. 3. IEEE, 2003, pp. III–733.
- [104] D. Grangier and S. Bengio, “A discriminative kernel-based approach to rank images from text queries,” *IEEE transactions on pattern analysis and machine intelligence*, vol. 30, no. 8, pp. 1371–1384, 2008.
- [105] W. Ali, F. Georgsson, and T. Hellstrom, “Visual tree detection for autonomous navigation in forest environment,” in *2008 IEEE Intelligent Vehicles Symposium*. IEEE, 2008, pp. 560–565.
- [106] L. Nanni and A. Lumini, “Ensemble of multiple pedestrian representations,” *IEEE Transactions on Intelligent Transportation Systems*, vol. 9, no. 2, pp. 365–369, 2008.
- [107] T. Mäenpää, J. Viertola, and M. Pietikäinen, “Optimising colour and texture features for real-time visual inspection,” *Pattern Analysis & Applications*, vol. 6, no. 3, pp. 169–175, 2003.
- [108] M. Turtinen, M. Pietikainen, and O. Silvén, “Visual characterization of paper using isomap and local binary patterns,” *IEICE transactions on information and systems*, vol. 89, no. 7, pp. 2076–2083, 2006.
- [109] M. Heikkilä and M. Pietikainen, “A texture-based method for modeling the background and detecting moving objects,” *IEEE transactions on pattern analysis and machine intelligence*, vol. 28, no. 4, pp. 657–662, 2006.
- [110] V. Kellokumpu, G. Zhao, and M. Pietikäinen, “Human activity recognition using a dynamic texture based method,” in *BMVC*, vol. 1, 2008, p. 2.
- [111] A. Oliver, X. Lladó, J. Freixenet, and J. Martí, “False positive reduction in mammographic mass detection using local binary patterns,” in *International Conference on Medical Image Computing and Computer-Assisted Intervention*. Springer, 2007, pp. 286–293.

- [112] S. Kluckner, G. Pacher, H. Grabner, H. Bischof, and J. Bauer, "A 3d teacher for car detection in aerial images," in *2007 IEEE 11th International Conference on Computer Vision*. IEEE, 2007, pp. 1–8.
- [113] A. Lucieer, A. Stein, and P. Fisher, "Multivariate texture-based segmentation of remotely sensed imagery for extraction of objects and their uncertainty," *International Journal of Remote Sensing*, vol. 26, no. 14, pp. 2917–2936, 2005.
- [114] S. Mohammad, D. Morris, and N. Thacker, "Texture analysis for the segmentation of optic disc in retinal images," in *2013 IEEE International Conference on Systems, Man, and Cybernetics*. IEEE, 2013, pp. 4265–4270.
- [115] S. Mohammad, D. Morris, and N. Thacker, "Segmentation of optic disc in retina images using texture," in *2014 International Conference on Computer Vision Theory and Applications (VISAPP)*, vol. 1. IEEE, 2014, pp. 293–300.
- [116] T. Morris and S. Mohammed, "Characterising glaucoma using texture," in *Proceedings of the 19th Conference on Medical Image Understanding and Analysis*. University of Lincoln, 2015, pp. 54–59.
- [117] Y. Bengio, I. Goodfellow, and A. Courville, *Deep learning*. MIT press Massachusetts, USA:, 2015, vol. 1.
- [118] U. Schmidt-Erfurth, A. Sadeghipour, B. S. Gerendas, S. M. Waldstein, and H. Bogunović, "Artificial intelligence in retina," *Progress in retinal and eye research*, vol. 67, pp. 1–29, 2018.
- [119] A. Krizhevsky, I. Sutskever, and G. E. Hinton, "Imagenet classification with deep convolutional neural networks," in *Advances in neural information processing systems*, 2012, pp. 1097–1105.
- [120] L. Liu, W. Ouyang, X. Wang, P. Fieguth, J. Chen, X. Liu, and M. Pietikäinen, "Deep learning for generic object detection: A survey," *International journal of computer vision*, vol. 128, no. 2, pp. 261–318, 2020.
- [121] M. D. Zeiler and R. Fergus, "Visualizing and understanding convolutional networks," in *European conference on computer vision*. Springer, 2014, pp. 818–833.

- [122] Y. Bengio, A. Courville, and P. Vincent, “Representation learning: A review and new perspectives,” *IEEE transactions on pattern analysis and machine intelligence*, vol. 35, no. 8, pp. 1798–1828, 2013.
- [123] K. Chatfield, K. Simonyan, A. Vedaldi, and A. Zisserman, “Return of the devil in the details: Delving deep into convolutional nets,” *arXiv preprint arXiv:1405.3531*, 2014.
- [124] J. Gu, Z. Wang, J. Kuen, L. Ma, A. Shahroudy, B. Shuai, T. Liu, X. Wang, G. Wang, J. Cai *et al.*, “Recent advances in convolutional neural networks,” *Pattern Recognition*, vol. 77, pp. 354–377, 2018.
- [125] Y. LeCun, Y. Bengio, and G. Hinton, “Deep learning,” *nature*, vol. 521, no. 7553, pp. 436–444, 2015.
- [126] P. Sermanet, D. Eigen, X. Zhang, M. Mathieu, R. Fergus, and Y. LeCun, “Overfeat: Integrated recognition, localization and detection using convolutional networks,” *arXiv preprint arXiv:1312.6229*, 2013.
- [127] J. Donahue, Y. Jia, O. Vinyals, J. Hoffman, N. Zhang, E. Tzeng, and T. Darrell, “Decaf: A deep convolutional activation feature for generic visual recognition,” in *International conference on machine learning*, 2014, pp. 647–655.
- [128] J. Yosinski, J. Clune, Y. Bengio, and H. Lipson, “How transferable are features in deep neural networks?” in *Advances in neural information processing systems*, 2014, pp. 3320–3328.
- [129] L. Torrey and J. Shavlik, “Transfer learning,” in *Handbook of research on machine learning applications and trends: algorithms, methods, and techniques*. IGI global, 2010, pp. 242–264.
- [130] M. Kuhn, K. Johnson *et al.*, *Applied predictive modeling*. Springer, 2013, vol. 26.
- [131] V. N. Vapnik, *The nature of statistical learning theory*. New York: Springer, 2013.
- [132] V. Vapnik and A. Lerner, “Pattern recognition using generalized portrait method,” *Automation and remote control*, vol. 24, pp. 774–780, 1963.

- [133] C. J. Burges, "A tutorial on support vector machines for pattern recognition," *Data mining and knowledge discovery*, vol. 2, no. 2, pp. 121–167, 1998.
- [134] C. Cortes and V. Vapnik, "Support-vector networks," *Machine learning*, vol. 20, no. 3, pp. 273–297, 1995.
- [135] J. Cervantes, F. Garcia-Lamont, L. Rodríguez-Mazahua, and A. Lopez, "A comprehensive survey on support vector machine classification: Applications, challenges and trends," *Neurocomputing*, vol. 408, pp. 189–215, 2020.
- [136] B. E. Boser, I. M. Guyon, and V. N. Vapnik, "A training algorithm for optimal margin classifiers," in *Proceedings of the fifth annual workshop on Computational learning theory*, 1992, pp. 144–152.
- [137] W. S. Noble, "What is a support vector machine?" *Nature biotechnology*, vol. 24, no. 12, pp. 1565–1567, 2006.
- [138] N. Japkowicz and S. Stephen, "The class imbalance problem: A systematic study," *Intelligent data analysis*, vol. 6, no. 5, pp. 429–449, 2002.
- [139] Y. Sun, A. K. Wong, and M. S. Kamel, "Classification of imbalanced data: A review," *International journal of pattern recognition and artificial intelligence*, vol. 23, no. 04, pp. 687–719, 2009.
- [140] E. Fix and J. Hodges, "Discriminatory analysis, nonparametric discrimination: consistency properties," CALIFORNIA UNIV BERKELEY, Tech. Rep., 1951.
- [141] T. Denoeux, "A k-nearest neighbor classification rule based on dempster-shafer theory," in *Classic works of the Dempster-Shafer theory of belief functions*. Springer, 2008, pp. 737–760.
- [142] T. Cover and P. Hart, "Nearest neighbor pattern classification," *IEEE transactions on information theory*, vol. 13, no. 1, pp. 21–27, 1967.
- [143] P. Cunningham and S. J. Delany, "k-nearest neighbour classifiers–," *arXiv preprint arXiv:2004.04523*, 2020.
- [144] S. Shan, W. Zhang, Y. Su, X. Chen, and W. Gao, "Ensemble of piecewise fda based on spatial histograms of local (gabor) binary patterns for face recognition," in *18th International Conference on Pattern Recognition (ICPR'06)*, vol. 4. IEEE, 2006, pp. 606–609.

- [145] N. I. Radwan, N. M. Salem, and M. I. El Adawy, "Histogram correlation for video scene change detection," in *Advances in computer science, engineering & applications*. Springer, 2012, pp. 765–773.
- [146] J. Puzicha, T. Hofmann, and J. M. Buhmann, "Non-parametric similarity measures for unsupervised texture segmentation and image retrieval," in *Proceedings of IEEE Computer Society Conference on Computer Vision and Pattern Recognition*. IEEE, 1997, pp. 267–272.
- [147] M. J. Swain and D. H. Ballard, "Color indexing," *International Journal of Computer Vision*, vol. 7, no. 1, pp. 11–32, Nov 1991. [Online]. Available: <https://doi.org/10.1007/BF00130487>
- [148] P. Cunningham, "Dimension reduction," in *Machine learning techniques for multimedia*. Springer, 2008, pp. 91–112.
- [149] C. C. Reyes-Aldasoro and A. Bhalerao, "The bhattacharyya space for feature selection and its application to texture segmentation," *Pattern Recognition*, vol. 39, no. 5, pp. 812–826, 2006.
- [150] H. Abdi and L. J. Williams, "Principal component analysis," *Wiley interdisciplinary reviews: computational statistics*, vol. 2, no. 4, pp. 433–459, 2010.
- [151] K. Pearson, "Liii. on lines and planes of closest fit to systems of points in space," *The London, Edinburgh, and Dublin Philosophical Magazine and Journal of Science*, vol. 2, no. 11, pp. 559–572, 1901.
- [152] A.-L. Cauchy, "Sur l'équation à l'aide de laquelle on détermine les inégalités séculaires des mouvements des planetes," *Exer. de math*, vol. 4, no. 1829, pp. 174–195, 1829.
- [153] C. Jordan, "Mémoire sur les formes bilinéaires." *Journal de mathématiques pures et appliquées*, vol. 19, pp. 35–54, 1874.
- [154] C. B. Boyer and U. C. Merzbach, "A history of mathematics," 1989.
- [155] I. Grattan-Guinness, *The Rainbow of Mathematics*. WW Norton & Company, 1997.
- [156] G. W. Stewart, "On the early history of the singular value decomposition," *SIAM review*, vol. 35, no. 4, pp. 551–566, 1993.

- [157] H. Hotelling, "Analysis of a complex of statistical variables into principal components." *Journal of educational psychology*, vol. 24, no. 6, p. 417–441, 1933.
- [158] A. Albarrak, F. Coenen, Y. Zheng *et al.*, "Age-related macular degeneration identification in volumetric optical coherence tomography using decomposition and local feature extraction," in *Proceedings of 2013 international conference on medical image, understanding and analysis*, 2013, pp. 59–64.
- [159] Y.-Y. Liu, M. Chen, H. Ishikawa, G. Wollstein, J. S. Schuman, and J. M. Rehg, "Automated macular pathology diagnosis in retinal oct images using multi-scale spatial pyramid and local binary patterns in texture and shape encoding," *Medical image analysis*, vol. 15, no. 5, pp. 748–759, 2011.
- [160] Y.-Y. Liu, M. Chen, H. Ishikawa, G. Wollstein, J. S. Schuman, and J. M. Rehg, "Automated macular pathology diagnosis in retinal oct images using multi-scale spatial pyramid with local binary patterns," in *International Conference on Medical Image Computing and Computer-Assisted Intervention*. Springer, 2010, pp. 1–9.
- [161] T. F. Cootes, C. J. Taylor *et al.*, "Statistical models of appearance for computer vision," 2004.
- [162] J. Reunanen, "Overfitting in making comparisons between variable selection methods," *Journal of Machine Learning Research*, vol. 3, no. Mar, pp. 1371–1382, 2003.
- [163] R. Kohavi, G. H. John *et al.*, "Wrappers for feature subset selection," *Artificial intelligence*, vol. 97, no. 1-2, pp. 273–324, 1997.
- [164] L. Burrell, O. Smart, G. K. Georgoulas, E. D. Marsh, and G. J. Vachtsevanos, "Evaluation of feature selection techniques for analysis of functional mri and eeg," in *DMIN*, 2007, pp. 256–262.
- [165] T. Ojala and M. Pietikäinen, "Texture classification," 2001, http://homepages.inf.ed.ac.uk/rbf/CVonline/LOCAL_COPIES/OJALA1/texclas.htm, Accessed: 01-Jan-2019.
- [166] R. W. Connors and C. A. Harlow, "A theoretical comparison of texture algorithms," *IEEE transactions on pattern analysis and machine intelligence*, no. 3, pp. 204–222, 1980.

- [167] J. H. du Buf, M. Kardan, and M. Spann, “Texture feature performance for image segmentation,” *Pattern recognition*, vol. 23, no. 3-4, pp. 291–309, 1990.
- [168] L. Liu, P. Fieguth, Y. Guo, X. Wang, and M. Pietikäinen, “Local binary features for texture classification: Taxonomy and experimental study,” *Pattern Recognition*, vol. 62, pp. 135–160, 2017.
- [169] C. Ferri, J. Hernández-Orallo, and R. Modroiu, “An experimental comparison of performance measures for classification,” *Pattern Recognition Letters*, vol. 30, no. 1, pp. 27–38, 2009.
- [170] H. He and Y. Ma, *Imbalanced learning: foundations, algorithms, and applications*. John Wiley & Sons, 2013.
- [171] P. Branco, L. Torgo, and R. Ribeiro, “A survey of predictive modelling under imbalanced distributions,” *arXiv preprint arXiv:1505.01658*, 2015.
- [172] R. Kohavi *et al.*, “A study of cross-validation and bootstrap for accuracy estimation and model selection,” in *Ijcai*, vol. 14, no. 2. Montreal, Canada, 1995, pp. 1137–1145.
- [173] G. James, D. Witten, T. Hastie, and R. Tibshirani, *An introduction to statistical learning*. Springer, 2013, vol. 112.
- [174] A. M. Molinaro, R. Simon, and R. M. Pfeiffer, “Prediction error estimation: a comparison of resampling methods,” *Bioinformatics*, vol. 21, no. 15, pp. 3301–3307, 2005.
- [175] J.-H. Kim, “Estimating classification error rate: Repeated cross-validation, repeated hold-out and bootstrap,” *Computational statistics & data analysis*, vol. 53, no. 11, pp. 3735–3745, 2009.
- [176] C. Haupt, A. B. Huber *et al.*, “How axons see their way—axonal guidance in the visual system,” *Front Biosci*, vol. 13, pp. 3136–3149, 2008.
- [177] R. Jerath, M. W. Crawford, and V. A. Barnes, “Functional representation of vision within the mind: A visual consciousness model based in 3d default space,” *Journal of Medical Hypotheses and Ideas*, vol. 9, no. 1, pp. 45–56, 2015.

- [178] H. Kolb, “Gross anatomy of the eye,” in *Webvision: The Organization of the Retina and Visual System [Internet]*. University of Utah Health Sciences Center, 2007.
- [179] G. D. Hildebrand and A. R. Fielder, “Anatomy and physiology of the retina,” in *Pediatric retina*. Springer, 2011, pp. 39–65.
- [180] M. D. Abràmoff, M. K. Garvin, and M. Sonka, “Retinal imaging and image analysis,” *IEEE reviews in biomedical engineering*, vol. 3, pp. 169–208, 2010.
- [181] L. A. Remington, *Clinical anatomy and physiology of the visual system*, 3rd ed. St. Louis: Elsevier/Butterworth-Heinemann, 2012.
- [182] C. Cavallotti and L. Cerulli, *Age-related changes of the human eye*. Springer Science & Business Media, 2008.
- [183] A. Cerulli, F. Regine, and G. Carella, “The aging of the choroid,” in *Age-Related Changes of the Human Eye*. Springer, 2008, pp. 217–238.
- [184] K. L. Pennington and M. M. DeAngelis, “Epidemiology of age-related macular degeneration (amd): associations with cardiovascular disease phenotypes and lipid factors,” *Eye and vision*, vol. 3, no. 1, pp. 1–20, 2016.
- [185] W. L. Wong, X. Su, X. Li, C. M. G. Cheung, R. Klein, C.-Y. Cheng, and T. Y. Wong, “Global prevalence of age-related macular degeneration and disease burden projection for 2020 and 2040: a systematic review and meta-analysis,” *The Lancet Global Health*, vol. 2, no. 2, pp. e106–e116, 2014.
- [186] J. Chen, K. M. Connor, L. E. Smith *et al.*, “Overstaying their welcome: defective cx3cr1 microglia eyed in macular degeneration,” *The Journal of clinical investigation*, vol. 117, no. 10, pp. 2758–2762, 2007.
- [187] A. Kassoff, J. Kassoff, J. Buehler, M. Eglow, F. Kaufman, M. Mehu, S. Kieval, M. Mairs, B. Graig, A. Quattrocchi *et al.*, “A randomized, placebo-controlled, clinical trial of high-dose supplementation with vitamins c and e, beta carotene, and zinc for age-related macular degeneration and vision loss: Areds report no. 8,” *Archives of Ophthalmology*, vol. 119, no. 10, pp. 1417–1436, 2001.
- [188] P. Karavitis, N. Pescosolido, and F. Pacella, “Many suggestions to protect the eyes in aging people,” in *Age-Related Changes of the Human Eye*. Springer, 2008, pp. 393–397.

- [189] I. D. Federation, "Idf diabetes atlas, 10th edn," Brussels, Belgium: 2021, <https://diabetesatlas.org>, Accessed: 17-Nov-2022.
- [190] D. C. KLONOFF and D. M. SCHWARTZ, "An economic analysis of interventions for diabetes," *DIABETES CARE*, vol. 23, no. 3, p. 391, 2000.
- [191] N. G. Congdon, D. S. Friedman, and T. Lietman, "Important causes of visual impairment in the world today," *Journal of the American Medical Association*, vol. 290, no. 15, pp. 2057–2060, 2003.
- [192] N. HR *et al.*, "A method of photographing fluorescence in circulating blood of the human eye." *Technical documentary report. SAM-TDR. USAF School of Aerospace Medicine*, vol. 60, pp. 1–4, 1960.
- [193] H. R. Novotny and D. L. Alvis, "A method of photographing fluorescence in circulating blood in the human retina," *Circulation*, vol. 24, no. 1, pp. 82–86, 1961.
- [194] K. Kogure and E. Choromokos, "Infrared absorption angiography." *Journal of applied physiology*, vol. 26, no. 1, pp. 154–157, 1969.
- [195] L. A. Yannuzzi, J. S. Slakter, J. A. Sorenson, D. R. Guyer, and D. A. Orlock, "Digital indocyanine green videoangiography and choroidal neovascularization." *Retina (Philadelphia, Pa.)*, vol. 12, no. 3, pp. 191–223, 1992.
- [196] G. Staurenghi, F. Bottoni, and A. Giani, "Clinical applications of diagnostic indocyanine green angiography," *Retina. London: Elsevier Saunders*, pp. 51–81, 2013.
- [197] D. Matsunaga, J. Yi, C. A. Puliafito, and A. H. Kashani, "Oct angiography in healthy human subjects," *Ophthalmic Surgery, Lasers and Imaging Retina*, vol. 45, no. 6, pp. 510–515, 2014.
- [198] R. F. Spaide, J. M. Klancnik, and M. J. Cooney, "Retinal vascular layers imaged by fluorescein angiography and optical coherence tomography angiography," *JAMA ophthalmology*, vol. 133, no. 1, pp. 45–50, 2015.
- [199] R. N. Johnson, A. D. Fu, H. R. McDonald, J. M. Jumper, E. Ai, E. T. Cunningham, and B. J. Lujan, "Fluorescein angiography: basic principles and interpretation," in *Retina Fifth Edition*. Elsevier Inc., 2012, pp. 2–50.

- [200] K. A. Kwiterovich, M. G. Maguire, R. P. Murphy, A. P. Schachat, N. M. Bressler, S. B. Bressler, and S. L. Fine, "Frequency of adverse systemic reactions after fluorescein angiography: results of a prospective study," *Ophthalmology*, vol. 98, no. 7, pp. 1139–1142, 1991.
- [201] M. Lopez-Saez, E. Ordoqui, P. Tornero, A. Baeza, T. Sainza, e. J. Zubeldia, M. Baeza, and M. L. Baeza, "Fluorescein-induced allergic reaction," *Annals of Allergy, Asthma & Immunology*, vol. 81, no. 5, pp. 428–430, 1998.
- [202] R. F. Spaide, J. G. Fujimoto, N. K. Waheed, S. R. Sadda, and G. Staurenghi, "Optical coherence tomography angiography," *Progress in retinal and eye research*, vol. 64, pp. 1–55, 2018.
- [203] D. Huang, E. A. Swanson, C. P. Lin, J. S. Schuman, W. G. Stinson, W. Chang, M. R. Hee, T. Flotte, K. Gregory, C. A. Puliafito *et al.*, "Optical coherence tomography," *science*, vol. 254, no. 5035, pp. 1178–1181, 1991.
- [204] J. Schottenhamml, E. M. Moul, S. Ploner, B. Lee, E. A. Novais, E. Cole, S. Dang, C. D. Lu, L. Husvogt, N. K. Waheed *et al.*, "An automatic, inter-capillary area based algorithm for quantifying diabetes related capillary dropout using oct angiography," *Retina (Philadelphia, Pa.)*, vol. 36, no. Suppl 1, p. S93, 2016.
- [205] J. G. Fujimoto, C. Pitris, S. A. Boppart, and M. E. Brezinski, "Optical coherence tomography: an emerging technology for biomedical imaging and optical biopsy," *Neoplasia*, vol. 2, no. 1-2, pp. 9–25, 2000.
- [206] J. A. Izatt, M. R. Hee, E. A. Swanson, C. P. Lin, D. Huang, J. S. Schuman, C. A. Puliafito, and J. G. Fujimoto, "Micrometer-scale resolution imaging of the anterior eye in vivo with optical coherence tomography," *Archives of ophthalmology*, vol. 112, no. 12, pp. 1584–1589, 1994.
- [207] M. R. Hee, J. A. Izatt, E. A. Swanson, D. Huang, J. S. Schuman, C. P. Lin, C. A. Puliafito, and J. G. Fujimoto, "Optical coherence tomography of the human retina," *Archives of ophthalmology*, vol. 113, no. 3, pp. 325–332, 1995.
- [208] C. A. Puliafito, M. R. Hee, C. P. Lin, E. Reichel, J. S. Schuman, J. S. Duker, J. A. Izatt, E. A. Swanson, and J. G. Fujimoto, "Imaging of macular diseases with optical coherence tomography," *Ophthalmology*, vol. 102, no. 2, pp. 217–229, 1995.

- [209] M. R. Hee, C. R. Bauman, C. A. Puliafito, J. S. Duker, E. Reichel, J. R. Wilkins, J. G. Coker, J. S. Schuman, E. A. Swanson, and J. G. Fujimoto, "Optical coherence tomography of age-related macular degeneration and choroidal neovascularization," *Ophthalmology*, vol. 103, no. 8, pp. 1260–1270, 1996.
- [210] M. R. Hee, C. A. Puliafito, C. Wong, J. S. Duker, E. Reichel, B. Rutledge, J. S. Schuman, E. A. Swanson, and J. G. Fujimoto, "Quantitative assessment of macular edema with optical coherence tomography," *Archives of ophthalmology*, vol. 113, no. 8, pp. 1019–1029, 1995.
- [211] J. Fingler, D. Schwartz, C. Yang, and S. E. Fraser, "Mobility and transverse flow visualization using phase variance contrast with spectral domain optical coherence tomography," *Optics express*, vol. 15, no. 20, pp. 12 636–12 653, 2007.
- [212] J. Fingler, C. Readhead, D. M. Schwartz, and S. E. Fraser, "Phase-contrast oct imaging of transverse flows in the mouse retina and choroid," *Investigative ophthalmology & visual science*, vol. 49, no. 11, pp. 5055–5059, 2008.
- [213] A. Mariampillai, B. A. Standish, E. H. Moriyama, M. Khurana, N. R. Munce, M. K. Leung, J. Jiang, A. Cable, B. C. Wilson, I. A. Vitkin *et al.*, "Speckle variance detection of microvasculature using swept-source optical coherence tomography," *Optics letters*, vol. 33, no. 13, pp. 1530–1532, 2008.
- [214] L. Yu and Z. Chen, "Doppler variance imaging for three-dimensional retina and choroid angiography," *Journal of Biomedical Optics*, vol. 15, no. 1, p. 016029, 2010.
- [215] A. Mariampillai, M. K. Leung, M. Jarvi, B. A. Standish, K. Lee, B. C. Wilson, A. Vitkin, and V. X. Yang, "Optimized speckle variance oct imaging of microvasculature," *Optics letters*, vol. 35, no. 8, pp. 1257–1259, 2010.
- [216] D. Y. Kim, J. Fingler, J. S. Werner, D. M. Schwartz, S. E. Fraser, and R. J. Zawadzki, "In vivo volumetric imaging of human retinal circulation with phase-variance optical coherence tomography," *Biomedical Optics Express*, vol. 2, no. 6, pp. 1504–1513, 2011.
- [217] L. An, T. Shen, and R. K. Wang, "Using ultrahigh sensitive optical microangiography to achieve comprehensive depth resolved microvasculature mapping for human retina," *Journal of Biomedical Optics*, vol. 16, no. 10, p. 106013, 2011.

- [218] G. Liu, W. Qi, L. Yu, and Z. Chen, “Real-time bulk-motion-correction free doppler variance optical coherence tomography for choroidal capillary vasculature imaging,” *Optics express*, vol. 19, no. 4, pp. 3657–3666, 2011.
- [219] Y. Jia, O. Tan, J. Tokayer, B. Potsaid, Y. Wang, J. J. Liu, M. F. Kraus, H. Subhash, J. G. Fujimoto, J. Hornegger *et al.*, “Split-spectrum amplitude-decorrelation angiography with optical coherence tomography,” *Optics express*, vol. 20, no. 4, pp. 4710–4725, 2012.
- [220] L. Conroy, R. S. DaCosta, and I. A. Vitkin, “Quantifying tissue microvasculature with speckle variance optical coherence tomography,” *Optics letters*, vol. 37, no. 15, pp. 3180–3182, 2012.
- [221] M. S. Mahmud, D. W. Cadotte, B. Vuong, C. Sun, T. W. Luk, A. Mariampillai, and V. X. Yang, “Review of speckle and phase variance optical coherence tomography to visualize microvascular networks,” *Journal of Biomedical Optics*, vol. 18, no. 5, p. 050901, 2013.
- [222] R. F. Spaide, J. G. Fujimoto, and N. K. Waheed, “Image artifacts in optical coherence tomography angiography,” *Retina (Philadelphia, Pa.)*, vol. 35, no. 11, p. 2163, 2015.
- [223] G. Coscas, M. Lupidi, F. Coscas, C. Français, C. Cagini, and E. H. Souied, “Optical coherence tomography angiography during follow-up: qualitative and quantitative analysis of mixed type i and ii choroidal neovascularization after vascular endothelial growth factor trap therapy,” *Ophthalmic research*, vol. 54, no. 2, pp. 57–63, 2015.
- [224] L. Kuehlewein, S. Sadda, and D. Sarraf, “Oct angiography and sequential quantitative analysis of type 2 neovascularization after ranibizumab therapy,” *Eye*, vol. 29, no. 7, pp. 932–935, 2015.
- [225] M. Al-Sheikh, N. A. Iafe, N. Phasukkijwatana, S. R. Sadda, and D. Sarraf, “Biomarkers of neovascular activity in age-related macular degeneration using optical coherence tomography angiography,” *Retina*, vol. 38, no. 2, pp. 220–230, 2018.
- [226] N. W. Muakkassa, A. T. Chin, T. De Carlo, K. A. Klein, C. R. Baumal, A. J.

- Witkin, J. S. Duker, and N. K. Waheed, "Characterizing the effect of anti-vascular endothelial growth factor therapy on treatment-naïve choroidal neovascularization using optical coherence tomography angiography," *Retina*, vol. 35, no. 11, pp. 2252–2259, 2015.
- [227] N. V. Palejwala, Y. Jia, S. S. Gao, L. Liu, C. J. Flaxel, T. S. Hwang, A. K. Lauer, D. J. Wilson, D. Huang, and S. T. Bailey, "Detection of non-exudative choroidal neovascularization in age-related macular degeneration with optical coherence tomography angiography," *Retina (Philadelphia, Pa.)*, vol. 35, no. 11, p. 2204, 2015.
- [228] X. Yao, M. N. Alam, D. Le, and D. Toslak, "Quantitative optical coherence tomography angiography: a review," *Experimental Biology and Medicine*, vol. 245, no. 4, pp. 301–312, 2020.
- [229] F. Corvi, M. Pellegrini, S. Erba, M. Cozzi, G. Staurenghi, and A. Giani, "Reproducibility of vessel density, fractal dimension, and foveal avascular zone using 7 different optical coherence tomography angiography devices," *American journal of ophthalmology*, vol. 186, pp. 25–31, 2018.
- [230] J. Yang, M. Yuan, E. Wang, and Y. Chen, "Comparison of the repeatability of macular vascular density measurements using four optical coherence tomography angiography systems," *Journal of ophthalmology*, vol. 2019, 2019.
- [231] A. Uji, S. Balasubramanian, J. Lei, E. Baghdasaryan, M. Al-Sheikh, E. Borrelli, and S. R. Sadda, "Multiple enface image averaging for enhanced optical coherence tomography angiography imaging," *Acta ophthalmologica*, vol. 96, no. 7, pp. e820–e827, 2018.
- [232] G. Litjens, T. Kooi, B. E. Bejnordi, A. A. A. Setio, F. Ciompi, M. Ghafoorian, J. A. Van Der Laak, B. Van Ginneken, and C. I. Sánchez, "A survey on deep learning in medical image analysis," *Medical image analysis*, vol. 42, pp. 60–88, 2017.
- [233] F. Jiang, Y. Jiang, H. Zhi, Y. Dong, H. Li, S. Ma, Y. Wang, Q. Dong, H. Shen, and Y. Wang, "Artificial intelligence in healthcare: past, present and future," *Stroke and vascular neurology*, vol. 2, no. 4, 2017.

- [234] Y. Zheng, M. H. A. Hijazi, and F. Coenen, “Automated “disease/no disease” grading of age-related macular degeneration by an image mining approach,” *Investigative ophthalmology & visual science*, vol. 53, no. 13, pp. 8310–8318, 2012.
- [235] D. S. W. Ting, L. R. Pasquale, L. Peng, J. P. Campbell, A. Y. Lee, R. Raman, G. S. W. Tan, L. Schmetterer, P. A. Keane, and T. Y. Wong, “Artificial intelligence and deep learning in ophthalmology,” *British Journal of Ophthalmology*, vol. 103, no. 2, pp. 167–175, 2019.
- [236] C. S. Lee, D. M. Baughman, and A. Y. Lee, “Deep learning is effective for classifying normal versus age-related macular degeneration oct images,” *Ophthalmology Retina*, vol. 1, no. 4, pp. 322–327, 2017.
- [237] C. S. Lee, A. J. Tying, N. P. Deruyter, Y. Wu, A. Rokem, and A. Y. Lee, “Deep-learning based, automated segmentation of macular edema in optical coherence tomography,” *Biomedical Optics Express*, vol. 8, no. 7, pp. 3440–3448, 2017.
- [238] M. Treder, J. L. Lauermann, and N. Eter, “Automated detection of exudative age-related macular degeneration in spectral domain optical coherence tomography using deep learning,” *Graefe’s Archive for Clinical and Experimental Ophthalmology*, vol. 256, no. 2, pp. 259–265, 2018.
- [239] Y.-Y. Liu, H. Ishikawa, M. Chen, G. Wollstein, J. S. Duker, J. G. Fujimoto, J. S. Schuman, and J. M. Rehg, “Computerized macular pathology diagnosis in spectral domain optical coherence tomography scans based on multiscale texture and shape features,” *Investigative ophthalmology & visual science*, vol. 52, no. 11, pp. 8316–8322, 2011.
- [240] P. P. Srinivasan, L. A. Kim, P. S. Mettu, S. W. Cousins, G. M. Comer, J. A. Izatt, and S. Farsiu, “Fully automated detection of diabetic macular edema and dry age-related macular degeneration from optical coherence tomography images,” *Biomedical Optics Express*, vol. 5, no. 10, pp. 3568–3577, 2014.
- [241] A. García-Floriano, Á. Ferreira-Santiago, O. Camacho-Nieto, and C. Yáñez-Márquez, “A machine learning approach to medical image classification: Detecting age-related macular degeneration in fundus images,” *Computers & Electrical Engineering*, vol. 75, pp. 218–229, 2019.

- [242] P. M. Burlina, N. Joshi, M. Pekala, K. D. Pacheco, D. E. Freund, and N. M. Bressler, “Automated grading of age-related macular degeneration from color fundus images using deep convolutional neural networks,” *JAMA ophthalmology*, vol. 135, no. 11, pp. 1170–1176, 2017.
- [243] Q. Zhang, C.-L. Chen, Z. Chu, F. Zheng, A. Miller, L. Roisman, J. R. de Oliveira Dias, Z. Yehoshua, K. B. Schaal, W. Feuer *et al.*, “Automated quantitation of choroidal neovascularization: a comparison study between spectral-domain and swept-source oct angiograms,” *Investigative ophthalmology & visual science*, vol. 58, no. 3, pp. 1506–1513, 2017.
- [244] K. Taibouni, Y. Chenoune, A. Miere, D. Colantuono, E. Souied, and E. Petit, “Automated quantification of choroidal neovascularization on optical coherence tomography angiography images,” *Computers in biology and medicine*, vol. 114, p. 103450, 2019.
- [245] E. Vaghefi, S. Hill, H. M. Kersten, and D. Squirrell, “Multimodal retinal image analysis via deep learning for the diagnosis of intermediate dry age-related macular degeneration: a feasibility study,” *Journal of ophthalmology*, vol. 2020, 2020.
- [246] J. Wang, T. T. Hormel, L. Gao, P. Zang, Y. Guo, X. Wang, S. T. Bailey, and Y. Jia, “Automated diagnosis and segmentation of choroidal neovascularization in oct angiography using deep learning,” *Biomedical Optics Express*, vol. 11, no. 2, pp. 927–944, 2020.
- [247] T. Ching, D. S. Himmelstein, B. K. Beaulieu-Jones, A. A. Kalinin, B. T. Do, G. P. Way, E. Ferrero, P.-M. Agapow, M. Zietz, M. M. Hoffman *et al.*, “Opportunities and obstacles for deep learning in biology and medicine,” *Journal of The Royal Society Interface*, vol. 15, no. 141, p. 20170387, 2018.
- [248] T. Perepelkina and A. B. Fulton, “Artificial intelligence (ai) applications for age-related macular degeneration (amd) and other retinal dystrophies,” in *Seminars in Ophthalmology*. Taylor & Francis, 2021, pp. 1–6.
- [249] K. Simonyan and A. Zisserman, “Very deep convolutional networks for large-scale image recognition,” *arXiv preprint arXiv:1409.1556*, 2014.

- [250] C. Szegedy, W. Liu, Y. Jia, P. Sermanet, S. Reed, D. Anguelov, D. Erhan, V. Vanhoucke, and A. Rabinovich, "Going deeper with convolutions," in *Proceedings of the IEEE conference on computer vision and pattern recognition*, 2015, pp. 1–9.
- [251] K. He, X. Zhang, S. Ren, and J. Sun, "Deep residual learning for image recognition," in *Proceedings of the IEEE conference on computer vision and pattern recognition*, 2016, pp. 770–778.
- [252] G. Huang, Z. Liu, L. Van Der Maaten, and K. Q. Weinberger, "Densely connected convolutional networks," in *Proceedings of the IEEE conference on computer vision and pattern recognition*, 2017, pp. 4700–4708.
- [253] M. Cimpoi, S. Maji, I. Kokkinos, and A. Vedaldi, "Deep filter banks for texture recognition, description, and segmentation," *International Journal of Computer Vision*, vol. 118, no. 1, pp. 65–94, 2016.
- [254] J. Deng, W. Dong, R. Socher, L.-J. Li, K. Li, and L. Fei-Fei, "Imagenet: A large-scale hierarchical image database," in *2009 IEEE conference on computer vision and pattern recognition*. Ieee, 2009, pp. 248–255.
- [255] M. Cimpoi, S. Maji, and A. Vedaldi, "Deep filter banks for texture recognition and segmentation," in *Proceedings of the IEEE conference on computer vision and pattern recognition*, 2015, pp. 3828–3836.
- [256] M. B. Lee, Y. H. Kim, and K. R. Park, "Conditional generative adversarial network-based data augmentation for enhancement of iris recognition accuracy," *IEEE Access*, vol. 7, pp. 122 134–122 152, 2019.
- [257] G. Wang, W. Kang, Q. Wu, Z. Wang, and J. Gao, "Generative adversarial network (gan) based data augmentation for palmprint recognition," in *2018 Digital Image Computing: Techniques and Applications (DICTA)*. IEEE, 2018, pp. 1–7.
- [258] A. Antoniou, A. Storkey, and H. Edwards, "Data augmentation generative adversarial networks," *arXiv preprint arXiv:1711.04340*, 2017.
- [259] C.-W. Hsu and C.-J. Lin, "A comparison of methods for multiclass support vector machines," *IEEE transactions on Neural Networks*, vol. 13, no. 2, pp. 415–425, 2002.

- [260] K.-B. Duan and S. S. Keerthi, "Which is the best multiclass svm method? an empirical study," in *International workshop on multiple classifier systems*. Springer, 2005, pp. 278–285.
- [261] S. Ramaswamy, P. Tamayo, R. Rifkin, S. Mukherjee, C.-H. Yeang, M. Angelo, C. Ladd, M. Reich, E. Latulippe, J. P. Mesirov *et al.*, "Multiclass cancer diagnosis using tumor gene expression signatures," *Proceedings of the National Academy of Sciences*, vol. 98, no. 26, pp. 15 149–15 154, 2001.
- [262] T. S. Furey, N. Cristianini, N. Duffy, D. W. Bednarski, M. Schummer, and D. Haussler, "Support vector machine classification and validation of cancer tissue samples using microarray expression data," *Bioinformatics*, vol. 16, no. 10, pp. 906–914, 2000.
- [263] Z. Yin and J. Hou, "Recent advances on svm based fault diagnosis and process monitoring in complicated industrial processes," *Neurocomputing*, vol. 174, pp. 643–650, 2016.
- [264] T. E. de Carlo, M. A. Bonini Filho, A. T. Chin, M. Adhi, D. Ferrara, C. R. Bauml, A. J. Witkin, E. Reichel, J. S. Duker, and N. K. Waheed, "Spectral-domain optical coherence tomography angiography of choroidal neovascularization," *Ophthalmology*, vol. 122, no. 6, pp. 1228–1238, 2015. [Online]. Available: <https://www.sciencedirect.com/science/article/pii/S0161642015001037>
- [265] A. H. Kashani, C.-L. Chen, J. K. Gahm, F. Zheng, G. M. Richter, P. J. Rosenfeld, Y. Shi, and R. K. Wang, "Optical coherence tomography angiography: a comprehensive review of current methods and clinical applications," *Progress in retinal and eye research*, vol. 60, pp. 66–100, 2017.
- [266] S. Liakopoulos, S. Ongchin, A. Bansal, S. Msutta, A. C. Walsh, P. G. Updike, and S. R. Sadda, "Quantitative optical coherence tomography findings in various subtypes of neovascular age-related macular degeneration," *Investigative ophthalmology & visual science*, vol. 49, no. 11, pp. 5048–5054, 2008.
- [267] S. R. Sadda, S. Liakopoulos, P. A. Keane, S. C. Ongchin, S. Msutta, K. T. Chang, and A. C. Walsh, "Relationship between angiographic and optical coherence tomographic (oct) parameters for quantifying choroidal neovascular lesions,"

Graefe's Archive for Clinical and Experimental Ophthalmology, vol. 248, no. 2, pp. 175–184, 2010.

- [268] A. Giani, C. Luiselli, D. D. Esmaili, P. Salvetti, M. Cigada, J. W. Miller, and G. Staurenghi, “Spectral-domain optical coherence tomography as an indicator of fluorescein angiography leakage from choroidal neovascularization,” *Investigative ophthalmology & visual science*, vol. 52, no. 8, pp. 5579–5586, 2011.
- [269] N. K. Waheed, T. De Carlo, A. Chin, and J. Duker, “Oct angiography in retinal diagnosis and treatment,” *Retinal Phys*, vol. 12, pp. 26–42, 2015.
- [270] A. C. Tan, G. S. Tan, A. K. Denniston, P. A. Keane, M. Ang, D. Milea, U. Chakravarthy, and C. M. G. Cheung, “An overview of the clinical applications of optical coherence tomography angiography,” *Eye*, vol. 32, no. 2, pp. 262–286, 2018.

Appendix A

Supplementary details for Chapter 2

A.1 Learned Category

Among the most widely utilised texture representation techniques that fall under the learned category are the CNN algorithms. The key building parts of CNN algorithms are the convolutional layers. The term “convolutional” in CNN algorithms suggests the use of a mathematical operation conventionally named convolution in the convolutional layers. The convolution operation is a specialised kind of linear transformation or operation and can therefore be explained as a matrix multiplication [117]. For instance, in the case of two dimensional image data, the matrix multiplication is typically performed between two dimensional arrays of weights or values normally named kernels or filters, and kernels sized by input data values usually referred to as patches or receptive fields. Figure A.1 shows an example of a convolution operation applied to a two dimensional input data.

A typical structure of a convolutional layer repeatedly employs three different types of operations, namely convolution, nonlinearity, and pooling functions [32, 117]. Figure A.2 presents the order of these typical components of operations in the convolutional layers of CNN algorithms. The first component is the convolution operation that involves using a number of kernels or filters [32, 117]. The values of these kernels are typically initialised with a random set of weights. The key innovation behind employing the convolution operation in CNN algorithms is that the kernel values or weights are learned instead of being manually specified or changed during training the CNN algorithm. These kernels are applied to every single overlapping area as described earlier in Figure A.1. Every single kernel is convolved and moved across the whole input data from top-left to bottom-right, hence allowing it to learn and discover certain types

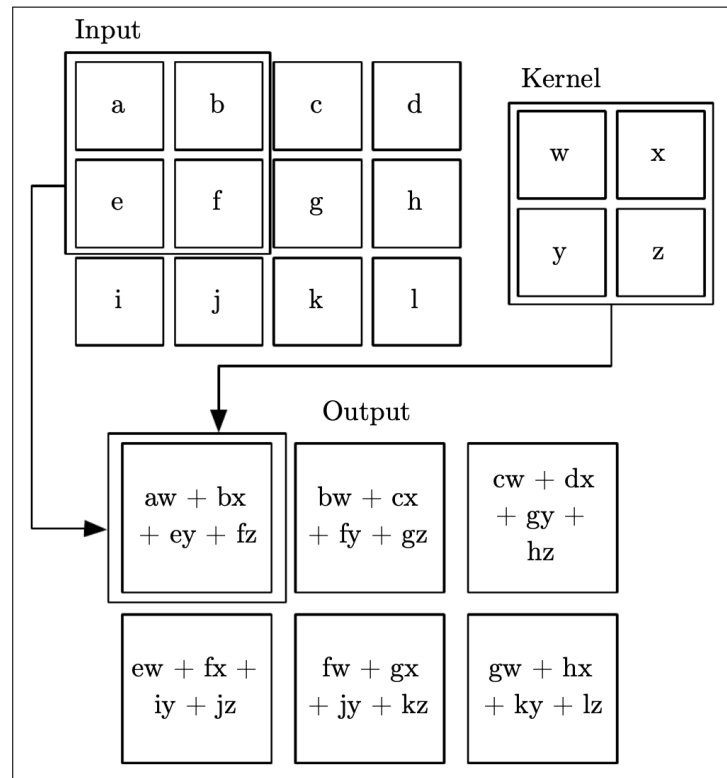


Figure A.1: An example of convolution operation applied to a two dimensional input data [117]. The convolution operation is applied systematically to every overlapping area in the input data specifically between a single kernel and multiple kernel sized patches of the input data. The output from convolving the kernel with the kernel sized patch of the input data values produces a single value. As the kernel moves across the input data and is multiplied with every kernel sized patch of the input data, this produces a two dimensional matrix representing the output values of the application of the convolution operation. The resulting two dimensional matrix represents a filtered version of the original input data. The arrows and boxes in the figure demonstrate how the upper left area (kernel sized patch) of the input data is convolved with the kernel and the resulting value is stored in the upper left of the output two dimensional matrix, which is a filtered version of the original input data (the convolution operation output matrix).

of features no matter where they are located.

The second operation involves the application of a nonlinear transfer or activation function, such as sigmoid or ReLU [32, 117]. The typical default choice of the activation function in CNN algorithms is the ReLU function [119]. This is because it gives the CNN algorithms the opportunity to learn more complex relationships and structures from the input data and also allows them to train much faster compared to using other activation functions such as the tanh activation function as demonstrated in [119]. The ReLU function is a simple mapping of the convolution operation output

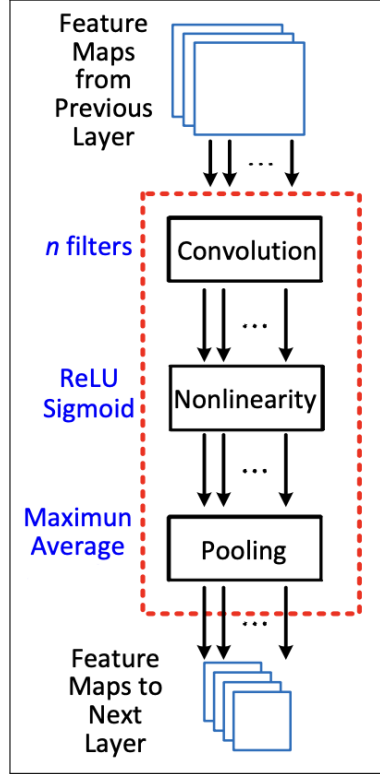


Figure A.2: Typical components of the convolutional layer in CNN algorithms [32]. The convolutional layer comprises three main operations, namely convolution, nonlinearity and pooling. When processing image data using a CNN algorithm, the input data to the deep convolutional layers are the feature maps produced from previous convolutional layers, however, the first convolutional layer takes pixel values as input.

matrix. For instance, it returns the value of 0 if the convolution operation output value is 0 or less, otherwise it returns the same convolution operation output value.

The third operation includes the utilisation of a local pooling or downsampling operation, such as maximum or average pooling operations [32, 117]. The pooling operation helps to make the representations of the convolution operation output almost invariant and more stable against minor translations of the input data [117]. This is typically accomplished by dragging a rectangular window much like a filter or a kernel of a size for instance 2×2 pixels and a stride length of two pixels, i.e.: two steps of pixels between rectangular windows, over the convolution operation output matrix after applying the ReLU function. For instance, in a case of using the maximum pooling operation, the process involves reporting the maximum value within a rectangular window of neighbouring values. A further key benefit of using the pooling operation is that it decreases the convolution operation output matrix size by a factor of 2 due to the stride length of 2 pixels [117]. Consequently, this reduces the computational

complexity and statistical burden on the subsequent convolution layers.

The final output of every convolution layer is a set of compact feature maps that summarise the presence of the features detected in the input data by the various previous operations in the convolution layer. These compact feature maps will be the input for the subsequent convolution layers in a CNN algorithm that has multiple convolution layers. The previously mentioned three components of operations in the convolutional layer are quite relevant to conventional signal processing methods commonly used in image texture analysis and representations [32,74]. However, the major differences between them are that the kernels or filters in the convolution operations step are learned directly from the input data instead of hand-engineered. Hence, this technique is very powerful since every single filter or kernel has the opportunity to learn a certain type of feature that can be most useful or relevant to the specific task being solved, for instance object recognition.

Since the CNN algorithms typically comprise a set of filters learned automatically in their convolution layers, various sets of feature maps are produced and passed to several subsequent convolution layers that are stacked up on top of each other. This stacking procedure of the convolutional layers in CNN algorithms is also a powerful technique. This is because it allows a hierarchical learning of the input data. This means early convolution layers can discover low level features such as lines, edges and bright or dark spots while deep convolution layers can discover increasingly high level and more sophisticated features, such as entire objects or shapes that clearly resemble cars, faces, cats, etc. that relate to the specific training data set under the constraints of the particular task being dealt with, for example, object segmentation or classification.

Depending upon the task to be accomplished, the learning in CNN algorithms can also be achieved in an end-to-end manner [32]. This means it is possible to use a CNN algorithm to represent textured images and to make predictions of target classes in solving an image classification task, for instance. This is typically achieved by reshaping or vectorising the output of the last convolutional layer into a single feature vector and feeding this vector into a fully connected layer (FC) or a stack of two or more deep FC layers. The outputs of FC layers are then passed to a sigmoid or a SoftMax activation function layer for end-to-end learning, hence generating the probabilities of target classes directly. Figure A.3 shows a typical structure of CNN algorithm that can be used to perform an end-to-end learning path for such a computer vision task for example image classification.

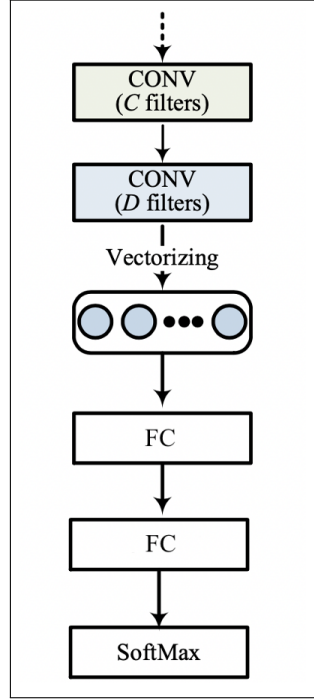


Figure A.3: A typical structure of CNN algorithm for an end-to-end learning task [32]. The top layers are the convolution layers (CONV). The output of the last CONV layer which is a set of compact feature maps are flattened out or vectorised into a single feature vector. This feature vector is then fed into a stack of two fully connected layers (FC layers). Finally, the outputs of FC layers are then passed to the final layer of CNN algorithm. This final layer employs a nonlinear transfer or activation function, such as a SoftMax in this example, in turn, to generate probabilities of target class predictions.

Following the major discovery point in 2012 of the special type of CNN algorithm developed by Krizhevsky et al. [119] commonly referred to as AlexNet that achieved remarkable image classification results, a huge number of various architectures of CNN algorithms that are generally much deeper and more complex have been developed to solve several image texture analysis tasks such as classification and localisation in recent years [32]. Examples of notable CNN algorithms proposed after AlexNet include VGGNet by Simonyan and Zisserman [249], GoogLeNet by Szegedy et al. [250], ResNet by He et al. [251], DenseNet by Huang et al. [252] and many more [32].

A fundamental aspect of the success of CNN algorithms in the context of texture representation is their extensive capability and power to utilise and leverage very large annotated and labelled texture data sets to automatically learn and discover very specific and high quality texture features that are very useful for solving highly challenging computer vision tasks, either texture classification or segmentation [32, 253].

Further aspects of the feasibility of CNN algorithms also include the abundance of public image texture repositories including ImageNet [254], which comprises of more than 15 million labelled images that belong to approximately 22,000 categories [119, 249]. Furthermore, the availability of special types and advanced computing technologies, namely graphics processing units (GPUs) that dramatically accelerate and incorporate a remarkable amount of computational capability, hence providing high-performance computing systems and facilitating the application of deep learning technologies [249].

In practice, training a CNN algorithm involves estimating a huge number of parameters i.e.: texture representations learned across all intermediate layers, typically in the range of millions [32]. Furthermore, it requires very large labelled or annotated data sets that are preferably closely relevant to the application domain. This is because training a CNN algorithm on a small size data set that is smaller than the number of parameters often results in overfitting [128]. Therefore, this can greatly affect the generalisation performance of the CNN algorithm to new, previously unseen data. Subsequently, this also can be a major barrier which rather limits the applicability of CNN algorithms in solving various specific domain problems for several reasons. For instance, this may especially occur when collecting a large enough data set is extremely expensive or only a limited amount of labelled or annotated data sets that represent a specific domain can be made available, e.g.: medical images.

Nevertheless, there are a number of major discoveries for such excellent techniques that can be used to mitigate the matter of inadequate data set size when utilising CNN algorithms. Among the most notable ones usually applied to texture image data sets include employing image data augmentation and transfer learning techniques [119, 128, 255]. The image data augmentation techniques are typically achieved by utilising a range of different types of operations that perform arbitrary transformations of texture images to artificially increase the image data set size. Examples of various types of operations usually applied include randomly changing the orientations of images, reflecting or flipping images horizontally and vertically, horizontal and vertical shift of images, applying random noise to images, randomly changing the brightness of images, arbitrary zooming in and out and random cropping of images [119, 256–258].

The transfer learning techniques, on the other hand, are generally accomplished by first training a base CNN algorithm on a base task using a base large data set [128]. Afterwards, the learned features in the pre-trained base CNN algorithm are repurposed, i.e.: transferred to another, new CNN algorithm that is to be trained towards a new task

using a new data set. This procedure tends generally to be successful if the representations or features learned are fairly universal features meaning that both data sets, the base and the new, share or exhibit certain patterns or features in common. This means that the learned features captured by the pre-trained base CNN algorithm are general or generic features that are applicable to details such as edges, curves, contours, extend lines and so on, in the sense that they may be relevant or appropriate to both the base and new tasks, instead of only being very specific towards a single task.

Consequently, the transfer learning techniques can be considered as powerful tools to allow using a large pre-trained base CNN algorithm for a new task using a new data set that is significantly smaller than the base data set without even being concerned about the risk of overfitting [128]. Several studies have taken advantage of transfer learning techniques to achieve a state-of-the-art performance when transferring from early layers as evidenced by [121, 126, 127], together demonstrating that the early layers of CNN algorithms do indeed capture features that are fairly universal while later layers capture features that are more specific to the original task and data set.

A common procedure in the transfer learning techniques is to copy the first n layers of the pre-trained base CNN algorithm to the first n layers of the new CNN algorithm that are to be used for a new task using a new data set [128]. This is because as mentioned earlier the early or first n layers typically learn features that are not specific to a certain task or data set, but instead they learn universal features that can be applicable to different tasks and data sets. However, the features learned of the pre-trained base CNN algorithm must ultimately shift from being general in the early layers to being increasingly domain specific in the last layers. Hence, the last layers of new CNN algorithm are initialised randomly and trained toward the new data set and task.

Broadly, there are two major common techniques that are normally employed in the transfer learning [32, 128]. The first technique is to transfer or copy certain early layers of a pre-trained CNN algorithm into a new CNN algorithm that will operate as a feature extraction method for the new task of interest. In this technique, the transferred or copied layers are typically left frozen or fixed. This means that the copied layers remain unchanged or altered during training of the new CNN algorithm on the new task and new data set. The later technique, on the other hand, is to perform finetuning or retraining of the transferred layers in the new CNN algorithm on the new task and new data set.

The choice of whether to leave the transferred layers of the new CNN algorithm

unchanged or to finetune them on the new task of interest depends on several factors [128]. Firstly, the size of the new data set and secondly, the number of parameters in the layers that will be transferred [32, 128]. When the size of the new data set is smaller than the number of parameters, finetuning usually results in overfitting. Hence, in the case of a situation like this, the transferred layers are often unaltered due to overfitting concerns. However, if the number of parameters is smaller than the size of the new data set in the sense that the new data set is large enough and overfitting is not an issue, the transferred layers can be finetuned on the new data set for the new task to improve generalisation performance. Indeed, when the size of new data set is extremely large, the utilisation of the transfer learning technique may be unnecessary. This is because the generic features learned in early layers can be simply learned from scratch on the new large data set.

Besides the ability of transfer learning techniques to address the matter of insufficient of data by leveraging previous knowledge learned from the base data set and task at the expense of improving the learning in the new data set and task, there are a further three potential benefits by which the transfer learning techniques might also provide improvements [129]. Firstly, they can help to boost the initial performance in the new task by using the transferred knowledge, hence providing a higher initial start skill. Experiments by Yosinski et al. [128] demonstrated that transferred representations from almost any n layers of a pre-trained base CNN algorithm can also generate enhancement of generalisation skill in the new CNN algorithm on a new task and data set.

Secondly, the amount of time that may be taken by the new CNN algorithm to fully learn on the new data set and task given the previous knowledge transferred is significantly less than the amount of time that may be taken to learn it from scratch. Therefore, they speed up the training on the new task and data set, and hence provide a higher performance slope. Thirdly, the potential ultimate overall performance level achievable in the new task with the utilisation of transfer learning techniques is greatly superior compared to the ultimate overall performance level without transfer learning techniques. Consequently, the converged ability of the new CNN algorithm is better, hence it provides a higher asymptote. Figure A.4 demonstrates these three possible benefits of utilising transfer learning techniques.

Despite the advantages of previously mentioned methods, namely, image data augmentation and transfer learning techniques that provide various solutions to the limited

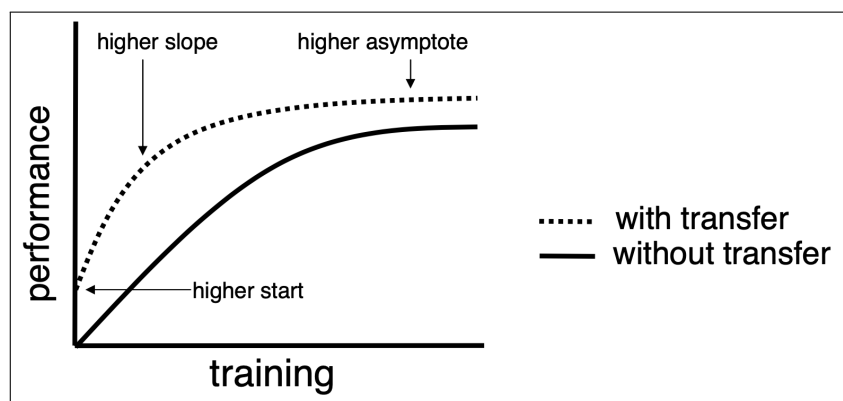


Figure A.4: Three potential benefits when exploiting transfer learning techniques [129].

availability of image data sets as well as boost the performance and generalisation ability of CNN algorithms, they suffer from a number of limitations. For example, image data augmentation techniques increase the number of images by performing arbitrary artificial transformations of images, however, these transformations can be inappropriate for several reasons. Specifically, they may misrepresent the original appearance of image data in undesirable ways. For instance, changes in orientation may change the original image dimensions. Perhaps one can rotate the images at right angles which in turn preserve the image dimensions. However, this will limit the increase in the number of images. This is because there are very few angles by which the images can be rotated.

A further very important issue with image data augmentation techniques is that they may open a wider problem which may require domain experts to investigate every single artificially created image. This is especially necessary when dealing with a very specific domain problem that includes for example microscopic or medical images. In this instance, trained clinicians or graders need to examine every single synthetic image generated to make sure that they do include the objects or areas of interest. However, this is not a straightforward task to reproduce the condition or examine the reproduced images due to several reasons. This is because it is not certain whether the reproduced images show or represent the correct areas of conditions in their original shape or known form. This is mainly due to the extensive dissimilarities and complexities that usually occur with medical images demonstrating different types of tiny cells or tissues of humans or animals. If the task under consideration deals with a general problem, such as identifying well known objects e.g.: cars, horses, chairs, tables and so on, image data augmentation techniques can serve as a great choice. Because the identification of these objects does not require a domain expert since any one can label

or examine the produced images. However, when it comes to a very sensitive domain specifically in the field of medicine where any error may be fatal, of course, this would present a major barrier towards the utilisation of image data augmentation techniques.

The application of transfer learning techniques, on the other hand, can also be inappropriate and may lead to undesirable consequences. This is because it is not very clear whether they will alleviate the lack of training data set as well as enhance the performance and generalisation until a base CNN algorithm trained on a related task is found and then some certain layers are transferred to a new CNN algorithm which is finally evaluated on the new data set and task. It is a multi-task pipeline that depends on several factors. These include the size of the new data set, the similarities and relationships between the base and new data sets and tasks, the choice of base CNN algorithm and many more.

Consequently, the application of transfer learning techniques can be regarded as an optimisation problem that may require domain expertise and knowledge for the base task and new task of interest that is dealt with to allow a reliable transfer. Of course, this should not be an issue when dealing with a generic problem such as finding well known objects, i.e.: car, animal, human, etc., that does not require a domain expert given the base data set is very large and diverse like ImageNet [254] and the new data set is relevant and not significantly different from the base data set. However, if the new data set represents some very specific domain, e.g.: medical or microscopic images, and there is no pre-trained base CNN algorithm on such an alike domain to be found, the utilisations of transfer learning techniques can be misleading.

A.2 Support Vector Machine (SVM)

Generally, the SVM classifier can be viewed as a mathematical entity for maximising a certain mathematical function in respect of a given data set [137]. However, the fundamental ideas behind the SVM classifier can be described without reading mathematical expressions or equations. In particular, there are four major concepts that need to be explained in order to understand the underlying essence of the SVM classifier for classification tasks so that one can have a deep insight of its function in real world applications. These basic concepts are the separating hyperplane, the maximum margin separating hyperplane, the soft margin hyperplane and the kernel function. To describe the SVM classifier in a working example, Noble [137] provides outstanding illustrative examples and comprehensive explanations including visualisations of these four

fundamental concepts for a binary classification problem using the SVM classifier as demonstrated in Figure A.5.

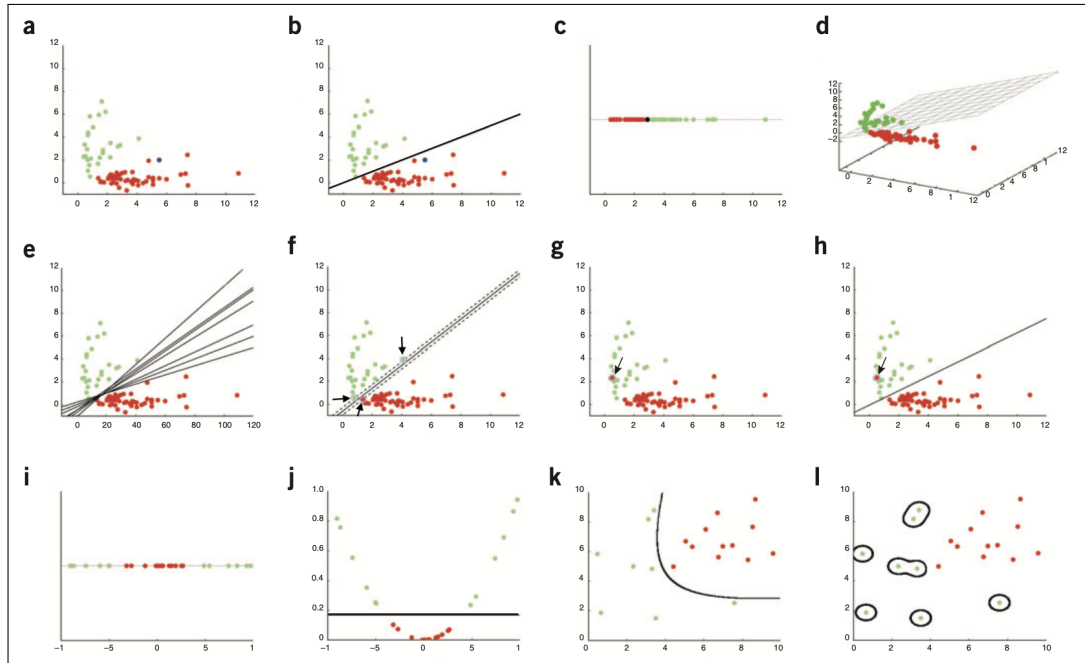


Figure A.5: Illustrative examples and visualisations of the SVM classifier in practical situations as well as comprehensive explanations of its four fundamental notions [137]. The data set used in these subfigures consists of different measurements derived from two different types of human genes, which represents two different classes of cancer. The two classes of cancer are mapped in the subfigures as green bullet points (●) for class **A** and red bullet points (●) for class **B**. (a) Shows a scatter plot of the two dimensional data set that represents two different classes of cancer. Each dimension in the scatter plot corresponds to the measurements of a given gene. The single blue bullet point (●) is an unknown data sample that is to be classified. The task of the SVM classifier is to assign a class label to the unknown data sample. (b) Displays the separating hyperplane. The inferred class label of the unknown data sample from this separating hyperplane is class **B**. (c) Presents the separating hyperplane of a one dimensional data set. The separating hyperplane is indicated as a single black bullet point (●). (d) Exhibits the separating hyperplane of a three dimensional data set. (e) Displays numerous potential separating hyperplanes. (f) Illustrates the maximum margin separating hyperplane. The three support vectors are indicated by three black arrows. (g) Demonstrates a data set that comprises “an outlier”, denoted by an arrow. (h) Displays the soft margin hyperplane and the outlier is denoted by an arrow. (i) Presents a nonseparable one dimensional data set. (j) Shows a separating nonseparable one dimensional data set that was previously visualised in (i). (k) Displays a situation of a linearly nonseparable two dimensional data set; however, it is linearly separable in four dimensions. (l) Illustrates a case in which the SVM classifier has overfitted a two dimensional data set.

The data set used by Noble [137] to describe the SVM classifier in a working example is plotted in Figure A.5a. This data set comprises a two dimensional data

set that consists of two different measurements derived from two different classes of human genes, which represents two different types of cancer. For simplicity, the two classes of cancer are plotted as green bullet points (●) for class **A** and red bullet points (●) for class **B** while the single blue bullet point (●) is an unknown data sample that is to be classified. The main task of the SVM classifier in this illustrative example is to learn the difference between the two different classes of cancer. Such that given an unlabelled data sample, for example the blue bullet point (●) the unknown data sample in Figure A.5a, the SVM classifier must predict whether it belongs to the green bullet points (●) class **A** or the red bullet points (●) class **B**.

The human eye is highly capable of recognising various patterns; for example, with a quick glance at Figure A.5a, one can easily recognise that class **A** forms a cluster in the upper left region and class **B** forms a cluster in the lower right region of the scatter plot. A simple general rule that may be determined from this scatter plot might state that any data sample represented in two dimensions is considered as being from class **A** if the value of one dimension is twice as high as the value of the other dimension, and vice versa for class **B**. In geometry, this simple rule relates to drawing a straight line between the two clusters, namely class **A** and class **B**, as depicted in Figure A.5b. Consequently, predicting the correct class label of the unknown data sample can be straightforward. This is because one can simply find the answer by examining whether the unknown data sample is located beside the class **A** cluster or the class **B** cluster of the separating straight line in the scatter plot.

To formally describe the notion of “the separating hyperplane”, consider a case in which the data set comprises an n -dimensional data set of measurements derived from human genes that characterises two different types of cancer. For instance, imagine a situation where the data set available contains only a single dimensional data set, i.e.: includes a single measurement of one class of human gene that characterises two different types of cancer. Subsequently, the space in which the corresponding single-dimensional data set resides is a single-dimensional straight line as demonstrated in Figure A.5c.

Hence, to distinguish between the two clusters, namely class **A** and class **B**, one can divide this straight line in the middle by using a single point such as the black bullet point (●) illustrated in Figure A.5c. A further possible situation includes a two dimensional data set and in this case, one can use a straight line to divide the space in half, as shown earlier in Figure A.5b. In case of a three-dimensional data set, one needs a plane to divide the space, as shown in Figure A.5d. This procedure can be

extrapolated mathematically to other higher dimensions depending upon the size of the data set used. Therefore, the typical term for the single point, straight line and plane that separate the space of any high dimensional space is a hyperplane, hence the term “separating hyperplane” [137].

The idea of handling the various classes of samples to be classified as points in a high dimensional space and identifying the separating hyperplane that separates the different classes is not exclusive to the SVM classifier [137]. However, the key difference that makes the SVM classifier quite distinctive from other hyperplane-based classification schemes is the way it operates to choose the separating hyperplane. Consider the enviable classification problem shown in Figure A.5a where two measurements derived from human genes are used to predict two different types of cancer that are completely separable. However, there is a large and perhaps infinite number of potential separating hyperplanes that may occur which can perfectly classify these two different classes of cancer as shown in Figure A.5e.

Given the aforementioned unique situation, one may run into a further issue, in particular, choosing the most appropriate class boundary, i.e.: the optimal separating hyperplane that provides the best classification performance. While there are numerous performance measures that can be employed for selecting the best separating hyperplane, for example, the accuracy metric, the accuracy-based performance measures, however, are generally inadequate [130]. This is because evaluating the classifier performance using a performance measure, e.g.: the accuracy metric, would be deemed equivalent since all these separating hyperplanes can provide perfect classification of the two different classes.

Nevertheless, Vapnik [131, 132] introduced an alternative and more appropriate metric termed the “margin” for judging the efficacy of the SVM classifier [130, 137]. Roughly speaking, the margin metric is defined as the maximal distance between the classification boundary, i.e.: the separating hyperplane, and the nearest training data points of at least one of the different classes, hence the term “maximum margin separating hyperplane” [130]. To illustrate this, Figure A.5f shows one potential separating hyperplane represented as a solid line. The two dashed lines on both sides of the separating hyperplane are located at the maximum possible distance from the separating hyperplane to the nearest training data points of at least one sample of the two different classes (at equal distances from the separating hyperplane).

In Figure A.5f, the three data samples of the two different classes equally have the same distance to the classification border, i.e.: the separating hyperplane, and these

three data samples are indicated by three black arrows. These three data samples are usually referred to as the support vectors of the SVM classifier, hence the term “Support Vector Machine (SVM)”. Both the solid and the two dashed lines construct the maximum margin separating hyperplane of the SVM classifier. Choosing this particular maximum margin separating hyperplane increases the SVM’s capability to generalise and classify previously unseen examples. A key success of the SVM classifier is generally attributed and driven by this theorem [137].

However, unless relying on pure luck, it would be hard to assume that the vast majority of data sets used in most real world classification problems could be easily separated by using a straight line. For instance, consider a realistic case similar to the one in Figure A.5g, which could potentially be encountered in most practical applications. As demonstrated in Figure A.5g, the data set comprises “an outlier”, the red bullet point (●) of class **B** cluster indicated by the arrow, which is located within the group of green bullet points (●) i.e.: class **A** cluster. Of course, if the data samples of the two different classes are not completely separable, it is always desirable to have a classifier that is capable of dealing with such insignificant errors in the data set. Intuitively, one may wish to accept a few anomalous data samples to be positioned exactly on or inside the margin or perhaps to drop at the incorrect side of the maximum margin separating hyperplane.

To accommodate situations like these, motivated by Boser et al. [136], Cortes and Vapnik [134] developed extensions to the maximum margin separating hyperplane by introducing “a soft margin hyperplane” to the SVM classifier to allow separating the training data set with a minimal number of errors [130, 134]. Technically, the soft margin hyperplane operates by allowing a few of the anomalous data samples to push their way through the maximum margin separating hyperplane without significantly affecting the overall classification performance, hence the term “soft margin hyperplane” [137]. Figure A.5h demonstrates the maximum margin separating hyperplane with the soft margin hyperplane solution technique to the problem visualised in Figure A.5g comprising one outlier, specified by a single black arrow. As seen in Figure A.5g, the single outlier, specifically the red bullet point (●) exists on the same side of the opposite class members i.e.: the class **A** cluster.

Indeed, no one desires the SVM classifier to allow for several incorrect classification cases such as these to occur. Consequently, introducing the soft margin hyperplane technique requires providing a user specified tuning parameter [137]. Roughly speaking, the typical task of the adjustable soft margin hyperplane parameter is to regulate

the number of data samples that are allowed to breach the maximum margin separating hyperplane. It also controls how far the anomalous data samples are allowed to go beyond the classification boundary line, e.g.: the maximum margin separating hyperplane. Selecting the appropriate value of this parameter can be, however, a relatively complicated task since it is always desirable to achieve a large margin separating hyperplane with respect to the correctly classified data samples as this increases the ability of the SVM classifier to predict the correct class labels of previously unseen data samples. Consequently, the most appropriate value of the soft margin hyperplane parameter should provide a compromise between the size of the margin and the number of potential hyperplane violations.

Despite the flexible solution that the soft margin hyperplane technique can provide, there are other challenging situations such as a single-dimensional but nonseparable data set. For instance, consider the analogous case demonstrated in Figure A.5i. This data set comprises only a single measurement of one class of human gene that describes two different categories of cancer. As can be seen from the distribution of the single human gene measurements in Figure A.5i, the values representing the class **B** cancer demonstrated in red bullet points (●) are all gathered close to zero while the other class **A** cancer illustrated in green bullet points (●) have values that are either significantly smaller or significantly greater than zero. However, the main problem with this data set is that no such appropriate separating hyperplane can be found to solve this classification problem. This is because neither the single point used in Figure A.5c nor the soft margin used in Figure A.5h can be used to separate the two various classes of cancer.

Nevertheless, when the different classes of samples are not completely separable, motivated by the findings of Boser et al. [136] which provide an extension to the linear nature of the SVM classifier to produce nonlinear classification boundaries, Cortes and Vapnik [134] proposed further enhancements to the early soft margin hyperplane technique to accommodate additional challenging situations such as the case in Figure A.5i by the means of introducing a “kernel function” [130, 137]. The application of kernel function allows the SVM classifier to construct extremely flexible decision or classification boundaries for the classification task of interest. Since the application of kernel function can lead to generating nonlinear classifiers, this generalisation is usually referred to as a “kernel trick” [130].

The kernel function can provide a proper solution to the classification problem demonstrated in Figure A.5i by introducing an extra dimension to the nonseparable

data set. In a typical way to add a new dimension to the data set, one can simply accomplish this by squaring every single value of the human gene [137]. As demonstrated in Figure A.5j, this naive operation, fortunately, separates the two different classes of cancer, **A** and **B**, by a straight line in the new two dimensional space. Therefore, the kernel function can be viewed as a mathematical trick that provides the SVM classifier with the great capability to solve a complex classification problem using a two dimensional data set that was originally driven from a one dimensional data set [137]. Consequently, the general task of the kernel function can be seen as projecting the data set from a low dimensional space to a higher dimensional space to facilitate solving a very challenging classification problem.

To grasp more insight into the kernel function task, consider the linearly nonseparable two dimensional data set plotted in Figure A.5k. Separating this data set with a straight line cannot be achieved without errors. However, employing a relatively simple kernel function that simply transforms the original data set from a two dimensional space into a four dimensional space will allow the data set to be linearly separated [137]. The newly constructed data set cannot be plotted in the four dimensional space; however, one can project the SVM classifier separating hyperplane in that new space back down to the original two dimensional space. The result of this operation is visualised as the contorted line in Figure A.5k. Inspired by this finding, it is potentially feasible to demonstrate that for a given data set of any dimension but with consistent classes, there is at least one kernel function that will allow the data set to be linearly separated [137]. The consistency of the classes here means that the data set does not include two identical measurements that represent two data samples from two opposite classes. Motivated by this observation, one can propose the idea of always projecting any data set into a higher dimensional space so as to be sure of finding the most appropriate separating hyperplane [137].

While the idea of projecting the data set under consideration into a higher dimensional space can be a reasonable proposal, it can present a further issue that is commonly known as the curse of dimensionality [137]. This is a phenomenon that normally occurs when the feature space becomes increasingly sparse due to a very high dimensional data set but does not occur in a low dimensional space. Therefore, as the feature space grows, i.e.: the number of features increases, the number of potential solutions, i.e.: the number of optimal separating hyperplanes also grows, however exponentially. This, in turn, can present a problem to the SVM classifier in deciding the most appropriate solution from a huge number of potential separating hyperplanes. Figure A.5l

displays what may occur when the SVM classifier is presented with a data set that is projected into a very high dimensional space.

The data set used in Figure A.5l and Figure A.5k is identical; however, the estimated hyperplane in Figure A.5l is drawn from a SVM classifier that utilises a very high dimensional kernel function. As can be seen from Figure A.5l, the classification boundary, i.e.: the separating hyperplane between the various classes is very specific to the samples in the training data set, hence it results in severe overfitting. Undoubtedly, this can negatively impact the generalisation performance of the SVM classifier when presented with new data samples [130, 137].

A further issue that can be encountered in most practical applications when using the SVM classifier to solve a classification problem using a new data set is the way of choosing the most appropriate kernel function. This is because it is always preferable that the kernel function chosen to solve the classification task should allow the data set under consideration to be separated perfectly, however, without presenting a huge number of irrelevant dimensions. Meeting this rigorous preference can be quite challenging; however, the only convincing way to meet this requirement is a procedure of trial-and-error [137].

A typical technique usually followed in the trial-and-error procedure is to start with a simple SVM classifier assuming the data set is linearly separable. It is then followed by conducting several experiments using a wide variety of the kernel functions available. The optimal kernel function can then be chosen based on a statistically rigorous method, such as employing cross validation strategy, for example, a resampling technique that involves experimenting with a set of kernel functions [130, 137]. Therefore, the right kernel function can be chosen properly while maintaining the overall objective that the SVM classifier does not overfit or underfit the training data set [130].

As explained up until now, perhaps the most obvious downside of the SVM classifier is that it can only handle a binary classification problem. Nevertheless, there have been considerable ongoing enhancements since its original development and an example of these extensions include handling classification of more than two classes [130, 259, 260]. Generalising the SVM classifier to solve multiclass classification problems is straightforward [137]. This is typically accomplished by employing any of a wide variety of multiclass classification techniques such as one-vs-the-rest (OVR), also occasionally referred to as one-vs-all (OVA) and one-vs-one (OVO) strategies.

The OVR or OVA strategy works by splitting the multiclass data set into several

binary classification problems. The process is then followed by training a number of separate SVM classifiers, i.e.: a single SVM classifier is trained on every single binary classification problem (one binary data set for every single class against all opposite classes). Classifications are then made using the SVM classifier that yields the highest confidence. Specifically, given n SVM classifiers trained on n classes, a new data sample is assigned to the class of the SVM classifier that returns the highest-class probability score [261].

The OVO strategy, on the other hand, works in a similar manner to the OVR or OVA strategy in splitting the multiclass data set into several binary classification problems. However, the key difference between them is that the OVO strategy splits the multiclass data set into a single data set for every single class against every single opposite class (one binary data set for every single class against every single opposite class). These simple multiclass classification strategies have been demonstrated to work quite well in a wide variety of practical classification applications such as the OVA strategy utilised in cancer classification [137, 261].

Overall, the SVM classifier tends to be a very reasonable choice for most classification problems as demonstrated in several studies [130, 137, 261, 262]. For instance, utilising a data set that includes around seven thousand human gene measurements to differentiate between various classes of cancer, the SVM classifier has been demonstrated to reach near perfect classification results [137, 262]. Moreover, using even a much larger data set, the SVM classifier was also demonstrated to perform significantly better than a wide variety of alternative classification algorithms for cancer classification tasks [137, 261].

While the demonstration so far has only considered employing the SVM classifier for cancer classification tasks, the SVM classifier can also be applied to a wide variety of domains including medical and industrial applications such as machine fault diagnosis using a small data set [263]. When taking all the aforementioned details about the SVM classifier into account, it becomes clear that the SVM classifier has been demonstrated to possess a robust theoretical underpinning since it can excellently reveal the implicit classification knowledge in various data sets of different domains [137, 263]. Furthermore, the SVM classifier demonstrated a great ability together with outstanding empirical classification results across various domains of applications with no matter of how big or small the data set utilised [137].

A.3 K-Nearest Neighbour (KNN)

The main rationale behind the development of the KNN classifier was primarily driven by the need to facilitate performing discrimination analysis when such reliable parametric probability density estimates are not feasible or are hard to define [141]. Therefore, the KNN classifier is a distribution free procedure, in the sense that it requires no prior statistical knowledge or assumption details to be available about the underlying form of data distribution for its application [141, 142]. Hence, this has made the KNN classifier more attractive to use in a wide variety of classification tasks, since details about the underlying data distribution are rarely available in most classification problems.

The KNN classifier is also widely known by other different names [143]. For instance, memory-based learning since the training data samples need to be in memory at run time, hence the name. Other names include lazy learning, so-called due to the fact that the induction is delayed until the run time or until a query is made to the classifier, and instance-based learning or example-based learning whereby the classification is based directly on the training data instances.

The main intuition underlying the KNN classifier is relatively straightforward to demonstrate since its construction is merely based on the class of individual samples from the training data set. For instance, new data samples are classified to the class of their k closest samples from the training data set. Figure A.6 demonstrates the KNN classifier in a working example to solve a binary classification problem in a two dimensional feature space. The data samples of two different classes are represented as orange colour filled circles (●) for Class 1 and blue colour filled squares (■) for Class 2 in the scatter plot in Figure A.6. These two different classes of samples are described by two different measurements, i.e.: feature values denoted as Predictor A and Predictor B in Figure A.6. The overall task of the KNN classifier in the example is to classify two different new data samples, represented by a black bullet point (●) and a black solid triangle (▲) based on the majority vote of five nearest neighbours in the training data set.

Based on the scatter plot in Figure A.6, the classification decision for the black solid triangle (▲) data sample is straightforward. This because the nearest neighbours of all five samples are from Class 2 (■) so the black solid triangle (▲) data sample is classified as belonging to Class 2 (■). However, the classification decision for the black bullet point (●) data sample is slightly more complicated. This is because the nearest neighbours of five samples are from a mixture of the two different classes, specifically

three neighbours from Class 1 (●) and two neighbours from Class 2 (■). Nevertheless, the most straightforward approach to resolve this situation is simply by assigning the majority class among the five nearest neighbours to the black bullet point (●) data sample. Consequently, the black bullet point (●) data sample is classified as belonging to Class 1 (●). Hence, the KNN classifier involves two main stages. It starts with the determination of the k nearest neighbours and then follows with the estimation of the class using those k nearest neighbours.

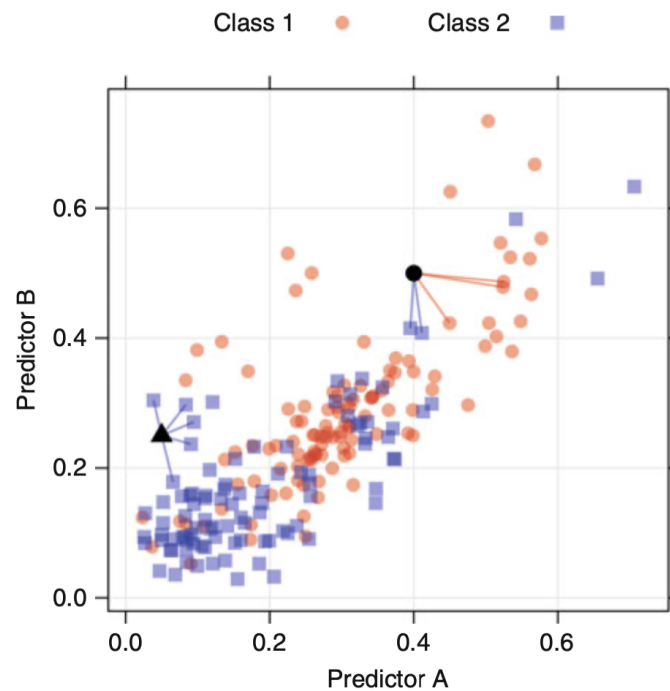


Figure A.6: An illustrative example of the KNN classifier in a binary classification situation [130]. A two dimensional data set is used in this example. Predictor A and Predictor B represent the values of two different feature measurements that quantify the two different classes, Class 1 (●) and Class 2 (■). Two new data samples, represented by a black bullet point (●) and a black solid triangle (▲), are classified based on the majority vote of five nearest neighbours i.e.: feature vectors in the training data set.

The determination of the k nearest neighbours is typically accomplished using a distance metric that measures how far the new data samples are from the k closest individual data samples in the training data set. Hence, the KNN classifier depends mainly on how the distances between data samples, i.e.: new data samples and k closest data samples, are quantified. While there are several distance metrics available, the most commonly utilised distance metric is the Euclidean distance, i.e.: the distances of the straight lines between the two new data samples and the five closest individual data samples in the training data set, as illustrated in Figure A.6.

Once the distances between data samples are defined, the class probability estimates of new data samples are determined based on the majority class among the k nearest neighbours in the training data set. In other words, the estimates of class probability for new data samples are computed as the proportion of k nearest neighbours set in each class [130]. The predicted class of every single new data sample is the class with the maximum probability estimates. However, if more classes, e.g.: two classes are equally tied to the maximum probability estimate, then the tie can be broken by considering ahead to the K plus 1 nearest neighbours or it can be broken at random [130].

The selected value of k nearest neighbours is five in the example illustrated in Figure A.6; however, other values of k are also possible. The value of k nearest neighbours is referred to as a tuning parameter of the KNN classifier since there is no well-established analytical formula available that can be employed to determine the most appropriate value of k [130]. Just similar to the parameters of other machine learning classification algorithms, for instance, the kernel function of the SVM classifier, the value of k needs to be determined carefully in a way that does not negatively impact the classification performance of the KNN classifier on previously unseen data samples.

Almost any machine learning classification algorithm with tuning parameters can be vulnerable to the risk of overfitting, and the KNN classifier is specifically susceptible to this problem [130]. This is because selecting very few neighbours, i.e.: a very small value of k , may cause the KNN classifier to overfit the individual data samples in the training data set. Similarly, choosing excessively numerous neighbours, i.e.: a very large value of k , may result in the KNN classifier not being sufficiently sensitive to produce a reasonable classification performance. Nevertheless, finding the optimal value of k nearest neighbours is usually determined in a similar manner to finding the optimal kernel function of the SVM classifier, that is based on a statistically rigorous method, such as employing a cross validation strategy, e.g.: a resampling technique that involves experimenting with a set of different k values.

Since the KNN classifier essentially depends on the distances between data samples, the scale of the feature values that describe data samples can introduce a great impact onto the distances between data samples, hence, dramatic influence on final classification results [130]. This is because the data samples described with measurements, i.e.: feature values that are based on a great variety of units or scales will produce distance measures that are biased towards the feature values with the greatest

scales. Consequently, the measurements with the greatest scales can contribute most to defining the distance measures between data samples, hence, can produce misleading classification results. Nevertheless, this potential bias is typically addressed through applying two popular data transformation methods, namely data centring and scaling techniques to the original measurements, i.e.: original feature values prior to applying the KNN classifier [130].

Before applying the aforementioned two data transformation methods, the mean and standard deviation of observable feature values must be estimated first, typically from the training data samples. Then, the feature values are centred by subtracting the mean from every single feature value, hence the term “data centring”. The result of this centring operation is a set of feature values that has a zero mean. Likewise, with the scaling technique, the feature values are scaled through dividing every single feature value by the standard deviation, hence the term “data scaling”. The result of this scaling operation is a set of feature values that has a common standard deviation of one. These statistical operations provide a great enhancement in terms of the feature values stability, hence, facilitating performing further statistical calculations as the KNN classifier specifically can benefit from the feature values being on a common scale [130]. When all the feature values are scaled to a standard range, this gives every single feature value the opportunity to contribute equally to calculating the distance measures in the KNN classifier. Nevertheless, the only downside of these data transformations methods is that the individual feature values are less interpretable as the transformed data are no longer represented in the original scales or units [130].

Generally, the KNN classifier is considered as one of the simplest machine learning classification algorithms as it is extremely easy to implement and very simple to understand [143]. Therefore, it is always considered as one of the first choices when seeking to solve a wide variety of classification problems. The KNN classifier holds several advantages that are the central key behind its current utility and wide applicability across various classification domains. Among the most important advantages of the KNN classifier are its simplicity and interpretability. For instance, the classification procedure is very clear and transparent in the sense that it is easy to implement and debug. In certain circumstances, such as solving medical image classification problems when interpreting and understanding the classification decisions are very useful, the KNN classifier can also serve as a great choice and a very effective approach where examining the closest neighbours provides valuable details as an explanation [143].

However, like other machine learning classification algorithms that have pros and

cons, the KNN classifier also has some disadvantages. For instance, if the delay in getting the classification results is an issue, the KNN classifier can have a poor run time performance when applied on a large training data set, since all the work is performed at run time. The KNN classifier can also be very sensitive to redundant or irrelevant feature values. This is because every single feature value typically contributes to distance or similarity measures, hence to the final classification decisions. Nevertheless, this sensitivity is usually eliminated by designing well representative features or by careful feature selection [143]. When dealing with very challenging classification tasks, the KNN classifier can sometimes be easily outperformed by more sophisticated machine learning classification algorithms such as the SVM classifier [143].

Appendix B

Supplementary details for Chapter 3

B.1 Optical Coherence Tomography Angiography (OCTA)

Broadly, the OCTA imaging technique works in a manner that is fairly analogous to the conventional cross-sectional OCT imaging technique. It starts by scanning a beam of light on the anterior eye or the retina to measure the depth of a certain ocular tissue structure as well as quantifying how much this tissue structure scatters or reflects light [202]. This measurement of scanning procedure is known as an axial scan or an A-scan. The cross-sectional OCT image is typically produced by successively obtaining several A-scans as the light beam is scanned in the transverse direction.

A three dimensional image data cube or volumetric data can, therefore, be generated by sequentially acquiring multiple cross-sectional OCT scans or images at different retinal locations covering a particular region of the retina in a raster scan pattern manner [202]. The raster scan pattern strategy is accomplished by acquiring several A-scans along a scan line to construct a cross-sectional OCT scan or image. Then, at the end of the scan line of the previous cross-sectional OCT scan, the scanning beam is swept back to start a new cross-sectional OCT scan but with a slight displacement away from the previous cross-sectional OCT scan. The aggregation of this scanning procedure forms the basis of the raster scan pattern strategy as well as generating the volumetric data.

However, the raster scan pattern strategy covers only a certain ocular region with a high density of A-scans and therefore cannot detect the motions of blood elements or

generate vascular contrasts. For discriminating motions of blood elements and producing vascular contrasts, the OCTA imaging technique recurrently and rapidly acquires multiple cross-sectional images from a certain region in the retina or any other ocular tissue area over various times and then investigates the various cross-sectional images captured for variations [202, 222]. This particular manner of imaging draws the fundamental characteristic of the OCTA imaging technique and the core difference from the conventional cross-sectional OCT imaging technique in imaging both retinal and choroidal vasculatures. Figure B.1 presents a simplified demonstration of how the OCTA imaging technique functions in a working example.

The variations between the various cross-sectional images captured are measured using motion contrast scanning technology. Figure B.2 demonstrates a simple example of how the motion contrast technology is employed to detect motions of blood flow and produce vascular contrasts through estimating the dissimilarity or variance between the various cross-sectional images captured rapidly over various times. This technology provides measurements that quantify precisely how much motions or movements of flow elements have occurred in a particular rapidly scanned region. This is accomplished by investigating the several cross-sectional images captured for variations as described in Figure B.2.

Typically, motionless or static elements are given very low values while high amounts of motions or moving elements are given high values [222]. These values are typically used to produce images of both choroidal as well as retinal vasculatures. Stated another way, since the greater part of the retina is a motionless tissue structure, the only anticipated motions in the choroid and retinal layers are blood flows or movements through the vessels [202]. Therefore, when several cross-sectional images are successively captured from a particular area, they will appear mostly very similar to each other except for the areas where the blood movements occur through the vessels.

At the regions where the blood moves through the vessels, the light reflectivity or scattering changes from one cross-sectional image to another [202]. By comparing the sequentially captured cross-sectional images, it is possible to characterise blood flow by looking for differences among the various cross-sectional images captured in a pairwise fashion, i.e.: on a pixel-by-pixel basis. This procedure is typically repeated several times at successive locations, densely and rapidly over a certain area, e.g.: the macula region that sits near the centre of the retina, to produce a volumetric OCTA data cube. This volumetric OCTA data cube provides a three dimensional imaging of the retinal and choroidal vasculature at a micro level. The time required to acquire

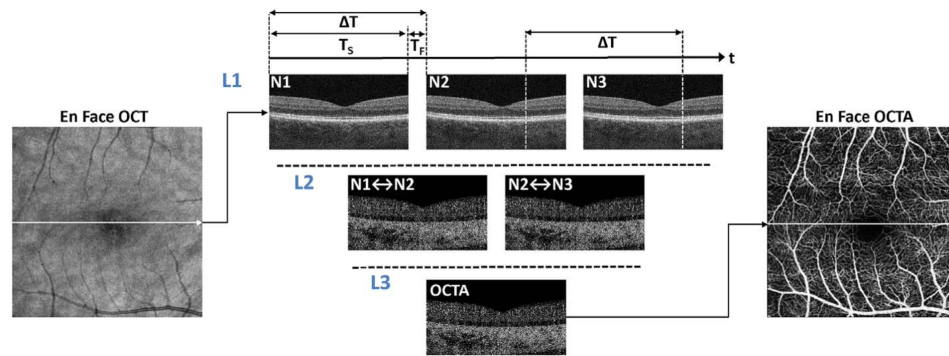


Figure B.1: A basic schematic that illustrates the manner in which the OCTA imaging technique functions in a working example to image the human eye [202]. The En Face OCT image, i.e.: the image that reveals the surface appearance of the retina tissue, shows the structural OCT image of the back of the eye that is centred around the macular region that will be densely scanned. As the OCTA imaging technique is a functional extension of the conventional OCT imaging technique, it starts by rapidly obtaining multiple repeated cross-sectional OCT scans from the same retinal location rapidly and repeatedly over various times. The line crossing the En Face OCT image corresponds to the same location from which multiple repeated cross-sectional OCT scans (N1, N2 and N3) as depicted in line 1 (L1) are rapidly acquired. The acquisition time (T_S) for every single cross-sectional OCT scan is determined as follows. The total number of A-scans per cross-sectional OCT scan times the A-scan rate i.e.: the maximal rate at which the A-scans are obtained during the cross-sectional OCT scan. The OCT beam is quickly scanned back to the original location during the fly back time (T_F). Another cross-sectional OCT scan is then repeated again after a time delay (ΔT), i.e.: an interscan time. The interscan time, ΔT , is determined by the sum of both the T_S and the T_F . Every A-scan that comprises a cross-sectional OCT scan is also repeated again at the interscan time. The interscan time plays a crucial rule in the imaging since it controls both the sensitivity and the saturation behaviour of the OCTA imaging technique. The sequential cross-sectional OCT scans (N1, N2 and N3) captured are then compared in a pairwise fashion, i.e.: on a pixel-by-pixel basis. This is to detect signal changes that occur due to movement of blood elements. The decorrelations or differences between them are then calculated and displayed as motion contrast images (N1 \leftrightarrow N2 and N2 \leftrightarrow N3) as depicted in line 2 (L2). The results calculated are then combined into a single OCTA cross-sectional image as depicted in line 3 (L3). This technique is typically repeated at successive locations densely and rapidly to produce the volumetric OCTA data cube over a particular area of the retina. The volumetric OCTA data cube generated provides a three dimensional imaging of the retinal and choroidal vasculature at a micro level. However, this volumetric OCTA data cube is typically evaluated and projected in depth to view en face two dimensional OCTA images from certain retinal and choroidal depth level slabs or layers. These en face OCTA images are analogous to the En Face OCT, FA and IGA images but with unprecedented depth resolved capabilities since the various retinal and choroidal layers can be selectively and individually segmented and displayed. The En Face OCTA images typically show blood vessels and flows in a monochrome display, i.e.: in colour over a greyscale. The En Face OCTA image in this figure demonstrates the superficial retinal layer. It can be clearly observed that the detail of retinal blood vessels in the En Face OCTA image is significantly richer compared to the En Face OCT image.

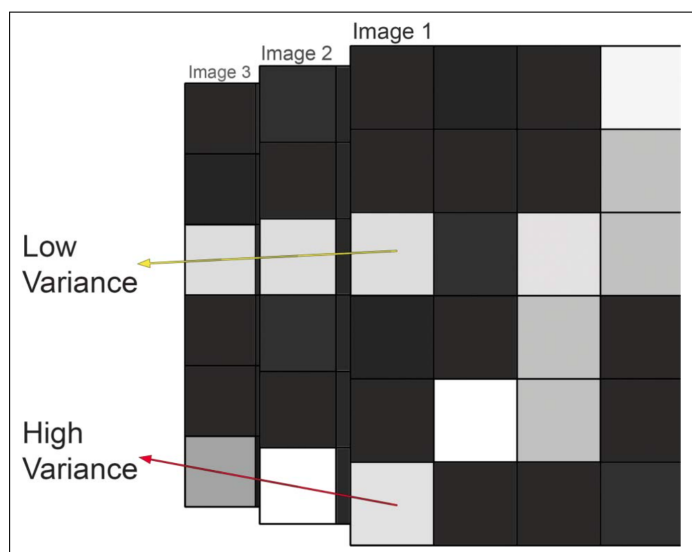


Figure B.2: Illustration of how the motion contrast technology is employed in the OCTA imaging technique by the means of variance [222]. Since the OCTA imaging technique rapidly image a certain region in the retina several times, three different images (Image 1, Image 2 and Image 3) are captured and compared using variance in this illustrative example. The yellow arrow that crosses the middle sequence of pixels shows the detected elements that have low variance. While these pixels appear much brighter than the background, they do not, however, change over the time between the various images captured. This is in contrast to the red arrow that intersects the below pixels that have high variance. While the below sequence of pixels in aggregate have the same mean value as the middle sequence of pixels, however, they demonstrate great variability between the various images captured over various times.

the volumetric OCTA data cube for a certain area of interest around the retina usually takes approximately six seconds [7].

Since the OCTA imaging technique is depth resolved, the volumetric OCTA data cube that comprises micro vasculature blood flow information is typically evaluated and projected in depth to visualise a specific depth level of different slabs of any individual retinal or choroidal layers displayed as two dimensional images [222]. These two dimensional images demonstrate high quality details about the various retinal capillary plexuses, i.e.: fine networks of blood vessels, and choroidal vasculature that appears in individual retinal or choroidal layers. These images are typically denoted or known by several names such as En Face OCTA images, OCTA images and OCT angiogram images. However, they all refer to the same thing as they demonstrate or reveal the surface appearance of a tissue layer, e.g.: a single layer of the retina or perhaps any other ocular tissue layer. The OCTA images typically demonstrate blood vessels and flows in a monochrome display, i.e.: in colour over a greyscale.

The OCTA imaging technique provides manual manipulation of the volumetric

OCTA data cube to allow scrolling inwards and outwards across both retinal and choroidal layers to visualise specific regions of vascular networks appearing in the various layers of the retina including the inner region of the choroid layer, i.e.: the choriocapillaris, or any other regions of interest. Nevertheless, the OCTA imaging technique also provides automated segmentation and visualisation of the volumetric OCTA data cube to construct clear OCTA images based on some specific depth levels and combinations of various retinal and choroidal layers allowing the automatic generation of four main distinct layers in total. Specifically, these four main layers are the superficial inner retina, the deep inner retina, the outer retina and the choriocapillaris layers. Figure B.3E-H provides examples of automated layer segmentation and visualisation by the OCTA imaging technique for the aforementioned layers namely the superficial inner retina, the deep inner retina, the outer retina and the choriocapillaris respectively for a healthy human eye.

As the OCTA imaging technique automatically produces images based on certain depth levels and combinations of various retinal and choroidal layers, the OCTA images of the above mentioned four main layers are typically determined and measured as follows. For instance, the OCTA image of the superficial inner retina layer is defined as a projection of the vasculature located in two retinal layers, namely the nerve fibre layer and the ganglion cell layer [7]. An OCTA image of the superficial inner retina layer is given in Figure B.3E. The OCTA image of the deep inner retina layer, on the other hand, comprises a projection of a combination of the vascular plexuses situated at the edge of the inner plexiform layer and the inner nuclear layer and the edge of the inner nuclear layer and the outer plexiform layer [7]. Figure B.3F provides an OCTA image of the deep inner retina layer.

The OCTA image of the outer retina layer typically comprises a projection of the outermost retinal layers, i.e.: the photoreceptor layer through to the choroid layer. The OCTA images of the outer retina layer usually demonstrate no blood vessels at all since the outermost retinal layers projected are typically avascular layers, i.e.: contain no vasculature. An OCTA image of the outer retina layer is given in Figure B.3G. The OCTA image of the choriocapillaris layer shows a projection of merely the inner area of choroid layer specifically the choriocapillaris layer. Figure B.3H illustrates an OCTA image of the choriocapillaris layer.

The range of imaging a particular physical area of interest, e.g.: the macula of retina, by the OCTA imaging technique, starts from a $2 \times 2 \text{ mm}$ up to a $12 \times 12 \text{ mm}$ field of view [7]. Examples of OCTA images captured with different fields of view,

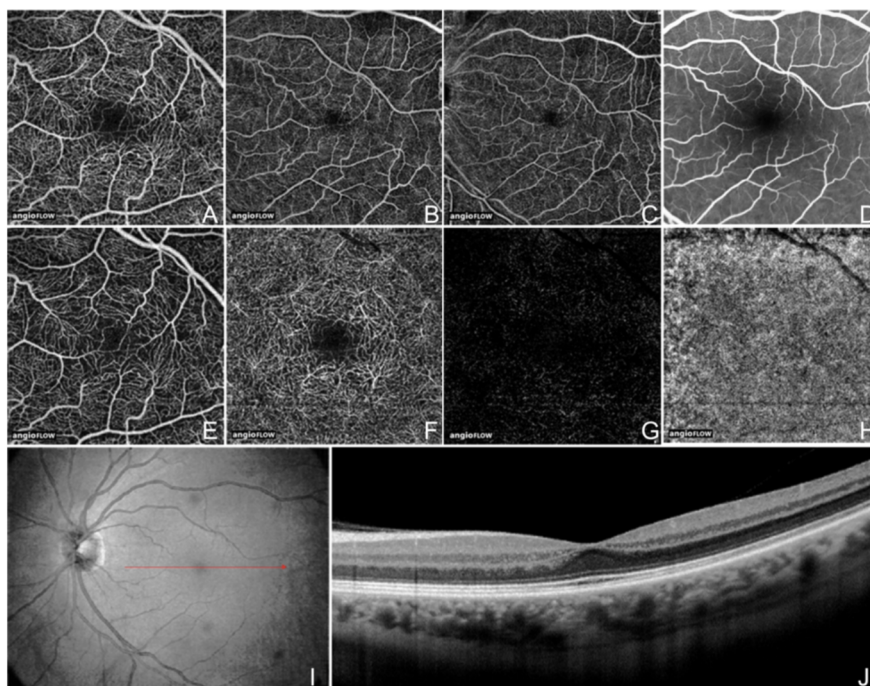


Figure B.3: Automated retinal and choroidal layers segmentation including visualisations with different fields of view by the OCTA imaging technique for a healthy human eye [7]. (A-C) Demonstrate OCTA images of the superficial inner retina captured around the macula region with various fields of view namely $3 \times 3 \text{ mm}$, $6 \times 6 \text{ mm}$ and $8 \times 8 \text{ mm}$, respectively. (D) Shows an image captured and cropped to approximately $8 \times 8 \text{ mm}$ around the macula region of the same patient, but using the FA imaging technique. It can be clearly seen that the textural appearance of the blood vessels in (D) demonstrates less vasculature detail than in (A-C) and as the field of view gets smaller, much richer vasculature details are obtained namely (A) displays better vasculature information than (B-C). (E-H) demonstrate $3 \times 3 \text{ mm}$ OCTA images of the superficial inner retina, the deep inner retina, the outer retina and the choriocapillaris layers, respectively. These OCTA images of the various retinal and choroidal layers are automatically extracted and segmented based on the depth level of every single layer by the default settings of the OCTA imaging technique. The textural appearance of these OCTA images varies between the different retinal and choroidal layers. For instance, the OCTA image of the outer retina in (G) shows generally absence of vasculature while the OCTA image of the choriocapillaris in (H) shows a typical homogenous texture appearance of capillaries, i.e.: extremely small and fine blood vessels. As the OCTA imaging technique is a functional extension of the conventional OCT imaging technique, (I) illustrates the structural OCT image of the back of the eye and the red arrow corresponds to the approximate location in which the cross-sectional OCT image demonstrated in (J) was sampled. This cross-sectional OCT image shows the full thickness of the region that was densely and rapidly scanned to generate OCTA images for the retinal and choroidal layers.

namely $3 \times 3 \text{ mm}$, $6 \times 6 \text{ mm}$ and $8 \times 8 \text{ mm}$, respectively are given in Figure B.3A-C. These various OCTA images demonstrate approximately the same superficial inner retina layer captured around the macula region. However, as the imaging field of view

becomes wider, i.e.: the imaging size of the physical area being scanned increases, the image quality can on the other hand be significantly decreased. This matter is mainly attributed to the fact that the OCTA imaging technique utilises the same number of cross-sectional images for imaging the areas of interest and does not take into account how large or small the range or size of the physical area or field of view is that will be visualised [7].

Nevertheless, several studies have determined that the OCTA images with $3 \times 3 \text{ mm}$ field of view appear to provide an outstanding resolution of various vascular layers of the eye. For instance, a study conducted by Matsunaga et al. [197] concluded that the $3 \times 3 \text{ mm}$ OCTA images were at least qualitatively similar to conventional imaging techniques, e.g.: the FA and IGA, in demonstrating essential vascular information. Furthermore, a recent study conducted by de Carlo et al. [7] deduced that vascular details visualised by the $3 \times 3 \text{ mm}$ OCTA images are far better than the presently available vascular images captured by conventional imaging techniques including the OCT, FA and IGA. Consequently, acquiring OCTA images with a small field of view can provide much richer details about the retinal and choroidal vasculature compared to those OCTA images with large fields of view.

Although the field of view of the $3 \times 3 \text{ mm}$ images may be criticised as being very small compared to the large field of view images captured by the FA and IGA imaging techniques, several studies indicated that the $3 \times 3 \text{ mm}$ OCTA images appear to provide better resolution as well as to show important details that are much better than the FA and IGA images [7]. Nevertheless, the OCTA imaging technique can also be performed repeatedly around various areas of interest during an imaging session [202]. Consequently, this can facilitate acquiring a comprehensive and a broad field of view about both choroidal and retinal vasculature information and can allow evaluating vascular response to treatments across various vascular areas in choroidal and retinal layers.

Despite the OCTA imaging technique being a few years old, i.e.: roughly a little more than ten years, and its initial introduction into clinical use was in 2014 as well as currently being in the initial stages of development, several studies have qualitatively reviewed and investigated in depth the feasibility of its data for detecting various ocular diseases as well as clinical assessments and have compared it with other existing gold standard angiographic imaging techniques, e.g.: FA, IGA and OCT [22, 202]. Examples of outstanding studies include the works by Matsunaga et al. [197] to qualitatively evaluate the OCTA imaging technique in measuring retinal vasculature of healthy human eyes; de Carlo et al. [7] to review the OCTA and compare it with the FA, IGA

and OCT imaging techniques; Spaide et al. [198] to compare the OCTA with FA in imaging the various retinal vascular layers; de Carlo et al. [264] to evaluate the ability of OCTA to clearly visualise CNV areas compared with FA; Spaide et al. [202] to establish a comprehensive guidance for obtaining the insight of how the OCTA imaging technique captures images of certain vascular layers of the eye described in a practical manner, and many more excellent comparative studies [5,265].

Nevertheless, the vast majority of the aforementioned studies have jointly demonstrated the potential of the OCTA imaging technique to generate outstanding retinal and choroidal vascular details that are far better and cannot be well distinguished by any other existing imaging techniques including the FA, IGA and OCT [7]. Figure B.4 provides a comprehensive comparison between different vascular images that demonstrate the appearance of abnormal retinal blood vessels as captured using various retinal vasculature imaging techniques specifically OCTA, OCT, FA and IGA, for an eye with CNV, a late stage of AMD disease. It can be easily appreciated that none of the aforementioned imaging techniques, namely the OCT, IGA and FA can provide images of choroidal and retinal blood vessels that demonstrate fine details about the CNV areas at a sufficient level that is at least comparable to the OCTA.

The utilities of OCTA imaging technique are extensively increasing across various domains, e.g.: on everyday clinical practice as well as for conducting research into understanding the pathophysiology of different retinal diseases [202]. These wide utilities of this innovative imaging modality are driven by several main factors. Among the most important ones include its capability to provide an advanced imaging of the various retinal and choroidal layers at micro vasculature levels in a noninvasive manner as well as unprecedented resolution and detail. Another important aspect is also the very short imaging time required by the OCTA to image the retinal and choroidal vascular information since it only takes a few seconds, while the FA and IGA imaging techniques typically require several minutes. Consequently, the OCTA can be particularly more desirable to be employed on a day-to-day clinical routine basis in such busy clinical circumstances.

Due to the nature of OCTA imaging technique, which does not require the injection of a contrast agent, i.e.: dye, as in the FA and IGA imaging techniques, and whereby the OCTA images are typically captured in just a matter of seconds, the scanning can be performed much more rapidly, specifically on every single patient visit to the clinic or the hospital [202]. Therefore, this can allow effective assessments of patients who need regular follow-up examinations to be performed and effective identification of those

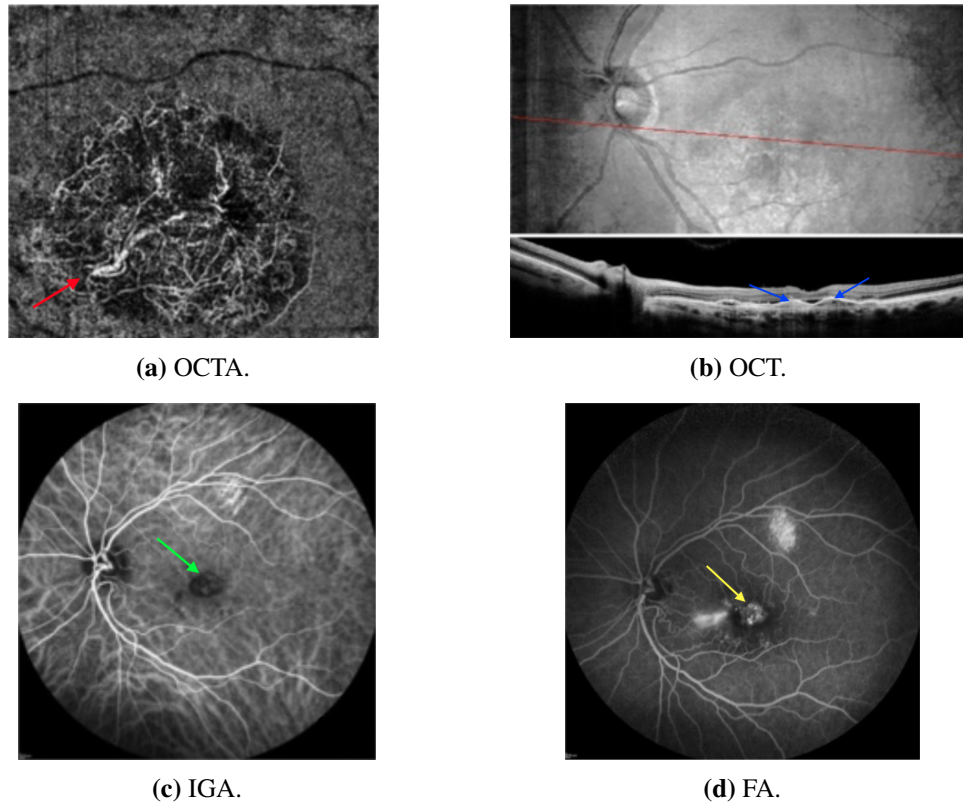


Figure B.4: Visualising images of abnormal choroidal and retinal blood vessels captured using various retinal vasculature imaging techniques specifically OCTA, OCT, FA and IGA, for an eye with CNV, a late stage of AMD disease [7]. (a) Shows an OCTA image with $6 \times 6 \text{ mm}$ field of view. In this OCTA image, the choroid layer with the capillaries i.e.: fine blood vessels known as choriocapillaris and the outer retina layer are displayed. It can be clearly seen that the abnormal blood vessels that forms a circular and irregular blood vessels network i.e.: the CNV indicated by a red arrow, in the middle of the image is surrounded by quiet homogenous choriocapillaris. These fine details of CNV have never been seen by any other retinal vasculature imaging techniques. (b) The top image illustrates a structural OCT image of the back of the eye and the red line corresponds to the location in which the 12 mm cross-sectional OCT image shown below was captured. This 12 mm cross-sectional OCT image demonstrates huge retinal layers detachments, disruptions and irregular contours that are major characteristics of identifying CNV areas in OCT images. The regions that are typically looked at for identifying abnormalities in cross-sectional OCT images for patients with AMD disease are approximately located around the areas indicated in blue arrows although in some situations the abnormalities may appear within and beyond these specified areas. (c) Displays an IGA image of the back of the eye and the area that is typically used to identify the abnormalities related to CNV is indicated with a green arrow. (d) Demonstrates an FA image of the back of the eye and the area that is typically used for detecting areas of abnormalities associated with CNV is indicated by a yellow arrow. It can be realised that none of the previous retinal vasculature imaging techniques namely the OCT, IGA and FA can visualise and image fine details about the CNV areas at a sufficiently similar level to the OCTA.

patients who are in extreme need of urgent treatment to be recognised in a suitable and timely manner [7]. Hence, these in turn can provide both a smooth and rapid streamlined clinical workflow to be achieved. The OCTA can also be an ideal imaging technique to those patients who cannot tolerate the FA or IGA imaging techniques due to the injection of intravenous dye. For instance, if the dye is not safe to use due to potential adverse reactions or certain contraindication circumstances such as the patient's pregnancy or kidney related problems [7, 200–202].

Although assessing retinal vascular changes related to vascular leakage or permeability may not be appreciable in the OCTA images compared to the FA and IGA images, the OCTA images are demonstrated to be the best among other angiogram images, e.g.: the OCT, FA and IGA images, as they allow the performance of precise delineation and size measurements of other serious retinal vascular pathologies, e.g.: CNV areas [7, 202]. Consequently, this can be particularly useful for identifying CNV areas in AMD disease where the exact localisation information of CNV areas is typically confirmed based on inferential judgments [7]. As the CNV typically perforates the Bruch's membrane, that is the innermost layer of the choroid layer, and grows into the subretinal layers, the precise localisation information of CNV areas may not be accurate with the FA or IGA imaging techniques as both techniques are not depth resolved [7].

Due the limited ability of structural en face OCT images to provide a reliable visualisation about the branching of CNV patterns, as the OCT imaging technique cannot distinguish blood flow and the cross-sectional OCT images can only provide details about retinal and choroidal thickening, there were no agreed-on criteria strictly based on using OCT imaging technique for identifying CNV areas [264]. To mitigate this limitation, the findings from the OCT data are typically used in combination with findings from other imaging techniques, e.g.: the FA to diagnose and identify CNV areas definitively [264, 266–268].]. The FA imaging technique is more ideal for visualising the blood vessels in the retina layer while the IGA imaging technique is typically utilised for visualising the choroid layer [7].

Nonetheless, the OCTA imaging technique can non-invasively visualise the various vasculatures that appear in retinal and the choroidal layers including other vasculatures that may appear in specific ocular tissue layers at a micro level. Consequently, these capabilities can eliminate the need of relying on conventional invasive imaging techniques, e.g.: the FA and IGA [264]. Hence, providing a more convenient, safe and effective imaging environment for evaluating and imaging various ocular tissue layers

as they can be imaged and evaluated by utilising only a single imaging instrument, i.e.: the OCTA imaging technique.

Despite the capacity of the OCTA imaging technique to provide useful information about retinal and choroidal vasculature as well as to deliver numerous advances as previously mentioned over other angiography gold standard imaging techniques, e.g.: the FA, IGA and OCT, it is necessary to understand its various limitations. An example of these limitations includes the limited field of view, i.e.: the limited imaging size of the ocular tissue area that will be visualised. Another obvious limitation is the incapability to visualise vascular leakage or permeability, which can be considered as both an advantage and a disadvantage [7, 269]. This is because the patterns of dye leakage as in the conventional imaging techniques, e.g.: the FA, IGA, are typically used as a clinical indication of vascular pathologies or anatomical anomalies, e.g.: vascular permeability [7, 197]. However, the dye leakage can obscure visualising essential vascular structures including other serious retinal vascular pathologies, e.g.: CNV areas in AMD disease [7, 197, 269].

Like most imaging techniques that employ a beam of light in the scanning procedure, the OCTA imaging technique has an increased risk of potential image artifacts, i.e.: noise such as uneven illumination [222, 231]. In addition to the unstable illumination issue with the OCTA images, any blinks or movements of the eye during the imaging procedure can also pose additional possible image artifacts that would make visually interpreting and understanding the OCTA images more challenging [7, 222, 269]. This is because the OCTA images are typically evaluated and projected in depth to view en face two dimensional OCTA images from certain retinal and choroidal depth level slabs or layers that have significantly higher contrast than structural en face OCT images. Hence, any motion due to the movements of the patient's eye or head can generate shearing deformations or gaps defects, manifest as bright strips or horizontal and vertical bright lines in the OCTA images [22, 202, 222].

The movements of the human eye are not only affected by action of the extraocular muscles i.e.: muscles that control movement of the eye, but also by movements of other human parts including the head and neck or even the whole body [202]. The texture of OCTA images can also contain some slight variations caused by changes in orientation, a relatively common issue with OCTA images [25, 27, 202, 222]. Although the subjects' eyes are not purposefully rotated, there may be some orientation changes to the texture of OCTA images when orbiting around the ocular tissue area of interest that is being scanned, e.g.: near the macula or fovea region [27]. Consequently, the

texture of OCTA images generated from various patients may not have a dominant orientation.

Despite the aforementioned limitations of the OCTA imaging technique, the outstanding advantages and advances provided by this innovative imaging modality should not be underestimated. Especially those driven by its outstanding features, like the noninvasive nature, the ability to obtain volumetric data that can be automatically projected and segmented to view specific retinal and choroidal depth level slabs or layers, the utility of motion contrast technique instead of the injection of intravenous dye, the extremely fast scanning ability as the scanning can be accomplished in just the course of seconds, the capacity to allow precise delineation, localisation information and size measurements of serious retinal vascular pathologies, e.g.: CNV areas and the capability to clearly visualise both the retinal and choroidal micro vasculature blood flow information [7]. An additional three certainly attention-grabbing aspects of the OCTA imaging technique are that it is reasonably inexpensive, accessible to approximately everybody and does not require skilled personnel, i.e.: trained photographers and interpreters to perform the imaging and the image interpretations as in the dye-based imaging techniques, e.g.: the FA and IGA [202,204].

Notably, the OCTA imaging technique is yet in its early stages of development, though, the rate of rapid improvements in the OCTA technology over the past few years has been phenomenal [202]. Moreover, there are numerous instances in which the OCTA imaging technique has shown to be equivalent or even far better than several conventional dye-based imaging techniques, e.g.: the FA and IGA, including the OCT imaging technique as evidenced by a wide variety of studies [5, 7, 197, 198, 202, 264, 265, 270]. Likewise, there are several occasions in which the OCTA imaging technique has proved to be a useful imaging tool for the detection and evaluation of various damaging ophthalmologic disorders, for example the AMD, DR, and glaucoma, among others [7].

The findings obtained by the OCTA imaging technique across various situations have also shown to be extraordinary as in some instances, the OCTA images have been demonstrated to distinguish certain vascular pathologies, e.g.: CNV areas that cannot even be clearly seen on the FA images [7, 202]. The OCTA imaging technique has revealed great promise by visualising pathologies affecting the choroid and the retina of the eye, for both to clinical utility and to perhaps improve the understanding of the pathogenesis and evolution of different retinal diseases, e.g.: the AMD [269].

None of the previously mentioned conventional imaging modalities, e.g.: the OCT,

FA and IGA, can provide alike capability nor can now be used in place of the OCTA imaging technique. Despite the aforementioned limitations associated with the OCTA imaging technique, it is already emerging as a useful, if not indispensable ophthalmic vasculature imaging modality especially appropriate for use in evaluating patients with AMD disease [18]. These matters specifically indicate the profound necessity and importance for the OCTA imaging technique to be exploited across various research and clinical disciplines to gain more insight into the pathophysiology of various ocular diseases and to accelerate its wide utility in daily clinical practice given the great imaging capabilities that it can deliver. Table B.1 provides a comprehensive comparison that summarises the key differences between the characteristics of the aforementioned imaging techniques, namely OCTA, OCT, FA and IGA.

Table B.1: A comprehensive summary of the differences between the key characteristics of the OCTA, OCT, FA and IGA imaging techniques.

Major characteristics	Ocular Vascular Imaging Modalities			
	OCTA	OCT	FA	IGA
Invasive imaging procedure	No	No	Yes	Yes
Require contrast dye injection	No	No	Yes	Yes
Laborious to perform	No	No	Yes	Yes
Potential allergic reactions	No	No	Yes	Yes
Require skilled photographers	No	No	Yes	Yes
Visualising individual vascular layers	Yes	No	No	No
Imaging at capillaries level	Yes	No	No	No
Wide imaging field of view	No	No	Yes	Yes
Visualise vascular permeability	No	No	Yes	Yes
Vascular detail obscured by dye leakage	No	No	Yes	Yes